

ASTRONOMICAL INSTITUTE
SLOVAK ACADEMY OF SCIENCES

SPECIAL ISSUE
**SPECTRAL LINE SHAPES IN
ASTROPHYSICS AND RELATED
TOPICS**

Based on lectures presented at
12th SERBIAN CONFERENCE ON SPECTRAL LINE SHAPES
IN ASTROPHYSICS (12th SCSLSA)

Vrdnik, Serbia, June 3-7, 2019

CONTRIBUTIONS
OF THE ASTRONOMICAL OBSERVATORY
SKALNATÉ PLESO

• VOLUME I •

Number 1



January 2020

Editorial Board

Editor-in-Chief

Augustín Skopal, *Tatranská Lomnica, The Slovak Republic*

Managing Editor

Richard Komžík, *Tatranská Lomnica, The Slovak Republic*

Editors

Drahomír Chochol, *Tatranská Lomnica, The Slovak Republic*

Július Koza, *Tatranská Lomnica, The Slovak Republic*

Aleš Kučera, *Tatranská Lomnica, The Slovak Republic*

Luboš Neslušan, *Tatranská Lomnica, The Slovak Republic*

Vladimír Porubčan, *Bratislava, The Slovak Republic*

Theodor Pribulla, *Tatranská Lomnica, The Slovak Republic*

Advisory Board

Bernhard Fleck, *Greenbelt, USA*

Arnold Hanslmeier, *Graz, Austria*

Marian Karlický, *Ondřejov, The Czech Republic*

Tanya Ryabchikova, *Moscow, Russia*

Giovanni B. Valsecchi, *Rome, Italy*

Jan Vondrák, *Prague, The Czech Republic*

©

Astronomical Institute of the Slovak Academy of Sciences
2020

ISSN: 1336-0337 (on-line version)

CODEN: CAOPF8

Editorial Office: Astronomical Institute of the Slovak Academy of Sciences
SK - 059 60 Tatranská Lomnica, The Slovak Republic

CONTENTS

List of participants	9
Preface	13
 Session A: ATOMIC PARAMETERS AND DATABASES	
A01: C.G.Parigger: Laser-plasma and stellar astrophysics spectroscopy	15
A02: P.A.M. van Hoof, G.C. Van de Steene, F. Guzmán, M. Dehghanian, M. Chatzikos and G.J. Ferland: Current and future development of the photoionization code Cloudy	32
A03: D. Jevremović, V.A. Srećković, B.P. Marinković and V. Vujčić: Databases for collisional and radiative processes in small molecules needed for spectroscopy use in astrophysics	44
A04: V.A. Srećković, Lj.M. Ignjatović, M.S. Dimitrijević, N.N. Bezuglov and A.N. Klyucharev: The collisional atomic processes in geocosmical plasmas: data needed for spectroscopy	55
A05: M.S. Dimitrijević, V.A. Srećković, A.A. Zalam, K. Miculis, D.K. Efimov, N.N. Bezuglov and A.N. Klyucharev: Autoionization widths of cold Rydberg atomic complexes	66
A06: N. Alwadie, A. Almodlej, N. Ben Nessib and M.S. Dimitrijević: Atomic structure of the carbon like ion Ca XV	86
A07: A. Murmantsev, A. Veklich, V. Boretskij and K. Lopatko: Hydrogen Balmer spectral lines in spectroscopy of underwater electric spark discharge plasma	96
 Session B: BROADENING EFFECTS IN SPECTRAL LINE SHAPES	
B01: J. Rosato, I. Hannachi and R. Stamm: Hydrogen Stark broadening calculations in white dwarf atmosphere conditions	105
B02: M. Christova, M.S. Dimitrijević and S. Sahal-Bréchet: Stark broadening of B I spectral lines within $2s^22p - 2s^2nd$ Spectral Series	111
B03: M.S. Dimitrijević: Stark broadening data for spectral lines of rare-earth elements: Example of Tb II and Tb IV	122
B04: R. Hamdi, N. Ben Nessib, S. Sahal-Bréchet and M.S. Dimitrijević: On the semiclassical perturbation Stark shifts of Ar II spectral lines	128
B05: A. Chougule, N. Przybilla, M.S. Dimitrijević and V. Schaffenroth: The impact of improved Stark-broadening widths on the modeling of double-ionized chromium lines in hot stars	139
B06: A. Almodlej, N. Alwadie, N. Ben Nessib and M.S. Dimitrijević: On the Stark broadening of some Cr II spectral lines in plasma	147

B07: R. Aloui, H. Elabidi and S. Sahal-Bréchet: Stark broadening and atomic data for Ar XVI	154
B08: Z. Majlinger, M.S. Dimitrijević and V.A. Srećković: Regularities and systematic trends on Lu III Stark widths	164
B09: V.A. Srećković, M.S. Dimitrijević and Lj.M. Ignjatović: The influence of collisional-ionization and recombination processes on spectral line shapes in stellar atmospheres and in the hydrogen clouds in broad-line region of AGNs	171
B10: M.S. Dimitrijević, V.A. Srećković and Lj.M. Ignjatović: Influence of the (n-n’)-mixing processes on the optical properties of the hydrogen clouds in the broad-line region of AGNs	179
B11: Lj.M. Ignjatović, V.A. Srećković and M.S. Dimitrijević: Photoionization of the alkali molecular ions in geo-cosmical plasmas	187

Session C: SPECTRAL LINE PHENOMENA IN STARS AND EXTRAGALACTIC OBJECTS

C01: G. Peach, S. Yurchenko, K. Chubb, I. Baraffe, M. Phillips and P. Tremblin: The resonance lines of sodium and potassium in brown dwarf spectra	193
C02: A.F. Zakharov, P. Jovanović, D. Borka and V. Borka Jovanović: Observational tests of general relativity and alternative theories of gravity with Galactic Center observations using current and future large observational facilities	203
C03: P. Jovanović, V. Borka Jovanović, D. Borka and L.Č. Popović: Possible observational signatures of supermassive black hole binaries in their Fe Kα line profiles	219
C04: L. Chmyreva and G. Beskin: On the possible connection between galactic featureless-spectrum sources and stellar-mass black holes	235
C05: P. Marziani, E. Bon, N. Bon, M.L. Martinez-Aldama, G.M. Stirpe, M. D’Onofrio, A. del Olmo, C.A. Negrete and D. Dultzin: Quasar emission lines as virial luminosity estimators	244
C06: S.N. Dodonov and A. Grokhovskaya: The density maps of the HS47.5-22 field	257
C07: M. Berton, I. Björklund, A. Lähteenmäki, E. Congiu, E. Järvelä, G. Terreran and G. La Mura: Line shapes in narrow-line Seyfert 1 galaxies: a tracer of physical properties?	270
C08: S. Panda, P. Marziani and B. Czerny: Main trends of the quasar main sequence - effect of viewing angle	293
C09: D. Kozlova, A.V. Moiseev and A.A. Smirnova: Extended ionized-gas structures in Seyfert 2 galaxy Mrk 78	309
C10: M.W. Ochmann, W. Kollatschny and M. Zetzl: Spectral changes and BLR kinematics of eruptive changing-look AGN	318

C11: E. Malygin, R. Uklein, E. Shablovinskaya, A. Grokhovskaya and A. Perepelitsyn: Medium-band photometric reverberation mapping of AGNs at $0.1 < z < 0.8$. Techniques and sample	328
C12: E. Shablovinskaya and V. Afanasiev: Intraday variability of the polarization vector in AGN S5 0716+714	341
C13: I. Jankov and D. Ilić: Narrow lines correlations in an SDSS sample of type 1 quasars	350
C14: M.A. Probst and W. Kollatschny: Preliminary Spectral Analysis of the NLS1 Galaxy WPVS48	360

The Contributions of the Astronomical Observatory Skalnaté Pleso
are available in a full version
in the frame of ADS Abstract Service
and can be downloaded in a usual way from the URL address:

‘http://adsabs.harvard.edu/article_service.html’

as well as from the web-site of
the Astronomical Institute of the Slovak Academy of Sciences
on the URL address:

‘<http://www.astro.sk/caosp/>’

The journal is covered/indexed by:

Thomson Reuters services (ISI)

Science Citation Index Expanded (also known as SciSearch[®])
Journal Citation Reports/Science Edition

SCOPUS

SPECIAL ISSUE
**SPECTRAL LINE SHAPES IN
ASTROPHYSICS AND RELATED TOPICS**

Edited by

Dragana Ilić, Anđelka Kovačević,
Luka Č. Popović, Evgeny Stambulchik

Based on lectures presented at
**12th SERBIAN CONFERENCE
ON SPECTRAL LINE SHAPES IN ASTROPHYSICS**

June 3 – 7, 2019, Vrdnik, Serbia

Faculty of Mathematics, University of Belgrade

<http://www.scslsa.matf.bg.ac.rs/>

Scientific Organizing Committee Local Organizing Committee

Dragana Ilić, co-chair (Serbia)

Evgeny Stambulchik, co-chair (Israel)

Victor Afanasiev (Russia)

Robert Beuc (Croatia)

Milan S. Dimitrijević (Serbia)

Darko Jevremović (Serbia)

Wolfram Kollatschny (Germany)

Evangelia Lyratzi (Greece)

Evencio Mediavilla (Spain)

Gillian Peach (United Kingdom)

Luka Č. Popović (Serbia)

Jagoš Purić (Serbia)

Sylvie Sahal-Bréchet (France)

Vladimir Srećković (Serbia)

Jack Sulentic (Spain)

Roland Stamm (France)

Anđelka Kovačević, chair

Saša Simić, secretary

Edi Bon

Nataša Bon

Maša Lakićević

Slađana Marčeta Mandić

Nenad Milovanović

Nemanja Rakić

Marko Stalevski



The participants of 12th SCSLSA in front of the Conference venue

LIST OF PARTICIPANTS

Afanasiev, Victor L.	Special Astrophysical Observatory of Russian Academy of Science, Russia
Aloui, Rihab	Ecole National Supérieure d'ingénieurs de Tunis, University of Tunis, Tunisia
Antoniou, Antonios	National and Kapodistrian University of Athens, Faculty of Physics, Department of Astrophysics, Astronomy and Mechanics, Greece
Ben Nessib, Nabil	Department of Physics and Astronomy, College of Sciences, King Saud University, Saudi Arabia
Berton, Marco	Finnish Centre for Astronomy with ESO, Finland
Bianchi, Stefano	University of Roma 3, Italy
Bon, Edi	Astronomical Observatory, Belgrade, Serbia
Bon, Nataša	Astronomical Observatory, Belgrade, Serbia
Borka, Duško	Atomic Physics Laboratory (040), Vinča Institute of Nuclear Sciences, Serbia
Borka Jovanović, Vesna	Atomic Physics Laboratory (040), Vinča Institute of Nuclear Sciences, Serbia
Chen, Sina	University of Padova, Italy
Chmyreva Elizaveta	Special Astrophysical Observatory of Russian Academy of Science, Russia
Chougule, Abhishek	Institute for Astro- and Particle Physics – Universität Innsbruck, Austria
Ciroi, Stefano	Department of Physics and Astronomy – Padova University, Italy
Czerny, Bozena	Center for Theoretical Physics, Poland
De Rosa, Gisella	Space Telescope Science Institute, USA
Dimitrijević, Milan S.	Astronomical Observatory, Belgrade, Serbia
Dodonov, Serguei	Special Astrophysical Observatory of Russian Academy of Science, Russia
Du, Pu	Institute of High Energy Physics, Chinese Academy of Sciences, China
Grokhovskaya, Aleksandra	Special Astrophysical Observatory of Russian Academy of Science, Russia
Hannachi, Ibtissem	Aix-Marseille Université, CNRS, PIIM UMR 7345, 13397 Marseille Cedex 20, France
Ilić, Dragana	Department of Astronomy, Faculty of Mathematics, University of Belgrade, Serbia
Jankov, Isidora	Department of Physics, University of Novi Sad, Serbia
Jevremović, Darko	Astronomical Observatory, Belgrade, Serbia
Jovanović, Predrag	Astronomical Observatory, Belgrade, Serbia

Kollatschny, Wolfram	Institute for Astrophysics, Göttingen, Germany
Koubiti, Mohammed	Aix-Marseille Université, France
Kovačević, Andjelka	Department of Astronomy, Faculty of Mathematics, University of Belgrade, Serbia
Kovačević Dojčinović, Jelena	Astronomical Observatory, Belgrade, Serbia
Kozlova, Daria	Ural Federal University, Institute of Natural Sciences and Mathematics; Special Astrophysical Observatory of Russian Academy of Science, Russia
Lakičević, Maša	Astronomical Observatory, Belgrade, Serbia
Lamy, Hervé	Royal Belgian Institute for Space Aeronomy, Belgium
Lyratzi, Evangelia	National and Kapodistrian University of Athens, Fac- ulty of Physics, Department of Astrophysics, Astron- omy and Mechanics, Greece
Majlinger, Zlatko	Astronomical Observatory, Belgrade, Serbia
Malović, Miodrag	Innovation Center of the Faculty of Technology and Metallurgy, University of Belgrade, Serbia
Malygin, Eugene	Kazan Federal University, Russia
Marčeta Mandić, Slađana	Department of Astronomy, Faculty of Mathematics, University of Belgrade, Serbia
Marziani, Paola	National Institute for Astrophysics (INAF), Italy
Meftah, Mohammed	Faculty of mathematics and matter sciences, Univer- sity Kasdi merbah, Ouargla, 30000, Algeria
Tayeb	Astronomical Observatory, Belgrade, Serbia
Milovanović, Nenad	European Southern Observatory, Headquarters, Ger- many
Møller, Palle	
Murmantsev, Aleksandr	Faculty of Radio Physics, Electronics and Computer Systems, Taras Shevchenko National University of Kyiv, Ukraine
Nagli, Lev	Ariel University, Israel
Nina, Aleksandra	Institute of Physics Belgrade, University of Belgrade, Serbia
Ochmann, Martin	Institute of Astrophysics, University of Göttingen, Germany
Panda, Swayamtrupta	Center for Theoretical Physics - PAS, Poland
Parigger, Christian	University of Tennessee Space Institute, USA
Peach, Gillian	University College London, UK
Popović, Luka Č.	Astronomical Observatory, Belgrade, Serbia
Probst, Malte Andrés	Institute of Astrophysics, University of Göttingen, Germany
Rakić, Nemanja	Faculty of Natural Sciences and Mathematics, Univer- sity of Banjaluka, Republic of Srpska, B&H
Rosato, Joel	Aix-Marseille University, France

Sahal-Bréchet, Sylvie	Paris Observatory, PSL LERMA, France
Savić, Đorđe V.	Astronomical Observatory, Belgrade, Serbia
Shablovinskaya, Elena	Special Astrophysical Observatory of Russian Academy of Science, Russia
Simić, Saša	Faculty of Sciences, Department of Physics, Kragujevac, Serbia
Spasojević, Djordje	Faculty of Physics, University of Belgrade, Serbia
Srećković, Vladimir A.	Institute of Physics, Belgrade, Serbia
Stalevski, Marko	Astronomical observatory, Belgrade, Serbia
Stambulchik, Evgeny	Weizmann Institute of Science, Israel
Stamm, Roland	Aix Marseille University, France
Stathopoulos, Dimitrios	National and Kapodistrian University of Athens, Faculty of Physics, Department of Astrophysics, Astronomy and Mechanics, Greece
Taylor, Joanna	Space Telescope Science Institute, USA
Touati, Kamel Ahmed	Lycée Professionnel, France
Tzimeas, Dimitrios	National and Kapodistrian University of Athens, Greece
Uklein, Roman	Special Astrophysical Observatory of Russian Academy of Science, Russia
van Hoof, Peter	Royal Observatory of Belgium
Vujčić, Veljko	Astronomical Observatory, Belgrade, Serbia
Vukčević, Miroslava	Astronomical Observatory, Belgrade, Serbia
Zakharov, Alexander	Institute of Theoretical and Experimental Physics

PREFACE

This Special Issue on "Spectral Line Shapes in Astrophysics and Related Topics" contains papers which were presented at the "12th Serbian Conference on Spectral Line Shapes in Astrophysics – 12th SCSLSA". The conference took place in the village called Vrdnik at the foothill of the scenic Fruška Gora mountain in the northern Serbia from June 3 to June 7, 2019. The uniqueness of this conference is in bringing together astronomers and physicists from Serbia and elsewhere to review the present stage of research, with the aim of improving our knowledge in this field, and to better understand the significance of emission/absorption lines for future astrophysical investigations. The program was divided into several sessions dedicated to spectral lines in stars and extragalactic objects, and spectral lines in laboratory and general plasma. One Special session "Broad lines in AGNs: The physics of emission gas in the vicinity of super-massive black hole" was organized in memory of the life and work of dr Alla Ivanovna Shapovalova (who sadly passed away in January 2019).

The 12th SCSLSA conference was attended by 70 participants from 20 countries. They presented 19 invited talks, 33 progress reports and 28 posters. In this Special Issue there are 32 papers published which are divided into three large sections: I. Atomic parameters and databases; II. Broadening effects in spectral line shapes, III. Spectral line phenomena in stars and extragalactic objects.

The organizers are indebted to the Ministry of Education, Science and Technological Development, as well as to "Telekom Srbija" for general support. Moreover, we thank the administration and financial departments of the Faculty of Mathematics for enormous support and help, as well as to the co-organizers Astronomical Observatory Belgrade and Faculty of Science, University of Kragujevac. We thank the members of the SOC and LOC for their help in preparing and running this conference. Finally, we owe an enormous thank you to all the referees for their hard work in peer-reviewing all contributions. Note here that all materials (programme, talks, presentations, photos, etc.) from this and previous SCSLSAs are available at <http://servo.aob.rs/eeditons/SCSLSA.php> through Serbian Virtual Observatory (<http://servo.aob.rs>).

D. Ilić, A. Kovačević, L. Č. Popović & E. Stambulchik
the editors

Laser-plasma and stellar astrophysics spectroscopy

Christian G. Parigger

*Physics and Astronomy Department, University of Tennessee,
University of Tennessee Space Institute, Center for Laser Applications,
411 B.H. Goethert Pkwy, Tullahoma, TN 37388, USA
(E-mail: cparigge@tennessee.edu)*

Received: June 6, 2019; Accepted: July 22, 2019

Abstract. This work examines time-resolved spectroscopy of the Balmer series lines in laboratory settings and applies results for interpretation of spectra from astrophysical objects. White dwarf stars reveal a variety of atomic or molecular line shapes in absorption depending on the age of these cooling stars. Laboratory investigations show emission profiles that are correlated with astrophysical records. For the hydrogen beta line, $H\beta$, and the hydrogen delta line, $H\delta$, of the Balmer series, line width and peak separation are indicators of electron density. In addition, widths of the hydrogen alpha line, $H\alpha$, and hydrogen gamma line, $H\gamma$, can be utilized along with $H\alpha$ shifts and $H\beta$ dipshifts. Of interest are experiments and analysis of laser- and astrophysical white-dwarf-plasma spectral line shapes, especially comparisons of transient laser-plasma-with gravitational white-dwarf- redshifts. Current and future research aspects include modeling of white-dwarf atmospheres for explanation of the very details of the astrophysical line shapes.

Key words: atomic and molecular spectroscopy – time-resolved spectroscopy – laser plasma – laser-induced optical breakdown – stellar astrophysics spectra – white dwarf stars – hydrogen

1. Introduction

Recorded emission spectra of astrophysical objects usually reveal absorption lines and bands. Analysis of the spectra allows one to make inferences about the star under investigation. In the visible region of the electromagnetic spectrum, $H\beta$ is of primary interest in the characterization of white dwarf (WD) stars. The temperature of the closest WD to earth, Sirius B (α CMa B), is of the order of 30 kK. Sirius B accompanies the brightest star Sirius A as seen from earth. However, instead of hydrogen absorption spectra, molecular carbon Swan absorption spectra are recorded for cooler WD's at a temperature of the order of 8 kK, viz. Procyon B (α CMi B), companion of the fifth brightest star seen from earth, namely, Procyon A. In the laboratory, hydrogen Balmer series emission spectra are recorded, including determination of temperature using the line-to-continuum ratio. The mass of WD stars is typically of the order of the mass of

the sun (M_{\odot}), but the WD radius is about the size of the earth, or 1/100 times that of the sun ($0.01 R_{\odot}$).

This work communicates experiments of laser plasma in hydrogen, gaseous mixtures of hydrogen and nitrogen, and air at standard ambient temperature and pressure. Ultra-pure hydrogen and gaseous mixtures experiments employ a laboratory cell for measurement of the Balmer series lines. Diatomic molecular recombination spectra are also recorded in laser-plasma of gaseous mixtures and laser-ablation plasma.

In recent hydrogen experiments, measurements address the first four Balmer series hydrogen lines – early in the plasma decay, neutral and ionized nitrogen lines are identified and appear first as the plasma cools. Plasma characteristics for time delays up to $0.275 \mu\text{s}$ were previously discussed albeit for exclusively hydrogen gas at 0.75 atm and ambient temperature (Parigger *et al.*, 2018). In this work, optical breakdown plasma is generated in a 1:1 hydrogen:nitrogen mixture at ambient temperature and 0.27-atm pressure (Parigger, 2019). Plasma diagnosis is applied for time delays in the range of $0.25 \mu\text{s}$ to $3.25 \mu\text{s}$. Nitrogen contributes to the breakdown plasma seven times more electrons than hydrogen in cases of full ionization. Time-resolved spectroscopy records emitted radiation with spatial radiation along the slit height for the $H\alpha$, $H\beta$, $H\gamma$, and $H\delta$ lines.

Laser-plasma diagnosis and characterization enjoy recent and significant interests in part due to needs for determination of chemical composition of materials. Specifically, laser-induced breakdown spectroscopy (LIBS, Miziolek *et al.*, 2018; Singh & Thakur, 2019) is preferred over spark-induced breakdown spectroscopy for chemical analysis. In stellar astrophysics however, hydrogen spectroscopy is essential for determination of atmospheres of stars, and related, for determination of the atmospheric composition of planets or exo-planets with established molecular data-bases (Tennyson & Yurchenko, 2012).

Typically, the micro-plasma is initiated with of the order of 10-nanosecond laser radiation and is recorded with time-resolved plasma spectroscopy (Kunze, 2009) for time delays up to a few μs for the recording of atomic hydrogen spectra, and for time delays of a few 10's of μs for molecular spectra. The accuracy of the $H\beta$ line is better than that of the $H\alpha$ line (Wiese, 1965) and recommendations for plasma spectroscopy include addition of trace amounts of hydrogen to accomplish accurate diagnosis (Wiese, 1965). Challenges in comparisons of laboratory and astrophysical plasma-spectra have been reviewed recently (Halenka *et al.*, 2015), i.e., comparisons of $H\beta$ line shapes of micro-plasma recorded with time-resolved emission spectroscopy and of $H\beta$ line shapes in astrophysical white dwarf macro-plasma absorption spectra that are measured continuously at various observatories.

2. Experimental details

Laboratory laser-plasma measurements employ a pulsed, Q-switched, Nd:YAG laser device (Q-Smart 850 Quantel laser, USA) operated at a pulse-width of 6 ns and a pulse energy of 850 mJ at the wavelength of 1064 nm. Laser-induced optical breakdown is generated by focusing 150 mJ per pulse of its fundamental radiation to achieve of the order of 1 TW/cm^2 in a cell containing a 1:1 mixture of hydrogen and nitrogen, introduced at a pressure of 0.135 atm each after establishing a nominal mercury-diffusion-pump vacuum in the cell of the order 10^{-5} mbar. A crossed CzernyTurner spectrometer (Jobin Yvon 0.64 m triple spectrometer, France) of 0.64-m focal length disperses the emission spectra. The pulsed radiation is focused into the cell with the beam propagating from the top and parallel to the vertical $100 \mu\text{m}$ spectrometer slit (Parigger, 2019). Further details of the experimental arrangement that is similar to the ultra-pure hydrogen experiments were communicated previously (Parigger *et al.*, 2014, 2018, 2019a,b).

The spectral resolution amounts to 0.1 nm for the selected 1200 g mm^{-1} holographic grating following corrections of the wavelength variation along the slit direction. Of the order of 24-nm spectral coverage for the 1024 pixels along the wavelength-dimension, the 0.1-nm resolution corresponds to an instrument-prompt width of on-average 4.25 pixels. Conversely, grouping four pixels along the slit dimensions corresponds to a spatial resolution of $54.4 \mu\text{m}$ as the pixel area amounts to $13.6 \mu\text{m} \times 13.6 \mu\text{m}$.

For 13 selected time delays from $0.25 \mu\text{s}$ to $3.25 \mu\text{s}$ and $0.025 \mu\text{s}$ gate-widths, micro-plasma data are captured. Of interest are the peak-separation and width of $\text{H}\delta$ and width of $\text{H}\gamma$ for electron densities in the range of 0.1 to $1 \times 10^{17} \text{ cm}^{-3}$, and comparisons with $\text{H}\beta$ and $\text{H}\alpha$ diagnostics. Integral inversion interrogates the lateral spatial distribution of the recorded line-of-sight plasma expansion.

3. Results

3.1. Line-of-sight measurements

A total of 52 two-dimensional data sets are recorded for the four $\text{H}\alpha$, $\text{H}\beta$, $\text{H}\gamma$, and $\text{H}\delta$ Balmer series lines, including several nitrogen and ionized nitrogen lines that occur especially for time delays in the range of 0.25 - $0.75 \mu\text{s}$ following plasma initiation. Fig. 1 portrays spectral radiance, using grey-scale representation, of individually scaled maps of the four hydrogen lines for a time delay of $3 \mu\text{s}$.

Features of Fig. 1 include expected Stark-width behavior (Holtsmark, 1919; Greene, 1961; Griem, 1974; Oks, 2017): (i) full-widths at half maximum increase from the $\text{H}\alpha$ line to the $\text{H}\delta$ line; (ii) the maximum signals decrease from $\text{H}\alpha$ to $\text{H}\delta$; (iii) peak-separation of the $\text{H}\beta$ (Ivković *et al.*, 2015) and $\text{H}\delta$ lines, and $\text{H}\beta$ dipshifts (Halenka *et al.*, 1989; Mijatović *et al.*, 1991). The occurrence of dips for

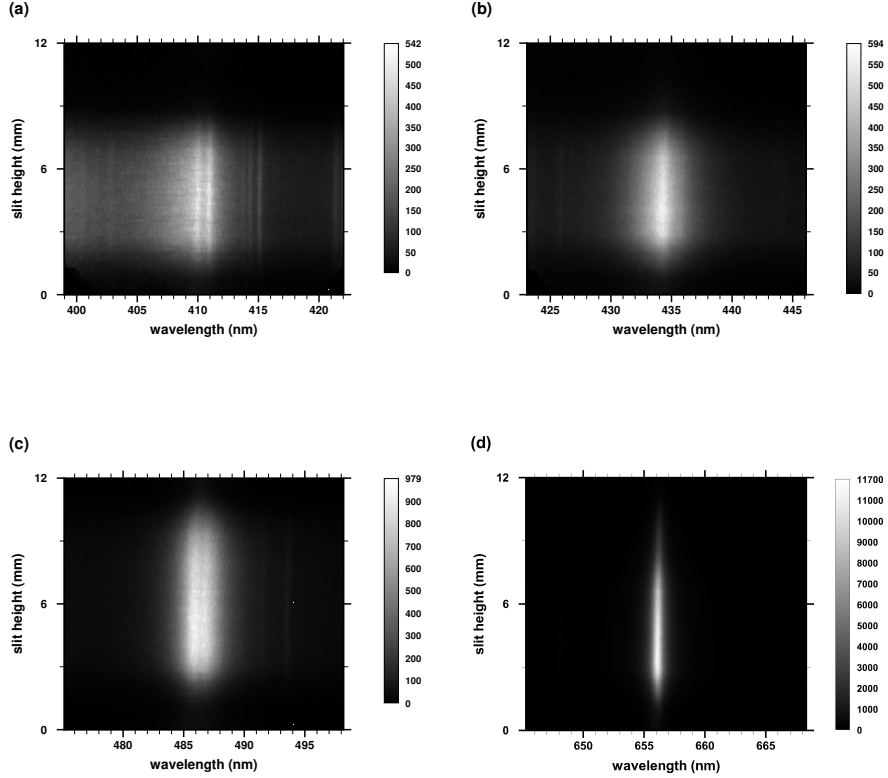


Figure 1. Balmer series hydrogen lines versus wavelength at $3\text{-}\mu\text{s}$ time delay, $0.025\text{-}\mu\text{s}$ gate. (a) $\text{H}\delta$, (b) $\text{H}\gamma$, (c) $\text{H}\beta$, and (d) $\text{H}\alpha$.

$\text{H}\beta$ and $\text{H}\delta$ are not due to self-absorption for electron densities of the order of 10^{17}cm^{-3} – predictions of Stark effects on $\text{H}\beta$ and $\text{H}\delta$ with associated absence of line-center components are part of the reason for E. Schrödinger (Schrödinger, 1926) receiving the Nobel Prize, shared with P. Dirac (Physics Nobel Prize, 1933).

In the images, detector dark-counts or background contributions are subtracted, sensitivity calibrations by reference to standard lamps are applied, and linear wavelength calibration is performed with penray lamps and by using calibrated spectrometer dials. The image of the spectrometer slit usually is slightly curved near the edges, consequently, wavelength calibrations are performed for each spectrum recorded along the slit. For the experiments reported here, four vertical pixels are combined to increase sensitivity requiring 256 individual wave-

length calibrations for each of four spectrometer positions. The 256 recorded, wavelength calibrated Balmer series spectra are slightly wavelength-shifted and interpolated for display of the data versus slit height and wavelength position. In other words, the displayed maps are corrected for the spectrometer-related wavelength variations along the slit height. Consequently, the maps in Fig. 1 are primed for analysis that employs integral inversion of the recorded line-of-sight data. However, data are first analyzed to determine variations and averages along the slit.

Analysis of the laboratory emission spectra utilizes established empirical formulae for H α and H β (Parigger *et al.*, 2018). For H α , the width, $\Delta\lambda_\alpha$, and shift, $\delta\lambda_\alpha$, are indicators for electron density,

$$\Delta\lambda_\alpha[\text{nm}] = 1.3 \left(\frac{N_e[\text{cm}^{-3}]}{10^{17}} \right)^{0.64 \pm 0.03}, \quad (1)$$

$$\delta\lambda_\alpha[\text{nm}] = 0.055 \left(\frac{N_e[\text{cm}^{-3}]}{10^{17}} \right)^{0.97 \pm 0.03}. \quad (2)$$

Analysis of H β offers three indicators of electron density: Width, $\Delta\lambda_\beta$, peak separation, $\delta\lambda_{\beta\text{-ps}}$, and dip shift, $\delta\lambda_{\beta\text{-ds}}$,

$$\Delta\lambda_\beta[\text{nm}] = 4.5 \left(\frac{N_e[\text{cm}^{-3}]}{10^{17}} \right)^{0.71 \pm 0.03}, \quad (3)$$

$$\delta\lambda_{\beta\text{-ps}}[\text{nm}] = 1.3 \left(\frac{N_e[\text{cm}^{-3}]}{10^{17}} \right)^{0.61 \pm 0.03}, \quad (4)$$

$$\delta\lambda_{\beta\text{-ds}}[\text{nm}] = 0.14 \left(\frac{N_e[\text{cm}^{-3}]}{10^{17}} \right)^{0.67 \pm 0.03}. \quad (5)$$

The H β dipshift allows one to measure electron density (Parigger *et al.*, 2019a) up to the H β Inglis-Teller limit (Inglis & Teller, 1939) of $60 \times 10^{17} \text{cm}^{-3}$. However, H β is preferred in a variety of astrophysics data-reduction efforts for electron densities of the order of 10^{17}cm^{-3} .

3.2. H δ and H γ line profiles

The analysis of the H δ and H γ data rely on computer simulations (Gigosos *et al.*, 2003), and in this work, on published Stark tables (Griem, 1974) that only show electron-density data in the range of 0.1 to $1 \times 10^{17} \text{cm}^{-3}$ for a temperature of 20 kK. From the Stark tables, H δ and H γ line-profiles can be constructed for electron densities, N_e , of 0.1 and $1 \times 10^{17} \text{cm}^{-3}$. Subsequently, H δ and H γ full-width half maximum (FWHM) can be determined for plasma diagnosis, moreover, H δ invites the use of peak separation (PS) as a diagnostic tool.

From log-log fitting of H γ and H δ data in the range of 0.1 to $1 \times 10^{17} \text{ cm}^{-3}$, one obtains for H δ FWHM, $\Delta\lambda_\delta$,

$$\Delta\lambda_\delta[\text{nm}] = 10 \left(\frac{N_e[\text{cm}^{-3}]}{10^{17}} \right)^{0.67}, \quad (6)$$

and the H δ peak-separation, $\Delta\lambda_{\delta\text{-ps}}$, in the range of 0.1 to $1 \times 10^{17} \text{ cm}^{-3}$ amounts to

$$\Delta\lambda_{\delta\text{-ps}}[\text{nm}] = 2.0 \left(\frac{N_e[\text{cm}^{-3}]}{10^{17}} \right)^{0.62}. \quad (7)$$

The H δ line shows peak separations just like the H β line. From log-log fitting, one obtains for H γ FWHM, $\Delta\lambda_\gamma$,

$$\Delta\lambda_\gamma[\text{nm}] = 6.0 \left(\frac{N_e[\text{cm}^{-3}]}{10^{17}} \right)^{0.72}. \quad (8)$$

Analysis of laser-plasma details requires both spatial and temporal resolutions. However, the average of the spectra along the slit-dimension are investigated first.

Fig. 2 displays signatures of the first four members of the Balmer series. The spectra are averaged over 220 individual spectral lines, and are also averaged over 100 accumulated laser-plasma events. Considering an average over 22,000 spectra, and with the nominal square-root reduction in variance by a factor of 148, further filtering of the data is not necessary.

3.3. Abel-inverted spectral maps

The recorded line-of-sight data can be further processed using inverse integral transforms in order to examine the spatial distribution of the expanding plasma. Motivation derives from recorded shadow-graphs depicted in Fig. 3.

Abel-inverted, first four Balmer lines data reveal minima at the center of the plasma (maps not included here), for example, for a time delay of $1.5 \mu\text{s}$ – illustrated in a recent publication (Parigger, 2019). These minima are representative of plasma expansion phenomena following initiation of optical breakdown. One can identify peak separation of the H δ and H β lines, respectively. The H δ map indicates that the background is shaded towards the UV, and there appear to be contributions from the H ϵ line (at the low wavelength side in the maps) just like in the recorded maps displayed in Fig. 1. The H δ line shows a shallower dip for higher electron density in the range of 0.1 to $1 \times 10^{17} \text{ cm}^{-3}$. However, the H β peak separation indicates an electron density of $1.5 \times 10^{17} \text{ cm}^{-3}$.

The Abel-inverted, $3.25 \mu\text{s}$ time-delay data display reasonably smooth line shapes for all four Balmer series lines. The H δ peak separation can be easily demarcated, but the H β peak separation is difficult to extract. In other words, The H δ line provides both PS and FWHM diagnostics as the electron density

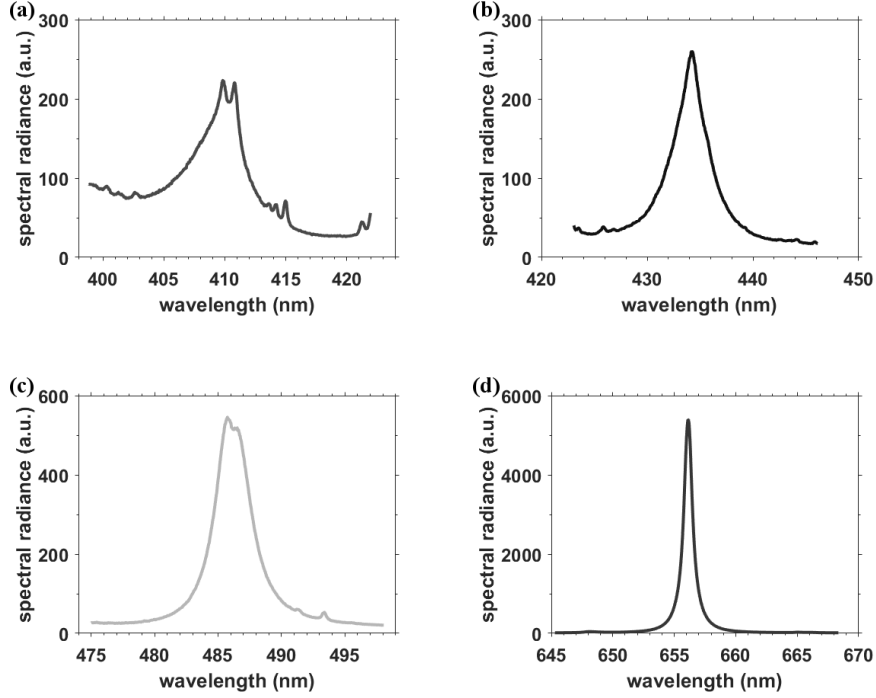


Figure 2. Average Balmer series hydrogen lines versus wavelength at $3\text{-}\mu\text{s}$ time delay, $0.025\text{-}\mu\text{s}$ gate. (a) $\text{H}\delta$, (b) $\text{H}\gamma$, (c) $\text{H}\beta$, and (d) $\text{H}\alpha$. The extra atomic lines, with magnitudes slightly larger than the background contributions, are due to nitrogen in the 1:1 hydrogen nitrogen mixture. In addition, the background contribution due to Bremsstrahlung radiation is larger for $\text{H}\delta$ than for $\text{H}\gamma$ and $\text{H}\beta$, with minute contributions to $\text{H}\alpha$.

decreases in the range of 0.1 to $1 \times 10^{17} \text{ cm}^{-3}$. A 1-nm peak separation at a time delay of $3.25 \mu\text{s}$ of the $\text{H}\delta$ line implies $N_e = 0.33 \times 10^{17} \text{ cm}^{-3}$.

Abel-inverted maps usually indicate undulations of the signal along the radial direction. Such undulations can be expected as the laser-plasma expands – in related experiments of optical breakdown in air, multiple reflections can be seen in shadowgraphs that are captured following optical breakdown in air. Similar phenomena as depicted in the air shadowgraphs are expected to occur for the hydrogen:nitrogen mixture. Fig. 3 displays recorded air-breakdown shadowgraphs to further elucidate multiple reflections that are likely causing undulations in the plasma core. The shadowgraph experiments recorded 125 images for each time delay, the selected images portray typical images.

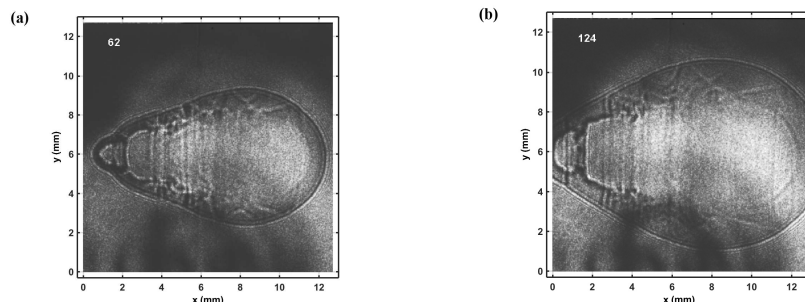


Figure 3. Shadowgraph of optical breakdown in laboratory air. The laser beam propagates from the right, images are captured using a second, imaging laser. The “bubble” on the laser side indicates absorption of laser radiation. Time delay: **(a)** $1.5 \mu\text{s}$, image 62. **(b)** $3 \mu\text{s}$, image 124.

3.4. Electron temperature and density

Analysis of the recorded spectra along the slit height aims to evaluate electron temperature, T_e , from Boltzmann plots. Moreover, electron density, N_e , determination relies on formulae and tables that describe Stark broadening in laser-plasma. Fig. 4 portrays a typical Boltzmann-plot from line-of-sight measurements at $3\text{-}\mu\text{s}$ time delay. The Boltzmann plot method utilizes Boltzmann distributions and determination of the slope to extract the temperature from the negative of $1/\text{slope}$. The intercept of the straight line is not used for evaluation of the temperature. For data points from the four Balmer series members close to the fitted line, one can infer local thermodynamic equilibrium. As data points deviate from the fitted line, deviations from equilibrium may be concluded – self-absorbed lines would also cause deviations of data points from the straight line, and equally, ambiguities in determination of the baseline. However, expansion dynamics may lead to variations in the integrated line intensities as well. Fig. 4 is obtained from the areas of the four Balmer series lines with area ratio $\text{area-H}\alpha:\text{H}\beta:\text{H}\gamma:\text{H}\delta$ equals $1.5:0.42:0.19:0.13$. Fig. 4 also shows error bars due to baseline uncertainties. The width ratio $\text{H}\alpha:\text{H}\beta:\text{H}\gamma:\text{H}\delta$ amounts to $0.84:2.6:2.7:5.2$, and the $\text{H}\beta$ and $\text{H}\delta$ peak separations are 0.74 and 1.1 nm, respectively. The electron densities inferred from the peak separations amount to $0.38 \times 10^{17} \text{cm}^{-3}$ and are consistent within error margins with electron densities obtained from the widths. Noteworthy, the uncertainties in the area and width determinations lead to estimated uncertainties of the electron density that are of the order of 10 to 20 per cent, equally for the electron density values computed from peak-separations. Automated analysis of the line-of-sight recorded data is further elaborated in Section 3.5, see Fig. 6.

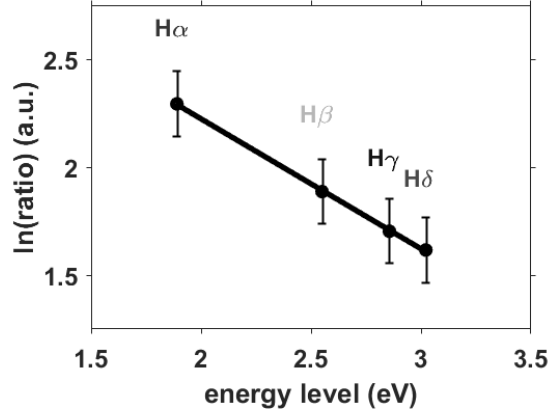


Figure 4. Electron temperature of 19.2 kK inferred from line-of-sight data at 4.8 mm slit height, 3- μ s time delay, 0.025- μ s gate.

The electron density is related to the hydrogen Balmer series FWHM to the power of the order of 1.5, however, detailed theory predictions and experimental results indicate slight deviations. Empirical equations are obtained from log-log fitting of FWHM and electron density. For red-shift of the H α line, the dependency on electron density is almost linear. As mentioned earlier, Stark broadening widths increase from H α to H γ . The use of H β peak-separation for N_e determination in laser-plasma adds a new diagnostic tool. Investigations of the H δ peak separation are communicated in this work for N_e in the range of 0.1 to $1 \times 10^{17} \text{ cm}^{-3}$ and applied for the hydrogen-nitrogen laser plasma.

For the 3.25- μ s time delay, electron densities largely agree when inferred from the widths of the four Balmer series lines and from the peak-separations of H β and H δ . However, there are subtle differences of N_e determined at 1.5 μ s time delay. One may conclude from the appearance of the measured emission spectra and the computed Abel-inverted spectra that super- to hyper-sonic laser-plasma expansion speeds affect the establishment of local thermodynamic equilibrium. Details are investigated in the next section. Tables 1 and 2 summarize a snapshot of the data analysis.

Table 1 displays measured FWHM and peak-separations. The values are determined from the spectra at a slit height of 4.8 mm by using Matlab[®] software “peakfit.m” (O’Haver, 2018). Table 2 reports the electron densities.

3.5. Plasma expansion dynamics

Laser-plasma generation with laser pulses of the order of 10 ns and pulse energies of 80 to 800 mJ in ambient laboratory conditions causes a shock wave that

Table 1. First four Balmer series FWHM and H δ and H β peak-separations from line-of-sight data at 4.8-mm slit height.

τ [μ s]	$\Delta\lambda_\delta$ [nm]	$\Delta\lambda_{\delta-ps}$ [nm]	$\Delta\lambda_\gamma$ [nm]	$\Delta\lambda_\beta$ [nm]	$\Delta\lambda_{\beta-ps}$ [nm]	$\Delta\lambda_\alpha$ [nm]
1.50	7.5 ± 1.5	1.4 ± 0.8	5.0 ± 0.2	4.2 ± 0.25	1.2 ± 0.2	1.17 ± 0.1
3.25	5.8 ± 0.3	1.1 ± 0.2	3.2 ± 0.2	2.6 ± 0.25	0.8 ± 0.15	0.78 ± 0.1

Table 2. First four Balmer series electron densities, N_e [10^{17} cm $^{-3}$], from line-of-sight data at 4.8-mm slit height.

τ [μ s]	$N_e(\delta)$	$N_e(\delta-ps)$	$N_e(\gamma)$	$N_e(\beta)$	$N_e(\beta-ps)$	$N_e(\alpha)$	average N_e
1.50	0.65	0.56	0.77	0.91	0.88	0.84	0.77
3.25	0.44	0.38	0.41	0.46	0.46	0.45	0.43

expands at a rate of one to a few mm μ s $^{-1}$, or a few km s $^{-1}$, give or take for time delays of the order of 1 μ s. Early in the plasma decay, expansion speeds of up to 80 km s $^{-1}$ are usually encountered that may be described in engineering terms as well above re-entry speeds or high hypersonic speeds. Several dozens of microseconds after plasma initiation, the shock wave reduces to the speed of sound.

In view of the "bubble" expanding in air and the associated isentropic expansion, one can determine electron density or temperature to elucidate the phenomena. Captured shadowgraphs can guide time-resolved spectroscopy, however, there should be an indication of the shockwave in spatially- and temporally-resolved measured spectra. One approach may utilize Radon- and Abel- inversion techniques (Pretzler *et al.*, 1992) that are generally known as computed tomography methods. Alternatively, one may closely investigate the captured spectra along the slit height. Fig. 5 compares electron density results for a time delay of 3.0 μ s. Increases in electron density at the plasma edges are indications of the expanding shock wave.

Systematic determination of the Stark widths from line-of-sight data is expected to reveal higher electron density near the shock wave than in the plasma core. Alternatively, determination of the area of the atomic Balmer series lines should indicate higher temperature near the shock wave than in the plasma center. Moreover, for time delays of several μ s – as the shockwave expanded beyond the interrogated volume – the plasma is expected to be homogeneous and indicate local thermodynamic equilibrium for electron densities in excess of 10^{16} cm $^{-3}$, as indicated by the necessary McWhirter criterion (McWhirter, 1965), and is expected to show higher temperature in the core.

The shock wave radius as function of time delay, τ , is evaluated with the Taylor-Sedov formula for spherical expansion (Campanella *et al.*, 2019),

$$R(\tau) = (E_p/\rho\tau^2)^{1/5}, \quad (9)$$

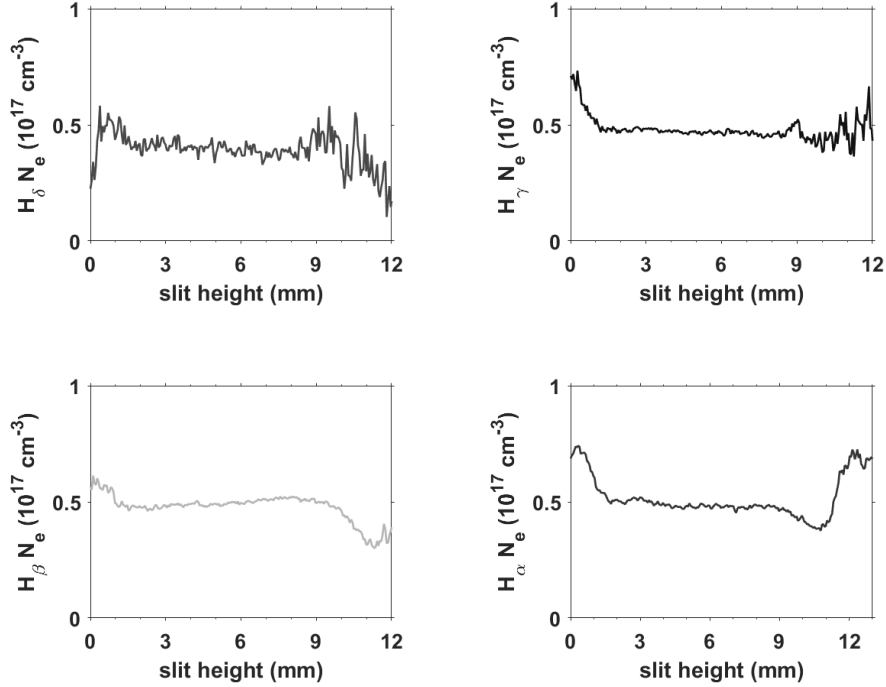


Figure 5. Electron density from line-of-sight data displayed in Fig. 1 at $3\text{-}\mu\text{s}$ time delay, $0.025\text{-}\mu\text{s}$ gate. (a) $\text{H}\delta$, (b) $\text{H}\gamma$, (c) $\text{H}\beta$, and (d) $\text{H}\alpha$.

where the laser-pulse energy, E_p , for the experiments amounts to 0.15 J , and the density of the 1:1 nitrogen hydrogen mixture, ρ , equals 0.37 kg m^{-3} . For $\tau = 3\text{ }\mu\text{s}$, one finds for the radius $R = 5.2\text{ mm}$. Fig. 6 illustrates the spectroscopic snapshot of the determined temperature profile for $\tau = 3\text{ }\mu\text{s}$.

Higher temperature is measured at slit-heights near 1.1 mm and 11.5 mm than in the central region, indicating the expanding shock wave. The predicted diameter of 10.4 mm for spherical expansion is identical with the diameter extracted from the spectra. Recording of shadowgraphs, see Fig. 3, indicates development of a largely symmetric bubble as time delay progresses beyond $1\text{ }\mu\text{s}$. While the displayed shadowgraphs are captured in ambient laboratory air, shock waves propagate about a factor of four faster in hydrogen than in air, thereby evolving in hydrogen into spherical appearance faster than in air. Furthermore, the reductions in temperature near 1.5 mm and 10 mm are also expected for expanding shockwaves that propagate at speeds well above the speed of sound. The absolute error margins of the temperature are estimated to be of the order of 25% due to ambiguities in determining the background contributions to the

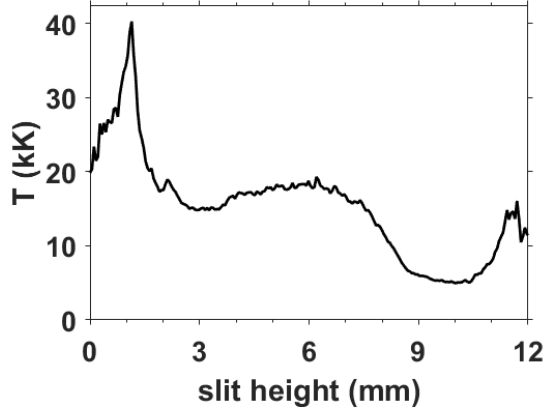


Figure 6. Electron temperature from line-of-sight data, 3- μ s time delay, 0.025- μ s gate. Average temperature: 15.4 kK.

line areas of the four Balmer series lines, yet the relative trends are consistent with expansion dynamics. The average temperature of the order of 15 kK is also consistent with previous measurements of average temperatures. However, as the shock wave expands, both density and temperature variations occur near the shock front.

4. Stellar astrophysical spectra

Well-known white dwarfs near the earth are Sirius B and Procyon B. Sirius B shows a temperature of 26 kK, and absorption spectra in the visible part of the electromagnetic spectrum are composed of hydrogen Balmer series lines. In turn, Procyon B at a temperature of 7.9 kK reveals molecular carbon Swan absorptions. Fig. 7 illustrates (Parigger *et al.*, 2018) recorded spectra (Giammichele *et al.*, 2012) that are accessible from the Montreal data-base (Dufour *et al.*, 2019).

The spectral resolution, $\lambda/\Delta\lambda$, equals 555 for the displayed Sirius B and Procyon B absorption spectra. Clearly, the Sirius B absorption spectra displays larger absorption of $H\gamma$ than of $H\beta$, $H\delta$ than $H\gamma$, etc. In turn, laboratory emission spectra display the usual Boltzmann factor dependency, i.e., the integrated emission of $H\beta$ is larger than that $H\gamma$, $H\gamma$ is larger than $H\delta$, etc. The key considerations for reconciling the apparent ambiguity are evaluation of white-dwarf opacities. The bound-bound opacity corresponds to the emission profile, but the wavelength-dependent bound-free opacity increases towards higher members of the Balmer series. In essence, the bound-free opacity needs to be evaluated prior to comparison of recorded astrophysical data with laboratory results (Tremblay

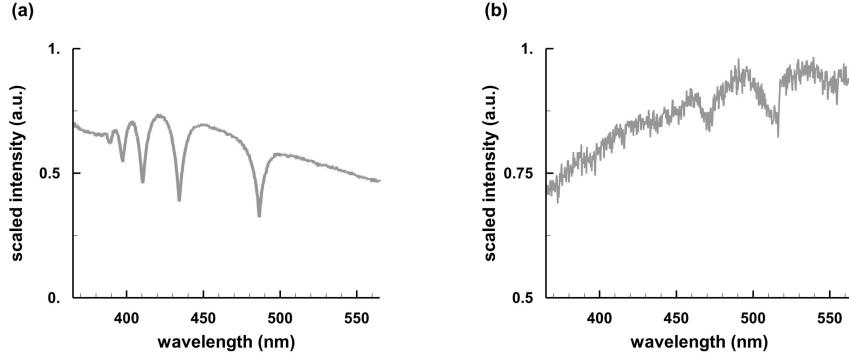


Figure 7. Sirius B and Procyon white dwarf spectra (Dufour *et al.*, 2019): (a) Sirius B at 26 kK; and (b) Procyon B at 8 kK.

& Bergeron, 2009). Conversely, as white dwarfs cool to the level of temperature seen for Procyon B, molecular absorption spectra can be demarcated. Carbon C_2 Swan spectra may be developed more convincingly, such as for the white dwarf GJ 841 B (Dufour *et al.*, 2019) that can be analyzed by fitting computed molecular spectra (Parigger *et al.*, 2019b).

Collection of spectra from white dwarf stars preferably occurs with a resolving power sufficient for determination of the gravitational shift. Recent data for the white dwarf star GD 394 B, recorded with an echelle spectrometer on November 15, 2015, with KOA-ID: HI.20151115.19364 (Keck Observatory Archive, 2015), shows a resolving power of $R = 38000$, or a resolution of $\Delta\lambda = 0.013$ nm.

Fig. 8(a) illustrates five overlapped regions of the recorded echelle spectra together with broad and narrow Lorentzian fits. Fig. 8(b) shows the expanded region of the central absorption. Both broad and narrow features of a WD astrophysical plasma are usually understood as absorptions from an outer region of the WD photosphere.

Analysis of the GD 394 B, $H\beta$ spectra (Parigger *et al.*, 2019a) shows narrow and broad photosphere absorption-widths of 0.39 nm and 7.3 nm that would indicate electron densities of 0.032 and $2.0 \times 10^{17} \text{ cm}^{-3}$, respectively. The electron density is determined from formulae that are valid for local thermodynamic equilibrium and that fulfil the necessary McWhirter criterion. Strictly speaking, then, the 0.39-nm width implies an electron density indicative of non-equilibrium conditions. In view of the astrophysical WD plasma, one may conclude that there is a rather broad, likely in local thermodynamic equilibrium WD photosphere yielding a broad line profile, and another region that is significantly less dense.

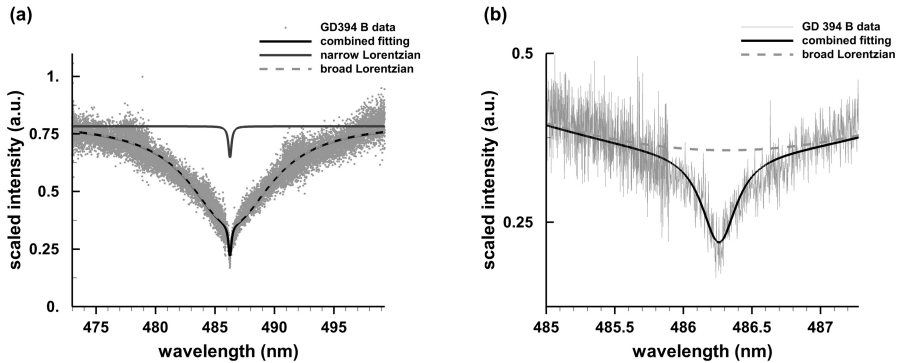


Figure 8. White dwarf GD 394 B, H β combined absorption profiles, recorded with the HIRES echelle spectrometer, KOA-ID: HI.20151115.19364 (Keck Observatory Archive, 2015). (a) Fitting with two Lorentzians and (b) Expanded region (Parigger *et al.*, 2019a).

Analysis of the white dwarf HG 7-85 from the Hyades cluster (Zuckerman *et al.*, 2013) yields consistent results (Parigger *et al.*, 2018) for broad Lorentzian center wavelength and gravitational shifts of 0.072 nm and 0.08 nm, respectively.

5. Discussion

Laboratory experiments are essential in establishing detailed appearances of Balmer series line shapes for analysis of observed white-dwarf spectra. Modeling of astrophysical spectra however involves fairly detailed computations of the radiative transfer equation that is also known as the Boltzmann transport equation. The emission spectra of specifically the H β and H γ lines reveal two peaks at line center as expected from treatments of the Stark effect in hydrogen. A spectral resolutions of the order of 5,000 is sufficient for capturing Balmer series members with time-resolved spectroscopy when using a crossed Czerny-Turner spectrometer and an intensified charge-coupled device. Typical spectral resolutions of the order of 50,000 are available with echelle spectrometers that are in use at observatories for continuous recording of astrophysical plasma from white dwarfs. Comparisons of laboratory spectra then requires adding individually recorded time-resolved spectra to obtain an average for comparison with white dwarf spectra. In other words, averaging of time-resolved spectra corresponds to averaging data for different electron densities. Consequently, details seen in the laboratory are absent in observed white dwarf spectra. Analysis of the white-dwarf spectra with at least two Lorentzians would indicate that at

least two regions indeed occur with different electron densities. The explored $H\gamma$ and $H\delta$ lines can provide additional diagnostics for white dwarfs, especially in the range of 0.1 to $1 \times 10^{17} \text{cm}^{-3}$. However, bound-free opacity effects would need to be included when using, say, the first four lines of the Balmer series. Analysis of white-dwarfs and other astrophysical objects such as active galactic nuclei from only one line, i.e., $H\beta$ may be preferred as bound-free effects may not be significant across one line and for purposes of determining widths and asymmetries of stellar $H\beta$ lines. Future work however should include new results from laboratory measurements that address specifically the shapes of lines used for diagnosis of astrophysical spectra.

Acknowledgements. The author appreciates the support in part by the Center for Laser Application, a State of Tennessee funded Accomplished Center of Excellence at the University of Tennessee Space Institute.

References

- Campanella, B., Legnaioli, S., Pagnotta, S., Poggialini, F., Palleschi, V. Shock Waves in Laser-Induced Plasmas. 2019, *Atoms*, **7**, 57
- Dufour, P., Blouin, S., Coutu, S., Fortin-Archambault, M., Thibeault, C., Bergeron, P., Fontaine, G. The Montreal White Dwarf Database: A Tool for the Community. Available online: <http://dev.montrealwhitedwarfdatabase.org> (accessed on 3 June 2019)
- Giammichele, N., Bergeron P., Dufour, P. Know your neighborhood: A detailed model atmosphere analysis of nearby white dwarfs. 2012, *Astrophys. J. Supp. Ser.*, **199**, 29–63
- Gigosos, M. A., González, M. Á., Cardenoso, V. Computer simulated Balmer-alpha, -beta and -gamma Stark line profiles for non-equilibrium plasmas diagnostics. 2003, *Spectrochim. Acta B At. Spectrosc.*, **58**, 1489-1504
- Greene, Jr., R. E. 1961, *The Shift and Shape of Spectral Lines*, Pergamon Press: Oxford, UK, 1961, Chapter 4, pp. 118–193
- Griem, H. R. 1974, *Spectral Line Broadening by Plasmas*, Academic Press: Cambridge, MA, USA, 1974
- Halenka, J., Vujičić, B., Djurović, S. Shift of the peaks of the $H\beta$ spectral line. 1989, *J. Quant. Spectrosc. Radiat. Trans.*, **42**, 571-573
- Halenka, J., Olchawa, W., Madej, J., Grabowski, B. Pressure shift and gravitational redshift of Balmer lines in white dwarfs: Rediscussion. 2015, *Astrophys. J.*, **808**, 131-140
- Holtzmark, J. Über die Verbreiterung von Spectrallinien. 1919, *Ann. Phys.*, **58**, 577-630
- Inglis, D. R., Teller, E. Ionic depression of series limits in one-electron spectra. 1939, *Astrophys. J.* **90**, 439–448

- Ivković, M., Konjević, N., Pavlović, Z. Hydrogen Balmer beta: The separation between line peaks for plasma electron density diagnostics and self-absorption test. 2015, *J. Quant. Spectrosc. Radiat. Trans.*, **154**, 1–8
- W. M. Keck Observatory Archive (KOA). Available online: <https://koa.ipac.caltech.edu> (accessed on 5 May 2018)
- Kunze, H.-J. 2009, *Introduction to Plasma Spectroscopy*, Springer: New York, NY, USA, 2009
- McWhirter, R. W. P. Spectral Intensities. 1965, *Plasma Diagnostic Techniques; Huddleston, R.H., Leonard, S.L., Eds.; Academic Press: New York, NY, USA, 1965; pp. 201–264*
- Mijatović, Z., Pavlov, M., Djurović, S. Shift of the H β line in dense hydrogen plasmas. 1991, *Phys. Rev. A*, **43**, 6095–6097
- Miziolek A. W., Palleschi V., Schechter, I., Eds. 2006, *Laser Induced Breakdown Spectroscopy*, Cambridge University Press: New York, NY, USA, 2006
- O’Haver T. C. Command-line peak fitter for time-series signals. Version 9.0, January 2018, *Mathworks File Exchange*. Available online: <https://www.mathworks.com/matlabcentral/fileexchange/23611-peakfit-m> (accessed June 4 2019)
- Oks, E. 2017, *Diagnostics of Laboratory and Astrophysical Plasmas Using Spectral Lineshapes of One-, Two-, and Three-Electron Systems*, World Scientific: Singapore, 2017; pp. 147
- Parigger, C. G., Woods, A. C., Witte, M. J., Swafford, L. D., Surmick, D. M. Measurement and Analysis of Atomic Hydrogen and Diatomic Molecular AlO, C₂, CN, and TiO Spectra Following Laser-induced Optical Breakdown. 2014, *J. Vis. Exp.*, **84**, e51250
- Parigger, C. G., Drake, K. A., Helstern, C. M., Gautam, G. Laboratory Hydrogen-Beta Emission Spectroscopy for Analysis of Astrophysical White Dwarf Spectra. 2018, *Atoms*, **6**, 36
- Parigger, C. G. Measurements of Gaseous Hydrogen-Nitrogen Laser-Plasma. 2019, *Atoms*, **7**, 61
- Parigger, C. G., Helstern, C. M., Gautam, G., Drake, K. A. Atomic and molecular line shapes in laboratory and selected astrophysical plasma. 2019, *J. Phys.: Conf. Ser.*, in press
- Parigger, C. G., Helstern, C. M., Gautam, G. Laser-Plasma and Self-Absorption Measurements with Applications to Analysis of Atomic and Molecular Stellar Astrophysics Spectra. 2019, *Atoms*, **7**, 63
- Pretzler, G., Jäger, H., Neger, T., Philipp, H., Woisetschläger, J. Comparison of Different Methods of Abel Inversion Using Computer Simulated and Experimental Side-On Data. 1992, *Z. Naturforsch.*, **47a**, 955–970
- Schrödinger, E. Quantisierung als Eigenwertproblem. 1926, *Ann. Phys.* **385**, 437–490
- Singh, J. P., Thakur S. N., Eds., 2019, *Laser Induced Breakdown Spectroscopy*, Elsevier Science: New York, NY, USA, 2019

- Tennyson, J., Yurchenko, S. N. ExoMol: Molecular line lists for exoplanet and other atmospheres. 2012, *Mon. Not. R. Astron. Soc.*, **425**, 21–33
- The Nobel Prize in Physics 1933. Available online: <https://www.nobelprize.org/prizes/physics/1933/summary/> (accessed on May 24 2019)
- Tremblay, P.-E., Bergeron, P. Spectroscopic Analysis of DA White dwarfs: Stark broadening of hydrogen lines including nonideal effects. 2009, *Astrophys. J.*, **696**, 1755–1770
- Wiese, W. L. Line Broadening. 1965, *Plasma Diagnostic Techniques*; Huddleston, R.H., Leonard, S.L., Eds.; Academic Press, New York, NY, USA, 1965; pp. 265–317
- Zuckerman, B., Xu, S., Klein, B., Jura, A. The Hyades cluster: Identification of a planetary system and escaping white dwarfs. 2013, *Astrophys. J.*, **770**, 140–141

Current and future development of the photoionization code Cloudy

P.A.M. van Hoof¹, G.C. Van de Steene¹, F. Guzmán²,
M. Dehghanian², M. Chatzikos² and G.J. Ferland²

¹ *Royal Observatory of Belgium, Ringlaan 3, B-1180 Brussels, Belgium*

² *Department of Physics and Astronomy, The University of Kentucky, Lexington, KY 40506, USA*

Received: July 31, 2019; Accepted: October 24, 2019

Abstract. The interstellar medium (ISM) plays a crucial role in the cycle of matter in every galaxy. The gas and dust that is present in the ISM is usually very far removed from (local) thermodynamic equilibrium, and in some cases may also not be in a steady-state equilibrium with its surroundings. The physics of this material is complex and you need a sophisticated numerical code to study it. For this purpose the open-source photoionization code Cloudy was created. It models the physical state of the gas and predicts the spectrum that it emits.

Cloudy is continually being developed to improve the treatment of the microphysical processes and the database of fundamental data that it uses. In this paper we will discuss how we are developing the code to improve our high-density predictions by implementing better collisional-radiative models for all ions. We will also briefly discuss the experimental mode in Cloudy to model gas that is not in steady-state equilibrium and present a preliminary model of recombining gas in a planetary nebula that is on the cooling track. We finish with a short discussion of how we are speeding up the code by using parallelization.

Key words: plasmas – ISM: general – planetary nebulae: general

1. Introduction

The space between stars is filled with a very tenuous gas called the interstellar medium (ISM) which plays a crucial role in the evolution of every galaxy. This medium is usually irradiated by strongly diluted radiation fields and is therefore far removed from local thermodynamic equilibrium (LTE). In some cases it may also not be in a steady-state equilibrium with its surroundings. The material in the ISM is generally primarily heated by stellar light, but other energy sources could be shocks, magnetic reconnection, cosmic rays, radioactive decay, etc. The gas may be ionized, neutral, or molecular and usually also contains dust grains. The geometry of the gas is often intricate, making solving the radiative transfer equations difficult. As a result the physics of this material is complex and you need a sophisticated numerical code to model the spectrum emitted by this gas.

For this purpose the open-source photoionization code Cloudy was created on 28 August 1978 in Cambridge, UK. The emphasis is on detailed treatment of microphysical processes, but it also needs simplifying assumptions, such as 1D spherical geometry¹ with simplified radiative transfer, no treatment of shocks, only a very basic treatment of magnetic fields, and no inclusion of radioactive decay. It models the physical state of the gas and predicts the spectrum emitted by that gas. It is the only code that can make a self-consistent model of a photoionized region and the neutral and molecular regions beyond the ionization front. Such a code needs a vast amount of atomic and molecular data. Cloudy is continually being developed to improve the treatment of the microphysical processes and the database of fundamental data that it uses, with the aim of making the code suitable for the widest possible range of physical conditions. In this paper we will briefly discuss our ongoing efforts to improve the code. We will also discuss the experimental mode in Cloudy to model gas that is not in steady-state equilibrium and show results from a preliminary model of a recombining planetary nebula (PN). In the final section we briefly discuss how we are speeding up the code using parallelization.

2. The ionization equilibrium

To meet our goal of modeling a wide range of physical conditions, Cloudy needs to be able to calculate the ionization balance over a wide range of densities. In very low-density gas, the ionization balance can be derived using the two-level or coronal approximation. Here it is assumed that all the material is in the ground state, and hence you only need to consider two states: the ground state of the current and the next ion. This approximation is valid because the time between two interactions is very long, giving the ion enough time to relax into the ground state after an excitation or recombination event. At very high densities, the collisional rates will be very fast, driving the gas into LTE. This implies that the ionization balance can be derived from the Saha-Boltzmann equation. Both limits are very easy to model, however at intermediate densities neither limit is valid and a complex numerical collisional-radiative model (CRM) is needed to obtain accurate predictions for the ionization balance. This is shown in Fig. 1.

A CRM solution requires many excited states to be included in the model atom as the average time between two interactions is too short for the electron to reach the ground state and excitations or ionizations from excited states become important. In recent years a considerable amount of effort was dedicated to prepare Cloudy for this task. Here we will describe the most important aspects of this work.

¹Christophe Morisset implemented pseudo-3D modeling based on Cloudy models using the pyCloudy package (Morisset, 2013).

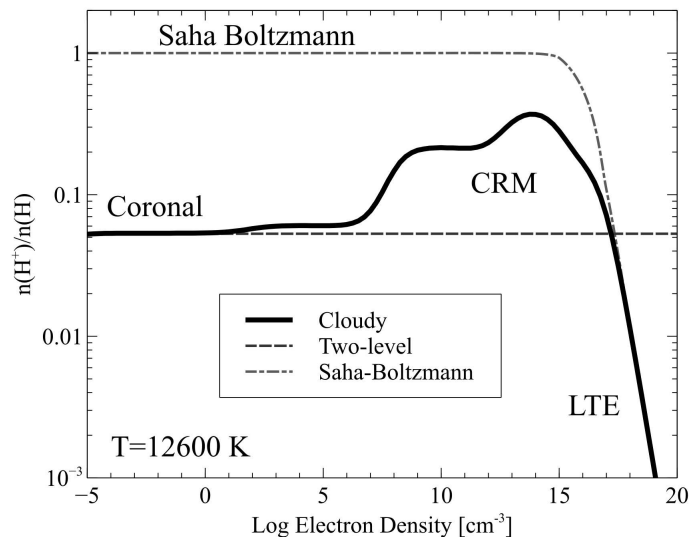


Figure 1. Ionization of hydrogen as a function of density. The solid line is the full numerical CRM solution, the dashed line is the ionization predicted by the two-level approximation, and the dashed-dotted line is the prediction of the Saha-Boltzmann equation. Figure taken from Ferland et al. (2017).

2.1. H- and He-like ions

For the H- and He-like iso-electronic sequences we use a custom approach for setting up the model atoms. This is done in such a way that the user can request an arbitrary number of levels. These can either be l -resolved or collapsed into states with the same principal quantum number n . Such an approach is possible by exploiting regularities in the atomic data resulting from the simple level structure of these ions. The original implementation of the He-like sequence is discussed in Porter et al. (2005); Bauman et al. (2005) and the H-like sequence in Luridiana et al. (2009). For the 2017 release of Cloudy we started a comprehensive review of these iso-electronic sequences, mainly focusing on the accuracy of the collisional data we use (Guzmán et al., 2016, 2017, 2019). This effort is still ongoing and will result in further updates in a future release.

The H- and He-like ions are unusual because the first excited level is much closer to the ionization threshold than to the ground state (see Fig. 2). This implies that in photoionized plasmas collisional excitation is generally unimportant, and the emission line spectra are produced by recombination. Recombination typically happens in highly excited Rydberg states, which are tightly coupled to the ionized continuum by collisional ionization and photoionization and their inverse processes. To make accurate predictions of the recombina-

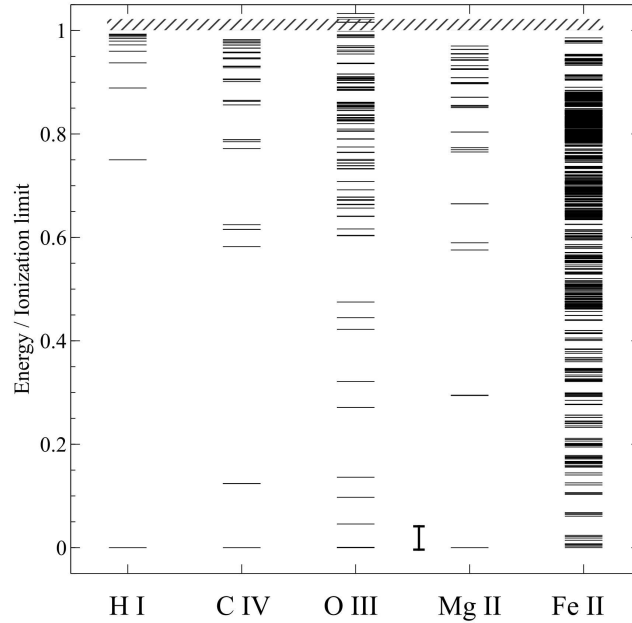


Figure 2. Experimental energy levels taken from NIST ASD (Kramida et al., 2014) for some species present in an ionized gas. The energies are given relative to the first ionization potential. Figure taken from Ferland et al. (2017).

tion spectrum, a very large model atom is needed. Cloudy is capable of setting up such a model atom, but the CPU and memory requirements are currently prohibitive. The reason for that is twofold. On the one hand, calculating the atomic data is too slow, while on the other hand solving the equations for the level populations takes too much time as every level is modeled explicitly. We will tackle the former problem by caching atomic data or moving them into data files (possibly in Stout format), rather than calculating them on the fly, and also by using better optimized algorithms. To alleviate the latter problem, we will implement the matrix condensation technique pioneered by Burgess & Summers (1969) and Brocklehurst (1970). This technique is akin to the superlevel technique often used in stellar atmospheres, which allows a significant reduction in the number of levels that are modeled, thus significantly speeding up the LU decomposition needed to solve the level populations. This will allow us to routinely model large model atoms and improve the accuracy of our recombination line predictions. This is e.g. needed for the measurement of the primordial helium abundance. These improvements will be offered in a future release of Cloudy.

2.2. More complex ions

Unlike H- and He-like ions, more complex ions have low-lying excited states. These can be collisionally excited, even in a photoionized plasma and thus can be an important source of cooling for the gas. Moreover, these ions can lack the regularities that H- and He-like ions have, e.g., due to configuration interaction shifting levels out of position. Because of this, a very different approach is needed compared to what we described above. We will need to tabulate the atomic data that are needed to model the atom. The level energies will normally be taken from experiments, while the transition probabilities and collision strengths typically come from large-scale computer models.

With the 2013 release of Cloudy we started moving these atomic data into external data files (until then, the data for a relatively small number of important lines were hardwired into the code). Initially we adopted the Chianti database (Dere et al., 1997; Landi et al., 2012) but we quickly realized that the scope of this database is insufficient for us to depend on it exclusively (e.g., it contains insufficient data for low ionization stages). So we decided to develop our own Stout database for atomic and molecular data. This database was introduced in the 2013 release of Cloudy (Ferland et al., 2013), but was only used for a very limited number of ions. With the 2017 release of Cloudy we moved many more ions to the Stout database, vastly increasing the number of levels and lines that can be modeled with Cloudy. A more detailed discussion of these points can be found in Ferland et al. (2017).

This is the first step towards full CRM treatment of these ions. However, more work is needed. Many of the entries in the Stout database are what we call “baseline” models. These contain level energies and transitions probabilities taken from NIST ASD (Kramida et al., 2014) but no collisional data. If for a given transition the collisional data are missing, Cloudy will use the g -bar approximation (Burgess & Tully, 1992) which is now widely viewed as unreliable, but is still better than having no data at all. To improve this situation, we have started a project to update the baseline models using the latest level energies and transition probabilities from NIST ASD and combining those with electron impact collisional data from the OPEN-ADAS database². This should vastly improve the quality of the predictions for these model atoms.

Solving the level populations and the ionization balance are however still not coupled in the sense that ionization from excited states is not considered for these complex ions (with only a handful of exceptions that are currently hardwired into the code). We aim to improve this situation in collaboration with the University of Cambridge by including both collisional ionization and photoionization processes from metastable states. All these improvements will be offered in a future release of Cloudy.

²<http://open.adas.ac.uk/>

3. Time-dependent modeling

For quite some time Cloudy has been able to model time-steady non-equilibrium dynamical flows (Henney et al., 2005, 2007). This capability was later extended to modeling time-dependent non-equilibrium conditions in the gas (Chatzikos et al., 2015). This feature is still considered experimental. Here we apply this method to the problem of a recombining PN.

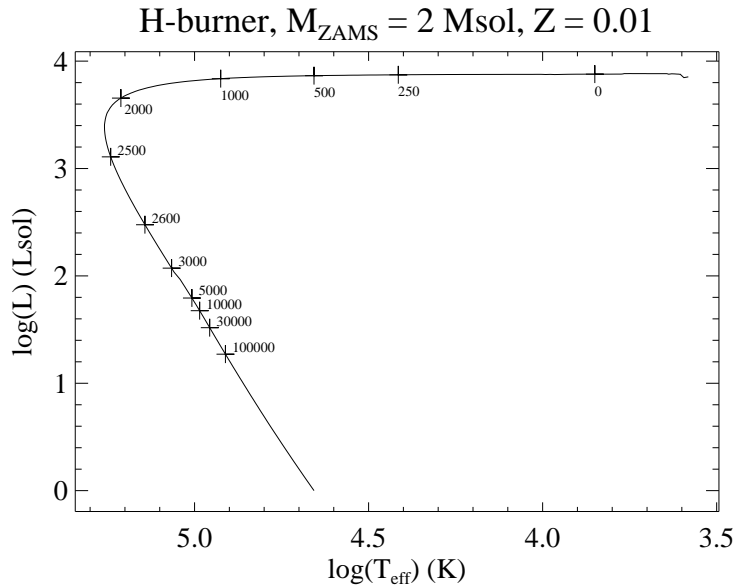


Figure 3. Evolutionary track from Miller Bertolami (2016). Ages in years since the star left the AGB are marked on the track.

When an intermediate-mass star nears the end of its life, it will experience thermal pulses during the asymptotic giant branch (AGB) part of its evolution. At this time the energy generation is via hydrogen shell burning, punctuated at regular intervals (10^4 – 10^5 yr) by helium flashes followed by short phases of quiescent helium burning. During these flashes, the remaining envelope of the star is removed in a superwind. When the envelope is nearly depleted, the star starts to heat up and ionizes the material that was ejected during the AGB phase, forming a new PN. Eventually the hydrogen burning shell runs out of fuel and the nuclear burning will shut down. At this time the luminosity of the star will quickly go down while it also will start to cool, eventually turning the star into a new white dwarf. This part of the evolution is called the cooling track.

When the star is on the cooling track, the PN will receive increasingly less ionizing photons. This implies that the outer parts of the PN can no longer be ionized and will start to recombine (e.g., van Hoof *et al.*, 2000). This is a non-equilibrium process that we can model with Cloudy. Here we present preliminary results. To have a realistic evolution of the luminosity as a function of time, we use the $2 M_{\odot}$ hydrogen-burning evolutionary track from Miller Bertolami (2016) with $Z = 0.01$. This track is shown in Fig. 3.

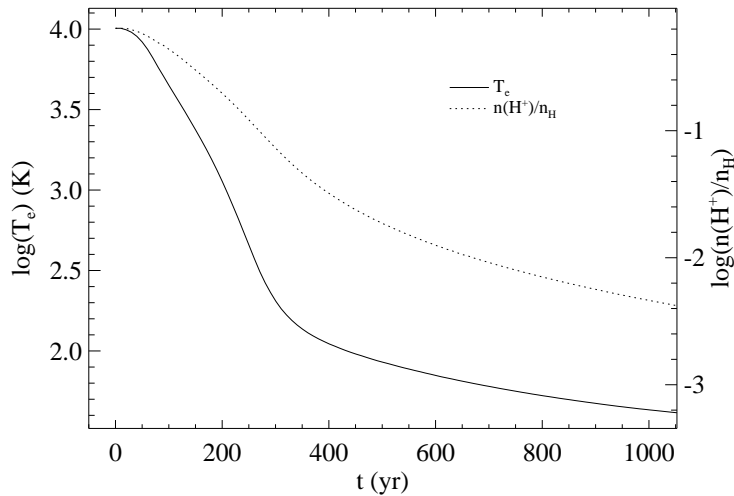


Figure 4. The evolution of the electron temperature and hydrogen ionization fraction as a function of time at a radius of 4×10^{15} m.

We will start the Cloudy model when the star is at the maximum temperature, $T_{\text{eff}} = 181.5$ kK. This point is reached after 2404 yr. It is currently not possible to vary the stellar temperature, so we assume that it stays constant at this value during the evolution. We model the spectrum of the star using the H-Ca grid of atmosphere models by Rauch (1997). The evolution of the luminosity as a function of time will be given by the evolutionary track, starting at a luminosity of $2455 L_{\odot}$. The gas is assumed to have a constant hydrogen density of 1000 cm^{-3} , a reasonable value for an evolved PN. The inner radius is set at 1.135×10^{15} m, which is the distance the gas would have traveled in 2404 yr assuming a canonical expansion velocity of 15 km s^{-1} . The outer radius is set at 5.395×10^{15} m, chosen to coincide with the ionization front at the start of the simulation. This implies an ionized mass of $0.75 M_{\odot}$. The gas is assumed to contain graphite dust (Martin & Rouleau, 1991).

The results of the model are shown in Figs. 4 and 5. The first shows that the electron temperature drops very quickly: the decrease from 10 116 K to 1000 K

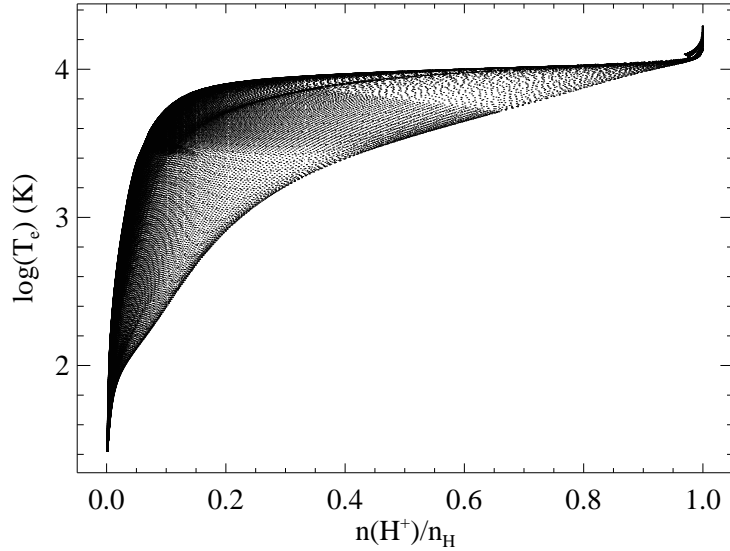


Figure 5. The electron temperature as a function of hydrogen ionization fraction is shown for every depth point of every time step of the model.

happens in less than 210 yr, while the hydrogen ionization fraction lags behind. When the electron temperature reaches 1000 K, hydrogen is still $\approx 18\%$ ionized. This can be seen even more clearly in Fig. 5 where we show the electron temperature as a function of the degree of ionization for all depths and every time step. From this it becomes clear that in a recombining PN it is possible to observe partially ionized gas at remarkably low temperatures: at 50% ionization, the electron temperature can be as low as 3410 K, at 20% ionization, as low as 815 K, and at 10% ionization as low as 250 K!

Roughly similar behavior can be observed for O^+ , while He^+ and N^+ also follow this trend, but with less extreme temperature lows. On the other hand, ions with a higher ionization potential, such as He^{2+} , C^{2+} , N^{2+} , and O^{2+} , do not show this behavior. Their recombination timescales are much shorter and they will have recombined before the gas has had the chance to cool by a significant amount. So in a recombining PN, you can have very cold gas that still has appreciable amounts of H^+ , He^+ , N^+ , and O^+ , but not many other ions (C^+ is also present, but that has a lower ionization potential and is still actively photoionized). This gas will still emit radiation due to the progressing recombination of these ions. These conclusions qualitatively agree with the earlier studies of Ferland & Truran (1981) who were modeling a nova shell and Binette & Robinson (1987) who were modeling an active galaxy.

It is well known that evolved PNe, such as NGC 6720 (the Ring nebula) and NGC 7293 (the Helix nebula), can have a large number of dense, molecular knots embedded in the ionized gas (Matsuura *et al.*, 2009). The origin of these knots is still debated. In O’Dell *et al.* (2007); van Hoof *et al.* (2010); Van de Steene *et al.* (2015) it has been proposed that these knots are not remnants of an earlier phase of evolution, but form in recombining gas when the star is on the cooling track. This leaves only one to two thousand years to form the knots in the case of NGC 6720 (O’Dell *et al.*, 2007). They would form as a result of an instability. When the recombining gas is cold, its internal pressure is low, making it susceptible to compression, e.g., by recombination radiation. The preliminary models presented in this paper show that this proposal could be viable. The recombining gas indeed cools on a very short timescale, but stays partially ionized, so that it still emits recombination radiation. This agrees with the assumptions made in van Hoof *et al.* (2010).

4. Parallelization

Modeling large model atoms as well as doing time-dependent modeling require a lot of work to be done by the CPU. To ease that burden, it is imperative that the code makes efficient use of the hardware resources that are available. This can be improved either through using SIMD (Single Instruction Multiple Data) instructions (also called code vectorization), or by using multiple cores in parallel since modern computers have more and more cores available.

In recent years an effort has been made to vectorize Cloudy. One way of achieving this is to simplify loops such that the compiler can recognize the potential to use SIMD instructions and generate these automatically while compiling. For this the loop needs to carry out only one or two simple tasks, otherwise the compiler will quickly be overwhelmed by the complexity and compile it using scalar instructions. So to achieve automatic vectorization, it may be beneficial to split one complex loop into multiple simpler ones. This task has been carried out in CPU-critical parts of the code.

In addition, we also created code primitives that were explicitly written to use SIMD instructions. These include routines to carry out reduction loops and vectorized transcendental functions (which apply transcendental functions to an array of arguments). Using code vectorization resulted in a moderate speedup of the code (roughly 20%). There likely is a potential to find further optimizations in the future. An added benefit is that any code that can be vectorized automatically by the compiler can also be parallelized automatically by the compiler using OpenMP.

Using multiple cores through parallelization promises more substantial time savings, but is also more complex to implement. In the past we have implemented parallelization at the highest level by calculating different models on different cores. This method is highly efficient, but can only be used in grid or optimizer

runs. For a single model different methods are needed. You can use parallelization on a low level by parallelizing individual loops as was already discussed above. This approach also opens the possibility of using graphics processors (though one drawback is that these are largely optimized for single-precision floating point math, while Cloudy often uses double-precision variables). Another possibility is mid-level parallelization, e.g. by solving the level populations of different ions on different cores, or by solving different grain size bins on different cores. These are ideas that still need to be tested and implemented in the future.

5. Concluding remarks

The interplay of physical processes in photoionized and photo-dissociation regions is very complex. Modeling these processes requires a large-scale code, and maintaining this requires a continuous effort. This includes adding the latest atomic and molecular data sets, implementing new and improved theory describing the physical processes, implementing faster and better numerical methods, and of course fixing bugs. In this paper we have highlighted a couple of the projects that we have recently undertaken, are in the process of implementing, or are planning to start in the future. These will allow Cloudy to make more accurate predictions. They will also make the code faster and more versatile. We hope that these efforts will improve the usefulness of Cloudy for our users.

References

- Bauman, R. P., Porter, R. L., Ferland, G. J., & MacAdam, K. B., J-Resolved He I Emission Predictions in the Low-Density Limit. 2005, *Astrophys. J.*, **628**, 541, DOI: 10.1086/430665
- Binette, L. & Robinson, A., Fossil nebulae in the context of active galaxies. I. Time evolution of a single cloud. 1987, *Astron. Astrophys.*, **177**, 11
- Brocklehurst, M., Level populations of hydrogen in gaseous nebulae. 1970, *Mon. Not. R. Astron. Soc.*, **148**, 417, DOI: 10.1093/mnras/148.4.417
- Burgess, A. & Summers, H. P., The Effects of Electron and Radiation Density on Dielectronic Recombination. 1969, *Astrophys. J.*, **157**, 1007, DOI: 10.1086/150131
- Burgess, A. & Tully, J. A., On the Analysis of Collision Strengths and Rate Coefficients. 1992, *Astron. Astrophys.*, **254**, 436
- Chatzikos, M., Williams, R. J. R., Ferland, G. J., et al., Implications of coronal line emission in NGC 4696*. 2015, *Mon. Not. R. Astron. Soc.*, **446**, 1234, DOI: 10.1093/mnras/stu2173

- Dere, K. P., Landi, E., Mason, H. E., Monsignori Fossi, B. C., & Young, P. R., CHIANTI - an atomic database for emission lines. 1997, *Astron. Astrophys., Suppl.*, **125**, 149, DOI: 10.1051/aas:1997368
- Ferland, G. J., Chatzikos, M., Guzmán, F., et al., The 2017 Release of Cloudy. 2017, *Revista Mexicana de Astronomía y Astrofísica*, **53**, 385
- Ferland, G. J., Porter, R. L., van Hoof, P. A. M., et al., The 2013 Release of Cloudy. 2013, *Revista Mexicana de Astronomía y Astrofísica*, **49**, 137
- Ferland, G. J. & Truran, J. W., An X-ray model for the nebula of nova DQ HER 1934. 1981, *Astrophys. J.*, **244**, 1022, DOI: 10.1086/158773
- Guzmán, F., Badnell, N. R., Williams, R. J. R., et al., H, He-like recombination spectra - I. l-changing collisions for hydrogen. 2016, *Mon. Not. R. Astron. Soc.*, **459**, 3498, DOI: 10.1093/mnras/stw893
- Guzmán, F., Badnell, N. R., Williams, R. J. R., et al., H-, He-like recombination spectra - II. l-changing collisions for He Rydberg states. 2017, *Mon. Not. R. Astron. Soc.*, **464**, 312, DOI: 10.1093/mnras/stw2304
- Guzmán, F., Chatzikos, M., van Hoof, P. A. M., et al., H-, He-like recombination spectra - III. n-changing collisions in highly excited Rydberg states and their impact on the radio, IR, and optical recombination lines. 2019, *Mon. Not. R. Astron. Soc.*, **486**, 1003, DOI: 10.1093/mnras/stz857
- Henney, W. J., Arthur, S. J., Williams, R. J. R., & Ferland, G. J., Self-Consistent Dynamic Models of Steady Ionization Fronts. I. Weak-D and Weak-R Fronts. 2005, *Astrophys. J.*, **621**, 328, DOI: 10.1086/427491
- Henney, W. J., Williams, R. J. R., Ferland, G. J., Shaw, G., & O'Dell, C. R., Merged Ionization/Dissociation Fronts in Planetary Nebulae. 2007, *Astrophys. J., Lett.*, **671**, L137, DOI: 10.1086/525023
- Kramida, A., Yu. Ralchenko, Reader, J., & and NIST ASD Team. 2014, NIST Atomic Spectra Database (ver. 5.2), [Online]. Available: <https://physics.nist.gov/asd> [2014, November 28]. National Institute of Standards and Technology, Gaithersburg, MD.
- Landi, E., Del Zanna, G., Young, P. R., Dere, K. P., & Mason, H. E., CHIANTI—An Atomic Database for Emission Lines. XII. Version 7 of the Database. 2012, *Astrophys. J.*, **744**, 99, DOI: 10.1088/0004-637X/744/2/99
- Luridiana, V., Simón-Díaz, S., Cerviño, M., et al., Fluorescent Excitation of Balmer Lines in Gaseous Nebulae: Case D. 2009, *Astrophys. J.*, **691**, 1712, DOI: 10.1088/0004-637X/691/2/1712
- Martin, P. G. & Rouleau, F., Extreme Ultraviolet Opacity with Interstellar Dust. 1991, in *Extreme Ultraviolet Astronomy*, ed. R. F. Malina & S. Bowyer, 341

- Matsuura, M., Speck, A. K., McHunu, B. M., et al., A “Firework” of H₂ Knots in the Planetary Nebula NGC 7293 (The Helix Nebula). 2009, *Astrophys. J.*, **700**, 1067, DOI: 10.1088/0004-637X/700/2/1067
- Miller Bertolami, M. M., New models for the evolution of post-asymptotic giant branch stars and central stars of planetary nebulae. 2016, *Astron. Astrophys.*, **588**, A25, DOI: 10.1051/0004-6361/201526577
- Morisset, C. 2013, pyCloudy: Tools to manage astronomical Cloudy photoionization code, Astrophysics Source Code Library
- O’Dell, C. R., Sabbadin, F., & Henney, W. J., The Three-Dimensional Ionization Structure and Evolution of NGC 6720, The Ring Nebula. 2007, *Astron. J.*, **134**, 1679, DOI: 10.1086/521823
- Porter, R. L., Bauman, R. P., Ferland, G. J., & MacAdam, K. B., Theoretical He I Emissivities in the Case B Approximation. 2005, *Astrophys. J., Lett.*, **622**, L73, DOI: 10.1086/429370
- Rauch, T., Implication of light metals (Li-Ca) on NLTE model atmospheres of compact hot stars. 1997, *Astron. Astrophys.*, **320**, 237
- Van de Steene, G. C., van Hoof, P. A. M., Exter, K. M., et al., Herschel imaging of the dust in the Helix nebula (NGC 7293). 2015, *Astron. Astrophys.*, **574**, A134, DOI: 10.1051/0004-6361/201424189
- van Hoof, P. A. M., van de Steene, G. C., Barlow, M. J., et al., Herschel images of NGC 6720: H₂ formation on dust grains. 2010, *Astron. Astrophys.*, **518**, L137, DOI: 10.1051/0004-6361/201014590
- van Hoof, P. A. M., Van de Steene, G. C., Beintema, D. A., et al., Properties of Dust Grains in Planetary Nebulae. I. The Ionized Region of NGC 6445. 2000, *Astrophys. J.*, **532**, 384, DOI: 10.1086/308536

Databases for collisional and radiative processes in small molecules needed for spectroscopy use in astrophysics

D. Jevremović¹, V.A. Srećković², B.P. Marinković² and V. Vujčić¹

¹ *Astronomical Observatory, Volgina 7, 11060 Belgrade, Serbia (E-mail: darko@aob.rs)*

² *Institute of Physics Belgrade, BU, Pregrevica 118, 11080 Zemun, Belgrade, Serbia, (E-mail: bratislav.marinkovic@ipb.ac.rs, vlada@ipb.ac.rs)*

Received: July 30, 2019; Accepted: December 12, 2019

Abstract. In this contribution we present a report on two atomic/molecular databases for collisional and radiative processes, BEAMDB and MolD, which are web services at the Serbian Virtual Observatory (SerVO) and nodes within the Virtual Atomic and Molecular Data Center (VAMDC). Within the BEAMDB there are mainly electron scattering cross section data, but having in mind the importance of spectroscopic data obtained by particle collisions, we also provide a number of electron energy loss spectra and threshold electron spectra. Electron loss spectroscopy with its complementarity to the photon absorption data, provides valuable information on the optically forbidden atomic and molecular transitions. The MolD database contains photodissociation cross sections for the individual ro-vibrational states of the diatomic molecular ions as well as corresponding data on molecular species and molecular state characterizations. The data can be used for further applications, e.g., for non-local thermal equilibrium modeling of early universe chemistry, modeling of the solar atmosphere, atmospheres of white dwarfs, etc.

Key words: Atomic processes – Planets and satellites: general – Line: profiles – Plasmas – ISM: clouds

1. Introduction

Obtaining crucial information on the different environments within our universe has become possible with advances in observational astronomy and computer modeling. For instance, data from new telescopes (e.g. ALMA) that will discover and explore the molecular universe (Saldaño et al., 2018; Zakharenko et al., 2019) require vast amount of atomic and molecular data for interpretation of observed spectra. As a consequence atomic and molecular databases have become essential for developing models and simulations of complex physical processes and for the interpretation of data provided by measurements e.g. in laboratory plasmas and in planetary atmospheres (Marinković et al., 2017b,a; Srećković et al., 2017a). In order to provide a repository of such large amounts of

data, the creation of a Virtual Observatory and Virtual Data Centre has been crucial (Dubernet et al., 2010, 2016; Jevremović et al., 2009; Srećković et al., 2017b).

In this contribution we present two atomic/molecular databases for collisional and radiative processes, BEAMDB and MolD, which are web services at the Serbian Virtual Observatory (SerVO) and nodes within the Virtual Atomic and Molecular Data Centre (VAMDC). The following section gives an overview of databases. A technical specification is described in Section 3 (an example for the data model is given in the appendix), while the Section 4 summarizes the material.

2. Database nodes

The Belgrade nodes of VAMDC are hosted by SerVO and currently contain two atomic/molecular databases of astrophysical importance, BEAMDB (`servo.aob.rs/emol`) and MolD (`servo.aob.rs/molD`). Both databases have been built using the specifications and rules required by the VAMDC project (see Dubernet et al. 2016; Moreau et al. 2018). The Belgrade nodes aim to provide a repository for cross sections and rates for reactions needed for astrophysical plasma modeling.

2.1. MolD

MolD as node of VAMDC contains photodissociation cross sections for the individual ro-vibrational states of the diatomic molecular ions, reaction rate coefficients as well as corresponding data on molecular species and molecular state characterisations. At the moment MolD contains data for photodissociation cross-sections of the molecular ions such as He_2^+ , H_2^+ , MgH^+ , HeH^+ , LiH^+ , NaH^+ , etc., and the corresponding averaged thermal photodissociation cross-sections (for details see e.g. table 1 from Marinković et al. 2017b representing species, states, etc.). The database is hosted at the Belgrade Astronomical Observatory, <http://servo.aob.rs> (Jevremović et al., 2009). The corresponding data are important for exploring the dense molecular clouds in the interstellar medium (ISM), surfaces of small bodies and satellites in our Solar System, modeling of different stellar atmospheres (see the papers Srećković et al. 2018; Vujčić et al. 2015). Collections of such data sets are as well important for the early Universe chemistry and also for understanding the molecular origins of life (Tielens, 2013; Mason et al., 2014).

Recently, the presence of the HeH^+ molecular ion was confirmed by Güsten et al. (2019) in the planetary nebula NGC 7027. These observations were made possible due to advances in terahertz spectroscopy and high-altitude observatories (Heyminck et al., 2012). This confirmation of the existence of HeH^+ in interstellar space requires investigation of this molecular ion, in particular the rates of radiative dissociation and association processes. In Fig. 1 we present

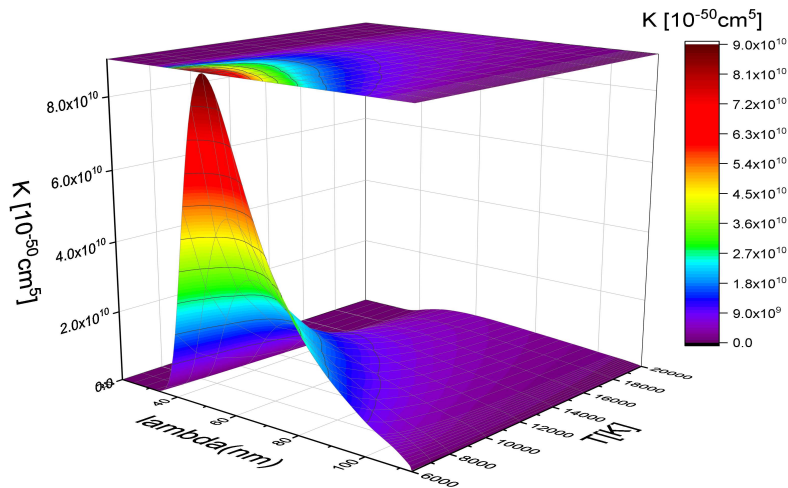


Figure 1. The behaviour of the photodissociation spectral rate coefficients $K(\text{bf})(\lambda; T)$ for the molecular ion HeH^+ .

the behavior of the spectral rate coefficient for photodissociation of the HeH^+ molecular ion. For details e.g. partial photodissociation cross sections for the individual ro-vibrational states and molecular state characterisation see MolD. Of course, here we should mention for example the importance of the results connected with the molecular ion H_2^+ (see Figure 4. from Srećković et al. 2017a) and its role in exploring of the interstellar medium, the early Universe chemistry as well as the modeling of different stellar atmospheres (see e.g. Coppola et al., 2013; Babb, 2015; Srećković et al., 2018).

2.2. BEAMDB

BEAMDB contains measured collisional data for electron interactions with atoms and molecules in the form of differential and integrated cross sections as well as energy loss of the spectra (Marinković et al., 2015). Two types of electron collision processes are featured in the collection, elastic electron scattering and electron excitation of atoms and electronic states of molecules. The BEAMDB is hosted at the Belgrade Astronomical Observatory, <http://servo.aob.rs>. One of the aims of BEAMDB is to collect data sets that are related to the electron interaction process which are important for exploring and modeling of different stellar atmospheres and spectroscopy plasma research (Marinković et al., 2017b). It focuses on atomic targets (neutral or ionized), small molecules (diatomic, triatomic, and four-atomic) as well as larger organic and biomolecules.

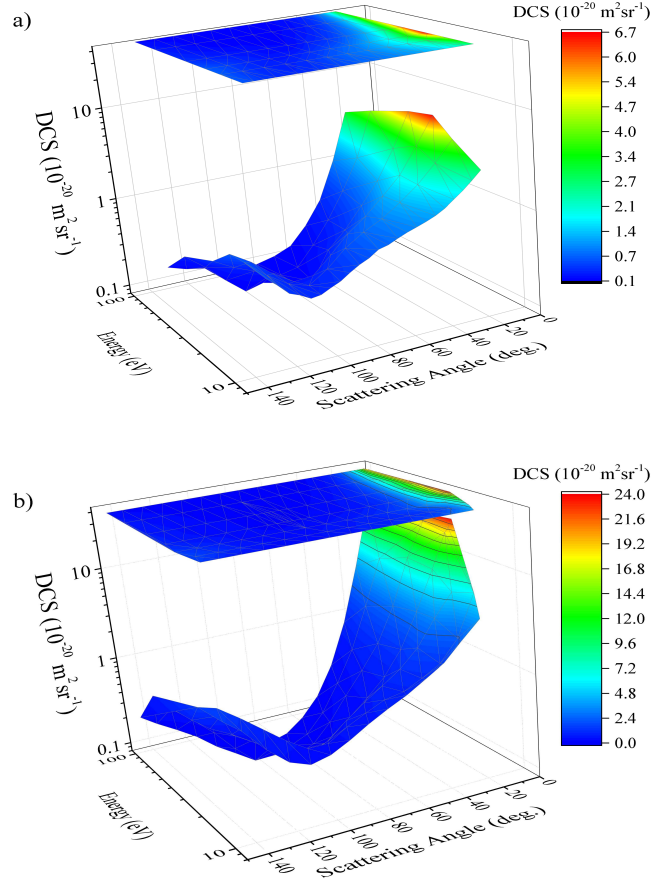


Figure 2. 3-D graph DCS data for electron elastic scattering by nitrous oxide versus electron incident energy and scattering angle. Panel a) data of Marinković and coauthors. panel b) data of Kitajima and coauthors.

Each conference on Spectral Line Shapes in Astrophysics and Plasmas is an opportunity to further develop and enlarge the content of the database with the hot topic atomic/molecular species. Also, special Workshops organized by the scientists in astrophysical and other plasmas contribute to the same aim, just to mention some recent ones: *The new view of comet coma processes after Rosetta: The importance of electrons*, organized at Comenius University; Bratislava in 2017 (Marinković, 2017), *Symposium on the Physics of Ionized Gases* held in 2018 in Belgrade (Marinković et al., 2018) or *Integrations of satellite and ground-*

based observations and multi-disciplinarity in research and prediction of different types of hazards in Solar system in Petnica, Serbia (Marinković *et al.*, 2019).

Comprehensive and up-to-date reviews on electron scattering data have been triennially realised by the IAU Division XII, Commission 14 working group: Atomic collisions (Peach *et al.*, 2009; Peach & Dimitrijević, 2012; Peach *et al.*, 2015). Data covered by BEAMDB for triatomic molecules include H₂O, H₂S and N₂O. An example of a 3-D graph representing differential cross section (DCS) data for electron elastic scattering by nitrous oxide versus electron incident energy and scattering angle is shown in Fig. 2. Two sets of data are presented from Marinković *et al.* (1986) (panel a)) and Kitajima *et al.* (1999) (panel b)) in the energy range from 10 eV to 100 eV. One can easily see the forward peaked nature of the elastic cross sections and the variation of magnitude in three orders. Kitajima *et al.* (2000) have contrasted two sets of data obtained at Sofia University, Tokyo, Japan and at Australian National University, Canberra, Australia, the first ones in the range from 1.5 eV to 100 eV and the second ones from 2 eV to 20 eV. The agreement among these two sets and older measurements is satisfactory having in mind the claimed experimental uncertainties.

3. Node maintenance

The most recent module of the VAMDC infrastructure was Query Store by Zwölf *et al.* (2016) - a mechanism that allows dynamic dataset citation. Adapting the recommendations from the Research Data Alliance (<https://www.rd-alliance.org/groups/data-citation-wg.html>), Query Store grapples with the on-line datasets citation challenges, from ever-evolving data sources. It should enhance visibility of data providers and reproducibility of data sets. Each data response is persisted and versioned so it can be recreated (Moreau *et al.*, 2018) - e.g. for the purpose of scientific verification. Furthermore, Query Store can communicate with other scientific services, such as registering a query to Zenodo and obtaining a DOI, see Zwölf *et al.* (2019).

Technically, Query Store required implementation of a new software layer in the existing NodeSoftware application and a set of asynchronous web services which log data requests (Zwölf *et al.*, 2019). On the side of the Belgrade server, updates of the NodeSoftware Django Web framework were necessary along with minor code alterations.

This contribution presents the continuation of the work performed on database development at Serbian Virtual Observatory. The SerVO is now addressing the challenge of upgrading software and continuous improvements of data processing. New data for targets like triatomic molecules as mentioned above have been constantly added in databases. Although at this moment we concentrate on the intermediate electron energy range from 10 eV to 100 eV (presented in Fig. 2), this range should be enlarged to 1 eV and 1000 eV, while there is an increasing interest towards very low energies, down to below 10 meV

(Kitajima et al., 2019) or to very high energies, up to 100 keV (García, 2019). By decreasing experimental uncertainties and increasing accuracies of theoretical methods, cross section data for rare gas atoms do serve as reference data with the well-established cross sections that may be used as test data in further endeavors.

On the MolD website (<http://servo.aob.rs/mold>), users can also calculate individual average thermal cross sections or plot them across the available spectrum. The fragment of code used for plotting is presented below. The code was shortened for concision. Also, in the appendix we show a sample XSAMS output of a typical query.

```
def plot(request, species_id, temperature):
    #retrieve molecule, processes and belonging wavelengths from the database
    molecule =Molecule.objects.get(inchikey=species_id)
    processes =RadiativeProcess.objects.filter(molecule_state__molecule=molecule)
    wavelengths =[int(i) for i in processes[0].x.data_values.split()]

    #define coefficients
    ...

    #calculate the cross sections for the wavelengths
    for process in processes:
        g =0.5 if (process.molecule_state.n % 2 ==0) else 1.5
        exponent=koef* float(process.molecule_state.energy)

        z +=g *(2 *process.molecule_state.n +1) *math.exp(-(exponent))

        cross_sections =[float(i) for i in process.y.data_values.split()]
        for i, cs in enumerate(cross_sections):
            s[i] +=g *(2 *process.molecule_state.n +1) *math.exp(-(exponent)) *cs

    results =[i/z for i in s]

    #generate random filename
    filename =str(uuid.uuid4()) +'.png'

    #plot and save
    plt.clf()
    plt.plot(wavelengths, results, 'ro')
    ...
    res =["{:.3E}".format(result) for result in results]
    t =filename, wavelengths, res
    return HttpResponse(json.dumps(t))
```

4. Future developments and concluding remarks

On the basis of the above, it can be concluded that analysed collisional and radiative atomic/molecular processes represent an important factor in the investigation of a lot of astrophysical environments and features of the interacting

radiation are important in their spectral analyses. The continuation of developments and services such as atomic/molecular databases and astronomical Virtual Observatories, is crucial in the field of astrophysics and modern science due to its rapid development and makes a huge impact on the way science is done in the developing world.

Acknowledgements. This work is made within projects of the Ministry of Education, Science and Technological Development of Serbia, grant numbers OI176002, III44002. Part of this work has been supported by the VAMDC and the SUP@VAMDC projects funded under the Combination of Collaborative Projects and Coordination and Support Actions Funding Scheme of The Seventh Framework Program. BPM recognizes support from MESTD-RS project OI 171020

References

- Babb, J. F., State Resolved Data for Radiative Association of H and H⁺ and for Photodissociation of H₂⁺. 2015, *Astrophys. J. Suppl. Ser.*, **216**, 21
- Coppola, C. M., Galli, D., Palla, F., Longo, S., & Chluba, J., Non-thermal photons and H₂ formation in the early Universe. 2013, *Mon. Notices Royal Astron. Soc.*, **434**, 114
- Dubernet, M. L., Antony, B. K., Ba, Y. A., et al., The virtual atomic and molecular data centre (VAMDC) consortium. 2016, *J. Phys. B*, **49**, 074003
- Dubernet, M. L., Boudon, V., Culhane, J. L., et al., Virtual atomic and molecular data centre. 2010, *J. Quant. Spectrosc. Radiat. Transf.*, **111**, 2151
- García, G., Invited Talk JS2. 2019, in *Proc. XX International Workshop on Low-Energy Positron and Positronium Physics, XXI International Symposium on Electron-Molecule Collisions and Swarms and V Workshop on Non-Equilibrium Processes POSMOL2019, 18 - 20 July 2019 Belgrade, Serbia, Book of Abstracts*, ed. D. Cassidy & et al., (Serbian Academy of Sciences and Arts and Institute of Physics Belgrade, Serbia, 2019), 7
- Güsten, R., Wiesemeyer, H., Neufeld, D., et al., Astrophysical detection of the helium hydride ion HeH⁺. 2019, *Nature*, **568**, 357
- Heyminck, S., Graf, U., Güsten, R., et al., GREAT: the SOFIA high-frequency heterodyne instrument. 2012, *Astron. Astrophys.*, **542**, L1
- Jevremović, D., Dimitrijević, M. S., Popović, L. Č., et al., The project of Serbian Virtual Observatory and data for stellar atmosphere modeling. 2009, *New Astron. Rev.*, **53**, 222
- Kitajima, M., Ejiri, T., Okumura, T., et al., Topical Lecture EMS 15. 2019, in *Proc. XX International Workshop on Low-Energy Positron and Positronium Physics, XXI International Symposium on Electron-Molecule Collisions and Swarms and V Workshop on Non-Equilibrium Processes POSMOL2019 18 - 20 July 2019 Belgrade, Serbia, Book of Abstracts*, ed. D. Cassidy & et al., (Serbian Academy of Sciences and Arts and Institute of Physics Belgrade, Serbia, 2019), 40

- Kitajima, M., Sakamoto, Y., Gulley, R., et al., Electron scattering from N₂O: absolute elastic scattering and vibrational excitation. 2000, *J. Phys. B*, **33**, 1687
- Kitajima, M., Sakamoto, Y., Watanabe, S., et al., Absolute elastic differential cross-sections for electron scattering by N₂O at 1.5–100 eV. 1999, *Chem. Phys. Lett.*, **309**, 414
- Marinković, B. P., Electron Impact Excitation data for H₂O, N₂O and H₂S triatomic molecules. 2017, in *Book of Abstracts, Workshop: The new view of comet coma processes after Rosetta: The importance of electrons, Comenius University; Bratislava, Slovakia, May 24 to 26 2017*, ed. N. Mason, J. Országh, P. Papp, & Š. Matejčík, The Workshop was organized under the ELEvaTE grant agreement number 692335, 10–11
- Marinković, B. P., Bredehöft, J., Vujčić, V., Jevremović, D., & Mason, N., Rosetta Mission: Electron Scattering Cross Sections-Data Needs and Coverage in BEAMDB Database. 2017a, *Atoms*, **5**, 46
- Marinković, B. P., Ivanović, S., Uskoković, N., & Nešić, M., Electron-impact cross sections for tholins: Coverage within BEAMDB databases. 2019, in *Proc. Integrations of satellite and ground-based observations and multi-disciplinarity in research and prediction of different types of hazards in Solar system*, ed. A. Nina, M. Radovanović, & V. A. Srećković, 10 - 13 May 2019, Petnica Science Center, Valjevo, Serbia, Book of Abstracts (Europlanet 2020 RI NA1 Innovation through Science Networking and Geographical Institute 'Jovan Cvijić' of Serbian Academy of Sciences and Arts, Belgrade, 2019), Abstract of Posters,, 47–48
- Marinković, B. P., Jevremović, D., Srećković, V. A., et al., BEAMDB and MolD - databases for atomic and molecular collisional and radiative processes: Belgrade nodes of VAMDC. 2017b, *Eur. Phys. J. D*, **71**, 158
- Marinković, B. P., Srećković, V. A., Jevremović, D., et al., BEAMDB and MolD Collisional and Radiative Databases at the Serbian Virtual Observatory. 2018, in *Proc. 29th Summer School and Int. Symp. on the Physics of Ionized Gases (SPIG2018), Contributed Papers & Abstracts of Invited Lectures, Topical Invited Lectures, Progress Reports and Workshop Lectures*, ed. G. Poparić, B. Obradović, D. Borka, & M. Rajković, (Vinča Institute of Nuclear Sciences and Serbian Academy of Sciences and Arts, Belgrade, 2018). Contributed Paper, 23–26
- Marinković, B. P., Szymtkowski, C., Pejčev, V., Filipović, D., & Vušković, L., Differential cross sections for elastic and inelastic scattering of electrons by N₂O in the range from 10 to 80 eV. 1986, *J. Phys. B*, **19**, 2365
- Marinković, B. P., Vujčić, V., Sushko, G., et al., Development of collisional data base for elementary processes of electron scattering by atoms and molecules. 2015, *Nucl. Instrum. Methods Phys. Res. B*, **354**, 90
- Mason, N. J., Nair, B., Jheeta, S., & Szymańska, E., Electron induced chemistry: a new frontier in astrochemistry. 2014, *Faraday discussions*, **168**, 235
- Moreau, N., Zwolf, C.-M., Ba, Y.-A., et al., The VAMDC Portal as a Major Enabler of Atomic and Molecular Data Citation. 2018, *Galaxies*, **6**, 105

- Peach, G. & Dimitrijević, M. S., Division XII / Commission 14 / Working Group Collision Processes. 2012, *Transactions of the International Astronomical Union, Series A*, **28**, 371
- Peach, G., Dimitrijević, M. S., & Barklem, P. S., Division B Commission 14 Working Group: Collision Processes. 2015, *Transactions of the International Astronomical Union, Series A*, **29**, 120
- Peach, G., Dimitrijević, M. S., & Stancil, P. C., Division XII / Commission 14 / Working Group Collision Processes. 2009, *Transactions of the International Astronomical Union, Series A*, **27**, 385
- Saldaño, H. P., Rubio, M., Jameson, K., & Bolatto, A. D., Molecular cloud properties in low-metallicity star forming regions. 2018, *Boletín de la Asociación Argentina de Astronomía La Plata Argentina*, **60**, 192
- Srećković, V. A., Dimitrijević, M. S., Ignjatović, L. M., Bezuglov, N., & Klyucharev, A., The Collisional Atomic Processes of Rydberg Hydrogen and Helium Atoms: Astrophysical Relevance. 2018, *Galaxies*, **6**, 72
- Srećković, V. A., Ignjatović, L. M., Jevremović, D., Vujčić, V., & Dimitrijević, M. S., Radiative and Collisional Molecular Data and Virtual Laboratory Astrophysics. 2017a, *Atoms*, **5**, 31
- Srećković, V. A., Jevremović, D., Vujčić, V., et al., Mol-D a Database and a Web Service within the Serbian Virtual Observatory and the Virtual Atomic and Molecular Data Centre. 2017b, in IAU Symposium, Vol. **325**, *Astroinformatics*, ed. M. Brescia, S. G. Djorgovski, E. D. Feigelson, G. Longo, & S. Cavuoti, 393–396
- Tielens, A., The molecular universe. 2013, *Reviews of Modern Physics*, **85**, 1021
- Vujčić, V., Jevremović, D., Mihajlov, A. A., et al., MOL-D: A Collisional Database and Web Service within the Virtual Atomic and Molecular Data Center. 2015, *J. Astrophys. Astron.*, **36**, 693
- Zakharenko, O., Lewen, F., Ilyushin, V. V., et al., Rotational spectroscopy of isotopic species of methyl mercaptan at millimeter and submillimeter wavelengths: CH₃SH. 2019, *Astron. Astrophys.*, **627**, A41
- Zwölf, C. M., Moreau, N., Ba, Y.-A., & Dubernet, M.-L., Implementing in the VAMDC the New Paradigms for Data Citation from the Research Data Alliance. 2019, *Data Science Journal*, **18**
- Zwölf, C. M., Moreau, N., & Dubernet, M.-L., New model for datasets citation and extraction reproducibility in VAMDC. 2016, *J. Mol. Spectrosc.*, **327**, 122

A. Node software

A.1. XSAMS generated output example

A sample query for Lithium cations with specific atomic numbers

```
select * where InchiKey='HSOYNNFNUCWPIZ-UHFFFAOYSA-N' and MoleculeQNJ=1 and MoleculeQNv=5
```

This is an annotated example of an XSAMS document returned from a query. The return data are from the MolD database node. The output was shortened for concision.

```
<?xml version="1.0" encoding="UTF-8"?>
<XSAMSData xmlns="http://vamdc.org/xml/xsams/1.0" xmlns:xsi="http://www.
  w3.org/2001/XMLSchema-instance" xmlns:cml="http://www.xml-cml.org/
  schema" xsi:schemaLocation="http://vamdc.org/xml/xsams/1.0 http://
  vamdc.org/xml/xsams/1.0">
<Sources><Source sourceID="BmolD-2019-07-25-20-5-16">
<Comments>Query was: select * where ((InchiKey = 'HSOYNNFNUCWPIZ-
  UHFFFAOYSA-N')) and MoleculeQNJ=1 and MoleculeQNV=5
Query Store Link: https://querystore.vamdc.eu/GetUUIDByToken?queryToken=
  mold:951f47f7-bdfb-45f0-8939-e7fc9f533a42:get</Comments>
<Year>2019</Year>
<Category>database</Category>
<ProductionDate>2019-07-25</ProductionDate>
</Source>
</Sources>
<Species>
<Molecules>
<Molecule speciesID="XmolD-3">
<MolecularChemicalSpecies>
<OrdinaryStructuralFormula><Value>LiH+</Value></OrdinaryStructuralFormula
  ><StoichiometricFormula>LiH+</StoichiometricFormula>
<ChemicalName><Value>Lithium hydride cation</Value></ChemicalName><InChI>
  1S/Li.H/q+1</InChI><InChIKey>HSOYNNFNUCWPIZ-UHFFFAOYSA-N</InChIKey>
<VAMDCSpeciesID></VAMDCSpeciesID>
<StableMolecularProperties>
</StableMolecularProperties>
</MolecularChemicalSpecies>
<MolecularState auxillary="true" stateID="SmolD-1259"><Description>
  ionized</Description> <MolecularStateCharacterisation> </
  MolecularStateCharacterisation>
<Case xsi:type="case:Case" caseID="dcs" xmlns:case="http://vamdc.org/xml/
  xsams/1.0/cases/dcs"><case:QNs></case:QNs></Case></MolecularState><
  MolecularState auxillary="false" stateID="SmolD-1273"><Description>r
  : 1, v: 5</Description> <MolecularStateCharacterisation><StateEnergy
  energyOrigin="SmolD-1259"><Value units="au">-.243083268582E-04
</Value></StateEnergy> </MolecularStateCharacterisation>
<Case xsi:type="case:Case" caseID="dcs" xmlns:case="http://vamdc.org/xml/
  xsams/1.0/cases/dcs"><case:QNs><case:v>5</case:v><case:J>1</case:J><
  /case:QNs></Case></MolecularState></Molecule>
</Molecules>
</Species>
<Processes>
<Radiative>
<AbsorptionCrossSection id="PmolD-CS1328"><SourceRef>BmolD-3</SourceRef><
  SourceRef>BmolD-4</SourceRef><SourceRef>BmolD-5</SourceRef><
```

```
Description></Description><X units="nm"><DataList count='151'>50 51
52 53 54 55 56 57 58 59 60 ...</DataList></X><Y units="cm2"><
DataList count='151'>0.714843E-21 0.732920E-21 0.750881E-21 0.769486
E-21 0.787933E-21 0.808199E-21 0.827278E-21 0.847998E-21 0.867653E
-21 0.889914E-21 ...
</DataList></Y><Species><SpeciesRef>XmolD-3</SpeciesRef><StateRef>SmolD
-1273</StateRef></Species><BandAssignment></BandAssignment></
AbsorptionCrossSection></Radiative>
</Processes>
</XSAMSData>
```

The collisional atomic processes in geo-cosmical plasmas: data needed for spectroscopy

V.A. Srećković¹, Lj.M. Ignjatović¹, M.S. Dimitrijević^{2,3},
N.N. Bezuglov⁴ and A.N. Klyucharev⁴

¹ *Institute of Physics Belgrade, BU, Pregrevica 118, 11080 Belgrade, Serbia
(E-mail: vlada@ipb.ac.rs)*

² *Astronomical Observatory, Volgina 7, 11060 Belgrade, Serbia*

³ *Sorbonne Université, Observatoire de Paris, Université PSL, CNRS, LERMA, F-92190, Meudon, France (E-mail: mdimitrijevic@aob.rs)*

⁴ *Department of Physics, Saint Petersburg State University, 7/9 Universitetskaya nab., 199034 St. Petersburg, Russia*

Received: July 16, 2019; Accepted: September 29, 2019

Abstract. The rate coefficients for the chemi-ionization (CI) processes in $\text{Na}^*(n) + \text{Na}$, $\text{Li}^*(n) + \text{Na}$, $\text{Li}^*(n) + \text{Li}$ and $\text{H}^*(n) + \text{Li}$ collisions are calculated for wide region of temperatures and the principal quantum numbers. The presented values of the rate coefficients are very useful for the improvement of modelling and analysis of different layers of weakly ionized plasmas in atmospheres of various stars where these and other CI processes could be important and could change the optical characteristics. Also, the results are of interest in spectroscopy of low temperature laboratory plasma.

Key words: Atomic processes – Planets and satellites: general – Line: profiles – Plasmas – ISM: clouds

1. Introduction

Collisional processes which include atoms and molecules in geo-cosmical plasmas, constantly attract attention of scientists (see e.g. Chary et al., 1999; Klyucharev et al., 2007). Among these processes, those involving highly excited Rydberg atoms are of particular interest (Gnedin et al., 2009; O’Keeffe et al., 2012). Primarily this can be attributed to a group of chemi-ionization (CI) processes in Rydberg atom collisions with ground state parent atoms. In a series of papers (Mihajlov et al., 2008; Mihajlov et al., 2011a; Mihajlov et al., 2011b; Mihajlov et al., 2016; Srećković et al., 2018), the group of atom-Rydberg atom collisional processes involving hydrogen and helium have been studied from the point of view of their effect on the optical (spectral line shapes) and kinetic properties of weakly ionized laboratory and astrophysical plasmas.

In this contribution we investigate CI processes for astrophysical usage for the case of alkali metals and give results which enable modeling of geo-cosmic weakly ionized plasma for wide range of plasma parameters. The obtained CI

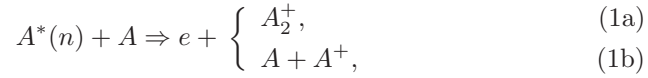
data are needed for modeling and research of cool stars, like white and brown dwarfs (Debes et al., 2012; Xu & Jura, 2014), lithium stars (Shavrina et al., 2001, 2003), sodium clouds around Io (Mendillo et al., 1990; Wilson et al., 2002), cometary tails (Cremonese et al., 2002, 1997), and primordial gas containing Li atoms and ions (Gnedin et al., 2009; Coppola et al., 2011), etc. Also, study of the CI collisional processes of alkali atoms are of basic interest for some laboratory spectroscopic investigation and technical applications (Vujčić et al., 2015; Efimov et al., 2017; Marinković et al., 2017; Pichler et al., 2017; Beuc et al., 2018a,b).

In Section 2 we describe the methods of calculation and then in Section 3 we give the results of the calculation. In Section 4 the conclusions are presented.

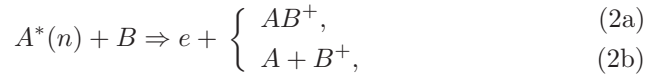
2. Theoretical remarks

2.1. The method of calculations

We will consider two types of CI processes: the symmetric processes



and the non-symmetric processes



where A , B , A^+ and B^+ are atoms and ions in the ground states, $A^*(n)$ is highly excited atom i.e. Rydberg atom, A_2^+ and AB^+ are the molecular ions in the ground electronic states. In Eq. (2) B atoms ionization potential is less than A ionization potential. The CI processes (1) and (2) can be divided to the associative ionization channel (a) with formation of molecular ions A_2^+ or AB^+ and to the non-associative ionization channel (b).

These processes have already been treated on the basis of the so-called dipole resonant mechanism (DRM), so we will briefly describe its main features. In this description of collisional ionisation and excitation events, these processes are induced by the dipole part of the electrostatic interaction between the outer Rydberg electron and the inner ion-atom system (see Fig. 1). A detailed description of the mechanism can be found in Mihajlov et al. (2012).

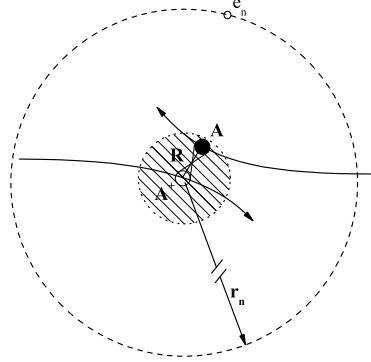


Figure 1. Schematic illustration of RA + A collision. Here R is the internuclear distance in the collision system, $r_n \sim n^2$ is the characteristic radius of Rydberg's atom A^* , e_n is outer electron and A and A^+ are atoms and their positive ions.

2.2. The CI rate coefficients

In accordance with the CI theory the partial rate coefficients $K^{(a)}(n, T)$ and the total ones $K^{(ab)}(n, T)$ can be presented with relations

$$K^{(a)}(n, T) = \int_0^{E_m^{(a)}(n)} v \sigma^{(a)}(n, E) f(v; T) dv, \quad K^{(ab)}(n, T) = \int_0^{\infty} v \sigma^{(ab)}(n, E) f(v; T) dv, \quad (3)$$

where the cross-sections $\sigma^{(a,ab)}(n, E)$ are given in Mihajlov et al. (2012), $E_m^{(a)}(n)$ is the upper limit of E relevant for the associative ionization process (1a) or (2a), and $f(v; T) = f_{cell}(v; T)$ is Maxwell distribution function. The rate coefficient $K^{(b)}(n, T)$ for the process (b) is obtained from $K^{(ab)}(n, T) = K^{(a)}(n, T) + K^{(b)}(n, T)$.

For understanding plasma chemistry and improvement of modelling and analysis of different layers of weakly ionized plasmas in atmospheres of various stars the cross sections and rate coefficients for reactions are needed (Mihajlov et al., 2011c; Srećković et al., 2017, 2018). In this contribution we investigate CI processes for astrophysical usage and give results which enable modeling of geo-cosmic weakly ionized plasma.

3. Results and Applications

3.1. The calculated quantities

In accordance with the described method, we calculate the rate coefficients $K^{(ab)}(n, T)$ for the extended range of principal quantum numbers $n \leq 25$ and temperatures $500 \text{ K} \leq T \leq 1500 \text{ K}$ for the CI processes in $\text{Li}^*(n) + \text{Na}$, $\text{Na}^*(n) + \text{Na}$ collisions, and $500 \text{ K} \leq T \leq 4000 \text{ K}$ for $\text{Li}^*(n) + \text{Li}$ and $\text{H}^*(n) + \text{Li}$ collisions in order to use in modelling and analysis of different layers of weakly ionized plasmas in atmospheres of various stars. We have extended the range of temperatures up to 4 000 K for lithium to enable the possible inclusion of CI processes in modelling of cool stars with low effective temperatures and enormous high Li abundances.

We note that the rate coefficient $K^{(ab)}(n, T)$ (for $\text{Li}^*(n) + \text{Li}$, $\text{Li}^*(n) + \text{Na}$, and $\text{Na}^*(n) + \text{Na}$) has the maximum between $n = 6$ and $n = 10$. The maximum position depend on temperature and moves to lower values of n with the increase of the temperature. A different behavior of $K^{(ab)}(n, T)$ is for the case of $\text{H}^*(n) + \text{Li}$ where the rate coefficient decreases with the increase of n , with different dependence on temperature. In the regions of lower T the process of associative CI, i.e. creation of molecular ions, in (1a) or (2a) collisions dominate in comparison with the non-associative CI channel except for the case of $\text{H}^*(n) + \text{Li}$ collisions where the associative channel is totally negligible for the analyzed conditions.

3.2. Fitting formula

In astrophysics, especially for the modeling of stellar atmospheres, fitting formula and coefficients as functions of temperature are needed, since such fitting coefficients are easier to be imported to the codes for stellar atmosphere modeling than tabulated data for a set of temperatures. To enable easy and more adequate use in laboratory as well as to allow a faster computation in stellar atmospheres modeling we construct a fitting formula. The results are in the form of a simple fitting formula:

$$\log(K^{(ab)}(n; T)) = k_1(n) + k_2(n) \cdot \log(T) + k_3(n) \cdot (\log(T))^2. \quad (4)$$

In Tabs. 1 and 2 the selected fits for $4 \leq n \leq 25$ are listed for the total rate coefficients of CI processes (1) and (2). It should be noted that fits in Tab. 1 are valid within the temperature range $500 \text{ K} \leq T \leq 1500 \text{ K}$ for $\text{Li}^*(n) + \text{Na}$, $\text{Na}^*(n) + \text{Na}$ collisions and in Tab. 2 are valid within the temperature range $500 \text{ K} \leq T \leq 4000 \text{ K}$ for $\text{Li}^*(n) + \text{Li}$ and $\text{H}^*(n) + \text{Li}$ collisions.

Table 1. The fits to the rate coefficient. The fits were made to the results over the range $500 \text{ K} \leq T \leq 1500 \text{ K}$.

n	$\text{Li}^*(n) + \text{Na}$			$\text{Na}^*(n) + \text{Na}$		
	k1	k2	k3	k1	k2	k3
4	-41.35531	18.67062	-2.69225	-46.51493	21.4718	-3.10971
5	-16.97267	4.48624	-0.58834	-29.28982	11.44201	-1.62003
10	-14.06446	2.72686	-0.34263	-11.58289	1.24937	-0.11571
15	-15.367	3.08165	-0.40038	-9.68059	0.23985	0.00292
20	-15.80875	2.96859	-0.38137	-9.50371	0.07705	0.00612
22	-15.8578	2.86113	-0.36295	-9.31387	-0.10334	0.03144
25	-16.2462	2.93717	-0.37582	-9.38528	-0.14156	0.03217

Table 2. Same as in Tab.1 but over the temperature range $500 \text{ K} \leq T \leq 4000 \text{ K}$.

n	$\text{Li}^*(n) + \text{Li}$			$\text{H}^*(n) + \text{Li}$		
	k1	k2	k3	k1	k2	k3
4	-35.12844	14.13288	-1.89755	-5.79278	-1.1651	0.13442
5	-23.31012	7.66745	-0.99756	-6.22763	-1.12647	0.12474
10	-11.29713	1.25562	-0.12888	-7.78576	-1.05661	0.11177
15	-9.71227	0.36138	-0.0305	-8.67836	-1.04816	0.11043
20	-9.45545	0.06564	0.00121	-9.23865	-1.08876	0.11676
22	-9.46101	0.00324	0.00775	-9.46812	-1.07506	0.11468
25	-9.5051	-0.07041	0.01609	-9.75651	-1.06821	0.11363

3.3. Astrophysical Targets

3.3.1. Li-rich stars

Study of CI processes may be of interest for the investigation and modelling of plasma in cold lithium stars (see North et al., 1998; Shavrina et al., 2001, 2003). Recently Li et al. (2018) found high-lithium abundance in newly discovered 12 low-mass, metal-poor, main-sequence stars, and in red giant stars in the Milky Way halo. Collisional processes including CI could be of interest for studying of lithium-rich stellar atmospheres as an additional canal for the creation of Li I atoms. The considered CI processes influence as well the ionization level and atom excited-state populations, so that they could affect the optical properties of the weakly ionized regions of alkali rich plasmas.

As it is known lithium is easily ionized and in the spectra of cool stars the Li I resonance line 6707.8 \AA is commonly observed. The lithium abundance data in such stars are mostly acquired from the spectral analysis of this particular line. The investigated CI processes, which influence atom excited-state populations and the ionization level, influence the optical properties and could be important

for the lithium spectra. Consequently the CI processes could be important for atmospheres of lithium-rich stars as an supplementary channel for the creation of the lithium atoms and RA atom populations. We give the data for extended range of temperatures for the calculation for lithium (see Tab. 2) to enable the possible inclusion of CI processes in $\text{Li}^*(n) + \text{Li}$ and $\text{H}^*(n) + \text{Li}$ collisions in modeling of cool stars with low effective temperatures ($T_{\text{eff}} \leq 6000$ K) and enormous high Li abundances (Li et al., 2018).

3.3.2. Primordial gas

It is known that in the early Universe the chemical composition of the primordial gas contained lithium, and during the cooling of Universe there is an epoch when conditions for presently investigated RA collisional processes were favorable (Gnedin et al., 2009; Puy et al., 2007). Collisional recombination, ionization and Rydberg states can play important role for the early Universe chemistry (Coppola et al., 2011). As concluded in (Coppola et al., 2011; Puy et al., 2007) LiH^+ represents the most abundant molecular species containing lithium at low redshift. Consequently, data on rate coefficients for CI processes in atom - Rydberg atom collisions of Li atoms presented in Tab. 2, may be of interest for the early Universe chemistry. We therefore computed the necessary quantities.

3.3.3. Io atmosphere

In Brown & Chaffee (1974) the first neutral sodium cloud near Jovian satellite Io has been detected (see also paper Brown, 1974; Fegley & Zolotov, 2000). Since the investigation of these sodium clouds are necessary to better understand the interaction between Io's atmosphere and Jovian magnetosphere and the processes in the Jovian surroundings (Mendillo et al., 1990; Wilson et al., 2002), the data on CI processes during alkali RA collisions may be of interest. In a recent paper Schaefer & Fegley (2005), authors estimated and expected abundance of lithium at Io.

The obtained CI rate coefficient $K^{(ab)}(n, T)$ (see Tab. 1) are calculated for a wide range of plasma parameter important for the models of Io's atmospheres (Strobel et al., 1994). CI processes may be important and could be used for accurately modelling and computer simulations. The investigation of these processes is needed for better understanding of the interaction between the Io's atmosphere and Jovian magnetosphere and of the processes in the Jovian environment. In Fig 2 the density and temperature altitude profiles for moderate-density (on panel a) left), and high-density (on panel a) right) of Io model atmospheres (Strobel et al., 1994; Moses et al., 2002) are presented. The Fig. 2 (panels b), c), d)) shows the total rate coefficient $K_{ci}^{(ab)}(n, T)$ for CI processes in $\text{Li}^*(n) + \text{Na}$, $\text{Li}^*(n) + \text{Li}$ and $\text{Na}^*(n) + \text{Na}$ collisions for modeled atmospheres of Io (Strobel et al., 1994; Moses et al., 2002). For both models it can be observed the growth of coefficients at higher altitudes. Also, one can see that the rate

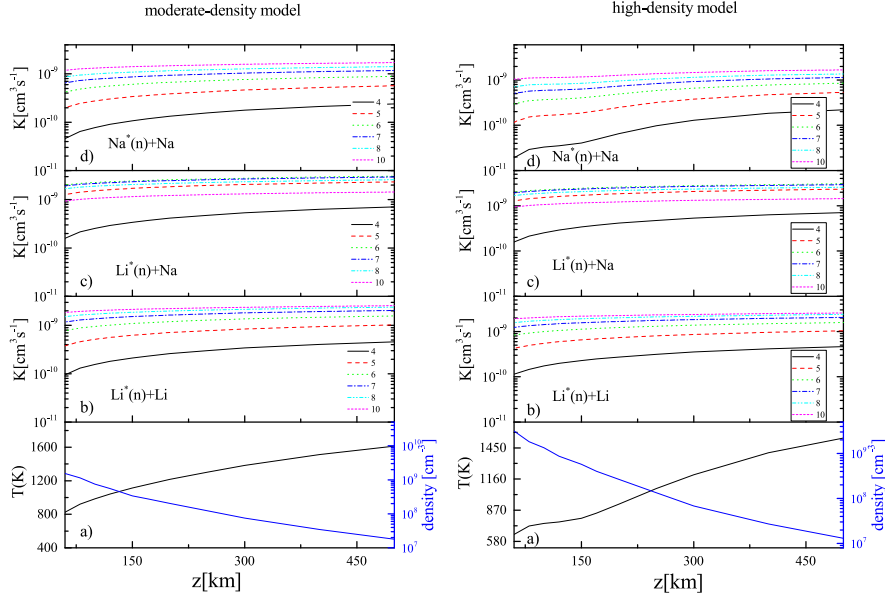


Figure 2. (left) Moderate-density model atmosphere of Io: the total rate coefficient $K_{ci}^{(ab)}(n, T)$ for CI processes in $\text{Li}^*(n) + \text{Na}$, $\text{Li}^*(n) + \text{Li}$ and $\text{Na}^*(n) + \text{Na}$ altitude profiles (panels b,c,d) for the corresponding model (a) (Strobel et al., 1994); (right) High-density model atmosphere of Io: the total rate coefficient $K_{ci}^{(ab)}(n, T)$ for CI processes in $\text{Li}^*(n) + \text{Na}$, $\text{Li}^*(n) + \text{Li}$ and $\text{Na}^*(n) + \text{Na}$ altitude profiles (panels b,c,d) for the corresponding model (a) (Strobel et al., 1994).

coefficients increase with the increase of the principal quantum number n and that they are the largest for the non-symmetric collisions.

3.3.4. Interstellar gas chemistry

The CI processes i.e. its associative channel (1(a) and 2(a)), are responsible for the formation of molecular ions and potentially important for molecular formations in interstellar gas (Dalgarno & Black, 1976). For knowing interstellar gas chemistry and for models of interstellar clouds the cross sections and rate coefficients for reactions (Srećković et al., 2018) are needed. The data for molecular ions LiNa^+ , LiH^+ , Li_2^+ and Na_2^+ are given and analysed in this contribution. The relative contribution (probability) of the associative channels (i.e. creation of molecular ions) are presented in Fig. 3 on the example of $\text{Na}^*(n) + \text{Na}$, $\text{Li}^*(n) + \text{Na}$, $\text{Li}^*(n) + \text{Li}$ collisions. As expected the probability for the creation of molecular ions as CI product is noticeable and higher at lower temperatures

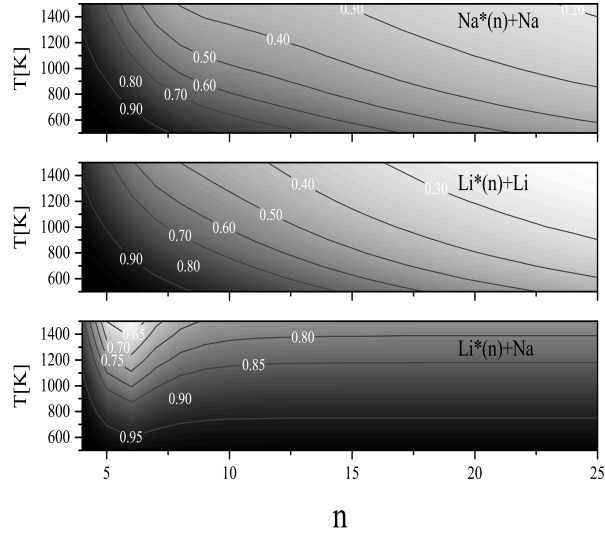


Figure 3. The surface plot of the quantity $K^{(a)}(n, T)/K^{(ab)}(n, T)$ i.e. probability of creation of molecular ions A_2^+ and AB^+ in CI collisions.

and n (see Fig. 3). Unlike presented cases in $H^*(n) + Li$ collisions the associative channel is totally negligible for the analyse conditions and consequently this channel could not be the main source of the LiH^+ molecular ion creation.

4. Summary

In this paper the rate coefficients for the CI processes in $Li^*(n) + Na$, $Li^*(n) + Li$, $H^*(n) + Li$ and $Na^*(n) + Na$ collisions were calculated. In order to enable the better and more adequate use of data, we present the results for the rate coefficients with a simple and accurate fitting formula. The calculated data have been applied to the models of atmosphere of Io. Also, the obtained rate coefficients could be very useful for the upgrading of modelling of different weakly ionized layers in atmospheres of various stars (solar like stars, lithium stars, etc) and low temperature laboratory plasmas. Note that the presented results indicate that considered CI processes are factors which influence on the ionization degree and atom excited-state populations in weakly ionized layers of atmospheres of various stars and must have a very significant influence on the optical properties of investigated atmospheres.

Acknowledgements. This work is made within projects of the Ministry of Education, Science and Technological Development of Serbia 176002 and III44002.

References

- Beuc, R., Movre, M., & Pichler, G., High Temperature Optical Spectra of Diatomic Molecules at Local Thermodynamic Equilibrium. 2018a, *Atoms*, **6**, 67
- Beuc, R., Peach, G., Movre, M., & Horvatić, B., Lithium, sodium and potassium resonance lines pressure broadened by helium atoms. 2018b, *Astron. Astrophys. Tran.*, **30**, 315
- Brown, R. A. & Chaffee, Jr., F. H., High-Resolution Spectra of Sodium Emission from Io. 1974, *Astrophys. J., Lett.*, **187**, L125
- Brown, R. A., Optical line emission from Io. 1974, in IAU Symposium, Vol. **65**, *Exploration of the Planetary System*, ed. A. Wozczyk & C. Iwaniszewska, 527–531
- Chary, R., Zuckerman, B., & Becklin, E. E., Observational constraints on the origin of metals in cool DA-type white dwarfs. 1999, in ESA Special Publication, Vol. **427**, *The Universe as Seen by ISO*, ed. P. Cox & M. Kessler, 289
- Coppola, C. M., Lodi, L., & Tennyson, J., Radiative cooling functions for primordial molecules. 2011, *Mon. Not. R. Astron. Soc.*, **415**, 487
- Cremonese, G., Boehnhardt, H., Crovisier, J., et al., Neutral Sodium from Comet Hale-Bopp: A Third Type of Tail. 1997, *Astrophys. J., Lett.*, **490**, L199
- Cremonese, G., Huebner, W. F., Rauer, H., & Boice, D. C., Neutral sodium tails in comets. 2002, *Adv. Space Res.*, **29**, 1187
- Dalgarno, A. & Black, J. H., Molecule formation in the interstellar gas. 1976, *Rep. Prog. Phys.*, **39**, 573
- Debes, J. H., Walsh, K. J., & Stark, C., The link between planetary systems, dusty white dwarfs, and metal-polluted white dwarfs. 2012, *Astrophys. J.*, **747**, 148
- Efimov, D., Bruvelis, M., Bezuglov, N., et al., Nonlinear Spectroscopy of Alkali Atoms in Cold Medium of Astrophysical Relevance. 2017, *Atoms*, **5**, 50
- Fegley, B. & Zolotov, M. Y., Chemistry of Sodium, Potassium, and Chlorine in Volcanic Gases on Io. 2000, *Icarus*, **148**, 193
- Gnedin, Y. N., Mihajlov, A. A., Ignjatović, L. M., et al., Rydberg atoms in astrophysics. 2009, *New Astron. Rev.*, **53**, 259
- Klyucharev, A. N., Bezuglov, N. N., Matveev, A. A., et al., Rate coefficients for the chemi-ionization processes in sodium- and other alkali-metal geocosmical plasmas. 2007, *New Astron. Rev.*, **51**, 547
- Li, H., Aoki, W., Matsuno, T., et al., Enormous Li Enhancement Preceding Red Giant Phases in Low-mass Stars in the Milky Way Halo. 2018, *Astrophys. J., Lett.*, **852**, L31
- Marinković, B. P., Jevremović, D., Srećković, V. A., et al., BEAMDB and MolD—databases for atomic and molecular collisional and radiative processes: Belgrade nodes of VAMDC. 2017, *Eur. Phys. J. D*, **71**, 158

- Mendillo, M., Baumgardner, J., Flynn, B., & Hughes, W. J., The extended sodium nebula of Jupiter. 1990, *Nature*, **348**, 312
- Mihajlov, A., Ignjatović, L. M., Srećković, V., & Djurić, Z., The influence of (n-n')-mixing processes in $\text{He}^*(n) + \text{He} (1s^2)$ collisions on $\text{He}^*(n)$ atoms populations in weakly ionized helium plasmas. 2008, *J. Quant. Spectrosc. Radiat. Transf.*, **109**, 853
- Mihajlov, A. A., Ignjatović, L. M., Srećković, V. A., & Dimitrijević, M. S., Chemi-ionization in Solar Photosphere: Influence on the Hydrogen Atom Excited States Population. 2011a, *Astrophys. J., Suppl.*, **193**, 2
- Mihajlov, A. A., Ignjatović, L. M., Srećković, V. A., & Dimitrijević, M. S., The influence of chemi-ionization and recombination processes on spectral line shapes in stellar atmospheres. 2011b, *Open Astron.*, **20**, 566
- Mihajlov, A., Sakan, N., Srećković, V., & Vitel, Y., Modeling of continuous absorption of electromagnetic radiation in dense partially ionized plasmas. 2011c, *J. Phys. A*, **44**, 095502
- Mihajlov, A. A., Srećković, V. A., Ignjatović, L. M., & Dimitrijević, M. S., Atom-Rydberg-atom chemi-ionization processes in solar and DB white-dwarf atmospheres in the presence of (n - n')-mixing channels. 2016, *Mon. Not. R. Astron. Soc.*, **458**, 2215
- Mihajlov, A. A., Srećković, V. A., Ignjatović, L. M., & Klyucharev, A. N., The Chemi-Ionization Processes in Slow Collisions of Rydberg Atoms with Ground State Atoms: Mechanism and Applications. 2012, *J. Clust. Sci.*, **23**, 47
- Moses, J. I., Zolotov, M. Y., & Fegley, B., Photochemistry of a Volcanically Driven Atmosphere on Io: Sulfur and Oxygen Species from a Pele-Type Eruption. 2002, *Icarus*, **156**, 76
- O'Keeffe, P., Bolognesi, P., Avaldi, L., et al., Experimental and theoretical study of the chemi-ionization in thermal collisions of Ne Rydberg atoms. 2012, *Phys. Rev. A*, **85**, 052705
- North, P., Polosukhina, N., Malanushenko, V., & Hack, M., The AP star HD 83368 may be a lithium-spotted pulsator. 1998, *Astron. Astrophys.*, **333**, 644
- Pichler, G., Makdisi, Y., Kokaj, J., et al., Superheating effects in line broadening of dense alkali vapors. 2017, in *J. Phys. Conf. Ser.*, Vol. **810**, *Journal of Physics Conference Series*, 012013
- Puy, D., Dubrovich, V., Lipovka, A., Talbi, D., & Vonlanthen, P., Molecular fluorine chemistry in the early Universe. 2007, *Astron. Astrophys.*, **476**, 685
- Schaefer, L. & Fegley, B., Alkali and halogen chemistry in volcanic gases on Io. 2005, *Icarus*, **173**, 454
- Shavrina, A. V., Polosukhina, N. S., Pavlenko, Y. V., et al., The spectrum of the roAp star HD 101065 (Przybylski's star) in the Li I 6708 Å spectral region. 2003, *Astron. Astrophys.*, **409**, 707

- Shavrina, A. V., Polosukhina, N. S., Zverko, J., et al., Lithium on the surface of cool magnetic CP stars. II. Spectrum analysis of HD 83368 and HD 60435 with lithium spots. 2001, *Astron. Astrophys.*, **372**, 571
- Srećković, V., Dimitrijević, M., Ignjatović, L., Bezuglov, N., & Klyucharev, A., The Collisional Atomic Processes of Rydberg Hydrogen and Helium Atoms: Astrophysical Relevance. 2018, *Galaxies*, **6**, 72
- Srećković, V., Ignjatović, L., Jevremović, D., Vujčić, V., & Dimitrijević, M., Radiative and Collisional Molecular Data and Virtual Laboratory Astrophysics. 2017, *Atoms*, **5**, 31
- Strobel, D. F., Zhu, X., & Summers, M. F., On the vertical thermal structure of Io's atmosphere. 1994, *Icarus*, **111**, 18
- Vujčić, V., Jevremović, D., Mihajlov, A. A., et al., MOL-D: A Collisional Database and Web Service within the Virtual Atomic and Molecular Data Center. 2015, *J. Astrophys. Astron.*, **36**, 693
- Wilson, J. K., Mendillo, M., Baumgardner, J., et al., The Dual Sources of Io's Sodium Clouds. 2002, *Icarus*, **157**, 476
- Xu, S. & Jura, M., The Drop during Less than 300 Days of a Dusty White Dwarf's Infrared Luminosity. 2014, *Astrophys. J., Lett.*, **792**, L39

Autoionization widths of cold Rydberg atomic complexes

M.S. Dimitrijević^{1,2}, V.A. Srećković³, Alaa Abo Zalam^{4,5},
K. Miculis^{6,7}, D.K. Efimov⁸, N.N. Bezuglov⁴ and A.N. Klyucharev⁴

¹ *Astronomical Observatory, Volgina 7, 11060 Belgrade, Serbia, (E-mail: mdimitrijevic@aob.rs)*

² *Sorbonne Université, Observatoire de Paris, Université PSL, CNRS, LERMA, F-92190, Meudon, France*

³ *Institute of Physics Belgrade, Pregrevica 118, 11080 Zemun, Belgrade, Serbia*

⁴ *Saint Petersburg State University, 7/9 Universitetskaya nab., St. Petersburg, 199034, Russia*

⁵ *Physics Department, Faculty of Science, Menoufia University, Menoufia, Egypt*

⁶ *University of Latvia, Institute of Atomic Physics and Spectroscopy, LV-1586 Riga, Latvia*

⁷ *Moscow State Engineering Physics Institute, Kashirskoe shosse 31, Moscow 115409, Russia*

⁸ *Instytut Fizyki im. Mariana Smoluchowskiego, Uniwersytet Jagielloński, 30-348 Kraków, Poland*

Received: July 10, 2019; Accepted: August 22, 2019

Abstract. We have considered two types of interactions between particles resulting in autoionization of the intermediate Rydberg collisional complex. The first type is caused by the charge exchange processes inside the ionic core of the complex and is responsible for the formation of the final associative ionization channel due to the departure of a Rydberg electron (RE) of the complex to the energy continuum. We have investigated the evolution of the orbital momentum L of RE and discovered a non-trivial time dependence of L , demonstrating a contrasting oscillatory structure in both direction orientation and its absolute value. The second type of interaction, dipole-dipole interaction, dominates in cold highly excited gaseous media and leads to Penning ionization of various pairs of Rydberg atoms. We have found the optimal quantum configurations of atomic pairs, which intensify the PI rates by several orders of magnitude, and become important suppliers of charged particles upon the evolution of Rydberg gas into cold plasma.

Key words: Atomic processes – Line: profiles – Plasmas

1. Introduction

In scientific literature, up until the early 1980s, astrophysical research largely focused on such global issues as star formation problems, planetary nebulae, and interstellar gas physics (Dalgarno, 1975). Currently, the subject of elementary collisional processes involving light and matter particles in the geospace environment is attracting more and more attention (see the results of the space mission 'Galileo Mission to Jupiter 1989-2003', Lopes & Williams 2005). Modern experimental techniques make it possible to compare the rate constants of various reactions obtained in the geospace environment with their terrestrial analogues (Gnedin et al., 2009), for example, for ion-recombination collisions in cold helium-saturated atmospheres of cooling stars of the White Dwarf type (DB White dwarfs, Mihajlov et al., 2003). Recombination processes result in populating highly excited states and are the important sources of the formation of Rydberg atoms/molecules in stellar atmospheres of late spectral types, interstellar nebulae and other space objects, including our solar system (see, for instance, Dalgarno 1975; Graham et al. 2012). The appearance of Rydberg particles plays a fundamental role in the Earth's lower ionosphere. In many situations (e.g., when solar flares occur) it exerts an uncontrollable influence on the propagation of satellite radio signals from the global positioning system (GPS, Buenker et al., 2013).

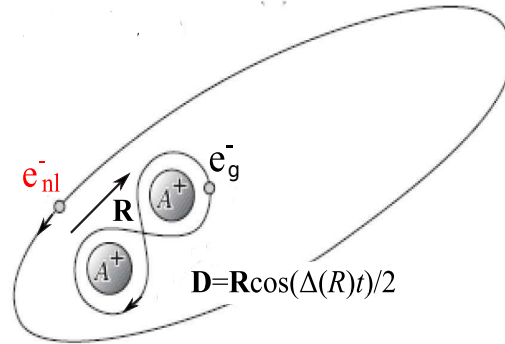
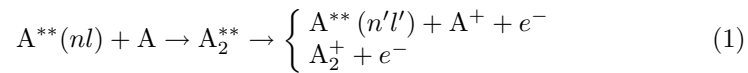


Figure 1. Schematic representation of the intermediate collisional complex A_2^{**} structure formed in the course of the reaction (1).

Autoionization processes of Rydberg atomic complexes A_2^{**} are inverse to recombination channels and may occur as intermediate states



in various collisional events involving atom A in the normal state and Rydberg atom $A^{**}(nl)$ with the principal and orbital quantum numbers n and l respectively. The theory for describing processes (1), which was called dipole resonance ionization (DRI), was based on Fermi's proposal (Fermi, 1934) to consider the intermediate formation A_2^{**} as a structure (see Fig. 1), consisting of positively charged atomic cores A^+ , generalized valence electron e_g^- of atom A and quasi-free Rydberg electron (RE) e_{nl}^- in a Keplerian orbit with binding energy $\varepsilon_{nl} = 1/2n^{*2}$, where n^* is the effective quantum number. Within the DRI model, the probability of realization of various output channels (the Penning channel and the associative channel) of reaction (1) is determined by the internal dipole moment \mathbf{D} of quasimolecule A_2^{**} . Moment $\mathbf{D} = \mathbf{R}(t) \cos(\Delta(R)t)/2$ arises in the process of recharging in the system ($A+A^+$) when changes in both the internuclear distance $\mathbf{R}(t)$ and the recharge frequency $\omega(t) = \Delta(R(t))$ are adiabatically slow (Janev & Mihajlov, 1980). Alternating dipole \mathbf{D} induces a quasi-monochromatic field $\mathbf{E}(t)$ that perturbs RE motion e_{nl}^- and leads to its "photoionization" as soon as frequency $\Delta(R)$ becomes greater than the RE binding energy ε_{nl} . The system is traditionally described in the adiabatic approximation using the corresponding potential curves of Rydberg complex A_2^{**} formed by RE e_{nl}^- and molecular ion A_2^+ (see Fig. 2).

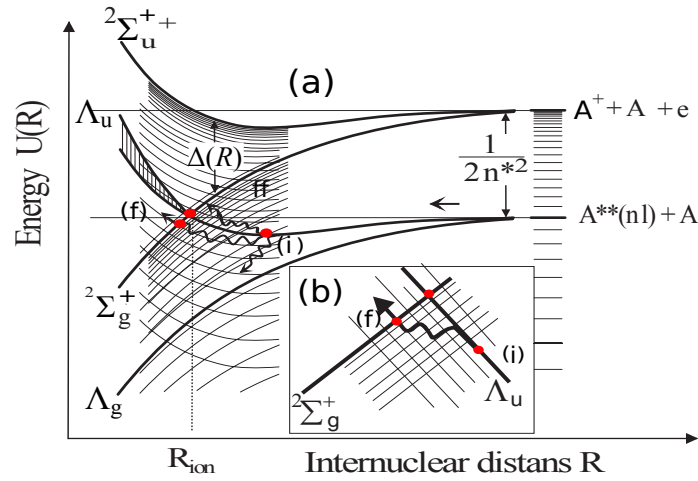


Figure 2. Illustration of the development of diffusion ionization in a quasi-molecule formed in the collision of two alkali metal atoms in the ground state A and in the highly excited state $A^{**}(nl)$. Box (b) shows one of the many possible evolutions of the initial excitation of a diatomic system.

Highly excited systems have specific features, when they interact with electromagnetic fields, due to the Coulomb condensation of quantum states near the

energy continuum. Both the Stark and the Zeeman effects cause multiple quasi-intersections of the Rydberg electron sublevels, which leads to RE chaotic motion along the dense grid of Rydberg states (see Fig. 2(b)) with the subsequent exit into the energy continuum. Such uncontrolled dynamic chaos (Zaslavsky, 2007) in the evolution of Hamiltonian systems is observed for single Rydberg atoms under the influence of external microwave fields (Koch & Van Leeuwen, 1995; Krainov, 2010), as well as for collisional Rydberg complexes with a strong intra-atomic dipole interaction (Klyucharev et al., 2007). In the case of molecular systems, diffusion migration of initial excitation can lead to dissociation of molecules (Dashevskaya et al., 2002).

Various aspects of the autoionization processes of Rydberg atomic formations were considered in works Gnedin et al. (2009); Klyucharev et al. (2007). They demonstrate, in particular, the important role of the dynamic chaos development for various ionization phenomena occurring in cold astrophysical environments. In continuation of these studies, in this article we present new numerical and analytical data related to the following problems. (i) Analysis of the nontrivial temporal dynamics of the angular momentum $L(t)$ of a Rydberg electron in electromagnetic fields, and (ii) the influence of this dynamics on the efficiency of the diffusion ionization. (iii) Analysis of constant rates Γ_N of the Penning autoionization of quasi-molecules formed by two cold Rydberg sodium atoms in different quantum states N , subject to the long-range dipole-dipole interaction.

Henceforth the atomic system of units is used, unless otherwise stated.

2. The problem of the Rydberg electron orbital momentum conservation upon diffusion ionization

The temporal evolution of the orbital momentum \mathbf{L} of the Rydberg intermediate complex largely determines the character and properties of atom-atom collisions of type (1). In the quasi-classical approximation, the absolute value \mathbf{L} is given by the relation $L = |\mathbf{L}| = l + 0.5$, where the term 0.5 is called the Langer correction (Landau & Lifshitz, 1977). In both the early Koch & Van Leeuwen (1995); Delone et al. (1983) and comparatively recent papers Krainov (2010); Bezuglov et al. (2002), which laid foundation for the studies on the dynamic stochasticization of highly excited states under the influence of microwave radiation, the authors relied on the important assumption of adiabatic invariance of L . This assumption was later questioned in Golubkov & Devdariani (2011). Within the framework of the theory of a multichannel quantum defect, this work demonstrated a change in the orbital quantum number l during inelastic collisions of heavy particles going through an intermediate state of a molecular ion. Another example refers to L-mixing processes in D-stratum of the Earth's atmosphere, which, *inter alia*, leads to occurrence of 'spectral windows' for incoherent radiation (Buenker et al., 2013).

Noteworthy is an important result in Bezuglov *et al.* (2002), which allows us to reduce the analysis of the effects of RE e_{nl}^- motion perturbation due to the intramolecular electric field $\mathbf{E}(t)$ (see the discussion of Fig. 1) to the case of a spatially homogeneous quasi-monochromatic microwave field influencing RE. This section investigates various aspects of the momentum L conservation for the corresponding model Hamiltonian

$$H(\mathbf{p}, \mathbf{r}, t) = \frac{\mathbf{p}^2}{2} - 1/r + (\mathbf{E}(t) \cdot \mathbf{r}); \quad (2)$$

$$\mathbf{E}(t) = \mathbf{E}_0 \cos(\omega_0 t + \theta), \quad (3)$$

which describes the interaction of a hydrogen atom with an external microwave field of frequency ω_0 and vector amplitude \mathbf{E}_0 .

2.1. The hydrogen atom in a slowly varying electric field

The main features of the dynamics of the angular momentum \mathbf{L} can be observed in a relatively simple and analytically solvable example of an almost stationary field (ω_0 is enough small - see below) with RE moving regularly. In the range of moderate amplitudes $E_0 = |\mathbf{E}_0|$ (see below), it is convenient to find the evolution of vector $\mathbf{L}(t)$ in the adiabatic approximation by averaging the equation for the rate of change $d\mathbf{L}/dt$ along the Coulomb electron trajectory: $d/dt \langle \mathbf{L} \rangle = -[\langle \mathbf{r} \rangle \mathbf{E}_0]$ (symbol $\langle \dots \rangle$ means averaging). The moderate disturbance implies minor changes in the parameters of the RE Keplerian orbits $\mathbf{r}(t)$ for the period $T = 2\pi n^3$ of classical motion. Here, a quasi-classical approach Landau & Lifshitz (1977) is used, in which, in accordance with Bohr's correspondence principle, the state with quantum numbers $\{n, l, m\}$ is juxtaposed with the classical trajectory with the following motion integrals (Landau & Lifshitz, 1976): energy $\varepsilon = -1/2n^2$, the modulus of angular momentum $L = l + 0.5$, and the projection $L_{pl} = m$ (m is azimuthal quantum number) on the direction of the polarization vector $\mathbf{e}_{pl} = \mathbf{E}_0/E_0$ of the external field.

It is easy to show that the mean value $\langle \mathbf{r} \rangle$ is directed along the semimajor axis (length $a = n^2$) of the Keplerian ellipse and, therefore, is expressed $\langle \mathbf{r} \rangle = 3a \cdot \langle \mathbf{A} \rangle / 2$ in terms of the Runge-Lenz vector (Laplace integral) $\mathbf{A} = [\mathbf{v}_e \mathbf{L}] - (\mathbf{r}/r)$ (Landau & Lifshitz, 1976) where \mathbf{v}_e is the RE velocity. The equation for evolution $\langle \mathbf{L} \rangle$, therefore, includes the average $\langle \mathbf{A} \rangle$, i.e.

$$\frac{d\langle \mathbf{L} \rangle}{dt} = -\frac{3}{2}a [\mathbf{E}_0 \langle \mathbf{A} \rangle]. \quad (4)$$

Evolution $\langle \mathbf{A} \rangle$, in turn, is related to vector $\langle \mathbf{L} \rangle$ (Landau & Lifshitz, 1976)

$$\frac{d\langle \mathbf{A} \rangle}{dt} = -\frac{3}{2} [\mathbf{E}_0 \langle \mathbf{L} \rangle]. \quad (5)$$

Note that $d\langle\varepsilon\rangle/dt = 0$, and the length $a = n^2 = n_0^2$ of the semimajor axis undergoes no evolution and remains adiabatically unchanged. Hereinafter, index '0' indicates the original (unperturbed) values of physical quantities at the moment of switching an external field. The closed system of equations (4) and (5) is reduced to two independent equations after the transition to new variables \mathbf{G}_\pm and the rescaling of time:

$$\mathbf{G}_\pm = n_0\langle\mathbf{L}\rangle \pm n_0^2\langle\mathbf{A}\rangle; \quad \tau = n_0t; \quad (6)$$

$$\frac{d}{d\tau}\mathbf{G}_\pm = \pm\frac{3}{2}[-\mathbf{E}_0\mathbf{G}_\pm]. \quad (7)$$

Equations (7) have an obvious geometric interpretation: vectors \mathbf{G}_\pm rotate around vector $-\mathbf{E}_0$ in the opposite directions with the circular frequency of the same modulus $\Omega_\tau = (3/2)E_0$ in units $1/\tau$ or $\Omega_t = (3/2)n_0E_0$ in units $1/t$. The corresponding revolution time is $T_E = 8\pi/(3n_0E_0)$. The validity range of equations (4)-(7) of our adiabatic model follows from two requirements: (i) smallness of rotation angles $\Delta\theta = \Omega_t T < 2\pi$ of vectors \mathbf{G}_\pm for the RE period of motion $T = 2\pi n_0^3$ and (ii) smallness of the field frequency ω_0 that may be expressed as

$$\omega_0 < 1.5E_0n_0 < 1/n^3. \quad (8)$$

Fields satisfying inequality (8) can be considered moderate, although they overlap the critical field value $E_{\text{cr}} = n_0^{-4}/16$, at which classical atom ionization occurs (Delone et al., 1983).

The modulus value $|\mathbf{A}|$ is equal to the eccentricity $|\mathbf{A}| = \sqrt{1 - (L/n_0)^2}$ of the Keplerian orbit (Landau & Lifshitz, 1976), and therefore for Rydberg states ($n_0 \gg 1$), the initial value $|\mathbf{A}_0|$ is close to unity. If we limit ourselves to the typical for experiments case of small values $l_0 \sim 1 \ll n_0$, then

$$\mathbf{G}_+^0 \approx -\mathbf{G}_-^0 \approx n_0^2\mathbf{A}_0, \quad (9)$$

as follows from (6). It can be seen that, due to the initial configuration of \mathbf{G}_\pm^0 (9), the dynamics (7) of vectors \mathbf{G}_\pm is determined by the mutual orientation of vectors \mathbf{A}_0 and \mathbf{E}_0 .

At the initial time ($t = 0$), vectors \mathbf{G}_\pm according to (9) are virtually directed in opposite directions, which gives $|\mathbf{L}_0| = |\mathbf{G}_+^0 + \mathbf{G}_-^0|/2n_0 = l_0 + 0.5 \approx 1$. With an increase in time t due to rotation around \mathbf{E}_0 , vectors \mathbf{G}_\pm approach each other. After a quarter of a turn at time $t = T_E/4$ the modulus of their half-sum, i.e. $n_0|\mathbf{L}|$, reaches the maximum value $\max(n_0|\mathbf{L}|) \approx n_0^2 \sin\varphi$, where φ is the angle between the directions of vectors \mathbf{A}_0 and $-\mathbf{E}_0$. Then the orbital momentum \mathbf{L} will be almost orthogonal to the plane with vectors \mathbf{A}_0 and \mathbf{E}_0 . If $\varphi = \pi/2$, the RE orbit becomes quasi-circular, because eccentricity $|\mathbf{A}| = \sqrt{1 - (L/n_0)^2} = 0$. With time t , vectors \mathbf{G}_\pm begin to diverge. When $t = T_E/2$ they acquire the opposite orientation again in the plane that is orthogonal to vector \mathbf{E}_0 ; the corresponding projections of \mathbf{G}_\pm change their signs as compared

to the initial values when $t = 0$. As a result, the angular momentum $\langle \mathbf{L} \rangle$ takes the position of vector \mathbf{L}_0 rotated around \mathbf{E}_0 by 180 degrees. Therefore $|\mathbf{L}|(t = T_E/2) = L_0$. The same directions of \mathbf{G}_\pm correspond to moment $t = 3/4 T_E$, and $|\mathbf{L}| \approx n_0 \sin \varphi$. Finally, at the end of the rotation period $t = T_E$, vectors $\mathbf{A}_0, \mathbf{L}_0$ occupy their initial '0' positions.

Fig. 3 illustrates the conclusions made about the character of the motion of RE in the initial state of 10p ($n_0 = 10, l_0 = 1$). Vectors $\mathbf{A}_0, \mathbf{E}_0, \mathbf{L}_0$ are chosen in a mutually orthogonal way, so that the RE orbit remains in (X, Y)-plane containing vectors $\mathbf{A}_0, \mathbf{E}_0$ with the angle between them $\varphi = \pi/2$. The direction of the momentum \mathbf{L} remains unchanged and coincides with Z-axis. In Fig. 3(a) the periodic oscillations of \mathbf{L}_Z projection within the segment $(-n_0 - 0.5, n_0 + 0.5) = (-10.5, 10.5)$ can be clearly seen. The corresponding conditionally periodic motion of RE (Fig. 3(b)) changes from quasi-circular ($\mathbf{L}_Z = \pm 10.5$) to quasi-rectilinear ($\mathbf{L}_Z = 0$) with a RE passing through the Coulomb center and changing the direction of rotation.

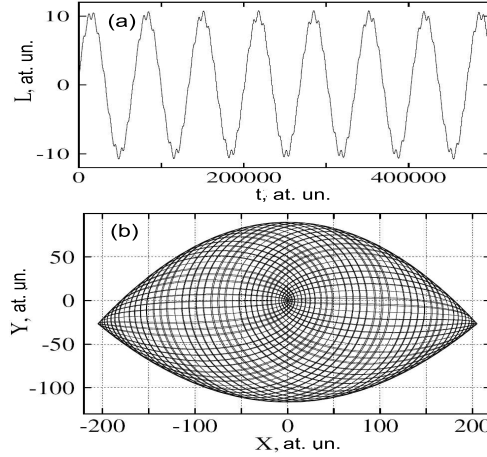


Figure 3. Time behavior of orbital momentum $\mathbf{L} = \mathbf{L}_Z$ (a) and electron path (b) in a steady electric field ($\omega_0 = 0$) with $E_0 = 0.98/(16n_0^4)$ amplitude and $\mathbf{A}_0 \perp \mathbf{E}_0$ configuration. RE initial state is 10p.

Another simple case of a two-dimensional motion of a RE in (X, Y)-plane is the situation of $\varphi = 0$, i.e. when $\mathbf{A}_0 \parallel \mathbf{E}_0$ and momentum \mathbf{L} is directed along the Z-axis. If the X-axis is directed along vector \mathbf{A}_0 , then it immediately follows from equation (5) that the increment of the current value of vector $\langle \mathbf{A} \rangle$ occurs along the Y-axis. As a result, the solution of the system of equations (6) and (7) is given by the following simple harmonic oscillations of vectors $\langle \mathbf{L} \rangle, \langle \mathbf{A} \rangle$

$$\langle \mathbf{L} \rangle = \mathbf{L}_0 \cos(1.5n_0 E_0 t), \quad (10)$$

$$\langle \mathbf{A} \rangle = \mathbf{A}_0 - (L_0/n_0) \sin(1.5n_0 E_0 t) \mathbf{e}_Y. \quad (11)$$

Evolution (10)-(11) corresponds to the periodic ‘pinching’ of Rydberg trajectories ($n_0 \gg 1$): the semi-major axis slightly changes its direction, while vector \mathbf{L} turning to zero transforms the orbital into a quasi-straight line.

Noteworthy, the appearance of an additional rotational motion of RE around the direction of the external electric field with frequency Ω_t causes, according to Bohr’s correspondence principles, the equidistant splitting of energy levels with the step size $\Delta \varepsilon = \Omega_t = (3/2) n_0 E_0$. This result is known from the quantum theory of the linear Stark effect (Landau & Lifshitz, 1977).

2.2. The case of stochastic motion in a microwave field

In the study of evolution of Rydberg states of a hydrogen atom interacting with a microwave field (Koch & Van Leeuwen, 1995; Krainov, 2010; Delone et al., 1983), approximation of conservation of momentum \mathbf{L} considerably facilitates the task due to the reduction of tridimensional RE dynamics to the issue of RE stochastic migration along a one-dimensional atomic level energy grid (Krainov, 2010). In the previous section, it was shown that the external field leads to a complex evolution of the RE Keplerian orbits, transferring them from the initially strongly elongated orbits to the quasi-circular ones and vice versa. Even with relatively small principal quantum numbers ($n_0 \sim 10$), the angular momentum modulus $\langle \mathbf{L} \rangle$ can vary significantly up to values $n_0 \sin \varphi$.

This section will demonstrate the notable changes of \mathbf{L} in microwave fields in the context of dynamic chaos conditions development and examine the validity of a one-dimensional model of diffusion ionization application. We shall start with an overview of key ideas of publications Krainov (2010); Delone et al. (1983) drawing upon the adiabatic constancy of RE orbital momentum $|\mathbf{L}|$.

(i) Global chaos is a threshold process for field amplitude E_0 and occurs when

$$E_0 > E_c \approx \frac{1}{n_0^4} \frac{1}{\chi_l (n_0^3 \omega_0)^{1/3}}; \quad L \leq L_c \approx (3/\omega_0)^{1/3}. \quad (12)$$

Values of χ_l parameter in $L \leq L_c$ region vary gradually from $\chi_0 \approx 35$ to $\chi_{l_c} \approx 22$. Value (12) for E_c critical amplitude was obtained for parameter $s = \omega_0 n_0^3 > 3$, i.e. under the condition of substantial non-adiabaticity of the excitation by the microwave field (see Eq. (8)).

(ii) When E_0 is a fixed value, expression (12) sets a $n_c \approx \sqrt[4]{1/(\chi_l E_0)}$ limit for the values of principal quantum numbers n separating the areas of RE random ($n > n_c$) and regular ($n < n_c$) motion. For the initial condition $n_0 > n_c$, publications Dashevskaya et al. (2002); Bezuglov et al. (2001) estimated the related time τ_{DI} of diffusion ionization as

$$\tau_{DI}(n_0) \approx 2\omega_0^{4/3} / (n_0 E_0^2), \quad (13)$$

which, similarly to relation (12), does not depend on L when $L \leq L_c$.

(iii) When the current value of orbital momentum $L(t) > L_c \sim (3/s)^{1/3}n_0 \sim n_0$ (which corresponds to RE orbits approximating to a circular orbit), dynamic resonance configuration peculiarities arise (Krainov, 2010; Delone *et al.*, 1983). Critical field values E_c in $L > L_c$ area increase drastically with practical blocking of the dynamic chaos condition and, accordingly, prohibition of diffusion ionization.

Analysis of phenomena with strong path stochastization requires the use of reliable tools for numerical computation of particle parameters. Such tools include symplectic integrators of motion equations (Hairer, 1999) for various physical problems, including complex integro-differential tasks related to the radiation energy transfer processes in optically dense media (Kazansky *et al.*, 2001) with a multi-level structure of atomic quantum states (Sydoryk *et al.*, 2008; Kirova *et al.*, 2017). A numeric algorithm of advanced stability for analyzing stochastic migration effects was suggested in publication Efimov *et al.* (2014). This algorithm is based on a combination of a symplectic integrator variety, also known as the split propagation technique, and Floquet technique (Chu & Telnov, 2004).

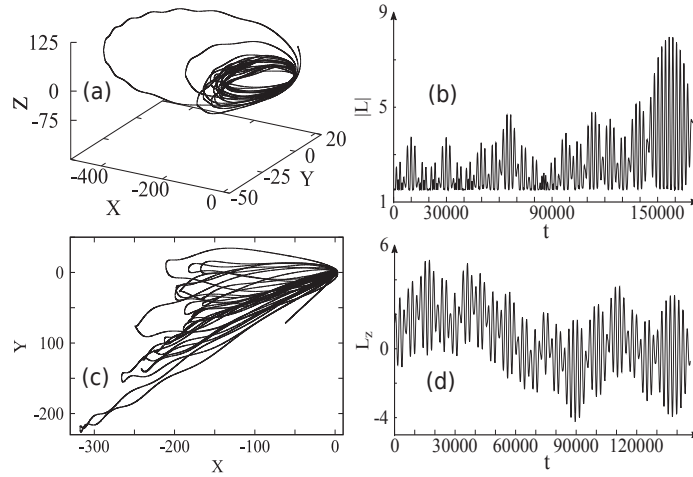


Figure 4. Rydberg electron trajectories in a hydrogen atom (boxes (a), (c)) and the related time behavior of the orbital momentum (boxes (c), (d)) for 10p initial state, at a microwave field frequency of $\omega_0 = 3/10^3$. Axial values are quoted in at. un.

The data obtained in Efimov *et al.* (2014) reflect invalidity of the approximation concerning invariance of angular momentum \mathbf{L} . As an example, motion paths and temporal evolution of orbital momentum under the conditions of diffusion ionization manifestation are shown in Fig. 4. We used the electron initial

state in a hydrogen atom equal to 10p ($n_0 = 10, l_0 = 1$). An electron is exposed to the impact of a $\omega_0 = 3/10^3$ frequency microwave field whose amplitude E_0 by far exceeds the threshold value E_c (12). Two typical initial configurations of \mathbf{E}_0 and \mathbf{A}_0 vectors were selected intentionally at $\varphi = \pi/2$ angle, which corresponds to the maximum change (see previous section 2.1) in $|\mathbf{L}|$ module or its projection L_Z for tridimensional ($E_0 = 6.5E_c$, Fig. 4, boxes (a), (b)) and bidimensional ($E_0 = 8.2E_c$, Fig. 4, boxes (c), (d)) paths respectively. All time dependencies are traceable until RE escape into the energy continuum. The results of the numerical calculations shown demonstrate a noticeable decrease in \mathbf{L} oscillation amplitude in the microwave field when global chaos occurs compared to regular motion (cf. boxes (a) in Fig. 3 and (d) in Fig. 4 for equal type configurations of the electric field and the electron initial state).

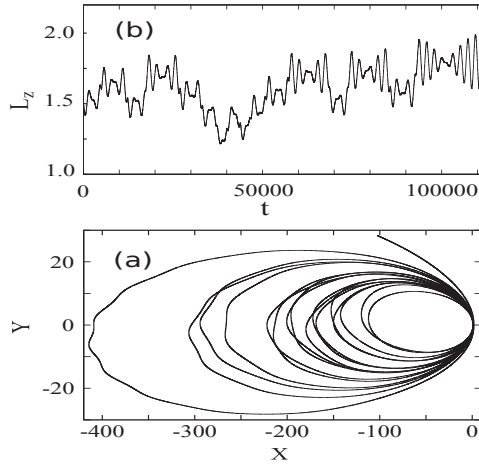


Figure 5. Similar to Fig. 3 for $\mathbf{A}_0 \parallel \mathbf{E}_0$ configuration and microwave field choice at frequency $\omega_0 = 3/10^3$ and amplitude $E_0 = 4.7E_c$.

RE random drift blocking starts when $L > L_c \approx (3/\omega_0)^{1/3}$. For the examples shown in Fig. 4 this corresponds to $L_c \approx 10$ value, i.e. L never exceeds the value $\approx 2/3L_c$ (see Fig. 4(b),(d)). Under the conditions of stochastic process development with $L < L_c$, the dependence of all diffusion factors on L appears to be weak (Krainov, 2010). To this extent the key conclusions from the monodimensional model of diffusion ionization suggested in publications Krainov (2010); Delone et al. (1983) retain their significance, since within the τ_{DI} time lapse (13) L values remain within L_c limits.

It should be noted that an exceptional configuration for $\mathbf{A}_0 \parallel \mathbf{E}_0$ vectors ($\varphi = 0$) in (X, Y) plane and $\mathbf{L} = L_Z \mathbf{e}_Z$ momentum exists. As follows from Fig. 5, $L_Z \approx \text{const}(= 1.5)$ approximation (box (a)) quite successfully matches

RE bidimensional motion (box (b)). The same configuration in the case of an adiabatic field ($\omega_0 \approx 0$) and a regular motion demonstrates significantly larger oscillations (10) of L_Z that lies within the interval $(-1.5, 1.5)$.

3. Autoionization widths of quasi-molecules formed by pairs of cold Rydberg atoms

Cold media are currently seen as promising physical objects in connection with the solution of a number of interdisciplinary applied problems, including both the issues of quantum information processing (Saffman *et al.*, 2010) and the physics of the unique ultra-cold plasma creation (Lyon & Rolston, 2016). Ultra-cold plasma is formed in magneto-optical traps in the ‘frozen’ Rydberg gas of alkali-metal atoms excited to the initial states with the principal quantum number of $n_0 \sim 50$, concentration $\rho_0 > 5 \cdot 10^{10} \text{cm}^{-3}$ and several μK temperature. It should be noted that ultra-cold plasma formation occurs through a diffusion stage (Tanner *et al.*, 2008) (see Fig. 6), which features formation of highly asymmetric Rydberg atomic pairs with different orbital l and principal quantum n numbers due to collisional processes.

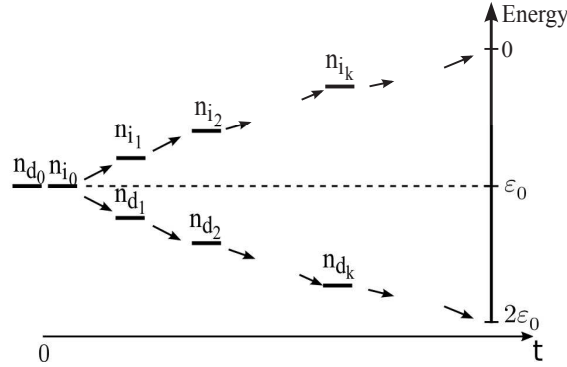


Figure 6. (Adopted from Tanner *et al.* 2008) Schematic of population diffusion over a band of energies for atomic pairs. The energy $\varepsilon_{id} = \varepsilon_{n_d} + \varepsilon_{n_i}$ of the $n_d n_i$ pairs of atoms initially identically excited ($n_{d_0} = n_{i_0} = n_0$) maintains its initial value $2\varepsilon_0 = -1/2n_0^{*2}$ because of the near resonance coupling between the two-atom quasimolecules $\tilde{n}_d \tilde{n}_i$. The energy axis corresponds to the individual atomic energies $\varepsilon_{n_d}, \varepsilon_{n_i}$.

The Penning ionization should be considered to be the most important type of collisional processes that create primary charged particles in cold media (Fig. 7).

$$A^{**} (n_d l_d) + A^{**} (n_i l_i) = A^{**} (n'_d l'_d) + A^+ + e (\varepsilon'_i l'_i). \quad (14)$$

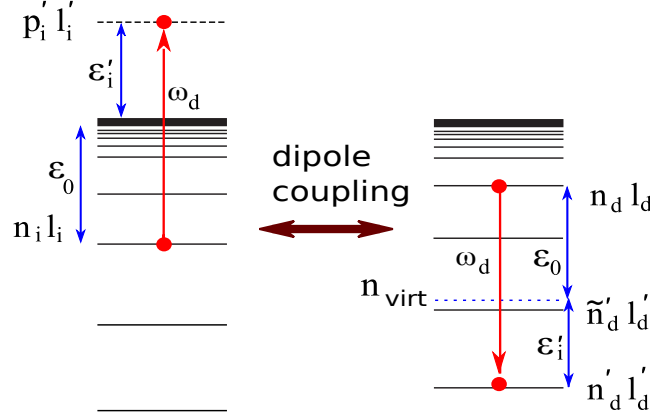


Figure 7. Auger-process illustration for resonance interaction between a Rydberg atomic pair $\{Ai^{**}, Ad^{**}\}$ and the energy continuum. The partial transition $N \rightarrow N'$ is presented.

Contrary to the associative ionization, the Penning ionization (PI) is a no-threshold reaction. Long-range dipole-dipole interaction between two Rydberg alkali-metal atoms results in a free electron escaping due to the Auger process: one of the atoms (d) undergoes a transition from state $n_d l_d$ to a deeper bound state $n_d' l_d'$, while the other atom (i) gains the released energy and jumps from state $n_i l_i$ to the continuum state $\varepsilon_i' l_i'$.

In this chapter, we analyze some nontrivial features of PI in Rydberg gases, which make PI an important source of charged particles in cold media.

3.1. Penning ionization (PI) cross sections

Our method for calculating PI cross section σ_{PI} for reaction (14) is based on the Katsuura-Smirnov model (Katsuura, 1965; Smirnov, 1981), where the main dynamic variable is the autoionization width $\Gamma_N = \tilde{\Gamma}_N/R^6$ of a pair of interacting atoms. If the atoms are in $N \equiv \{N_d = n_d l_d, N_i = n_i l_i\}$ quantum states at a fixed internuclear distance R , the reduced Penning width $\tilde{\Gamma}_N$ consists of partial widths $\tilde{\Gamma}_{NN'}$ corresponding to individual bound-free atom transitions $N \rightarrow N'$ (see Fig. 7): $\tilde{\Gamma}_N = \sum_{N'} \tilde{\Gamma}_{NN'}$. The partial widths (a.u.)

$$\tilde{\Gamma}_{NN'} = |D_{N'_D N_D}|^2 \frac{c\sigma_{ph}}{\pi |\omega_d|}, \quad (15)$$

include dipole matrix elements $D_{N'_D N_D}$ for the bound-bound d-atom transitions and the photoionization cross section σ_{ph} for the i-atom, in accordance with

its transition into continuum. Frequency of a partial atomic transition ω_d determines the energy that the d-atom transfers to the i-atom (see Fig. 7) in the dipole-dipole interaction. The ionization condition means that $\omega_d \geq \varepsilon_0$, where the i-atom binding energy $\varepsilon_0 = 1/(2n_i^{*2})$ is expressed through the effective quantum number $n_i^* = n_i - \delta_i$ and the quantum defect δ_i . The hatched line in Fig. 7 shows the position of an imaginary level n_{virt} that is lower than the $n_d l_d$ state by amount ε_0 and, therefore, determines the position of the ionization limit: $n'_d < n_{virt}$.

In the Katsuura-Smirnov model, the PI cross-section σ_{PI} of two colliding Rydberg atoms, subject to the long-range dipole-dipole interaction, is determined directly by width $\tilde{\Gamma}_N$

$$\sigma_{PI} = 3.37 \cdot \tilde{\Gamma}_N^{2/5} / v^{2.5}, \quad (16)$$

where v is the relative velocity of the atoms. Therefore, PI specifics identification is related to the analysis of $\tilde{\Gamma}_N$ behavior in various quantum configurations N of atomic pairs.

Publication Bezuglov & Borodin (1999) suggests simple quasi-classical formulas for calculating radiation constants of optical transitions in alkali-metal atoms, which were used in the surveys of PI autoionization widths $\tilde{\Gamma}_N$ for symmetric pairs ($n_d = n_i$) of rubidium atoms (Amthor et al., 2009) and asymmetric pairs ($n_d \neq n_i$) of hydrogen atoms (Efimov et al., 2016). This chapter includes an analysis of PI effects in a cold Rydberg gas of sodium atoms. The accuracy of our presented below numerical results, based on the semi-classical approach, is better than 15% (Efimov et al., 2016).

3.2. Optimal Rydberg atomic pairs

Fig. 8 shows the values of autoionization width $\tilde{\Gamma}_N$ as functions of principal quantum numbers n_d, n_i of H and Na atomic pairs. In the first place, a higher PI efficiency for sodium atoms (by an order of magnitude) can be observed. Noteworthy also is a contrasting oscillatory structure $\tilde{\Gamma}_N$ present in n_d and n_i variations. These oscillations belong to PI distinctive features and are caused by the rapid decrease of dipole matrix elements $D_{N'_d N_D}(\omega_d)$ and photoionization cross sections $\sigma_{ph}(\varepsilon'_i)$ with the decrease of their arguments (Sobelman, 1992). Therefore, $\tilde{\Gamma}_N$ peak corresponds to the occurrence of threshold ionization values $\varepsilon'_i = 0$, which for atomic levels in Fig. 7 corresponds to superimposition of the $\tilde{n}'_d l'_d$ actual state on the n_{virt} virtual level. Their divergence leads to the decrease of $\tilde{\Gamma}_N$, while the convergence results in its growth, i.e. in oscillations.

Some specific features of surfaces in Fig. 8 include $\tilde{\Gamma}_N$ dependence on the quantum number n_d at fixed values n_i of the ionized i-atom. The set of such dependences is shown for H, Na and K s-s atomic pairs in Fig. 9. A rapid increase of $\tilde{\Gamma}_N$ with the de-excited d-atom size $\sim n_d^{*2}$ reduction can be clearly seen.

This is a purely quantum effect caused by an ‘average’ reduction of ω_d and ε'_i arguments for the functions $D_{N'_d N_D}, \sigma_{ph}$ with the n_d value decrease. For each

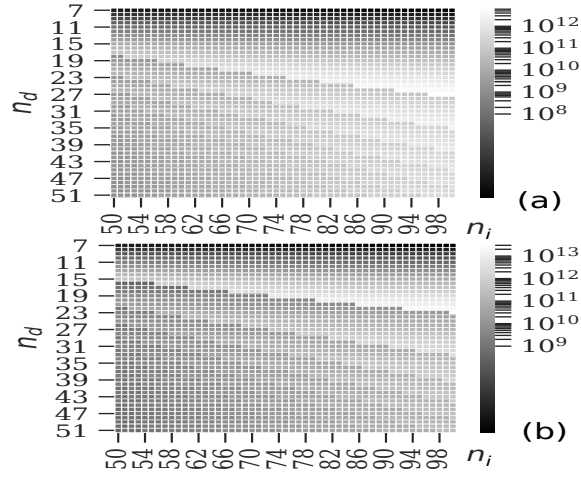


Figure 8. Dependence of reduced autoionization width $\tilde{\Gamma}_N$ (at. un.) on principal quantum numbers n_d , n_i of a diatomic quasi-molecule. The cases of (a) s-s ($l_d = 0, l_i = 0$) configuration for hydrogen atomic pairs and (b) s-p ($l_d = 0, l_i = 1$) configuration for sodium atoms have been considered.

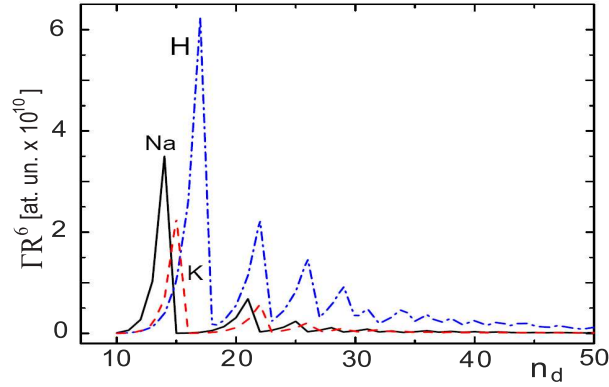


Figure 9. Reduced autoionization widths $\tilde{\Gamma}_N = R^6 \Gamma_N$ for the cases of s-s- ($l_d = 0, l_i = 0$) H, Na and K atomic pairs configurations at the fixed value $n_i = 50$.

type of atomic pairs presented in Fig. 9 an optimal $n_d^{(opt)}(n_i)$ value for the i-atom exists when the maximum peak of $\tilde{\Gamma}^{(opt)}(n_i)$ occurs. The occurrence of the optimal pair $(n_d^{(opt)}, n_i)$ corresponds, thus, to the coincidence of the energy of virtual level n_{virt} and the energy $\tilde{\varepsilon}'_d$ of $\tilde{n}'_d l'_d$ state, which is the nearest to

$n_d^{(opt)}l_d$ initial state (see Fig. 7):

$$\varepsilon_d^{(opt)} - \tilde{\varepsilon}'_d = \gamma_d^{(\min)} \left(n_d^{(opt)} - \delta_{l_d} \right)^{-3} = (n_i - \delta_{l_i})^{-2} / 2. \quad (17)$$

The positive parameter $\gamma_d^{(\min)} > 0$ assumes the minimum value for the difference between effective quantum numbers for l_d - and l'_d -series. Relation (17) describes well the position of $n_d^{(opt)}$ for all the three atomic types shown in Fig. 9.

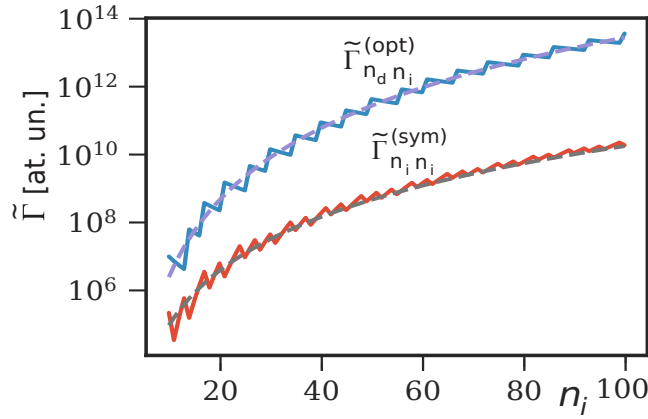


Figure 10. The reduced PI widths $\tilde{\Gamma}_N$ for symmetric (sim) and optimal (opt) pairs in relation to the principal quantum number n_i of the ionized atom. The case of s-p ($l_d = 0, l_i = 1$) configuration for sodium atoms pairs has been considered. The dashed curves correspond to the analytical results.

The order of magnitude of PI efficiency increase when a symmetric pair ($n_d = n_i, n_i$) is replaced by an optimal pair ($n_d^{(opt)}, n_i$) is shown in Fig. 10. The respective gain $\Lambda = \tilde{\Gamma}^{(opt)} / \tilde{\Gamma}^{(sym)}$ when $n_i \sim 100$ achieves three orders of magnitude.

3.3. Analytical results

Quasi-classical representations of partial values $\tilde{\Gamma}_{NN'}$ (15) allow obtaining analytical assessment of PI processes efficiency for individual, yet important from the practical standpoint cases of $\Gamma_{N'}$ autoionization widths for symmetric/ optimal pairs. Omitting the rather cumbersome calculations, which will be included in another publication Abo *et al.* (In progress), we shall provide only the final

results:

$$\langle \tilde{\Gamma}_{n_d n_i}^{(sim)} \rangle (n_i) \simeq \Pi_{l_d l_i}^{(sym)} \frac{1 + 34\sqrt{2}/(3n_i^*)}{\left(1 + 4\sqrt{2} \cdot \Xi_{l_d l_i}^{(sym)}/n_i^*\right)^{17/3}} n_i^{*16/3} \quad (18)$$

$$\langle \tilde{\Gamma}_{n_d n_i}^{(opt)} \rangle (n_i) \simeq \Pi_{l_d l_i}^{(opt)} \frac{\left(1 - \Xi_{l_d l_i}^{(opt)}/n_i^{*2/3}\right)^4}{\left(1 + 3 \cdot \Xi_{l_d l_i}^{(opt)}/n_i^{*2/3}\right)^{10/3}} n_i^{*19/3}. \quad (19)$$

Parameters $\Pi_{l_d l_i}^{(sim/opt)}$, $\Xi_{l_d l_i}^{(sim/opt)}$ included in formulas (18) and (19) are functions of only orbital $\{l_d, l_i\}$ configurations of pairs. The former parameter type (Π) regulates the numeric values of PI rate constants. In the case of hydrogen atoms both parameters $\Pi_{l_d l_i}^{(sim/opt)}$ prove to be constant, i.e. $\Pi_{l_d l_i}^{(sim)} = 1.070$; $\Pi_{l_d l_i}^{(opt)} = 1.899$, and do not depend on $\{l_d, l_i\}$. The latter parameter type (Ξ), which is nondimensional, is responsible for the oscillatory structure (see Fig. 10) of PI rate constants. Concerning oscillation-averaged values $\langle \tilde{\Gamma}_N \rangle$ of Penning widths, the value $\Xi_{l_d l_i}^{(sim/opt)} = 0.5$ could be assumed in the first approximation.

Table 1. Π (a.u.) and Ξ parameters values for primary configurations of sodium atomic pairs. For reference: 1 a.u. = $0.906 \cdot 10^{-33}$ cm⁶/s.

	s-s	s-p	s-d	s-f	p-s	p-p	p-d	p-f
$\Pi^{(sim)}$	0.127	0.449	0.318	0.433	0.0992	0.34	0.244	0.332
$\Xi^{(sim)}$	0.69	0.41	0.11	0.11	1.4	0.96	0.69	0.69
$\Pi^{(opt)}$	2.53	9.266	6.17	8.87	0.927	3.64	2.41	3.29
$\Xi^{(opt)}$	0.66	0.59	0.41	0.5	0.65	0.69	0.48	0.5
	d-s	d-p	d-d	d-f	f-s	f-p	f-d	f-f
$\Pi^{(sim)}$	0.356	1.24	0.886	1.23	0.3	1.03	0.754	1.08
$\Xi^{(sim)}$	0.98	0.69	0.41	0.5	0.98	0.59	0.41	0.61
$\Pi^{(opt)}$	0.71	2.73	1.9	2.51	0.61	1.81	1.25	1.71
$\Xi^{(opt)}$	0.5	0.43	0.3	0.31	0.82	0.41	0.32	0.31

In the general case of arbitrary atoms of alkali-metal elements, both parameter types Π , Ξ can be considered adjustable, while formulas (18) and (19) can be used for rapid estimation of PI autoionization widths. Tab. 1 includes, by way of example, data on Π -, Ξ -values for the primary orbital configurations of Na atomic pairs. The ‘average’ quantity of such calculations can be assessed by the data shown in Fig. 10, where the hatched curves were obtained with the aid of formulas (18) and (19) using the data for s-p pair parameters from Tab. 1.

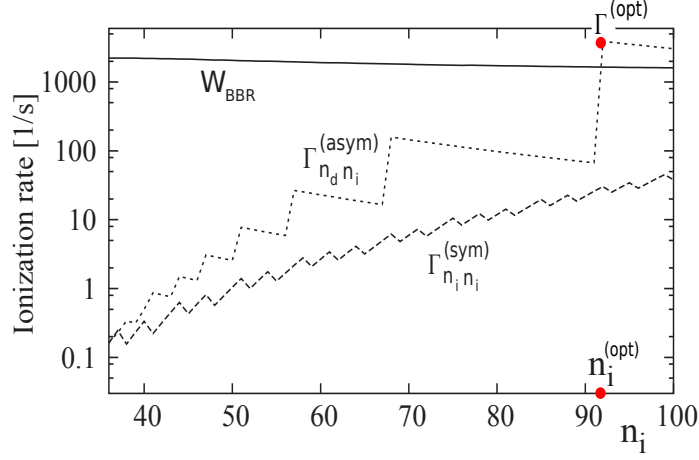


Figure 11. Growth of Penning ionization rates (Γ) during diffusion of the atomic population. The black-body radiation-induced ionization rate W_{BBR} (Efimov et al., 2016) is exhibited as a solid line as well.

3.4. Role of asymmetric atomic pairs in cold Rydberg gases

Both the collisions with electrons and the evolution of population of Rydberg atom pairs via resonant energy transfer lead to the diffusion of the atomic population over a range of Rydberg states (see Fig. 6). Upon this diffusion following the laser excitation of Rydberg hydrogen atomic pairs with $n_{i_0} = n_{d_0} = n_0 = 36$ and the concentration $\rho_0 = 2.3 \cdot 10^{11} \text{cm}^{-3}$ (see Fig. 11), the growth of one of the initial quantum numbers $n_0 \rightarrow n_i$ may increase the initial autoionization rate $\Gamma_{n_0 n_0}^{(sim)}$ by three orders of magnitude, while the simultaneous lowering of the other quantum number $n_0 \rightarrow n_d$ can increase $\Gamma_{n_i n_i}^{(sim)}$ by another two or three orders of magnitude (see Fig. 11). The aggregated gain of $\Gamma_{n_d n_i}^{(asim)}$ compared to the initial rate ($\sim 0.1 \text{s}^{-1}$) can be as large as $\sim 10^4 - 10^5$, and this may strongly enhance the role of PI in the destabilization of cold Rydberg gases via formation of cold plasmas.

The shown findings of the analysis of PI effects in cold Rydberg media allow drawing the following conclusions. Contrary to hydrogen atoms, alkali element atoms feature strong dependence of PI processes efficiency on orbital quantum numbers (see Tab. 1). This is related to the wide variety of δ_l quantum defects of atomic series. Values of parameters $\Pi^{(opt)}$ in the majority of the cases (see Tab. 1) exceed the "hydrogen reference" value 1.899. Therefore, PI processes involving highly excited states of all atoms of alkali-metal elements may play a dominant role as sources of primary charged particles at the diffusion stage of a cold Rydberg gas evolution into a cold plasma.

4. Conclusion

The paper provides the results of research into the features of autoionization processes in highly excited atomic complexes associated with the evolution of the orbital moment L of Rydberg electrons (RE). Two types of interaction between the complex particles are considered. The first type of interaction is characteristic of reactions of the associative ionization type. It is caused by the charge exchange processes inside the complex ionic core, which results in a quasimonochromatic microwave electric field. The latter perturbs the motion of RE on the Keplerian orbit with the principal quantum number n and leads to its departure to the energy continuum. We have simulated such type of ionization for a hydrogen atom under the influence of external radiation of frequency ω_0 and amplitude E_0 . The results of the analytical consideration in the adiabatic approximation are given. A nontrivial evolution of the orbital moment, having oscillations in both the direction and the absolute value of L with the maximum possible amplitude equal to $n+0.5$, has been discovered. Violation of adiabaticity causes the appearance of irregular motion zones in the RE energy space. When E_0 exceeds the critical value E_c (12), these zones merge into a single whole with a departure to the energy continuum. The evolution of L continues to demonstrate a complex oscillation structure with a slightly suppressed amplitude $\approx 2n/3$ of the oscillations. The latter turns out to be less than the critical value $L_c \sim n$, and does not lead to any violation of conditions for the one-dimensional diffusion ionization model feasibility.

The second type of interaction between Rydberg particles – dipole-dipole interaction – dominates in ultra-cold gaseous media. The non-threshold transfer of excitation energy between REs leads to the resonance Penning autoionization (PI) of atomic pairs. An important feature of PI is the nontrivial dependence of the rate constants on both the size ($\sim n^2$) and the orbital moments of the atoms. We have found optimal, highly asymmetric configurations of Rydberg atomic pairs for all alkali metals, leading to explosive intensification (by several orders of magnitude) of free electron formation due to PI processes. This property makes PI an important source of primary charged particle formation when cold Rydberg plasma is created.

Acknowledgements. This work is made within projects of the Ministry of Education, Science and Technological Development of Serbia, grant numbers 176002, III44002.

References

- Abo, Z., Miculis, K., Bruvelis, M., et al., Strong enhancement of Penning ionization in cold Rydberg gases II: Tom and Jerry pairs for alkali-metal atoms. In progress, *J. Phys. B*

- Amthor, T., Denskat, J., Giese, C., et al., Autoionization of an ultracold Rydberg gas through resonant dipole coupling. 2009, *Eur. Phys. J. D*, **53**, 329
- Bezuglov, N. & Borodin, V., Generalized correspondence rules for quasi-classical dipole matrix elements. 1999, *Opt. Spectrosc.*, **86**, 467
- Bezuglov, N., Borodin, V., Eckers, A., & Klyucharev, A., A quasi-classical description of the stochastic dynamics of a Rydberg electron in a diatomic quasi-molecular complex. 2002, *Opt. Spectrosc.*, **93**, 661
- Bezuglov, N., Borodin, V., Kazanskii, A., et al., Analysis of Fokker-Planck type stochastic equations with variable boundary conditions in an elementary process of collisional ionization. 2001, *Opt. Spectrosc.*, **91**, 19
- Buenker, R. J., Golubkov, G., Golubkov, M., Karpov, I., & Manzheliy, M., Relativity laws for the variation of rates of clocks moving in free space and GPS positioning errors caused by space-weather events. 2013, in *Global Navigation Satellite Systems-From Stellar to Satellite Navigation* (IntechOpen)
- Chu, S.-I. & Telnov, D. A., Beyond the Floquet theorem: generalized Floquet formalisms and quasienergy methods for atomic and molecular multiphoton processes in intense laser fields. 2004, *Phys. Rep.*, **390**, 1
- Dalgarno, A. 1975, in book *Rydberg States of Atoms and Molecules*, by R. F. Stebbings, F. B. Dunning, Cambridge, UK: Cambridge University Press
- Dashevskaya, E., Litvin, I., Nikitin, E., Oref, I., & Troe, J., Classical diffusion model of vibrational predissociation of van der Waals complexes Part III. Comparison with quantum calculations. 2002, *Phys. Chem. Chem. Phys.*, **4**, 3330
- Delone, N. B., Krainov, B., & Shepelyanskii, D., Highly-excited atoms in the electromagnetic field. 1983, *Sov. Phys. Usp.*, **26**, 551
- Efimov, D., Bezuglov, N., Klyucharev, A., et al., Analysis of light-induced diffusion ionization of a three-dimensional hydrogen atom based on the Floquet technique and split-operator method. 2014, *Opt. Spectrosc.*, **117**, 8
- Efimov, D., Miculis, K., Bezuglov, N., & Ekers, A., Strong enhancement of Penning ionization for asymmetric atom pairs in cold Rydberg gases: the Tom and Jerry effect. 2016, *J. Phys. B*, **49**, 125302
- Fermi, E., Sopra lo spostamento per pressione delle righe elevate delle serie spettrali. 1934, *Il Nuovo Cimento (1924-1942)*, **11**, 157
- Gnedin, Y. N., Mihajlov, A. A., Ignjatović, L. M., et al., Rydberg atoms in astrophysics. 2009, *New Astron. Rev.*, **53**, 259
- Golubkov, G. & Devdariani, A., Associative ionization in slow collisions of atoms. 2011, *Russ. J. Phys. Chem. B*, **5**, 892
- Graham, W. G., Fritsch, W., Hahn, Y., & Tanis, J. *Recombination of atomic ions*, Vol. **296** (Springer Science & Business Media)
- Hairer, E., Numeral geometric integration. 1999, *Université de Geneve, Geneve*
- Janev, R. & Mihajlov, A., Resonant ionization in slow-atom-Rydberg-atom collisions. 1980, *Phys. Rev. A*, **21**, 819

- Katsuura, K., Remarks on excitation transfer between unlike molecules. 1965, *J. Chem. Phys.*, **43**, 4149
- Kazansky, A., Bezuglov, N., Molisch, A., Fuso, F., & Allegrini, M., Direct numerical method to solve radiation trapping problems with a Doppler-broadening mechanism for partial frequency redistribution. 2001, *Phys. Rev. A.*, **64**, 022719
- Kirova, T., Cinins, A., Efimov, D., et al., Hyperfine interaction in the Autler-Townes effect: The formation of bright, dark, and chameleon states. 2017, *Phys. Rev. A*, **96**, 043421
- Klyucharev, A., Bezuglov, N., Matveev, A., et al., Rate coefficients for the chemi-ionization processes in sodium-and other alkali-metal geocosmical plasmas. 2007, *New Astron. Rev.*, **51**, 547
- Koch, P. & Van Leeuwen, K., The importance of resonances in microwave ionization of excited hydrogen atoms. 1995, *Phys. Rep.*, **255**, 289
- Krainov, V., Ionization of atoms in strong low-frequency electromagnetic field. 2010, *J. Exp. Theor. Phys.*, **111**, 171
- Landau, L. & Lifshitz, E., *Mechanics* (Nauka, Moscow, 1973); English tran., Course of theoretical physics. Vol. 1. Mechanics. 1976, *Permagon Press, Oxford-New York-Toronto*
- Landau, L. & Lifshitz, E. 1977, *Quantum Mechanics* Pergamon Press
- Lopes, R. M. & Williams, D. A., Io after Galileo. 2005, *Rep. Prog. Phys.*, **68**, 303
- Lyon, M. & Rolston, S., Ultracold neutral plasmas. 2016, *Rep. Prog. Phys.*, **80**, 017001
- Mihajlov, A. A., Ignjatović, L. M., Dimitrijević, M. S., & Djurić, Z., Symmetrical Chemi-Ionization and Chemi-Recombination Processes in Low-Temperature Layers of Helium-rich DB White Dwarf Atmospheres. 2003, *Astrophys. J. Suppl.*, **147**, 369
- Saffman, M., Walker, T. G., & Mølmer, K., Quantum information with Rydberg atoms. 2010, *Rev. Mod. Phys.*, **82**, 2313
- Smirnov, B. M., Ionization in low-energy atomic collisions. 1981, *Soviet Physics Uspekhi*, **24**, 251
- Sobelman, I. *Atomic spectra and radiative transitions*, , Vol. **12** (Springer Science & Business Media)
- Sydoryk, I., Bezuglov, N., Beterov, I., et al., Broadening and intensity redistribution in the Na (3 p) hyperfine excitation spectra due to optical pumping in the weak excitation limit. 2008, *Phys. Rev. A.*, **77**, 042511
- Tanner, P. J., Han, J., Shuman, E., & Gallagher, T., Many-body ionization in a frozen Rydberg gas. 2008, *Phys. Rev. Lett.*, **100**, 043002
- Zaslavsky, G. M. 2007, *The Physics of Chaos in Hamiltonian Systems* (the 2dn Edition Imperial College Press)

Atomic structure of the carbon like ion Ca XV

N. Alwadie^{1,2}, A. Almodlej¹, N. Ben Nessib^{1,3}
and M.S. Dimitrijević^{4,5}

¹ *Department of Physics and Astronomy, College of Sciences, King Saud University, Saudi Arabia*

² *Department of Physics, College of Sciences, King Khalid University, Saudi Arabia*

³ *GRePAA, INSAT, Centre Urbain Nord, University of Carthage, Tunis, Tunisia*

⁴ *Astronomical Observatory, Volgina 7, 11060 Belgrade 38, Serbia*

⁵ *Sorbonne Université, Observatoire de Paris, Université PSL, CNRS, LERMA, F-92190 Meudon, France*

Received: July 31, 2019; Accepted: September 28, 2019

Abstract. Energy levels, oscillator strengths and transition probabilities for the multicharged carbon like Ca XV ion have been calculated using the pseudo-relativistic Hartree-Fock (HFR) approach using the new Cowan atomic structure code 2018. Results have been compared with NIST database and other calculated data. There are great lack on atomic structure data of Ca XV and obtained new data will be important for plasma diagnostic and astrophysical modeling.

Key words: spectral lines – energy levels – oscillator strengths – transition probabilities

1. Introduction

Carbon-like ions are highly abundant elements and their lines are prominent in both stellar and interstellar spectra and they are interesting for possible astrophysical plasma diagnostic applications (Al-Modlej *et al.*, 2018). One example of them is calcium (Ca) which has a nuclear charge $Z=20$ and it has cosmic abundances in astrophysical spectra (Träbert *et al.*, 2018). Carbon-like ions are also important for investigation in plasma physics, fusion research and plasma technologies.

In general, we can obtain ionized calcium by Tokamaks which are proven light sources suitable for measuring spectra of astrophysical relevance (Träbert *et al.*, 2018), as well as by the solar flare plasma where Extreme Ultra-Violet (EUV) solar emission lines of highly ionized calcium have been recorded (Nahar, 2017).

Indeed, what is interesting now is the study of Ca XV, a highly charged carbon-like ion that typically exists in high temperature plasmas and plays an important role for diagnostics and modeling.

Researchers have done some important experimental studies on spectral lines of Ca XV where the diagnostic potential of these lines was noted. It is worth mentioning that the data on atomic properties are not only relevant to spectroscopy, but these values are of interest in a variety of other fields in physics and technology (Colón and Alonso-Medina, 2010). As an example, the diagnostic emission lines have been frequently observed in solar EUV spectra of carbon-like Ca XV by Dere (1978). Moreover, Ca XV was detected in the Extreme-Ultraviolet Explorer satellite spectrum of the star ξ Bootis A (Laming and Drake, 1999). Also, EUV emission lines of Ca XV in solar and laboratory spectra were studied by Keenan *et al.* (2003).

Recently, the most important experimental study in this field was by Trbert *et al.* (2018), where they investigated the emission line intensity pattern of highly charged Ca and Ar in the EUV in a laboratory plasma, by using a Tokamak plasma discharge in hydrogen carrying some Ar and intermittently seeded with Ca. The task is done injecting these elements by laser pulse into a plasma dominated by hydrogen. Fortunately, the results of the study of spectrum for Ca produced a fair number of spectral lines. The data of this experimental study have been compared with databases especially CHIANTI (Dere *et al.*, 2019). Most importantly, they found that Ca XV is particularly rich in lines in the EUV spectral range and the strongest line was $2s^2 2p^2 \ ^1D_2 - 2s 2p^3 \ ^1D_2^o$ at $\lambda = 161.1 \text{ \AA}$.

In the present work, we calculated energy levels for the configuration expansion: $2s^2 2p^2$, $2s^2 2p 3p$, $2s^2 2p 4p$, $2s 2p^3$, $2s^2 2p 3s$, $2s^2 2p 4s$, $2s^2 2p 5s$ and $2s^2 2p 3d$. Also, we computed oscillator strengths and transition probabilities corresponding to some spectral lines of the carbon like Ca XV ion using a relativistic configuration interaction method based on numerical wave functions calculated with a single configurations Hartree-Fock Relativistic (HFR) approach including core-polarization potential and the corresponding corrections in the matrix elements because for any system considered, complex like Ca XV ion, both relativistic and correlation effects could be relevant. So, all our calculations were in the framework of the HFR by means of a recent version of the Cowan computer code adapted by Kramida (2018).

We describe in Section 2 the theoretical calculations and then in Section 3 the results of the atomic structure of Ca XV ion. The conclusions are presented in Section 4.

2. Hartree-Fock Relativistic method

For the hydrogen atom, the Schrödinger equation is solved exactly, but for a system consisting of a multi-electron atom or molecule, we must use approx-

imate methods such as the HFR method, where the Schrödinger equation for N -electrons atom wavefunction can be written as:

$$\left[\sum_{i=1}^N \left(-\frac{1}{2} \nabla_{r_i}^2 - \frac{Z}{r_i} \right) + \sum_{i<j}^N \frac{1}{r_{ij}} \right] \Psi(q_1, q_2, \dots, q_N) = E \Psi(q_1, q_2, \dots, q_N) \quad (1)$$

where q_i denotes the set of the discrete spin variable of electron i and continuous spatial coordinates r_i .

In this method, the many wave functions are written as a linear superposition of products of single-particle spin orbitals wave functions but these wave functions, anti-symmetric for N -electrons, must satisfy the Pauli principle. So, this product is written as a determinant known as the Slater Determinant (Bransden & Joachain, 2003):

$$\Psi(q_1, q_2, \dots, q_N) = \frac{1}{\sqrt{N!}} \begin{vmatrix} u_\alpha(q_1) & u_\beta(q_1) & \dots & u_\nu(q_1) \\ u_\alpha(q_2) & u_\beta(q_2) & \dots & u_\nu(q_2) \\ \vdots & \dots & \dots & \vdots \\ u_\alpha(q_N) & u_\beta(q_N) & \dots & u_\nu(q_N) \end{vmatrix} \quad (2)$$

The functions $u_\lambda(q_i)$ satisfy the HartreeFock Relativistic equation (Al-Towyan *et al.*, 2016; Colón and Alonso-Medina, 2010):

$$\left[-\frac{1}{2} \nabla_{r_i}^2 - \frac{Z}{r_i} \right] u_\lambda(q_i) + \left[\sum_{\mu} \int u_{\mu}^*(q_i) \frac{1}{r_{ij}} u_{\mu}(q_j) dq_j \right] u_\lambda(q_i) - \left[\sum_{\mu} \int u_{\mu}^*(q_j) \frac{1}{r_{ij}} u_{\lambda}(q_j) dq_j \right] u_\lambda(q_i) = E_\lambda u_\lambda(q_i) \quad (3)$$

where $\lambda, \mu = \alpha, \beta, \dots, \nu$ and the summation over μ extends over the N occupied spin-orbitals.

We note from Eq. (2) that the determinant vanishes if two electrons are the same. That means the Hartree wavefunction is anti-symmetric with respect to the interchange of any set of space-spin coordinates of any two particles, but its Hamiltonian must be invariant under this condition. From here it was necessary to introduce the relativistic corrections with a Breit-Pauli Hamiltonian including mass-variation term, one-body Darwin term and Blume-Watson spin-orbit term which contain the part of the Breit interaction that can be reduced to a one-body operator, also treated by the perturbation theory Alonizan *et al.* (2016).

In previous works (Alonizan *et al.* (2016), for example), we obtained better results with HFR method comparing to similar methods as TFDA potential method; which gives advantage of this method.

The Cowan (CW) code, a suite of four atomic structure programs (RCN, RCN2, RCG and RCE) version 2018 (Kramida, 2018), uses this HFR method. The three first codes are for *ab initio* atomic structure calculations and the

fourth one (RCE) is used to have least-squares fit calculations using an iterative procedure (Cowan, 1981).

3. Atomic structure of the ion Ca XV

We performed calculations of energy levels for the carbon-like ion Ca XV by the suite of atomic structure codes of Cowan adapted by Kramida (2018). The configuration expansion of the basis set used in this work consists of 3 even parity configurations: $2s^2 2p^2$ and $2s^2 2p np$ ($n=3,4$) and 5 odd parity configurations: $2s 2p^3$, $2s^2 2p ns$ ($n=3,4,5$) and $2s^2 2p 3d$.

The calculated values of energy levels and oscillator strengths obtained with this code have been compared with other theoretical methods (Ekman *et al.*, 2014), and with data from NIST database (Kramida *et al.*, 2018).

3.1. Energy levels of the ion Ca XV

In Tables 1 to 5, we list energy levels of the configurations $2s^2 2p^2$, $2s 2p^3$, $2s^2 2p ns$ ($n = 3, 4, 5$), $2s^2 2p np$ ($n = 3, 4$), $2s^2 2p 3d$ for Ca XV ion. The obtained values are compared with those of NIST atomic database (Kramida *et al.*, 2018) and with Ekman *et al.* (2014) values which are calculated using the Multi-Configuration Hartree-Fock (MCHF) method.

Table 1. "Energy levels for the configuration $2s^2 2p^2$ of Ca XV." E(NIST) are from NIST database, E(CW) are the energy levels calculated by using the Cowan (CW) code, and E(EK) calculated using (MCDHF) by Ekman *et al.* All energies are in cm^{-1} .

Conf.	Term	J	E(NIST)	E(CW)	E(EK)
$2s^2 2p^2$	3P	0	0	0	0
$2s^2 2p^2$	3P	1	17559	16353	17553
$2s^2 2p^2$	3P	2	35923	35171	35920
$2s^2 2p^2$	1D	2	108600	104491	108736
$2s^2 2p^2$	1S	0	197670	214620	197839

For the configuration $2s^2 2p^2$, CW code gives close to results to NIST. The results differ by about 4% from the NIST values, while, Ekman *et al.* values are very close to the NIST database values by 0.1%.

For the configuration $2s 2p^3$, the CW code gives values 5.6% higher than NIST database. Ekman *et al.* values are roughly the same differing by only 0.02% from the NIST ones.

Table 2. Same as Table 1, but for configuration $2s\ 2p^3$ of Ca XV.

Conf.	Term	J	E(NIST)	E(CW)	E(EK)
$2s\ 2p^3$	$^5S^o$	2	275900	311928	275788
$2s\ 2p^3$	$^3D^o$	3	500230	533862	500273
$2s\ 2p^3$	$^3D^o$	2	496680	529034	496724
$2s\ 2p^3$	$^3D^o$	1	497570	529652	497632
$2s\ 2p^3$	$^3P^o$	1	582780	607890	582942
$2s\ 2p^3$	$^3P^o$	2	585670	611053	585800
$2s\ 2p^3$	$^3P^o$	0	581730	606177	581886
$2s\ 2p^3$	$^1D^o$	2	729650	759011	730043
$2s\ 2p^3$	$^3S^o$	1	728880	757132	729176
$2s\ 2p^3$	$^1P^o$	1	814380	835599	814815

Table 3. Same as Table 1, but for configurations $2s^2\ 2p\ ns$ ($n = 3, 4, 5$) of Ca XV.

Conf.	Term	J	E(NIST)	E(CW)	E(EK)
$2s^2\ 2p3s$	$^3P^o$	0	-	4392032	4079795
$2s^2\ 2p3s$	$^3P^o$	1	-	4396297	4084845
$2s^2\ 2p3s$	$^3P^o$	2	-	4428144	4115926
$2s^2\ 2p3s$	$^1P^o$	1	-	4441352	4134012
$2s^2\ 2p4s$	$^3P^o$	0	-	4395728	5520070
$2s^2\ 2p4s$	$^3P^o$	1	-	4396731	5522133
$2s^2\ 2p4s$	$^3P^o$	2	-	4431652	5556429
$2s^2\ 2p4s$	$^1P^o$	1	-	4433840	5561725
$2s^2\ 2p5s$	$^3P^o$	0	-	4657441	-
$2s^2\ 2p5s$	$^3P^o$	1	-	4657861	-
$2s^2\ 2p5s$	$^3P^o$	2	-	4693386	-
$2s^2\ 2p5s$	$^1P^o$	1	-	4694256	-

For the configurations $2s^2\ 2p\ ns$ ($n = 3, 4, 5$) and $2s^2\ 2p\ np$ ($n = 3, 4$) the NIST values do not exist for comparison. It should be noted that, we have obtained new energy values that do not exist in Ekman *et al.* for the configuration $2s^2\ 2p\ 5s$ and for the term $2s^2\ 2p\ 4p\ ^1S$.

Table 4. Same as Table 1, but for configurations $2s^2 2p np$ ($n = 3, 4$) of Ca XV.

Conf.	Term	J	E(NIST)	E(CW)	E(EK)
$2s^2 2p3p$	3S	1	-	4476007	4257457
$2s^2 2p3p$	1P	1	-	4446957	4228086
$2s^2 2p3p$	3D	1	-	4424400	4205709
$2s^2 2p3p$	3D	2	-	4445944	4229376
$2s^2 2p3p$	3D	3	-	4472023	4255295
$2s^2 2p3p$	3P	0	-	4475994	4250224
$2s^2 2p3p$	3P	1	-	4494910	4270847
$2s^2 2p3p$	3P	2	-	4501838	4276163
$2s^2 2p3p$	1D	2	-	4528268	4314496
$2s^2 2p3p$	1S	0	-	4567681	4361378
$2s^2 2p4p$	3S	1	-	4491238	5618735
$2s^2 2p4p$	1P	1	-	4487896	5612050
$2s^2 2p4p$	3D	1	-	4450829	5572096
$2s^2 2p4p$	3D	2	-	4456178	5583680
$2s^2 2p4p$	3D	3	-	4488453	5613455
$2s^2 2p4p$	3P	0	-	4459660	5590557
$2s^2 2p4p$	3P	1	-	4455693	5582839
$2s^2 2p4p$	3P	2	-	4491171	5619232
$2s^2 2p4p$	1D	2	-	4496043	5631037
$2s^2 2p4p$	1S	0	-	4501924	-

Table 5. Same as Table 1, but for configuration $2s^2 2p 3d$ of Ca XV.

Conf.	Term	J	E(NIST)	E(CW)	E(EK)
$2s^2 2p3d$	$^3F^o$	2	4363300	3951477	4363635
$2s^2 2p3d$	$^3F^o$	3	4379400	3963833	4378814
$2s^2 2p3d$	$^3F^o$	4	-	3988654	4401309
$2s^2 2p3d$	$^1D^o$	2	-	3966033	4385007
$2s^2 2p3d$	$^3D^o$	1	4399500	3975409	4402470
$2s^2 2p3d$	$^3D^o$	2	4411500	3991878	4413002
$2s^2 2p3d$	$^3D^o$	3	4426400	4000316	4425526
$2s^2 2p3d$	$^3P^o$	2	4435400	4006954	4433389
$2s^2 2p3d$	$^3P^o$	1	4434500	4008947	4435381
$2s^2 2p3d$	$^3P^o$	0	-	4010358	4436968
$2s^2 2p3d$	$^1F^o$	3	4475000	4032514	4474373
$2s^2 2p3d$	$^1P^o$	1	4473400	4032524	4475119

Moreover, with respect to the configuration $2s^2 2p 3d$, some values of ${}^3F_4^o$, ${}^1D^o$ and ${}^3P_0^o$ terms in NIST database do not exist and for the existing data, the CW code gives results 9.6% higher than the NIST values but Ekman *et al.* values stays very close at the same rate from NIST. Indeed, we recommend the use of our CW results, because of the fact that we got new values with the CW code that are not present in the NIST database.

3.2. Oscillator strengths of the ion Ca XV

Instead of the absorption oscillator strengths f_{ij} or the emission oscillator strengths f_{ji} , we use the weighted oscillator strengths gf :

$$gf = g_i f_{ij} = g_f f_{ji} \quad (4)$$

The weighted oscillator strengths and transition probabilities for selected allowed transitions $2s^2 2p^2 {}^3P - 2s 2p^3 {}^3S^o$, $2s^2 2p^2 {}^3P - 2s 2p^3 {}^3P^o$ and $2s^2 2p^2 {}^3P - 2s 2p^3 {}^3D^o$ were computed using the CW code adapted by Kramida (2018).

Tables from 6 to 8 give the weighted oscillator strengths and transition probability values of these transitions for Ca XV ion obtained *ab initio* by CW code and just compared with Ekman *et al.* (2014) values which are calculated using the MCHF method because there is no data to compare in NIST atomic database (Kramida *et al.*, 2018).

Table 6. Weighted oscillator strengths and transition probabilities for the transition ($2s^2 2p^2 {}^3P - 2s 2p^3 {}^3S^o$) of Ca XV ion. $\log gf(\text{CW})$, $\log gf(\text{EK})$ and $gA(\text{CW})$ and $gA(\text{EK})$ are the weighted oscillator strengths and transition probabilities calculated by us and by Ekman *et al.* using the Cowan and (MCDHF) respectively. g_i and g_k are respectively the statistical wights of the term ${}^3P - {}^3S^o$.

λ (nm)	g_i	g_k	$\log gf$		gA	
			(CW)	(EK)	(CW)	(EK)
13.9	5	3	-0.317	-0.462	1.68E+11	1.11E+11
13.5	3	3	-0.599	-0.762	9.22E+10	5.82E+10
13.2	1	3	-1.076	-1.249	3.21E+10	2.00E+10

So, for the results of weighted oscillator strengths $\log gf$ for selected transitions, we found that our results for $2s^2 2p^2 {}^3P - 2s 2p^3 {}^3P^o$ transitions were in a good agreement (the difference is 3.6% for $\log gf$) with the values of Ekman *et al.* Also, for the other transitions, the results differ from the Ekman *et al.* values by about 20% for $2s^2 2p^2 {}^3P - 2s 2p^3 {}^3S^o$ and 17% for $2s^2 2p^2 {}^3P - 2s 2p^3 {}^3D^o$.

On the other hand, the results for transition probabilities gA for selected transitions were compared to the values of the Ekman *et al.*: The CW calculated

Table 7. Same as Table 6, but for the transition ($2s^2 2p^2 \ ^3P - 2s \ 2p^3 \ ^3P^o$) of Ca XV.

λ (nm)	g_i	g_k	$\log gf$		gA	
			(CW)	(EK)	(CW)	(EK)
17.46058	5	3	-1.34	-1.32	1.01E+10	9.54E+09
17.36467	5	5	-0.59	-0.61	5.75E+10	4.91E+10
16.95419	3	1	-1.25	-1.25	1.31E+10	1.20E+10
16.90512	3	3	-1.07	-1.12	1.98E+10	1.61E+10
16.8152	3	5	-1.68	-1.54	4.94E+09	6.15E+09
16.45036	1	3	-1.41	-1.37	9.59E+09	9.66E+09

Table 8. Same as Table 6, but for the transition ($2s^2 2p^2 \ ^3P - 2s \ 2p^3 \ ^3D^o$) of Ca XV.

λ (nm)	g_i	g_k	$\log gf$		gA	
			(CW)	(EK)	(CW)	(EK)
20.25	5	5	-1.790	-2.105	2.64E+09	1.11E+09
20.22	5	3	-2.992	-3.365	1.66E+08	6.15E+07
20.05	5	7	-0.500	-0.699	5.24E+10	2.88E+10
19.51	3	5	-0.644	-0.815	3.98E+10	2.34E+10
19.48	3	3	-1.399	-1.616	7.02E+09	3.72E+09
18.88	1	3	-0.956	-1.126	2.07E+10	1.24E+10

data for $2s^2 \ 2p^2 \ ^3P - 2s \ 2p^3 \ ^3P^o$ transition was in average less than 13% higher of the Ekman *et al.* values, but for $2s^2 \ 2p^2 \ ^3P - 2s \ 2p^3 \ ^3S^o$ transition was in average 57% higher of the Ekman *et al.* values and for $2s^2 \ 2p^2 \ ^3P - 2s \ 2p^3 \ ^3D^o$ transition the difference reach 100%.

4. Conclusion

When comparing the calculated energy levels with experimental values from NIST and the results from Ekman *et al.*, we find that our results for configurations $2s^2 \ 2p^2$, $2s \ 2p^3$ and $2s^2 \ 2p \ 3d$ were close to the NIST database by about 4% to 9%. While, for the other configurations, there are no values to compare with them in NIST, but we found values in the Ekman *et al.* for these configurations except the $2s^2 \ 2p \ 5s$ configuration. So, we got new values with the CW code for the ($2s^2 \ 2p \ 5s$) configuration and for the term ($2s^2 \ 2p \ 4p \ ^1S$) that did not exist before in any experimental data.

As for the results obtained with CW code for all the above transitions of weighted oscillator strengths $\log gf$ are in a good agreement with the values of Ekman *et al.* Also, the results of transition probabilities gA for selected transitions are close to Ekman *et al.* values. For example, the weighted oscillator

strengths and transition probabilities for $2s^2 2p^2 \ ^3P - 2s \ 2p^3 \ ^3P^o$ transitions are in average 3.6% for $\log gf$ and 12% for gA different from the values of Ekman *et al.*

As we mentioned before, there is no abundant data for Ca XV transitions in NIST database, where there are only 14 lines for it (Kramida *et al.*, 2018). So, this study is extremely important to overcome this great lack on atomic structure data for Ca XV ion and it provides the missing values of NIST database and supports the results given by Ekman *et al.* for the weighted oscillator strengths gf and transition probabilities gA which will be very important for the atomic data needed in astrophysical spectroscopy and laboratories.

Acknowledgements. This project was funded by the National Plan for Science, Technology and Innovation (MAARIFAH), King Abdulaziz City for Science and Technology, Kingdom of Saudi Arabia, Award Number (12-MAT2879-02).

References

- Al-Modlej, A., Alraddadi, R.A.B., and Ben Nessib, N.: Energy levels and oscillator strengths for carbon isoelectronic sequence from C I to Ne V 2018, *Eur. Phys. J. Plus* **133**, 379. DOI: 10.1140/epjp/i2018-12192-9
- Alonizan, N., Qindeel, R., & Ben Nessib, N., Atomic structure calculations for neutral oxygen. 2016, *International Journal of Spectroscopy*, **2016** DOI: 10.1155/2016/1697561
- Al-Towyan, A., Nessib, N.B., Alonizan, N., Qindeel, R., and Yacoub, N.: Stark widths dependence on electron temperature for neutral chromium spectral lines 2016, *Eur. Phys. J. Plus* **131**, 9. DOI: 10.1140/epjp/i2016-16009-7
- Bransden, B. & Joachain, C. 2003, *Physics of Atoms and Molecules*, Prentice Hall
- Colón, C., and Alonso-Medina, A.: Calculation of oscillator strengths, transition probabilities and radiative lifetimes of levels in Sn III 2010, *J. Phys. B: At. Mol. Phys.* **43**, 165001. DOI: 10.1088/0953-4075/43/16/165001
- Cowan, R.D.: *The theory of atomic structure and spectra* 1981, *Los Alamos Series in Basic and Applied Sciences*.
- Dere, K.P.: Spectral lines observed in solar flares between 171 and 630 Angstroms. 1978, *Astron. J.* **221**, 1062. DOI: 10.1086/156110
- Dere, K.P., Del Zanna, G., Young, P.R., Landi, E., and Sutherland, R.S.: CHIANTI—An Atomic Database for Emission Lines. XV. Version 9, Improvements for the X-Ray Satellite Lines 2019, *The Astrophysical Journal Supplement Series* **241**, 22. DOI: 10.3847/1538-4365/ab05cf
- Ekman, J., Jönsson, P., Gustafsson, S., Hartman, H., Gaigalas, G., Godefroid, M.R., and Froese Fischer, C.: Calculations with spectroscopic accuracy: energies, transition rates, and Landé g_J -factors in the carbon isoelectronic sequence from Ar XIII to Zn XXV 2014, *Astron. Astrophys.* **564**, A24. DOI: 10.1051/0004-6361/201323163

- Keenan, F.P., Aggarwal, K.M., Katsiyannis, A.C., and Reid, R.H.G.: Extreme Ultraviolet Emission Lines of Ca xv in Solar and Laboratory Spectra 2003, *Solar Physics* **217**, 225. DOI: 10.1023/B:SOLA.0000006871.49518.eb
- Kramida, A., A Suite of Atomic Structure Codes Originally Developed by RD Cowan Adapted for Windows-Based Personal Computers. Available: <https://catalog.data.gov/dataset/a-suite-of-atomic-structure-codes-originally-developed-by-r-d-cowan-adapted-for-windows-ba> [2019, January 10]. DOI: 10.18434/T4/1502500
- Kramida, A., Yu. Ralchenko, Reader, J., & and NIST ASD Team. 2018, NIST Atomic Spectra Database (ver. 5.6.1), [Online]. Available: <https://physics.nist.gov/asd> [2019, April 18]. National Institute of Standards and Technology, Gaithersburg, MD.
- Laming, J.M., and Drake, J.J.: Stellar Coronal Abundances. VI. The First Ionization Potential Effect and ξ Bootis A: Solar-like Anomalies at Intermediate-Activity Levels 1999, *Astron. J.* **516**, 324. DOI: 10.1086/307112
- Nahar, S.N.: Photoionization of Ca XV with high energy features 2017, *New Astronomy* **51**, 69. DOI: 10.1016/j.newast.2016.08.010
- Träbert, E., Beiersdorfer, P., Lepson, J.K., Reinke, M.L., and Rice, J.E.: EUV Spectra and Line Ratios of Multiply Ionized Calcium and Argon Atoms in a Laboratory Plasma 2018, *Astron. J.* **865**, 148. DOI: 10.3847/1538-4357/aadba7

Hydrogen Balmer spectral lines in spectroscopy of underwater electric spark discharge plasma

A. Murmantsev¹, A. Veklich¹, V. Boretskij¹ and K. Lopatko²

¹ *Taras Shevchenko National University of Kiev, 63/13, Volodymyrska str., Kyiv 01601, Ukraine*

² *National University of Life and Environmental Sciences of Ukraine, Kyiv, Ukraine*

Received: July 31, 2019; Accepted: December 2, 2019

Abstract. The behavior of the Balmer series spectral line profiles in the underwater electric spark discharge plasma between copper granules is investigated. Specially developed pulse power source is used to initiate a discharge between copper granules immersed into the deionized water. Typical values of voltage are of 40 – 200 V, current is up to 600 A and pulse frequency is in the range of 0.2 – 2 kHz. The voltage, applied to electrodes, caused a current flow along the chain of closely arranged granules in the stochastic switching mode. Optical emission spectroscopy methods are used for diagnostics of such discharge plasma. Profiles of $H\alpha$ and $H\beta$ hydrogen lines, exposed to the Stark mechanism of spectral lines' broadening, are used to determine electron density. The Boltzmann plot of copper lines' intensities are used to determine the plasma temperature.

Key words: underwater spark discharge – Boltzmann plot – Balmer lines – profiles – Stark broadening

1. Introduction

The investigation of underwater discharge plasma is of great interest to scientists because of its practical use in biology and electrochemistry. This discharge is used as a high-efficient method for the water treatment, surface treatment and plasma sterilizations (Babaeva & Kushner, 2008; Bruggeman & Leys, 2009; Clements et al., 1987). Underwater discharge is widely used for synthesis of micro- and nanoparticles (Lopatko et al., 2015; Cressault et al., 2013). It was found that colloidal solutions with nanoparticles are the most suitable form for biological usage (Lopatko et al., 2009). It is known that the solutions of silver and copper nanoparticles have bactericidal, antiviral, antifungal and antiseptic effects (Xiu et al., 2012), what makes them essential biocide products.

Unfortunately, nowadays there is no exact physical model of such underwater discharge, which increases the interest in studying it, improving of dynamic process in discharge and optimization of generation of colloidal substance process. For improvement of these discharge characteristic and increase quality of

the output solution, it is important to understand main discharge plasma parameters, such as excitation temperature and electron density. Optical emission spectroscopy (OES) is one of the most common methods for determination of these parameters. Specifically, copper and hydrogen spectral lines are widely used for it. Cu I spectral lines are well-studied and widely used (usually Cu I 515.3 nm, broadened by quadratic Stark effect Konjević & Konjević 1986) for electron density measurements (Babich et al., 2014; Fesenko et al., 2014; Venger et al., 2017) as well as Hydrogen lines (Venger et al., 2017; Nikiforov et al., 2015; Wang et al., 2019; Jovičević et al., 2004).

In previous work the $H\alpha$ shape was studied in underwater spark discharge (Tmenova et al., 2017) and in underwater arc discharge with $H\beta$ spectral line (Venger et al., 2017). Electron density, obtained in Venger et al. (2017) from the width of $Cu I$ 515.3 nm and $H\alpha$ spectral lines were of the same order of magnitude for all the studied power modes, values of N_e , obtained from the width of $H\beta$ line were by two orders of magnitude lower for the cases of arc current of 660 and 800 A, and by one order of magnitude lower for the case of 1000 A. It aroused interest to study the behavior of $H\beta$ spectral line profile in underwater spark discharge.

Thus, the main goals of the presented work are investigation of Balmer spectral lines behavior in underwater electric spark discharge, determination of electron density and excitation temperature from $Cu I$ and $H\alpha$ spectral line profile as well as enrolment of $H\beta$ spectral line to electron density measurements by OES. It should give additional methods for future investigation of underwater spark discharge to find correlation of discharge plasma parameters and properties of colloidal substance.

2. Experimental setup

Specially developed pulse power source was used to initiate a discharge between copper granules immersed into the deionized water. Implementation of the low-voltage spark discharges was carried out on the experimental setup, which is shown in Fig.1. It consists of a pulse generator 1, control unit 2, measuring and auxiliary devices: oscilloscope 3, Rogowsky coil 4, voltage divider 5; and discharge chamber 6.

The voltage, applied to electrodes, caused a current flow along the chain of closely arranged granules in the stochastic switching mode. Investigation of the influence of process variables on dispersion and morphology of the products of metal granules erosion during the formation of local spark discharges was carry out. It was performed by varying of electrical parameters of the discharge circuit.

It must be noted, the investigations were carried out in two modes, which differ by generation power. The higher power (second) mode, as it turn out, must be used due to the fact, that $H\beta$ was not observe or was comparable

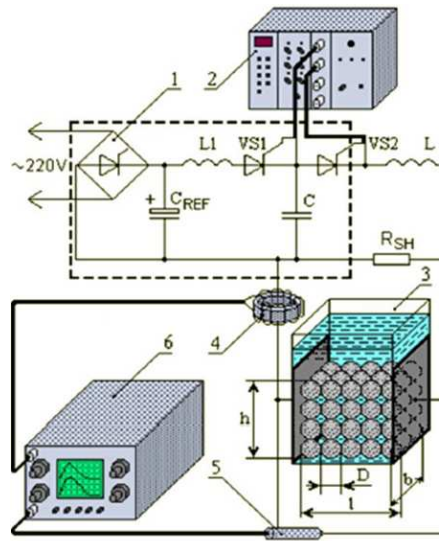


Figure 1. Scheme of experimental setup, that consists of a pulse generator 1, control unit 2, measuring and auxiliary devices: oscilloscope 3, Rogowsky coil 4, voltage divider 5; and discharge chamber 6.

with noise at lower power (first mode). Typical values of voltage were of 40 – 200 V, currents were 100 – 300 A in the first mode and 400 – 600 A in the second mode and pulse frequency was in the range of 0.2 – 2 kHz. As a result of a spark-erosion process, the formation of colloidal fraction was observed. Its morphology markedly differs from a micro fraction and is a common for metallurgical processes at low pressure, namely, the formation of a solid phase resulting from evaporation followed by condensation.

Spectra with Balmer and copper spectral lines were registered by Solar LS SDH-IV spectrometer with a 4-position manually switchable diffraction gratings turret in this investigation. Spectra were registered by CCD (Toshiba TCD 1304 AP, 3648 px). Two spectrometer ranges in two different modes were used to extend the studied spectral range. The first mode was realized in spectral range of 450-910 nm with 0.09 nm spectral resolution, the second mode - in 290-610 nm with 0.18 nm spectral resolution. Spectral sensitivity of this device was determined by tungsten band-lamp and was taken into account in spectral data treatment.

3. Results and Discussions

Fig.2a and 2b show spectra with marked spectral lines, registered in the first and second modes, correspondingly.

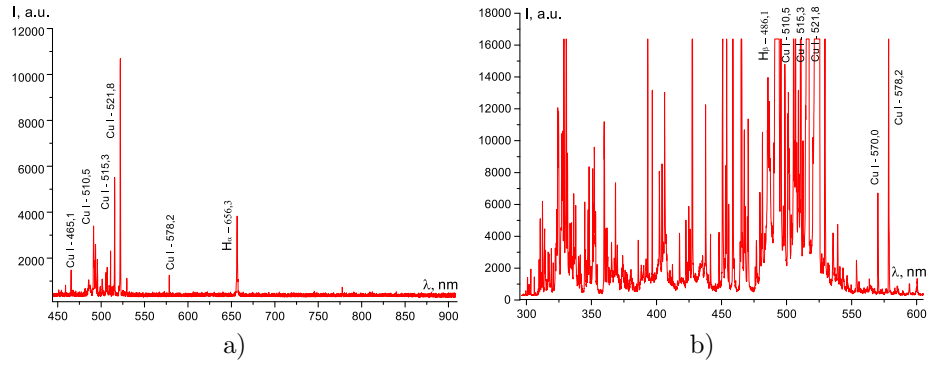


Figure 2. Registered spectra: (a) - the first mode; (b) - the second mode.

The electron density in plasma at the first mode was obtained from the width of *Cu I* 515.3 nm and *Hα* spectral lines. The Voigt function was used in this study to account for spectrometer instrument function, as well as, to determine the Stark width (see Fig.3a and 3b). Other broadened mechanisms (such as resonance broadening, van der Waals broadening etc.) were neglected in this study e.g. (Nikiforov et al., 2015; Laux et al., 2003; Marinov et al., 2014).

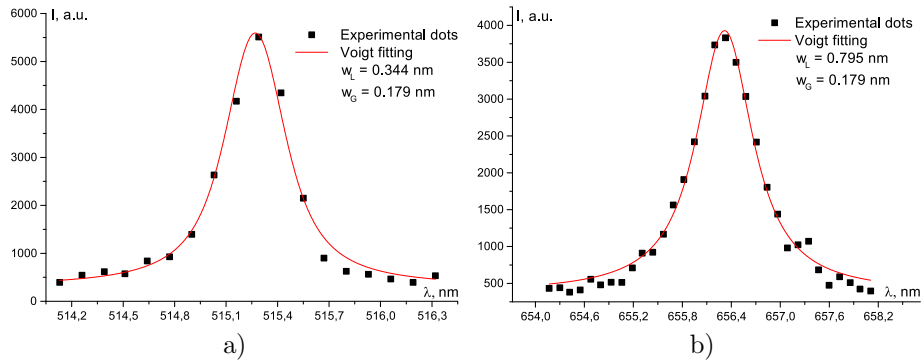


Figure 3. Voigt fitting of spectral line profile of: (a) - *Cu I* 515.3 nm; (b) - *Hα* 656.3 nm.

Electron density, obtained from the widths of *Cu I* 515.3 nm and *Hα* spectral lines, was of $9.9 \times 10^{16} \text{ cm}^{-3}$ and $6.7 \times 10^{16} \text{ cm}^{-3}$, respectively. Plasma excitation temperature was determined by Boltzmann plot technique. Fig.4 shows typical

Boltzmann plot, obtained by *Cu I* 465.1, 510.5, 515.3, 521.8 and 578.2 nm spectral lines. It was found from this plot, that excitation temperature in this plasma source was of 10500 ± 900 K.

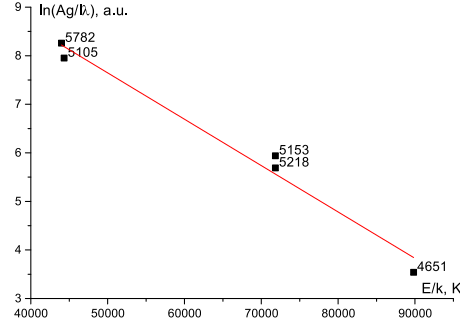


Figure 4. Boltzmann plot on the base of *Cu I* spectral lines.

As one can see from Fig.2b, the spectrum becomes very complicated at the second mode and a lot of spectral lines were exposed. The use of *Cu I* 515.3 nm spectral line was not possible, since it went beyond of the CCD dynamic range. That is why the *Cu I* 570.0 nm, in assumption that it broadened by quadratic Stark effect (Konjević & Konjević (1986)), and $H\beta$ spectral lines were used for electron density measurements (see Fig.5a and 5b). $H\alpha$ (656.3 nm) spectral line was not registered in this mode due to limited spectral range (290-610 nm).

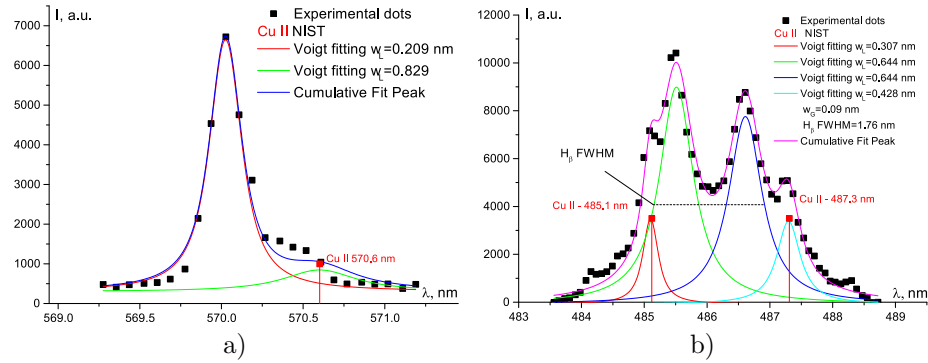


Figure 5. Voigt fitting of spectral line profile of: (a) - *Cu I* 570.0 nm; (b) - $H\beta$ 486.1 nm.

$H\beta$ was approximated by four peaks Voigt profile (Fig.5a) due to two reasons. Firstly, this line had complex shape, specifically, it had dip in the center of line. Secondly, it was overlapped by *Cu II* 485.1 and 487.3 nm spectral lines.

In a similar way it was taken into account (by two peaks Voigt profile) the overlapping of *Cu I* 570.0 nm and *Cu II* 570.6 nm spectral lines (Fig.5b).

The electron density, obtained from $H\beta$ width, can be determined in accordance with Konjević et al. (2012):

$$N_e[m^{-3}] = 10^{22} * (w_S[nm]/0.94666)^{1.49}, \quad (1)$$

where w_S is a Stark width. It must be noted, that w_S not equal width of Lorentz part of the Voigt function (w_L) (Konjević et al., 2012) and must be determined in accordance with Kelleher (1981):

$$w_S = (w_M^{1.4} - w_{D,I}^{1.4})^{1/1.4}, \quad (2)$$

where w_M is the measured FWHM, $w_{D,I}^2 = w_D^2 + w_I^2$ (w_D - Doppler width, w_I - width of instrument function).

The value of electron density, obtained from $H\beta$ width was of $1.73 \times 10^{16} \text{ cm}^{-3}$, from *Cu I* 570.0 nm width - $6.92 \times 10^{17} \text{ cm}^{-3}$.

As one can see, electron density values, obtained from width of *Cu I* 515.3 nm and $H\alpha$ spectral lines are of the same order of magnitude. As for $H\beta$ spectral line, electron density value, obtained from the width of this line is by one order of magnitude lower in comparison of value, obtained from the width of *Cu I* 570.0 nm spectral line. That is the similar results, obtained in previous work (Venger et al., 2017) and, obviously, must be as a subject of future investigation.

The impact of other broadening mechanisms were estimated on base of experimentally obtained plasma parameters (temperature and electron density) to testify the aforementioned neglect. The relations showed by Griem (1974) were used.

Van der Waals broadening. Calculations of van der Waals widths were carry out for different perturbers, specifically, for *H*, *O* and *Cu*. It was assumed that the temperature is 1 eV for the second mode, electron density provided predominantly by copper atoms. Concentrations of such atoms were calculated by Saha equation and were $7 \times 10^{15} \text{ cm}^{-3}$ and $2 \times 10^{17} \text{ cm}^{-3}$ for the first and the second modes, respectively. The ratios between intensities of Cu and H lines were found from the spectra (see Fig.2) to calculate the concentration of Hydrogen atoms of $4 \times 10^{18} \text{ cm}^{-3}$ and $8 \times 10^{18} \text{ cm}^{-3}$ for the first and the second modes, respectively. Polarizability of *H* and *O* was taken from Allen (1976), and for *Cu*, it was taken from Sarkisov et al. (2019). It was estimated that maximal value of van der Waals width was 0.03 nm for $H\alpha$ spectral line with Cu as a perturber.

Resonance broadening. The values of resonance broadening width were lower than 0.003 nm for copper spectral lines and lower than 0.002 nm for Balmer lines.

The values of resonance and van der Waals broadening are much lower than observed line widths, which confirms neglect of other mechanisms except Stark broadening.

Optical Thickness of plasma was estimated additionally. The opacities for different spectral lines were calculated in assumption of the Boltzmann distribu-

tion of atom energy level population. The value of optical thickness for $H\alpha$, $H\beta$ and $Cu I$ 570.0 nm spectral lines were 0.02, 0.004 and 0.006 respectively. The plasma radii were assumed of 1 mm in this case. These results give the reason to disregard the contribution of opacity in data treatment.

4. Conclusions

The behavior of Balmer spectral line profiles, in particular, $H\alpha$ and $H\beta$ was investigated. OES was used for determination of excitation temperature and electron density in plasma of underwater spark discharge.

The values of electron density at lower power mode, obtained from widths of $H\alpha$ and $Cu I$ 515.3 nm spectral lines are the same in order of magnitude. In contrast to this, in the second mode, $H\beta$ and $Cu I$ 570.0 nm spectral lines give different results of electron density which coincide with behavior, observed in previous experiment.

Presently, on the one hand, it is impossible to talk about aptitude of electron density measurements in plasma of underwater spark discharge from the $H\beta$ spectral line profile. On the other hand, such method can be considered potential for such aims. Thus, such investigation should be continued and implemented in other ways in future studies.

References

- Allen, C. W. 1976, *Astrophysical Quantities*
- Babaeva, N. & Kushner, M., Streamer Branching: The Role of Inhomogeneities and Bubbles. 2008, *IEEE Trans. Plasma Sci.*, **38**, 892, DOI: 10.1109/TPS.2008.922434
- Babich, I. L., Boretskij, V. F., Veklich, A. N., & Semenyshyn, R. V., Spectroscopic data and Stark broadening of Cu I and Ag I spectral lines: Selection and analysis. 2014, *Adv. Space Res.*, **54**, 1254, DOI: 10.1016/j.asr.2013.10.034
- Bruggeman, P. & Leys, C., TOPICAL REVIEW: Non-thermal plasmas in and in contact with liquids. 2009, *J. Ph. D. Appl. Phys.*, **42**, 053001, DOI: 10.1088/0022-3727/42/5/053001
- Clements, J., Sato, M., & Davis, R., Preliminary investigation of pre-breakdown phenomena and chemical reactions using a pulsed high-voltage discharge in water. 1987, *IEEE Trans. Ind. Appl.*, **23**, 224, DOI: 10.1109/TIA.1987.4504897
- Cressault, Y., Teulet, P., Gleizes, A., et al., Peculiarities of metal nanoparticles generation by underwater discharges for biological applications. 2013, in XXXIth International Conference on Phenomena in Ionized Gases, Vol. **1**, , 14–19

- Fesenko, S., Veklich, A., Boretskij, V., et al., Properties of thermal air plasma with admixing of copper and carbon. 2014, in *Journal of Physics Conference Series*, Vol. **550**, *J. Phys. Conference Series*, 012008
- Griem, H. R. 1974, *Spectral line broadening by plasmas*
- Jovičević, S., Ivković, M., Konjević, N., Popović, S., & Vušković, L., Excessive Balmer line broadening in microwave-induced discharges. 2004, *J. Appl. Phys.*, **95**, 24, DOI: 10.1063/1.1629133
- Kelleher, D., Stark broadening of visible neutral helium lines in a plasma. 1981, *J. Quant. Spectrosc. Radiat. Transfer*, **25**, 191, DOI: [https://doi.org/10.1016/0022-4073\(81\)90089-3](https://doi.org/10.1016/0022-4073(81)90089-3)
- Konjević, N., Ivković, M., & Sakan, N., Hydrogen Balmer lines for low electron number density plasma diagnostics. 2012, *Spectrochimica Acta*, **76**, 16, DOI: 10.1016/j.sab.2012.06.026
- Konjević, R. & Konjević, N., Stark broadening and shift of neutral copper spectral lines. 1986, *Fizika*, **18**, 327
- Laux, C. O., Spence, T. G., Kruger, C. H., & Zare, R. N., Optical diagnostics of atmospheric pressure air plasmas. 2003, *Plasma Sources Science Technology*, **12**, 125, DOI: 10.1088/0963-0252/12/2/301
- Lopatko, K., Aftandiliants, Y., & Kalenska, S., Colloidal Solution of Metal. 2009, *Ukrainian Patent*, 12
- Lopatko, K., Aftandiliants, Y., Veklich, A., et al., Enrichment of colloidal solutions by nanoparticles in underwater spark discharge. 2015, *Probs. At. Sci. and Tech.*, **10**, 267
- Marinov, I., Starikovskaia, S., & Rousseau, A., Dynamics of plasma evolution in a nanosecond underwater discharge. 2014, *Journal of Physics D Applied Physics*, **47**, 224017, DOI: 10.1088/0022-3727/47/22/224017
- Nikiforov, A. Y., Leys, C., Gonzalez, M. A., & Walsh, J. L., Electron density measurement in atmospheric pressure plasma jets: Stark broadening of hydrogenated and non-hydrogenated lines. 2015, *Plasma Sources Science Technology*, **24**, 034001, DOI: 10.1088/0963-0252/24/3/034001
- Sarkisov, G. S., Hamilton, A., & Sotnikov, V., Dynamic dipole polarizability of gold and copper atoms for 532- and 1064-nm wavelengths. 2019, *Phys. Rev. A*, **99**, 012503, DOI: 10.1103/PhysRevA.99.012503
- Tmenova, T., Veklich, A., Boretskij, V., et al., Optical emission spectroscopy of plasma of underwater electric spark discharge between metal granules. 2017, *Probs. At. Sci. and Tech.*, **107**, 132
- Venger, R., Tmenova, T., Valensi, F., et al., Detailed Investigation of the Electric Discharge Plasma between Copper Electrodes Immersed into Water. 2017, *Atoms*, **5**, 40, DOI: 10.3390/atoms5040040

- Wang, H., Wandell, R. J., Tachibana, K., Voráč, J., & Locke, B. R., The influence of liquid conductivity on electrical breakdown and hydrogen peroxide production in a nanosecond pulsed plasma discharge generated in a water-film plasma reactor. 2019, *J. Phys. D. Appl. Phys.*, **52**, 075201, DOI: 10.1088/1361-6463/aaf132
- Xiu, Z.-m., Zhang, Q.-b., Puppala, H. L., Colvin, V. L., & Alvarez, P. J. J., Negligible Particle-Specific Antibacterial Activity of Silver Nanoparticles. 2012, *Nano Letters*, **12**, 4271, DOI: 10.1021/nl301934w

Hydrogen Stark broadening calculations in white dwarf atmosphere conditions

J. Rosato, I. Hannachi and R. Stamm

*Laboratoire PIIM, UMR 7345 Aix-Marseille Université / CNRS, F-13397
Marseille Cedex 20, France
(E-mail: joel.rosato@univ-amu.fr)*

Received: July 26, 2019; Accepted: August 22, 2019

Abstract. We discuss a selection of problems involved in hydrogen Stark broadening calculations in white dwarf atmosphere conditions. The ion dynamics issue, the description of quadrupolar interactions, and the Zeeman splitting due to strong magnetic fields are successively considered. Calculations of the H β line shape are performed as an illustration.

Key words: White dwarfs – Stark effect – Zeeman effect

1. Introduction

Studies of white dwarf atmospheres have shown that the majority of white dwarfs have an atmosphere of pure hydrogen as a result of gravitational settling, which removes helium and heavier elements from the atmosphere and moves them towards inner layers [Fontaine & Michaud (1979); Rohrmann (2001)]. These atmospheres can be considered as hydrogen plasmas, which are similar to some that can be created in laboratory experiments [Parigger et al. (2018)]. Such white dwarfs are classified as being of the DA type due to the strong hydrogen absorption lines they present. The electron density in a white dwarf atmosphere is high enough (up to 10^{17} cm $^{-3}$, and higher) so that the line shapes are dominated by Stark broadening and, hence, can serve as a probe of the electron density N_e . In this work, we give a review of specific issues which are involved in the modeling of Stark broadening in white dwarf atmospheres. Calculations of the H β line shape are performed as an illustration.

2. Stark broadening with ion dynamics

We first give a summary of the line broadening formalism involved in line shape calculations. We focus on the spectral profile of a single line, without considering the contribution of continuum radiation; the latter can be addressed by using a dedicated model for the atomic populations, such as in [Tremblay & Bergeron (2009)]. Consider an atom that emits or absorbs a photon (for the sake of clarity in discussions, it will always be referred to as the “emitter”) in the presence of charged particles located at its vicinity. The electric field they generate modifies

the energy level structure of the emitter (Stark effect), and the resulting spectral lines are broader. The spectrum of a Stark-broadened line is proportional to the Fourier transform of the dipole autocorrelation function:

$$I(\omega) \propto \text{Re} \int_0^\infty dt \{ \text{Tr}[\rho \mathbf{d}(0) \cdot \mathbf{d}(t)] \} e^{i\omega t}. \quad (1)$$

Here, $\mathbf{d}(t)$ denotes the atomic dipole operator expressed in the Heisenberg picture, ρ is the density operator, $\text{Tr}(\dots)$ denotes a trace over the atomic states and the brackets $\{\dots\}$ correspond to an average over the perturbers. The dipole at time t is related to its initial value through $\mathbf{d}(t) = U^\dagger(t) \mathbf{d}(0) U(t)$, where $U(t) \equiv U(t, 0)$ is the evolution operator from time 0 to t . The latter obeys the time-dependent Schrödinger equation:

$$i\hbar \frac{dU}{dt}(t) = [H_0 + V(t)]U(t). \quad (2)$$

Here, H_0 is the Hamiltonian corresponding to the unperturbed atom and $V(t) = -\mathbf{d} \cdot \mathbf{E}(t)$ is the Stark effect term; $\mathbf{E}(t)$ is the electric field generated at the emitter's location by the perturbers. In the framework of the so-called "standard model", the ions are assumed motionless and the electrons are described within a collisional picture in terms of a relaxation ("collision") operator K_e . In practice, these two assumptions yield the substitution $-\mathbf{d} \cdot \mathbf{E}(t) \rightarrow -\mathbf{d} \cdot \mathbf{E}_i(0) - iK_e$ in the Stark effect term; the Schrödinger equation has an exponential solution and the line shape is obtained from a matrix inversion (e.g. Griem (1974) for details). The standard model provides a good estimate of the line broadening but it can be inaccurate in regimes such that the ions move significantly during the characteristic decorrelation time for the dipole (usually referred to as the "time-of-interest" t_i ; it is of the order of the inverse line width). An illustration of this inaccuracy is given in Figure 1. The spectral profile of H β has been calculated assuming a pure and completely ionized hydrogen plasma, of density $N_e = N_i = 10^{17} \text{ cm}^{-3}$ and temperature $T_e = T_i = 1 \text{ eV}$. These values correspond to white dwarf atmosphere conditions. For the sake of clarity, the broadening due to electrons has not been retained in the calculations. The calculation with account of ion dynamics has been done using a computer simulation technique, developed previously for tokamak plasma spectroscopy applications [Rosato et al. (2009)]. As can be seen in the figure, the ion dynamics yields a spectrum larger than that expected from a static ion model. This result is in agreement with early studies of ion dynamics [e.g. Stamm et al. (1986)]; a noticeable result is that the dip at the center is less pronounced. A criterion for the static approximation for ions to hold is that the collision time $\tau_c = r_0/v$ (with $r_0 \sim N_i^{-1/3}$ and $v \sim \sqrt{2T_i/m_i}$) must be larger than the time-of-interest. In the conditions considered here, the ratio t_i/τ_c is of the order of several tens of percents, which indicates that ion dynamics effects cannot be neglected.

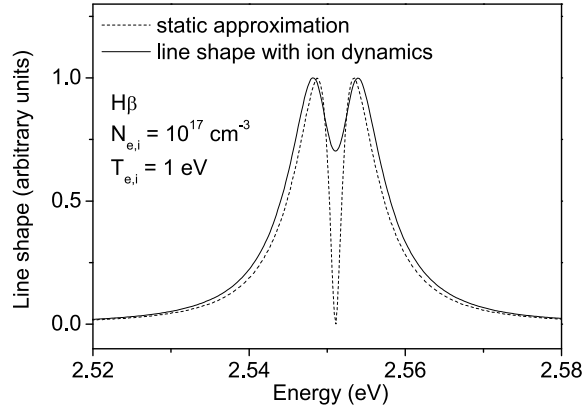


Figure 1. Spectral profile of H β calculated in white dwarf atmosphere conditions, assuming a static model for ions and retaining the ion dynamics during the time-of-interest. The ion dynamics results in an additional broadening of the line. In particular, the dip present at the center of the line is less pronounced.

3. Quadrupolar interaction

The Stark effect Hamiltonian $V = -\mathbf{d} \cdot \mathbf{E}$ corresponds to the first-order term in a multipole expansion; in dense media, the mean distance between an emitter and a perturber can be small enough so that higher-order terms need to be retained. Other-than-dipole interactions can result in an asymmetry of the spectral lines [Djurović et al. (2009); Halenka et al. (2015); Gomez et al. (2016)]. Figure 2 shows an illustration of such an asymmetry in white dwarf atmosphere conditions. The H β line shape has been calculated with account of the quadrupolar interaction, assuming the same plasma parameters as in the previous section. The quadrupolar interaction is described through an additional term in the Hamiltonian, $V_Q = -(1/3)\mathbf{Q} : \nabla\mathbf{E}$, where the quadrupolar moment is defined as $\mathbf{Q} = -e(3\mathbf{r}\mathbf{r} - r^2\mathbf{I})/2$ with \mathbf{r} being the position of the atomic electron and \mathbf{I} being the identity matrix. The broadening due to electrons has not been retained here, again for clarity purposes. As can be seen in the figure, the blue component of the line is higher than the red component. This asymmetry is all the more pronounced that the density is high. Specific investigations using line shape codes have been carried out recently in order to address this effect [SLSP workshop; <http://plasma-gate.weizmann.ac.il/slsp/>] and calculations are still underway. In particular, a pending issue is the relative importance of multipolar interactions with respect to the quadratic Stark effect (namely: the coupling between states of different principal quantum numbers), which is important in high density

regimes and also yields an asymmetry. These two effects must be treated on an equal footing in calculations in order to have an accurate description of spectra.

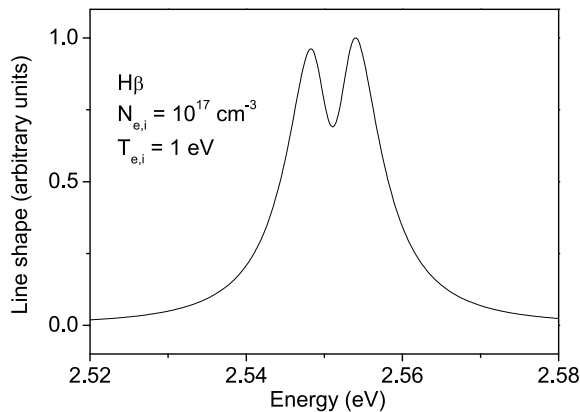


Figure 2. The quadrupolar interaction yields an asymmetry. Here, the $H\beta$ line shape has been calculated with the same conditions as in Fig. 1.

4. Zeeman effect

A significant amount of white dwarf spectra exhibit lines with a triplet structure, which is a feature of the presence of strong magnetic fields [Külebi et al. (2009); Kepler et al. (2013)]. Simple estimates based on the separation between the components indicate that the magnetic field can attain several kiloteslas. The combined action of electric and magnetic fields on lines has recently been addressed in white dwarf atmosphere conditions [Rosato et al. (2017); Kieu et al. (2017)]. A pending issue is the description of the overlapping and the mixing between two consecutive lines (e.g., $H\beta$ and $H\gamma$) in regimes such that the Zeeman splitting is comparable to the separation between the lines. A proper description of a spectrum should account both for the linear Zeeman perturbation $-\boldsymbol{\mu} \cdot \mathbf{B}$ (with $\boldsymbol{\mu}$ being the atomic magnetic moment) and the quadratic perturbation $e^2(\mathbf{B} \times \mathbf{r})^2/8m_e$ [Garstang (1977)]. Figure 3 shows an example where such a situation occurs. The $H\beta$ line shape has been calculated assuming the same plasma conditions as above. A value of 2 kT has been taken for the magnetic field and the observation angle θ has been set equal to 90° . The spectrum presents many components, which is a feature of the quadratic Zeeman effect. The plot in dashed line corresponds to a calculation of $H\beta$ neglecting the energy level mixing and the solid line corresponds to a calculation where mixing with the $n = 5$

level is retained. As can be seen, there is an overall shift of the spectrum towards the red direction. This shift is a feature of the repulsion between energy levels due to an external perturbation; it is expected from basic time-independent perturbation theory. A noticeable result is that not all components are shifted with the same amplitude. Calculations are presently underway in order to better characterize this effect.

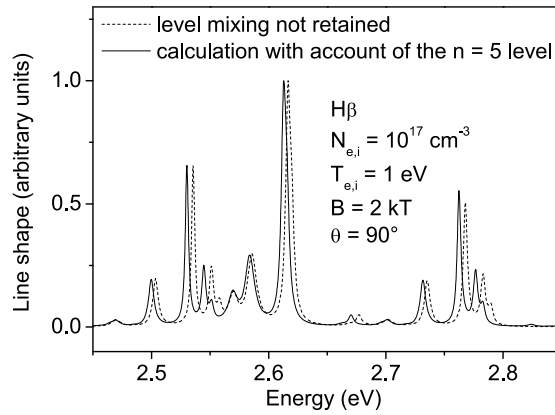


Figure 3. Some white dwarfs have a strong magnetic field; as a result, the spectral lines are subject to both linear and quadratic Zeeman effects. The quadratic Zeeman effect can induce a mixing between energy levels of different principal quantum number, which must be retained in a calculation if accuracy is sought for. Here, the figure shows an example where such a situation occurs. The calculation neglecting energy level mixing (dashed line) yields an overall shift of the spectrum. Not all components are shifted with the same amplitude.

5. Conclusion

We have identified several problems involved in the modeling of hydrogen Stark line shapes in conditions relevant to white dwarf atmospheres. A line can be broader due to ion dynamics effects, and, on the other hand, it can be asymmetric due to quadrupolar interactions. These two effects must be accounted for in models if accuracy is sought for in a spectroscopic diagnostic. An additional issue that must be addressed is the presence of quadratic Zeeman effect and its influence on energy level mixing. The $H\beta$ calculations we have done indicate a significant shift of the overall spectrum. New calculations are presently ongoing in order to better quantify this effect. An additional issue that will be addressed

is the modification of the particle trajectories due to the magnetic field, and how this alters spectral line shapes. New investigations will be done along the lines of previous works [Rosato et al. (2018); Alexiou (2019)].

Acknowledgements. This work has been carried out within the framework of the French Research Federation for Magnetic Fusion Studies.

References

- Alexiou, S. 2019, *Atoms*, **7**, 52
- Djurović, S. et al. 2009, *Phys. Rev. E*, **79**, 046402
- Fontaine, G. & Michaud, G. 1979, *Astrophys. J.*, **231**, 826
- Garstang, R. H. 1977, *Rep. Prog. Phys.*, **40**, 105
- Gomez, T. A. et al. 2016, *Phys. Rev. A*, **94**, 022501
- Griem, H. R. 1974, *Spectral Line Broadening by Plasmas*, ed. A. Press (London)
- Halenka, J. et al. 2015, *Astrophys. J.*, **808**, 131
- Kepler, S. O. et al. 2013, *Mon. Not. R. Astron. Soc.*, **429**, 2934
- Kieu, N. et al. 2017, *Atoms*, **5**, 44
- Külebi, B. et al. 2009, *Astron. Astrophys.*, **506**, 1341
- Parigger, C. G. et al. 2018, *Atoms*, **6**, 36
- Rohrmann, R. D. 2001, *Mon. Not. R. Astron. Soc.*, **323**, 699
- Rosato, J., Ferri, S., & Stamm, R. 2018, *Atoms*, **6**, 12
- Rosato, J. et al. 2009, *Phys. Rev. E*, **79**, 046408
- Rosato, J. et al. 2017, *Atoms*, **5**, 36
- Stamm, R. et al. 1986, *Phys. Rev. A*, **34**, 4144
- Tremblay, P.-E. & Bergeron, P. 2009, *Astrophys. J.*, **696**, 1755

Stark broadening of B I spectral lines within $2s^22p - 2s^2nd$ Spectral Series

Magdalena Christova¹, Milan S. Dimitrijević^{2,3} and
Sylvie Sahal-Bréchet³

¹ *Department of Applied Physics, Faculty of Applied Mathematics and Informatics, Technical University - Sofia, Kl. Ohridski Blvd 8, 1000 Sofia, Bulgaria, (E-mail: mchristo@tu-sofia.bg)*

² *Astronomical Observatory, Volgina 7, 11060 Belgrade, Serbia, (E-mail: mdimitrijevic@aob.rs)*

³ *Sorbonne Université, Observatoire de Paris, Université PSL, CNRS, LERMA, F-92190, Meudon, France, (E-mail: mdimitrijevic@aob.rs, sylvie.sahal-brechet@obspm.fr)*

Received: August 13, 2019; Accepted: September 15, 2019

Abstract. Stark broadening parameters of neutral boron spectral lines within one series $2s^22p - 2s^2nd$ ($n = 3 - 8$) have been presented. The dependence of: temperature, electron density and principal quantum number has been studied. The contribution in Stark width and shift of different perturbers (electrons, protons and ionized helium ions) has been obtained. Results are applicable for astrophysical and laboratory plasma diagnostics.

Key words: Atomic data – Atomic processes – Line: profiles – Plasmas

1. Introduction

The study reports calculated Stark broadening parameters (widths and shifts) of boron spectral lines. The impact semi-classical perturbation formalism has been applied (Sahal-Bréchet, 1969a,b). Data on boron lines, including Stark broadening, are of interest in astrophysics but also for laboratory (Blagojević et al., 1999), fusion (Iglesias et al., 1997) and laser produced (Nicolosi et al., 1978) plasmas investigations as well as for laser research and development (Wang et al., 1992).

The story of origin of the formation of LiBeB trio starts from the middle of the twentieth century (Burbridge et al., 1957; Penzias, 1978) and stays unsolved up to now (Lyubimkov, 2018). In the whole nuclear realm, the light elements LiBeB are exceptional since they are both, simple and rare. A general trend in nature is that the abundance of the elements versus the mass number draws a globally decreasing curve (Vangioni-Flam & Cassé, 1999; Vangioni-Flam et al., 2000). Lithium, beryllium, and boron are of great interest for two sets of reasons, which might be categorized as cosmological and related to stellar structure (Duncan et al., 1998). Heretofore, it was reported in the literature, that the rare

and fragile light nuclei, lithium, beryllium and boron are not generated in the normal course of stellar nucleosynthesis (except ${}^7\text{Li}$, in the galactic disk) and are, in fact, destroyed in stellar interiors. The standard Big Bang nucleosynthesis (BBN) theory is not effective to explain the generation of ${}^6\text{Li}$, ${}^9\text{Be}$, ${}^{10}\text{B}$, ${}^{11}\text{B}$ (Schramm, 1993; Thomas *et al.*, 1993), what is reflected in the low abundance of these simple species. Recently, according to Lyubimkov (2018), there are modern data indicating that first chemical elements up to oxygen are formed in Big Bang nucleosynthesis. Nevertheless, the abundance questions are among unsolved problems. Lithium, beryllium, and boron are a unified group of elements from the standpoint of evolution, since they burn up in stars in the same process, (p, α) reactions. The stellar structure interest stems from the fact that Li, Be and B undergo nuclear reactions at relatively low temperatures, approximately 2.5, 3.5, and 5×10^6 K at densities similar to those in the Sun. Since these temperatures are reached not far below the convection zone and well outside the core in solar-type stars, circulation and destruction of the light elements can result in observable abundance changes. Observations of these changes can provide an invaluable probe of stellar structure and mixing. Both Li and Be abundances are greatly reduced in the giants from their initial main-sequence values. Duncan *et al.* (1998) report the B abundance of two giants and one dwarf in the Hyades, the latter included to evaluate explicitly the boron abundance prior to giant-branch evolution. They demonstrate empirically that boron contributes to the absorption spectra of cool stars. HST measurements of boron abundances of these objects have permitted a test of one of the basic predictions of stellar evolution theory: the growth of the convection zone as a star evolves up the giant branch.

On the basis of Hubble Space Telescope Goddard High Resolution Spectrograph, the boron abundance has been derived for the young Orion solar-type member BD - 05°1317 and reported by Cunha *et al.* (1999). According to their conclusion, the real interstellar boron abundance and its comparison with the stellar values remains uncertain. The boron abundance derived from spectra of B-type stars of the Orion association is consistent with the expectation that it should be similar to those of the solar system, but it is considerably higher than the interstellar boron abundance for several lines of sight, including some toward Orion. Question of low boron abundance emerges, why interstellar gas and young stars have boron abundance lower 4 or 5 times since the Solar system was formed (Cunha *et al.*, 1999). The light trace elements lithium, beryllium, and boron play a major and significant role in the formation of the primordial fireball, interstellar, intergalactic space, stellar surfaces and interiors (Venn *et al.*, 2002). This role arises because boron nuclei are destroyed by warm protons, and thus even quite shallow mixing of the atmosphere with the interior reduces the surface abundance by bringing boron-depleted material to the surface. The importance of latest nuclei data, including boron to carbon ratio, from space station experiment Alpha Magnetic Spectrometer (AMS-02) is outlined by Niu & Li (2018). Using the abundant information carried by cosmic rays about

their sources and propagation environments, the properties of the structure of the Galaxy, the interstellar medium (ISM) and even dark matter (DM) in the Galaxy could be investigated.

In hot stars, boron alone is observable and a study on boron abundance of B-type stars has been presented in Venn et al. (2002). Stark broadening is important for hot stars. The present-day boron abundance is a principal goal of most of studies on hot stars since it could improve our understanding of the Galactic chemical evolution of boron. It is shown that boron is a tracer of some various processes affecting a surface composition of hot stars that are not included in the standard models of stellar evolution. Boron abundances are a clue to unraveling the nonstandard processes that affect young hot stars. Stark broadening is often needed for abundances determination of hot stars. In Popović et al. (1999b) errors in abundances have been analyzed, in the case that Stark broadening is not taken into account, especially for A-type stars.

In Duncan et al. (1998) the importance of light element abundance for the giant-branch evolution is underlined. Spectral lines of boron ions have been observed in stellar spectra. B I lines have been observed in F and G stars (Duncan et al., 1997). Especially for white dwarfs, Stark broadening mechanism is usually the principal one and Stark broadening data for various atomic and ionic lines are of particular interest for WDs (Popović et al., 1999b; Tankosić et al., 2003; Milovanović et al., 2004; Simić et al., 2006; Dimitrijević et al., 2011; Dufour et al., 2011; Simić et al., 2013, 2014). For A type and late B type stars from the main sequence this broadening mechanism may be of interest (Lanz et al., 1988; Popović et al., 1999a,b, 2001a,b; Dimitrijević et al., 2003a,b; Tankosić et al., 2003; Dimitrijević et al., 2004; Milovanović et al., 2004; Dimitrijević et al., 2005; Simić et al., 2005a,b, 2009, 2013, 2014).

The increasing astrophysical importance of Stark broadening data for various atoms and ions of trace elements, arises with the development of satellite born telescopes. They provide high-resolution spectra of earlier inaccessible quality. Well-resolved line profiles for many white dwarfs, where Stark broadening is important, have been and will be registered by the Space Telescope Imaging Spectrograph (STIS), Cosmic Origins Spectrograph (COS) and Goddard High Resolution Spectrograph (GHRS), Far Ultraviolet Spectroscopy Explorer (FUSE), the International Ultraviolet Explorer and others.

Consequently the origin and evolution of boron, are of particular interest and the corresponding Stark broadening data are needed (Tankosić et al., 2003).

Recently, we have calculated Stark broadening parameters for 157 multiplets of helium-like boron (B IV) multiplets (Dimitrijević et al., 2014, 2016). To complete as much as possible the corresponding Stark broadening data needed in astrophysics, laboratory-, technological-, fusion-, and laser produced-plasma physics, our aim is to present in this work new theoretical determinations of Stark broadening parameters (full widths at half intensity and shifts) within the impact semi-classical perturbation approach for B I multiplets and to study their regularities within a spectral series.

2. Theory

Interactions between an atom (ion, or molecule) and surrounding particles (perturbers) in a gas or plasma provoke broadening and shift of spectral line profile when this atom emits or absorbs light. This broadening is known as pressure broadening. The width of the profile at half maximum of the intensity and the shift of spectral line profile are broadening parameters. They depend from the temperature and density of the medium and could be used for spectroscopic diagnostics. When the perturbers are charged particles the observed broadening is called Stark broadening. The plasma in the Universe exists in a huge interval of temperatures and densities and Stark broadening could be notable or dominant in many domains. At temperatures of the order of 10^4 K and densities of 10^{13} - 10^{15} cm^{-3} , Stark broadening is powerful for modelling and analysing spectra of moderately hot (A) and hot (B) types of stars (Sahal-Br  chot, 2010). Especially, Stark broadening is the dominant collisional line broadening process in all layers of the atmosphere of white dwarfs. Stark broadening theory is successfully applied for the purposes of spectroscopic diagnostics and modelling. For such purposes the knowledge of numerous atomic data and spectral profiles is required. The white dwarfs are very faint objects and observed profiles of trace elements, as boron in the present case, are useful probes for modern spectroscopic diagnostics. Interpretation of the spectra of white dwarfs allows to understand the evolution of these very old stars, which are close to death.

Sahal-Br  chot theory of Stark broadening (Sahal-Br  chot, 1969a,b) has been applied in this study. The theory is based on the semi-classical perturbation formalism. According to this theory, the full half width (W) and the shift (d) of an isolated line originating from the transition between the initial level i and the final level f is expressed as:

$$W = 2N \int v f(v) dv \left(\sum_{i' \neq i} \sigma_{ii'}(v) + \sum_{f' \neq f} \sigma_{ff'}(v) + \sigma_{el} \right) \quad (1)$$

$$d = N \int v f(v) dv \int_{R_3}^{R_D} 2\pi \rho d\rho \sin(2\varphi_p). \quad (2)$$

where i' and f' are perturbing levels, n_e and v are the electron density and the velocity of perturbers respectively, and $f(v)$ is the Maxwellian distribution of electron velocities.

The inelastic contribution in the width (cross sections $\sigma_{ii'}(v)$, and $\sigma_{ff'}(v)$) can be expressed by an integration of the transition probability $P_{ii'}$ over the impact parameter ρ :

$$\sum_{i' \neq i} \sigma_{ii'}(v) = \frac{1}{2} \pi R_1^2 + \int_{R_1}^{R_D} 2\pi \rho d\rho \sum_{i' \neq i} P_{ii'}(\rho, v). \quad (3)$$

The elastic collision cross section for the width is given by

$$\sigma_{el} = 2\pi R_2^2 + \int_{R_2}^{R_D} 2\pi\rho d\rho \sin^2 \delta, \quad (4)$$

$$\delta = (\varphi_p^2 + \varphi_q^2)^{\frac{1}{2}}. \quad (5)$$

The phase shifts ϕ_p and ϕ_q are caused by the polarization and quadrupole potential interactions, respectively. The symmetrization procedure, cut-off parameters R_1 , R_2 , R_3 and Debye cut-off R_d are described in Sahal-Bréchet (1969a,b). This theoretical method has been developed by later innovations and optimizations, described in details in Sahal-Bréchet et al. (2014).

3. Results

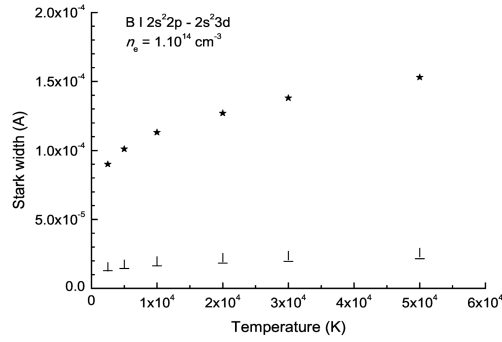


Figure 1. Stark broadening width for $2s^2 2p - 2s^2 3d$ transition for electron density 10^{14} cm^{-3} versus temperature from different type of perturbers: electrons - star; protons - vertical dash; ionized helium ions - horizontal dash.

Stark broadening impact parameters, full width at half maximum of intensity (FWHM - W) and shift (d) for B I lines within one spectral series have been calculated. Semi-classical perturbation method (Sahal-Bréchet, 1969a,b), has been applied. Electrons, protons, and helium ions have been examined as perturbers and their contribution to the total Stark broadening parameters has been discussed. The temperature interval of interest is (2500 - 50 000) K, and those for electron density is $10^{11} - 10^{20} \text{ cm}^{-3}$. The role of temperature and electron density has been studied. Energy levels needed for these calculations, have been taken from Kramida & Ryabtsev (2007), while for the needed oscillator

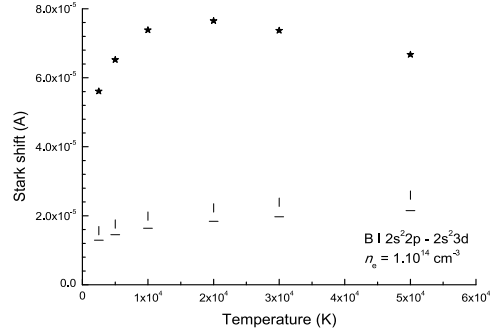


Figure 2. Same as in Fig. 1 but for the shift.

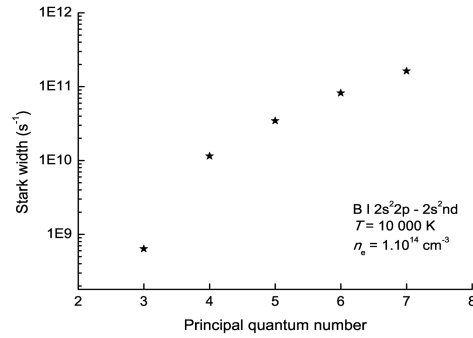


Figure 3. Electron broadening width for spectral lines within $2s^22p - 2s^2nd$ ($n = 3 - 8$) spectral series *versus* principal quantum number. The electron density is 10^{14} cm^{-3} and the temperature - 10 000 K.

strengths Bates & Damgaard (1949) method has been used, together with the tables of Oertel & Shomo (1968).

Studied lines belong to one spectral series $2s^22p - 2s^2nd$ for $n = 3 - 8$. The Stark width and shift of $2s^22p - 2s^23d$ spectral line have been illustrated in Figs.1 and 2 respectively. The total Stark width and shift are due to interactions with electrons, protons and ionized helium ions. The contribution of every type of perturbers has been estimated and shown in the figure. All components of the width slowly increase with the temperature. The proton width is almost the same as the width from He^+ ions, while the electron width is more than five times greater. The proton-impact shift as well as shift from He^+ ion impacts

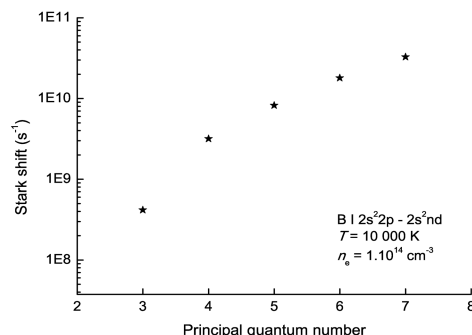


Figure 4. Same as in Fig. 5 but for the shift.

also increase with the temperature, while electron shift reach a maximum at 20000 K and slowly decreases for higher values.

The variation of electron width and shift versus principal quantum number within one spectral series has been presented in Figs. 3 and 4 respectively. We can see a regular increase of widths and shifts with the increase of principal quantum number, as expected. This regular behavior can be used for interpolation of new data if we have spectral series where Stark broadening parameters are not known for all transitions.

4. Conclusion

Stark broadening impact parameters of B I spectral lines within the series $2s^22p - 2s^2nd$ ($n = 3 - 8$) have been calculated. The role of the: temperature, electron density and principal quantum number has been studied. The contribution to Stark width and shift of different perturbers (electrons, protons and ionized helium ions) has been obtained. Results are applicable for astrophysical and laboratory plasma diagnostics.

References

- Bates, D. R., Damgaard, A., The Calculation of the Absolute Strengths of Spectral Lines. 1949, *Philos. Trans. R. Soc. London A*, **242**, 101
- Blagojević, B., Popović, M. V., Konjević, N., & Dimitrijević, M. S., Stark Broadening Parameters of Analogous Spectral Lines Along the Lithium and Beryllium Isoelectronic Sequences. 1999, *J. Quant. Spectrosc. Radiat. Transfer*, **61**, 361

- Burbridge, E. M., Burbridge, G. R., Fowler, W. A., & Hoyle, F., Synthesis of the Elements in Stars. 1957, *Rev. Mod. Phys.*, **29**, 547
- Cunha, K., Smith, V. V., & Lambert, D. L., The Boron Abundance of the Orion G-Dwarf Member BD -05°1317. 1999, *ApJ*, **519**, 844
- Cunha, K., Lambert, D. L., Lemke, M., Gies, D. R., & Roberts, L. C., Boron Abundances of B Stars of the Orion Association. 1997, *ApJ*, **478**, 211
- Dimitrijević, M. S., Jovanović, P., & Simić, Z., Stark broadening of neutral germanium spectral lines. 2003a, *A&A*, **410**, 735
- Dimitrijević, M. S., Ryabchikova, T., Popović, L. Č., Shulyak, D., & Tsymbal, V., On the influence of Stark broadening on Si I lines in stellar atmospheres. 2003b, *A&A*, **404**, 1099
- Dimitrijević, M. S., Dačić, M., Cvetković, Z., & Simić, Z., Stark broadening of Ga I spectral lines. 2004, *A&A*, **425**, 1147
- Dimitrijević, M. S., Ryabchikova, T., Popović, L. Č., Shulyak, D., & Khan, S., On the influence of Stark broadening on Cr I lines in stellar atmospheres, 2005, *A&A*, **435**, 1191
- Dimitrijević, M. S., Kovačević, A., Simić, Z., & Sahal-Bréchet, S., Stark Broadening of Several Ne II, Ne III and O III Spectral Lines for the Stark-B Database. 2011, *Baltic Astronomy*, **20**, 580
- Dimitrijević, M. S., Christova, M., Simić, Z., Kovačević, A., & Sahal-Bréchet, S., Stark broadening of B IV lines for astrophysical and laboratory plasma research. 2014, *Adv. Space Res.*, **54**, 1195
- Dimitrijević, M.S., Christova, M., Simić, Z., Kovačević, A., & Sahal-Bréchet, S., Stark broadening of B IV spectral lines. 2016, *Mon. Not. R. Astron. Soc.*, **460**(2), pp. 1658-1663
- Dufour, P., Ben Nessib, N., Sahal-Bréchet, S., & Dimitrijević, M. S., Stark Broadening of Carbon and Oxygen Lines in Hot DQ White Dwarf Stars: Recent Results and Applications. 2011, *Baltic Astronomy*, **20**, 511
- Duncan, D. K., Peterson, R. C., Thorburn, J. A., & Pinsonneault, M. H., Boron Abundances and Internal Mixing in Stars. I. The Hyades Giants. 1998, *ApJ*, **499**, 871
- Duncan, D. K., Primas, F., Rebull, L. M., Boesgaard, A. M., Deliyannis, Constantine P., Hobbs, L. M., King, J. R., & Ryan, S. G., The Evolution of Galactic Boron and the Production Site of the Light Elements. 1997, *ApJ*, **488**, 338
- Griem, H. R., *Spectral line Broadening by Plasmas*. 1974, McGraw-Hill, New York
- Iglesias, E., Griem, H., Welch, B., & Weaver, J., UV Line Profiles of B IV from a 10-Ps KrF-Laser-Produced Plasma. 1997, *Astrophys. Space Sci.*, **256**, 327

- Kramida, A. E. & Ryabtsev, A. N., A critical compilation of energy levels and spectral lines of neutral boron. 2007, *Phys. Scr.*, **76**, 544-557
- Lanz, T., Dimitrijević, M. S., & Artru, M. C., Stark broadening of visible Si II lines in stellar atmospheres. 1988, *A&A*, **192**, 249
- Lyubimkov, L. S., Light Chemical Elements in Stars: Mysteries and Unsolved Problems. 2018, *Astrophysics*, **61(2)**, 262-285
- Milovanović, N., Dimitrijević, M. S., Popović, L. Č., & Simić, Z., Importance of collisions with charged particles for stellar UV line shapes: Cd III. 2004, *A&A*, **417**, 375
- Nicolosi, P., Garifo, L., Jannitti, E., Malvezzi, A. M., & Tondello, G., Broadening and self-absorption of the resonance lines of H-like light ions in laser-produced plasmas. 1978, *Nuovo Cimento B*, **48**, 133
- Niu, J.-S., & Li, T., Galactic cosmic-ray model in the light of AMS-02 nuclei data. 2018, *Phys. Rev. D*, **97**, 023015
- Oertel, G. K., & Shomo, L. P., Tables for the Calculation of Radial Multipole Matrix Elements by the Coulomb Approximation. 1968, *ApJS*, **16**, 175
- Penzias, A., *Nobel Lecture 1978, The origin of the elements*
- Popović, L. Č., Dimitrijević, M. S., & Ryabchikova, T., The electron-impact broadening effect in CP stars: the case of La II, La III, Eu II, and Eu III lines. 1999a, *A&A*, **350**, 719
- Popović, L. Č., Dimitrijević, M. S., & Tankosić, D., The Stark broadening effect in hot star atmospheres: Au I and Au II lines. 1999b, *A&AS*, **139**, 617
- Popović, L. Č., Milovanović, N., & Dimitrijević, M. S., The electron-impact broadening effect in hot star atmospheres: The case of singly- and doubly-ionized zirconium. 2001a, *A&A*, **365**, 656
- Popović, L. Č., Simić, S., Milovanović, N., & Dimitrijević, M. S., Stark Broadening Effect in Stellar Atmospheres: Nd II Lines. 2001b, *ApJS*, **135**, 109
- Proffitt, C. R., & Quigley, M. F., Boron Abundances in Early B Stars: Results from the B III Resonance Line in IUE Data. 2001, *ApJ*, **548**, 429
- Proffitt, C. R., Jönsson, P., Litzén, U., Pickering, J. C., & Wahlgren, G. M., Goddard High-Resolution Spectrograph Observations of the B III Resonance Doublet in Early B Stars: Abundances and Isotope Ratios. 1999, *ApJ*, **516**, 342
- Sahal-Bréchet, S., Impact Theory of the Broadening and Shift of Spectral Lines due to Electrons and Ions in a Plasma. 1969a, *A&A*, **1**, 91
- Sahal-Bréchet, S., Impact Theory of the Broadening and Shift of Spectral Lines due to Electrons and Ions in a Plasma (Continued). 1969b, *A&A*, **2**, 322

- Sahal-Bréchet, S., European Virtual Atomic Data Centre - VAMDC. 2010, *J. Phys.: Conf. Ser.*, **257**, 012028
- Sahal-Bréchet, S., Dimitrijević, M. S., & Ben Nessib, N., Neutral and Ionized Atoms Perturbed by Collisions With Electrons and Ions: An Outline of the Semiclassical Perturbation (SCP) Method and of the Approximations Used for the Calculations. 2014, *Atoms*, **2**, 225
- Sahal-Bréchet, S., Dimitrijević, M.S., & Moreau, N., Virtual Laboratory Astrophysics: the STARK-B database for spectral line broadening by collisions with charged particles and its link to the European project VAMDC. 2012, *J. Phys.: Conf. Ser.*, **397**, 012019
- Sahal-Bréchet, S., Dimitrijević, M. S., & Moreau, N. 2019, STARK-B database, [online]. Available: <http://starkb.obspm.fr> [August 6, 2019]. Observatory of Paris, LERMA and Astronomical Observatory of Belgrade
- Sahal-Bréchet, S., Dimitrijević, M. S., Moreau, N., & Ben Nessib, N., The STARK-B database VAMDC node: a repository for spectral line broadening and shifts due to collisions with charged particles. 2015, *Phys. Scripta*, **90**, 054008
- Schramm, D. N., Primordial nucleosynthesis. 1993, in: Prantzos, et al. (Eds.), *Origin and Evolution of the Elements*, Cambridge University Press, Cambridge, p. 112
- Shore, B. W., & Menzel, D., Generalized Tables for the Calculation of Dipole Transition Probabilities. 1965, *ApJS*, **12**, 187
- Simić, Z., Dimitrijević, M. S., Popović, L. Č., & Dačić, M., Stark Broadening of F III Lines in Laboratory and Stellar Plasma. 2005a, *J. Appl. Spectrosc.*, **72**, 443
- Simić, Z., Dimitrijević, M. S., Milovanović, N., & Sahal-Bréchet, S., Stark broadening of Cd I spectral lines. 2005b, *A&A*, **441**, 391
- Simić, Z., Dimitrijević, M. S., Popović, L. Č., & Dačić, M., Stark broadening parameters for Cu III, Zn III and Se III lines in laboratory and stellar plasma. 2006, *New Astron.*, **12**, 187
- Simić, Z., Dimitrijević, M. S., & Kovačević, A., Stark broadening of spectral lines in chemically peculiar stars: Te I lines and recent calculations for trace elements. 2009, *New Astron. Rev.*, **53**, 246
- Simić, Z., Dimitrijević, M. S., & Sahal-Bréchet, S., Stark broadening of resonant Cr II $3d^5-3d^44p$ spectral lines in hot stellar atmospheres. 2013, *MNRAS*, **432**, 2247
- Simić, Z., Dimitrijević, M. S., & Popović, L. Č., Stark broadening data for spectral lines of rare-earth elements: Nb III. 2014, *Adv. Space Res.*, **54**, 1231

- Tankosić, D., Popović, L. Č., & Dimitrijević, M. S., The electron-impact broadening parameters for Co III spectral lines. 2003, *A&A*, **399**, 795
- TFR Group, Doyle, J. G., & Schwob, J. L., Intercombination to resonance line intensity ratio for He-like oxygen and carbon ions in TFR Tokamak plasmas. 1982, *J. Phys. B*, **15**, 813
- Thomas, D., Schramm, D. N., Olive, K. A., & Fields, B. D., Primordial Nucleosynthesis and the Abundances of Beryllium and Boron. 1993, *ApJ*, **406**, 569
- Vangioni-Flam, E., & Cassé, M., Cosmic Lithium-Beryllium-Boron Story. 1999, *Astrophys. Space Sci.*, **265**, 77
- Vangioni-Flam, E., Cassé, M., & Audouze, J., Lithium-beryllium-boron: origin and evolution. 2000, *Phys. Rep.*, **333-334**, 365
- Venn, K. A., Brooks, A. M., Lambert, D. L., Lemke, M., Langer, N., Lennon, D. J., & Keenan, F. P., Boron Abundances in B-Type Stars: A Test of Rotational Depletion during Main-Sequence Evolution. 2002, *ApJ*, **565**, 571
- Wang, J. S., Griem, H. R., Huang, Y. W., & Böttcher, F., Measurements of line broadening of B V H_α and L_δ in a laser-produced plasma. 1992, *Phys. Rev. A*, **45**, 4010

Stark broadening data for spectral lines of rare-earth elements: Example of Tb II and Tb IV

Milan S. Dimitrijević^{1,2}

¹ *Astronomical Observatory, Volgina 7, 11060 Belgrade 38, Serbia*

² *Sorbonne Université, Observatoire de Paris, Université PSL, CNRS,
LERMA, F-92190 Meudon, France*

Received: August 14, 2019; Accepted: September 28, 2019

Abstract. Stark full widths at half maximum (FWHM) for five multiplets of Tb II and 8 multiplets of Tb IV have been calculated for electron density of 10^{17} cm^{-3} by using the symplified modified semiempirical (SMSE) method. The calculations were performed for temperatures from 5 000 K to 80 000 K, in the region where the used theory is applicable.

Key words: Spectral lines – Plasma – Atomic data – Stark broadening

1. Introduction

The lanthanides are a series of 15 chemical elements with atomic numbers 57 through 71, from lanthanum to lutetium. Along with the chemically similar elements scandium and yttrium, they are often collectively known as the rare earth elements (REE). Stark broadening of rare-earth atom and ion spectral lines is of considerable importance in astrophysics due to rare-earth peak of abundance distribution of chemical elements. Consequently, a lot of spectral lines of these elements have been and will be observed in stellar spectra, in particular due to the development of space astronomy. For example, instruments like the Goddard High Resolution Spectrograph (GHRS) on the Hubble Space Telescope, enable us to obtain spectral lines with unprecedented resolution and accuracy.

The data on Stark broadening of rare-earth elements are scarce, first because of the lack of reliable atomic data for the corresponding calculations. The semiclassical perturbation theory (SCP) for Stark broadening of isolated lines (Sahal-Bréchet, 1969a,b) can be used only for some scandium and yttrium ions. In some cases the modified semiempirical method (MSE - Dimitrijević & Konjević 1980) or the symplified modified semiempirical method (SMSA - Dimitrijević & Konjević 1987) can be applied, but in many cases there is not enough atomic data even for the simplest calculations and regularities and systematic trends can only be used for very rough estimates (Popović & Dimitrijević, 1998). Concerning Stark broadening data for REE spectral lines, up to now data are

published for six multiplets of Sc II, calculated by using MSE (Popović & Dimitrijević, 1996), ten of Sc III, using SCP (Dimitrijević & Sahal-Bréchet, 1992), four of Sc X and ten of Sc XI, using SCP (Dimitrijević & Sahal-Bréchet, 1998a), six of Y II using MSE (Popović & Dimitrijević, 1996), 32 of Y III, using SCP (Dimitrijević & Sahal-Bréchet, 1998b), three of La II, six of La III, 284 of Nd II, by using SMSE (Popović et al., 2001b) seven of Eu II, by using MSE, one of Eu III by using SMSE (Popović et al., 1999), four of Yb III, by using MSE (Dimitrijević, 2019), 27 of Lu III, by using MSE (Majlinger et al., 2015) and four of Lu IV, by using MSE, (Dimitrijević, 2019)

The significance of Stark broadening data, including data for REE elements, is increasing in astrophysics due to the increasing possibility of obtaining high resolution spectra. Rauch et al. (2007) underlined that they “are of crucial importance for sophisticated analysis of stellar spectra by means of NLTE model atmospheres”. Spectral lines of neutral and ionized terbium are present and observed in stellar spectra. For example, the terbium abundance was derived by Siqueira Mello et al. (2014) for the moderately r-process-enhanced star CS 30315-029, based on three weak Tb II lines. Elkin et al. (2015) found Tb III lines in ro Ap star HD 213637 and Sachkov et al. (2008) in ro Ap star 10 Aql. Tb I, Tb II and Tb III lines have been found and in the spectrum of the extreme roAp star HD 101065, known as Przybylski’s star (Cowley et al., 2000).

Since there is neither experimental or theoretical data for Stark broadening of Tb II and Tb IV, we calculated here Stark full widths at half maximum (FWHM) for five transitions of Tb II and eight transitions of Tb IV by using the simplified modified semiempirical method (Dimitrijević & Konjević, 1987), since there is not enough atomic data for more advanced calculations.

2. Notes about calculations

In cases when we do not have enough data for more sophisticated theoretical calculations, or when, for example in astrophysics for model atmosphere or radiative transfer calculations, a lot of spectral lines, with the corresponding data should be taken into account. Here the simplified modified semiempirical formula (Dimitrijević & Konjević, 1987) for Stark widths of isolated, singly, and multiply charged ion lines might be very useful. This formula may be used in the case when the nearest atomic energy level, having an allowed dipole transition from, or to, the initial or final energy level of the spectral line considered is far enough away so that the influence of elastic collisions is dominant.

By using the simplified modified semiempirical (SMSE) method (Dimitrijević & Konjević, 1987), the most advanced method applicable in present case due to the lack of a corresponding set of atomic data, we calculated Stark full widths at half maximum (FWHM) due to collisions with electrons, for five transitions of Tb II and eight of Tb IV, for an electron density of 10^{17} cm^{-3} and for a temperature interval from 5 000 K up to 20 000 K or 40 000 K, depending

on the limits of validity of the SMSE method, in the case of Tb II, while for Tb IV the temperature interval is from 5 000 K to 80 000 K. Energy levels and ionization potentials for these calculations have been taken from Martin et al. (1978) and Kramida et al. (2019).

3. Results and discussion

Table 1. This table gives electron-impact broadening (Stark broadening) Full Widths at Half Intensity Maximum (W) for Tb II spectral lines, for a perturber density of 10^{17} cm^{-3} and temperatures from 5 000 to 40 000 K. Also is given quantity $3kT/2\Delta E$, where ΔE is the energy difference between closest perturbing level and the closer of initial and final levels.

Transition	Temp.	W[Å]	$3kT/2\Delta E$
Tb II (${}^6\text{H}_{15/2}^o$) $6s_{1/2}(15/2,1/2)$ -	5000.	0.393	0.734
(${}^6\text{H}_{15/2}^o$) $6p_{1/2}(15/2,1/2)$	10000.	0.278	1.47
3934.1	20000.	0.196	2.94
Tb II (${}^6\text{H}_{15/2}^o$) $6s_{1/2}(15/2,1/2)$ -	5000.	0.350	0.556
(${}^6\text{H}_{15/2}^o$) $6p_{3/2}(15/2,3/2)$	10000.	0.247	1.11
3610.5	20000.	0.175	2.22
Tb II (${}^6\text{H}_{13/2}^o$) $6s_{1/2}(13/2,1/2)$ -	5000.	0.393	0.529
(${}^6\text{H}_{13/2}^o$) $6p_{1/2}(13/2,1/2)$	10000.	0.278	1.06
3938.3	20000.	0.196	2.12
Tb II (${}^6\text{H}_{13/2}^o$) $6s_{1/2}(13/2,1/2)$ -	5000.	0.344	0.417
(${}^6\text{H}_{13/2}^o$) $6p_{3/2}(13/2,3/2)$	10000.	0.243	0.834
3567.3	20000.	0.172	1.67
	40000.	0.122	3.34
Tb II (${}^6\text{H}_{11/2}^o$) $6s_{1/2}(11/2,1/2)$ -	5000.	0.397	0.449
(${}^6\text{H}_{11/2}^o$) $6p_{1/2}(11/2,1/2)$	10000.	0.281	0.897
3966.1	20000.	0.198	1.79
	40000.	0.140	3.59

The results obtained for Stark widths for Tb II spectral lines are presented in Table 1 and those for Tb IV are in Table 2. The wavelengths given in Tables 1 and 2 are calculated from the energy levels used. In the last column is $3kT/2\Delta E$, representing the ratio of the average energy of free electrons, $E = 3kT/2$, and the energy difference between the initial (i) or final (f) and the closest perturbing

Table 2. Same as in Table 1, but for Tb IV, for temperature interval 5000 - 80 000 K.

Transition	Temp.	W[Å]	3kT/2ΔE
Tb IV ($^8S^o$)5d $^9D^o$ -	5000.	0.275E-01	0.122
($^8S_{7/2}^o$)6p $_{1/2}$ (7/2,1/2) $_3$	10000.	0.195E-01	0.243
1338.7	20000.	0.138E-01	0.486
	40000.	0.974E-02	0.973
	80000.	0.689E-02	1.95
Tb IV ($^8S^o$)5d $^9D^o$ -	5000.	0.273E-01	0.119
($^8S_{7/2}^o$)6p $_{1/2}$ (7/2,1/2) $_4$	10000.	0.193E-01	0.239
1324.5	20000.	0.136E-01	0.477
	40000.	0.964E-02	0.955
	80000.	0.682E-02	1.91
Tb IV ($^8S^o$)5d $^9D^o$ -	5000.	0.255E-01	0.106
($^8S_{7/2}^o$)6p $_{1/2}$ (7/2,3/2) $_5$	10000.	0.180E-01	0.211
1323.3	20000.	0.128E-01	0.423
	40000.	0.902E-02	0.845
	80000.	0.638E-02	1.69
Tb IV ($^8S^o$)6s $^9S^o$ -	5000.	0.161	0.122
($^8S_{7/2}^o$)6p $_{1/2}$ (7/2,1/2) $_3$	10000.	0.114	0.243
2331.8	20000.	0.807E-01	0.486
	40000.	0.570E-01	0.973
	80000.	0.403E-01	1.95
Tb IV ($^8S^o$)6s $^9S^o$ -	5000.	0.156	0.122
($^8S_{7/2}^o$)6p $_{1/2}$ (7/2,1/2) $_4$	10000.	0.111	0.243
2289.3	20000.	0.782E-01	0.486
	40000.	0.553E-01	0.973
	80000.	0.391E-01	1.95
Tb IV ($^8S^o$)6s $^9S^o$ -	5000.	0.128	0.122
($^8S_{7/2}^o$)6p $_{3/2}$ (7/2,3/2) $_5$	10000.	0.904E-01	0.243
2027.1	20000.	0.639E-01	0.486
	40000.	0.452E-01	0.973
	80000.	0.319E-01	1.95
Tb IV ($^8S^o$)6s $^9S^o$ -	5000.	0.250E-01	0.107
($^8S_{7/2}^o$)6p $_{3/2}$ (7/2,3/2) $_4$	10000.	0.177E-01	0.214
1203.8	20000.	0.125E-01	0.429
	40000.	0.884E-02	0.858
	80000.	0.625E-02	1.72
Tb IV ($^8S^o$)5d $^7D^o$ -	5000.	0.135	0.107
($^8S_{7/2}^o$)6p $_{3/2}$ (7/2,3/2) $_5$	10000.	0.953E-01	0.214
2056.2	20000.	0.674E-01	0.429
	40000.	0.477E-01	0.858
	80000.	0.337E-01	1.72

level (i' or f'). Here, T is the temperature and k Boltzmann constant. The larger of these values for the initial and final levels are taken, i.e.:

$$\Delta E = \text{Max}[E/\Delta E_{i,i'}, E/\Delta E_{f,f'}] \quad (2)$$

This is the validity condition for the SMSE method used. The $3kT/2\Delta E$ is equal to one at the threshold for the corresponding inelastic transition. If it is lower, than elastic collisions are dominant and the SMSE method is completely applicable and valid. For values larger than one, the inelastic collisions start become more and more important with its increase. Up to the value of around two, the results are acceptable. Data for the slightly higher values in Table 1, are given in order to enable better interpolation. The behavior of Starks widths with electron density is linear within the limits of validity of the SMSE method. These are the first published data for Stark width of Tb II and Tb IV and there is no other theoretical or experimental data to compare with.

4. Conclusion

New Stark FWHM for five lines of singly charged, and eight lines for triply charged terbium ion have been calculated in this work using the simplified modified semiempirical formula (Dimitrijević & Konjević, 1987). There is no other theoretical or experimental Stark broadening data for these emitters, so that the data presented are of interest for stellar plasma analysis, as well as for laboratory plasma diagnostics and laser produced plasma investigation.

References

- Cowley, C. R., Ryabchikova, T., Kupka, F., Bord, D. J., Mathys, G., & Bidelman, W. P. 2000, Abundances in Przybylski's star. *MNRAS*, 317, 299309.
- Dimitrijević, M. S. 2019, Stark widths of Yb III and Lu IV spectral lines, *Atoms*, 7, 10.
- Dimitrijević, M. S., & Konjević, N., Stark widths of doubly- and triply-ionized atom lines. 1980, *J. Quant. Spectrosc. Radiat. Transf.*, 24, 451.
- Dimitrijević, M.S., & Konjević, N. 1987. Simple estimates for Stark broadening of ion lines in stellar plasma. *A&A*, 172, 345-349.
- Dimitrijević, M. S., & Sahal-Bréchet, S. 1992. Stark Broadening of Spectral Lines of Multicharged Ions of Astrophysical Interest. IV. Sc III and Ti IV Lines. *A&AS*, 95, 121-128.
- Dimitrijević, M. S., & Sahal-Bréchet, S. 1998a. Stark broadening of spectral lines of multicharged ions of astrophysical interest. XXI. Sc X, Sc XI, Ti XI and Ti XII spectral lines. *A&AS*, 131, 143-144.
- Dimitrijević, M. S., & Sahal-Bréchet, S. 1998b. Stark Broadening of Y III Spectral Lines. *J. Appl. Spectrosc.*, 65, 492-498.

- Elkin, V. G., Kurtz, D. W., & Mathys, G. 2015, Time resolved spectroscopy of the cool Ap star HD 213637. *MNRAS*, 446, 41264131.
- Kramida, A., Ralchenko, Yu., Reader, J., & - NIST ASD Team 2018, NIST Atomic Spectra Database. Gaithersburg, MD: National Institute of Standards and Technology. (ver. 5.6.1), [Online]. Available: <https://physics.nist.gov/asd> [2019, August 13].
- Majlinger, Z., Simić, Z., & Dimitrijević, M. S. 2015, On the Stark Broadening of Lu III Spectral Lines. *J. Astrophys. Astron.*, 36, 671.
- Martin, W. C., Zalubas, R., & Hagan, L. 1978, Atomic Energy Levels The Rare-Earth Elements, *Nat. Stand. Ref. Data Ser.*, NSRDS-NBS 60, 1-422.
- Popović, L. Č., & Dimitrijević, M. S. 1996, Stark widths for astrophysically important ns-np transitions in Sc II, Y II and Zr II spectra. *A&AS*, 120, 373-374.
- Popović, L. Č., & Dimitrijević, M. S. 1998, A program for electron-impact broadening parameter calculations of ionized rare-earth element lines. *Contrib. Astron. Obs. Skalnaté Pleso*, 27, 353-355.
- Popović, L. Č., Dimitrijević, M.S., & Ryabchikova, T. 1999, The electron-impact broadening effect in CP stars: The case of La II, La III, Eu II, and Eu III lines. *A&A*, 350, 719724.
- Popović, L. Č., Simić, S., Milovanović, N., & Dimitrijević, M. S. 2001, Stark Broadening Effect in Stellar Atmospheres: Nd II Lines. 2001, *ApJS*, 135, 109.
- Rauch, T., Ziegler, M., Werner, K., Kruk, J. W., Oliveira, C. M., Putte, D. V., Mignani, R. P., & Kerber, F. 2007, High-resolution FUSE and HST ultraviolet spectroscopy of the white dwarf central star of Sh 2-216. *Astrophysics*, 470, 317329.
- Sachkov, M., Kochukov, O., Ryabchikova, T., Leone, F., Bagnulo, S., & Weiss, W. W. 2008. Spectroscopic study of pulsations in the atmosphere of roAp star 10 Aql. *Contrib. Astron. Obs. Skalnaté Pleso*, 38, 323-328.
- Sahal-Bréchet, S. 1969a, Impact Theory of the Broadening and Shift of Spectral Lines due to Electrons and Ions in a Plasma. *A&A*, 1, 91-123.
- Sahal-Bréchet, S. 1969b, Impact Theory of the Broadening and Shift of Spectral Lines due to Electrons and Ions in a Plasma (Continued). *A&A*, 2, 322-354.
- Simić, Z., Dimitrijević, M. S., & Popović, L. Č. 2014, Stark broadening data for spectral lines of rare-earth elements: Nb III. *Adv. Space Res.*, 54, 1231.
- Siqueira Mello, C., Hill, V., Barbuy, B., Spite, M., Spite, F., Beers, T. C., Caffau, E., Bonifacio, P., Cayrel, R., François, P., Schatz, H., & Wanajo, S. 2014, High-resolution abundance analysis of very metal-poor r-I stars. *A&A*, 565, A93.

On the semiclassical perturbation Stark shifts of Ar II spectral lines

R. Hamdi^{1,2}, N. Ben Nessib³, S. Sahal-Bréchet⁴ and
M.S. Dimitrijević^{5,4}

¹ *Deanship of Joint First Year, Department of Physics, Umm Al-Qura University, Makkah, Saudi Arabia.*

² *Groupe de Recherche en Physique Atomique et Astrophysique, Faculté des Sciences de Bizerte, Université de Carthage, Tunisia., (E-mail: rafik.hamdi@istls.rnu.tn)*

³ *Department of Physics and Astronomy, College of Science, King Saud University. PO Box 2455, Riyadh 11451, Saudi Arabia.*

⁴ *Sorbonne Université, Observatoire de Paris, Université PSL, CNRS, LERMA, F-92190, Meudon, France*

⁵ *Astronomical Observatory, Volgina 7, 11060 Belgrade, Serbia.*

Received: August 5, 2019; Accepted: September 28, 2019

Abstract. We present in this paper Stark shifts as a function of temperature for 20 spectral lines of Ar II belonging to 4p - 4d transition array. Calculations are made using semiclassical perturbation approach in impact approximation. Atomic data used in this calculation are carried out using Hartree-Fock method with relativistic corrections. Singly charged argon (Ar II) spectral lines are observed in many astrophysical plasmas. Ar II spectral lines are also important for laboratory plasmas and laser physics and technology.

Key words: atomic data – atomic processes – line: formation

1. Introduction

Inert gas such as argon produces very favorable conditions for stable discharges. For this reason argon plasmas are very attractive for testing the methods of plasma spectroscopy (Wiese, 1988). Singly charged argon (Ar II) spectral lines have been widely observed and studied in laboratory plasma. For example, Belmonte et al. (2014) measured transition probabilities for same UV lines of Ar II. Djurović et al. (2013) reported Stark broadening parameters measurements of Ar II UV lines. Gajo et al. (2013) measured Stark widths and shifts of Ar II spectral lines in the visible part of the spectrum. Ar II spectral lines are also used in plasma diagnostic. Alonso-Medina & Colón (2007) used Ar II spectral lines for the determination of temperature and electron density of laser induced lead plasma. Beside laboratory plasmas, singly charged argon spectral lines are also of interest for argon laser (Dimitrijević & Csillag, 2006). Ar II spectral lines

are also observed in stellar atmospheres. Vennes et al. (2018) performed abundance analysis of hot subdwarfs, they found a remarkable excess of argon with respect to oxygen in the hot subdwarf J2205-3141. Based on high resolution, high signal to noise observations of Ar II absorption lines, Brown et al. (1992) obtained abundances of argon in main-sequence B-type stars.

Stark broadening parameters are of interest for a number of applications such as laser physics, laser produced plasmas, modelling and investigation of stellar atmospheres in particular determination of chemical abundance. Stark broadening data are also useful for laboratory plasmas diagnostic. Corfdir et al. (2019) used Stark shift as a temperature diagnostic of Cu dominated plasma.

In this paper, we present Stark shifts for twenty Ar II spectral lines belonging to 4p - 4d transition array. Our Stark shift are given as a function of temperature for collisions with electrons, protons singly charged helium and singly charged argon. Our calculation are carried out using semiclassical perturbation approach (Sahal-Bréchet, 1969a,b) (SCP). SCP method need a set of atomic data sufficiently complete. In this work the needed set of atomic data is calculated using Hartree-Fock method with relativistic corrections (Cowan, 1981).

2. The method

Our Stark shifts are calculated using semiclassical perturbation approach. A detailed description of this formalism with all the innovations is given in Sahal-Bréchet (1969a,b, 1974, 1991); Fleurier et al. (1977); Dimitrijević et al. (1991); Dimitrijević & Sahal-Bréchet (1996); Sahal-Bréchet et al. (2014) and earlier papers.

The shift (d) (in angular frequency units) of an electron-impact shifted spectral line can be expressed as:

$$d = N \int v f(v) dv \int_{R_3}^{R_D} 2\pi \rho d \rho \sin(2\varphi_p) \quad (1)$$

where N is the electron density, $f(v)$ the Maxwellian velocity distribution function for electrons, ρ denotes the impact parameter of the incoming electron.

The phase shift φ_p due to the polarization potential (r^{-4}), is given in Section 3 of Chapter 2 in Sahal-Bréchet (1969a) and R_D is the Debye radius. The cut-off R_3 is described in Section 1 of Chapter 3 in Sahal-Bréchet (1969a).

SCP calculation of Stark shift need a relatively large number of atomic data comparing to modified semi-empirical method (Dimitrijević & Konjević, 1980). In this work, atomic data needed for SCP calculation are determined using Hartree-Fock method with relativistic corrections (Cowan, 1981). We use as for the width calculations an atomic model including 24 configurations: $3s^2 3p^5$; $3s^2 3p^4 nl$ ($nl = 4p, 4f, 5p, 5f, 6p, 6f, 6h, 7p, 7f, 7h$) (odd parity) and $3s 3p^6$; $3s^2 3p^4 n'l'$ ($n'l' = 3d, 4s, 4d, 5s, 5d, 5g, 6s, 6d, 6g, 7s, 7d, 7g$) (even parity). We use

an *ab initio* procedure. In Tab.1, we compare our wavelengths and oscillator strengths with the values taken from NIST database (Kramida et al., 2018). We can see from Tab.1 that our wavelengths and oscillator strengths are in good agreement with NIST values. Only electric dipole transitions (E1) are taken into account in our calculations. We have checked that the use of magnetic dipole (M1) and electric quadrupole (E2) transitions have no influence on the results.

3. Results and discussion

Table 1. Our calculated wavelengths and oscillator strengths compared with the values taken from NIST database (Kramida et al., 2018).

Lower level (i)	Upper level (j)	λ (Å)		f_{ij}	
		This work	NIST	This work	NIST
(³ P) 4p ⁴ P _{3/2} ^o	(³ P) 4d ⁴ D _{5/2}	3465.74	3514.39	0.377	0.378
(³ P) 4p ⁴ P _{1/2} ^o	(³ P) 4d ⁴ D _{3/2}	3484.51	3535.32	0.265	0.21
(³ P) 4p ⁴ P _{5/2} ^o	(³ P) 4d ⁴ D _{5/2}	3428.10	3467.75	0.220	0.227
(³ P) 4p ⁴ P _{1/2} ^o	(³ P) 4d ⁴ D _{1/2}	3463.75	3509.78	0.373	0.471
(³ P) 4p ⁴ P _{5/2} ^o	(³ P) 4d ⁴ D _{3/2}	3406.92	3454.09	0.0385	0.0375
(³ P) 4p ⁴ P _{5/2} ^o	(³ P) 4d ⁴ P _{5/2}	3108.72	3139.02	0.0796	0.077
(³ P) 4p ⁴ P _{3/2} ^o	(³ P) 4d ⁴ P _{3/2}	3180.37	3212.52	0.0108	0.0081
(³ P) 4p ⁴ P _{1/2} ^o	(³ P) 4d ⁴ P _{1/2}	3251.51	3281.71	0.0730	0.068
(³ P) 4p ⁴ P _{5/2} ^o	(³ P) 4d ⁴ P _{3/2}	3148.64	3181.04	0.0454	0.037
(³ P) 4p ⁴ P _{3/2} ^o	(³ P) 4d ⁴ P _{1/2}	3216.28	3243.69	0.0888	0.0833
(³ P) 4p ⁴ P _{3/2} ^o	(³ P) 4d ⁴ P _{5/2}	3139.64	3169.67	0.104	0.11
(³ P) 4p ⁴ P _{5/2} ^o	(³ P) 4d ² F _{7/2}	3091.66	3146.42	0.000438	0.00059
(³ P) 4p ⁴ D _{3/2} ^o	(³ P) 4d ⁴ D _{3/2}	3772.17	3872.17	0.0367	0.034
(³ P) 4p ⁴ D _{7/2} ^o	(³ P) 4d ⁴ D _{7/2}	3686.67	3780.84	0.184	0.17
(³ P) 4p ⁴ D _{5/2} ^o	(³ P) 4d ⁴ D _{5/2}	3734.16	3826.81	0.0693	0.0617
(³ P) 4p ⁴ D _{1/2} ^o	(³ P) 4d ⁴ D _{1/2}	3782.32	3880.33	0.0453	0.0524
(³ P) 4p ⁴ D _{7/2} ^o	(³ P) 4d ⁴ D _{5/2}	3670.06	3763.50	0.0328	0.0284
(³ P) 4p ⁴ D _{5/2} ^o	(³ P) 4d ⁴ D _{7/2}	3751.35	3844.73	0.014	0.0137
(³ P) 4p ⁴ D _{3/2} ^o	(³ P) 4d ⁴ D _{5/2}	3798.15	3900.36	0.0295	0.025
(³ P) 4p ⁴ D _{1/2} ^o	(³ P) 4d ⁴ D _{3/2}	3807.09	3911.58	0.0432	0.035

Our calculated Stark shifts are presented in Tab.2 (see appendix) for twenty spectral lines belonging to 4p-4d transition array for a perturber density of 10^{17} cm⁻³ and for a set of temperatures from 5 000 K to 60 000 K. Stark shifts are given for electron- proton- singly ionized helium and singly ionized argon impact broadening, in this way we take into account the most important perturbers in stellar atmospheres and laboratory plasmas as well as for example for argon lasers. Since our results are obtained using calculated energy levels, a

correction to the shifts due to the difference between calculated and observed wavelengths is introduced using Eq. (8) of Hamdi et al. (2013). All wavelengths given in Tab. 2 are taken from NIST database (Kramida et al., 2018). The impact approximation is valid for all values given in Tab. 2 since the collision volume (V) multiplied by the perturbation density (N) is much less than one. When the impact approximation reaches its limit of validity ($0.1 < N V \leq 0.5$), the value is preceded by an asterisk.

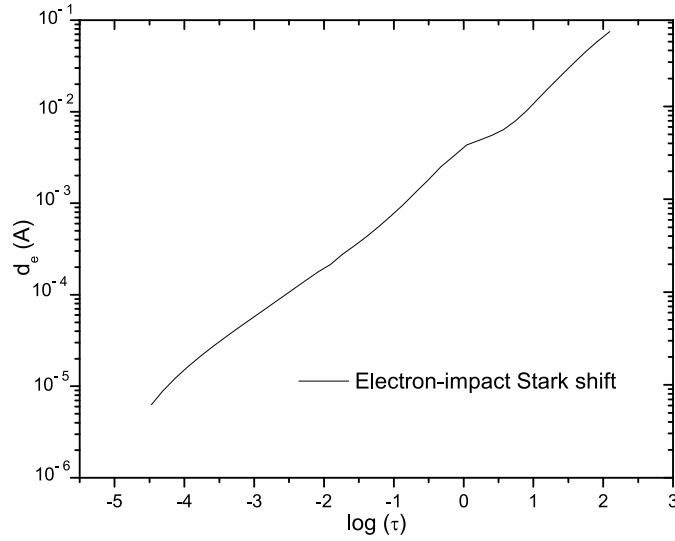


Figure 1. Electron-impact Stark shift for Ar II (3P) $4p\ 4P_{3/2}^o - ({}^3P)$ $4d\ 4D_{5/2}$ ($\lambda = 3514.39\ \text{\AA}$) spectral line as a function of logarithm of Rosseland optical depth ($\log \tau$). Electron-impact Stark shift is shown for an atmospheric model (Kurucz, 1979) with surface gravity $\log g = 4.5$ and effective temperature $T_{eff} = 10\ 000\ \text{K}$.

In Hamdi et al. (2019), we have compared our Stark shifts with experimental results (Djeniže et al., 1989; Dzierzega & Musiol, 1994; Aparicio et al., 1998; Djurović et al., 2013) for Ar II spectral lines. We found good agreement with experimental results except for some transitions. For example, the agreement with Djurović et al. (2013) was 27% for 4p-4d transitions except for four transitions. Concerning Stark widths, the comparison with experiments is made in Hamdi et al. (2017, 2018) for 212 spectral lines and we found an agreement generally good. For example, the average agreement for 4p-4d transitions was

10% comparing with Djurović et al. (2013) and 20% comparing with Pellerin et al. (1997).

In Fig. 1, we present the electron-impact Stark shift for Ar II (^3P) $4\text{p } ^4\text{P}_{3/2}^{\circ}$ - (^3P) $4\text{d } ^4\text{D}_{5/2}$ ($\lambda = 3514.39 \text{ \AA}$) spectral line as a function of logarithm of Rosseland optical depth ($\log \tau$) for an A-type star. Electron-impact Stark shift is shown for an atmospheric model (Kurucz, 1979) with surface gravity $\log g = 4.5$ and effective temperature $T_{eff} = 10\,000 \text{ K}$. Fig. 1 shows that the value of the electron-impact Stark shift in the deeper atmospheric layer is about 0.1 \AA . The theoretical resolving power of the high-resolution echelle spectrometer for the Keck TenMeter Telescope is of the order of $> 250,000$, but practical realizations may be approximately $36,000$. For $\lambda = 3514.39 \text{ \AA}$, this resolving power enables to register shifts of 0.08 \AA . Since new generations of terrestrial telescopes, as for example European Extremely Large Telescope of 39.3 m will have even greater resolving power, shifts from deepest layers in Fig. 1 will be measurable with such telescopes in the near future.

4. Conclusion

We have presented Stark shifts for twenty 4p-4d spectral lines of Ar II ion calculated using semiclassical perturbation approach and a set of atomic data calculated using Hartree-Fock method with relativistic corrections. The accuracy of our method was checked in our previous work (Hamdi et al. 2019). The accuracy of the atomic data used as input parameters for SCP calculation of Stark shifts is also verified by comparing our wavelengths and our oscillator strengths with the values of NIST database. We hope that our results will be of interest for the investigation of laboratory and astrophysical plasmas.

Acknowledgements. This work is part of the project 176002 “Influence of collisional processes on astrophysical plasma line shapes” supported by the Ministry of Education, Science and Technological Development of Serbia. This work has been also supported by the Paris Observatory, the CNRS and the PNPS (Programme National de Physique Stellaire, INSU-CNRS), France. This work has also been supported by the LABEX Plas@par project, and received financial state aid managed by the Agence Nationale de la Recherche, as part of the programme “Investissements d’avenir” under the reference ANR--11--IDEX--0004--02.

References

- Alonso-Medina, A. & Colón, C., Stark widths of several Pb III spectral lines in a laser-induced lead plasma. 2007, *Astron. Astrophys.*, **466**, 399, DOI: 10.1051/0004-6361:20066113
- Aparicio, J.A., Gigosos, M.A., González, V.R., Pérez, C., de la Rosa, M.I., & Mar, S., Measurement of Stark broadening and shift of singly ionized Ar lines. 1998, *J. Phys. B*, **31**, 1029. DOI: 10.1088/0953-4075/31/5/011

- Belmonte, M. T., Djurović, S., Peláez, R. J., Aparicio, J. A. & Mar, S., Improved and expanded measurements of transition probabilities in UV Ar II spectral lines. 2014, *Mon. Not. R. Astron. Soc.*, **445**, 3345, DOI: 10.1093/mnras/stu2006
- Brown, P. J. F., Dufton, P. L., Keenan, F. P., Holmgren, D. E. & Warren, G. A., The determination of accurate cosmic abundances from B-type stellar spectra. 1992, in Lecture Notes in Physics, Vol. **401**, *The Atmospheres of Early-Type Stars*, ed. U. Heber & C.S. Jeffery, 33
- Corfdir, P., Lantz, G., Abplanalp, M., Sütterlin, P., Kassubek, F., Delachaux, T. & Bator, M., Stark shift measurement as a temperature diagnostic of Cu-dominated thermal plasmas. 2019, *Journal of Physics D*, **52**, 5203, DOI: 10.1088/1361-6463/ab188e
- Cowan, R. D. 1981, *The theory of atomic structure and spectra*
- Dimitrijević, M. S. & Csillag, L., Influence of spectral line broadening on the mode structure of He-Kr and He-Ar gas lasers. 2006, *Journal of Applied Spectroscopy*, **73**, 458, DOI: 10.1007/s10812-006-0100-6
- Dimitrijević, M. S. & Konjević, N., Stark widths of doubly- and triply-ionized atom lines. 1980, *J. Quant. Spectrosc. Radiat. Transf.*, **24**, 451, DOI: 10.1088/0031-8949/54/1/008
- Dimitrijević, M. S. & Sahal-Bréchet, Stark broadening of neutral helium lines. 1984, *J. Quant. Spectrosc. Radiat. Transf.*, **31**, 301, DOI: 10.1016/0022-4073(84)90092-X
- Dimitrijević, M. S. & Sahal-Bréchet, Stark broadening of Li II spectral lines. 1996, *Physica Scripta*, **54**, 50, DOI: 10.1088/0031-8949/54/1/008
- Dimitrijević, M. S., Sahal-Bréchet, S. and Bommier, V., Stark broadening of spectral lines of multicharged ions of astrophysical interest. I - C IV lines. II - SI IV lines. 1991, *Astron. Astrophys., Suppl.*, **89**, 581,
- Djenžić, S., Malešević, M., Srećković, A., Milosavljević, M. & Purić, P., Stark broadening and shift of singly-ionized argon spectral lines in higher multiplets. 1989, *J. Quant. Spectrosc. Radiat. Transf.*, **42**, 429, DOI: 10.1016/0022-4073(89)90011-3
- Djurović, S., Belmonte, M. T., Peláez, R. J., Aparicio, J. A. & Mar, S., Stark parameter measurement of Ar II UV spectral lines. 2013, *Mon. Not. R. Astron. Soc.*, **433**, 1082, DOI: 10.1093/mnras/stt787
- Fleurier, C., Sahal-Bréchet, S. & Chapelle, J., Stark profiles of some ion lines of alkaline earth elements. 1977, *J. Quant. Spectrosc. Radiat. Transf.*, **17**, 595, DOI: 10.1016/0022-4073(77)90019-X
- Gajo, T., Mijatović, Z., Savić, I., Djurović, S. & Kobilarov, R., Stark widths and shifts of Ar II spectral lines in visible part of spectrum. 2013, *J. Quant. Spectrosc. Radiat. Transf.*, **127**, 119, DOI: 10.1016/j.jqsrt.2013.05.005
- Dzierzega, K. & Musiol, K., Stark broadening and shift for Ar II lines. 1994, *J. Quant. Spectrosc. Radiat. Transf.*, **52**, 747. DOI: 10.1016/0022-4073(94)90040-X
- Hamdi, R., Ben Nessib, N., Dimitrijević, M. S. & Sahal-Bréchet, S., Stark broadening of Pb IV spectral lines. 2013, *Mon. Not. R. Astron. Soc.*, **431**, 1039, DOI: 10.1093/mnras/stt228

- Hamdi, R., Ben Nessib, N., Sahal-Bréchet, S. & Dimitrijević, M. S., Stark Widths of Ar II Spectral Lines in the Atmospheres of Subdwarf B Stars. 2017, *Atoms*, **5**, 26, DOI: 10.3390/atoms5030026
- Hamdi, R., Ben Nessib, N., Sahal-Bréchet, S. & Dimitrijević, M. S., Semiclassical perturbation Stark widths of singly charged argon spectral lines. 2018, *Mon. Not. R. Astron. Soc.*, **475**, 800, DOI: 10.1093/mnras/stx3209
- Hamdi, R., Ben Nessib, N., Sahal-Bréchet, S. & Dimitrijević, M. S., Semiclassical perturbation Stark shifts of singly charged argon spectral lines. 2019, *Mon. Not. R. Astron. Soc.*, **488**, 2473, DOI: 10.1093/mnras/stz1835
- Kramida, A., Ralchenko, Yu., Reader, J. & NIST ASD Team, 2018, NIST Atomic Spectra Database (ver. 5.6.1). National Institute of Standards and Technology, Gaithersburg, MD. Available at: <https://physics.nist.gov/asd>. DOI: <https://doi.org/10.18434/T4W30F>
- Kurucz, R. L., Model atmospheres for G, F, A, B, and O stars. 1979, *Astrophys. J., Suppl.*, **40**, 1, DOI: 10.1086/190589
- Pellerin, S., Musiol, K., & Chapelle, J., Measurement of atomic parameters of singly ionized argon lines. III. Stark broadening parameters. 1997, *J. Quant. Spectrosc. Radiat. Transf.*, **57**, 377. DOI: 10.1016/S0022-4073(96)00134-3
- Sahal-Bréchet, S., Impact Theory of the Broadening and Shift of Spectral Lines due to Electrons and Ions in a Plasma. 1969, *Astron. Astrophys.*, **1**, 91,
- Sahal-Bréchet, S., Impact Theory of the Broadening and Shift of Spectral Lines due to Electrons and Ions in a Plasma (Continued). 1969, *Astron. Astrophys.*, **2**, 322,
- Sahal-Bréchet, S., Stark Broadening of Isolated Lines in the Impact Approximation. 1974, *Astron. Astrophys.*, **35**, 319,
- Sahal-Bréchet, S., Broadening of ionic isolated lines by interactions with positively charged perturbers in the quasistatic limit. 1991, *Astron. Astrophys.*, **245**, 322,
- Sahal-Bréchet, S., Dimitrijević, M. S. & Ben Nessib, N., Widths and Shifts of Isolated Lines of Neutral and Ionized Atoms Perturbed by Collisions With Electrons and Ions: An Outline of the Semiclassical Perturbation (SCP) Method and of the Approximations Used for the Calculations. 2014, *Atoms*, **2**, 225, DOI: 10.3390/atoms2020225
- Vennes, S., Németh, P. & Kawka, A., A FEROS Survey of Hot Subdwarf Stars. 2018, *Open Astronomy*, **27**, 7, DOI: 10.1515/astro-2018-0005
- Wiese, W. L., The atomic transition probabilities of argon - a continuing challenge to plasma spectroscopy. 1988, *J. Quant. Spectrosc. Radiat. Transf.*, **40**, 421, DOI: 10.1016/0022-4073(88)90130-6

A. Stark shifts results

Table 2. Electron-, proton-, singly charged helium and singly-charged argon-impact Stark shifts for Ar II lines calculated using semiclassical perturbation approach (Sahal-Bréchet 1969a,b) and a set of atomic data is calculated using Cowan code (Cowan 1981), for a perturber density of 10^{17} cm $^{-3}$ and temperatures of 5000 to 60 000 K. Wavelength of the transitions (in Å) and parameter C (Dimitrijević & Sahal-Bréchet 1984) are also given. This parameter when divided with the corresponding Stark width gives an estimate for the maximal perturber density for which the line may be treated as isolated. d_e : electron-impact Stark shift, d_{H^+} : proton-impact Stark shift, d_{He^+} : singly charged helium-impact Stark shift, d_{Ar^+} : singly charged argon-impact Stark shift. Cells preceded by an asterisk mean that the impact approximation reaches its limit of validity ($0.1 < NV \leq 0.5$). Empty cells mean that the impact approximation is not valid.

Transition	T (K)	d_e (Å)	d_{H^+} (Å)	d_{He^+} (Å)	d_{Ar^+} (Å)
$(^3P) 4p \ ^4P_{3/2}^o - (^3P) 4d \ ^4D_{5/2}$ 3514.39 Å C= 0.56E+20	5000.	0.344	0.206E-01	*0.171E-01	
	10000.	0.265	0.321E-01	*0.259E-01	*0.185E-01
	20000.	0.207	0.423E-01	0.347E-01	*0.253E-01
	30000.	0.184	0.478E-01	0.388E-01	*0.284E-01
	40000.	0.167	0.522E-01	0.431E-01	*0.314E-01
	60000.	0.147	0.580E-01	0.465E-01	*0.335E-01
$(^3P) 4p \ ^4P_{1/2}^o - (^3P) 4d \ ^4D_{3/2}$ 3535.32 Å C= 0.54E+20	5000.	0.342	0.205E-01	*0.169E-01	
	10000.	0.261	0.319E-01	*0.257E-01	*0.191E-01
	20000.	0.206	0.421E-01	0.346E-01	*0.263E-01
	30000.	0.183	0.473E-01	0.388E-01	*0.292E-01
	40000.	0.166	0.519E-01	0.426E-01	*0.324E-01
	60000.	0.146	0.577E-01	0.459E-01	*0.347E-01
$(^3P) 4p \ ^4P_{5/2}^o - (^3P) 4d \ ^4D_{5/2}$ 3476.75 Å C= 0.55E+20	5000.	0.316	0.192E-01	*0.159E-01	
	10000.	0.241	0.301E-01	*0.243E-01	*0.181E-01
	20000.	0.188	0.398E-01	0.325E-01	*0.248E-01
	30000.	0.169	0.447E-01	0.367E-01	*0.278E-01
	40000.	0.152	0.491E-01	0.400E-01	*0.307E-01

Table 2. continued

Transition	T (K)	d_e (Å)	d_{H^+} (Å)	d_{He^+} (Å)	d_{Ar^+} (Å)
$(^3P) 4p \ ^4P_{1/2}^o - (^3P) 4d \ ^4D_{1/2}$ 3509.78 Å C= 0.55E+20	5000.	0.343	0.205E-01	*0.170E-01	
	10000.	0.264	0.320E-01	*0.258E-01	*0.192E-01
	20000.	0.206	0.422E-01	0.346E-01	*0.265E-01
	30000.	0.184	0.477E-01	0.387E-01	*0.295E-01
	40000.	0.166	0.521E-01	0.429E-01	*0.326E-01
	60000.	0.147	0.578E-01	0.463E-01	*0.350E-01
$(^3P) 4p \ ^4P_{5/2}^o - (^3P) 4d \ ^4D_{3/2}$ 3454.09 Å C= 0.52E+20	5000.	0.326	0.195E-01	*0.161E-01	
	10000.	0.250	0.304E-01	*0.246E-01	*0.183E-01
	20000.	0.196	0.402E-01	0.330E-01	*0.252E-01
	30000.	0.176	0.452E-01	0.371E-01	*0.280E-01
	40000.	0.159	0.495E-01	0.407E-01	*0.310E-01
	60000.	0.140	0.551E-01	0.439E-01	*0.331E-01
$(^3P) 4p \ ^4P_{5/2}^o - (^3P) 4d \ ^4P_{5/2}$ 3139.02 Å C= 0.16E+20	5000.	0.288	0.206E-01	*0.173E-01	
	10000.	0.222	0.322E-01	*0.254E-01	
	20000.	0.174	0.425E-01	*0.347E-01	*0.264E-01
	30000.	0.154	0.475E-01	0.388E-01	*0.293E-01
	40000.	0.140	0.525E-01	0.430E-01	*0.323E-01
	60000.	0.122	0.573E-01	0.464E-01	*0.347E-01
$(^3P) 4p \ ^4P_{3/2}^o - (^3P) 4d \ ^4P_{3/2}$ 3212.52 Å C= 0.21E+20	5000.	0.308	0.217E-01	*0.183E-01	
	10000.	0.239	0.340E-01	*0.267E-01	
	20000.	0.188	0.449E-01	*0.365E-01	*0.279E-01
	30000.	0.166	0.501E-01	0.408E-01	*0.308E-01
	40000.	0.151	0.555E-01	0.455E-01	*0.341E-01
	60000.	0.134	0.605E-01	0.490E-01	*0.365E-01
$(^3P) 4p \ ^4P_{1/2}^o - (^3P) 4d \ ^4P_{1/2}$ 3281.70 Å C= 0.28E+20	5000.	0.348	0.245E-01	*0.205E-01	
	10000.	0.272	0.380E-01	*0.301E-01	
	20000.	0.214	0.504E-01	*0.410E-01	*0.313E-01
	30000.	0.189	0.565E-01	0.458E-01	*0.349E-01
	40000.	0.173	0.625E-01	0.504E-01	*0.381E-01
	60000.	0.151	0.679E-01	0.544E-01	*0.417E-01
$(^3P) 4p \ ^4P_{5/2}^o - (^3P) 4d \ ^4P_{3/2}$ 3181.04 Å C= 0.20E+20	5000.	0.302	0.212E-01	*0.180E-01	
	10000.	0.234	0.334E-01	*0.262E-01	
	20000.	0.184	0.440E-01	*0.358E-01	*0.274E-01
	30000.	0.163	0.491E-01	0.400E-01	*0.302E-01
	40000.	0.148	0.544E-01	0.446E-01	*0.334E-01
	60000.	0.131	0.593E-01	0.480E-01	*0.357E-01

Table 2. continued

Transition	T (K)	d_e (Å)	d_{H^+} (Å)	d_{He^+} (Å)	d_{Ar^+} (Å)
$(^3P) 4p \ ^4P_{3/2}^o - (^3P) 4d \ ^4P_{1/2}$ 3243.69 Å C= 0.28E+20	5000.	0.341	0.239E-01	*0.200E-01	
	10000.	0.265	0.371E-01	*0.294E-01	
	20000.	0.210	0.492E-01	*0.401E-01	*0.305E-01
	30000.	0.185	0.552E-01	0.447E-01	*0.340E-01
	40000.	0.169	0.610E-01	0.492E-01	*0.372E-01
60000.	0.148	0.663E-01	0.531E-01	*0.407E-01	
$(^3P) 4p \ ^4P_{1/2}^o - (^3P) 4d \ ^4P_{3/2}$ 3249.80 Å C= 0.21E+20	5000.	0.315	0.222E-01	*0.187E-01	
	10000.	0.244	0.349E-01	*0.274E-01	
	20000.	0.191	0.459E-01	*0.374E-01	*0.285E-01
	30000.	0.170	0.513E-01	0.417E-01	*0.315E-01
	40000.	0.153	0.567E-01	0.465E-01	*0.349E-01
60000.	0.136	0.619E-01	0.501E-01	*0.373E-01	
$(^3P) 4p \ ^4P_{3/2}^o - (^3P) 4d \ ^4P_{5/2}$ 3169.67 Å C= 0.16E+20	5000.	0.294	0.210E-01	*0.176E-01	
	10000.	0.226	0.329E-01	*0.259E-01	
	20000.	0.177	0.435E-01	*0.354E-01	*0.269E-01
	30000.	0.157	0.485E-01	0.395E-01	*0.299E-01
	40000.	0.142	0.536E-01	0.439E-01	*0.329E-01
60000.	0.125	0.585E-01	0.473E-01	*0.354E-01	
$(^3P) 4p \ ^4P_{5/2}^o - (^3P) 4d \ ^2F_{7/2}$ 3146.42 Å C= 0.22E+20	5000.	0.347	0.268E-01	*0.222E-01	
	10000.	0.271	0.406E-01	*0.323E-01	
	20000.	0.215	0.544E-01	*0.441E-01	*0.340E-01
	30000.	0.189	0.604E-01	*0.497E-01	*0.376E-01
	40000.	0.173	0.675E-01	0.544E-01	*0.414E-01
60000.	0.151	0.733E-01	0.583E-01	*0.444E-01	
$(^3P) 4p \ ^4D_{3/2}^o - (^3P) 4d \ ^4D_{3/2}$ 3872.14 Å C= 0.63E+20	5000.	0.404	0.245E-01	*0.202E-01	
	10000.	0.309	0.382E-01	*0.308E-01	*0.229E-01
	20000.	0.240	0.504E-01	0.414E-01	*0.314E-01
	30000.	0.214	0.567E-01	0.466E-01	*0.349E-01
	40000.	0.194	0.620E-01	0.510E-01	*0.387E-01
60000.	0.171	0.689E-01	0.549E-01	*0.413E-01	
$(^3P) 4p \ ^4D_{7/2}^o - (^3P) 4d \ ^4D_{7/2}$ 3780.84 Å C= 0.65E+20	5000.	0.376	0.231E-01	*0.191E-01	
	10000.	0.286	0.361E-01	*0.291E-01	*0.218E-01
	20000.	0.221	0.478E-01	0.391E-01	*0.298E-01
	30000.	0.196	0.537E-01	0.441E-01	*0.330E-01
	40000.	0.177	0.586E-01	0.482E-01	*0.367E-01
60000.	0.155	0.649E-01	0.520E-01	*0.391E-01	

Table 2. continued

Transition	T (K)	d_e (Å)	d_{H^+} (Å)	d_{He^+} (Å)	d_{Ar^+} (Å)
$(^3P) 4p \ ^4D_{5/2}^o - (^3P) 4d \ ^4D_{5/2}$ 3826.81 Å C = 0.65E+20	5000.	0.382	0.235E-01	*0.194E-01	
	10000.	0.290	0.366E-01	*0.296E-01	*0.221E-01
	20000.	0.226	0.485E-01	0.397E-01	*0.302E-01
	30000.	0.201	0.545E-01	0.447E-01	*0.337E-01
	40000.	0.182	0.597E-01	0.487E-01	*0.373E-01
	60000.	0.159	0.657E-01	0.527E-01	*0.399E-01
$(^3P) 4p \ ^4D_{1/2}^o - (^3P) 4d \ ^4D_{1/2}$ 3880.33 Å C = 0.65E+20	5000.	0.413	0.250E-01	*0.207E-01	
	10000.	0.317	0.390E-01	*0.313E-01	*0.234E-01
	20000.	0.246	0.514E-01	0.422E-01	*0.323E-01
	30000.	0.219	0.581E-01	0.472E-01	*0.359E-01
	40000.	0.198	0.634E-01	0.523E-01	*0.398E-01
	60000.	0.174	0.706E-01	0.564E-01	*0.426E-01
$(^3P) 4p \ ^4D_{7/2}^o - (^3P) 4d \ ^4D_{5/2}$ 3763.50 Å C = 0.63E+20	5000.	0.363	0.225E-01	*0.185E-01	
	10000.	0.274	0.350E-01	*0.284E-01	*0.210E-01
	20000.	0.212	0.463E-01	0.378E-01	*0.289E-01
	30000.	0.189	0.521E-01	0.428E-01	*0.323E-01
	40000.	0.170	0.573E-01	0.467E-01	*0.357E-01
	60000.	0.149	0.627E-01	0.501E-01	*0.381E-01
$(^3P) 4p \ ^4D_{5/2}^o - (^3P) 4d \ ^4D_{7/2}$ 3844.73 Å C = 0.67E+20	5000.	0.395	0.242E-01	*0.199E-01	
	10000.	0.301	0.377E-01	*0.305E-01	*0.227E-01
	20000.	0.234	0.498E-01	0.408E-01	*0.312E-01
	30000.	0.207	0.561E-01	0.459E-01	*0.345E-01
	40000.	0.187	0.612E-01	0.504E-01	*0.384E-01
	60000.	0.164	0.683E-01	0.543E-01	*0.410E-01
$(^3P) 4p \ ^4D_{3/2}^o - (^3P) 4d \ ^4D_{5/2}$ 3900.36 Å C = 0.67E+20	5000.	0.391	0.241E-01	*0.199E-01	
	10000.	0.297	0.377E-01	*0.305E-01	*0.226E-01
	20000.	0.230	0.500E-01	0.408E-01	*0.310E-01
	30000.	0.204	0.562E-01	0.461E-01	*0.348E-01
	40000.	0.186	0.617E-01	0.502E-01	*0.383E-01
	60000.	0.162	0.675E-01	0.540E-01	*0.410E-01

The impact of improved Stark-broadening widths on the modeling of double-ionized chromium lines in hot stars

A. Chougule^{1,2}, N. Przybilla¹, M.S. Dimitrijević²
and V. Schaffenroth³

¹ *Institut für Astro- und Teilchenphysik, Universität Innsbruck,
Technikerstr. 25/8, A-6020 Innsbruck, Austria
(E-mail: abhishek.rajeshchougule@gmail.com)*

² *Astronomical Observatory, Volgina 7, 11060 Belgrade 38, Serbia*

³ *Institute for Physics and Astronomy, University of Potsdam,
Karl-Liebknecht-Str. 24/25,
14476 Potsdam, Germany,*

Received: July 31, 2019; Accepted: November 6, 2019

Abstract. Stellar atmosphere modeling and chemical abundance determinations require the knowledge of spectral line shapes. Spectral lines of chromium in various ionization stages are common in stellar spectra but detailed data on Stark broadening for them is scarce. Recently we reported on the first calculations of Stark widths for several $4s-4p$ transitions of double-ionized chromium, employing the Modified Semi-Empirical approach (MSE). In this work we present applications of the data to spectrum synthesis of Cr III lines in the ultraviolet region of hot stars. The ATLAS9 model atmosphere code and the line-formation code SURFACE were used with the assumption of local thermodynamic equilibrium. The improvements of adopting the MSE broadening tables instead of approximate Stark broadening coefficients are investigated for a total of 56 Cr III lines visible in HST/STIS spectra of the B3 subgiant star Iota Herculis and the subdwarf B-star Feige 66.

Key words: Line: profiles – Stars: abundances

1. Introduction

Most of our knowledge of the physical conditions of astrophysical systems relies on the observations of electromagnetic radiation emitted by them. For example, a stellar spectrum can reveal many properties of stars, such as their chemical composition, temperature, density, distance, mass, luminosity, and radial motion using Doppler shift measurements. The stellar spectral lines are not infinitely sharp but have a finite width due to various physical processes. Each of these processes introduces a characteristic shape that can be expressed in the form of a line profile function $\phi(\nu)$ where the parameters of a normalized line profile ($\int \phi(\nu) d\nu = 1$) are the central frequency ν_0 , the Full Width at Half Maximum

(FWHM) and the profile value at the central frequency $\phi(\nu_0)$. The knowledge of spectral line shapes is required for stellar atmosphere modeling and chemical abundance determinations. In this work, we focus on the study of line broadening in stars due to collisions with neighboring charged particles, i.e., Stark broadening, in particular for double-ionized chromium Cr III.

1.1. Stark broadening

In plasma, collisional interactions between emitters/absorbers – atoms and ions, and charged particles – free electrons and ions, results in the broadening of spectral lines, called Stark broadening. The corresponding line profile, due to the application of the impact approximation – the interactions are separated in time –, and the isolated line approximation – neighboring energy levels do not overlap –, (Baranger, 1958), results in a Lorentzian profile generally defined by the corresponding FWHM and shift. The FWHM governs the shape of the line while shift (which is usually less than the width), determines the position relative to the central wavelength of the line, and it is not so important for studying the influence of Stark broadening in stellar spectra and has been neglected in our work. The isolated line approximation holds true for most of the spectral lines originating from stellar atmosphere (Griem & Ralchenko, 2000) as well as for spectral lines considered in this work, for electron densities of interest.

In order to produce a synthetic stellar spectrum that can be compared to observations, line broadening mechanisms other than Stark broadening also need to be taken into consideration, like the natural line width and Doppler broadening. The resulting line profile is a convolution of the individual profile functions, known as Voigt profile. Hence, any change in the FWHM due to Stark broadening is reflected in the resulting synthetic stellar spectrum. It is worth noting that the FWHM is proportional to the damping constant describing a spectral line. In fact, damping constants have been widely used for stellar spectral synthesis. In our investigation, for the calculation of synthetic spectra based on approximate Stark broadening data, the damping constants obtained using the methods described in Sec. 2.1 were used. On the other hand, for the calculation of synthetic spectra based on the broadening tables, the MSE calculated FWHMs were included into the input file.

2. Method

We study and compare the effects of improved Stark broadening tables for Cr III lines (Dimitrijević & Chougule, 2018) and approximate Stark broadening constants as described in Castelli (2005) on the calculation of synthetic stellar spectra. We also compare these spectra with observations, for the B3 subgiant star Iota Herculis and the subdwarf B-star Feige 66.

2.1. Approximate Stark broadening data

As reported in Castelli (2005), the Stark damping constant used for line computation is a fit by Peytremann (1972) to the detailed calculations by Sahal-Br echot & Segre (1971):

$$\gamma_{\text{Stark}} = 10^{-8} n^{*5} N_e \text{ (s}^{-1}\text{)} \quad (1)$$

Here, $n^* = \left[\frac{E_H Z_{\text{eff}}^2}{\chi_{\text{ion}} - \chi_k} \right]^{\frac{1}{2}}$ and is known as the effective quantum number of the state k (upper state). The ionization energy of hydrogen is given by $E_H = 13.6 \text{ eV}$, Z_{eff} is the effective charge (e.g., 1 for Cr I, 2 for Cr II, etc.), χ_{ion} is the ionization potential, and χ_{upper} is the excitation potential of the upper level. If the upper level is above the ionization potential, because it ionizes to an excited level of the parent, n^* is set to 5. The damping constant γ_{Stark} is related to the half-half width (W) listed by Griem & Peach (1975) via the expression:

$$\frac{\gamma_{\text{stark}}}{N_e} = \frac{2\pi c(2W)}{\lambda_0^2} \frac{1}{N_e}$$

where $N_e = 10^{16} \text{ cm}^{-3}$ for neutral atoms and $N_e = 10^{17} \text{ cm}^{-3}$ for ions. In the Kurucz's line lists, the W values from Griem & Peach (1975) are usually for $T=10,000 \text{ K}$.

2.2. Improved Stark broadening data

The improved Stark broadening data of Dimitrijević & Chougule (2018) were calculated using the Modified Semi-empirical (MSE) approach (Dimitrijević & Konjević, 1980; Dimitrijević & Kršljanin, 1986; Dimitrijević & Popović, 2001). The accuracy of the MSE approach is estimated to be about $\pm 50\%$ in general (Dimitrijević & Popović, 2001) and it has been tested on numerous occasions (Dimitrijević, 1990). Even for emitters with very complex spectra (e.g. Xe II and Kr II) good agreement of the MSE approach with experimental measurements (in the range $\pm 30\%$) can be achieved (Popović & Dimitrijević, 1996, 1998).

2.3. Stellar spectral synthesis

A hybrid non local thermodynamic equilibrium (non-LTE) approach was used for the model calculations as presented by Nieva & Przybilla (2007) for B-type main-sequence stars and Przybilla et al. (2006) for sdB stars. The model stellar atmospheres were assumed to be in LTE and were computed with the ATLAS9 code (Kurucz, 1993). Subsequently, deviations from LTE (non-LTE) were considered in the line-formation computations with DETAIL and SURFACE (Giddings 1981; Butler & Giddings 1985; recently extended and updated by K. Butler). The non-LTE calculations for hydrogen and helium were based on model atoms of Przybilla & Butler (2004) and Przybilla (2005), respectively. The

line formation calculations for chromium were performed assuming LTE because the lack of a proper non-LTE model atom, based on input data described by Schaffenroth (2015). Both, calculations with the approximate Stark broadening coefficients and with the MSE tables were performed for the two test stars, with atmospheric parameters adopted from Nieva & Przybilla (2012) and O’Toole & Heber (2006), respectively. Effective temperature T_{eff} , (logarithmic) surface gravities $\log(g)$ and logarithmic chromium abundances relative to hydrogen are summarised in Tab. 1.

Table 1. Properties of the stars under consideration.

Star	$\log(g)$	T_{eff}	Cr abundance
Feige 66	5.83	34,500K	-4.70
Iota Herculis	3.80	17,500K	-6.40

2.4. Comparison with observations

The synthetic spectra were compared to observations of Cr III lines in the UV spectral range. Data obtained with the Space Telescope Imaging Spectrograph (STIS) installed on the Hubble Space Telescope (HST) were downloaded from the Mikulski Archive for Space Telescopes. Both the spectra were observed employing the NUV-MAMA detector and the E230M grating, providing a resolving power of 30,000 in the wavelength range 1605Å to 3100Å, at moderate signal-to-noise ratios.

3. Results

The MSE Stark broadening tables included for stellar spectral synthesis correspond to a perturber density of 10^{17} cm^{-3} and temperatures from 5000 K up to 80,000 K. A comparison of 56 Cr III synthetic spectral lines based on approximate Stark broadening data with those based on MSE broadening tables was done in the stars Feige 66 and Iota Herculis. As the influence of Stark broadening is seen in the wings of the spectral lines, strong lines are expected to show this effect in their line profiles. For the star Feige 66, the difference in line shapes was quite prominent for almost all the Cr III spectral lines under investigation (see Fig. 1) because the high-density atmosphere pronounces the differences. On the other hand, the difference in line shapes was very small in case of the star Iota Herculis (see Fig. 2) due to its lower-density subgiant atmosphere. Some of the basic properties of the two stars are as summarized in Tab. 1.

In order to compare with the observation (Fig. 3 and Fig. 4), the theoretical spectra were convolved with the rotational, macroturbulent, and the instrumental profiles. Due to low signal-to-noise ratio of the observed spectra and line

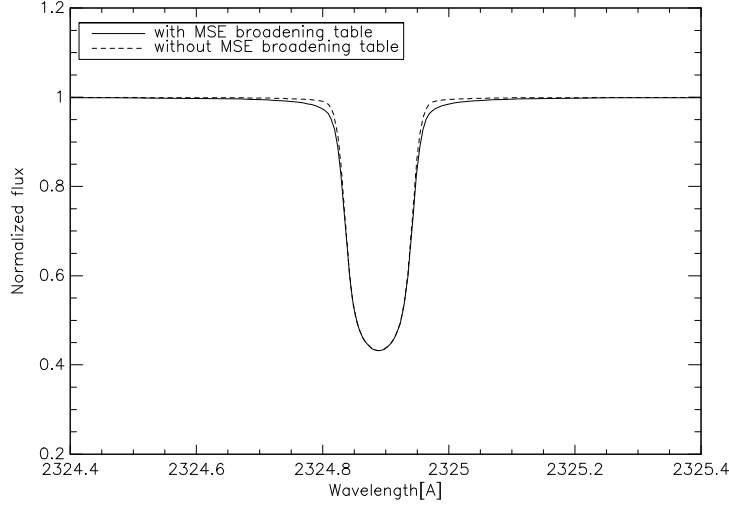


Figure 1. Comparison of the Cr III synthetic spectral lines corresponding to the transition $3d^3(4F)4s^3F - 3d^3(4F)4p^3G^o$, 2324.889Å in Feige 66. The difference in the line profiles can be seen clearly in the wings.

blends, only a few lines were found suitable for comparison with the synthetic spectra.

4. Conclusions

We have shown that the strong Cr III lines can react sensitively to the choice of Stark broadening parameters, depending on the perturber densities. Use of the MSE tables yields significantly broader line profiles in the case of the high-density sdB star Feige 66, while the differences are negligible for the subgiant Iota Herculis. The effects on the abundance determination still need to be quantified, but can already be qualified as being significant. The situation found here is therefore similar to the case of the star HD 133792, for which Dimitrijević et al. (2007) have investigated the impact of Stark broadening data for Cr II lines computed using the semiclassical perturbation approach on the analysis of a high signal-to-noise spectrum. There, the improved data were found to be important, in particular for the interpretation of the chromium abundance stratification.

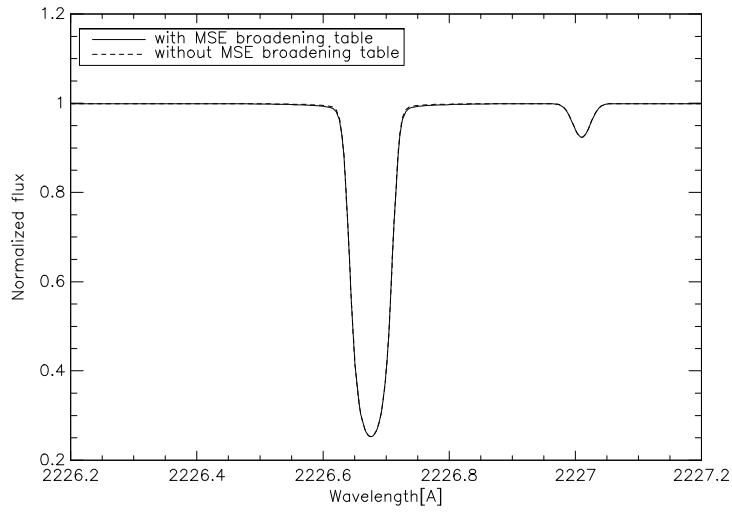


Figure 2. Comparison of the Cr III synthetic spectral lines corresponding to the transition $3d^3(4F)4s^5F - 3d^3(4F)4p^5G^o$, 2226.676\AA in Iota Herculis. The difference in the line profiles is very small.

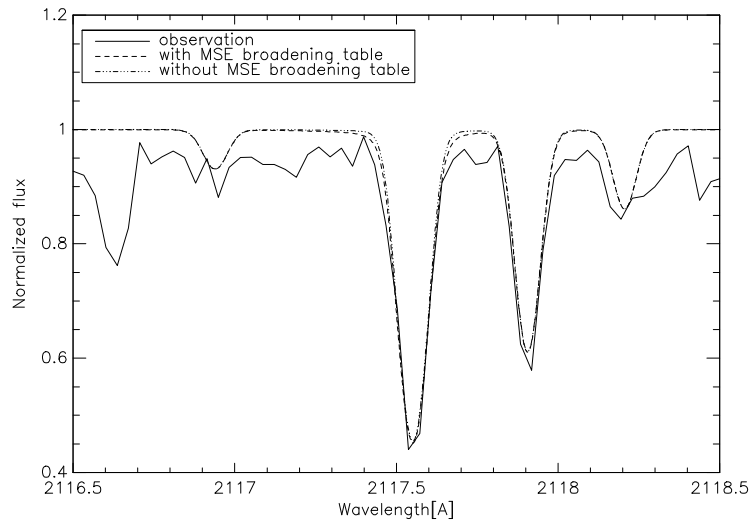


Figure 3. Comparison of the Cr III synthetic spectral lines corresponding to the transition $3d^3(4F)4s^5F - 3d^3(4F)4p^5F^o$, 2117.5\AA with observation in Feige 66.

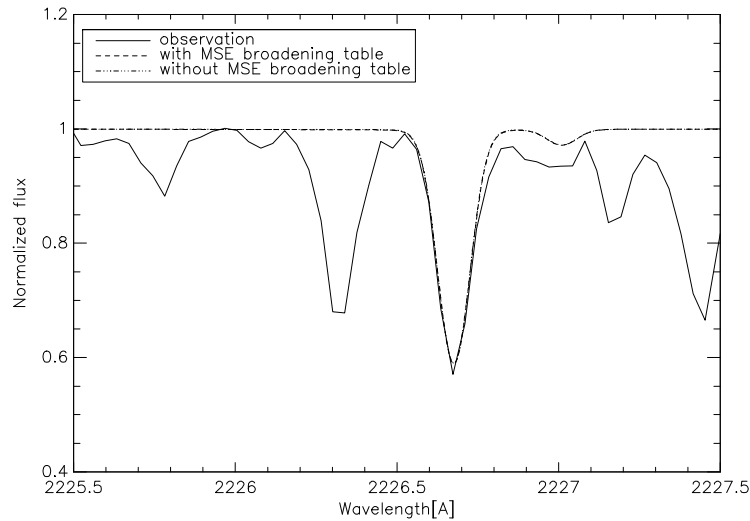


Figure 4. Comparison of the Cr III synthetic spectral lines corresponding to the transition $3d^3(4F)4s^5F - 3d^3(4F)4p^5G^o$, 2226.676\AA with observation in Iota Herculis.

Acknowledgements. A.C. would like to thank the organizers of the 12th Serbian Conference on Spectral Line Shapes in Astrophysics for financial support and the University of Innsbruck for granting a doctoral scholarship from the Promotion of Young Researchers Program. V.S. acknowledges funding by the Deutsches Zentrum für Luft- und Raumfahrt, grant 50 OR 1110, under which, part of the work was conducted.

References

- Baranger, M., General Impact Theory of Pressure Broadening. 1958, *Physical Review*, **112**, 855, DOI: 10.1103/PhysRev.112.855
- Butler, K. & Giddings, J. R. 1985, in Newsletter of Analysis of Astronomical Spectra, No. 9 (Univ. London)
- Castelli, F., Kurucz's WIDTH code and INPWIDTH. 2005, *Memorie della Societa Astronomica Italiana Supplementi*, **8**, 44
- Dimitrijević, M. & Chougule, A., Stark Broadening of Cr III Spectral Lines: DO White Dwarfs. 2018, *Atoms*, **6**, 15, DOI: 10.3390/atoms6020015
- Dimitrijević, M. S., Accuracy of line broadening data. 1990, in *Accuracy of Element Abundances from Stellar Atmospheres*, ed. R. Wehrse, Lecture Notes in Physics 356 (Springer Verlag), **31**, 44
- Dimitrijević, M. S. & Konjević, N., Stark widths of doubly- and triply-ionized atom lines. 1980, *J. Quant. Spectrosc. Radiat. Transf.*, **24**, 451, DOI: 10.1016/0022-4073(80)90014-X

- Dimitrijević, M. S. & Kršljanin, V., Electron-impact shifts of ion lines: modified semiempirical approach. 1986, *Astron. Astrophys.*, **165**, 269
- Dimitrijević, M. S. & Popović, L. Č., Modified Semiempirical Method. 2001, *Journal of Applied Spectroscopy*, **68**, 893
- Dimitrijević, M. S., Ryabchikova, T., Simić, Z., Popović, L. Č., & Dačić, M., The influence of Stark broadening on Cr II spectral line shapes in stellar atmospheres. 2007, *Astron. Astrophys., Suppl. Ser.*, **469**, 681, DOI: 10.1051/0004-6361:20077054
- Giddings, J. R. 1981, PhD. Thesis, University of London
- Griem, H. R. & Peach, G., Spectral Line Broadening by Plasmas. 1975, *Physics Today*, **28**, 61, DOI: 10.1063/1.3068826
- Griem, H. R. & Ralchenko, Y. V., Electron collisional broadening of isolated lines from multiply-ionized atoms. 2000, *J. Quant. Spectrosc. Radiat. Transf.*, **65**, 287, DOI: 10.1016/S0022-4073(99)00074-6
- Kurucz, R. 1993, CD-ROM No. 13 (Cambridge, Mass: SAO)
- Nieva, M. F. & Przybilla, N., Hydrogen and helium line formation in OB dwarfs and giants. A hybrid non-LTE approach. 2007, *Astron. Astrophys.*, **467**, 295, DOI: 10.1051/0004-6361:20065757
- Nieva, M. F. & Przybilla, N., Present-day cosmic abundances. A comprehensive study of nearby early B-type stars and implications for stellar and Galactic evolution and interstellar dust models. 2012, *Astron. Astrophys.*, **539**, A143, DOI: 10.1051/0004-6361/201118158
- O’Toole, S. J. & Heber, U., Abundance studies of sdB stars using UV echelle HST/STIS spectroscopy. 2006, *Astron. Astrophys.*, **452**, 579, DOI: 10.1051/0004-6361:20053948
- Peytremann, E., Theoretical Effect of Various Broadening Parameters on Ultraviolet Line Profiles. 1972, *Astron. Astrophys.*, **17**, 76
- Popović, L. Č. & Dimitrijević, M. S., Stark broadening of Xe II lines. 1996, *Astron. Astrophys., Suppl.*, **116**, 359
- Popović, L. Č. & Dimitrijević, M. S., Stark broadening parameters for Kr II lines from 5s-5p transitions. 1998, *Astron. Astrophys., Suppl.*, **127**, 295, DOI: 10.1051/aas:1998351
- Przybilla, N., Non-LTE modelling of the He I 10830 Å line in early-type main sequence stars. 2005, *Astron. Astrophys.*, **443**, 293, DOI: 10.1051/0004-6361:20053412
- Przybilla, N. & Butler, K., Non-LTE Line Formation for Hydrogen Revisited. 2004, *Astrophys. J.*, **609**, 1181, DOI: 10.1086/421316
- Przybilla, N., Nieva, M. F., & Edelmann, H., NLTE Analyses of sdB Stars: Progress and Prospects. 2006, *Baltic Astronomy*, **15**, 107
- Sahal-Bréchet, S. & Segre, E. R. A., Semi-Classical Calculations of Electron and Ion Collisional Broadening of the Strongest U. V. Ionic Lines of Astrophysical Interest. 1971, *Astron. Astrophys.*, **13**, 161
- Schaffenroth, V. 2015, Ph.D. Thesis, University of Erlangen-Nuremberg

On the Stark broadening of some Cr II spectral lines in plasma

A. Almodlej¹, N. Alwadie^{1,2}, N. Ben Nessib^{1,3} and
M. S. Dimitrijević^{4,5}

¹ *Department of Physics and Astronomy, College of Sciences, King Saud University, Saudi Arabia*

² *Department of Physics, College of Sciences, King Khalid University, Saudi Arabia*

³ *GRePAA, INSAT, Centre Urbain Nord, University of Carthage, Tunis, Tunisia*

⁴ *Astronomical Observatory, Volgina 7, 11060 Belgrade 38, Serbia*

⁵ *Sorbonne Université, Observatoire de Paris, Université PSL, CNRS, LERMA, F-92190 Meudon, France*

Received: July 31, 2019; Accepted: September 28, 2019

Abstract. New electron-impact line widths for eight Cr II multiplets have been calculated within the modified semiempirical (MSE) approach. Needed energy levels and radial integrals are calculated by different methods. The Stark widths are obtained as a function of temperature, for perturber density of 10^{17} cm^{-3} and have been compared with the approximate formula of Cowley and with recent experimental results. The obtained results are of interest for diagnostic and modeling of laboratory and stellar plasmas. The obtained data will be included in the STARK-B database, which is part of the Virtual Atomic and Molecular Data Center VAMDC.

Key words: Spectral lines – Plasma – Atomic data – Stark broadening

1. Introduction

Chromium in various ionization stages has been observed in the spectra of white dwarf atmospheres, where the Stark broadening is usually dominant broadening mechanism, especially in deeper atmospheric layers (Simić *et al.*, 2006; Hamdi *et al.*, 2008; Dufour *et al.*, 2011; Hamdi *et al.*, 2014; Dimitrijević and Chougule, 2018). In order to determine chromium abundance in such stars, as well as for opacity calculations and more sophisticated stellar atmosphere modeling, we need the corresponding Stark broadening data. Such data are also of interest for laboratory plasma diagnostics and modeling, as well as for investigation of fusion and laser produced plasmas where addition of different impurities may change different plasma parameters.

Nine Cr I spectral line widths, due to Stark broadening, are calculated by Dimitrijević *et al.* (2005). Seven multiplets belonging to 4s-4p transitions of Cr

II spectral lines are calculated by Dimitrijević *et al.* (2007) and nine resonant Cr II multiplets by Simić *et al.* (2013). Stark spectral line widths of six Cr III transitions are calculated by Dimitrijević and Chougule (2018). Cr VI spectral line widths for two multiplets are calculated by Dimitrijević *et al.* (2017). In this work, in order to provide new Stark broadening data for stellar and laboratory plasma research, we calculate Stark spectral line widths for eight Cr II multiplets for an electron density of 10^{17} cm^{-3} and a range of temperature between 5 000 K and 50 000 K. The obtained results will be in STARK-B database (<http://stark-b.obspm.fr/>, Sahal-Bréchet *et al.* (2015)) which is included in Virtual Atomic and Molecular Data Center (VAMDC Consortium <http://vamdc.org> Dubernet *et al.* (2016), Moreau *et al.* (2018)).

2. Method of calculations

The modified semiempirical approach (MSE) by Dimitrijević and Konjević (1980) has its origin from the semiempirical approach (SE) by Griem (1968) where Stark widths are calculated as a function of inelastic cross sections for the emitter collisions with perturbers, expressed using the empirical Gaunt factors $g(x)$, within the impact approximation taking into account the elastic collisions approximately, by extrapolation of Gaunt factors below the threshold for inelastic collisions:

$$W_{SE} = N \frac{8\pi}{3} \frac{\hbar^2}{m^2} \left(\frac{2m}{\pi kT} \right)^{1/2} \frac{\pi}{\sqrt{3}} \left[\sum_{i'} R_{i'i}^2 g \left(\frac{E}{\Delta E_{i'i}} \right) + \sum_{f'} R_{f'f}^2 g \left(\frac{E}{\Delta E_{f'f}} \right) \right] \quad (1)$$

where $\Delta E = |E - E_j|$.

In the MSE approach (Dimitrijević and Konjević, 1980) a modified Gaunt factors $\tilde{g}(x) = 0.7 - \frac{1.1}{Z} + g(x)$ is used for $\Delta n = 0$:

$$\begin{aligned} W_{MSE} = N \frac{8\pi}{3} \frac{\hbar^2}{m^2} \left(\frac{2m}{\pi kT} \right)^{1/2} \frac{\pi}{\sqrt{3}} & \left[R_{l_i, l_i+1}^2 \tilde{g} \left(\frac{E}{\Delta E_{l_i, l_i+1}} \right) \right. \\ & + R_{l_i, l_i-1}^2 \tilde{g} \left(\frac{E}{\Delta E_{l_i, l_i-1}} \right) \\ & + R_{l_f, l_f+1}^2 \tilde{g} \left(\frac{E}{\Delta E_{l_f, l_f+1}} \right) + R_{l_f, l_f-1}^2 \tilde{g} \left(\frac{E}{\Delta E_{l_f, l_f-1}} \right) \\ & \left. + \sum_{i'} (R_{i'i}^2)_{\Delta n \neq 0} g \left(\frac{3kT n_i^{*3}}{4Z^2 E_H} \right) + \sum_{f'} (R_{f'f}^2)_{\Delta n \neq 0} g \left(\frac{3kT n_f^{*3}}{4Z^2 E_H} \right) \right] \quad (2) \end{aligned}$$

where $Z-1$ is the ionic charge and n_i^* and n_f^* are the effective principal quantum numbers of initial and final transition level respectively (in its original form, the spectral line width depends only on the upper principal quantum number). The effective principal quantum number n_j^* is related by the energy level E_j as:

$$(n_j^*)^2 = Z^2 \frac{E_H}{E_{ion} - E_j} \quad (3)$$

where E_H is the hydrogen atom energy.

Energy levels needed in our MSE calculations are taken from the NIST database (Kramida *et al.*, 2018), oscillator strengths were calculated using the method of Bates and Damgaard (1949) and tables of Oertel and Shomo (1968). For higher levels, the method described in van Regemorter *et al.* (1979) was applied.

The MSE is valid for singly and multicharged ions and the number of input atomic data is minimized. In the MSE approach, only the matrix elements of transitions with $\Delta n = 0$ should be calculated, while other transitions are separated and grouped together. The advantage of this method is that smaller number of atomic data is needed for calculation than the more sophisticated calculations in semiclassical perturbation (SCP) ones (Sahal-Br  chot *et al.*, 2014). Accuracy of MSE results is usually within an error bars of ± 50 percent.

The Cowley formula (Cowley, 1971) was used extensively in astrophysics, for example it was used by Majlinger *et al.* (2017):

$$W_{Cowley} = N \frac{\pi}{c} \frac{\hbar^2}{m^2} \left(\frac{2m}{\pi kT} \right)^{1/2} \frac{\lambda^2}{Z^2} \left[(n_i^*)^4 + (n_f^*)^4 \right] \quad (4)$$

where λ is the wavelength of the line.

3. Results and discussion

We evaluated Stark widths using the MSE approach for 8 selected Cr II spectral lines. The Stark widths are calculated for an electron density of 10^{17} cm^{-3} , which is usually used in tables for ion emitters, and for different temperature values. To make the usage of obtained results for modelisation of stellar atmospheres and spectra easier, as well as for radiative transfer calculations, and to prepare our results for the implementation in the STARK-B database, we used the formula from Sahal-Br  chot *et al.* (2011) for fitting calculated data within the range 5 000 K 50 000 K with temperature:

$$\log(W) = a_0 + a_1 \log(T) + a_2 \log^2(T) \quad (5)$$

where, W is the FWHM Stark width in \AA , T is the temperature in Kelvin and a_0 , a_1 and a_2 are the fitting parameters obtained for electron density of 10^{17} cm^{-3} .

Stark width (FWHM) values for temperatures from 5 000 K to 50 000 K are given in Table 1, since this temperature interval is interesting for plasma diagnostic of white dwarf atmospheres and laser produced plasmas.

In this Table 1, W_{MSE} is our calculated Stark width using the MSE approach (Equation 1) and W_{Cowley} using Equation 4. The wavelengths in Table 1 are calculated from the corresponding energy levels given as the input so that they may differ from the observed ones.

We give in Table 2, the fitting parameters a_0 , a_1 and a_2 with the R correlation coefficient in %.

Table 1. Stark electron-impact widths (full widths at half maximum, FWHM) for Cr II spectral lines: W_{MSE} , calculated by using the modified semiempirical (MSE) method; W_{Cowley} , calculated by using the approximate formula of Cowley. The temperatures are from 5000 K up to 50000 K and the electron density is 10^{17} cm^{-3} .

Transition	Temp.	W_{MSE}	W_{Cowley}
Cr II $3d^4(a^1G)4s^2P - 3d^4(a^1G)4p^2P^o$ 3172.07 Å $3kT/2\Delta E = 0.349$	5000	1.58E-01	1.65E-01
	10000	1.12E-01	1.17E-01
	20000	7.92E-02	8.26E-02
	30000	6.47E-02	6.75E-02
	50000	5.01E-02	5.23E-02
Cr II $3d^4(a^3F)4s^2F - 3d^4(a^3F)4p^2F^o$ 3028.12 Å $3kT/2\Delta E = 1.14$	5000	1.43E-01	152E-01
	10000	1.01E-01	1.08E-01
	20000	7.16E-02	7.62E-02
	30000	5.84E-02	6.22E-02
	50000	4.53E-02	4.82E-02
Cr II $3d^4(^3G)4s^2G - 3d^4(^3G)4p^2G^o$ 3107.56 Å $3kT/2\Delta E = 0.327$	5000	1.55E-01	1.65E-01
	10000	1.09E-01	1.17E-01
	20000	7.73E-02	8.27E-02
	30000	6.31E-02	6.75E-02
	50000	4.89E-02	5.23E-02
Cr II $3d^4(a^1G)4s^2G - 3d^4(a^1G)4p^2G^o$ 2777.27 Å $3kT/2\Delta E = 0.302$	5000	1.17E-01	1.27E-01
	10000	8.24E-02	9.01E-02
	20000	5.83E-02	6.37E-02
	30000	4.76E-02	5.20E-02
	50000	3.69E-02	4.03E-02
Cr II $3d^4(a^3P)4s^4P - 3d^4(a^3P)4p^4D^o$ 2943.75 Å $3kT/2\Delta E = 0.307$	5000	1.26E-01	1.34E-01
	10000	8.92E-02	9.47E-02
	20000	6.31E-02	6.69E-02
	30000	5.15E-02	5.47E-02
	50000	3.99E-02	4.23E-02
Cr II $3d^4(^3H)4s^4H - 3d^4(^3H)4p^4H^o$ 2981.09 Å $3kT/2\Delta E = 0.311$	5000	1.28E-01	1.36E-01
	10000	9.07E-02	9.61E-02
	20000	6.41E-02	6.80E-02
	30000	5.24E-02	5.55E-02
	50000	4.06E-02	4.30E-02
Cr II $3d^4(^3D)4s^4D - 3d^4(^3D)4p^4D^o$ 2846.26 Å $3kT/2\Delta E = 0.297$	5000	1.17E-01	1.26E-01
	10000	8.28E-02	8.92E-02
	20000	5.85E-02	6.31E-02
	30000	4.78E-02	5.15E-02
	50000	3.70E-02	3.99E-02
Cr II $3d^4(^5D)4s^6D - 3d^4(^5D)4p^6F^o$ 2850.70 Å $3kT/2\Delta E = 0.297$	5000	1.17E-01	1.26E-01
	10000	8.26E-02	8.89E-02
	20000	5.84E-02	6.29E-02
	30000	4.77E-02	5.13E-02
	50000	3.70E-02	3.98E-02

Table 2. Fitting parameters for approximate formula (5). $R^2(\%)$ is the square of the correlation coefficient.

Transition	$\lambda(\text{\AA})$	a_0	a_1	a_2	$R^2(\%)$
$3d^4(a^1G)4s^2P - 3d^4(a^1G)4p^2P^o$	3172.07	1.00340	-0.47920	-0.00235	0.9999976
$3d^4(a^3F)4s^2F - 3d^4(a^3F)4p^2F^o$	3028.12	1.02325	-0.50967	0.00126	0.9999966
$3d^4(^3G)4s^2G - 3d^4(^3G)4p^2G^o$	3107.56	1.12564	-0.54132	0.00487	0.9999823
$3d^4(a^1G)4s^2G - 3d^4(a^1G)4p^2G^o$	2777.27	0.99869	-0.53851	0.00448	0.9999913
$3d^4(a^3P)4s^4P - 3d^4(a^3P)4p^4D^o$	2943.75	0.92591	-0.48882	-0.00127	0.9999993
$3d^4(^3H)4s^4H - 3d^4(^3H)4p^4H^o$	2981.09	0.93937	-0.49250	-0.00075	0.9999985
$3d^4(^3D)4s^4D - 3d^4(^3D)4p^4D^o$	2846.26	0.90349	-0.49312	-0.00082	0.9999991
$3d^4(^5D)4s^6D - 3d^4(^5D)4p^6F^o$	2850.70	0.97414	-0.52729	0.00325	0.9999963

We compared in Table 3 our results with those obtained experimentally by Aguilera *et al.* (2014). For spectral line widths within a multiplet, we used the formula:

$$W_{line} = \left(\frac{\lambda_{line}}{\lambda_{Mult}} \right)^2 W_{Mult} \quad (6)$$

where W_{line} and λ_{line} are for the particular line within the multiplet; W_{Mult} and λ_{Mult} are the values for the multiplet.

Table 3. Comparison of our MSE Stark width calculations W_{MSE} with experimental widths W_{Agl} from Aguilera *et al.* (2014). Lines are sorted by wavelength.

Transition	Multiplet	$\lambda(\text{\AA})$	W_{Agl}	W_{MSE}	$\frac{W_{Agl}}{W_{MSE}}$
$3d^4(a^1G)4s - 3d^4(a^1G)4p$	$c^2G w^2G^o$	2774.43	6.96E-02	6.30E-02	0.91
$3d^4(^5D)4s - 3d^4(^5D)4p$	$a^6D z^6F^o$	2835.63	6.91E-02	5.00E-02	0.72
$3d^4(^3D)4s - 3d^4(^3D)4p$	$c^4D w^4D^o$	2838.78	6.41E-02	5.50E-02	0.86
$3d^4(^5D)4s - 3d^4(^5D)4p$	$a^6D z^6F^o$	2843.25	6.94E-02	5.10E-02	0.73
$3d^4(^5D)4s - 3d^4(^5D)4p$	$a^6D z^6F^o$	2849.83	6.98E-02	5.10E-02	0.73
$3d^4(^5D)4s - 3d^4(^5D)4p$	$a^6D z^6F^o$	2855.67	7.00E-02	5.00E-02	0.71
$3d^4(^5D)4s - 3d^4(^5D)4p$	$a^6D z^6F^o$	2860.93	7.03E-02	5.00E-02	0.71
$3d^4(^5D)4s - 3d^4(^5D)4p$	$a^6D z^6F^o$	2862.57	7.04E-02	4.70E-02	0.67
$3d^4(^3G)4s - 3d^4(^3G)4p$	$b^2G x^2G^o$	2927.08	8.27E-02	7.90E-02	0.96
$3d^4(^3P)4s - 3d^4(a^3P)4p$	$b^4P y^4D^o$	2930.85	7.50E-02	6.60E-02	0.88
$3d^4(^3P)4s - 3d^4(a^3P)4p$	$b^4P y^4D^o$	2935.13	7.53E-02	6.60E-02	0.88
$3d^4(^3P)4s - 3d^4(a^3P)4p$	$b^4P y^4D^o$	2961.72	7.66E-02	6.20E-02	0.81
$3d^4(^3H)4s - 3d^4(^3H)4p$	$a^4H z^4H^o$	2971.90	7.71E-02	7.10E-02	0.92
$3d^4(^3P)4s - 3d^4(a^3P)4p$	$b^4P y^4D^o$	2976.71	7.74E-02	6.00E-02	0.78
$3d^4(^3H)4s - 3d^4(^3H)4p$	$a^4H z^4H^o$	2979.74	7.75E-02	7.00E-02	0.90
$3d^4(^3H)4s - 3d^4(^3H)4p$	$a^4H z^4H^o$	2989.19	7.80E-02	6.80E-02	0.87
$3d^4(^3F)4s - 3d^4(a^3F)4p$	$b^2F z^2F^o$	3028.12	8.55E-02	7.70E-02	0.90
$3d^4(^3P)4s - 3d^4(a^3P)4p$	$a^2P z^2P^o$	3172.07	9.47E-02	7.80E-02	0.82

We obtain for all the considered lines 0.82 as a mean value of the ratio $\frac{W_{Agl}}{W_{MSE}}$ with a standard deviation of $s=0.088$, so the calculated values are approximately 20 % higher than the experimental ones.

4. Conclusions

We calculated Stark electron-impact widths using the MSE method for a range of temperatures from 5 000 K to 50 000 K and for an electron density of 10^{17} cm^{-3} . These new eight Cr II Stark widths calculated in this work, for the lines where other theoretical Stark broadening data are missing, are of interest for stellar plasma, laboratory plasma diagnostics, laser produced plasma, as well as for analysis and modeling of stellar atmospheres. An extension of the Stark broadening calculations to other lines of Cr II will be an interesting future work and also applications of the atomic and spectroscopic data of these lines to typical stars where Stark broadening is an important mechanism in their atmospheres.

Acknowledgements. This project was funded by the National Plan for Science, Technology and Innovation (MAARIFAH), King Abdulaziz City for Science and Technology, Kingdom of Saudi Arabia, Award Number (12-MAT2879-02).

References

- Aguilera, J.A., Aragón, C., and Manrique, J.: Experimental Stark widths and shifts of Cr II spectral lines 2014, *Mon. Not. R. Astron. Soc.* **438**, 841.
- Bates, D.R., and Damgaard, A.: The Calculation of the Absolute Strengths of Spectral Lines 1949, *Phil. Transact. Roy. Soc. London A* **242**, 101.
- Cowley, C.R.: An approximate Stark broadening formula for use in spectrum synthesis 1971, *Observatory* **91**, 139.
- Dimitrijević, M., and Chougule, A.: Stark Broadening of Cr III Spectral Lines: DO White Dwarfs 2018, *Atoms* **6**, 15.
- Dimitrijević, M.S., and Konjević, N.: Stark widths of doubly- and triply-ionized atom lines. 1980, *J. Quant. Spectrosc. Radiat. Transfer* **24**, 451.
- Dimitrijević, M.S., Ryabchikova, T., Popović, L.Č., Shulyak, D., and Khan, S.: On the influence of Stark broadening on Cr I lines in stellar atmospheres 2005, *Astron. Astrophys.* **435**, 1191.
- Dimitrijević, M.S., Ryabchikova, T., Simić, Z., Popović, L.Č., and Dačić, M.: The influence of Stark broadening on Cr II spectral line shapes in stellar atmospheres 2007, *Astron. Astrophys.* **469**, 681.
- Dimitrijević, M.S., Simić, Z., and Sahal-Bréchet, S.: On the Stark broadening of Cr VI spectral lines in astrophysical plasma 2017, *J. Phys. Conf. Series*, 012021.
- Dubernet, M.L., et al.: The virtual atomic and molecular data centre (VAMDC) consortium 2016, *J. Phys. B: At. Mol. Phys.* **49**, 074003.
- Dufour, P., Ben Nessib, N., Sahal-Bréchet, S., and Dimitrijević, M.S.: Stark Broadening of Carbon and Oxygen Lines in Hot DQ White Dwarf Stars: Recent Results and Applications 2011, *Balt. Astron.* **20**, 511.

- Griem, H.R.: Semiempirical Formulas for the Electron-Impact Widths and Shifts of Isolated Ion Lines in Plasmas 1968, *Phys. Rev.* **165**, 258.
- Hamdi, R., Ben Nessib, N., Milovanović, N., Popović, L.Č., Dimitrijević, M.S., and Sahal-Bréchet, S.: Atomic data and electron-impact broadening effect in DO white dwarf atmospheres: SiVI 2008, *Mon. Not. R. Astron. Soc.* **387**, 871.
- Hamdi, R., Ben Nessib, N., Sahal-Bréchet, S., and Dimitrijević, M.S.: Stark widths of Ar III spectral lines in the atmospheres of subdwarf B stars 2014, *Adv. Space Res.* **54**, 1223.
- Kramida, A., Yu. Ralchenko, Reader, J., & and NIST ASD Team. 2018, NIST Atomic Spectra Database (ver. 5.6.1), [Online]. Available: <https://physics.nist.gov/asd> [2019, April 18]. National Institute of Standards and Technology, Gaithersburg, MD.
- Majlinger, Z., Simić, Z., and Dimitrijević, M.S.: Stark broadening of Zr IV spectral lines in the atmospheres of chemically peculiar stars 2017, *Mon. Not. R. Astron. Soc.* **470**, 1911.
- Moreau, N., Zwolf, C.-M., Ba, Y.-A., Richard, C., Boudon, V., and Dubernet, M.-L.: The VAMDC Portal as a Major Enabler of Atomic and Molecular Data Citation 2018, *Galaxies* **6**, 105.
- Oertel, G.K., and Shomo, L.P.: Tables for the Calculation of Radial Multipole Matrix Elements by the Coulomb Approximation. 1968, *Astrophys. J., Suppl. Ser.* **16**, 175.
- Sahal-Bréchet, S., Dimitrijević, M.S., and Ben Nessib, N.: Comparisons and Comments on Electron and Ion Impact Profiles of Spectral Lines 2011, *Balt. Astron.* **20**, 523.
- Sahal-Bréchet, S., Dimitrijević, M., and Ben Nessib, N.: 2014, *Atoms* **2**, 225.
- Sahal-Bréchet, S., Dimitrijević, M.S., Moreau, N., and Ben Nessib, N.: The STARK-B database VAMDC node: a repository for spectral line broadening and shifts due to collisions with charged particles 2015, *Phys. Scr.* **90**, 054008.
- Simić, Z., Dimitrijević, M.S., Popović, L.Č., and Dačić, M.D.: Stark broadening parameters for Cu III, Zn III and Se III lines in laboratory and stellar plasma 2006, *New Astron.* **12**, 187.
- Simić, Z., Dimitrijević, M.S., and Sahal-Bréchet, S.: Stark broadening of resonant Cr II $3d^5-3d^44p$ spectral lines in hot stellar atmospheres 2013, *Mon. Not. R. Astron. Soc.* **432**, 2247.
- van Regemorter, H., Binh Dy, H., and Prudhomme, M.: Radial transition integrals involving low or high effective quantum numbers in the Coulomb approximation 1979, *J. Phys. B: At. Mol. Phys.* **12**, 1053.

Stark broadening and atomic data for Ar XVI

R. Aloui¹, H. Elabidi^{2,3} and S. Sahal-Bréchet⁴

¹ *Laboratoire de Spectroscopie et Dynamique Moléculaire, LSDM, École Nationale Supérieure d'ingénieurs de Tunis, University of Tunis, Tunisia
(E-mail: rihabaloui88@gmail.com)*

² *Department of Physics, Deanship of the Foundation Year, Umm Al-Qura University, Makkah Almukarramah, Saudi Arabia*

³ *Groupe de Recherche en Physique Atomique et Astrophysique, LSDM, Faculté des Sciences de Bizerte, Université de Carthage, Tunisia*

⁴ *Sorbonne Université, Observatoire de Paris, Université PSL, CNRS, LERMA, F-92190 Meudon, France*

Received: August 1, 2019; Accepted: August 16, 2019

Abstract. Stark broadening and atomic data calculations have been developed for the recent years, especially atomic and line broadening data for highly ionized ions of argon. We present in this paper atomic data (such as energy levels, line strengths, oscillator strengths and radiative decay rates) for Ar XVI ion and quantum Stark broadening calculations for 10 Ar XVI lines. Radiative atomic data for this ion have been calculated using the University College London (UCL) codes (SUPERSTRUCTURE, DISTORTED WAVE, JAJOM) and have been compared with other results. Using our quantum mechanical method, our Stark broadening calculations for Ar XVI lines are performed at electron density $N_e = 10^{20} \text{ cm}^{-3}$ and for electron temperature varying from 7.5×10^5 to 7.5×10^6 K. No Stark broadening results in the literature to compare with. So, our results come to fill this lack of data.

Key words: line:profiles– stars– atomic data– Stark line broadening.

1. Introduction

Lithium-like ions are of importance in astrophysical and magnetized plasmas. Many emission lines of highly ionized argon, such as Ar IX–XVIII, were studied in Dere et al. (2001). Many Li-like transitions were useful for the determination of chemical abundances (Lemen et al., 1986). The number of the previous publications shows the importance of the Li-like ions: In Aggarwal & Keenan (2013), the authors reported the atomic data for Li-like ions with $12 \leq Z \leq 20$. In Whiteford et al. (2002), the authors performed the calculations of energy levels for Ar XVI ion by using AUTOSTRUCTURE (AS) code of Badnell (1997). Recently, in McKeown et al. (2004), the authors calculated the energy levels and radiative rates for Ar XVI and Fe XXIV. Atomic and line broadening data of highly ionized atoms are required in plasma physics. These parameters are used in the opacity calculations. They were also required for the modelling of fusion

plasmas (Peacock et al., 1997) as many elements were presented as impurities in the reactor walls. They determined the chemical abundances of elements and they used to test various theoretical approximations (Dimitrijević, 2003). Theoretical atomic data for Ar XVI were required for the modelling and diagnostics of plasmas and not available from measurements (McKeown et al., 2004).

Argon ions played a great role in technological devices and plasma applications (Djurović et al., 2011). We choose to study Ar XVI because of its ground configuration $1s^2 2s^1$ (with one external electron on closed shells), this ion is like hydrogen, thus their atomic properties can be calculated *ab initio* with a great accuracy. Therefore we perform another calculations to assess a precision of the available data, and that results can be applied with confidence in plasma diagnostics. Despite the importance of these parameters for stellar plasma research, for the interpretation of high-resolution spectra from astrophysical sources, the line broadening data of Ar XVI are totally missing in the literature. To fill this lack, we calculated their parameters using our quantum mechanical method. We hope that our results enrich the databases of astrophysicists. In the present work, the calculations of atomic data are computed by the sequence of UCL (University College, London) atomic packages (SUPERSTRUCTURE (Eissner et al., 1974)/DW (Eissner, 1998)/JAJOM (Saraph, 1978)). In Elabidi et al. (2014); Elabidi & Sahal-Bréchet (2018); Aloui et al. (2018, 2019), the authors adapted these packages to provide Stark broadening data for several argon lines missing in the literature. This method gave acceptable results. In Aloui et al. (2018), we calculated the Stark widths for Ar VII spectral lines. In Aloui et al. (2019), we computed quantum Stark broadening data for Ar VIII and Ar IX lines.

2. Outline of our line broadening method

To perform the present line broadening calculations, we have used our quantum mechanical method obtained in Elabidi et al. (2004, 2008). The expression of the full width at half-maximum (valid at temperatures and densities studied here), W is given by the following expression:

$$W = 2N \left(\frac{\hbar}{m} \right)^2 \left(\frac{2m\pi}{k_B T} \right)^{\frac{1}{2}} \times \int_0^{\infty} \Gamma_w(E) \exp\left(-\frac{\epsilon}{k_B T}\right) d\left(\frac{\epsilon}{k_B T}\right), \quad (1)$$

where the integration is over the Maxwellian velocity distribution, m is the electron mass, k_B is the Boltzmann constant, N is the electron density, T denotes

the electron temperature, ϵ is the incident electron energy, and

$$\begin{aligned} \Gamma_w(\epsilon) = & \sum_{J_i^T J_f^T l K_i K_f} \frac{[K_i, K_f, J_i^T, J_f^T]}{2} \\ & \times \left\{ \begin{matrix} J_i K_i l \\ K_f J_f 1 \end{matrix} \right\}^2 \left\{ \begin{matrix} K_i J_i^T s \\ J_f^T K_f 1 \end{matrix} \right\}^2 \\ & \times [1 - (\text{Re}(\mathbf{S}_i)\text{Re}(\mathbf{S}_f) + \text{Im}(\mathbf{S}_i)\text{Im}(\mathbf{S}_f))], \end{aligned} \quad (2)$$

where $L_i + S_i = J_i$, $J_i + l = K_i$ and $K_i + s = J_i^T$. L is the atomic orbital angular momentum, S is the spin of the target, l is the electron orbital momentum. The superscript T designates the operators of the total system (electron+ion). \mathbf{S}_i (\mathbf{S}_f) represent the scattering matrix elements for the initial (final) levels in intermediate coupling. $\text{Re}(\mathbf{S})$ and $\text{Im}(\mathbf{S})$ denotes the real and the imaginary parts of the \mathbf{S} -matrix, respectively. $\left\{ \begin{matrix} abc \\ def \end{matrix} \right\}$ designate 6-j symbols and we use the notation $[x, y, \dots] = (2x + 1)(2y + 1)\dots$

To calculate both \mathbf{S}_i and \mathbf{S}_f , we use the same incident electron energy $\epsilon = mv^2/2$. The SUPERSTRUCTURE (SST) code (Eissner et al., 1974) calculates the atomic structure in intermediate coupling, where configuration interaction and relativistic corrections (spin-orbit, mass, Darwin and one-body) are included according the Breit-Pauli approach (Bethe & Salpeter, 1957). The radial wave functions are determined by diagonalization of the non relativistic Hamiltonian using orbitals calculated in a scaled Thomas FermiDirac Amaldi (TFDA) potential. The potential depends on scaling parameters λ_l that have been obtained by a selfconsistent energy minimization on the term energies included in our calculations. The DISTORTED WAVE (DW) code (Eissner, 1998) performs the electron-ion scattering calculations and produces reaction matrices \mathbf{R} in LS coupling. The JAJOM code (Saraph, 1978) treats the scattering calculations in intermediate coupling. This code uses the term coupling coefficients (TCC) -resulting of SST calculations- and these matrices in LS coupling (obtained by DW) to calculate collision strengths and reactance matrices \mathbf{R} in intermediate coupling. This resulting matrices \mathbf{R} and the $\text{Re} \mathbf{S}(\text{Im} \mathbf{S})$ which are obtained using JAJPOLARI program -the transformed of JAJOM code- (Elabidi & Dubau, unpublished results) and RtoS program (Dubau, unpublished results) have been used as input data suitable for the formula (2). $\text{Re} \mathbf{S}$ and $\text{Im} \mathbf{S}$ are assessed by the expressions below:

$$\text{Re} \mathbf{S} = (1 - \mathbf{R}^2) (1 + \mathbf{R}^2)^{-1}, \text{Im} \mathbf{S} = 2\mathbf{R} (1 + \mathbf{R}^2)^{-1} \quad (3)$$

3. Results and discussions

3.1. Structure and radiative data

Structural and radiative atomic data have been calculated using the SUPERSTRUCTURE code of Eissner et al. (1974). We have used 6 configurations: $1s^2$ (2s, 2p, 3s, 3p, 3d and 4s). These configurations give rise to 6 terms and 9 levels of fine structure. The code (SST) provides also the scaling parameters ($\lambda_s = 1.3116$, $\lambda_p = 0.9392$ and $\lambda_d = 0.8683$). In Table 1, we display the present energy levels for Ar XVI in cm^{-1} and compare them with the experimental results of NIST (Kramida et al., 2018), with those calculated in McKeown et al. (2004) (GRASP) who used the GRASP (General purpose Relativistic Atomic Structure Package) code (Dyall et al., 1989), with those calculated from McKeown et al. (2004) (CIV3) who used the CIV3 code of Hibbert (1975), and with those from Whiteford et al. (2002) (AS) who used the AUTOSTRUCUTRE code (Badnell, 1997). As it is shown in Table 1, the average errors between our results and all the other ones are less than 1%.

The absorption oscillator strengths f_{ij} and radiative rates A_{ji} (in s^{-1}) for a transition $i \rightarrow j$ are related by the following expression (Aggarwal & Keenan, 2013):

$$f_{ij} = \frac{mc}{8\pi^2 e^2} \lambda_{ji}^2 \frac{\omega_j}{\omega_i} A_{ji} = 1.49 \times 10^{-16} \lambda_{ji}^2 \frac{\omega_j}{\omega_i} A_{ji}, \quad (4)$$

Table 1. Present fine structure energy levels E (in cm^{-1}) for Ar XVI ion compared with NIST values (Kramida et al., 2018), with GRASP values: the calculated results from McKeown et al. (2004) who used the GRASP code of Dyall et al. (1989), with CIV3 values: the results from McKeown et al. (2004) who used the CIV3 code from Hibbert (1975), and with AS values: the results obtained by Whiteford et al. (2002) who used the AS code (Badnell, 1997).

k	Level	E	NIST	GRASP	CIV3	AS
1	2s $^2S_{1/2}$	0.0	0.0	0.0	0.0	0.0
2	2p $^2P^{\circ}_{1/2}$	258659.	257026.	258563.03	259759.16	257860.71
3	2p $^2P^{\circ}_{3/2}$	283924.	282603.	285218.22	284263.50	283275.87
4	3s $^2S_{1/2}$	4176900.	4176030.	4176030.	4177350.	4179640.
5	3p $^2P^{\circ}_{1/2}$	4248504.	4246950.	4247060.	4248110.	4250730.
6	3p $^2P^{\circ}_{3/2}$	4255873.	4254180.	4255150.	4255370.	4258250.
7	3d $^2D_{3/2}$	4283042.	4281030.	4281730.	4282300.	4285880.
8	3d $^2D_{5/2}$	4285399.	4283560.	4284110.	4284660.	4288250.
9	4s $^2S_{1/2}$	5606962.	5605700.	5605740.	5607210.	5610400.

where m and e are the electron mass and charge, respectively, c is the velocity of light, λ_{ji} is the transition wavelength in  , and ω_i and ω_j are the statistical weights of the lower (i) and upper (j) levels, respectively. Similarly, the oscillator strengths f_{ij} (dimensionless) and the line strength S (in atomic units, 1 a.u. = 6.460×10^{-36} cm² esu²) are related by the following standard equations for the electric dipole (E1) transitions:

$$A_{ji} = \frac{2.0261 \times 10^{18}}{\omega_j \lambda_{ji}^3} S^{E1} \text{ and } f_{ji} = \frac{303.75}{\omega_i \lambda_{ji}} S^{E1} \quad (5)$$

Table 2 displays present radiative decay rates A_{ji} (in s⁻¹) for Ar XVI transitions which are compared with GRASP and CIV3 results from McKeown et al. (2004), and with AS results from Whiteford et al. (2002). The difference between our results and these references (McKeown et al., 2004; Whiteford et al., 2002) varies from nearly 0% to 19%. The maximum error for radiative decay rates in CIV3 results (Δ_{CIV3} is about 19%) in the transition $4s^2S_{1/2} - 2p^2P^{\circ}_{1/2}$ (9-2). But the average value of errors still acceptable, is about 4%. According to this comparison we note that our A_{ji} values are relatively close to the other

Table 2. Present radiative decay rates: A_{ij} (in s⁻¹), compared with GRASP values: the results from McKeown et al. (2004) who used the GRASP code of Dyaal et al. (1989), with CIV3 values: the results from McKeown et al. (2004) who used the CIV3 code of Hibbert (1975), and with AS values: the results from Whiteford et al. (2002) who used the AS code of Badnell (1997) for Ar XVI transitions. i and j are labelling the levels as in Table 1.

$i - j$	A_{ij}	GRASP	CIV3	AS	Δ_{GRASP}	Δ_{CIV3}	Δ_{AS}
2 - 1	1.179E+09	1.166E+09	1.195E+09	1.170E+09	1.10	1.36	0.76
3 - 1	1.564E+09	1.552E+09	1.573E+09	1.540E+09	0.77	0.58	1.53
4 - 2	1.836E+11	2.012E+11	1.880E+11	1.970E+11	9.59	2.40	7.30
4 - 3	3.879E+11	4.097E+11	3.900E+11	3.860E+11	5.62	0.54	0.49
5 - 1	1.433E+12	1.449E+12	1.440E+12	1.420E+12	1.12	0.49	0.91
5 - 4	1.530E+08	1.494E+08	1.468E+08	1.490E+08	2.35	4.05	2.61
6 - 1	1.423E+12	1.424E+12	1.425E+12	1.430E+12	0.07	0.14	0.49
6 - 4	2.051E+08	2.042E+08	1.974E+08	2.020E+08	0.44	3.75	1.51
7 - 2	3.619E+12	3.639E+12	3.630E+12	3.670E+12	0.55	0.30	1.41
7 - 3	7.203E+11	7.229E+11	7.219E+11	7.190E+11	0.36	0.22	0.18
7 - 5	1.111E+07	1.052E+07	1.073E+07	1.160E+07	5.31	3.42	4.41
7 - 6	1.079E+06	9.733E+05	1.047E+06	1.130E+06	9.80	2.97	4.73
8 - 3	4.330E+12	4.338E+12	4.335E+12	4.320E+12	0.18	0.12	0.23
8 - 6	8.308E+06	7.580E+06	8.088E+06	8.680E+06	8.76	2.65	4.48
9 - 2	8.715E+10	9.192E+10	7.044E+10	7.550E+10	5.47	19.17	13.37
9 - 3	1.649E+11	1.846E+11	1.514E+11	1.490E+11	11.95	8.19	9.64
9 - 5	5.693E+10	5.270E+10	5.268E+10	5.410E+10	7.43	7.47	4.97
9 - 6	1.121E+11	1.074E+11	1.086E+11	1.060E+11	4.19	3.12	5.44

ones (GRASP, CIV3, AS). Present absorption oscillator strengths f_{ij} ($i \rightarrow j$) and our line strengths S for Ar XVI transitions are reported in Table 3 and compared with GRASP results from McKeown et al. (2004). The percentage errors between the present two parameters (S and f_{ij}) and GRASP results vary from nearly 0% to 12%, for the both parameters. We found the maximum error in $4s\ 2S_{1/2}-2p\ 2P^{\circ}_{3/2}$ (9–3) transition nearly to 12%. Also the average value of errors still acceptable, is about 3%.

3.2. Line broadening results

We perform the calculations of Stark broadening for 10 Ar XVI lines. Quantum results W are calculated using our expression (1) and using 6 configurations. We use a range of electron temperature from 7.5×10^5 to 7.5×10^6 K and at electron density $N_e = 10^{20}$ cm $^{-3}$. Present calculations are reported in Table 4. We can prove that with the electron temperature and density values chosen in the present work, the condition of the impact approximation is valid: this approximation means that the duration τ of an interaction must be much smaller than the mean interval between two collision ΔT (Baranger, 1958):

$\tau \ll \Delta T$. τ can be expressed as $\tau \approx \frac{\rho_{typ}}{v_{typ}}$, where ρ_{typ} is a typical impact parameter, and v_{typ} presents a mean typical velocity. ΔT is of the order of the

Table 3. Present line strengths S and absorption oscillator strengths f_{ij} are compared with GRASP values: the results from McKeown et al. (2004) who used the GRASP code of Dyall et al. (1989) for Ar XVI transitions.

Levels $i - j$	S			f_{ij}		
	Present	GRASP	$\Delta_{GRASP}(\%)$	Present	GRASP	$\Delta_{GRASP}(\%)$
2 – 1	0.067234	0.066430	1.20	2.641E–02	2.610E–02	1.17
3 – 1	0.134921	0.133900	0.76	5.818E–02	5.772E–02	0.79
4 – 2	0.003014	0.003309	9.79	1.793E–02	1.968E–02	9.76
4 – 3	0.006490	0.006869	5.84	1.919E–02	2.029E–02	5.73
5 – 1	0.018447	0.018690	1.32	1.190E–01	1.205E–01	1.26
5 – 4	0.411389	0.409700	0.41	4.474E–02	4.426E–02	1.07
6 – 1	0.036441	0.036530	0.24	2.356E–01	2.360E–01	0.17
6 – 4	0.822315	0.823300	0.12	9.863E–02	9.855E–02	0.08
7 – 2	0.109613	0.110500	0.81	6.700E–01	6.749E–01	0.73
7 – 3	0.022235	0.022380	0.65	6.753E–02	6.790E–02	0.55
7 – 5	0.532594	0.529100	0.66	2.794E–02	2.731E–02	2.25
7 – 6	0.106206	0.105700	0.48	2.190E–03	2.110E–03	3.65
8 – 3	0.200116	0.201100	0.49	6.081E–01	6.104E–01	0.38
8 – 6	0.955857	0.953300	0.27	2.143E–02	2.075E–02	3.17
9 – 2	0.000562	0.000594	5.69	4.570E–03	4.824E–03	5.56
9 – 3	0.001079	0.001210	12.14	4.360E–03	4.889E–03	12.13
9 – 5	0.022417	0.020760	7.39	4.625E–02	4.283E–02	7.39
9 – 6	0.044880	0.043020	4.14	4.605E–02	4.413E–02	4.17

Table 4. Present quantum Stark widths W for ten Ar XVI lines at electron density $N = 10^{20} \text{ cm}^{-3}$ for different temperatures, the wavelengths λ are taken from the SUPERSTRUCTURE (SST) code of Eissner et al. (1974).

Transition	$T(10^5 \text{ K})$	$W(\text{Å})$	Transition	$T(10^5 \text{ K})$	$W(\text{Å})$
$2p \ ^2P^{\circ}_{1/2} - 2s \ ^2S_{1/2}$ $\lambda = 386.61 \text{ Å}$ 2-1	7.5	1.216E-02	$3p \ ^2P^{\circ}_{3/2} - 2s \ ^2S_{1/2}$ $\lambda = 23.50 \text{ Å}$ 6-1	7.5	1.735E-04
	10	1.065E-02		10	1.496E-04
	15	8.854E-03		15	1.212E-04
	30	6.510E-03		30	8.474E-05
	50	5.205E-03		50	6.452E-05
	75	4.338E-03		75	5.109E-05
$2p \ ^2P^{\circ}_{3/2} - 2s \ ^2S_{1/2}$ $\lambda = 352.21 \text{ Å}$ 3-1	7.5	1.002E-02	$3d \ ^2D_{3/2} - 2p \ ^2P^{\circ}_{1/2}$ $\lambda = 24.85 \text{ Å}$ 7-2	7.5	2.144E-03
	10	8.782E-03		10	1.594E-03
	15	7.304E-03		15	1.012E-03
	30	5.377E-03		30	4.361E-04
	50	4.302E-03		50	2.293E-04
	75	3.588E-03		75	1.380E-04
$3s \ ^2S_{1/2} - 2p \ ^2P^{\circ}_{1/2}$ $\lambda = 25.52 \text{ Å}$ 4-2	7.5	2.434E-04	$3d \ ^2D_{3/2} - 2p \ ^2P^{\circ}_{3/2}$ $\lambda = 25.01 \text{ Å}$ 7-3	7.5	1.968E-03
	10	2.098E-04		10	1.465E-03
	15	1.697E-04		15	9.326E-04
	30	1.170E-04		30	4.040E-04
	50	8.832E-05		50	2.137E-04
	75	6.996E-05		75	1.292E-04
$3s \ ^2S_{1/2} - 2p \ ^2P^{\circ}_{3/2}$ $\lambda = 25.69 \text{ Å}$ 4-3	7.5	2.467E-04	$4s \ ^2S_{1/2} - 2p \ ^2P^{\circ}_{3/2}$ $\lambda = 18.79 \text{ Å}$ 9-3	7.5	9.741E-05
	10	2.128E-04		10	8.428E-05
	15	1.722E-04		15	6.858E-05
	30	1.187E-04		30	4.807E-05
	50	8.953E-05		50	3.697E-05
	75	7.089E-05		75	2.996E-05
$3p \ ^2P^{\circ}_{1/2} - 2s \ ^2S_{1/2}$ $\lambda = 23.54 \text{ Å}$ 5-1	7.5	1.756E-04	$4s \ ^2S_{1/2} - 3p \ ^2P^{\circ}_{3/2}$ $\lambda = 74.01 \text{ Å}$ 9-6	7.5	2.940E-02
	10	1.516E-04		10	2.412E-02
	15	1.235E-04		15	1.735E-02
	30	8.836E-05		30	8.672E-03
	50	6.704E-05		50	4.831E-03
	75	5.245E-05		75	2.969E-03

inverse of collisional line width, which can be roughly expressed as equal to $N_e v_{typ} \rho_{typ}^2$. Thus, the validity condition of the impact approximation can be written as $\rho_{typ} \ll N_e^{-1/3}$. ρ_{typ}^3 is called the 'collision volume' that must be smaller than the volume of perturber N_e^{-1} . The condition of the impact approximation can be written in terms of temperature and the orbital momentum of the perturber. The classical angular momentum $L = \rho m v$ can be related to the eigenvalues of the corresponding quantum-mechanical operator \mathbf{L}^2 by $L^2 = (\rho m v)^2 = \hbar^2 l(l+1) \implies \rho^2 = \frac{\hbar^2 l(l+1)}{(m v)^2}$, using that $E = \frac{1}{2} m v^2 = \frac{3}{2} k_B T$, we find $\rho_{typ} = \frac{\hbar l_{typ}}{\sqrt{m k_B T_{typ}}} \approx 3 \times 10^{-10} \text{ m}$. We use $T_{typ} = 7.5 \times 10^6$, and with $N_e = 10^{20} \text{ cm}^{-3}$, we see that $\rho_{typ} \ll N_e^{-1/3} = 10^{-6.67} \text{ m}$. There are no other results in the literature to compare with the present Stark width calculations. The good agreement found between our atomic data and other results shows that our line broadening calculations have acceptable accuracy. Other experimental or theoretical results of Ar XVI line broadening would be very helpful to confirm our calculations.

4. Conclusions

In the present paper, we have performed quantum Stark broadening calculations for 10 Ar XVI lines for the range of electron temperatures from 7.5×10^5 to 7.5×10^6 K and an electron density of $N_e = 10^{20} \text{ cm}^{-3}$. Six configurations have been used in our calculations. The present structural and radiative parameters have been calculated using the UCL (SST/DW/JAJOM) codes. These parameters have been used in our line broadening calculations. To the best of our knowledge, there are no other results for the Stark broadening in the literature to compare with them. New calculations or measurements of line widths for this ion may be interesting for checking our calculations.

References

- Aggarwal, K. M. & Keenan, F. P., Energy levels, radiative rates, and electron impact excitation rates for transitions in Li-like ions with $12 \leq Z \leq 20$. 2013, *At. Data Nucl. Data Tables*, **99**, 156, DOI: doi:10.1016/j.adt.2012.03.001
- Aloui, R., Elabidi, H., Hamdi, R., & Sahal-Br  chot, S., Quantum Stark broadening data for Ar VIII and Ar IX lines. 2019, *Mon. Not. R. Astron. Soc.*, **484**, 4801, DOI: <https://doi.org/10.1093/mnras/stz303>
- Aloui, R., Elabidi, H., Sahal-Br  chot, S., & Dimitrijevi  , M. S., Quantum and Semiclassical Stark Widths for Ar VII Spectral Lines. 2018, *Atoms*, **6**, 20, DOI: <https://doi.org/10.3390/atoms6020020>
- Badnell, N. R., On the effects of the two-body non-fine-structure operators of the Breit - Pauli Hamiltonian. 1997, *J. Phys. B: At., Mol. Opt. Phys.*, **30**, 1, DOI: <https://doi.org/10.1088/0953-4075/30/1/005>
- Baranger, M., General Impact Theory of Pressure Broadening. 1958, *Phys. Rev.*, **112**, 855, DOI: [DOI:https://doi.org/10.1103/PhysRev.112.855](https://doi.org/10.1103/PhysRev.112.855)
- Bethe, H. A. & Salpeter, E. E. 1957, *Quantum Mechanics of One- and Two-Electron Atoms*
- Dere, K. P., Landi, E., Young, P. R., & Del Zanna, G., CHIANTIAN Atomic Database for Emission Lines. IV. Extension to XRay Wavelengths. 2001, *Astrophys. J., Suppl.*, **134**, 331, DOI: <https://doi.org/10.1086/320854>
- Dimitrijevi  , M. S., Stark Broadening in Astrophysics (Applications of Belgrade School Results and Collaboration With Former Soviet Republics). 2003, *Astron. Astrophys. Trans.*, **22**, 389, DOI: 10.1080/1055679031000108167
- Djurovi  , S., Mar, S., Pel  ez, R. J., & Aparicio, J. A., Stark broadening of ultraviolet Ar III spectral lines. 2011, *Mon. Not. R. Astron. Soc.*, **414**, 1389, DOI: <https://doi.org/10.1111/j.1365-2966.2011.18470.x>

- Dyall, K. G., Grant, I. P., Johnson, C. T., Parpia, F. A., & Plummer, E. P., GRASP: A general-purpose relativistic atomic structure program. 1989, *Comput. Phys. Commun.*, **55**, 425, DOI: doi:10.1016/0010-4655(89)90136-7
- Eissner, W., The UCL distorted wave code. 1998, *Comput. Phys. Commun.*, **114**, 295, DOI: [https://doi.org/10.1016/S0010-4655\(98\)00082-4](https://doi.org/10.1016/S0010-4655(98)00082-4)
- Eissner, W., Jones, M., & Nussbaumer, H. J., Techniques for the calculation of atomic structure and radiative data including relativistic corrections. 1974, *Comput. Phys. Commun.*, **8**, 270, DOI: [https://doi.org/10.1016/0010-4655\(74\)90019-8](https://doi.org/10.1016/0010-4655(74)90019-8)
- Elabidi, H., Ben Nessib, N., Cornille, M., Dubau, J., & Sahal-Bréchet, S., Electron impact broadening of spectral lines in Be-like ions: quantum calculations. 2008, *J. Phys. B: At. Mol. Opt. Phys.*, **41**, 025702, DOI: 10.1088/0953-4075/41/2/025702
- Elabidi, H., Ben Nessib, N., & Sahal-Bréchet, s., Quantum mechanical calculations of the electron-impact broadening of spectral lines for intermediate coupling. 2004, *J. Phys. B: At. Mol. Opt. Phys.*, **37**, 63, DOI: doi:10.1088/0953-4075/37/1/004.
- Elabidi, H. & Sahal-Bréchet, S., Quantum mechanical Stark widths for Ar V and Ar VI lines: scaling with temperature. 2018, *Mon. Not. R. Astron. Soc.*, **480**, 697, DOI: 10.1093/mnras/sty1858.
- Elabidi, H., Sahal-Bréchet, S., & Dimitrijević, M. S., Quantum Stark broadening of Ar XV lines. Strong collision and quadrupolar potential contributions. 2014, *Adv. Space Res.*, **54**, 1184, DOI: doi:10.1016/j.asr.2013.08.017
- Hibbert, A., CIV3 A general program to calculate configuration interaction wave functions and electric-dipole oscillator strengths. 1975, *Comput. Phys. Commun.*, **9**, 141, DOI: 10.1016/0010-4655(75)90103-4
- Kramida, A., Ralchenko, Y., Reader, J., & NIST ASD Team. 2018, *NIST Atomic Spectra Database (ver. 5.5.6)*, [Online]. Available: <https://physics.nist.gov/asd> [2018, July 25]
- Lemen, J. R., Sylwester, J., & Bentley, R. D., Determination of the calcium elemental abundance for 43 flares from SMM-XRP solar X-ray spectra. 1986, *Adv. Space Res.*, **6**, 245, DOI: doi:10.1016/0273-1177(86)90153-5
- McKeown, K., Aggarwal, K. M., Keenan, F. P., & Rose, S. J., Energy levels and radiative rates for Li-like Ar XVI and Fe XXIV. 2004, *Phys. Scr.*, **70**, 295, DOI: <https://doi.org/10.1088/0031-8949/70/5/006>
- Peacock, N. J., Barnsley, R., Coffey, I. H., et al., X-ray spectroscopic diagnostics of core ion confinement in large (JET) and medium size (COMPASS) tokamaks. 1997, *Fusion Eng. Des.*, **34**, 171, DOI: 10.1016/s0920-3796(96)00633-3

- Saraph, H. E., Fine structure cross sections from reactance matrices-a more versatile development of the program jajom. 1978, *Comput. Phys. Commun.*, **15**, 247, DOI: 10.1016/0010-4655(78)90095-4
- Whiteford, A. D., Badnell, N. R., Ballance, C. P., Loch, S. D. O'Mullane, M. G., & Summers, H. P., Excitation of Ar^{15+} and Fe^{23+} for diagnostic application to fusion and astrophysical plasmas. 2002, *J. Phys. B: At., Mol. Opt. Phys.*, **35**, 3729, DOI: 10.1088/0953-4075/35/17/309

Regularities and systematic trends on Lu III Stark widths

Zlatko Majlinger¹, Milan S. Dimitrijević¹, and
Vladimir A. Srećković²

¹ *Astronomical Observatory, Volgina 7, 11060 Belgrade, Serbia, (E-mail: mdimitrijevic@aob.rs)*

² *Institute of Physics Belgrade, BU, Pregrevica 118, 11080 Zemun, Belgrade, Serbia*

Received: August 10, 2019; Accepted: September 28, 2019

Abstract. Regularity and systematic trend analysis has been performed on the Stark widths of 27 Lu III spectral lines calculated elsewhere by modified semiempirical method. Possible correlation of those Stark widths with corresponding effective principal quantum numbers or effective ionization potentials have been also considered and discussed. Results obtained in such a way can be used for quick estimate of some other unknown Stark width data for the ions in the same homologous or isoelectronic sequence, especially if the conditions are not satisfied to use more accurate theoretical methods.

Key words: Atomic processes – Line: profiles – Plasmas

1. Introduction

Stark widths values are important in many fields of science and technology. For example, in astrophysics, line widths are useful for analysis, synthesis and interpretation of stellar spectra for all types of stars, investigation of chemical abundances of elements, solar opacity calculations and analysis of radiative transfer through the stellar atmospheres. (Majlinger et al., 2017b).

Regularities and systematic trends are common properties among the Stark widths and shifts (Wiese & Konjević, 1982). Those properties are very usually found among the atomic data, helping to interpolate or quickly estimate needed Stark broadening parameters.

Today the method producing the largest number of Stark broadening parameters is the semiclassical perturbation one (see e.g. Sahal-Bréchet, 1969a,b). If there are no atomic data to use this method adequately one can use the modified semiempirical method, MSE (Dimitrijević & Konjević, 1980). However, in the absence of data needed to calculate Stark broadening parameters, or if the conditions to use these methods are not satisfied, simple estimates become very useful tools, and sometimes become also the only way for finding Stark widths and shifts. Although we lose on accuracy when those estimates are performed,

they are still helpful when the great number of broadening parameters needs to be calculated, and if great accuracy of results is not necessary.

In this work we are focused on investigation of regularities and systematic trends based on Stark widths of 27 spectral lines of Lu III calculated elsewhere (Majlinger et al., 2015) by MSE method, in order to enable quick and simple estimations of the Stark widths.

2. Method

This study is purely empirical and it is performed as the similar statistical research for Stark broadening parameters of Zr IV spectral lines (Majlinger et al., 2017a). Estimation methods used here can be also divided into two groups:

- a) estimates based on theory – for example, Cowley’s formula (Cowley, 1971), or simplified MSE (Dimitrijević & Konjević, 1987), and
- b) estimates derived from purely statistical analysis of existing data, like the methods of Purić and Lakićević (see for example Purić & Šćepanović 1999, or Lakićević 1983), or estimates derived from systematic trends based on specific examples of Stark widths (Wiese & Konjević, 1982).

We search the estimation formula in same two versions as in paper mentioned above (Majlinger et al., 2017a). The first is in dependence on the so-called effective ionization potential (see for example Purić & Šćepanović 1999, or Lakićević 1983) for the atomic energy level j , $\chi_j = E_{ion} - E_j$:

$$W_{E_1} = a_1 \cdot Z^{c_1} \cdot \lambda^2 \cdot N \cdot f(T) \cdot (\chi_j)^{-b_1} \quad (1)$$

where $j = i, f$, for upper - initial i or lower - final f atomic energy level, and the second in dependence on the effective principal quantum number n_j^*

$$W_{E_2} = a_2 \cdot Z^{c_2} \cdot \lambda^2 \cdot N \cdot f(T) \cdot (n_j^*)^{-b_2} \quad (2)$$

The relation between effective principal quantum number and effective ionization potential χ_j is given by:

$$n_j^{*2} = \frac{Z^2 E_H}{\chi_j}. \quad (3)$$

where $Z - 1$ is ionic charge, n_j^* - effective principal quantum number of upper or lower level, W_E estimated Stark width in \AA , λ wavelength in \AA , N - perturber density in m^{-3} , E_H - hydrogen atom ionization energy, E_{ion} - ionization energy, E_j - energy of upper or lower atomic energy level. Coefficients a , b and c in equations (1) and (2) are independent of temperature, ionization potential and electron density for a given transition.

Example of first type Eq.(1) estimation formula are Purić & Šćepanović (1999) or Lakićević (1983) estimates, while example of second type Eq.(2) is formula of Cowley. In our estimates in this work we assume that the condition:

$$\frac{3kT}{2|E_j - E_{j'}|} \leq 2, \quad (4)$$

where k is Boltzmann's constant and $E_{j'}$ is the closest perturbing level, is satisfied. In that case, Gaunt factor from MSE theory is constant (Dimitrijević & Konjević 1980, and Griem 1968) and the use of temperature function

$$f(T) = T^{-1/2} \quad (5)$$

is a proper choice for spectral widths of isolated ion lines in the case of low temperatures (Elabidi et al. 2009, Elabidi & Sahal-Bréchet 2011). However, it is not recommended to use any of these estimates above temperature limit, and it is the reason why results of W_C mostly decrease faster with temperature than W_{MSE} in Table 2 (Majlinger et al., 2015). So we scaled all of our analysed widths on temperature $T = 10000$ K, where we assume that lower temperature limit condition Eq.(4) is satisfied, at least in the case of our considered Lu III lines.

First, we compare the results obtained by Cowley formula (Cowley, 1971) and MSE results, both already published in Majlinger et al. (2015). Our experiences on Zr IV spectral lines show that modified Cowley formula (see, for example, Kilian et al. 1991, and Przybilla et al. 2016) which includes both upper and lower state influences gives better accuracy than old Cowley equation which is based only on upper state influence (for further detailed see Majlinger et al. 2017a). So we used Cowley's estimating formula in a form:

$$W_{E2A} = a_2 \cdot Z^{c_2} \cdot \lambda^2 \cdot N \cdot f(T) \cdot [(n_{upper*})^{b_2} + (n_{lower*})^{b_2}] \quad (6)$$

with parameters $a_2 = 1.1075 \cdot 10^{-30}$, $b_2 = 4$ and $c_2 = -2$ (according to Kilian et al. 1991), instead in form (2).

Also we test the possibility to use the statistical estimates of Jagoš Purić for quick prediction of unknown Stark widths. Comparing the great amount of Stark width data from STARK-B database (Sahal-Bréchet et al. 2014; Sahal-Bréchet et al. 2015a), Purić and his co-workers found the correlation between Stark width and difference between ionization energy and energy of the upper state (which is, according to Purić, called upper effective ionization potential) and offered set of different estimating formulae.

3. Results and Discussion

We calculated Stark Full Width at Half intensity Maximum (FWHM) for 27 Lu III transitions by using the so-called "generalized" estimating formula (Purić

Table 1. Comparison of Stark Full widths at half intensity maximum for spectral lines of Lu III obtained by "generalized" method of Purić & Šćepanović (1999) for all types of transitions, W_{PS} , and the method of Purić et al. (2008), for 3s-3p transitions, applied here for all s-p transitions, W_P , with widths obtained by MSE method (W_{MSE}) and with Cowleys method (W_C) calculated in Majlinger et al. (2015). All estimates are done for temperature of $T = 10000$ K and perturber density of $N = 10^{23} \text{m}^{-3}$.

<i>Transition</i>	$\lambda[\text{Å}]$	$W_{PS}[\text{Å}]$	$W_P[\text{Å}]$	W_{PS}/W_{MSE}	W_P/W_{MSE}	W_P/W_C
$(^1S)5d^2D_{3/2} - (^1S)5f^2F_{5/2}^o$	1001.2	0.166		10.6		
$(^1S)5d^2D_{5/2} - (^1S)5f^2F_{5/2}^o$	1031.5	0.176		10.5		
$(^1S)5d^2D_{5/2} - (^1S)5f^2F_{7/2}^o$	1030.3	0.177		10.6		
$(^1S)5d^2D_{3/2} - (^1S)6p^2P_{1/2}^o$	3058.8	0.165		1.05		
$(^1S)5d^2D_{3/2} - (^1S)6p^2P_{3/2}^o$	2564.3	0.135		1.18		
$(^1S)5d^2D_{5/2} - (^1S)6p^2P_{1/2}^o$	2773.4	0.158		1.18		
$(^1S)5d^2D_{3/2} - (^1S)7p^2P_{1/2}^o$	1056.5	0.144		2.24		
$(^1S)5d^2D_{3/2} - (^1S)7p^2P_{3/2}^o$	1029.8	0.153		2.44		
$(^1S)5d^2D_{5/2} - (^1S)7p^2P_{3/2}^o$	1062.0	0.163		2.45		
$(^1S)5f^2F_{5/2}^o - (^1S)7d^2D_{3/2}$	5871.3	15.0		10.6		
$(^1S)5f^2F_{5/2}^o - (^1S)7d^2D_{5/2}$	5750.3	14.8		11.0		
$(^1S)5f^2F_{7/2}^o - (^1S)7d^2D_{5/2}$	5788.1	15.0		10.9		
$(^1S)6s^2S_{1/2} - (^1S)6p^2P_{1/2}^o$	2604.1	0.120	0.0926	0.83	0.643	0.73
$(^1S)6s^2S_{1/2} - (^1S)6p^2P_{3/2}^o$	2236.9	0.103	0.0684	0.94	0.628	0.67
$(^1S)6s^2S_{1/2} - (^1S)7p^2P_{1/2}^o$	996.4	0.128	0.0136	2.1	0.219	0.20
$(^1S)6s^2S_{1/2} - (^1S)7p^2P_{3/2}^o$	972.7	0.137	0.0129	2.3	0.215	0.19
$(^1S)6p^2P_{1/2}^o - (^1S)6d^2D_{3/2}$	1854.6	0.316		3.2		
$(^1S)6p^2P_{3/2}^o - (^1S)6d^2D_{3/2}$	2100.1	0.405		3.2		
$(^1S)6p^2P_{3/2}^o - (^1S)6d^2D_{5/2}$	2066.0	0.404		3.2		
$(^1S)6p^2P_{1/2}^o - (^1S)7s^2S_{1/2}$	2071.2	0.316	0.138	2.82	1.23	0.69
$(^1S)6p^2P_{3/2}^o - (^1S)7s^2S_{1/2}$	2382.3	0.418	0.216	2.75	1.42	0.82
$(^1S)6d^2D_{3/2} - (^1S)5f^2F_{5/2}^o$	7536.4	9.40		6.7		
$(^1S)6d^2D_{5/2} - (^1S)5f^2F_{5/2}^o$	8010.9	10.6		6.7		
$(^1S)6d^2D_{5/2} - (^1S)5f^2F_{7/2}^o$	7938.7	10.5		6.8		
$(^1S)7p^2P_{1/2}^o - (^1S)7d^2D_{3/2}$	4491.3	8.79		8.4		
$(^1S)7p^2P_{3/2}^o - (^1S)7d^2D_{3/2}$	5047.5	11.1		7.5		
$(^1S)7p^2P_{3/2}^o - (^1S)7d^2D_{5/2}$	4957.8	11.0		7.8		

& Šćepanović, 1999) derived from the large scale semiclassical perturbation and MSE calculations for all types of transitions, in order to test its applicability in the case of a complex ion like Lu III. We considered also the expression presented in (Purić et al. 2008, p. 805, Fig 1a), which is derived from large number of published theoretical and experimental data for Stark widths for multiply charged ions of different elements along the periodic table for transitions of type 3s – 3p. There is no such transitions in Lu III spectrum but in order to test its applicability to other transitions of the s-p type, we calculated also Stark widths for 6 s-p Lu III lines. After conversion of width from angular frequency units to

Angstroms (see for example, Hamdi et al. 2013, p. 1045, Eq. 7), coefficient value a_1 is recalculated to be $a_1 = 1.134 \cdot 10^{-27}$ while $b_1 = 3.33$ and $c_1 = 5.2$ remain in relation (1) as in Purić et al. (2008). The comparison with our MSE results and calculations using Cowley's method, both from Majlinger et al. (2015) are presented in Table 1. These results are calculated for temperature of $T = 10000$ K and perturber density of $N = 10^{23} \text{m}^{-3}$.

First of all, we can see the regularity of results for lines within the same multiplet. In such cases, we get approximately the same values of Stark broadening parameters, as expected. In the case of our calculation using the "generalized" expression of (Purić & Šćepanović, 1999), the average ratio with MSE results is 5.18 with extremes 11 and 0.83. The average ratio of Stark widths calculated according to Purić et al. 2008 and using MSE, for six s-p transitions is 0.73, with highest and lowest values of 1.30 and 0.215, while the average value for comparison with calculations using Cowley's formula is 0.55 with maximal and minimal value 0.82 and 0.19. We can conclude that the "general" method of Purić & Šćepanović (1999), derived for all types of transitions, is not reliable in the case of Lu III. However, if we make an analysis taking into account the type of transition we can see that the averaged ratio with MSE results is 9.4 for d-f, 3.65 for p-d and 1.96 for s-p transitions. In fact, only for s-p transitions we have a possibility for rough estimate of Stark widths which are not available.

We have already noticed (Majlinger et al., 2015) that method of Purić & Šćepanović (1999), derived from statistical analysis for ions of all elements in the periodic table and all known transitions (rearranged coefficients using in Eq. 1 are in this case $a_1 = 3.27 \times 10^{-28}$, $b_1 = 3.1$ and $c_1 = 5.2$), is expected to be more accurate for very small ionic charge (e.g. $Z = 1$) and for very large ionic charge (e.g. $Z = 5$), where results of their statistics is standing in the lower or higher end of correlation line in Fig. 1 in Purić & Šćepanović (1999), e.g. for the smallest and for the greatest values of Stark widths. For Lu III $Z = 3$, our 27 Stark widths of spectral lines lie in the middle of this correlation line, where maximal standard deviation is observed. This is one reason why method of Purić & Šćepanović (1999) give better results in comparison with MSE for Zr IV (Majlinger et al., 2017a,b) while in the present case differences are even an order of magnitude for d-f transitions. Moreover, Purić & Šćepanović (1999) did their statistical analysis on the great amount of theoretical data, including the results obtained with different theories and for all types of transitions. On our opinion, this mixture of different methods, as well as different types of transitions which are not equally represented (smaller number of data for transitions with higher ℓ), can produce a large statistical noise, resulting with so large discrepancy of data, because every method, theoretical or empirical, has its own different accuracy, and the theoretical details for different types of transitions are different.

And finally, we try to find estimation based on systematic trend among 27 calculated MSE results. Any systematic trend we found is log-log correlation

between Stark widths and corresponding wavelengths of spectral lines:

$$\log W_{MSE} = 2.245 \log \lambda - 8.403 \quad (7)$$

with correlation coefficient of around 96.5%.

4. Conclusion

We confirmed the possibility to use for s-p transitions of Lu III approximate formula for Stark width estimation given in reference Purić et al. (2008), comparing results for Stark widths of 6 spectral lines of Lu III, obtained by those formula and MSE results calculated and published elsewhere (Majlinger et al., 2015) as well as with calculations from Majlinger et al. (2015) using the method of Cowley (1971), but see also Kilian et al. (1991). The method of Purić et al. (2008) is not applicable for d-f and p-d transitions of Lu III, but for s-p transitions can provide a very rough estimate.

References

- Cowley, C., An approximate Stark broadening formula for use in spectrum synthesis. 1971, *Observatory*, **91**, 139
- Dimitrijević, M. & Konjević, N., Stark widths of doubly- and triply-ionized atom lines. 1980, *J. Quant. Spectrosc. Radiat. Transf.*, **24**, 451
- Dimitrijević, M.S., & Konjević, N. 1987. Simple estimates for Stark broadening of ion lines in stellar plasma. 1987, *Astron. Astrophys.*, **172**, 345.
- Elabidi, H. & Sahal-Bréchet, S., Checking the dependence on the upper level ionization potential of electron impact widths using quantum calculations. 2011, *Eur. Phys. J. D*, **61**, 285
- Elabidi, H., Sahal-Bréchet, S., & Nessib, N. B., Quantum Stark broadening of 3s–3p spectral lines in Li-like ions; Z-scaling and comparison with semi-classical perturbation theory. 2009, *Eur. Phys. J. D*, **54**, 51
- Griem, H. R., Semiempirical formulas for the electron-impact widths and shifts of isolated ion lines in plasmas. 1968, *Phys. Rev.*, **165**, 258
- Hamdi, R., Ben Nessib, N., Dimitrijević, M. S., & Sahal-Bréchet, S., Stark broadening of Pb IV spectral lines. 2013, *Mon. Notices Royal Astron. Soc.*, **431**, 1039
- Kilian, J., Montenbruck, O., & Nissen, P., Chemical abundances in early B-type stars. II-Line identification and atomic data for high resolution spectra. 1991, *Astron. Astrophys. Suppl.*, **88**, 101
- Lakićević, J., Estimated Stark widths and shifts of neutral atom and singly charged ion resonance lines. 1983, *Astron. Astrophys.*, **127**, 37

- Majlinger, Z., Dimitrijević, M., & Simić, Z., Regularities and Systematic Trends on Zr IV Stark Widths. 2017a, *Atoms*, **5**, 49
- Majlinger, Z., Simić, Z., & Dimitrijević, M. S., On the Stark Broadening of Lu III Spectral Lines. 2015, *J. Astrophys. Astron.*, **36**, 671
- Majlinger, Z., Simić, Z., & Dimitrijević, M. S., Stark broadening of Zr IV spectral lines in the atmospheres of chemically peculiar stars. 2017b, *Mon. Notices Royal Astron. Soc.*, **470**, 1911
- Przybilla, N., Fossati, L., Hubrig, S., et al., B fields in OB stars (BOB): Detection of a magnetic field in the He-strong star CPD- 57o 3509. 2016, *Astron. Astrophys.*, **587**, A7
- Purić, J., Dojčinović, I., Nikolić, M., et al., Stark Parameter Regularities of Multiply Charged Ion Spectral Lines Originating from the Same Transition Array. 2008, *Astrophys. J.*, **680**, 803
- Purić, J. & Šćepanović, M., General Regularities of Stark Parameters for Ion Lines. 1999, *Astrophys. J.*, **521**, 490
- Sahal-Bréchet, S., Impact Theory of the Broadening and Shift of Spectral Lines due to Electrons and Ions in a Plasma. 1969a, *Astron. Astrophys.*, **1**, 91
- Sahal-Bréchet, S., Impact Theory of the Broadening and Shift of Spectral Lines due to Electrons and Ions in a Plasma (Continued). 1969b, *Astron. Astrophys.*, **2**, 322
- Sahal-Bréchet, S., Dimitrijević, M. S., & Moreau, N., STARK-B database, [online]. Available: <http://stark-b.obspm.fr> [June 9, 2015]. 2015a, *Paris Observatory and Astronomical Observatory of Belgrade*
- Sahal-Bréchet, S., Dimitrijević, M. S., Moreau, N., & Ben Nessib, N., The Stark-B database VAMDC node for spectral line broadening by collisions with charged particles. 2014, in *SF2A-2014: Proceedings of the Annual meeting of the French Society of Astronomy and Astrophysics*, ed. J. Ballet, F. Martins, F. Bounaud, R. Monier, & C. Reylé, 515–521
- Sahal-Bréchet, S., Dimitrijević, M. S., Moreau, N., & Nessib, N. B., The STARK-B database VAMDC node: A repository for spectral line broadening and shifts due to collisions with charged particles. 2015b, *Phys. Scr.*, **90**, 054008
- Wiese, W. & Konjević, N., Regularities and similarities in plasma broadened spectral line widths (Stark widths). 1982, *J. Quant. Spectrosc. Radiat. Transf.*, **28**, 185

The influence of collisional-ionization and recombination processes on spectral line shapes in stellar atmospheres and in the hydrogen clouds in broad-line region of AGNs

V.A. Srećković¹, M.S. Dimitrijević^{2,3} and Lj.M. Ignjatović¹

¹ *Institute of Physics Belgrade, Pregrevica 118, 11080 Zemun, Belgrade, Serbia, (E-mail: vlada@ipb.ac.rs)*

² *Astronomical Observatory, Volgina 7, 11060 Belgrade, Serbia, (E-mail: mdimitrijevic@aob.rs)*

³ *Sorbonne Université, Observatoire de Paris, Université PSL, CNRS, LERMA, F-92190, Meudon, France*

Received: July 16, 2019; Accepted: August 22, 2019

Abstract. In this paper, the importance of $H^*(n) + H(1s)$ collisional ionization as well as the influence of inverse recombination processes in different environments has been investigated within the regions $2 \leq n \leq 20$ and $4\,000\text{ K} \leq T \leq 20\,000\text{ K}$. The interpretation of this influence is based on existing method of describing inelastic processes in symmetrical atom-Rydberg-atom collisions. These processes have effect on ionization and the populations of hydrogen excited atoms in moderately ionized plasma layers. From the results it follows that the investigation of these processes is of interest for the research and modelling of such medium.

Key words: Atomic processes – Galaxies: active – Line: profiles – Plasmas

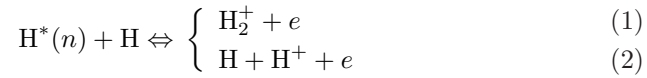
1. Introduction

The processing of line spectra with radiative transfer calculations requires spectroscopic data as well as collisional data (e.g., cross sections, rate coefficients, atomic parameters, etc Baron & Hauschildt 1998; Mihajlov et al. 2011a; Ignjatović et al. 2014; Srećković et al. 2018a). The fact that the ionization processes which involve highly excited atoms (Mihajlov et al., 2012; Srećković et al., 2017) influence the ionization level and atom excited-state populations, could influence the optical properties of the weakly ionized regions (Mihajlov et al., 2011b) of very dense parts of the clouds in broad line region (BLR) of active galactic nuclei (AGN), and potentially be important for the spectroscopy and modeling of such environment (Crosas & Weisheit, 1993; Osterbrock & Ferland, 2006).

Consequently, it is essential to find out at what plasma conditions such processes become important and to eliminate uncertainties of the rate coefficients

due to hydrogen collisions (Barklem, 2007; Srećković *et al.*, 2018a), so that they can be properly included in numerical simulations (Ferland *et al.*, 1998, 2017).

If an atom is in a state of sufficiently high principal quantum number n it means that the valence electron is far from the ionic core, and such atom appears hydrogenic. It is commonly accepted to call such atoms as Rydberg atoms with electron excited into a high lying Rydberg state, with large principal quantum number. For Rydberg atoms even inelastic thermal collisions can be sufficiently energetic to lead to ionization reactions (Gnedin *et al.*, 2009; Mihajlov *et al.*, 2012). These types of reactions are collisional ionization processes of associative ionization and the non-associative ionization



and the corresponding inverse recombination processes where $\text{H}^*(n)$ represents a high n Rydberg state of an atom H and e is a free electron, where $\text{H} = \text{H}(1s)$. Here the processes (1) and (2) are theoretically considered as factors of influence on the populations of excited atoms in the weakly ionized hydrogen plasmas. It means that the efficiency of these processes should be compared with the efficiency of the collisional processes $\text{H}^*(n) + e \Leftrightarrow \text{H}^+ + 2e$ and $\text{H}^+ + e \Rightarrow \text{H}^*(n) + \varepsilon_\lambda$. For the considered conditions of weakly ionized hydrogen plasmas the rate coefficients for collisional ionisation and collisional recombination processes are calculated as well.

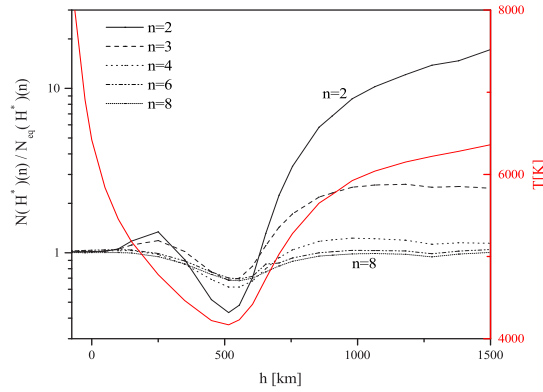


Figure 1. The ratio $N(\text{H}^*)(n)/N(\text{H}_{eq}^*)(n)$, as a function of height h . The index "eq" denotes that excited atom densities correspond to thermodynamical equilibrium conditions for given T .

Let us note the fact concerning (1) and (2) collision processes. Namely the considered processes strongly influence to the excited state populations and the free electron density (Mihajlov et al., 2011b). As the consequence of these facts, the significant change of the shape of the hydrogen atomic spectral lines is expected in different environments (see e.g. Gnedin et al. 2009). Also, let us emphasize the fact that the importance of these processes for non-local thermodynamic equilibrium (LTE) modeling of different atmosphere should be further investigated. In Fig. 1, deviations of non-LTE populations of excited hydrogen atom states with $2 \leq n \leq 8$, in solar photosphere are illustrated (see Mihajlov et al. 2011b). One can see that these deviations are particularly pronounced for $n = 2$. This deviation is noticeable, illustrating the importance of taking into account the considered processes ab initio in the modeling.

2. The collisional ionisation/recombination data

As in the previous papers (Mihajlov et al., 2011b; Mihajlov et al., 2012), for the hydrogen Rydberg states ($n \gg 1$) we will treat processes (1) and (2) on the basis of dipole resonant mechanism. Such processes are considered as a result of resonant energy conversion within the electronic component of the collisional system $H^*(n) + H(1s)$, which is realized inside the region $R \ll r_n$, where the collisional system can be presented as $[H^+ + H(1s)] + e_n$, and which is caused by the dipole part of the interaction of the outer electron e_n with the subsystem $[H^+ + H(1s)]$. The parameter $r_n \sim n^2$ is the characteristic radius of Rydberg atom $H^*(n)$ and R is the inter-nuclear distance in the collision system $H^*(n) + H(1s)$. The processes (1) and (2) for the $2 \leq n \leq 4$ will be considered separately as in Mihajlov et al. (2011b), due to the behaviour of the adiabatic potential curves of atom-atom collisional systems. Here we presented a brief description of the method with the basic theory (for details, see Mihajlov et al. 2012; O’Keeffe et al. 2012).

The aim of this work is to find out at what plasma conditions collisional ionisation/recombination become important and to update values and eliminate uncertainties of the rate coefficients due to hydrogen collisions (Barklem, 2007; Srećković et al., 2018a) in order that they can be properly included in numerical simulations and modelling (Ferland et al., 1998, 2017) as well as in the A&M databases (Vujčić et al., 2015; Dubernet et al., 2016; Marinković et al., 2017).

The corresponding partial rate coefficients of the collisional ionisation/ recombination processes (1) and (2) are denoted here with $K_{ci,cr}^{(a,b)}(n; T)$, where T is the temperature of the considered plasma. Using these partial rate coefficients we determined the total ones $K_{ci,cr}(n, T)$, namely,

$$K_{ci,cr}(n, T) = K_{ci,cr}^{(a)}(n, T) + K_{ci,cr}^{(b)}(n, T), \quad (3)$$

which characterizes the efficiency of the considered collisional processes together (for details see Mihajlov et al. 2011b). Here we will consider collisional ionisa-

tion/ recombination processes within the regions $2 \leq n \leq 20$ and $4\,000\text{ K} \leq T \leq 20\,000\text{ K}$. Relative contribution of associative and non-associative channels i.e.

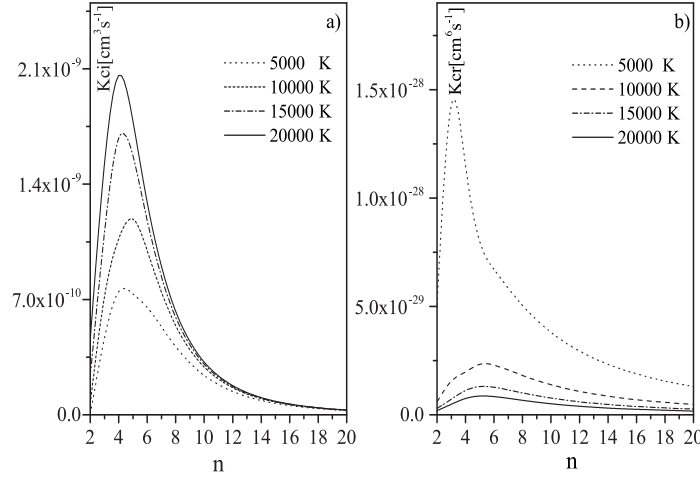


Figure 2. The calculated values of rate coefficients for collisional ionization and recombination $K_{ci}(n, T)$ and $K_{cr}(n, T)$.

partial collisional ionisation/ recombination for given n and T can be characterized by corresponding branch factor i.e. ratio $K_{ci}^{(a,b)}(n, T)/K_{ci}(n, T)$. This provides important information about presence of molecular ion H_2^+ .

The total collisional ionization $I_{ci}(n, T)$, and collisional recombination $I_{cr}(n, T)$ fluxes caused by the processes (1) and (2), can be expressed as,

$$I_{ci}(n, T) = K_{ci}(n, T) \cdot N_n N_1, \quad I_{cr}(n, T) = K_{cr}(n, T) \cdot N_1 N_i N_e. \quad (4)$$

This is performed under the standard assumption that in e.g. photosphere plasmas $T_e = T_a = T$, where T_e and T_a are the electron and atom temperatures and T is their common value. Let $I_{i;ea}(n, T) = K_{ea}(n, T) \cdot N_n N_e$, $I_{r;eei}(n, T) = K_{eei}(n, T) \cdot N_i N_e N_e$ and $I_{r;ph}(n, T) = K_{ph}(n, T) \cdot N_i N_e$ are the fluxes caused by ionization and recombination processes where N_1 , N_n , N_i , and N_e are, respectively, the densities of the ground and excited states of a hydrogen atom, of ion, and of free electron in the considered plasma with given T .

Using these expressions, we can calculate quantities i.e. flux ratio $\frac{I_{ci}(n, T)}{I_{i;ea}(n, T)}$ which characterize the relative efficiency of partial ionization processes (1) and (2) together and the impact electron-atom ionization in the considered plasma.

3. Results and Discussion

The values of the total ionization and recombination rate coefficients $K_{ci}(n, T)$ and $K_{cr}(n, T)$, obtained in the described way, are presented in Fig. 2. These results cover the regions $2 \leq n \leq 20$ and $4000 \text{ K} < T \leq 20000 \text{ K}$ which are relevant for moderately ionized plasma layers in different environments.

In order to allow for a faster usage of the calculated results we provide a fit to numerical results of the form (Sahal-Bréchet et al., 2014)

$$\log(K_{ci,cr}(T)) = \sum_{i=0}^2 a_i (\log(T))^i. \quad (5)$$

The fits are valid over the temperature range of $4000 \text{ K} \leq T \leq 20000 \text{ K}$ (see Mihajlov et al. (2011a); Srećković et al. (2018a); Srećković et al. (2018b)). This enables the easy inclusion of these processes in the modeling not only the very dense parts of the clouds in AGN BLR but also moderately ionized layers of the Sun and solar like stars. The parameters are provided in Tab. 1 for selected excited states ($n = 4, 5$).

Table 1. The fits of the Eq. (5) to the rate coefficients (Mihajlov et al., 2011a; Srećković et al., 2018a). A portion is shown here for guidance regarding its form and content.

n	a_0	a_1	a_2
K_{ci}			
4	19.91758	-15.14785	1.98009
5	-20.60455	5.21174	-0.57122
K_{cr}			
4	35.17003	-30.09052	3.52731
5	-15.84169	-4.85018	0.41418

These results, and further analysis show that associative channel is dominant for lower n and T . This provides important information about presence of molecular ion H_2^+ . The importance of associative channel decreases with temperature increase when non-associative channel take dominant place.

In Fig. 3 the behavior of flux ratio $\frac{I_{ci}(n,T)}{I_{i,ea}(n,T)}$ for $2 \leq n \leq 8$, for the plasma condition with neutral hydrogen atom in the ground state densities 10^{13} cm^{-3} and the electron density of $0.01 N_1$, at $T = 8000 \text{ K}$, is shown. For $2 \leq n \leq 5$ the efficiency of the considered collisional ionization processes is at least comparable with the electron-atom impact ionization. The same conclusion goes for influence of the collisional recombination processes together on the same block of excited hydrogen atom states.

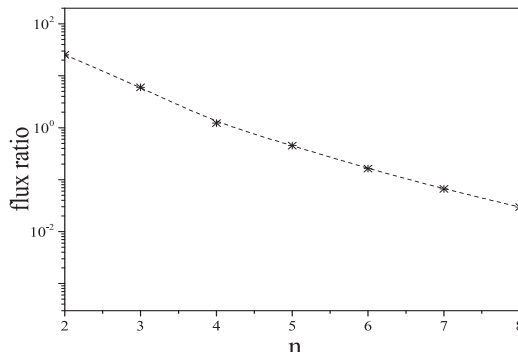


Figure 3. Behavior of the quantity i.e. flux ratio $\frac{I_{ei}(n,T)}{I_{i;ea}(n,T)}$ as a function of n , for the neutral hydrogen atom ground state densities $N_1 = 10^{13} \text{ cm}^{-3}$ and temperatures $T = 8000 \text{ K}$ with the electron density $0.01 N_1$.

Analyzing the flux ratio the influence of investigated processes increases linearly with hydrogen density, and, for example for 10^{13} cm^{-3} some optical characteristics may be different than for 10^{12} cm^{-3} , due to changes in electron density, energy level populations, formation of hydrogen molecules, etc. In future it will be very useful to do an analysis (e.g with the code CLOUDY) in order to see changes in optical characteristics.

About this issue, in Mihajlov *et al.* (2007) was examined the atmosphere of a M red dwarf with an effective temperature of 3800 K. For the examined atmosphere, the profiles of a number of spectral lines of the hydrogen atom were calculated (see also Gnedin *et al.* (2009)). Profiles are synthesized with PHOENIX code with Stark broadening contribution. Analyses show that the collisional-ionization/recombination processes, influence on the population of the hydrogen excited states and the electron densities, and have a very strong effect on the shape of the spectral lines (see also Gnedin *et al.* 2009; Srećković *et al.* 2018a).

4. Conclusions

The presented data and analyses demonstrate the fact that the considered ionization/recombination processes, influence on the ionization level and atom excited-state populations and have a noticeable influence on the optical properties of very dense parts of the clouds in the BLR of AGNs where the neutral hydrogen densities are larger than 10^{12} cm^{-3} since in such conditions they dominate over the relevant concurrent electronatom collision processes. The calculated values of the rate coefficients are also very useful for the modelling and

analysis of similar layers in the photospheres of Sun and solar like stars and laboratory plasmas (Barklem, 2007; Fontenla et al., 2009) and for the study of their influence during the cosmological recombination epoch (Chluba et al., 2010). Note that the obtained results point to further directions of the investigation. In future it will be very useful to do an analysis with the code CLOUDY in order to see changes in optical characteristics i.e. on the line shapes.

Acknowledgements. This work is made within projects of the MESTD of the Republic of Serbia Grants OI176002, III44002.

References

- Barklem, P. S., Non-LTE Balmer line formation in late-type spectra: effects of atomic processes involving hydrogen atoms. 2007, *Astron. Astrophys.*, **466**, 327
- Baron, E. & Hauschildt, P. H., Parallel Implementation of the PHOENIX Generalized Stellar Atmosphere Program. 1998, *Astrophys. J.*, **495**, 370
- Chluba, J., Vasil, G. M., & Dursi, L. J., Recombinations to the Rydberg states of hydrogen and their effect during the cosmological recombination epoch. 2010, *Mon. Not. R. Astron. Soc.*, **407**, 599
- Crosas, M. & Weisheit, J. C., Hydrogen molecules in quasar broad-line regions. 1993, *Mon. Not. R. Astron. Soc.*, **262**, 359
- Dubernet, M. L., Antony, B. K., Ba, Y. A., et al., The virtual atomic and molecular data centre (VAMDC) consortium. 2016, *J. Phys. B*, **49**, 074003
- Ferland, G. J., Chatzikos, M., Guzmán, F., et al., The 2017 Release Cloudy. 2017, *Rev. Mex. Astron. Astrofis*, **53**, 385
- Ferland, G. J., Korista, K. T., Verner, D. A., et al., CLOUDY 90: Numerical Simulation of Plasmas and Their Spectra. 1998, *Publ. Astron. Soc. Pac.*, **110**, 761
- Fontenla, J. M., Curdt, W., Haberreiter, M., Harder, J., & Tian, H. Semiempirical Models of the Solar Atmosphere. III. Set of Non-LTE Models for Far-Ultraviolet/Extreme-Ultraviolet Irradiance Computation. 2009, *Astrophys. J.*, **707**, 482
- Gnedin, Y. N., Mihajlov, A., Ignjatović, L. M., et al., Rydberg atoms in astrophysics. 2009, *New Astron. Rev.*, **53**, 259
- Ignjatović, L. M., Mihajlov, A., Srećković, V., & Dimitrijević, M., Absorption non-symmetric ion-atom processes in helium-rich white dwarf atmospheres. 2014, *Mon. Notices Royal Astron. Soc.*, **439**, 2342
- Marinković, B. P., Jevremović, D., Srećković, V. A., et al., BEAMDB and MolD-databases for atomic and molecular collisional and radiative processes: Belgrade nodes of VAMDC. 2017, *Eur. Phys. J. D*, **71**, 158
- Mihajlov, A. A., Jevremović, D., Hauschildt, P., et al., Influence of chemi-ionization and chemi-recombination processes on hydrogen line shapes in M dwarfs. 2007, *Astron. Astrophys.*, **471**, 671

- Mihajlov, A., Sakan, N., Srećković, V., & Vitel, Y., Modeling of continuous absorption of electromagnetic radiation in dense partially ionized plasmas. 2011a, *J. Phys. A*, **44**, 095502
- Mihajlov, A., Srećković, V., Ignjatović, L. M., & Klyucharev, A., The chemi-ionization processes in slow collisions of Rydberg atoms with ground state atoms: mechanism and applications. 2012, *J. Clust. Sci.*, **23**, 47
- Mihajlov, A. A., Ignjatović, L. M., Srećković, V. A., & Dimitrijević, M. S., Chemi-ionization in Solar Photosphere: Influence on the Hydrogen Atom Excited States Population. 2011b, *Astrophys. J., Suppl.*, **193**, 2
- O’Keeffe, P., Bolognesi, P., Avaldi, L., et al., Experimental and theoretical study of the chemi-ionization in thermal collisions of Ne Rydberg atoms. 2012, *Phys. Rev. A*, **85**, 052705
- Osterbrock, D. E. & Ferland, G. J. 2006, *Astrophysics of gaseous nebulae and active galactic nuclei* (University science books)
- Sahal-Bréchet, S., Dimitrijević, M. S., Moreau, N., & Ben Nessib, N., The STARK-B database as a resource for STARK widths and shifts data: State of advancement and program of development. 2014, *Adv. Space Res.*, **54**, 1148
- Srećković, V., Dimitrijević, M., Ignjatović, L., Bezuglov, N., & Klyucharev, A., The Collisional Atomic Processes of Rydberg Hydrogen and Helium Atoms: Astrophysical Relevance. 2018a, *Galaxies*, **6**, 72
- Srećković, V. A., Dimitrijević, M. S., & Ignjatović, L. M., Atom-Rydberg atom chemi-ionization/recombination processes in the hydrogen clouds in broad-line region of AGNs. 2018b, *Mon. Not. R. Astron. Soc.*, **480**, 5078
- Srećković, V., Ignjatović, L., Jevremović, D., Vujčić, V., & Dimitrijević, M., Radiative and Collisional Molecular Data and Virtual Laboratory Astrophysics. 2017, *Atoms*, **5**, 31
- Vujčić, V., Jevremović, D., Mihajlov, A., et al., MOL-D: A Collisional Database and Web Service within the Virtual Atomic and Molecular Data Center. 2015, *J. Astrophys. Astron.*, **36**, 0

Influence of the $(n-n')$ -mixing processes on the optical properties of the hydrogen clouds in the broad-line region of AGNs

M.S. Dimitrijević^{1,2}, V.A. Srećković³ and Lj.M. Ignjatović³

¹ *Astronomical Observatory, Volgina 7, 11060 Belgrade, Serbia*

² *Sorbonne Université, Observatoire de Paris, Université PSL, CNRS, LERMA, F-92190 Meudon, France (E-mail: mdimitrijevic@aobrs)*

³ *Institute of Physics Belgrade, Pregrevica 118, 11080 Zemun, Belgrade, Serbia, (E-mail: vlada@ipb.ac.rs)*

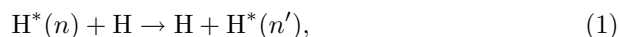
Received: July 16, 2019; Accepted: October 29, 2019

Abstract. The role of $(n-n')$ -mixing processes in active galactic nuclei broad-line region (BLR) clouds has been studied. Our investigation indicates that these collisional processes must have influence on the populations of the excited hydrogen atoms in moderately ionized layers of dense parts of the BLR clouds and are of interest for its modelling and research. We provide results potentially important for the spectroscopy and modeling of the BLR clouds, as well as for the study of hydrogen Rydberg states.

Key words: Galaxies: active – atomic processes – Plasmas

1. Introduction

In the papers Mihajlov et al. (2005); Gnedin et al. (2009); Mihajlov et al. (2016) authors drew attention to the importance of inelastic processes in slow collisions of Rydberg state atoms with ground state hydrogen atoms (i.e. excitation/de-excitation processes) in solar and stellar atmospheres



where H are hydrogen atoms in their ground states, $\text{H}^*(n)$ and $\text{H}^*(n')$ are hydrogen atoms in a highly excited (Rydberg) state.

These authors concluded that $(n-n')$ -mixing processes (Eq. 1) significantly influence on the populations of hydrogen Rydberg atoms (RA) in weakly ionized layers of stellar atmospheres and particularly in Solar photosphere and the lower chromosphere and need to be added in any modelling and investigation of these regions. In Barklem (2007) and Mashonkina (2009) the $(n-n')$ -mixing processes have also been analyzed together with others, and the conclusion was that there is a great need for their further investigation, since in many cases there are uncertainties in the rate coefficients of hydrogen collisions (see also Srećković et al., 2018a,b).

In active galactic nuclei (AGN), especially in the region of the moderately ionized layers of dense parts of the broad-line region (BLR), in which physical conditions are closer to stellar atmospheres than to photoionized nebulae (Ilić et al., 2007; Negrete et al., 2012; Ilić et al., 2017; Bon et al., 2018; Osterbrock & Ferland, 2006). In the BLR clouds temperature may drop to the much lower values where the gas is weakly ionized with huge number of hydrogen atoms in excited states, due to the high density and large optical depths (Crosas & Weisheit, 1993; Negrete et al., 2012; Netzer, 2013). Consequently, it is of interest to investigate the influence of the mentioned collisional processes Srećković et al. (2018c).

That is the reason why we have extended the investigation of these processes and calculated their rate coefficients for a wider region of plasma parameters and for quantum numbers n up to 20 in order to be potentially used in AGN modeling. The results presented here cover the range of temperatures $2000 \text{ K} \leq T \leq 30000 \text{ K}$, broader than the regions relevant for weakly ionized layers of dense parts of the BLR clouds (see e.g. Crosas & Weisheit, 1993; Negrete et al., 2012), so that the data presented here can be also used for investigation of the atmospheres of Sun and Sun-like stars etc. (Mihajlov et al., 2011; Mihajlov et al., 2011; Srećković et al., 2014). Also, study of these processes are of interest for some laboratory spectroscopical investigation and technical applications (Dubernet et al., 2016; Marinković et al., 2017).

We describe in Section 2 the methods of calculation and then in Section 3 we give the results of the calculation. In Section 4 the conclusions are presented.

2. Method

2.1. The resonant mechanism

On the basis of the resonant mechanism (Mihajlov et al., 2012; Srećković et al., 2013, 2018c) the $(n-n')$ -mixing processes (Eq. 1) are characterized as a product of the resonant energy exchange between the outer electron e and the electronic component of the subsystem $\text{H}^+ + \text{H}$ (Fig.1). The system $\text{H}^*(n) + \text{H}$ is described as: $e + (\text{H}^+ + \text{H})$, where e is the outer electron of the hydrogen RA $\text{H}^*(n)$. For describing the subsystem $(\text{H}^+ + \text{H})$ electronic states, the adiabatic electronic ground state, or the first excited state of the molecular ion were used.

2.2. The $(n-n')$ -mixing rate coefficients

The procedure of obtaining the rate coefficients for the processes (Eq. 1) is described in detail in Mihajlov et al. (2004); Srećković et al. (2013) and only the corresponding final expressions are given here. The rate coefficients $K_{n;n+p}^{mix}(T)$ for the mixing processes between two excited levels with main quantum numbers

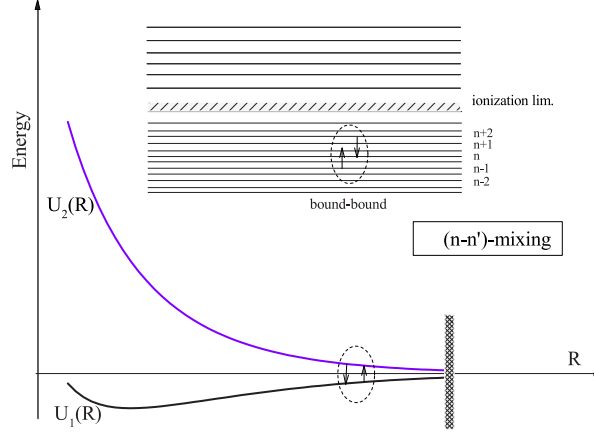


Figure 1. The schematic presentation of the (n-n')-mixing processes. R presents the internuclear distance, $U_1(R)$ and $U_2(R)$ are the potential energy curves of the initial and final electronic state of considered system.

n and $n + p$, can be expressed as a function of the temperature T as

$$K_{n;n+p}^{mix}(T) = \frac{2\pi}{3\sqrt{3}} \frac{(ea_0)^2}{\hbar} \cdot n^{-5} \cdot g_{n;n+p} \times \int_{R_{min}(n,n+p)}^{R_{max}(n,n+p)} X(R) \cdot \exp\left[-\frac{U_2(R)}{kT}\right] \frac{R^4 \cdot dR}{a_0^5}, \quad (2)$$

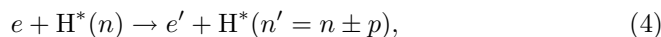
where $T_e = T_a = T$, T_e and T_a are the electron and atom temperatures and T is their common value, $g_{n;n+p}$ is the Gaunt factor, $R_{min}(n, n+p)$ and $R_{max}(n, n+p)$ are quantities defined in Mihajlov et al. (2008), a_0 is the atomic unit of length, e is the value of electron charge, R is the internuclear distance, \hbar and k are the Planck and Boltzmann constants and $U_2(R)$ is the potential curve of the first excited electronic states of the considered system. $X(R)$ is defined as the function $X(R) = \frac{\Gamma(3/2; \frac{|U_1(R)|}{kT})}{\Gamma(3/2)}$, where $\Gamma(3/2; x)$ and $\Gamma(3/2)$ are the corresponding values of the incomplete and complete Gamma functions. The rate coefficients for the corresponding inverse deexcitation processes are

$$K_{n;n-p}^{mix}(T) = K_{n-p;n}^{mix}(T) \cdot \frac{(n-p)^2}{n^2} \cdot \exp\left(\frac{\epsilon_{n-p;n}}{kT}\right), \quad (3)$$

where $\epsilon_{n-p;n} = \epsilon_n - \epsilon_{n-p}$ and $\epsilon_n = -Ry/n^2$, Ry is the Rydberg constant (for details see Mihajlov et al., 2008).

2.3. The relative efficiency

To estimate the relative efficiency of processes defined in Eq. (1) in comparison to concurrent electron-atom mixing processes i.e. electron-excited atom collisional excitation/de-excitation processes



we use the parameter $F_n^{(\pm)}(T)$

$$F_n^{(\pm)}(T) = \frac{\sum_{p=1}^5 K_{n;n\pm p}^{mix}(T)N(n)N(1)}{\sum_{p=1}^5 K_{n;n\pm p}^{ea}(T)N(n)N_e} = \frac{\sum_{p=1}^5 K_{n;n\pm p}^{mix}(T)}{\sum_{p=1}^5 K_{n;n\pm p}^{ea}(T)}\eta, \quad (5)$$

where $N(n)$ is the population of the excited atom states, N_e is the density of free electrons and the parameter $\eta = N(1)/N_e$. Here quantity $K_{n;n\pm p}^{ea}(T_e = T)$ is the rate coefficient for the electron-atom process (Eq.4) taken from Vriens & Smeets (1980). The expressions $K_{n;n\pm p}^{mix}(T)N(n)N(1)$ and $K_{n;n\pm p}^{ea}(T)N(n)N_e$ are the partial atom- and electron-Rydberg atom excitation and deexcitation fluxes.

3. Results and Discussion

The rate coefficients $K_{n;n\pm p}^{mix}(T)$ for mixing processes (Eq.1) are calculated for the following parameters $4 \leq n \leq 20$, $1 \leq p \leq 5$ and $2000 \text{ K} \leq T \leq 30000 \text{ K}$. Here we give the results only for temperatures $\leq 10000 \text{ K}$, which are relevant for the moderately ionized layers of dense parts of the BLR clouds and data for higher temperatures are of interest for other moderately ionized astrophysical plasmas. In Fig. 2 the excitation rate coefficients are presented for selected excited states $n = 4, \dots, 13$ and temperature T in the range $3\,000 - 10\,000 \text{ K}$ relevant for the moderately ionized layers of dense parts of the BLR clouds.

We have calculated the values of the parameter $F_n^{(+)}$ for $4 \leq n \leq 8$ in order to compare the relative influence of $(n-n')$ -mixing processes (Eq.1) and influence of concurrent electron-atom excitation processes (Eq.4) for the physical conditions which could be relevant in the BLR of AGNs (see Fig. 3). It can be noted that the $(n-n')$ -mixing processes for $n \leq 5$ are dominating over the concurrent ones in the lower temperature regime (Eq.4, bottom panel) whereas for $6 \leq n \leq 8$ both processes are comparable (see Fig. 3). Also the processes (Eq.1) are comparable with concurrent excitation processes (Eq.4) only for lower n in the parts of the BLR with higher temperatures. On Fig. 3 the shaded area ($2 \leq n \leq 4$) present extrapolated values due to the missing reliable data for the corresponding rate coefficients. The only existing rate coefficients in the literature for $n = 2$ and 3 are data from Drawin (1968) which are not recommended (see Barklem 2007, Srećković et al. 2018c). We note that these rate coefficients for $n = 2$ and 3 are of great importance and the impact of processes (see Eq.1) should be much

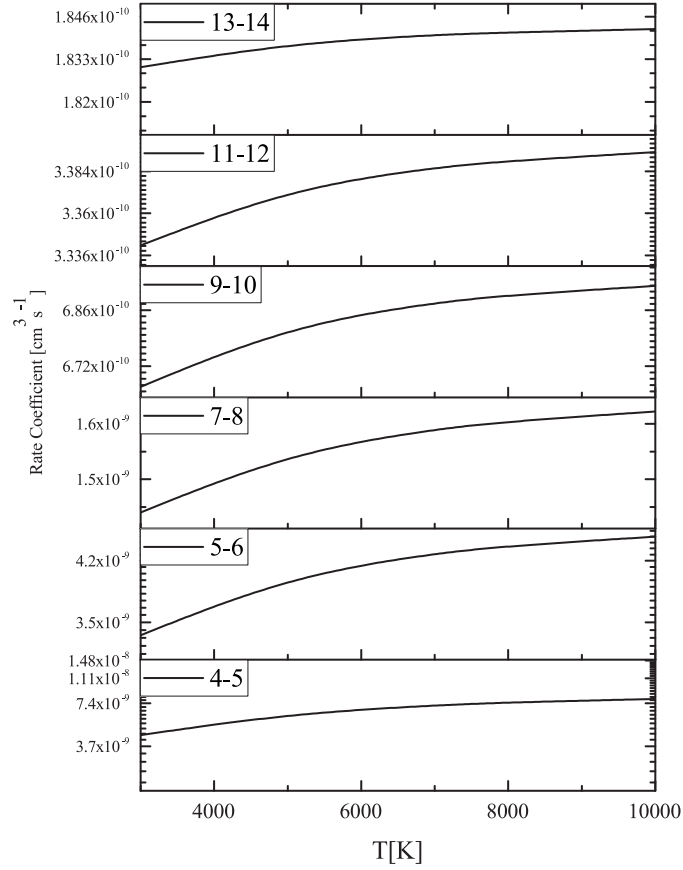


Figure 2. Plot of excitation rate coefficients for processes $\text{H}^*(n) + \text{H} \rightarrow \text{H} + \text{H}^*(n')$, for selected excited states $n = 4, \dots, 13$ and temperature T in the range 3 000 - 10 000K.

higher on the populations of hydrogen excited atoms of the AGNs in comparison to the concurrent processes.

The presented results demonstrate that these processes must have a noticeable influence on the optical properties of the weakly ionized regions of dense parts of the BLR clouds and that they should be used in the models. In addition, they could be helpful for modeling of various stellar atmospheres with low effective temperatures, as well as for the research of Rydberg states of hydrogen and the analysis of their influence during the cosmological recombination epoch

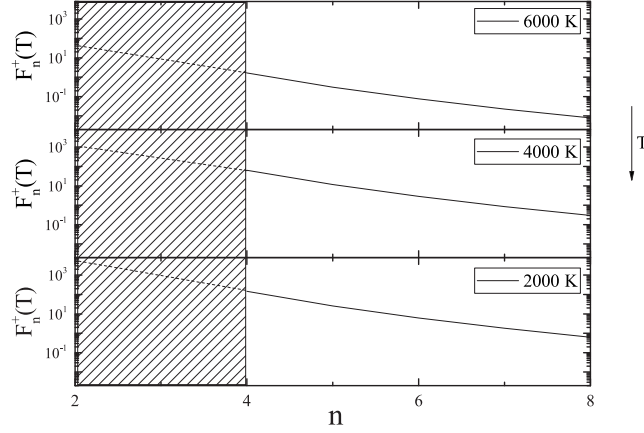


Figure 3. Efficiencies $F_n^{(+)}$ of the analyzed processes for $4 \leq n \leq 8$ and temperatures 6000 K (upper panel), 4000 K (middle panel), and 2000 K (bottom panel). The extrapolated values below $n = 4$ (see text) are shown in the left shaded region.

(Fontenla et al., 2009; Przybilla & Butler, 2004; Barklem, 2007; Mashonkina, 2009).

4. Conclusion

Our primary task in this paper was determination of rate coefficients for parameters that exists in BLR clouds in order to be used in the corresponding models. The results demonstrate the fact that the considered $(n-n')$ -mixing processes must have a significant influence on the populations of excited hydrogen atoms in cooler and denser parts of the BLR clouds in AGNs in comparison to the concurrent processes and must have influence on the optical properties.

Acknowledgements. This work is made within projects of the Ministry of Education, Science and Technological Development of Serbia, 176002, III44002.

References

- Barklem, P. S., Non-LTE Balmer line formation in late-type spectra: effects of atomic processes involving hydrogen atoms. 2007, *Astron. Astrophys.*, **466**, 327
- Bon, N., Bon, E., & Marziani, P., AGN Broad Line Region variability in the context of Eigenvector 1: case of NGC 5548. 2018, *Frontiers in Astronomy and Space Sciences*, **5**, 3

- Crosas, M. & Weisheit, J. C., Hydrogen molecules in quasar broad-line regions. 1993, *Mon. Not. R. Astron. Soc.*, **262**, 359
- Drawin, H.-W., Zur formelmäßigen Darstellung des Ionisierungsquerschnitts für den Atom-Atomstoß und über die Ionen-Elektronen-Rekombination im dichten Neutralgas. 1968, *Z. Phys.*, **211**, 404
- Dubernet, M.-L., Antony, B., Ba, Y.-A., et al., The virtual atomic and molecular data centre (VAMDC) consortium. 2016, *J. Phys. B*, **49**, 074003
- Fontenla, J. M., Curdt, W., Haberreiter, M., Harder, J., & Tian, H., Semiempirical Models of the Solar Atmosphere. III. Set of Non-LTE Models for Far-Ultraviolet/Extreme-Ultraviolet Irradiance Computation. 2009, *Astrophys. J.*, **707**, 482
- Gnedin, Y. N., Mihajlov, A., Ignjatović, L. M., et al., Rydberg atoms in astrophysics. 2009, *New Astron. Rev.*, **53**, 259
- Ilić, D., Popović, L. Č., Ciroi, S., La Mura, G., & Rafanelli, P., Physical Properties of the BLR of AGN: Boltzmann-Plot vs. CLOUDY Models. 2007, in American Institute of Physics Conference Series, Vol. **938**, *Spectral Line Shapes in Astrophysics*, ed. L. C. Popovic & M. S. Dimitrijevic, 70–75
- Ilić, D., Shapovalova, A. I., Popović, L. Č., et al., Long-term monitoring of the broad-line region properties in a selected sample of AGN. 2017, *Frontiers in Astronomy and Space Sciences*, **4**, 12
- Marinković, B. P., Jevremović, D., Srećković, V. A., et al., BEAMDB and MolD–databases for atomic and molecular collisional and radiative processes: Belgrade nodes of VAMDC. 2017, *Eur. Phys. J. D*, **71**, 158
- Mashonkina, L., Atomic data necessary for the non-LTE analysis of stellar spectra. 2009, *Phys. Scr.*, **134**, 014004
- Mihajlov, A., Sakan, N., Srećković, V., & Vitel, Y., Modeling of the continuous absorption of electromagnetic radiation in dense Hydrogen plasma. 2011, *Open Astron.*, **20**, 604
- Mihajlov, A. A., Ignjatović, L. M., & Dimitrijević, M. S., Processes of (n - n')-mixing in collisions of Rydberg H*(n) atoms with H(1s) in the Solar atmosphere. 2005, *Astron. Astrophys.*, **437**, 1023
- Mihajlov, A. A., Ignjatovic, L. M., Djuric, Z., & Ljepojevic, N. N., The rate coefficients for the processes of (n - n')-mixing in collisions of Rydberg atoms H*(n) with H(1s) atoms. 2004, *J. Phys. B*, **37**, 4493
- Mihajlov, A. A., Ignjatović, L. M., Srećković, V. A., & Dimitrijević, M. S. 2011, *Astrophys. J., Suppl.*, **193**, 2
- Mihajlov, A. A., Ignjatović, L. M., Srećković, V. A., & Djurić, Z., The influence of (n-n')-mixing processes in He*(n)+He(1s²) collisions on He*(n) atoms populations in weakly ionized helium plasmas. 2008, *J. Quant. Spectrosc. Radiat. Transf.*, **109**, 853
- Mihajlov, A. A., Srećković, V. A., Ignjatović, L. M., & Dimitrijević, M. S., Atom-Rydberg-atom chemi-ionization processes in solar and DB white-dwarf atmospheres

- in the presence of (n - n')-mixing channels. 2016, *Mon. Not. R. Astron. Soc.*, **458**, 2215
- Mihajlov, A. A., Srećković, V. A., Ignjatović, L. M., & Klyucharev, A. N., The Chemi-Ionization Processes in Slow Collisions of Rydberg Atoms with Ground State Atoms: Mechanism and Applications. 2012, *J. Clust. Sci.*, **23**, 47
- Negrete, C. A., Dultzin, D., Marziani, P., & Sulentic, J. W., Broad-line Region Physical Conditions in Extreme Population A Quasars: A Method to Estimate Central Black Hole Mass at High Redshift. 2012, *Astrophys. J.*, **757**, 62
- Netzer, H. 2013, *The Physics and Evolution of Active Galactic Nuclei*, Cambridge: Cambridge University Press
- Osterbrock, D. E., & Ferland, G. J. 2006, *Astrophysics of gaseous nebulae and active galactic nuclei*, 2nd. ed. by D.E. Osterbrock and G.J. Ferland. Sausalito, CA: University Science Books
- Przybilla, N. & Butler, K., Non-LTE Line Formation for Hydrogen Revisited. 2004, *Astrophys. J.*, **609**, 1181
- Srećković, V., Dimitrijević, M., Ignjatović, L., Bezuglov, N., & Klyucharev, A., The Collisional Atomic Processes of Rydberg Hydrogen and Helium Atoms: Astrophysical Relevance. 2018a, *Galaxies*, **6**, 72
- Srećković, V., Ignjatović, L., & Dimitrijević, M., Symmetric Atom–Atom and Ion–Atom Processes in Stellar Atmospheres. 2018b, *Atoms*, **6**, 1
- Srećković, V. A., Dimitrijević, M. S., & Ignjatović, L. M., Atom-Rydberg atom chemi-ionization/recombination processes in the hydrogen clouds in broad-line region of AGNs. 2018c, *Mon. Not. R. Astron. Soc.*, **480**, 5078
- Srećković, V. A., Mihajlov, A. A., Ignjatović, L. M., & Dimitrijević, M. S., Excitation and deexcitation processes in atom-Rydberg atom collisions in helium-rich white dwarf atmospheres. 2013, *Astron. Astrophys.*, **552**, A33
- Srećković, V. A., Mihajlov, A. A., Ignjatović, L. M., & Dimitrijević, M. S., Ion-atom radiative processes in the solar atmosphere: quiet Sun and sunspots. 2014, *Adv. Space Res.*, **54**, 1264
- Vriens, L. & Smeets, A. H. M., Cross-section and rate formulas for electron-impact ionization, excitation, deexcitation, and total depopulation of excited atoms. 1980, *Phys. Rev. A*, **22**, 940

Photoionization of the alkali molecular ions in geo-cosmical plasmas

Lj.M. Ignjatović¹, V.A. Srećković¹ and M.S. Dimitrijević^{2,3}

¹ *Institute of Physics Belgrade, BU, Pregrevica 118, 11080 Belgrade, Serbia
(E-mail: vlada@ipb.ac.rs)*

² *Astronomical Observatory, Volgina 7, 11060 Belgrade, Serbia (E-mail:
mdimitrijevic@aob.rs)*

³ *Sorbonne Université, Observatoire de Paris, Université PSL, CNRS,
LERMA, F-92190, Meudon, France*

Received: July 16, 2019; Accepted: September 29, 2019

Abstract. Opacities of the solar and stellar atmospheres are caused by a large number of radiative processes. Within development of more sophisticated stellar atmosphere models, we can further investigate known processes and include all processes not considered before. We calculate the average cross-section and rate coefficients for the photodissociation of the alkali molecular ions Li_2^+ , Na_2^+ and LiNa^+ ready for further use with a particular accent to the applications for astro plasma research and low temperature laboratory plasma research.

Key words: Atomic processes – Line: profiles – Plasmas – ISM: clouds

1. Introduction

The influence of some hydrogen and helium radiative processes on the optical characteristics of the stellar atmospheres was already established (see e.g. Fontenla et al., 2006; Ignjatović et al., 2009). Here we keep in mind such symmetric and non-symmetric radiative processes as photoabsorption/emission described in Srećković et al. (2017) and Marinković et al. (2017)

Recently, in the papers Mihajlov et al. (2007); Ignjatović et al. (2014); Srećković et al. (2014); Babb (2015); Heays et al. (2017) has been pointed out that the photodissociation of the diatomic molecular ion in the symmetric and non-symmetric cases, are of astrophysical relevance and could be important in modeling of specific stellar atmosphere layers and they should be included in some chemical models. In the symmetric case, it was considered the processes of molecular ion photodissociation and inverse photoassociation:



where A and A^+ are atom and ion in their ground states, and A_2^+ is molecular-ion in the ground electronic state. In the non-symmetric case, the similar processes of photodissociation/ photoassociation are:



where B is an atom whose ionization potential is less than the corresponding value for atom A . AB^+ is also molecular-ion in the ground electronic state.

For the solar atmosphere, A designates atom H(1s) and B one of the relevant metal atoms Si, Ca, Na, Mg. Also there are cases where $A=He$, and $B=H$, Mg, Si, Na, Ca (Mihajlov *et al.*, 2007; Ignjatović *et al.*, 2014; Srećković *et al.*, 2014). For the helium-rich white dwarf atmospheres A designate He($1s^2$) and B H(1s), and eventually oxygen or carbon (Ignjatović *et al.*, 2009; Mihajlov *et al.*, 2013). Recently, Srećković *et al.* (2017, 2018) show the importance of including the symmetric processes (1) with $A = H(1s)$ in the solar atmosphere models like Fontenla *et al.* (2006). Also, for modeling the DB white dwarf atmospheres results for case $A = He(1s^2)$ have been used (Koester, 2010).

It is well known (Puy *et al.*, 2007) that the chemical composition of the primordial gas consists of electrons and species such as: helium - He, He⁺, He²⁺ and HeH⁺; hydrogen - H, H⁻, H⁺, H₂⁺ and H₂; deuterium - D, D⁺, HD, HD⁺ and HD⁻; lithium - Li, Li⁺, Li⁻, LiH⁻ and LiH⁺. One can see that among them are species like molecular ions A_2^+ and AB^+ whose role in the primordial star formation is important (see also Coppola *et al.*, 2011; Glover *et al.*, 2014).

The average cross-section for the photodissociation and the corresponding spectral absorption coefficients of the alkali molecular ions Li₂⁺, Na₂⁺ and LiNa⁺ are calculated for the wide region of temperatures and wavelengths. The presented results are ready for further use with a particular accent to the applications for astro plasma research and low temperature laboratory plasma research created in gas discharges, where plasma conditions may be favorable for processes investigated here (Pichler *et al.*, 2017; Beuc *et al.*, 2018).

We describe in Section 2 the methods of calculation and then in Section 3 the results of the calculation. The conclusions are presented in Section 4.

2. The methods of calculation

In accordance with the Ignjatović *et al.* (2014) the mean thermal photodissociation cross section, is

$$\sigma^{(phd)}(\lambda, T) = \frac{\sum_{J,v} (2J+1) e^{-\frac{E_{J,v}}{kT}} \cdot \sigma_{J,v}(\lambda)}{\sum_{J,v} (2J+1) e^{-\frac{E_{J,v}}{kT}}}, \quad (3)$$

and $\sigma_{J,v}(\lambda)$ is the partial photodissociation cross-section for the ro-vibrational states with given quantum numbers J and v , and $E_{J,v}$ - the energies of these states with the respect to the ground ro-vibrational states. Here $E_{J,v} = E_{dis} + \epsilon_{J,v}$, where E_{dis} is the dissociative energy of the molecular ion, and the energies $\epsilon_{J,v} < 0$ are determined as in Srećković *et al.* (2014); Srećković *et al.* (2017) together with the wave functions of the considered ro-vibrational states. Within

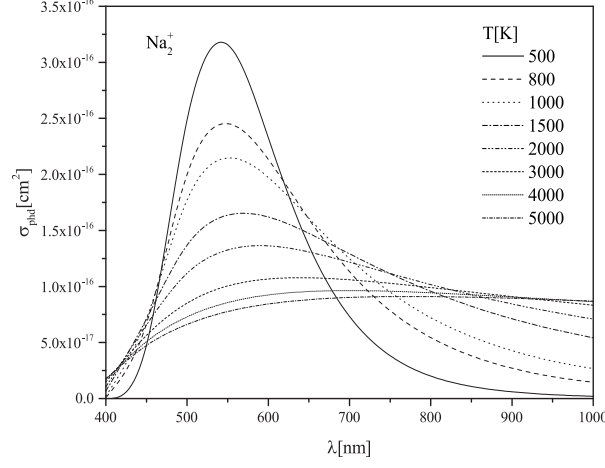


Figure 1. The behaviour of the averaged cross-section $\sigma_{phd}(\lambda, T)$ for photodissociation of the Na_2^+ molecular ion, as a function of λ and T .

the dipole approximation the partial cross-sections $\sigma_{J,v}(\lambda)$ are given by

$$\sigma_{J,v}(\lambda) = \frac{8\pi^3}{3\lambda} \left[\frac{J+1}{2J+1} |D_{J,v;J+1,E'_{imp}}|^2 + \frac{J}{2J+1} |D_{J,v;J-1,E'_{imp}}|^2 \right], \quad (4)$$

$$D_{J,v;J\pm 1,E'_{imp}} = \langle in, J, v; R | D_{in,fin}(R) | fin, J \pm 1, E' \rangle, \quad (5)$$

where $E' = \epsilon_{J,v} + \epsilon_\lambda$, E'_{imp} and E' and $D_{in,fin}(R)$ are given in Srećković et al. (2014). $D_{in;fin}(R)$ is the electronic dipole matrix element

$$D_{in;fin}(R) = \langle in; R | \mathbf{D}(R) | fin; R \rangle, \quad (6)$$

where \mathbf{D} is the operator of the dipole moment of the considered system.

The photodissociation spectral rate coefficient can be calculated using expression

$$K(\lambda, T) = \sigma^{(phd)}(\lambda, T) \cdot \chi^{-1}(T), \quad (7)$$

where the factor $\chi(T) = N(A)N(B^+)/N(AB^+)$ is given by the relation

$$\chi(T) = \frac{g_1 g_2}{g_{12}} \left(\frac{\mu k T}{2\pi \hbar^2} \right)^{\frac{3}{2}} \cdot \frac{1}{\sum_{J,v} (2J+1) e^{\frac{E_{dis} - E_{J,v}}{kT}}}, \quad (8)$$

where g_1 , g_2 and g_{12} are the electronic statistical weights of the species, A , B^+ and AB^+ respectively, and $\sigma^{(phd)}(\lambda, T)$ is given by Eqs. (3)-(5).

3. Results and discussion

The results for the average photodissociation cross-section $\sigma^{(phd)}(\lambda, T)$ on the example of the Na_2^+ molecular ion are illustrated by Fig. 1. The curves in this figure show the behavior of $\sigma^{(phd)}(\lambda, T)$ as a function of λ for a wide range of temperatures T , which are relevant for modeling geo-cosmical plasmas (Klyucharev *et al.*, 2007). The values of the Li_2^+ , Na_2^+ , LiNa^+ rate coefficient $K(\lambda, T)$, defined by Eq. (7), are presented in Fig. 2 for $500 \text{ K} \leq T \leq 5\,000 \text{ K}$ in order to enable easier use (interpolation) of this results (see e.g. Ignjatović *et al.*, 2019). This allows direct calculation of the spectral absorption coefficients during the process of applying an atmosphere model with the given parameters and composition of plasma.

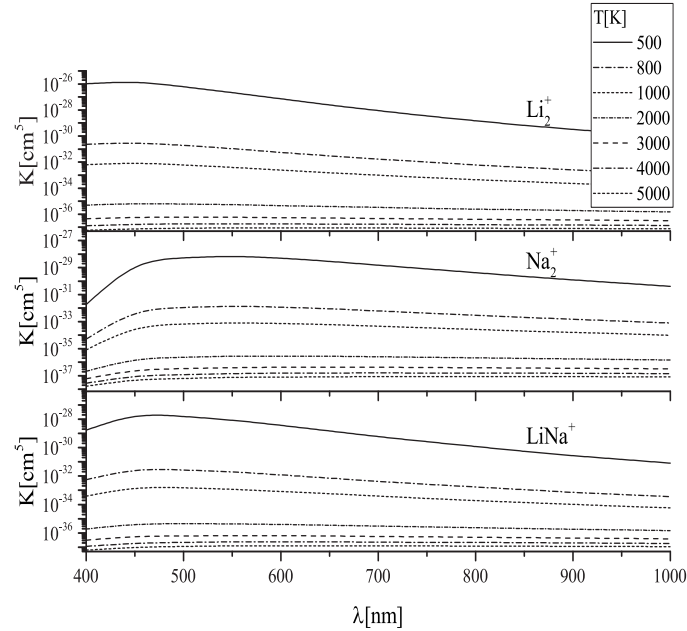


Figure 2. The plot of the spectral rate coefficients for photodissociation of the Li_2^+ , Na_2^+ , LiNa^+ , as a function of λ and T .

These figures show that exist a noticeable difference between temperature dependence of the mean thermal photo-ionization cross section and the corresponding spectral rate coefficient. The results obtained during this investigation will be implemented in the MolD database (Vujčić *et al.*, 2015; Marinković *et al.*, 2017, 2019).

4. Conclusions and Discussion

We determine the average cross-section for the photodissociation processes and the corresponding spectral rate coefficient of the alkali molecular ions Li_2^+ , Na_2^+ , LiNa^+ in the region $\lambda \leq 1000$ nm. The calculated data are useful for modelling and investigation of cool stars, especially brown and white dwarfs, lithium stars, Io's cloud of sodium atoms, and primordial gas containing Li atoms and ions. Also, the presented results are also important in theoretical and laboratory spectroscopic plasmas research.

Acknowledgements. This work is made within projects of the MESTD of Serbia, grant numbers 176002, III44002.

References

- Babb, J. F., State resolved data for radiative association of H and H^+ and for Photodissociation of H_2^+ . 2015, *Astrophys. J. Suppl. Ser.*, **216**, 21
- Beuc, R., Peach, G., Movre, M., & Horvati, B., Lithium, sodium and potassium resonance lines pressure broadened by helium atoms. 2018, *Astron. Astrophys. Trans.*, **30**, 315
- Coppola, C. M., Longo, S., Capitelli, M., Palla, F., & Galli, D., Vibrational level population of H_2 and H_2^+ in the early universe. 2011, *Astrophys. J. Suppl. Ser.*, **193**, 7
- Fontenla, J. M., Avrett, E., Thuillier, G., & Harder, J., Semiempirical Models of the Solar Atmosphere. I. The Quiet- and Active Sun Photosphere at Moderate Resolution. 2006, *Astrophys. J.*, **639**, 441
- Glover, S. C. O., Chluba, J., Furlanetto, S. R., Pritchard, J. R., & Savin, D. W., Chapter Three - Atomic, Molecular, and Optical Physics in the Early Universe: From Recombination to Reionization. 2014, *Advances in Atomic Molecular and Optical Physics*, **63**, 135
- Heays, A., Bosman, A., & van Dishoeck, E., Photodissociation and photoionisation of atoms and molecules of astrophysical interest. 2017, *Astron. Astrophys.*, **602**, A105
- Ignjatović, L. M., Mihajlov, A. A., Sakan, N. M., Dimitrijević, M. S., & Metropoulos, A., The total and relative contribution of the relevant absorption processes to the opacity of DB white dwarf atmospheres in the UV and VUV regions. 2009, *Mon. Notices Royal Astron. Soc.*, **396**, 2201
- Ignjatović, L. M., Mihajlov, A. A., Srećković, V. A., & Dimitrijević, M. S., Absorption non-symmetric ion-atom processes in helium-rich white dwarf atmospheres. 2014, *Mon. Notices Royal Astron. Soc.*, **439**, 2342
- Ignjatović, L. M., Srećković, V., & Dimitrijević, M., The collisional atomic processes of Rydberg alkali atoms in geo-cosmical plasmas. 2019, *Mon. Notices Royal Astron. Soc.*, **483**, 4202

- Klyucharev, A. N., Bezuglov, N. N., Matveev, A. A., et al., Rate coefficients for the chemi-ionization processes in sodium- and other alkali-metal geocosmical plasmas. 2007, *New.Astr.Rev.*, **51**, 547
- Koester, D., White dwarf spectra and atmosphere models . 2010, *Mem. S.A.It.*, **81**, 921
- Marinković, B. P., Jevremović, D., Srećković, V. A., et al., BEAMDB and MolD-databases for atomic and molecular collisional and radiative processes: Belgrade nodes of VAMDC. 2017, *Eur. Phys. J. D*, **71**, 158
- Marinković, B. P., Srećković, V. A., Vujčić, V., et al., BEAMDB and MOLDDatabases at the Serbian Virtual Observatory for Collisional and Radiative Processes. 2019, *Atoms*, **7**, 11
- Mihajlov, A., Ignjatović, L. M., Sakan, N., & Dimitrijević, M., The influence of H_2^+ -photo-dissociation and $(H+H^+)$ -radiative collisions on the solar atmosphere opacity in UV and VUV regions. 2007, *Astron. Astrophys.*, **469**, 749
- Mihajlov, A. A., Ignjatović, L. M., Srećković, V. A., Dimitrijević, M. S., & Metropoulos, A., The non-symmetric ion-atom radiative processes in the stellar atmospheres. 2013, *Mon. Notices Royal Astron. Soc.*, **431**, 589
- Pichler, G., Makdisi, Y., Kokaj, J., et al., Superheating effects in line broadening of dense alkali vapors. 2017, in *J. Phys. Conf. Ser.*, Vol. **810**, *J. Phys. Conf. Ser.*, 012013
- Puy, D., Dubrovich, V., Lipovka, A., Talbi, D., & Vonlanthen, P., Molecular fluorine chemistry in the early Universe. 2007, *Astron. Astrophys.*, **476**, 685
- Srećković, V., Dimitrijević, M., Ignjatović, L., Bezuglov, N., & Klyucharev, A., The Collisional Atomic Processes of Rydberg Hydrogen and Helium Atoms: Astrophysical Relevance. 2018, *Galaxies*, **6**, 72
- Srećković, V. A., Ignjatović, L. M., Jevremović, D., Vujčić, V., & Dimitrijević, M. S., Radiative and Collisional Molecular Data and Virtual Laboratory Astrophysics. 2017, *Atoms*, **5**, 31
- Srećković, V. A., Mihajlov, A. A., Ignjatović, L. M., & Dimitrijević, M. S., Ion-atom radiative processes in the solar atmosphere: Quiet Sun and sunspots. 2014, *Adv. Space Res.*, **54**, 1264
- Vujčić, V., Jevremović, D., Mihajlov, A. A., et al., MOL-D: A Collisional Database and Web Service within the Virtual Atomic and Molecular Data Center. 2015, *J. Astrophys. Astron.*, **36**, 693

The resonance lines of sodium and potassium in brown dwarf spectra

G. Peach¹, S. Yurchenko¹, K. Chubb², I. Baraffe³, M. Phillips³, and P. Tremblin⁴,

¹ *Department of Physics and Astronomy, University College London WC1E 6BT, UK*

(E-mail: g.peach@ucl.ac.uk)

² *SRON, Netherlands Institute for Space Research*

³ *Department of Physics and Astronomy, University of Exeter, UK*

⁴ *Maison de la Simulation CEA Saclay, Paris*

Received: August 14, 2019; Accepted: September 12, 2019

Abstract. Accurate pressure broadened line profiles of alkali resonance doublets are needed for the modelling of atmospheres of cool stars and for generating their synthetic spectra in the region 400 - 900 nm. When the lines utterly dominate their region of the spectrum, it becomes important to represent the profiles accurately over the whole range from the line centre to the far line wings. In this paper we examine the theories of spectral line shapes that have been used and carry out new calculations of the line shapes for the resonance lines of sodium and potassium broadened by helium.

Key words: spectral line broadening calculations – alkali resonance doublets – cool stars: synthetic spectra

1. Introduction

The cool atmospheres of brown dwarfs are characterised by the formation of molecules and condensates. The highly wavelength dependent opacity of abundant molecules such as water, methane and ammonia dominate the infrared spectra of these substellar objects, while at shorter wavelengths the spectrum is shaped by the neutral alkali metals as more refractory elements are sequestered in condensate species. In particular the sodium and potassium resonance doublets, centered at 0.59 and 0.77 microns respectively, play a unique role in shaping the spectrum between 0.4-1.0 microns. H₂ and He are present at high atmospheric densities in the range ($\sim 10^{19}$ - 10^{21} cm⁻³) and they collisionally broaden the resonance lines at wavenumbers up to ± 3000 cm⁻¹ from the line centre.

Using our state-of-the-art 1D radiative-convective equilibrium model ATMO, we are developing a grid of model substellar atmospheres and investigating the impact of Na and K line shapes on predicted brown dwarf spectra. We find that there are large differences between the various published line shape calculations

and this can affect the predicted spectra. Most notably these uncertainties occur in the near-infrared due to the extent of the red wing of the K resonance lines.

Previous calculations have used various theories to obtain line shapes for alkali resonance lines broadened by helium. In the centre of the line the profile is Lorentzian, and half-half widths have been obtained for lithium, sodium and potassium broadened by helium, see Mullanphy *et al.* (2007), Peach and Whittingham (2009) and Kielkopf *et al.* (2012). Quasistatic theory has been used by Burrows and Volobuyev (2003) and Beuc *et al.* (2018) to describe the behaviour in the far line wings. A unified theory developed by Allard *et al.* (1999) is used by Allard *et al.* (2003) to obtain line profiles for a wide range of frequencies.

In this paper, an alternative method for obtaining complete line profiles is described and is applied to the resonance lines of sodium and potassium broadened by helium.

2. The Hamiltonian for the atom-perturber system

Large quantum chemistry calculations provide very accurate potentials for the electronic states of atom-atom systems at short and intermediate separations. This approach is limited to low excited electronic states. The present problems involve low-energy atom-atom scattering processes for excited electronic states. Our requirement is for the accurate representation of potentials at medium and large interatomic separations.

In this work a three-body model is adopted; two atomic cores a and b and one active electron, i.e. $\text{Na}^+ + \text{He} + e^-$ and $\text{K}^+ + \text{He} + e^-$. Atomic units are used, with lengths in Bohr radii, $a_0 = 0.0529177209$ nm and energies in Hartrees, $E_h = \alpha^2 m_e c^2 = 27.211384$ eV.

The electron-core interaction is specified by

$$V_{a,b}(r) = -\frac{Z}{r}(1 + \delta + \delta' r) \exp(-\gamma r) - \frac{z}{r} - \frac{\alpha_d^{a,b}}{2r^4} F_1(r), \quad (1)$$

where r is the electron-core separation, $Z + z$ is the nuclear charge, α_d^a and α_d^b are the dipole polarisabilities of the cores a and b and $F_1(r)$ is a cutoff factor. Parameters γ , δ and δ' are varied to reproduce the positions of known energy levels for $z \neq 0$, and phase shifts for scattering for $z = 0$. The fits also predict the correct number of nodes in the wave functions, see Peach (1982).

The core-core interaction is given by

$$V_c(R) \simeq -z_a^2 \frac{\alpha_d^b}{2R^4} - z_b^2 \frac{\alpha_d^a}{2R^4} + \text{short-range terms}, \quad (2)$$

where R is the separation between the two cores a and b with charges z_a and z_b respectively. Options considered for the short-range term are:

- (a) Use the three-body model itself to generate the potential.

(b) Use a simple analytic form based on perturbation theory.

Choices (a) and (b) differ only for $R \leq R_A + R_B$ where R_A and R_B are the mean radii of Na^+ and K^+ .

The three-body interaction is given by

$$V_3(\mathbf{r}_a, \mathbf{r}_b, \mathbf{R}) \simeq z_b \frac{\alpha_d^a}{r_a^2 R^2} P_1(\hat{r}_a \cdot \hat{R}) + z_a \frac{\alpha_d^b}{r_b^2 R^2} P_1(-\hat{r}_b \cdot \hat{R}) \quad (3)$$

for R large, where \mathbf{r}_a and \mathbf{r}_b are the position vectors of the electron relative to the atomic cores a and b . $\mathbf{R} = (\mathbf{r}_a - \mathbf{r}_b)$ and $P_1(\hat{r} \cdot \hat{R})$ is a Legendre polynomial.

On using (1), (2) and (3), the Hamiltonian for the system then becomes

$$H = -\frac{1}{2}\nabla^2 + V_a(r_a) + V_b(r_b) + V_c(R) + V_3(\mathbf{r}_a, \mathbf{r}_b, \mathbf{R}). \quad (4)$$

A set of atomic basis states on one or both centres is used and the Hamiltonian matrix diagonalized to obtain the electronic energies.

The principles and problems involved in the construction of the potentials are:

- (a) The long-range interactions are based on well-known perturbation theory.
- (b) No existing data for the molecules NaHe and KHe are used to fix any variable parameters.
- (c) Positions of virtual states in the electron-core model potentials are sensitive to the precise fit.
- (d) Model potentials can be l -dependent or l -independent.
- (e) A different potential may have to be used for ground states, e.g. $\text{He}(1s^2)$.

3. Theory of spectral line broadening

3.1. Baranger theory

The main references for the discussion that follows are Baranger (1958) and Peach and Whittingham (2009). The impact theory has been widely used, but is actually only an approximation to the general theory developed by Baranger in this his first important paper.

The line profile $I(\omega)$ is defined in terms of a correlation function $C(s)$ by

$$I(\omega) = \mathcal{R} \frac{1}{\pi} \int_0^\infty C(s) \exp(i\Delta\omega s) ds, \quad (5)$$

where ω is the angular frequency, $\Delta\omega$ is the angular frequency separation from the line centre and s is a time variable. \mathcal{R} denotes 'real part of'. Baranger showed that $C(s)$ can be written as

$$C(s) = \exp[-N g(s)], \quad (6)$$

where N is the perturber density and $g(s)$ is split into two parts, i.e.

$$g(s) = g_1(s) + g_2(s). \quad (7)$$

Only the first term $g_1(s)$ is used here as in many circumstances the second term, $g_2(s)$, can be neglected.

We consider the transition $n_i L_i \rightarrow n_f L_f$ between states $n_i L_i M_i$ and $n_f L_f M_f$ of the alkali atom. The wave function describing the scattering by a potential $V_\Lambda(r)$ is given by

$$\psi_\Lambda(\mathbf{r}) = \sum_{l=0}^{\infty} (2l+1) i^l \exp(i\eta_{\Lambda l}) \frac{1}{k^{\frac{1}{2}} r} F_{\Lambda l}(k, r) P_l(\hat{\mathbf{k}} \cdot \hat{\mathbf{r}}), \quad (8)$$

where $P_l(\hat{\mathbf{k}} \cdot \hat{\mathbf{r}})$ is a Legendre polynomial and the radial functions $F_{\Lambda l}(k, r)$ are solutions of the equation

$$\left[\frac{d^2}{dr^2} - \frac{l(l+1)}{r^2} - 2MV_\Lambda(r) + k^2 \right] F_{\Lambda l}(k, r) = 0. \quad (9)$$

The potential $V_\Lambda(r)$ and the atom-atom separation r are in atomic units and M is the reduced mass of the emitter-perturber pair in units of the electron mass m . The momentum k in atomic units is given by

$$k = \frac{Mmv a_0}{\hbar}, \quad (10)$$

where v is the relative velocity of the emitter and perturber and a_0 is the Bohr radius. The asymptotic form of $F_{\Lambda l}(k, r)$ is specified by

$$F_{\Lambda l}(k, r) \simeq k^{-\frac{1}{2}} \sin(kr - \frac{1}{2}l\pi + \eta_{\Lambda l}), \quad (11)$$

where $\eta_{\Lambda l} \equiv \eta_{\Lambda l}(k)$ is the elastic scattering phase shift, and as $r \rightarrow 0$

$$F_{\Lambda l}(k, r) \propto r^{l+1}. \quad (12)$$

For the cases considered here, the scattering matrix elements S_i and S_f are given by

$$S_i \equiv \langle l\Lambda_i | S | l\Lambda_i \rangle = \exp(2i\eta_{\Lambda_i l}); \quad \Lambda_i = |M_i| \quad (13)$$

and

$$S_f \equiv \langle l\Lambda_f | S | l\Lambda_f \rangle = \exp(2i\eta_{\Lambda_f l}); \quad \Lambda_f = |M_f|. \quad (14)$$

Then we obtain

$$N g_1(s) = (w + id) s, \quad (15)$$

where

$$w + id = \mathcal{C} \frac{\lambda^{1/2}}{M^{3/2}} \sum_{M_i M_f \mu} \left(\begin{matrix} L_i & 1 & L_f \\ M_i & \mu & M_f \end{matrix} \right)^2 \int_0^\infty \exp(-u) du \\ \times \sum_{l=0}^{\infty} (2l+1) \{i \exp[i(\eta_{\Lambda_i} - \eta_{\Lambda_f})]\} \\ \times [2M \int_0^\infty F_{\Lambda_i l}(k, r) \Delta V F_{\Lambda_f l}(k, r) dr] \quad (16)$$

and $\begin{pmatrix} a & b & c \\ d & e & f \end{pmatrix}$ is a 3- j coefficient.

The quantities introduced here are defined by

$$\Delta V = V_{\Lambda_i} - V_{\Lambda_f} \quad (17)$$

and

$$\mathcal{C} = N 4\sqrt{\pi} \frac{\hbar a_0}{m}; \quad u = \frac{E}{\kappa T} = \frac{\lambda k^2}{M}; \quad \lambda = \frac{\hbar^2}{2ma_0^2 \kappa T}, \quad (18)$$

where κ is the Boltzmann constant, T is the temperature and E refers to the energy of the relative motion. All the dimensional information is contained in the factor \mathcal{C} . It then follows from (5), (6), (15) and (16) that w and d are the half-half width and shift of the Lorentz profile given by

$$I(\omega) = \frac{1}{\pi} \frac{w}{(\Delta\omega - d)^2 + w^2}. \quad (19)$$

3.2. The impact approximation

The well-known impact theory is obtained directly from (16) by replacing the wave functions $F_{\Lambda_i l}(k, r)$ and $F_{\Lambda_f l}(k, r)$ by their asymptotic forms (11), so that

$$w + id = \mathcal{C} \frac{\lambda^{1/2}}{M^{3/2}} \sum_{M_i M_f \mu} \left(\begin{matrix} L_i & 1 & L_f \\ M_i & \mu & M_f \end{matrix} \right)^2 \int_0^\infty \exp(-u) du \\ \times \sum_{l=0}^{\infty} (2l+1) \frac{1}{2} [1 - S_i S_f^*]. \quad (20)$$

In addition, if the Born approximation is made, the phase shifts in (11) are calculated from the expression

$$\tan(\eta_{\Lambda l}) = -2Mk \int_0^\infty r^2 V_{\Lambda}(r) [j_l(kr)]^2 dr \quad (21)$$

for all values of l . In (21), $j_l(kr)$ is a spherical Bessel function of the first kind where

$$kr j_l(kr) \simeq \sin(kr - \frac{1}{2}l\pi) \quad (22)$$

as $r \rightarrow \infty$, c.f. (11). The Born impact theory is then obtained directly from equations (13), (14) and (20).

3.3. The one-perturber approximation

Finally we consider the one-perturber approximation. We define the quantity

$$P(\omega) = \int_0^\infty F_{\Lambda_i l}(k_i, r) \mathcal{D}(r) F_{\Lambda_f l}(k_f, r) dr; \quad \mathcal{D}(r) \equiv \frac{D(r)}{D(\infty)}, \quad (23)$$

where in general, $k_i \neq k_f$. The dipole moment for the transition $\Lambda_i \rightarrow \Lambda_f$ is $D(r)$, which tends to a constant, $D(\infty)$, as $r \rightarrow \infty$. Then $P(\omega)$ is given by

$$(k_i^2 - k_f^2) P(\omega) = 2M \int_0^\infty F_{\Lambda_i l} \Delta V \mathcal{D} F_{\Lambda_f l} dr - \int_0^\infty \frac{d\mathcal{D}}{dr} \left(F_{\Lambda_i l} \frac{dF_{\Lambda_f l}}{dr} - F_{\Lambda_f l} \frac{dF_{\Lambda_i l}}{dr} \right) dr, \quad (24)$$

where

$$(k_i^2 - k_f^2) = \frac{2mMa_0^2}{\hbar} \Delta\omega. \quad (25)$$

We now neglect the second term on the right-hand side of (24), as experience shows that it is negligible compared with the first term. The profile in the line wings is then given by

$$L(\omega) = [P(\omega)]^2 \quad (26)$$

and we obtain

$$I(\omega) \simeq \frac{1}{\pi} \frac{w}{\Delta\omega^2}; \quad |\Delta\omega| \gg w, \quad |\Delta\omega| \gg |d|. \quad (27)$$

If the ranges of validity of the Baranger theory and the one-perturber approximations overlap, then the correlation function $C(s)$ can be replaced by

$$C(s) = 1 - N g_1(s) \quad (28)$$

and we can use these equations to obtain a unification of the two profiles $L(\omega)$ and $I(\omega)$.

Then the Lorentz profile in (19) is replaced by

$$I(\omega) = \frac{1}{\pi} \frac{w(0)}{(\Delta\omega - d)^2 + w(0)^2} \frac{w(\Delta\omega)}{w(0)}, \quad (29)$$

where

$$w(\Delta\omega) = C \frac{\lambda^{1/2}}{M^{3/2}} \sum_{M_i M_f \mu} \left(\frac{L_i \ 1 \ L_f}{M_i \ \mu \ M_f} \right)^2 \int_0^\infty \exp(-u) du \times \sum_{l=0}^\infty (2l+1) \left[2M \int_0^\infty F_{\Lambda_i l}(k_i, r) \Delta V F_{\Lambda_f l}(k_f, r) dr \right]^2, \quad (30)$$

and

$$u = \frac{\lambda k_i^2}{M}. \quad (31)$$

If the wave functions in (30) are replaced by their asymptotic forms and we set $k_i = k_f$, $\Delta\omega = 0$. Then in (30) $w \equiv w(0)$ and $w(0)$ is identical with the expression for w given by (20).

This procedure will be valid for lower perturber densities, but will break down at high densities when the correlation function $C(s)$ in (6) must be evaluated directly and the Fourier transform in (5) performed.

4. Results and discussion

Calculations have been completed for the widths of the sodium and potassium resonance lines broadened by helium using the interaction potentials described in earlier work, see Mullamphy et al. (2007) and Peach (2011). The extensive temperature range chosen, $100 \text{ K} \leq T \leq 10000 \text{ K}$, serves two purposes. It provides the data required for the analysis of the spectra of cool stars, but also tests the range of validity of the various theoretical approximations discussed in this paper.

The main computational issues arise from the slow convergence of the sum over angular momenta l for the higher temperatures and the associated requirement for a greater number of points to be chosen for the integration over energy.

The radial equation describing the scattering wave function is integrated directly to determine the exact wave functions and their phase shifts for smaller values of l , $l \leq l_0$ say, and the Born approximation is then used to evaluate phase shifts for $l_0 < l \leq l_{max}$. The Born approximation for the scattering amplitude in its closed form is used to complete the summation up to $l = \infty$. Careful checks are made to determine the optimum values of l_0 and l_{max} at each energy.

Our results are shown in Tab. 1-Tab. 4. In Tab. 1 and Tab. 2 the half-half widths, $w(0)$, and shifts d are shown for the resonance lines of sodium and potassium. The results for $w(0)$ using the one-perturber and Baranger theories are compared and there is close agreement over the whole temperature range. In Tab. 3, the present results for $w(0)$ for sodium and potassium are compared with the earlier close-coupling calculations of Mullamphy et al. (2007) who use the impact approximation. There is very close agreement for the sodium lines; the agreement for the potassium lines is slightly less good, but this can be attributed to the fact that a small modification to the K-He potential was introduced in the present work.

Finally in Tab. 4, $w(\Delta\omega)/N$ is listed for sodium as a function of wavenumber $w\nu = \Delta\omega/(2\pi c)$ to demonstrate the asymmetry in the line when the profile is extended out to the far wings.

5. Conclusions

In the present calculations we have demonstrated that the formalism and the computational techniques that have been developed can be successfully applied to obtain complete line profiles from the line centre to the line wings for all temperatures and for the lower perturber densities for which the one-perturber approximation is valid. The one-perturber term, $w(\Delta\omega)/N$, is generated for a wide range of values of temperature $T(\text{K})$ and $\Delta\omega$ which can then be interpolated to provide input into the atmospheric models.

Table 1. $w(0)/N$ and d/N (in units of 10^{-21} MHz m³/atom) for the transition Na 3p²P–3s²S at 589.36 nm

$T(K)$	One-perturber $w(0)/N$	Baranger $w(0)/N$	Theory d/N
100.0	0.1741	0.1733	-0.0303
200.0	0.2310	0.2306	-0.0343
300.0	0.2713	0.2711	-0.0368
500.0	0.3319	0.3318	-0.0407
700.0	0.3792	0.3791	-0.0433
1000.0	0.4373	0.4372	-0.0457
1500.0	0.5146	0.5146	-0.0483
2000.0	0.5775	0.5775	-0.0502
2500.0	0.6314	0.6314	-0.0517
3000.0	0.6789	0.6789	-0.0529
5000.0	0.8307	0.8307	-0.0570
10000.0	1.0855	1.0855	-0.0622

A grid of model substellar atmospheres is being developed and these new profiles for the Na and K resonance lines will be incorporated into the models. We also intend to include the contribution from transitions where the emitter-perturber system occupies a bound state supported by the initial or final potentials for the molecular states Λ_i and Λ_f . These are known to contribute in the far red wings of the lines considered in this paper.

Table 2. $w(0)/N$ and d/N (in units of 10^{-21} MHz m³/atom) for the transition K 4p²P–4s²S at 767.83 nm

$T(K)$	One-perturber $w(0)/N$	Baranger $w(0)/N$	Theory d/N
100.0	0.1979	0.1979	-0.0325
200.0	0.2713	0.2713	-0.0378
300.0	0.3233	0.3233	-0.0380
500.0	0.3986	0.3986	-0.0359
700.0	0.4551	0.4551	-0.0341
1000.0	0.5222	0.5222	-0.0329
1500.0	0.6101	0.6100	-0.0334
2000.0	0.6819	0.6813	-0.0353
2500.0	0.7446	0.7427	-0.0377
3000.0	0.8012	0.7971	-0.0402
5000.0	0.9861	0.9702	-0.0490
10000.0	1.2808	1.2504	-0.0620

Table 3. $w(0)/N$ (in units of 10^{-21} MHz m³/atom) ^aMullamphy et al. (2007), ^bpresent work

atom	$T(K)$	$w(0)/N^a$	$w(0)/N^b$
Sodium			
	450.0	0.3167	0.3166
	480.0	0.3252	0.3257
	1000.0	0.4367	0.4372
	2000.0	0.5781	0.5775
	3000.0	0.6813	0.6789
Potassium			
	410.0	0.3463	0.3647
	1000.0	0.5032	0.5222
	2000.0	0.6799	0.6813
	3000.0	0.8109	0.7971

Table 4. $w(\Delta\omega)/N$ (in units of 10^{-21} MHz m³/atom) for the transition Na 3p²P–3s²S at 589.36 nm at $T(K) = 1000$ K

$w\nu(\text{cm}^{-1})$	$w(-\Delta\omega)/N$	$w(+\Delta\omega)/N$
0.0	0.4372	0.4372
5.0	0.4392	0.4424
10.0	0.4444	0.4521
15.0	0.4524	0.4662
20.0	0.4631	0.4842
25.0	0.4763	0.5058
50.0	0.5726	0.6507
100.0	0.8494	1.0185
200.0	1.4315	1.7516
300.0	2.1897	2.3863
500.0	3.0461	3.3882
1000.0	5.4202	4.7610
1500.0	7.7315	4.9751
2000.0	9.7106	4.3831
2500.0	12.072	3.3667
3000.0	10.410	2.0039

References

- Allard, N.F., Royer, A., Kielkopf, J.F., Feautrier, N.: 1999, *Phys. Rev. A* **60**, 1021
- Allard, N.F., Allard, F., Hauschildt, P.H., Kielkopf, J.F., Machin, L.: 2003, *Astron. Astrophys.* **411**, L473
- Baranger, M.: 1958, *Phys. Rev. A* **111**, 481
- Beuc, R., Peach, G., Movre, M., Horvatić, B.: 2018, *Astron. and Astrophys. Trans.* **30**, 315
- Burrows, A., Volobuyev, M.: 2003 *Astrophys. J.* **583**, 985
- Kielkopf, J.F., Allard, N.F., Babb, J.: 2012, *EAS Publications Series* **58**, 75
- Mullamphy, D.F.T., Peach, G., Venturi, V., Whittingham, I.B., Gibson, S.J.: 2007, *J. Phys. B: At. Mol. Opt. Phys.* **40**, 1141
- Peach, G.: 1982, *Comment. At. Mol. Phys.* **11**, 101
- Peach, G.: 2011, *Baltic Astron.* **20**, 516
Errata: headings 'Impact Theory — Baranger Theory' in tables 5-9 to be replaced by 'Baranger Theory — V d Waals Theory'
- Peach, G., Whittingham, I.B.: 2009, *New Astron. Rev.* **53**, 227

Observational tests of general relativity and alternative theories of gravity with Galactic Center observations using current and future large observational facilities

A.F. Zakharov^{1,2,3}, P. Jovanović⁴, D. Borka⁵ and
V. Borka Jovanović⁵

¹ *Institute of Theoretical and Experimental Physics, B. Cheremushkinskaya 25, 117218 Moscow, Russia, (E-mail: zakharov@itep.ru)*

² *Bogoliubov Laboratory of Theoretical Physics, Joint Institute for Nuclear Research, 141980 Dubna, Russia*

³ *National Research Nuclear University MEPhI (Moscow Engineering Physics Institute), 115409, Moscow, Russia*

⁴ *Astronomical Observatory, Volgina 7, P.O. Box 74, 11060 Belgrade, Serbia*

⁵ *Atomic Physics Laboratory (040), Vinča Institute of Nuclear Sciences, University of Belgrade, P.O. Box 522, 11001 Belgrade, Serbia*

Received: July 31, 2019; Accepted: September 15, 2019

Abstract. It is established that there are supermassive black holes in centers of galaxies. A supermassive black hole with mass around $4 \times 10^6 M_{\odot}$ is located at the Galactic Center. Such an approach for the Galactic Center looks rather natural, in spite of that consequences of model must be checked with observations. We discuss opportunities to check this with forthcoming observations of shadows in mm band for the Galactic Center as it was done recently for M87*. Observations of bright stars moving near the Galactic Center gives another opportunity to evaluate gravitational potential. We discuss opportunities to use these observations to constrain alternative theories of gravity.

Key words: supermassive black holes – general relativity – alternative theories of gravity

1. Introduction

Astronomers believe that supermassive black holes are located in centers of galaxies, including our Galaxy. However, for the Galactic Center theorists proposed many different models (including exotic ones), such as a dense cluster of stars (Reid, 2009), fermion balls (Munyanza & Viollier, 2002), boson stars (Jetzer, 1992; Torres, Capozziello & Lambiase, 2000), neutrino balls (De Paolis et al., 2001). Later, some of these models have been ruled out, or the range of parameters of these models is significantly constrained with consequent observations (Reid, 2009).

Now it is accepted that there is a super-massive black hole at the Galactic Center (see, e.g., recent reviews Reid 2009; Zakharov 2017, 2018a, 2019).

It is well-known that the universal gravity law was discovered with efforts of J. Kepler, R. Hooke and I. Newton, see, for instance, a popular interesting review on the subject by Arnold (2000). Using planet observations Kepler found three laws of planet motions in our Solar system, Hooke understood that Kepler's laws could be explained if gravity force is inversely proportional to squared distance and wrote the idea in his letter to Newton (Arnold, 2000; Taton & Wilson, 2003). Newton proved that the Hooke'd hypothesis is correct and vice versa Newton showed that the inverse square law follows from Kepler's law on ellipticity of stellar orbits. Therefore, a law for an interaction could be obtained from an analysis of trajectories of moving objects. Similarly, later E. Rutherford used α particles to investigate an atomic structure and A. Einstein created a modification of Newtonian gravity and explained the Mercury anomaly with his theoretical approach.

To evaluate its gravitational potential near a black hole, one can analyze trajectories of test particles moving in the potential, and as a result one could constrain the parameters of the potential. In this article we discuss opportunities to use photons or massive objects as test particles to evaluate gravitational potential near the Galactic Center using the conventional approach of general relativity and models obtained in the framework of alternative theories of gravity. If we speak about observable quantities at the first case we consider size and shape of shadows around supermassive black holes in Sgr A* and M87*, at the second case, one analyzes trajectories of bright stars near the Galactic Center.

2. Shadows around black holes

As it was noted one could use photons as test particles and analyze the images around supermassive black holes including the Galactic Center. We remind papers where the authors discussed issues connected with the subject. Assuming that there is a luminous screen behind a black hole Bardeen considered the apparent shape of a Kerr black hole located between a luminous screen and a distant observer (Bardeen, 1973). Critical sets of impact parameters occupied by plunge parabolic orbits of particles and of photons has been considered by Young (1976) for the Kerr – Newman – de-Sitter metric (the apparent shape of a black hole could be obtained from the region of critical photon orbits, with a reflection in respect to the rotation axis). Later, Luminet (1979) showed a silhouette of a Schwarzschild black hole, and images of thin accretion disks around a spherical symmetric black hole. However, earlier, visible shapes of circular orbits around Schwarzschild and Kerr black holes had been shown by Cunningham & Bardeen (1973), see also beautiful pictures of accretion disks around a Kerr black hole had been reproduced recently for the *Interstellar* movie (James et

al., 2015), where one could recognize shadows since for rotating black holes the authors considered truncated disks with inner radii $r_{\text{inner}} > r_{\text{ISCO}}$.

It is well-known that photon geodesics in a Kerr metric are characterized by only two parameters (integrals of motion), called ξ and η (Chandrasekhar, 1983). One could introduce a function $\eta_{cr}(\xi)$ of critical values of ξ and η which correspond to unstable spherical photon orbits with $r = \text{const}$ (r is the radial Boyer – Lindquist coordinate). This set separates plunge and scatter regions (Zakharov, 1986). In the book by Chandrasekhar (1983), a parametric representation of the functions $\eta_{cr}(r)$ and $\xi(r)$ was used. Such a representation of these functions used by Chandrasekhar (1983) is not suitable since a topology of sets $\{\xi, \eta\}$ corresponding to scatter and plunge regions is not presented properly, for instance, in Fig. 39 in book by Chandrasekhar (1983) curve $\eta_{cr}(r)$ is shown for $\eta < 0$, while it is known that for pairs $(\xi, \eta) \in M = \{(\xi, \eta) | -a^2 + 2a|\xi| - \xi^2 \leq \eta < 0\}$ one has photon capture since geodesics with constants of motion correspond to vortex motion and these photon geodesics do not cross the equatorial plane (Yakovlev, 1975), while for other pairs (ξ, η) with $\eta < 0$ photon geodesics do not exist. In addition, in paper by Zakharov (1986) it was shown that maximum $\eta_{cr}(r)$ is 27 and it corresponds to $\xi = -2a$. This useful property of $\eta_{cr}(r)$ function was not discussed by Chandrasekhar (1983). Such a property could be expressed as a property of shadow for observers in the equatorial plane as it was done by Zakharov et al. (2005a) and now it is widely used in the literature to evaluate a spin from future shadow observations.

We would like to remind that in paper by Zakharov (1986), it was noted that this function $\eta_{cr}(\xi)$ separates scatter and plunge photon orbits, namely, photons are plunging for positive η only if $(\xi, \eta) \in S$, where

$$S = \{(\xi, \eta) | 0 \leq \eta < \eta_{cr}(\xi) \quad \& \quad \xi_1 < \xi < \xi_2\}, \quad (1)$$

and ξ_1 and ξ_2 are the critical impact parameters of the retrograde and direct unstable photon circular equatorial orbits, respectively (Zakharov, 1986); all length quantities are expressed in M units, while η is expressed in M^2 units

$$\xi_1 = -6 \cos \left(\frac{\arccos a}{3} + \frac{2}{3}\pi \right) - a \quad (2)$$

and

$$\xi_2 = 6 \cos \frac{\arccos(-a)}{3} - a. \quad (3)$$

Pairs $(\xi, \eta) \in S$ correspond to double roots of the polynomial $R(r)$ governing the radial motion of photons (Zakharov, 1986) (we would like to note that this condition is valid for black holes but not for naked singularities). In addition, in paper by Zakharov (1986) it was proven that the maximal value of the function $\eta_{cr}(\xi)$ is 27 and $\eta_{cr}(-2a) = 27$; the radial Boyer – Lindquist coordinate value for this orbit reads $r(-2a) = 3$. Therefore, one can see that the representation of the function $\eta_{cr}(\xi)$, as it was done by Zakharov (1986), is more clear than

the parametric representation of this function as it was done by Chandrasekhar (1983), and one could easily recognize scatter and plunge orbits, and prove that the maximal value of $\eta_{cr}(\xi)$ does not depend on the black hole spin a .

At the first glance, a model with a luminous screen behind a black hole, studied by Bardeen (1973); Chandrasekhar (1983), does not look realistic, because in astronomy there is no luminous screen behind a black hole, and the sizes of a silhouette (shadow) are too small to be detectable in seventies and eighties of the last century for masses and distances of known black holes – for example the super-massive black hole at the Galactic Center has the angular size of the shadow, as observed from the Earth, around $50 \mu as$, however, now this shadow size is large enough to be reconstructed with advanced VLBI facilities in the mm-band (similarly to the Event Horizon Telescope) or more precisely bright structures with such sizes could be observed and dark shadow could be reconstructed from observed distribution of bright structure. In this case, one could say that it would be possible to observe unseeable (Doeleman, 2017).

Based on ideas introduced by Chandrasekhar (1983), Zakharov (1986) and Holz & Wheeler (2002), Zakharov et al. (2005a) reformulated results about the properties of the $\eta_{cr}(\xi)$ function obtained earlier by Zakharov (1986), and considered different types of the shadow shapes for the Kerr black holes, and different position angles of a distant observer. In addition, Zakharov et al. (2005a) showed that for an equatorial plane position of a distant observer, maximal impact parameter $|\beta_{max}|$ in the z -direction (which coincides with the black hole rotation-axis direction) is $\sqrt{27}$ (in GM/c^2 units), and $\beta_{max} = \sqrt{27}$ for $\alpha = 2a$, or $|\beta(2a)| = \sqrt{27}$ (Zakharov et al., 2005a), if we consider the function $\beta(\alpha)$ for the critical impact parameters separating plunge and scatter regions of photons ($\beta(\alpha)$ is expressed through function $\eta_{cr}(\xi)$ and a position angle of a distant observer). It means that for an observer in the equatorial plane, $|\beta_{max}|$ remains the same, the shadow is deformed in the direction which is parallel to equatorial plane, and such a deformation depends on the black hole spin a . This theoretical property of the black hole shadow is widely used to evaluate the black hole spin from observations. For instance, Hioki and Maeda (2009) proposed to use such parameters (radius and distortion parameter for shadows) to evaluate the black hole spin from observations. Therefore, evaluations of the shadow sizes around the black holes could help to estimate of the black hole parameters (Zakharov et al., 2005a,b; Zakharov, 2014, 2015; Cherepashchuk, 2016, 2017; Bisnovatyikogan & Tsupko, 2017; Dokuchaev & Nazarova, 2017; Cunha & Herdeiro, 2018; Shaikh, 2018, 2019; Dokuchaev & Nazarova, 2019). Opportunities to compare predictions of general relativity and alternative theories of gravity with measuring the shadow size for the black hole at the Galactic Center has been discussed by Zakharov et al. (2012); Johannsen et al. (2016).

Some time ago Falcke, Melia & Agol (2000); Melia & Falcke (2001) simulated the shadows for supermassive black holes and showed that the black hole silhouette could be formed in a rather natural way (see also Falcke, Melia & Agol (2013); Johannsen (2016) for more recent reviews). The authors used a toy

model for their analysis, and they concluded that the strong gravitational field bends trajectories of photons emitted by accreting particles, and an observer could see a dark spot (shadow) around a black hole position or more precisely one could reconstruct a shape of shadow analyzing bright structure distributions. For the black hole at the Galactic Center the size of the shadow is around $3\sqrt{3}R_S$ (where $R_S \approx 10 \mu\text{as}$), as is the angular size of the Schwarzschild radius. Based on results of simulations, Falcke, Melia & Agol (2000); Melia & Falcke (2001) concluded that the shadow may be detectable at mm and sub-mm wavelengths, however, scattering may be very significant at cm wavelengths, so there are very small chances to observe the shadows at the cm band. The ground – space interferometer Radioastron (which was launched in 2011 and it finished its operation in the beginning of 2019) had the shortest wave length around 1.3 cm, therefore, it was no chance to reconstruct shadow structure in spite of nice angular resolution around $7 \mu\text{as}$ at 1.3 cm. We should mention that the results obtained by Falcke, Melia & Agol (2000); Melia & Falcke (2001) are rather general, in spite of their specific model. Strictly speaking, it is impossible to see darkness (shadows) in astronomical observations and people try to investigate structures of bright spots near shadows since shadows are formed by envelopes of bright images – analyzing structures of images one could reconstruct shadows (Broderick & Loeb, 2006). Further simulations and observations for M87* were confirmed these claims.

There is a tremendous progress in evaluation of minimal size of a spot detectable by recent observational techniques near the Sgr A^* (Shen et al., 2005; Doeleman et al., 2008; Doeleman, 2008). For example, Doeleman et al. (2008); Doeleman (2008) evaluated a bright spot size as small as $37_{-10}^{+16} \mu\text{as}$ for the VLBI technique in mm-band, but a boundary of a dark spot (shadow) has to be bright, and the related size of the bright boundary has been evaluated, and, therefore, the theoretical estimate of the shadow size and the bright spot size obtained from the observations should have similar values. These activities, including design and construction of new facilities, observations, and data analysis, are important steps to create the so-called the Event Horizon Telescope (Doeleman et al., 2009; Doeleman, 2017), see also for a more recent information¹. The idea is to create a world-wide VLBI network to observe pictures of the supermassive black hole at the Galactic Center and in the galaxy M87 center. As the project authors claimed, they are developing a Earth size telescope because lengths of arms are comparable with the Earth diameter, however, one should remind that earlier the authors of the ground – space interferometer Radioastron declared that they created the telescope much bigger than Earth since its longest arm length is about 3×10^5 km (Kardashev, 1997, 2009, 2013). As it was mentioned earlier, initially, it was expected to analyze bright accretion structures near the black hole horizon at the Galactic Center, but consequent observations and estimates showed that the shortest wavelength of Radioastron is around 1.3 cm,

¹<http://eventhorizontelescope.org/>.

and it is too long to observe a shadow at the Galactic Center since electron scattering is blurring a shadow image. A turbulence is an important issue and it could distort images of the bright spots near the shadows (Broderick et al., 2016).

2.1. Shadow reconstruction for M87*

On April 10, 2019 the Event Horizon Telescope (EHT) collaboration reported results of the shadow reconstruction for observations of M87* on four days in April 2017 at 1.3 mm wavelength (EHT Collaboration: Akiyama et al., 2019a,b,c,d,e,f). M87 is a giant elliptical galaxy with a rather massive black hole in its center. Earlier, there were different estimates of the black hole mass at M87*. Data analysis of EHT observations in April 2017 supported a black hole mass estimate around $6.5 \times 10^9 M_{\odot}$, which was also discussed earlier in the literature. Distance toward M87 is around 17 Mpc. The shadow diameter is around $(42 \pm 0.3) \mu as$.² Accuracy of image reconstruction is not better than $25 \mu as$, it means that the image reconstruction presented by EHT Collaboration: Akiyama et al. (2019a) is not unique. Generally speaking, these results are consistent with predictions in the framework of conventional black hole model in general relativity, therefore, general relativity passed one significant test more. However, many alternatives for this approach are not rule out yet (EHT Collaboration: Akiyama et al., 2019a), it is rather natural since a number of alternatives (sometimes exotic ones) have very similar features observed with EHT as it was demonstrated earlier in computer simulations, differences for alternative approaches may be very tiny, as shown by (Vincent et al., 2016; Mizuno et al., 2018) where the authors discussed shadow formation for the boson star and the black hole models, see also discussion by Cunha et al. (2015, 2016).

3. Observations of bright stars near the Galactic Center as tool to evaluate gravitational potential

The closest supermassive black hole is located in our Galactic Center and astronomers observe the Galactic Center in different spectral bands. Moreover, such an object is a natural laboratory to test general relativity and check its possible alternatives in a weak gravitational field limit and in the future in a strong gravitational field limit. In 2018 the GRAVITY collaboration reported about the discovery of general relativity effects for S2 star observations near its pericenter passage in May 2018 (GRAVITY Collaboration: Abuter et al., 2018a). We would like to remind that British astronomers observed light deflection from foreground stars during Solar eclipse in May 1919 (Dyson, Eddington

²In spite of different distances toward Sgr A* and M87* and different black hole masses in these objects angular sizes of Schwarzschild radii (therefore shadow diameters) have similar sizes. This case reminds the coincidence of angular sizes for Sun and Moon.

& Davidson, 1920) and they tested three different options, namely, a) there is no a deflection of light by gravitating body; b) a deflection of light is describing by a Newtonian theory; c) a deflection of light is describing by general relativity and after an analysis of their observations astronomers concluded that general relativity is better fitting observations and we had to adopt general relativity instead of Newtonian theory as an universal gravity theory. Similarly, the GRAVITY team showed that general relativity (or more precisely the first post-Newtonian correction of general relativity) is much better describing relativistic redshifts for S2 star near its pericenter passage. It means that general relativity passed one significant test more and we have an additional argument that general relativity is an universal theory of gravity.

There is a very interesting and challenging opportunity to monitor bright IR stars moving around the Galactic Center. Two groups of astronomers use such an opportunity and observe these stars with largest telescopes which are equipped with adaptive optics facilities. American group led by A. Ghez uses the twin Keck 10 m telescopes and this group participates in a development of the Thirty Meter Telescope at Hawaii. Another European group uses four VLT telescopes which have four 8 m telescopes and four 1.8 m telescopes and these telescopes joined in the GRAVITY interferometer facilities. Later, European astronomers will use the European Extremely Large Telescope (E-ELT) to improve an accuracy of bright star orbit reconstruction. Observations of bright stars showed that these stars move along elliptical orbits and therefore, one could conclude that a gravitational potential of point like mass around $M_{SBH} = 4 \times 10^6 M_{\odot}$ could be adopted as the first approximation. After than one could try to find deviations from elliptical orbits which could represent the relativistic effect which is similar to Mercury anomaly discovered by U. Le Verrier in 1859 and explained by A. Einstein in 1915. S2 star is one of the most interesting object to test a gravitational potential at the Galactic Center. This star has eccentricity $e = 0.88$, period $T = 16$ yr and an expected visible relativistic precession of its orbit is around $\Delta s \approx 0.83$ mas (Gillessen et al., 2017; Chu et al., 2017) if we assume that extended mass distributions inside its orbit do not have a significant impact on relativistic precession. Currently the Keck uncertainty in the S2 star orbit reconstruction is around $\sigma_{Keck} \approx 0.16$ mas (Hees et al., 2017), while for Thirty Meter Telescope(TMT) which will be constructed within a several years $\sigma_{TMT} \approx 0.015$ mas.

4. First discoveries with GRAVITY

4.1. Gravitational redshift of S2 star near its pericenter passage

There is a rapid improvement of accuracy of S2 star orbit reconstruction, for example for the European team, since in 1990s a precision of SHARP facilities were around 4 mas, in 2000s NACO had a precision around 0.5 mas, but in 2018 GRAVITY reached a precision around $30 \mu as$ (GRAVITY Collaboration:

Abuter et al., 2018a). It is well-known that measurement of gravitational redshift is one of the classical tests of general relativity. The GRAVITY collaboration estimated gravitational redshift in the orbit of S2 star near its pericenter passage in May 2018 and showed that observational data are much better fitted with GR model in the first PN approximation in comparison with Newtonian one. Therefore, general relativity successfully passed its test for the Galactic Center. It means that almost after 100 years since the confirmation of the GR prediction about a deflection of light during Solar eclipse in 1919 Dyson, Eddington & Davidson (1920), astronomers checked GR prediction at high distances from our Solar system. A theoretical background for gravitational redshift evaluation if sources are moving in binary system was developed by Kopeikin & Ozernoy (1999); Alexander (2005); Zuker et al. (2006). S2 star passed pericenter in May 2018 and after analysis of these observational data it was clear that relativistic corrections for gravitational redshift have to be taken into account near this passage. At the pericenter S2 moves with a total space velocity $V_{\text{peri}} \approx 7650$ km/s therefore $\beta_{\text{peri}} = V_{\text{peri}}/c = 2.55 \times 10^{-2}$ (GRAVITY Collaboration: Abuter et al., 2018a). Considering the first post-Newtonian correction for a total gravitational redshift could expressed in the following form (Kopeikin & Ozernoy, 1999; Alexander, 2005; Zuker et al., 2006; GRAVITY Collaboration: Abuter et al., 2018a)³

$$z_{\text{GR}} = \frac{\Delta\lambda}{\lambda} = B_0 + B_{0.5}\beta + B_1\beta^2 + \mathcal{O}(\beta^3), \quad (4)$$

where $B_1 = B_{1,tD} + B_{1,grav}$, $B_{1,tD} = B_{1,grav} = 0.5$, $B_{1,tD}$ is the special relativistic transverse Doppler effect, $B_{1,grav}$ is the general relativistic gravitational redshift, $B_{0.5} = \cos\theta$, where θ is the angle between the velocity vector and line of sight (Alexander, 2005), the redshift B_0 is independent on a star velocity β and

$$B_0 = z_{\odot} + z_{\text{gal}} + z_{\text{star}} + \frac{1}{2}\Upsilon_0, \quad (5)$$

therefore, the redshift B_0 consists of four terms, the first term z_{\odot} is due a total motion of the Sun and the Earth in respect to Galactic Center and blue shift due to potential of the Sun and the Earth, z_{gal} is redshift due to Galaxy potential, z_{star} is redshift due to the star's potential, the redshift $\frac{1}{2}\Upsilon_0 = \frac{GM}{2a}$ due to the location of star in the SMBH potential (Alexander, 2005). The GRAVITY collaboration evaluated the total redshift from spectroscopical observations $z \approx \frac{200 \text{ km/s}}{c}$ (GRAVITY Collaboration: Abuter et al., 2018a). One could represent the total redshift obtained from spectroscopical observations in the following form (GRAVITY Collaboration: Abuter et al., 2018a)

$$z_{\text{tot}} = z_K + f(z_{\text{GR}} - z_K), \quad (6)$$

³Results of precise measurements of gravitational redshift with Galileo satellites on elliptical orbits have been published recently (Delva et al., 2018; Herrmann et al., 2018).

where $z_K = B_0 + B_{0.5}\beta$ is the Keplerian redshift, $f = 0$ corresponds to Keplerian (Newtonian) fit, while $f = 1$ corresponds to PPN(1) fit. The GRAVITY collaboration found that $f = 0.90 \pm 0.09|_{\text{stat}} \pm 0.15|_{\text{sys}}$ and the authors also concluded that S2 data are inconsistent with a pure Newtonian dynamics with a very high confidence level. Later, the estimate for redshift parameter has been corrected $f = 1.04 \pm 0.05$ with a significance level around 20σ (GRAVITY Collaboration: Abuter et al., 2019). Similarly, the GRAVITY collaboration evaluated f -value from observational data comparing Schwarzschild precession and Newtonian fit for a point like mass (without any precession) and they concluded that the f -value is much closer to GR quantity ($f = 0.94 \pm 0.09$). The Keck team obtained similar results (Do et al., 2019), namely, the authors found that $f = 0.87 \pm 0.17$ and the Newtonian model $f = 0$ has to be rejected with 5σ confidence level.

A comprehensive review on constraints of alternative theory parameters from observations of bright stars around the Galactic Center is given by GRAVITY Collaboration: Amorim et al. (2019).

4.2. Observations of motions of hot spots near the innermost stable circular orbit (ISCO)

The GRAVITY collaboration reported about observations of two bright flares near the Galactic Center on July 22 and July 28, 2018, as well as a fainter flare on May 27, 2018 (GRAVITY Collaboration: Abuter et al., 2018b). The authors noted that the position centroids exhibited clockwise looped motion on the sky, on scales of typically $150 \mu\text{as}$ over a few tens of minutes, corresponding to about 30% the speed of light. Meanwhile, the flares exhibited continuous rotation of the polarization angle, with about the same $45(\pm 15)$ min period as that of the centroid motions. These observations are very important to reconstruct magnetic field distribution near the Galactic Center. Typical radius of spot orbits are around $7 M_{\text{SBH}}$ (in mass units), while the ISCO radius is $6 M_{\text{SBH}}$ for a Schwarzschild black hole. It means the motions of these flares is very close to boundary of stability for bounded orbits.

4.3. Spatially resolved rotation of broad line region for 3C273

The GRAVITY collaboration observed not only the Galactic Center but also bright quasars including 3C273. Recently the authors reported observations of a spatial offset (with a spatial resolution of 10^{-5} arcseconds, or about 0.03 parsecs for a distance of 550 million parsecs) between the red and blue photo-centres of the broad Paschen- α line of the quasar 3C 273⁴ perpendicular to the direction

⁴3C 273 is the first quasar ever been identified. Initially it was observed with Parkes Radio Telescope by Lunar occultation method. M. Schmidt found its redshift $z \approx 0.158$ with Palomar 200-in telescope (Schmidt, 1963). 3C273 is the closest and brightest quasar. Analyzing old photo plates where there were 3 C273 images, Soviet astronomers and Sharov and Efremov found variabilities with time scale T_{var} around a few days (Sharov & Efremov, 1963). It means that a size 3 C273 is less than cT_{var} (where c is a speed of light) or less than the Solar system

of its radio jet (GRAVITY Collaboration: Sturm et al., 2018). The data are fitted by a conventional broad-line-region model of a thick disk of gravitationally bound material orbiting a black hole of $3 \times 10^8 M_\odot$. The authors concluded that disk radius is around 150 light days and since earlier a radius of 100 – 400 light days was evaluated previously using reverberation mapping, therefore, these estimates obtained with data analysis if new GRAVITY observations are consistent with previous ones.

5. Constraints on alternative theories of gravity with observations of bright stars near the Galactic Center

5.1. Graviton mass constraints

A theory of massive gravity was introduced by Fierz & Pauli (1939). Later, a number of pathologies such as Zakharov – Veltman – Van Dam – Iwasaki discontinuity, presence of ghosts were found etc. However, in last years theorists created theories of massive gravity without such defects, see recent review on the subject by de Rham et al. (2017). Different ways to evaluate graviton mass were discussed by Goldhaber and Nieto (2010). The LIGO collaboration treated a theory with massive graviton as a feasible alternative theory of gravity and in the first paper where they reported about the first detection of gravitational waves from a merger of two black holes (it was detected on September 14, 2015 and it is called GW150914), about the discovery (Abbott et al., 2016) the team constrained the graviton Compton wavelength $\lambda_g > 10^{13}$ km which could be interpreted as a constraint for a graviton mass $m_g < 1.2 \times 10^{-22}$ eV. Later, this constraint was improved by Abbott et al. (2017a) where the authors found $m_g < 7.7 \times 10^{-23}$ eV from analysis of the GW170104 event signal

From observations of GW signal and corresponding electromagnetic counterparts in different spectral bands from binary neutron star merger GW170817 which represent a kilonova explosion discussed earlier in the literature constraints on speed of gravitational waves from binary neutron star merger have been found $-3 \times 10^{-15} < (v_g - c)/c < 7 \times 10^{-16}$ (Abbott et al., 2017b). Since graviton energy is $E = hf$, therefore, assuming a typical LIGO frequency range $f \in (10, 100)$, from the dispersion relation one could obtain a graviton mass estimate $m_g < 3 \times (10^{-21} - 10^{-20})$ eV which slightly a more worse estimate than previous ones obtained from binary black hole signals detected by the LIGO team (Zakharov et al., 2018a). Assuming Yukawa gravitational potential of a form

$$\Phi_Y(r) = -\frac{GM}{(1+\delta)r} \left[1 + \delta e^{-\frac{r}{\lambda}} \right], \quad (7)$$

size. A very challenging task was arisen to propose a theoretical model for a huge energy release from a very small space region.

and $\delta = 1$ for massive graviton case. Therefore, this representation for gravitational potential can be used to find the lower bound for Compton wavelength λ_g for graviton, i.e. the upper bound for its mass

$$m_{g(\text{upper})} = h c / \lambda_g. \quad (8)$$

In paper by Borka et al. (2013) we found constraints on Yukawa gravity parameters (λ, δ) from observational data on S2 star orbit. Later, we obtained constraints on graviton mass $m_g < 2.9 \times 10^{-21}$ eV from available observational data for S2 star trajectory (Zakharov et al., 2016a) (see also papers by Zakharov et al. (2016b, 2017a,b) for more details). In these considerations we used available data for S2 star trajectory constrain graviton mass. Later, Keck group followed our ideas to improve our estimates with new observational data $m_g < 1.6 \times 10^{-21}$ eV Hees et al. (2017). In paper Zakharov et al. (2018b) we evaluated discovery potential to improve a graviton mass estimate with future observational data for S2 and other bright stars observed with VLT and Keck telescopes, in particular, we evaluated orbital precession for Yukawa potential and obtained an upper limit for a graviton mass assuming that GR predictions about orbital precessions for bright stars moving around the Galactic Center will be confirmed with future observations.

As it was shown by Zakharov et al. (2018b) the longest Compton wavelength could be expressed as

$$\Lambda \approx \frac{c}{2} \sqrt{\frac{(a\sqrt{1-e^2})^3}{3GM}} \approx \sqrt{\frac{(a\sqrt{1-e^2})^3}{6R_S}}, \quad (9)$$

or therefore, after observations of bright stars for several decades an upper bound for a graviton mass could reach around 5×10^{-23} eV.

5.2. Tidal charge constraints

The line element of the spherically symmetric Reissner – Nordström – de-Sitter metric is

$$ds^2 = -f(r)dt^2 + f(r)^{-1}dr^2 + r^2d\theta^2 + r^2\sin^2\theta d\phi^2, \quad (10)$$

where function $f(r)$ is defined as

$$f(r) = 1 - \frac{2M}{r} + \frac{Q^2}{r^2} - \frac{1}{3}\Lambda r^2, \quad (11)$$

M is a black hole mass, Q is its charge and Λ is cosmological constant. In the case of a tidal charge as it was considered by Dadhich et al. (2001), Q^2 could be negative and in this case Q^2 term reflects a presence of an extra dimension. In paper by Zakharov (2018b) it was shown that a total relativistic advance for metric (10) in the first post-Newtonian approximation is

$$\Delta\theta(\text{total}) := \frac{6\pi M}{L} - \frac{\pi Q^2}{ML} + \frac{\pi\Lambda a^3\sqrt{1-e^2}}{M}. \quad (12)$$

and apocenter shift dependences on eccentricity and semi-major axis are the same for Schwarzschild and Reissner – Nordström cases while corresponding factors ($6\pi M$ and $-\frac{\pi Q^2}{M}$) are different, therefore, it is very hard to separate an impact of a tidal charge and black hole mass evaluation uncertainties. For $Q^2 > 0$, there is an apocenter shift due to a presence of the corresponding term in the opposite direction in respect to GR advance. In paper by Zakharov (2018b) bounds in Q^2 and Λ are presented for current and future accuracies for Keck and Thirty Meter telescopes which were discussed by Hees et al. (2017). Similarly to Zakharov (2018b,c) if we adopt uncertainty $\sigma_{\text{GRAVITY}} = 0.030$ mas for the GRAVITY facilities as it was used by GRAVITY Collaboration: Abuter et al. (2018a) ($\delta_{\text{GRAVITY}} = 2\sigma_{\text{GRAVITY}}$) or in this case $\Delta\theta(GR)_{S2} = 13.84\delta_{\text{GRAVITY}}$ for S2 star and assuming again that GR predictions about orbital precession of S2 star will be confirmed with δ_{GRAVITY} accuracy (or $\left|\frac{\pi Q^2}{ML}\right| \lesssim \delta_{\text{GRAVITY}}$), one could conclude that

$$|Q^2| \lesssim 0.432M^2, \quad (13)$$

or based on results of future observations one could expect to reduce essentially a possible range of Q^2 parameter in comparison with a possible hypothetical range of Q^2 parameter in comparison with current and future Keck data.

6. Conclusions

The Particle Data Group (PDG) which is an international consortium of scientists and it collects and reanalyzes results related to the properties of particles, fundamental interaction, astrophysics and cosmology. The PDG issues the Reviews which summarize properties of elementary particles and describe the current status of elementary particle physics, general relativity and cosmology. Our estimate of graviton mass was included in PDG Review update 2019 together with a few other papers where graviton mass constraints are given⁵.

As it was shown that precise observations of bright stars is very efficient tool to check alternative theories of gravity and to investigate a presence of an extended mass distribution near the Galactic Center as it was investigated earlier by Zakharov et al. (2007). We obtained the graviton mass constraints from an analysis of S2 star trajectory and the bounds are consistent and comparable with the constraints presented recently by the LIGO-Virgo collaboration. In our current studies we discuss an opportunities to evaluate parameters of supermassive black hole, stellar cluster and dark matter cloud near the Galactic Center or evaluate parameters of alternative gravity model analyzing apocenter (pericenter) advance after at least one star revolution. However, in the future when astrometric accuracy will be significantly improved one will have a possibility to evaluate a static gravitational potential at the Galactic Center analyzing

⁵<http://pdg.lbl.gov/2019/listings/rpp2019-list-graviton.pdf>.

only small part of stellar orbit similarly to consideration by Kosmo O'Neil et al. (2019), where it was shown that around 40% (or even smaller) of stellar phase coverage is enough for an orbit reconstruction. However, if a contribution of time-dependent component of gravitational potential caused by stellar encounters is significant an orbit reconstruction problem may be more complicated.

Acknowledgements. P.J., D.B. and V.B.J. wish to acknowledge the support by the Ministry of Education, Science and Technological Development of the Republic of Serbia through the project 176003 "Gravitation and the large scale structure of the Universe". We appreciate an anonymous referee for careful reading of our manuscript and useful remarks.

References

- Abbott, B. P., Abbott, R., Abbott, T. D. et al.: 2016, *Phys. Rev. Lett.* **116**, 061102
- Abbott, B. P., Abbott, R., Abbott, T. D. et al.: 2017a *Phys. Rev. Lett.* **118**, 221101
- Abbott, B. P., Abbott, R., Abbott, T. D. et al.: 2017b *Astrophys. J. Lett.* **848**, L13
- Alexander, T.: 2005, *Phys. Rep.* **419**, 65
- Arnold, V. I.: 2000, *Huygens and Barrow, Newton and Hooke. Pioneers in Mathematical Analysis and Catastrophe Theory from Evolvents to Quasicrystals*, (Birkhäuser Verlag, Basel - Boston - Berlin).
- Bardeen, J. M.: 1973, in *Black holes (Les Astres Occlus)*, ed. by C. de Witt and B.S. de Witt (Gordon Breach, New-York – London – Paris, 1973), p. 215.
- Bisnovatyi-Kogan, G. S. & Tsupko, O. Yu.: 2017, *Universe* **3**, 57
- Borka, D., Jovanović, P., Borka Jovanović, V. & Zakharov, A. F.: 2013, *J. Cosm. Astropart. Phys. (JCAP)* **11**, 050
- Broderick A. E. & Loeb, A.: 2006, *Astrophys. J.* **636**, L109
- Broderick, A. E., Fish, V. L., Johnson, M. D. et al.: 2016, *Astrophys. J.* **820**, 137
- Chandrasekhar, S.: 1983, *The Mathematical Theory of Black Holes*, (Clarendon Press, Oxford).
- Cherepashchuk, A. M.: 2016, *Physics-Uspokhi* **59**, 70
- Cherepashchuk, A.M.: 2017, *Astron. Rep.* **61**, 265
- Chu, D. S., Do, T., Hees, A. et al.: 2018, *Astrophys. J.* **854**:12 (10pp)
- Cunha, P. V. P., Herdeiro, C. A. R., Radu, E. & Runarsson, H. F.: 2015, *Phys. Rev. Lett.* **115**, 211102
- Cunha, P. V. P., Grover, J., Herdeiro, C. A. R. et al. : 2016, *Phys. Rev. D* **94**, 104023
- Cunha, P. V. P. & Herdeiro, C. A. R.: 2018, *Gen. Relativ. Grav. D* **50**, 42
- Cunningham, C. T. & Bardeen, J. M.: 1973, *Astrophys. J* **183**, 237
- Dadhich, D., Maartens, R., Papadopoulos, Ph. & Rezania, V.: 2001, *Phys. Lett. B* **487**, 1

- Delva, P., Puchades, N. Schönemann, E. et al.: 2018, *Phys. Rev. Lett.* **121**, 231101
- De Paolis, F., Inghrosso, G., Nucita, A.A. et al. : 2001, *Astron. Astrophys.* **376**, 853
- Do, T., Hees, A., Ghez, A. et al.: 2019, *Science* **365**, 664; arXiv:1907.10731v1 [astro-ph.GA]
- Doeleman, S. S.: 2008, *J. Phys.: Conf. Ser.* **131**, 012055
- Doeleman, S.: 2017, *Nat. Astron.* **1**, 646
- Doeleman, S. S. et al.: 2008, *Nature* **455**, 78
- Doeleman, S. S., Agol, E., Backer, D. et al.: 2009, arXiv:0906.3899 [astro-ph.CO]
- Dokuchaev, V. I. & Nazarova, N. O.: 2017, *JETP Lett.* **106**, 637
- Dokuchaev, V. I. & Nazarova, N. O.: 2019, *Universe* **5**, 183
- Dyson, F. W., Eddington A. S. & Davidson, C.: 1920, *Phil. Trans. R. Soc. London. Series A*, **220**, 291
- EHT Collaboration: Akiyama, K., Alberdi, A., Alef, W. et al.: 2019a, *Astrophys. J. Lett.* **875**, L1 (Paper I)
- EHT Collaboration: Akiyama, K., Alberdi, A., Alef, W. et al.: 2019b, *Astrophys. J. Lett.* **875**, L2 (Paper II)
- EHT Collaboration: Akiyama, K., Alberdi, A., Alef, W. et al.: 2019c, *Astrophys. J. Lett.* **875**, L3 (Paper III)
- EHT Collaboration: Akiyama, K., Alberdi, A., Alef, W. Alberdi, A., Alef, W. et al.: 2019d, *Astrophys. J. Lett.* **875**, L4 (Paper IV)
- EHT Collaboration: Akiyama, K., Alberdi, A., Alef, W. et al.: 2019e, *Astrophys. J. Lett.* **875**, L5 (Paper V)
- EHT Collaboration: Akiyama, K., Alberdi, A., Alef, W. et al.: 2019f, *Astrophys. J. Lett.* **875**, L6 (Paper VI)
- Falcke, H., Melia, F. & Agol, E., 2000, *Astrophys. J.* **528**, L13
- Falcke, H. & Markoff, S. B.: 2013, *Class. Quan. Grav.* **30**, 244003
- Fierz, M. & Pauli, W.: 1939, *Proc. Roy. Soc. Lond. A* **173**, 211
- Gillessen, S, Plewa, P. M., Eisenhauer, F. et al.: 2017, *Astrophys. J.* **837**:30 (19pp)
- Goldhaber, A. S. & Nieto, M. M.: 2010, *Rev. Mod. Phys.* **82**, 939
- de Rham, C., Deskins, J. T. & Tolley, A. J. et al.: 2017, *Rev. Mod. Phys.* **89**, 025004
- GRAVITY Collaboration: Abuter, R., Amorim, A., Anugu, N. et al.: 2018a, *Astron. & Astrophys. Lett.* **615**, L15
- GRAVITY Collaboration: Abuter, R., Amorim, A., Bauböck, M. et al.: 2018b, *Astron. & Astrophys. Lett.* **618**, L10
- GRAVITY Collaboration: Sturm, E., Dexter, J., Pfuhl, O. et al.: 2018, *Nature* **563**, 657
- GRAVITY Collaboration: Abuter, R., Amorim, A., Bauböck, M. et al.: 2019, *Astron. & Astrophys. Lett.* **625**, L10

- GRAVITY Collaboration: Amorim, A., Bauböck, M., Benisty, M., et al.: 2019, *Month. R. Astron. Soc.* **489**, 4606; arXiv:1908.06681v1[astro-ph.GA]
- Hees, A., Do, T., Ghez, A. M. et al.: 2017, *Phys. Rev. Lett.* **118**, 211101
- Herrmann, S., Finke, F., Lülff M. et al.: 2018, *Phys. Rev. Lett.* **121**, 231102
- Hioki, K. & Maeda, K.: 2009, *Phys. Rev. D* **80**, 024042.
- Holz, D. E. & Wheeler, J. A.: 2002, *Astrophys. J.* **578**, 330
- James, O., von Tunzelmann, E., Franklin P. & Thorne, K. S.: 2015, *Class. Quant. Grav.* **32**, 065001
- Jetzer, P.: 1992, *Phys. Rep.* **220**, 163
- Johannsen, T.: 2016, *Class. Quant. Grav.* **33**, 113001
- Johannsen, T., Broderick, A. E., Plewa, P. M. et al.: 2016, *Phys. Rev. Lett.* **116**, 031101
- Kardashev, N.S.: 1997, *Exper. Astron.* **7**, 329
- Kardashev, N.S.: 2009, *Physics – Uspekhi* **52**, 1127
- Kardashev, N. S., Khartov, V. V., Abramov, V. V. et al.: 2013, *Astron. Rep.* **57**, 153
- Kopeikin, S. M. & Ozernoy, L. M.: 1999, *Astrophys. J.* **523**, 771
- Kosmo O’Neil, K., Martinez, G. D. & Hees, A. et al.: 2019, *Astron. J.* **158**:4 (21pp)
- Luminet, P.: 1979, *Astron & Astrophys.* **75**, 228
- Melia, F. & Falcke, H.: 2001, *Ann. Rev. Astron. Astrophys.* **39**, 309
- Mizuno, Y., Younsi, Z., Fromm, C. M., et al.: 2018, *Nature Astron.* **2**, 585
- Munyaneza, F. & Viollier, R. D.: 2002, *Astrophys. J.* **564**, 274
- Reid, M.: 2009, *Intern. J. Mod. Phys. D* **18**, 889
- Schmidt, M.: 1963, *Nature* **197**, 1040
- Shaikh, R.: 2018, *Phys. Rev. D* **98**, 024044
- Shaikh, R.: 2019, *Phys. Rev. D* **100**, 024028
- Sharov, A. S. & Efremov, Yu. N.: 1963, *Commission 27 of the I. A. U. Information Bulletin on Variable Stars*, Number 23, Konkoly Observatory, Budapest, 18 April 1963.
- Shen, Z. Q., Lo, K. Y., Liang, M.-C. et al. : 2005, *Nature* **438**, 62
- Taton, R. & Wilson, C.: 2003, *The Planetary Astronomy from the Renaissance to the Rise of Astrophysics*, (Cambridge University Press, Cambridge).
- Torres, D. F., Capozziello, S. & Lambiase, G.: 2000, *Phys. Rev. D* **62**, 104012
- Vincent, F. H., Meliani, Z., Grandclément, P. et al. : 2016, *Class. Quant. Grav.* **33**, 105015
- Yakovlev, D. G.: 1975, *Sov. Phys. JETP* **41**, 179
- Young, P.: 1976, *Phys. Rev. D* **14**, 3281
- Zakharov, A. F.: 1986, *Sov. Phys. JETP* **64**, 1
- Zakharov, A. F.: 2014, *Phys. Rev. D* **90**, 062007

- Zakharov, A. F.: 2015, *J. Astrophys. Astron.* **36**, 539
- Zakharov, A. F.: 2017, *J. Phys.: Conf. Ser.* **934**, 012037
- Zakharov, A. F.: 2018a, *Intern. J. Mod. Phys. D* **27**, 1841009
- Zakharov, A. F.: 2018b, *Eur. Phys. J. C* **78**, 689
- Zakharov, A.: 2018c, *Eur. Phys. J. Web Conf.*, **125**, 01010
- Zakharov, A. F.: 2019, *Intern. J. Mod. Phys. D* **28**, 1941003
- Zakharov, A. F., Jovanović, P., Borika, D. & Borika Jovanović, V.: 2016a, *J. Cosm. Astropart. Phys. (JCAP)* **05**, 045
- Zakharov, A. F., Jovanović, P., Borika, D. & Borika Jovanović, V.: 2016b, *Eur. Phys. J. Web Conf.* **125**, 01011
- Zakharov, A. F., Jovanović, P., Borika, D. & Borika Jovanović, V.: 2017a, *J. Phys.: Conf. Series* **798** 012081
- Zakharov, A. F., Jovanović, P., Borika, D. & Borika Jovanović, V.: 2017b, *Eur. Phys. J. Web of Conf.* **138**, 010010
- Zakharov, A. F., Jovanović, P., Borika, D. & Borika Jovanović, V.: 2018a, *Intern. J. Mod. Phys.: Conf. Ser.* **47**, 1860096
- Zakharov, A. F., Jovanović, P., Borika, D. & Borika Jovanović, V.: 2018b, *J. Cosm. Astropart. Phys. (JCAP)* **04**, 050
- Zakharov, A.F., Nucita, A.A., De Paolis F., & Ingrosso, G.: 2005a, *New Astron.* **10**, 479
- Zakharov, A.F., Nucita, A.A., De Paolis F., & Ingrosso, G.: 2005b, *Astron. & Astrophys.* **442**, 795
- Zakharov, A.F., Nucita, A.A., De Paolis, F. & Ingrosso, G.: 2007, *Phys. Rev. D* **76**, 062001
- Zakharov, A.F., Nucita, A.A., De Paolis F. & Ingrosso, G.: 2012, *New Astron. Rev.* **56**, 64
- Zucker, S., Alexander, T., Gillessen, S. et al.: 2006, *Astrophys. J.* **639**, L21

Possible observational signatures of supermassive black hole binaries in their Fe K α line profiles

P. Jovanović^{1,*}, V. Borka Jovanović², D. Borka² and L.Č. Popović¹

¹ *Astronomical Observatory, Volgina 7, P.O. Box 74, 11060 Belgrade, Serbia*
**(E-mail: pjovanovic@aob.rs)*

² *Atomic Physics Laboratory (040), Vinča Institute of Nuclear Sciences,
University of Belgrade, P.O. Box 522, 11001 Belgrade, Serbia*

Received: July 10, 2019; Accepted: October 24, 2019

Abstract. Here we study the potential observational signatures of supermassive black hole binaries (SMBHBs) in the Fe K α line profiles emitted from the accretion disks around their components. We simulated the Fe K α line emission from the relativistic accretion disks using ray tracing method in Kerr metric. The obtained profiles from the SMBHBs are then compared with those in the case of the single supermassive black holes (SMBHs). We considered two models of the SMBHBs: a model when the secondary SMBH is embedded in the accretion disk around the primary, causing an empty gap in the disk, and a model with clearly separated components, where the accretion disks around both primary and secondary give a significant contribution to the composite Fe K α line emission of a such SMBHB. The obtained results showed that both models of SMBHBs can leave imprints in the form of ripples in the cores of the emitted Fe K α line profiles, which may look like an absorption component in the line profile. However, in the case of the composite line profiles emitted from two accretion disks, these ripples could have much higher amplitudes and strongly depend on orbital phase of the system, while for those emitted from a disk with an empty gap, the corresponding ripples mostly have lower amplitudes and do not vary significantly with orbital phase. The present day X-ray telescopes are not able to detect such signatures in the observed X-ray spectra of SMBHBs. However this will be possible with the next generation of X-ray observatories, which will also enable application of such effects as a tool for studying the properties of these objects.

Key words: black hole physics – supermassive black holes – accretion disks – line: profiles

1. Introduction

Nowadays, it is widely accepted that binary systems of SMBHs originate in galactic mergers (Begelman et al., 1980), and that their coalescences are the powerful emitters of low-frequency (nHz) gravitational waves (GWs) which are currently probed by pulsar timing arrays (PTA, Sesana et al., 2018), and which

will be main targets for future space-based interferometers. Searches for (active) SMBHBs are currently ongoing, resulting with more than 100 candidates (see e.g. Sesana et al., 2018, and references therein), and were significantly intensified after the first observation of merging stellar mass black hole binary performed by LIGO Scientific Collaboration and Virgo Collaboration (2016).

One of the most powerful methods for SMBHB searches is the spectroscopy (in different spectral bands). As two SMBHBs in a galactic merger become gravitationally bound and start to orbit around their center of mass, the emission lines from SMBHB components start to shift due to their radial velocities (see e.g. Popović, 2012; Bon et al., 2012; Li et al., 2016, for examples in optical band). In such a case, a strong X-ray emission in the broad Fe $K\alpha$ line at 6.4 keV could arise from accretion disks around both SMBHBs, and could be therefore affected by the Doppler shifts due to the orbital motion of the binary (Yu and Lu, 2001; Jovanović et al., 2014), since the radial velocities of its components could reach $\approx 1.5 \times 10^4$ km/s in the case when the separation between them is $10^{-3} - 10^{-2}$ pc (see Table 1 in Popović, 2012). Such, double relativistic Fe $K\alpha$ lines and periodic X-ray variability are expected to be detected from very massive ($M > 10^8 M_\odot$) and cosmologically nearby ($z_{cosm} < 1$) SMBHBs (Sesana et al., 2012).

The Fe $K\alpha$ line is produced by fluorescent emission from a very compact region around a SMBHB (Fabian et al., 1989, 2000), and thus it represents powerful diagnostic tool for studying physics and structure of such regions (see e.g. Jovanović et al., 2008; Jovanović & Popović, 2009; Jovanović, 2012; Popović, 2012), as well as the masses and spins of SMBHBs (see e.g. Jovanović et al., 2011; Reynolds, 2014). X-ray reflection spectroscopy, which is based on the studies of the observed broad Fe $K\alpha$ line profiles, is nowadays proven to be an especially powerful technique for the robust black hole spin measurements across the wide range of black hole masses, from the stellar-mass black holes in the X-ray binaries to the SMBHBs in the Active Galactic Nuclei (AGN), as well as for the reverberation of the relativistically broadened iron line which is already detected in the observed X-ray spectra of some AGN (for more details see the review by Reynolds (2014), and references therein).

In the case of SMBHBs, the line emitting regions could have different structures, depending on the mass ratios of the components, separation between them and parameters of their accretion disks (Jovanović et al., 2014). In some cases the secondary SMBHB could be even embedded in the accretion disk around the primary, causing an empty annular gap in it (McKernan et al., 2013), similarly to the empty gap in circumbinary disk of Mrk 231 (see Fig. 1 in Yan et al., 2015). Namely, it is well known that a SMBHB with small mass ratio ($q \ll 1$) can exchange angular momentum with its disk, distorting its density and causing the secondary SMBHB to migrate inward (see e.g. McKernan et al., 2013, and references therein). If a secondary has a very low mass, it is subjected to a very rapid Type I migration, and it cannot significantly affect the Fe $K\alpha$ line emitted from the disk, neither can create an empty cavity in it. However, if the

secondary is sufficiently massive (i. e. if the mass ratio of the SMBHB exceeds the critical value of $q \geq 10^{-4}$), it will be subjected to a Type II migration, and it will open an empty annular gap in the disk, analogous to the gaps in protoplanetary disks, significantly affecting the emitted Fe K α line (McKernan et al., 2013).

Here we study the possibility to detect the SMBHB signatures in their observed Fe K α line profiles by nowadays and future X-ray detectors. For this purpose we studied two models of the SMBHBs: (1) model with clearly separated components, where the accretion disks around both primary and secondary SMBHs significantly contribute to their composite line emission, and (2) model in which the secondary SMBH is embedded in the accretion disk around primary, causing an empty gap in the disk.

This paper is organized as follows: the simulations of X-ray radiation from two accretion disks with different parameters, as well as the procedure how to obtain the simulated Fe K α line profiles for two mentioned models of SMBHBs are described in Section 2, the obtained results are presented in Section 3 and briefly discussed in Section 4, and finally, in Section 5 we point out our main conclusions.

2. Models of accretion disks around two components of a SMBHB and their barycentric orbits

2.1. Accretion disk models

In order to study the potential observational signatures of SMBHBs in the Fe K α line profiles emitted from the relativistic accretion disks around their SMBH components, we performed the numerical simulations of disk emission based on ray-tracing method in Kerr metric, taking into account only those photon trajectories reaching the observer's sky plane (Fantoni et al., 1997; Cadez et al., 1998; Jovanović et al., 2008; Jovanović & Popović, 2009; Jovanović, 2012). We assumed that disk emissivity $\varepsilon(r)$ follows power law: $\varepsilon(r) = \varepsilon_0 \cdot r^p$, where ε_0 is an emissivity constant, and p is an emissivity index (see Jovanović, 2012, for more details). In the case of the SMBHB model with empty gap, this power law disk emissivity was modified so that $\varepsilon(r) = 0$ over the annulus representing the gap (see below text for more details).

Due to several effects, photons emitted from a disk at energy E_{em} (or wavelength λ_{em}) will be observed by an observer at infinity at energy E_{obs} (or wavelength λ_{obs}), causing the energy shift g or, equivalently, the usual redshift in wavelength z (for more details see e.g. Jovanović et al., 2016, and references therein):

$$g = \frac{E_{obs}}{E_{em}} = \frac{\lambda_{em}}{\lambda_{obs}} = \frac{1}{1+z}. \quad (1)$$

By integrating the observed flux at each observed energy over the whole disk image, one can obtain the corresponding simulated line profile emitted from the

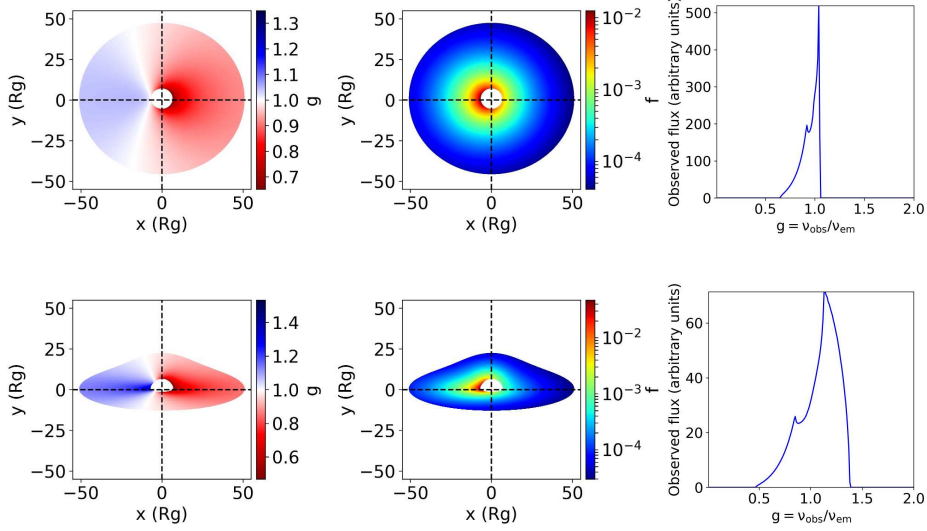


Figure 1. Simulated images of the relativistic accretion disk in Kerr metric around a SMBH, colored according to energy shift g (left) and observed flux (middle), as well as the corresponding simulated non-normalized line profile (right). Top panel corresponds to “disk model A” and bottom to “disk model B” (see §2 for the particular values of disk parameters).

previously calculated accretion disk image (Jovanović, 2012):

$$F_{obs}(E_{obs}) = \int_{image} \varepsilon(r) g^4 \delta(E_{obs} - gE_0) d\Xi \quad (2)$$

Taking into account the results of some previous studies (see e.g. Jovanović, 2012, and references therein), we assumed the following parameters for modeling the accretion disks around the primary and secondary SMBHs: both SMBHs are assumed to be slowly rotating with the same small spin: $a_{BH} = 0.1$, inner radii of both disks are fixed to $R_{in} = R_{ms} = 5.67 R_g$ (where R_{ms} is the radius of the marginally stable orbit, and $R_g = GM/c^2$ - the gravitational radius of the SMBH with mass M), their outer radii are also assumed to be the same: $R_{out} = 50 R_g$, as well as their emissivity indices: $p = -2.5$. We simulated the SMBHB signatures for two different disk inclinations: $\theta_{obs} = 25^\circ$ (labeled as “disk model A” for the further reference) and $\theta_{obs} = 75^\circ$ (“disk model B”). The resulting simulated disk images, colored according to the energy shifts g and the observed fluxes F , as well as the corresponding simulated non-normalized line profiles are presented in Fig. 1 for both disk models. As it can be seen from this figure, disk inclination significantly affects the width and intensity of

the resulting line profiles, which was the main reason why we assumed these particular two disk models.

Since, as already mentioned, the appearance of double relativistic Fe K α lines and periodic X-ray variability are expected to be detected from very massive and cosmologically nearby SMBHBs (Sesana et al., 2012), we assumed a large mass of the primary SMBH: $M_1 = 5 \times 10^8 M_\odot$ and small angular diameter distance to the binary system of SMBHBs: $D_A = 20$ Mpc, corresponding to $z_{cosm} \approx 0.0045$ for $\Omega_M = 0.315$, $\Omega_\Lambda = 0.685$ and $H_0 = 67.4 \text{ km s}^{-1} \text{ Mpc}^{-1}$ (Planck Collaboration, 2018). For mass ratio of the SMBHB we adopted the value $q = 0.5$, corresponding to the mass of the secondary of $M_2 = 2.5 \times 10^8 M_\odot$. Thus, the total mass of the SMBHB is almost an order of magnitude less than the mass of the central SMBH of M87, estimated from its shadow by Event Horizon Telescope Collaboration (Event Horizon Telescope Collaboration, 2019), and it is within the mass limit of $1.6 \times 10^9 M_\odot$ for the SMBHBs out to the distance of the Virgo Cluster (≈ 16 Mpc), obtained from 11-year data set for low frequency gravitational waves by NANOGrav PTA collaboration (Aggarwal et al., 2019). This resulted with simulated accretion disk around the primary with outer radii of $R_{out} = 50 R_g \approx 250$ AU which on the observer's sky corresponds to $\approx 12.5 \mu\text{as}$, giving a total apparent size of the disk's image of $\sim 25 \mu\text{as} \times 25 \mu\text{as}$.

Regarding the assumed size of the accretion disks, we took into account the results of some observational studies of AGN with single SMBHBs in their centers, which suggest that the broad Fe K α line is emitted from the innermost regions of their accretion disks, extending between R_{ms} and a few dozens of R_g (see e.g. Ballantyne & Fabian, 2005, for an example in the case of radio galaxy 4C 74.26). This is also in accordance with so called "standard model of accretion disk" (Shakura & Sunyaev, 1973), according to which the spectrum of radiation emitted from the disk depends on the distance to the central SMBH, so that the innermost part of the disk between R_{ms} and several tens of R_g emits X-rays, its central part between $\sim 100 R_g$ and $\sim 1000 R_g$ emits UV radiation, while its outer part located thousands R_g from the SMBH, emits the optical radiation. Taking this into account, and since we are here investigating only the Fe K α line emission from a SMBHB, we assumed that the outer radii of its both disks are equal to the outer radii of their Fe K α line emitting regions, for which we adopted the following value: $R_{out} = 50 R_g$.

On the other hand, the outer parts of an accretion disk in a close SMBHB (i.e. when semimajor axis a is small), could be subjected to the tidal disruption by the gravitational field of the second component. Therefore, the maximum size of the accretion disks in such a SMBHB is determined by the gravitational interaction between its components, and it is a function of their mass ratio q (for more details see e.g. Paczynski, 1977). An accretion disk with outer radius R_{out} would be tidally disrupted if the semimajor axis a of the SMBHB is less than the following limit for tidal disruption (Safarzadeh et al., 2019):

$$a_t = R_{out} \left(1 + q^{1/3} \right). \quad (3)$$

In this study, the outer radii of the disks are $R_{out} \approx 250$ AU, which corresponds to the following limit for tidal disruption: $a_t \approx 450$ AU. As it can be seen from Table 1, the semimajor axes of both studied orbits significantly exceed this limit ($a \gg a_t$), and thus the accretion disks around both components are not subjected to the tidal disruption during their orbital motion.

2.2. Keplerian barycentric orbits of SMBHBs

The first of two studied SMBHB models assumes that its clearly separated primary and secondary components are moving around their common center of mass along Keplerian orbits which, due to their radial velocities, causes Doppler shifts in the Fe K α lines emitted from their accretion disks.

To model Keplerian barycentric orbits of a binary system of SMBHBs, we apply the same procedure which is commonly used for the binary stars (for more details see e.g. Hilditch, 2001). As a first step, we can adopt some masses of the primary and secondary components M_1 and M_2 , or alternatively, just mass of the primary and mass ratio between the secondary and primary: $q = \frac{M_2}{M_1}$. We also need to assume some separation between the components a (i.e. semimajor axis of their relative orbit)¹. The orbital period of the binary can be then obtained from the third Kepler's law:

$$P^2 = \frac{4\pi^2 a^3}{G(1+q)M_1}. \quad (4)$$

If we denote time with t and time of the pericenter passage with τ , then the next step is to calculate the mean anomaly M (and also orbital phase Φ):

$$M = \frac{2\pi}{P}(t - \tau) = 2\pi\Phi. \quad (5)$$

Assuming some orbital eccentricity e , the corresponding eccentric anomaly E can be obtained by solving the Kepler's Equation:

$$M = E - e \sin E, \quad (6)$$

and the true anomaly θ can be calculated from E according to:

$$\theta = 2 \arctan \left(\sqrt{\frac{1+e}{1-e}} \tan \frac{E}{2} \right). \quad (7)$$

Finally, the true barycentric orbits (i.e. those in the orbital plane) of the primary and secondary SMBHBs are then represented by polar equations of the ellipse

¹Sub-parsec SMBHBs are of special interest for this investigation, since several observational studies indicated the existence of such SMBHBs in the cores of some AGN (see e.g. Bon et al., 2012).

$r_{1,2}(\theta)$:

$$r_{1,2}(\theta) = \frac{a_{1,2}(1-e^2)}{1+e\cos\theta}, \quad (8)$$

where $a_1 = \frac{qa}{1+q}$ and $a_2 = \frac{a}{1+q}$ are their semimajor axes².

The corresponding apparent orbits (in rectangular coordinates) can be calculated by projecting the true orbits on the observers sky plane using the remaining three Keplerian orbital elements (orbital inclination i , longitude of the ascending node Ω and longitude (or argument) of pericenter ω):

$$\begin{aligned} x_{1,2} &= r_{1,2} \cos\theta [\cos\Omega \cos\omega - \sin\Omega \sin\omega \cos i] \\ &\quad + r_{1,2} \sin\theta [-\cos\Omega \sin\omega - \sin\Omega \cos\omega \cos i] \\ y_{1,2} &= r_{1,2} \cos\theta [\sin\Omega \cos\omega + \cos\Omega \sin\omega \cos i] \\ &\quad + r_{1,2} \sin\theta [-\sin\Omega \sin\omega + \cos\Omega \cos\omega \cos i]. \end{aligned} \quad (9)$$

Radial velocities of the components are given by the following expression (Hilditch, 2001):

$$V_{1,2}^{rad}(\theta) = K_{1,2} [\cos(\theta + \omega) + e \cdot \cos\omega] + \gamma, \quad (10)$$

where $K_{1,2}$ are the semiaplitudes of the velocity curves:

$$K_{1,2} = \frac{2\pi a_{1,2} \sin i}{P\sqrt{1-e^2}}, \quad (11)$$

and γ is systemic velocity (which is assumed to be 0 km/s in our simulations). Assuming that $V_{1,2}^{rad} \ll c$, Doppler shifts in wavelength ($z_{1,2}$) and energy ($g_{1,2}$) due to radial velocities of the components are given by:

$$z_{1,2} \approx \frac{V_{1,2}^{rad}}{c}, \quad g_{1,2} = \frac{1}{1+z_{1,2}}. \quad (12)$$

The total redshift factor g_{tot} , representing the net effect of both relativistic effects and radial velocities of the components, can be then obtained from Eqs. (1) and (12):

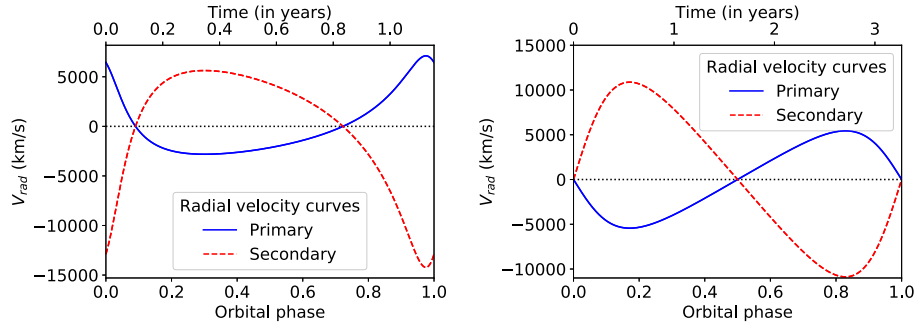
$$g_{tot} = \frac{1}{1+z+z_{12}} = \frac{1}{\frac{1}{g} + \frac{1}{g_{1,2}} - 1}. \quad (13)$$

We studied the influence of Doppler shifts on the observed disk emission by calculating the simulated line profiles according to the expression (2), but using the total redshift factor g_{tot} instead of g .

²One should also take into account that the orientations of two barycentric orbits differ by 180° within the orbital plane.

Table 1. Adopted orbital elements for two Keplerian orbits of a SMBHB with mass ratio $q = 0.5$.

	a		Period (yr)	e	i ($^\circ$)	Ω ($^\circ$)	ω ($^\circ$)
	(AU)	(pc)					
<i>orbit 1</i>	1×10^3	0.005	1.16	0.5	30	0	30
<i>orbit 2</i>	2×10^3	0.01	3.27	0.25	60	0	90

**Figure 2.** Radial velocities of the components in a SMBHB with mass ratio $q = 0.5$, for orbit 1 (*left*) and for orbit 2 (*right*).

3. Results and discussion

To study the observational signatures of the first SMBHB model, we performed simulations of the X-ray radiation from such a SMBHB with mass ratio $q = 0.5$ for two different Keplerian orbits of its components, denoted as “orbit 1” and “orbit 2”, and determined by the orbital elements which are summarized in Table 1. As it can be seen from this table, the obtained orbital periods are on the order of a few years, which means that we simulated electromagnetic signatures in the Fe $K\alpha$ line of the nearby SMBHBs with semimajor axes of $\sim 10^{-3} - 10^{-2}$ pc, periods of a few years and masses above $\sim 10^8 M_\odot$, and such SMBHBs are targets of present PTAs like NANOGrav, which search for their gravitational wave signatures (see e.g. Aggarwal *et al.*, 2019).

The obtained radial velocities of the components in the case of both orbits from Table 1 are presented in Fig. 2. It can be seen from this figure that the radial velocity of the secondary SMBH can go far beyond 10,000 km/s, which is sufficient to induce significant Doppler shift in the X-ray radiation from its accretion disk.

As a next step, we used the obtained radial velocities to simulate the X-ray radiation from this SMBHB during different orbital phases along each of two orbits, assuming different models of accretion disks around its components. Two

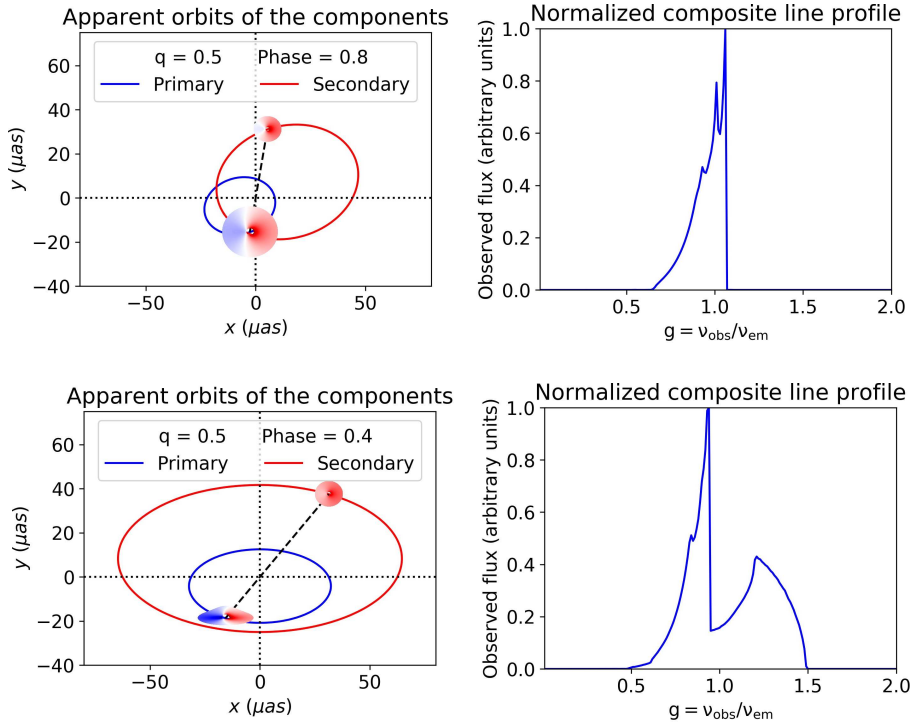


Figure 3. *Left:* Simulated images of the accretion disks around the primary and secondary components of a SMBHB with $q = 0.5$ for “disk A” around both primary and secondary during orbital phase 0.8 along “orbit 1” (*top panel*), as well as for “disk B” around primary and “disk A” around secondary during orbital phase 0.4 along “orbit 2” (*bottom panel*). *Right:* The corresponding simulated composite Fe $K\alpha$ line profiles.

examples of the obtained results are presented in Fig. 3 and they correspond to the orbital phase $\Phi = 0.8$ along “orbit 1” in the case when “disk A” is around both components (top panel), as well as to the orbital phase $\Phi = 0.4$ along “orbit 2” in the case when “disk B” is around the primary and “disk A” around the secondary component (bottom panel). The disk images, colored according to the total redshift factor g_{tot} , are presented in the left parts of each panel of Fig. 3, while their right parts show the corresponding simulated composite Fe $K\alpha$ line profiles. As it can be seen from this figure, this model of SMBHB induces the appearance of the ripples in the cores of the simulated composite Fe $K\alpha$ line profiles. The amplitudes of these ripple effects strongly depend on the assumed parameters of the accretion disks around both primary and secondary SMBHBs, the orbital elements of their Keplerian orbits, as well as on the particular orbital phase (i.e. time) at which, here a simulation and in reality an observation, is

made. Moreover, as demonstrated in Jovanović *et al.* (2014), the mass ratio q also has a strong influence on the amplitudes of these ripples, since the ratio between the fractions of the composite Fe K α line flux, contributed by the accretion disks around the secondary and the primary, roughly corresponds to q . Since a highly inclined disk produces a wide line profile, as demonstrated in Fig. 1, the ripple in the bottom panel of Fig. 3 is much wider and deeper than the one in the top panel because it is created in the component of the Fe K α line which is emitted from the highly inclined “disk B” around the primary SMBH.

We also investigated the flux variability in different parts of the Fe K α line for different phases during one orbital period. The flux variability of the total line profile, its red part ($E < 6.2$ keV), core ($6.2 \text{ keV} \leq E \leq 6.6$ keV) and blue part ($E > 6.6$ keV) are presented in Fig. 4 by black, red, green and blue lines, respectively. Two panels in Fig. 4 refer to the same disk parameters and orbital elements as the corresponding panels in Fig. 3, but for 10 different orbital phases (including those from Fig. 3). As it can be seen from Fig. 4, this model of SMBHBs induces the highest flux variability in the core of the Fe K α line. Taking into account that the presented results refer to only one orbital period, it can be easily deduced that the same variability pattern would also repeat during all successive orbital periods. Therefore, in the case of such a SMBHB, a periodic variability of the X-ray radiation in the Fe K α line should be expected, which is in good agreement with the similar predictions of Sesana *et al.* (2012).

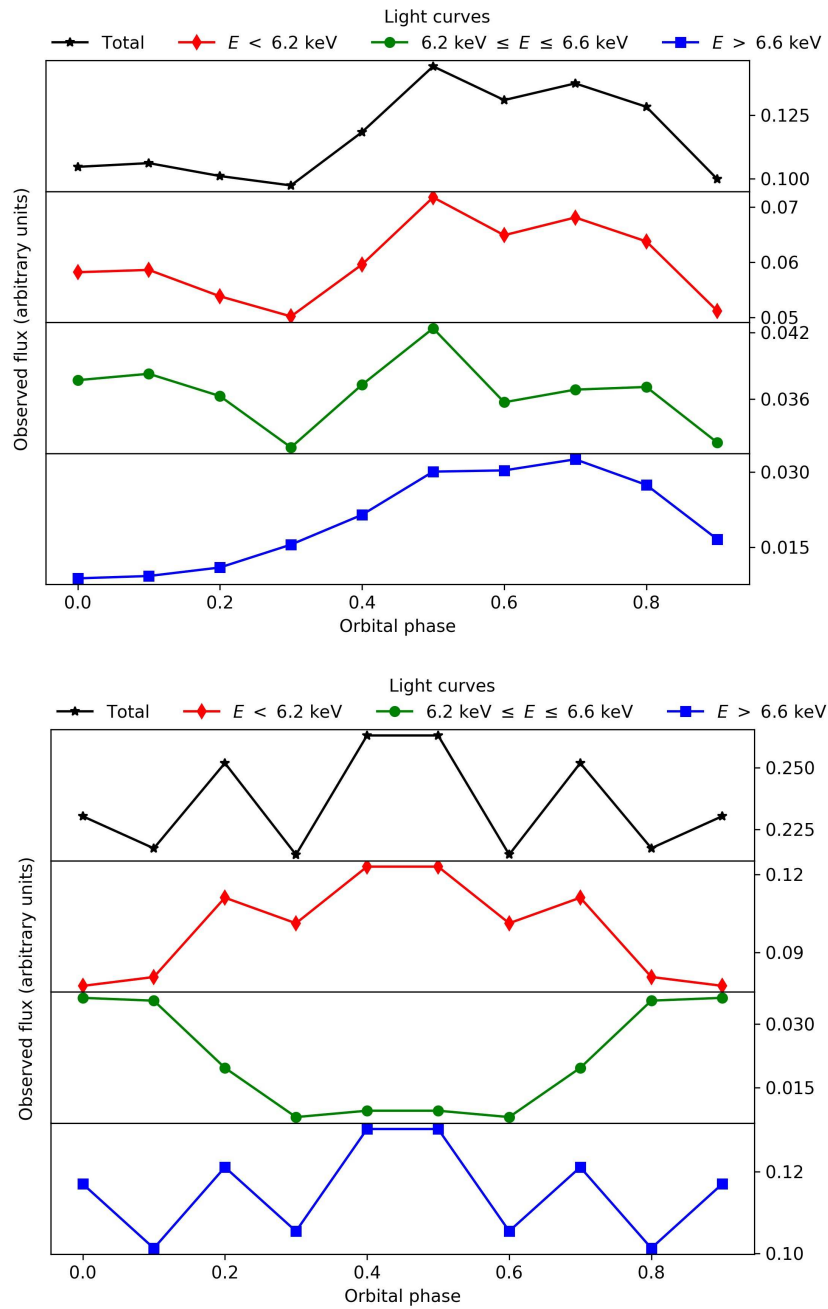


Figure 4. Flux variability (from top to bottom) of the total Fe $K\alpha$ line profile (black line), its red part (red line), core (green line) and blue part (blue line) during 10 different orbital phases and for the same disk parameters and orbital elements as in the corresponding panels of Fig. 3.

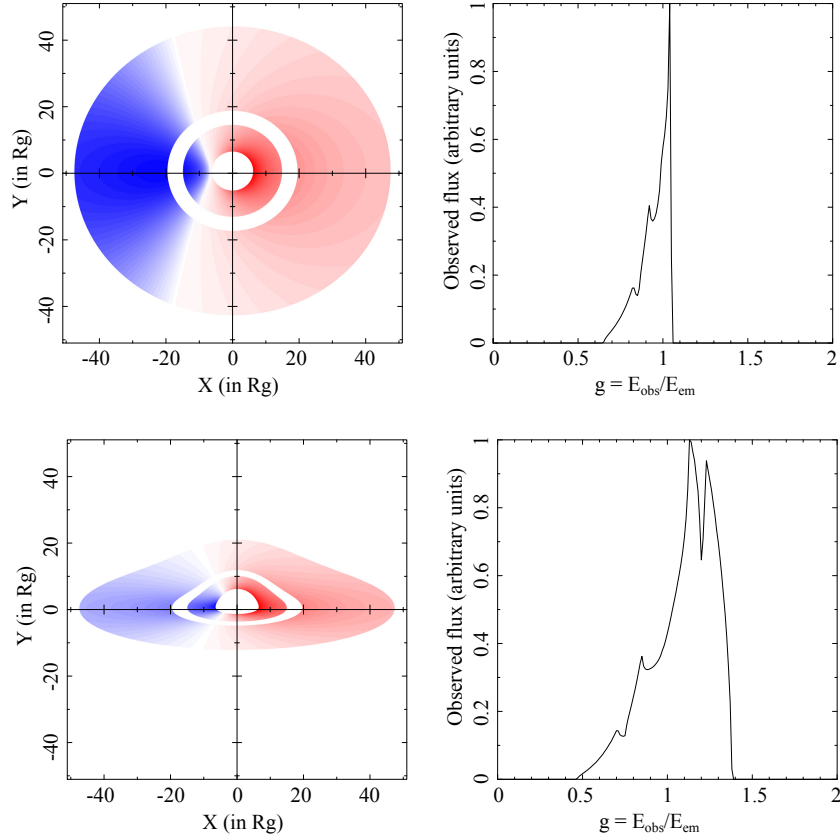


Figure 5. Illustrations of two relativistic accretion disks with an empty gap extending from $15R_g$ to $20R_g$ (*left*), and the corresponding simulated Fe $K\alpha$ line profiles (*right*). Top panel corresponds to the first, and bottom panel to the second model of accretion disks, as described in §2.

We studied the observational signatures of the second SMBHB model using the similar simulations of the X-ray radiation from the accretion disk around its primary SMBH, in which its secondary SMBH cleared an empty gap. We performed these simulations for both disk models from §2 and for different positions and widths of the empty gap, i.e. for different values of its inner and outer radii. Two examples of the obtained results in the case of “disk A” and “disk B”, each with an empty gap extending between $15 R_g$ and $20 R_g$, are shown in the left panels of Fig. 5, while the corresponding simulated Fe $K\alpha$ line profiles are shown in the right panels of the same figure. Taking into account that the gap is formed in the accretion disk around the primary, and for the sake of simplicity, we expressed its radii in the units defined by gravitational radius

$R_g = R_{g1}$ (and mass) of the primary SMBH, in which the both gaps from the left panels of Fig. 5 have the widths of $5 R_{g1}$. On the other hand, the gap width can be also expressed in different units of gravitational radius R_{g2} for the secondary SMBH (or equivalently, in terms of its mass), assuming that it is twice as large as the outer radius of the accretion disk around the secondary, for which we adopted the value of $50 R_{g2}$, as previously mentioned. Under these assumptions: $5 R_{g1} = 100 R_{g2}$, resulting with the following value for the mass ratio of the SMBHB: $q = \frac{R_{g2}}{R_{g1}} = 0.05$, as well as with the mass of the secondary SMBH of $M_2 = 2.5 \times 10^7 M_\odot$. Therefore, this SMBHB has an order of magnitude lower mass ratio than the previously described model, but which is still significantly larger than the limit of $q = 10^{-4}$ below which the secondary SMBH is not able to open a gap in the disk around the primary (see e.g. McKernan et al., 2013, for more details). Another important difference between these two models is an assumption that in the latter case, there is no Fe K α line emission from the gap, i. e. that the "minidisk" around the secondary SMBH (which is embedded in the gap) gives a negligible contribution to the total line emission of the binary. Such scenario is preferable, although one cannot completely exclude a possibility that some gas can enter the gap and feed a "minidisk" around the secondary which, as a consequence, could create some additional Fe K α line emission (see McKernan et al., 2013, and references therein).

It can be seen from Fig. 5 that in such a case an empty annular gap in the accretion disk around primary could have significant influence on the resulting line shape, inducing the appearance of the similar ripples as in the case of the first SMBHB model, which is in good agreement with the results of some previous studies (see e.g. McKernan et al., 2013). However, these ripple effects in the second SMBHB model, besides having the lower amplitudes, strongly depend only on the positions and widths of empty gap (or in other words, on its radii), but they do not noticeably vary with time (or orbital phase), since we assumed that the inner and outer radii of the gap are also time independent. In reality, on the other hand, the secondary SMBH would slowly spiral down towards the primary, so the radii and width of empty gap would also change with time, inducing a slow time variability of the resulting ripple effects.

4. Discussion

As it was shown in the previous section, both studied SMBHB models predict occurrences of the ripples in the cores of emitted Fe K α line profiles. Thus, an important related issue is the possibility to detect such effects in the observed spectra of SMBHB candidates using nowadays and future X-ray detectors, which depends on their spectral resolution and signal-to-noise ratio (S/N).

The presented simulated line profiles were calculated over 200 bins of width $\Delta E = 0.064$ keV, which corresponds to the spectral resolution of $E/\Delta E = 100$

at 6.4 keV. On the other hand, the spectral resolutions of some modern X-ray observatories are: $E/\Delta E \sim 20 - 50$ in the case of XMM-Newton, ~ 600 at 6 keV for Suzaku, and $\sim 100 - 1000$ in 0.1–10 keV range for Chandra. Therefore, the performed simulations provide spectral resolution which is comparable to those of modern X-ray detectors, and according just to this property, the SMBHB signatures in the form of ripple effects in their observed Fe $K\alpha$ line profiles should be detectable even by nowadays X-ray detectors.

However, this is not achievable yet due to insufficient S/N of the modern instruments. Namely, in the ray-tracing simulations S/N depends on the number of photons emitted from a simulated disk (Milošević *et al.*, 2018), which in our case was 5000×5000 . Such a large number of photons in our simulations provides much higher S/N ratio than in the current observations by XMM-Newton and Chandra, which is the main cause for difficult detection of SMBHB signatures in the currently observed line profiles, in spite of similar spectral resolutions. However, the planned future X-ray observatories (like Advanced Telescope for High Energy Astrophysics – ATHENA) will be equipped with high signal-to-noise and high spectral resolution instruments ($E/\Delta E \sim 2800$ in 0.2–12 keV range) and will enable the detection of the SMBHB signatures in the observed Fe $K\alpha$ line profiles.

5. Conclusions

We simulated the Fe $K\alpha$ line profiles emitted from the following two models of SMBHBs:

- (i) a model in which both primary and secondary SMBHs are surrounded by an accretion disk and they are orbiting around their center of mass, and
- (ii) a model in which the secondary SMBH clears an empty gap (or cavity) in the disk around primary.

We can summarize the obtained results of these simulations as follows:

- (i) Both models leave detectable ripples in the emitted Fe $K\alpha$ line profiles which may look like an absorption component in the line profile;
- (ii) In the first model, such ripples in the composite line profiles are caused by Doppler shifts due to orbital motion, and depend on:
 - orbital phase of SMBHB (time) and cause the periodical variability of the line shapes,
 - mass ratio between the secondary and primary SMBHs,
 - parameters of the accretion disks (e.g. inclination) around both primary and secondary,
 - Keplerian orbital elements, which could potentially enable reconstruction of the observed radial velocity curves and their fitting with Keplerian orbits (see e.g. Bon *et al.*, 2012, for an example);

- (iii) In the second model, these ripples do not significantly change in time, but instead:
- they depend on the parameters of the disk around the primary (especially on the disk inclination),
 - their amplitudes strongly depend on the width and distance of the empty gap from the central SMBH, and hence they could be used for constraining the mass ratios and separations between the components in this type of SMBHBs;
- (iv) Spectral resolutions and, especially S/N, of modern X-ray detectors are not sufficient to study in details such signatures of SMBHBs, however this will be possible with the next generation of X-ray observatories, such as ATHENA.

Acknowledgements. This work has been supported by Ministry of Education, Science and Technological Development of the Republic of Serbia, through the projects: 176003 "Gravitation and the Large Scale Structure of the Universe" and 176001 "Astrophysical Spectroscopy of Extragalactic Objects". The authors would like to thank an anonymous referee for very useful and helpful comments and suggestions which significantly improved the presentation of the paper.

References

- Aggarwal, K., et al.: 2019, *Astrophys. J.* **880**, 116
- Ballantyne, D. R., Fabian, A. C.: 2005, *Astrophys. J.* **622**, L97
- Begelman, M.C., Blandford, R.D., and Rees, M.J.: 1980, *Nature* **287**, 307
- Bon, E., Jovanović, P., Marziani, P., Shapovalova, A. I., Bon, N., Borka Jovanović, V., Borka, D., Sulentic, J., Popović, L. Č.: 2012, *Astrophys. J.* **759**, 118
- Cadez, A., Fanton, C., Calivani, M.: 1998, *New Astron.* **3**, 647
- Event Horizon Telescope Collaboration, Akiyama, K. et al.: 2019, *Astrophys. J.* **875**, L1
- Fabian, A. C., Rees, M. J., Stella, L., White, N. E.: 1989, *Mon. Not. R. Astron. Soc.* **238**, 729
- Fabian, A. C., Iwasawa, K., Reynolds, C. S., Young, A. J.: 2000, *Publ. Astron. Soc. Pacific* **112**, 1145
- Fanton, C., Calivani, M., Felice, F., Cadez, A.: 1997, *Publ. Astron. Soc. Jpn* **49**, 159
- Hilditch, R. W.: 2001, *An Introduction to Close Binary Stars*, Cambridge University Press, New York
- Jovanović, P., Popović, L. Č.: 2008, *Fortschr. Phys.* **56**, 456
- Jovanović, P., Popović, L. Č.: 2009, chapter in the book *Black Holes and Galaxy Formation*, Nova Science Publishers Inc, Hauppauge NY, USA, 249-294 (arXiv:0903.0978)
- Jovanović, P., Borka Jovanović, V., Borka, D.: 2011, *Baltic Astron.* **20**, 468

- Jovanović, P.: 2012, *New Astron. Rev.* **56**, 37
- Jovanović, P., Borka Jovanović, V., Borka, D., Bogdanović, T.: 2014, *Adv. Space Res.* **54**, 1448
- Jovanović, P., Borka Jovanović, V., Borka, D., Popović, L. Č.: 2016, *Astrophys. Space Sci.* **361**, 75
- Li, Y.-R., Wang, J.-M., Ho, L.C., Lu, K.-X., Qiu, J., Du, P., Hu, C., Huang, Y.-K., Zhang, Z.-X., Wang, K., and Bai, J.-M.: 2016, *Astrophys. J.* **822**, 4
- LIGO Scientific Collaboration and Virgo Collaboration, Abbott, B.P. et al.: 2016, *Physical Review Letters* **116**, 061102
- McKernan, B., Ford, K. E. S., Kocsis, B., Haiman, Z.: 2013, *Mon. Not. R. Astron. Soc.* **432**, 1468
- Milošević, M., Pursiainen, M., Jovanović, P., Popović, L. Č.: 2018, *Int. J. Mod. Phys. A* **33**, 1845016
- Paczynski, B.: 1977, *Astrophys. J.* **216**, 822
- Planck Collaboration, Aghanim, N. et al.: 2018, *arXiv:1807.06209*
- Popović, L. Č.: 2012, *New Astron. Rev.* **56**, 74
- Reynolds, C. S.: 2014, *Space Science Reviews* **183**, 277
- Safarzadeh, M., Loeb, A., Reid, M.: 2019, *Mont. Not. Royal Astron. Soc.* **488**, L90
- Sesana, A., Roedig, C., Reynolds, M.T., and Dotti, M.: 2012, *Mon. Not. R. Astron. Soc.* **420**, 860
- Sesana, A., Haiman, Z., Kocsis, B., and Kelley, L.Z.: 2018, *Astrophys. J.* **856**, 42
- Shakura, N. I., Sunyaev, R. A.: 1973, *Astron. Astrophys.* **500**, 33
- Yan, C.-S., Lu, Y., Dai, X., Yu, Q.: 2015, *Astrophys. J.* **809**, 117
- Yu, Q., and Lu, Y.: 2001, *Astron. Astrophys.* **377**, 17

On the possible connection between galactic featureless-spectrum sources and stellar-mass black holes

L. Chmyreva¹ and G. Beskin¹

Special Astrophysical Observatory, Nizhnij Arkhyz 369167, Russia

Received: July 31, 2019; Accepted: December 3, 2019

Abstract. The problem of direct detection of a black hole event horizon still remains unresolved. Isolated stellar-mass black holes could be ideal objects for solving this problem, since the event horizon would not be screened by the surrounding interstellar plasma due to its low accretion rate. We search for black hole candidates in their presumed birth locations, computed in the assumption that they could have originated in high-mass binaries. Theories predict that isolated black holes should exhibit featureless flat spectra covering the entire electromagnetic range. Objects classified as DC dwarfs (cool white dwarfs with featureless continuum spectra) are among such galactic sources, and they also constitute a good sample for searching for possible black hole candidates among them. We analyze sources with available spectral, photometric, and proper motion data. The final list contains 5 sources that fit the selection criteria.

1. Introduction

Direct detection of a black hole (BH) event horizon is a problem that still remains largely unsolved. Searching for isolated stellar-mass black holes, spherically accreting interstellar medium (ISM) of low density, is of great importance, as such objects are ideal for detecting and studying the event horizon. The spectrum of such a black hole was first calculated by Shvartsman (1971). He demonstrated that an emitting halo of accreted matter forms around such objects and generates optical featureless emission. The majority of such emission comes from the regions near the horizon, at approximately $(3 - 5)r_g$, where r_g is the Schwarzschild radius. It is therefore possible to observe the interaction of a BH with its surrounding environment.

An isolated stellar mass black hole would be subject to low-rate ($10^{-6} - 10^{-9} \dot{M}_{Edd}$) spherical accretion of the ISM. It should exhibit synchrotron emission in the increased magnetic field if (1) the thermal electrons are in the range of $10^{14} - 10^{16}$ Hz and (2) the nonthermal ones are in the range of $10^{16} - 10^{19}$ Hz. This combination of both radiated components yields a practically flat spectrum from infrared to γ -rays. The hard spectral component is highly variable due to the emission of nonthermal electron blobs (for details, see Beskin & Karpov

2005, and references therein). For typical ISM parameters, a BH seen from a distance of 100 pc would exhibit the following features:

- 16 – 25^m optical source
- highly variable bright X-ray counterpart
- variable component of optical emission $\sim 18 - 27^m$
- time scale of the variability $\sim 10^{-4}$ s
- relative flare amplitudes $\sim 0.2 - 6\%$ in various spectral bands
- proper motion.

Spherical accretion onto isolated stellar-mass black holes has been investigated by numerous authors, including early works of Zeldovich & Novikov (1971); Novikov & Thorne (1973); Shapiro (1973); Bisnovatyi-Kogan & Ruzmaikin (1974); Meszaros (1975). The first solution to the spherical accretion problem was derived by Bondi (1952). Spectra for the resulting accretion flow were calculated by Ipser & Price (1982) and McDowell (1985). Heckler & Kolb (1996) proposed searching for isolated black holes using data from the Sloan Digital Sky Survey (SDSS). Their estimates used a spherical accretion model, and the method of Ipser & Price (1982) was used to compute the spectrum. Chisholm et al. (2003) searched for nearby isolated BH using optical and X-ray data and reported the positions and colors of 55 BH candidates and estimated their likelihood to be black holes.

As we mentioned above, theories predict that the main observational manifestation of a BH is a featureless flat spectrum (Shvartsman 1971; Beskin & Karpov 2005). In this work, we seek sources with flat spectra and no significant spectral features over a large range of wavelengths, very fast variability, and luminosity within the predicted boundaries. Our search for possible candidates consists of two parts:

- a search restricted to specific regions in the sky as described below, and
- a general search involving an all-sky investigation of featureless-spectrum sources such as DC dwarfs (cool white dwarfs with helium-dominated atmospheres and featureless spectra with no lines) and BL Lacertae.

2. Method

In the first part, the sky regions where the search was performed are determined as follows. With at least 50% of stars known to be members of binary or multiple systems (Batten, 1967; Duquennoy & Mayor, 1991; Halbwachs et al., 2003), it is safe to assume that many BHs, as well as relatively young neutron stars (NS) that we observe as radio pulsars, originated in high-mass binaries. In BH+NS pairs, the more massive BH would have formed in the first supernova explosion in the system, which has a roughly 40% chance of staying gravitationally bound (Bethe & Brown 1998). The second supernova explosion, in which a pulsar is born, generally disrupts the system. The high velocities pulsars obtained in the

process (Hobbs et al. 2005) can be used to trace them back to their birthplaces, restricting therefore the BH-candidate search area (Prokhorov & Popov, 2002; Chmyreva et al., 2010).

In the second part, work on which is now in progress, the search for BH candidates is not restricted to specific regions, but is done throughout the whole sky. Such a search would concentrate on sources with already measured spectra available in public databases. Specifically, we are looking for sources with featureless flat spectra across the entire electromagnetic range, as described above and fitting the other criteria. To this end, we investigate the available catalogs for white dwarfs of DC spectral type, BL Lacertae objects that have not been confirmed and might be galactic sources with proper motions available in GAIA Data Release 2, and also any objects marked as "unknown" and whose spectra have no significant lines and could not be classified. A high signal-to-noise ratio is desired, since noisy spectra cannot be truly considered featureless. Such sources are then analyzed according to the other selection criteria described above.

3. Candidate selection

In order to identify the regions in the sky suitable for the search according to the first part of the method, we created an initial sample of 16 isolated radio pulsars with measured proper motions and parallaxes, relatively small spin-down ages, and no previous associations that fit the criteria. To compute the sky-projected areas of their births, 100,000 trajectories were simulated for each pulsar, tracing them back according to their age estimates. The birthplaces of 4 youngest pulsars in the sample, J0139+5814, J0922+0638, J0358+5413, and J1935+1616, the first two of which are shown in Figure 1 as an example, have demonstrated the best results and were analyzed for possible objects of interest.

We used publicly available databases including but not limited to ROSAT, FERMI, XMM-Newton, FIRST, WISE, 2MASS, GALEX, SDSS, SIMBAD, ATNF, NED, LAMOST. First, we selected all non-optical sources that fall into the 3-sigma contours of the pulsar birth locations (5 γ -ray sources, 250 X-ray sources, 1800 radio sources). These non-optical sources were then cross-identified with each other and with possible optical counterparts within their positional error ellipses. For this, we used the SDSS database (where available), and other catalogs otherwise. We constructed spectral energy distributions (SEDs) for the candidates with a hard-energy range component, and demonstrated that they are very similar to those of BL Lacertae objects. In addition to sources with a hard component, we also considered optical sources classified as blue objects and white dwarfs, as their observational manifestations are similar to those of the objects of interest. The spectra of 14 of the pre-selected candidates are shown in Figure 2. The spectrum of another candidate classified as a DC-type dwarf is shown in Figure 3.

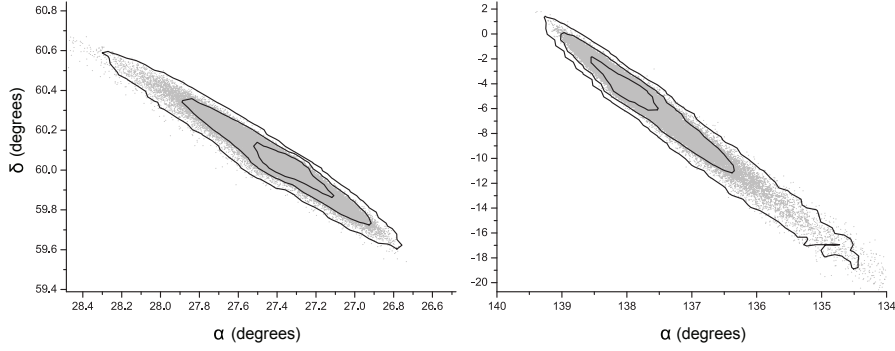


Figure 1. Simulated birthplaces of pulsars J0139+5814 (left) and J0922+0638 (right). The axes show the right ascension (α) and declination (δ).

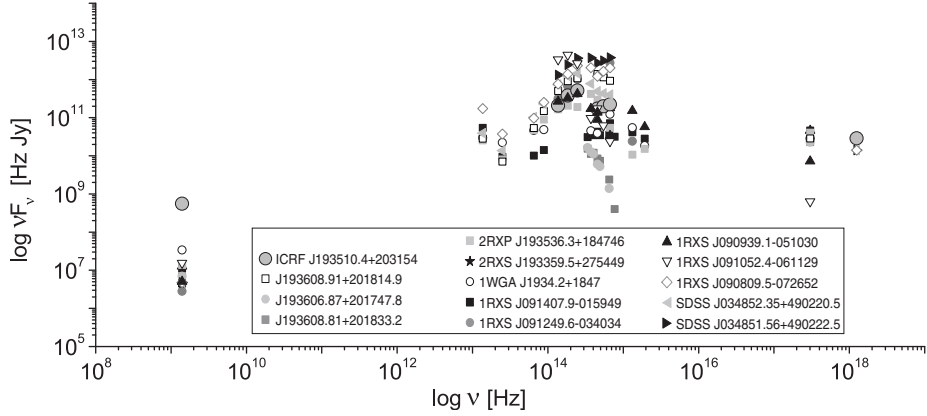


Figure 2. Spectra of 14 pre-selected candidates with a hard component. The object names are specified in the box. The larger grey circles indicate the only source among the 14 that has a γ -ray component.

After this pre-selection, the sample of candidates consisted of 94 objects, including several multiple identifications of a single source, which were eliminated at the later stages of analysis. We then proceeded to eliminate the candidates using the following criteria. First, we checked the sample for artifacts and crossed off the list all sources with unreliable photometry, as well as extended and polarized sources. Several sources with clearly stellar, galactic, and quasar spectra, as well as spectra which clearly showed lines were also eliminated. The GAIA DR2 database allowed us to use accurate parallax (distance) and proper motion measurements, further restricting the sample to contain only sources with distances

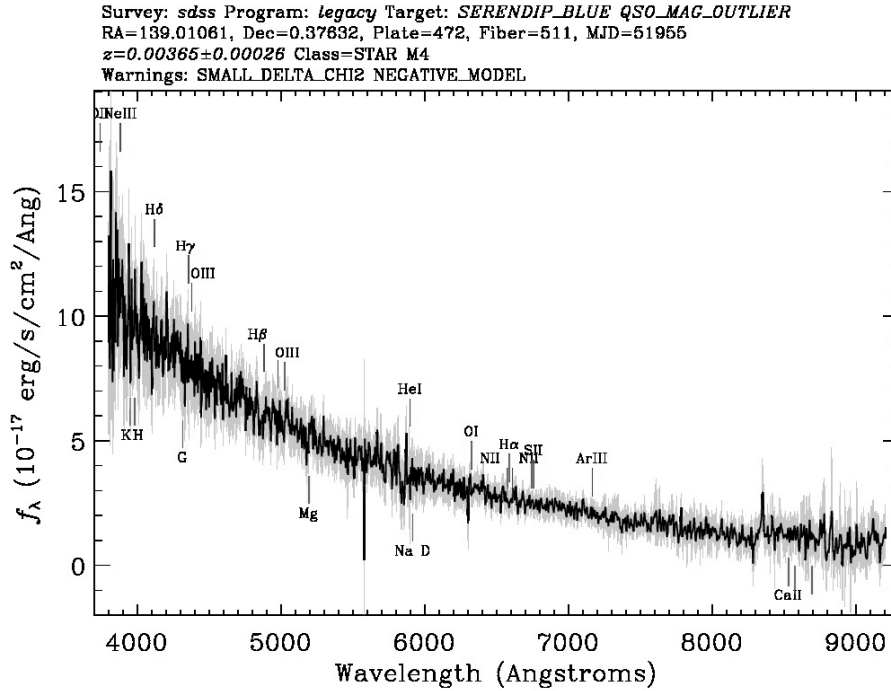


Figure 3. SDSS spectrum of a candidate classified as a DC-type dwarf.

and velocities which would place them inside the (3D) birth location boundary. We then discarded objects with no measured proper motions or proper motions with a large error, as such sources cannot be reliably considered as galactic. The remaining sources were faint and had no spectral data available, and we therefore used SDSS *ugriz*, *BVR*, or *JHK* colors depending on the available photometry to classify them. For well-measured sources, we simply used a Planck curve fit to eliminate stars. For sources with only a few points measured, we used color-color diagrams to keep only the sources located primarily in the regions dominated by white dwarfs and quasars. After this procedure, we were left with a list of 12 candidates. None of them have variability measurements. Four of these candidates have insufficient data available to reject them, and we therefore keep them on the list for now. For the remaining 8 sources, we used the relation described by Beskin & Karpov (2005), specifically, formula (77) in that paper, to compute the theoretical luminosities expected for a stellar-mass BH located at the point in space where the candidates are. We took into account the ISM densities (calculated using the 3D distribution of dust in the galaxy (Green et al., 2018) and the total column density of interstellar hydrogen), distances and proper motions from GAIA DR2. Using theoretical BH masses and space velocities estimated

from proper motions, we computed a grid of magnitudes possible for a BH located in this region of the galaxy. After comparing these computed magnitudes with those of the candidates, we rejected a further 3 sources. The remaining 5 sources fit the luminosity criteria: J035738.16+525934.4, J035757.63+525928.7, J193559.9+205305.7, J035717.10+511525.4, J035239.08+513344.1. These are all faint sources, $m_V \sim 19$ -21, located within 300 pc. Two of them have hard components. Figure 4 shows the computed magnitude distributions for BHs located at the positions of these 5 sources. These candidates, as well as the 4 with insufficient data for rejection were marked for further investigation. The subject of our future work would involve obtaining spectra for these sources and checking their variability.

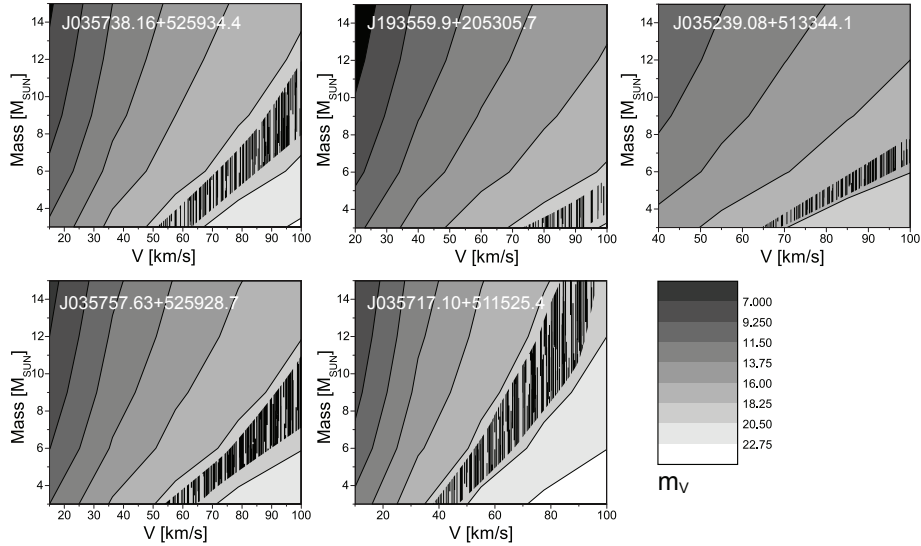


Figure 4. Theoretical magnitude distribution for BHs located at the positions of the 5 candidates. The positions of these sources are marked by black. The name of the object is indicated at the top of each graph in white.

In the second part of our work, now in progress, we seek BH candidates throughout the whole sky, not restricted to specific sky regions. We now concentrate on objects for which the spectra are already measured and publicly available. Databases like SDSS, LAMOST, and others, have a number of objects whose spectra are marked as "unknown" due to either a lack of spectral features, or poor quality. Some examples of such spectra are shown in Figure

5. These sources and others with similar featureless spectra are of primary interest to us, especially if they have counterparts in other spectral domains. A high signal-to-noise ratio is preferred in order to rule out the presence of lines with equivalent widths $> 5\text{\AA}$. Therefore, DC-type white dwarfs, unconfirmed BL Lacertae objects, and sources of unidentified spectral type with no significant spectral features are our primary objects of interest in the corresponding catalogs. Such sources will be analyzed further using the method described above in order to refine their classification. Those among them that are shown to fit the other selection criteria may be considered as BH candidates. These results will be published in our upcoming paper.

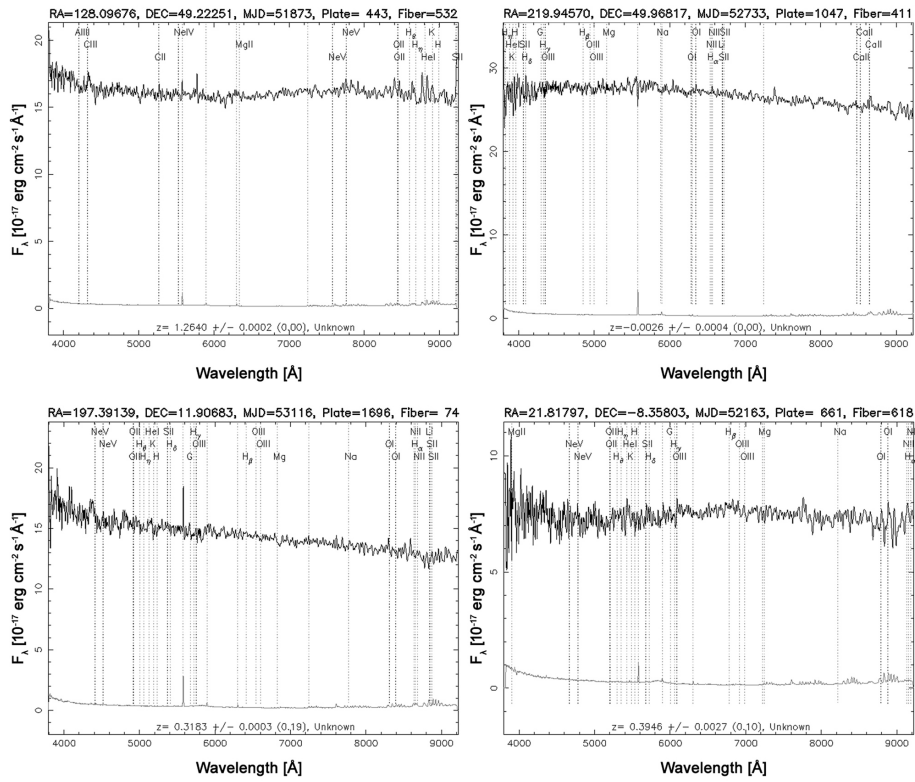


Figure 5. Examples of unidentified spectra in the SDSS.

4. Results

We have performed a search for stellar-mass BH candidates. Looking for BHs is an important task directly related to the problem of direct detection of BH event horizons, for which they can be viewed as ideal probes. Many now-isolated BHs may have originated in high mass binaries where the other component is a neutron star. Tracing the trajectories of the neutron stars to their birth places, we placed restrictions on the locations of possible BH candidates, deriving four promising regions in the sky for the search.

Within those areas, we selected all sources with a hard spectral component, and identified them with their optical counterparts using the SDSS database. Blue objects and DC-dwarfs were also considered. A list of 94 candidates was made in the process, from which we eliminated all sources with unreliable photometry, as well as extended and polarized sources. The several objects with available spectra were also crossed off the list due to their clearly stellar, galactic, or quasar nature. We then used the accurate parallax and proper motion data from the GAIA database to further restrict the sample to objects located within the considered spatial region. Multi-band photometric data were used to classify the remaining sources, thereby shortening the list down to 12 objects.

Theoretical luminosities were then computed for stellar-mass BHs located at the positions of the candidates. The theoretical magnitudes were compared with the observed ones, which allowed us to finalize the preliminary list of BH candidates which fit the observational criteria. There are 5 sources on the list; their coordinates are as follows (α , δ): 03:57:38.19 +52:59:34.4, 03:57:57.64 +52:59:29.1, 19:35:59.92 +20:53:07.0, 03:57:17.10 +51:15:25.4, 03:52:39.09 +51:33:44.1. Long-term observations of these sources are planned as the next step to narrow the list down further, both to obtain their spectra and monitor them for photometric variations (no spectra or variability information are currently available for these objects). Such observations would allow us to obtain evidence that one or more of these sources are, in fact, possible BHs.

5. Conclusions

We have performed a search for stellar-mass black hole candidates within 4 restricted regions of space, computed in the assumption that BHs have originally formed in high-mass binaries. The search in these areas yielded a list of 5 candidates, J035738.16+525934.4, J035757.63+525928.7, J193559.9+205305.7, J035717.10+511525.4, and J035239.08+513344.1, which may be considered as a preliminary result. These 5 sources were targeted for further investigation, and will be observed in order to obtain their spectra, as well as data on their variability. This result shows that at least several sources fit the selection criteria (are consistent with the theoretical expectations of a stellar mass black hole as observed from Earth), and that a full-sky search will provide many more

candidates. This full-sky search, as well as obtaining observed data for the 5 candidates, is the subject of our upcoming work.

References

- Batten, A. H. 1967, *Ann. Rev. Astron. Astrophys.*, **5**, 25
- Beskin, G. M. & Karpov, S. V. 2005, *Astron. Astrophys.*, **440**, 223
- Bethe, H. A. & Brown, G. E. 1998, *Astrophys. J.*, **506**, 780
- Bisnovatyi-Kogan, G. S. & Ruzmaikin, A. A. 1974, *Astrophys. Space Sci.*, **28**, 45
- Bondi, H. 1952, *Mon. Not. R. Astron. Soc.*, **112**, 195
- Chisholm, J. R., Dodelson, S., & Kolb, E. W. 2003, *Astrophys. J.*, **596**, 437
- Chmyreva, E. G., Beskin, G. M., & Biryukov, A. V. 2010, *Astronomy Letters*, **36**, 116
- Duquenooy, A. & Mayor, M. 1991, *Astron. Astrophys.*, **500**, 337
- Green, G. M., Schlafly, E. F., Finkbeiner, D., et al. 2018, *Mon. Not. R. Astron. Soc.*, **478**, 651
- Halbwachs, J. L., Mayor, M., Udry, S., & Arenou, F. 2003, *Astron. Astrophys.*, **397**, 159
- Heckler, A. F. & Kolb, E. W. 1996, *Astrophys. J., Lett.*, **472**, L85
- Hobbs, G., Lorimer, D. R., Lyne, A. G., & Kramer, M. 2005, *Mon. Not. R. Astron. Soc.*, **360**, 974
- Ipsier, J. R. & Price, R. H. 1982, *Astrophys. J.*, **255**, 654
- McDowell, J. 1985, *Mon. Not. R. Astron. Soc.*, **217**, 77
- Meszaros, P. 1975, *Astron. Astrophys.*, **44**, 59
- Novikov, I. D. & Thorne, K. S., *Black holes (Les Astres Occlus)*, Edited by C. DeWitt and B. DeWitt, Gordon and Breach, N.Y. 1973, 343–450
- Prokhorov, M. E. & Popov, S. B. 2002, *Astronomy Letters*, **28**, 536
- Shapiro, S. L. 1973, *Astrophys. J.*, **180**, 531
- Shvartsman, V. F. 1971, *Soviet Astron.*, **15**, 377
- Zeldovich, Y. B. & Novikov, I. D., *Relativistic astrophysics. Vol.1: Stars and relativity*, University of Chicago Press. 1971

Quasar emission lines as virial luminosity estimators

P. Marziani¹, E. Bon², N. Bon², M.L. Martinez-Aldama³,
G.M. Stirpe⁴, M. D’Onofrio⁵, A. del Olmo⁶, C.A. Negrete⁷
and D. Dultzin⁷

¹ *National Institute for Astrophysics (INAF), Padua Astronomical Observatory, Padua, (E-mail: paola.marziani@inaf.it) Italy*

² *Astronomical Observatory, Belgrade, Serbia*

³ *Center for Theoretical Physics, Polish Academic of Sciences, Warsaw, Poland*

⁴ *INAF - Osservatorio Astrofisica e Science dello Spazio, Bologna, Italy*

⁵ *Dipartimento di Fisica ed Astronomia “Galileo Galilei,” Università di Padova, Padova, Italia*

⁶ *Instituto de Astrofisica de Andalucia (CSIC), Granada, Spain*

⁷ *Instituto de Astronomia, UNAM, Mexico, D.F., Mexico*

Received: July 30, 2019 ; Accepted: August 22, 2019

Abstract. Quasars accreting matter at very high rates (known as extreme Population A [xA]) may provide a new class of distance indicators covering cosmic epochs from present day up to less than 1 Gyr from the Big Bang. We report on the developments of a method that is based on “virial luminosity” estimates from measurements of emission line widths of xA quasars. The approach is conceptually equivalent to the virial estimates based on early and late type galaxies. The main issues related to the cosmological application of luminosity estimates from xA quasar line widths are the identification of proper emission lines whose broadening is predominantly virial over a wide range of luminosity, and the assessment of the effect of the emitting region orientation with respect to the line of sight. We report on recent developments concerning the use of the AlIII λ 1860 intermediate ionisation line and of the Hydrogen Balmer line H β as “virial broadening estimators.”

1. Introduction: a main sequence for quasars

The Main Sequence (MS) is a powerful tool to organize type-1 quasar diversity (see e.g., Marziani et al., 2018, for a recent review). The MS concept originated from the first eigenvector (E1) of a Principal Component Analysis carried out on a sample of ≈ 80 Palomar-Green quasars (Boroson & Green, 1992). The E1 MS was first associated with anti-correlations between strength of FeII λ 4570 and width of H β as well as strength of FeII λ 4570 and [OIII] prominence. Over

the years, several parameters related to the accretion process and the accompanying outflows were found to be also associated with the fundamental relation between prominence of singly-ionized iron emission and broad Balmer line width (Sulentic et al., 2000, 2007). For an exhaustive list see Sulentic et al. (2011); Fraix-Burnet et al. (2017). Since 1992, the E1 MS has been found in increasingly larger samples, and the MS potential was fully recognized following an SDSS-based analysis of a large sample of several tens of thousands of quasars (Shen & Ho, 2014).

The optical plane of the MS is defined by the FWHM of the $H\beta$ broad component vs the parameter R_{FeII} that is defined as $R_{\text{FeII}} = I(\text{FeII}\lambda 4570)/I(H\beta)$, the ratio between the integrated flux of the FeII λ 4570 blend of multiplets, and that of the $H\beta$ broad component (Sulentic et al., 2000). The data are distributed as an elbow-shaped figure (Fig. 1) if a restriction to low- z and relatively low luminosity is applied; if higher luminosity sources are included the MS takes a wedge-like form (as in case of Shen & Ho 2014).

It is not surprising that a measure of FeII emission can lead a fundamental correlation, as singly-ionized emission is extended from the UV to the NIR, and can dominate the thermal balance of the broad line region (BLR, Marinello et al., 2016). FeII emission is self-similar but its intensity with respect to Hydrogen Balmer line $H\beta$ changes. The width of $H\beta$ is mainly associated with the broadening due to the emitting gas dynamics via Doppler effect. A correlation between the two parameters points towards a coupling between physical and dynamical conditions within the line emitting region, as further discussed in § 2.

Quasar spectra show a wide range of line profiles, line shifts, line intensities and differences in dynamical conditions and ionization levels of the BLR, systematically changing along the sequence. It is expedient to identify spectral types along the MS (Fig. 1) and to distinguish between Population A ($\text{FWHM}(H\beta) \leq 4000 \text{ km s}^{-1}$) and Population B ($\text{FWHM}(H\beta) > 4000 \text{ km s}^{-1}$). Pop. A sources include prototypical Narrow Line Seyfert 1 IZw1 as well as sources with relatively little FeII, such as Mark 335. The appearance of the spectrum suggests a relatively low degree of ionization, with significant FeII, weak [OIII] $\lambda\lambda$ 4959,5007 and weak high-ionization lines in general. Pop. B objects show not only broader lines but also higher ionization, weak FeII and strong [OIII]. A prototypical source is NGC 5548 (Sulentic et al., 2000). Regarding internal line shifts in the spectra of individual quasars, it is helpful to distinguish between low- and high-ionization lines (HILs and LILs). Internal line shifts between HILs and LILs are mainly associated with HIL blueshifted emission.

The MS is probably due to a combination of effects dependent on Eddington ratio, viewing angle, and metal content (Panda et al. 2019 and references therein). The connection between observational and accretion parameters is not well-mapped as yet, but the quasar MS could be aptly considered as the analogous of the MS in the stellar H-R diagram (Sulentic et al., 2001, 2008).

Even if our understanding is not complete, it is possible to exploit some well-defined properties in particular sectors “spectral types” along the MS. A second key element that makes it possible to consider quasars even as “Eddington standard candles” (i.e., sources with a small scatter around a fixed value of the Eddington ratio in place of a luminosity measure) has been the ability to recognize that the part of the BLR emitting the LIL is eminently virialized. In the following we will summarize in which way quasar emission lines can be considered as virial broadening estimators (VBE, §2) and identify a particular class of quasars (§3) for which the assumption of an almost constant Eddington ratio is likely to be verified. We stress the analogy with stellar systems (§4.1) and consider redshift-independent estimates of luminosity made possible by the scaling between virial broadening and luminosity itself (§5).

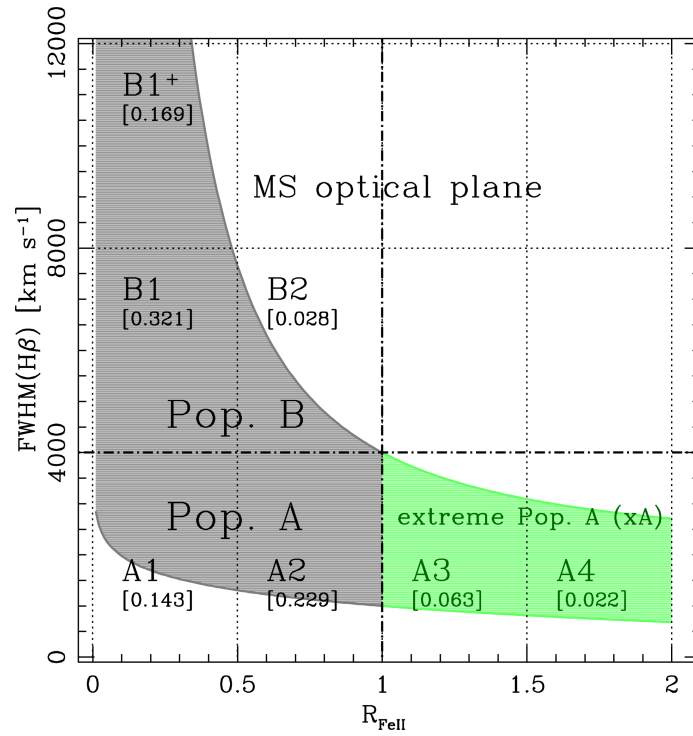


Figure 1. A sketch outlining the occupation of optical plane of the quasar MS. The plane has been subdivided in spectral types, and the region of extreme Population A has been shaded green. The numbers in square brackets are the relative prevalence in the ST along the sequence, from the sample of Marziani et al. (2013a).

2. A virialized and a wind system

The origin of the broadening of quasar emission lines has been a contentious issue for decades after quasar discovery and it is as yet not fully understood. Reverberation-mapping campaign have provided direct evidence of a large mass concentration in a very small volume of space, with broadening for lines emitted by different ionic species becoming larger and their distance decreasing with increasing ionisation potential (Peterson & Wandel, 1999). At the same time, internal line shifts (measured soon after the quasar discovery, Burbidge & Burbidge 1967) complicated the interpretation of the spectra of individual quasars. A turning point was the ability offered by the FOS on board HST to observe the HIL CIV 1549 and to compare it to a strong LIL such as $H\beta$ (Corbin & Boroson, 1996; Marziani et al., 1996). It was found that the CIV line showed prominent blueshift while the $H\beta$ remained almost unshifted with respect to the rest frame of the quasars. If we assume that a line whose profile appears symmetric and unshifted with respect to rest frame can be considered as a marker of a virialized emitting region, this result provided support to the idea that the BLR were composed of two sub-regions, one emitting predominantly HIL in an outflow scenario and one associated with a flattened distribution of gas coplanar with the accretion disk (possibly the accretion disk itself, Collin-Souffrin et al. 1988; Elvis 2000; see Fig. 2). Later, it was found that a virialized system emitting mainly LILs coexists with outflowing gas in Pop. A sources, even at the highest luminosity (Sulentic et al., 2017; Vietri, 2017; Coatman et al., 2017).

3. Extreme Population A

Selection and physical conditions of Extreme Population A is made possible by the MS that allows for the definition of spectral types, in addition to the two Populations defined earlier. Spectral types within Pop. A are due to a gradient of R_{FeII} (Boroson & Green, 1992; Sulentic et al., 2000; Shen & Ho, 2014; Du et al., 2016; Panda et al., 2019).

Extreme Pop. A quasars (xA) are selected applying simple criteria from diagnostic emission line intensity ratios:

1. $R_{\text{FeII}} \text{ FeII}\lambda 4570 \text{ blend}/H\beta \gtrsim 1.0$;
2. $\text{UV AIII } \lambda 1860/\text{SiIII } \lambda 1892 \gtrsim 0.5$ and $\text{SiIII } \lambda 1892/\text{CIII } \lambda 1909 \gtrsim 1$

UV and optical selection criteria are equivalent, and lead to the identification as xA of $\sim 10\%$ of all quasars in low- z , optically selected samples. xA spectra show distinctively strong FeII emission and Lorentzian Balmer line profiles, and $\text{FWHM}(H\beta) \approx \text{FWHM}(\text{AIII } 1860)$ whenever it has been possible to cover both lines for the same object (Negrete et al. 2013; Marziani & Sulentic 2014). This means that the AIII 1860 FWHM is a virial broadening estimator equivalent to $H\beta$ (del Olmo et al. 2019, in preparation). The measurements of the 1900 blend

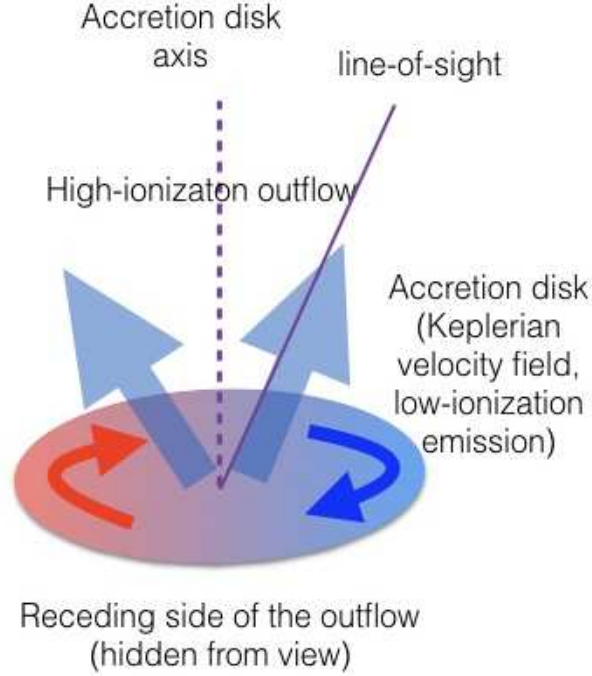


Figure 2. A sketch illustrating the principle of a virialized sub-region co-existing with an outflowing component. The sketch is highly simplified and accounts for the systematic blueshifts of HILs, large when the HI Balmer lines are narrower, but does not take into account the systematic changes in accretion modes expected along the sequence.

and specifically of the AlIII line allows for the consideration of xA quasars at high z ($\gtrsim 1.2$).

The UV spectrum of xA quasars at $z \sim 2$ shows symmetric low-ionization and blueshifted high-ionization lines even at the highest luminosity (Martínez-Aldama et al. 2018, and reference therein). The CIV and the 1900 blend lines have low equivalent width: about one-half of xAs are weak lined quasars following the definition of Diamond-Stanic et al. (2009).

Observed diagnostic ratios (CIV/AlIII, CIV/HeII, AlIII/SiIII) imply extreme values for density (high, $n \gtrsim 10^{12-13} \text{ cm}^{-3}$), ionization (low, $U \sim 10^{-3}$) and extreme values of metallicity ($Z \gtrsim 20Z_{\odot}$, Martínez-Aldama et al. 2018, Sniegowska et al. 2019 in preparation). These values are inferred by considering curves of constant intensity ratios in the plane ionization parameter versus density from arrays of CLOUDY simulations (Negrete et al., 2012). A crossing

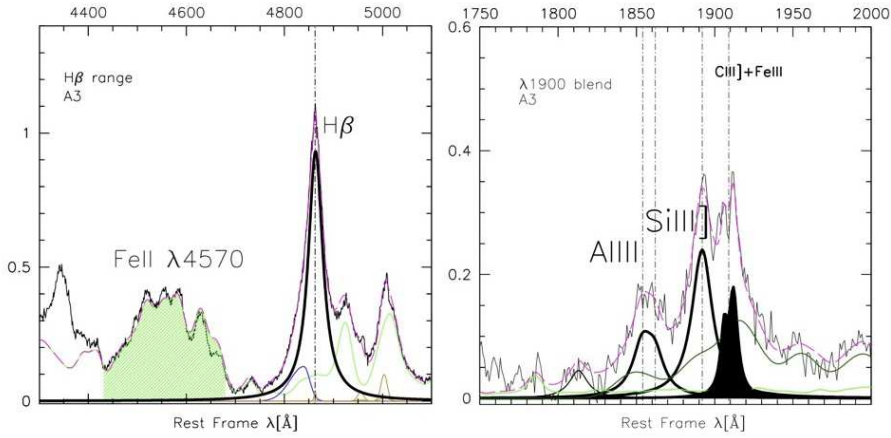


Figure 3. Examples of the $H\beta$ (left, Marziani et al. 2013b) and 1900 \AA (right, Bachev et al. 2004) spectral region (after continuum subtraction) in low redshift extreme Eddington candidates, selected from the optical criterion $R_{\text{FeII}} > 1$. The ratio R_{FeII} is obtained by measuring the flux of the FeII blend at 4570 \AA (pale green shaded area), and the flux of $H\beta$. The thick black lines trace broad lines whose FWHM can be used as virial broadening estimator, $\text{AlIII}\lambda 1860$, $\text{SiIII]}\lambda 1892$, and $H\beta$ but not $\text{CIII]}\lambda 1909$ (shaded dark). $H\beta$ and the UV lines have been found to provide consistent FWHM measures in agreement with $H\beta$ at low- L . Green lines show FeII templates (pale), and the FeIII template in the UV (dark). The magenta dashed lines show models of the total line emission.

point defined by the isopleth of constant intensity ratios identifies the physical conditions that predict all considered intensity ratios. The very high density inferred from the weakness of $\text{CIII]}\lambda 1909$, and the maximum radiative output per unit mass suggests that the LIL Emitting regions could be a dense compact remnant of a more conventional LIL-BLR.

4. Extreme Population A quasars: virial broadening

There are several lines of evidence suggesting that the R_{FeII} is correlated with Eddington ratio. Among them, we mention the fundamental plane of the accretion black holes correlations (Du et al., 2016) which is a restatement of the correlation of Eddington ratio R_{FeII} , adding a second correlate associated with the LIL profile. Extreme Population A ($R_{\text{FeII}} \gtrsim 1$) show extreme L/L_{Edd} along the MS with small dispersion (Marziani & Sulentic, 2014) (MS14). Accretion disk theory predicts low radiative efficiency at high accretion rate; L/L_{Edd} saturates toward a limiting values; (Mineshige et al., 2000; Abramowicz et al., 1988; Sadowski, 2011). This seems to be what is occurring to xA sources.

A virial luminosity estimate for large samples of xA quasars is possible if:

1. xA quasars radiate close to Eddington limit $L/L_{\text{Edd}} \propto L/M_{\text{BH}} \sim 1$. The exact value of the the Eddington ratio is not relevant, provided that L/L_{Edd} scatters little around a well-defined value. At this point we are able to recognize only xA quasars at one extreme of the MS, but the same approach could be applied to other sources along the MS, were their Eddington ratio known with high precision.
2. Virial motions are the broadening source of the low-ionization BLR.
3. xA quasars have similar BLR physical parameters, an assumption that is justified by the spectral similarity over a large range in luminosity. This implies that BLR radius rigorously scales with the square root of the luminosity.

If we know a virial broadening estimator δv (in practice, the FWHM of a low-ionization line), we can derive a z -independent, “virial” luminosity, $L_{\text{vir}} \propto (n_{\text{H}}U)^{-1}(\delta v)^4$. The virial luminosity can be written as $L = \mathcal{L}_0 \text{FWHM}^4$, where the constant depends on the fraction of ionizing luminosity, the average frequency of ionizing photons, and the photon flux. These are all intrinsic properties of quasars.

4.1. $L \propto (\delta v)^a$: not only for quasars

The $L \propto \text{FWHM}^4$ is a law analogous to the Tully-Fisher and the early formulation of the Faber Jackson laws for early-type galaxies (Faber & Jackson, 1976; Tully & Fisher, 1977). Galaxies and even clusters of galaxies are virialized systems that globally follows a law $\propto \sigma^4$ (Fig. 4). The main difference with quasars is that the velocity dispersion of stellar system is by far not as strongly dependent on the viewing angle as the FWHM of quasar LILs.

5. Interpretation of the virial luminosity estimates for quasars

5.1. Virial luminosity and redshift-based luminosity

The sketch of Fig. 2 suggests that the viewing angle of the plane of the accretion disk should substantially affect the projection of the virial velocity field along the line-of-sight. In other words, the FWHM is strongly dependent on the viewing angle θ defined as the angle between the line of sight and the axis of the accretion disk plane.

The virial luminosity is applicable to xA quasars over a wide range of luminosity and redshift. If we compare the virial luminosity to the conventional estimate of luminosity from redshift, H_0 and the Ω_s we find that there is an overall consistency with redshift-based concordance luminosity. At the same time we

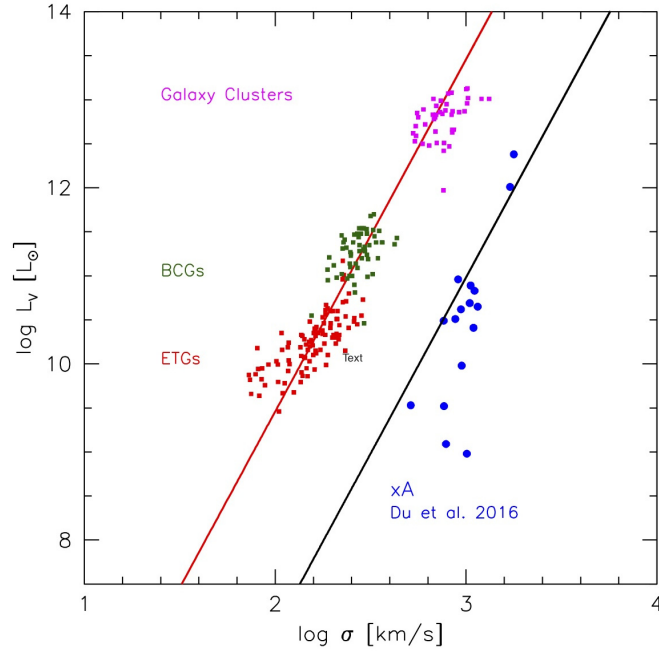


Figure 4. Relation between virial broadening and luminosity, for several classes of virialized stellar systems and quasars. Data points refers to early-type galaxies (ETGs, red squares), brightest cluster galaxies (BCGs, dark-green squares), clusters of galaxies (magenta squares) from the wide-field nearby galaxy-cluster survey and are as used in D’Onofrio et al. (2019), and xA quasars from the sample of Du et al. (2016). The filled lines trace two relations with $L \propto \sigma^4$.

measure a significant scatter $\sigma \sim 0.5$ dex (Fig. 5; 0.3 dex can be reached by improving the statistics of larger samples, as done in Marziani et al. 2017, but a substantial statistical scatter is expected to remain even in large samples of excellent data).

An analysis aimed at the cosmological exploitation of the virial luminosity is ongoing. Work to improve the accuracy of black hole mass and Eddington ratio using θ is also in progress. At this point, however, it is perhaps more interesting to try to understand the origin of the scatter between virial luminosity and conventional luminosity $L(z, H_0, \Omega_M, \Omega_\Lambda)$, where the cosmological parameter have been assumed to have values consistent with the concordance ones.

The difference between the virial L and $L(z, H_0, \Omega_M, \Omega_\Lambda)$ as a function of redshift for the sample of Negrete et al. (2018) is shown in the left panel of Fig. 5. The scatter is due in part to measurement errors. The FWHM enters to the fourth power in the L expression; a 10% error, achievable with high S/N

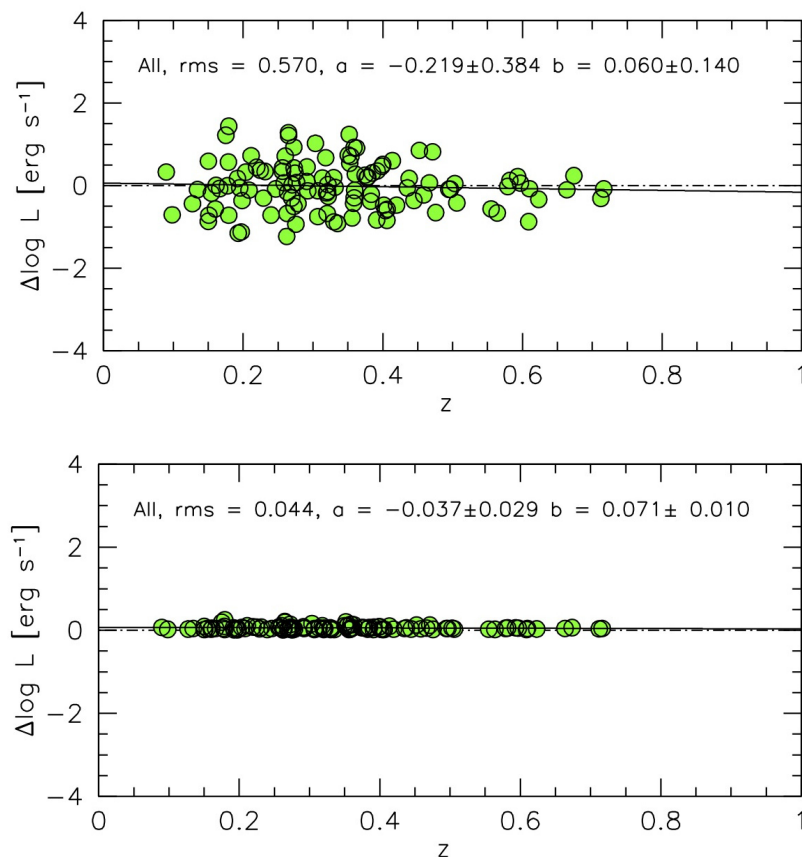


Figure 5. Quasar luminosity estimates: residuals as a function of redshift z of virial luminosity estimated from the $H\beta$ FWHM minus luminosity $L(z, H_0, \Omega_M, \Omega_\Lambda)$ from redshift before orientation correction (above), and after (below). Data are from the low- z quasar sample of Negrete et al. (2018).

data would imply a ≈ 0.17 dex error on luminosity (see Marziani & Sulentic 2014 for a preliminary error budget). More than measurement errors, it is likely that orientation accounts for most of the scatter, especially if lines are emitted in a flattened system. There is growing evidence that this is the case (Mejía-Restrepo et al., 2018; Afanasiev et al., 2019; Marziani et al., 2019) although the expression of the form factor connecting virial broadening δv_K and line FWHM ($\delta v_K^2 = f \text{FWHM}^2$) in the form $f = 1/4(\kappa^2 + \sin^2 \theta)$, where κ can be interpreted as the ratio between an isotropic velocity component and the

virial velocity, we found that all objects in the sample of Negrete et al. (2018) can be accounted for by the effect of the viewing angle within $0 \lesssim \theta \lesssim 50$ degrees (in the right panel of Fig. 5 residuals are zeroed if $f^{1/2}\text{FWHM}$ is used as a VBE). Orientation might be really the main source of scatter between virial and conventional luminosity estimates. More details are given by Negrete et al. (2018), and a more conclusive analysis will be hopefully presented in forthcoming studies.

6. Conclusion

The MS offer contextualization of quasar observational and physical properties. Extreme Population A (xA) quasars at the high R_{FeII} end of the MS appear to radiate at extreme L/L_{Edd} . xA quasars show a relatively high prevalence (10%) and are easily recognizable. Low ionization lines are apparently emitted in a highly-flattened, virialized BLR, and the consistency between virial and redshift-based luminosity estimates supports this basic interpretation also for xA quasars. Several methods to derive redshift-independent L values based on intrinsic properties of quasars have been proposed in the last few years (Wang et al., 2013; La Franca et al., 2014; Risaliti & Lusso, 2015); xA quasars might be suitable as “Eddington standard candles” especially if orientation effects can be accounted for.

Acknowledgements. PM and MDO acknowledge funding from the INAF PRIN-SKA 2017 program 1.05.01.88.04. PM is also grateful for support via a STSM of the COST Action CA16104, Gravitational waves, black holes and fundamental physics that allowed her participation to the SCSLSA12. AdO acknowledges financial support from the Spanish Ministry of Economy and Competitiveness through grant AYA2016-76682-C3-1-P and from the State Agency for Research of the Spanish MCIU through the Center of Excellence Severo Ochoa award for the Instituto de Astrofísica de Andalucía (SEV-2017-0709). E.B. and N.B. acknowledge support from the Ministry of Education, Science and Technological Development of the Republic of Serbia through the projects Astrophysical Spectroscopy of Extragalactic Objects (176001) and Gravitation and structure of the Universe on large scales (176003).

References

- Abramowicz, M. A., Czerny, B., Lasota, J. P., & Szuszkiewicz, E., Slim accretion disks. 1988, *Astrophys. J.*, **332**, 646, DOI: 10.1086/166683
- Afanasiev, V. L., Popović, L. Č., & Shapovalova, A. I., Spectropolarimetry of Seyfert 1 galaxies with equatorial scattering: black hole masses and broad-line region characteristics. 2019, *Mon. Not. R. Astron. Soc.*, **482**, 4985, DOI: 10.1093/mnras/sty2995
- Bachev, R., Marziani, P., Sulentic, J. W., et al., Average Ultraviolet Quasar Spectra in the Context of Eigenvector 1: A Baldwin Effect Governed by the Eddington Ratio? 2004, *ApJ*, **617**, 171, DOI: 10.1086/425210

- Boroson, T. A. & Green, R. F., The emission-line properties of low-redshift quasi-stellar objects. 1992, *ApJS*, **80**, 109, DOI: 10.1086/191661
- Burbidge, G. R. & Burbidge, E. M. 1967, *Quasi-stellar objects* (San Francisco, Freeman)
- Coatman, L., Hewett, P. C., Banerji, M., et al., Correcting C IV-based virial black hole masses. 2017, *Mon. Not. R. Astron. Soc.*, **465**, 2120, DOI: 10.1093/mnras/stw2797
- Collin-Souffrin, S., Dyson, J. E., McDowell, J. C., & Perry, J. J., The environment of active galactic nuclei. I - A two-component broad emission line model. 1988, *MNRAS*, **232**, 539
- Corbin, M. R. & Boroson, T. A., Combined Ultraviolet and Optical Spectra of 48 Low-Redshift QSOs and the Relation of the Continuum and Emission-Line Properties. 1996, *Astrophys. J., Suppl.*, **107**, 69, DOI: 10.1086/192355
- Diamond-Stanic, A. M., Fan, X., Brandt, W. N., et al., High-redshift SDSS Quasars with Weak Emission Lines. 2009, *Astrophys. J.*, **699**, 782, DOI: 10.1088/0004-637X/699/1/782
- D’Onofrio, M., Sciaratta, M., Cariddi, S., Marziani, P., & Chiosi, C., The Parallelism between Galaxy Clusters and Early-type Galaxies. I. The Light and Mass Profiles. 2019, *Astrophys. J.*, **875**, 103, DOI: 10.3847/1538-4357/ab1134
- Du, P., Wang, J.-M., Hu, C., et al., The Fundamental Plane of the Broad-line Region in Active Galactic Nuclei. 2016, *Astrophys. J., Lett.*, **818**, L14, DOI: 10.3847/2041-8205/818/1/L14
- Elvis, M., A Structure for Quasars. 2000, *Astrophys. J.*, **545**, 63, DOI: 10.1086/317778
- Faber, S. M. & Jackson, R. E., Velocity dispersions and mass-to-light ratios for elliptical galaxies. 1976, *Astrophys. J.*, **204**, 668, DOI: 10.1086/154215
- Fraix-Burnet, D., Marziani, P., D’Onofrio, M., & Dultzin, D., The Phylogeny of Quasars and the Ontogeny of Their Central Black Holes. 2017, *Frontiers in Astronomy and Space Sciences*, **4**, 1, DOI: 10.3389/fspas.2017.00001
- La Franca, F., Bianchi, S., Ponti, G., Branchini, E., & Matt, G., A New Cosmological Distance Measure Using Active Galactic Nucleus X-Ray Variability. 2014, *Astrophys. J., Lett.*, **787**, L12, DOI: 10.1088/2041-8205/787/1/L12
- Marinello, M., Rodríguez-Ardila, A., Garcia-Rissmann, A., Sigut, T. A. A., & Pradhan, A. K., The Fe II Emission in Active Galactic Nuclei: Excitation Mechanisms and Location of the Emitting Region. 2016, *Astrophys. J.*, **820**, 116, DOI: 10.3847/0004-637X/820/2/116
- Martínez-Aldama, M. L., Del Olmo, A., Marziani, P., et al., Highly Accreting Quasars at High Redshift. 2018, *Frontiers in Astronomy and Space Sciences*, **4**, 65, DOI: 10.3389/fspas.2017.00065
- Marziani, P., del Olmo, A., Martínez-Carballo, M. A., et al., Black hole mass estimates in quasars. A comparative analysis of high- and low-ionization lines. 2019, *Astron. Astrophys.*, **627**, A88, DOI: 10.1051/0004-6361/201935265
- Marziani, P., Dultzin, D., Sulentic, J. W., et al., A main sequence for quasars. 2018, *Frontiers in Astronomy and Space Sciences*, **5**, 6

- Marziani, P., Negrete, C. A., Dultzin, D., et al., Highly accreting quasars: a tool for cosmology? 2017, in IAU Symposium, Vol. **324**, *IAU Symposium*, 245–246
- Marziani, P. & Sulentic, J. W., Highly accreting quasars: sample definition and possible cosmological implications. 2014, *Mon. Not. R. Astron. Soc.*, **442**, 1211, DOI: 10.1093/mnras/stu951
- Marziani, P., Sulentic, J. W., Dultzin-Hacyan, D., Calvani, M., & Moles, M., Comparative Analysis of the High- and Low-Ionization Lines in the Broad-Line Region of Active Galactic Nuclei. 1996, *ApJS*, **104**, 37, DOI: 10.1086/192291
- Marziani, P., Sulentic, J. W., Plauchu-Frayn, I., & del Olmo, A., Is Mg II 2800 a Reliable Virial Broadening Estimator for Quasars? 2013a, *AAP*, **555**, 89, 16pp
- Marziani, P., Sulentic, J. W., Plauchu-Frayn, I., & del Olmo, A., Low-Ionization Outflows in High Eddington Ratio Quasars. 2013b, *ApJ*, **764** [e-print:[arXiv]1301.0520]
- Mejía-Restrepo, J. E., Lira, P., Netzer, H., Trakhtenbrot, B., & Capellupo, D. M., The effect of nuclear gas distribution on the mass determination of supermassive black holes. 2018, *Nature Astronomy*, **2**, 63, DOI: 10.1038/s41550-017-0305-z
- Mineshige, S., Kawaguchi, T., Takeuchi, M., & Hayashida, K., Slim-Disk Model for Soft X-Ray Excess and Variability of Narrow-Line Seyfert 1 Galaxies. 2000, *Publ. Astron. Soc. Jap.*, **52**, 499, DOI: 10.1093/pasj/52.3.499
- Negrete, A., Dultzin, D., Marziani, P., & Sulentic, J., BLR Physical Conditions in Extreme Population A Quasars: a Method to Estimate Central Black Hole Mass at High Redshift. 2012, *ApJ*, **757**, 62
- Negrete, C. A., Dultzin, D., Marziani, P., et al., Highly accreting quasars: The SDSS low-redshift catalog. 2018, *Astron. Astrophys.*, **620**, A118, DOI: 10.1051/0004-6361/201833285
- Negrete, C. A., Dultzin, D., Marziani, P., & Sulentic, J. W., Reverberation and Photoionization Estimates of the Broad-line Region Radius in Low-*z* Quasars. 2013, *Astrophys. J.*, **771**, 31, DOI: 10.1088/0004-637X/771/1/31
- Panda, S., Marziani, P., & Czerny, B., The Quasar Main Sequence explained by the combination of Eddington ratio, metallicity and orientation. 2019, *arXiv e-prints*, arXiv:1905.01729
- Peterson, B. M. & Wandel, A., Keplerian Motion of Broad-Line Region Gas as Evidence for Supermassive Black Holes in Active Galactic Nuclei. 1999, *Astrophys. J., Lett.*, **521**, L95, DOI: 10.1086/312190
- Risaliti, G. & Lusso, E., A Hubble Diagram for Quasars. 2015, *Astrophys. J.*, **815**, 33, DOI: 10.1088/0004-637X/815/1/33
- Sadowski, A., Slim accretion disks around black holes, PhD Thesis. 2011, *ArXiv e-prints* [e-print:[arXiv]1108.0396]
- Shen, Y. & Ho, L. C., The diversity of quasars unified by accretion and orientation. 2014, *Nature*, **513**, 210, DOI: 10.1038/nature13712
- Sulentic, J., Marziani, P., & Zamfir, S., The Case for Two Quasar Populations. 2011, *Baltic Astronomy*, **20**, 427

- Sulentic, J. W., Bachev, R., Marziani, P., Negrete, C. A., & Dultzin, D., C IV λ 1549 as an Eigenvector 1 Parameter for Active Galactic Nuclei. 2007, *ApJ*, **666**, 757, DOI: 10.1086/519916
- Sulentic, J. W., del Olmo, A., Marziani, P., et al., What does CIV λ 1549 tell us about the physical driver of the Eigenvector quasar sequence? 2017, *Astron. Astrophys.*, **608**, A122, DOI: 10.1051/0004-6361/201630309
- Sulentic, J. W., Marziani, P., & Calvani, M., An H-R diagram for AGN? 2001, in AIP CP, Vol. **599**, *X-ray Astronomy: Stellar Endpoints, AGN, and the Diffuse X-ray Background*, 963–966
- Sulentic, J. W., Marziani, P., & Dultzin-Hacyan, D., Phenomenology of Broad Emission Lines in Active Galactic Nuclei. 2000, *ARA&A*, **38**, 521, DOI: 10.1146/annurev.astro.38.1.521
- Sulentic, J. W., Zamfir, S., Marziani, P., & Dultzin, D., Our Search for an H-R Diagram of Quasars. 2008, *Revista Mexicana de Astronomia y Astrofisica Conference Series*, **32**, 51
- Tully, R. B. & Fisher, J. R., A new method of determining distances to galaxies. 1977, *Astron. Astrophys.*, **54**, 661
- Vietri, G., The LBT/WISSH quasar survey: revealing powerful winds in the most luminous AGN. 2017, in American Astronomical Society Meeting Abstracts, Vol. **229**, *American Astronomical Society Meeting Abstracts*, 302.06
- Wang, J.-M., Du, P., Valls-Gabaud, D., Hu, C., & Netzer, H., Super-Eddington Accreting Massive Black Holes as Long-Lived Cosmological Standards. 2013, *Physical Review Letters*, **110**, 081301, DOI: 10.1103/PhysRevLett.110.081301

The density maps of the HS47.5-22 field

S. N. Dodonov¹ and A. Grokhovskaya¹

*Special Astrophysical Observatory of the Russian Academy of Science,
Nizhnii Arkhyz, 369167, Russia*

Received: July 31, 2019; Accepted: November 14, 2019

Abstract. We study the reconstruction of overdensity maps of galaxies as function of redshift in the range $0 < z < 0.8$ using data from 1-m Schmidt Telescope of Byurakan Astrophysical Observatory (Armenia) in 16 medium band ($\sim 250\text{\AA}$) and four broad band (u,g,r,i) filters. The data used in this work homogeneously cover 2.39 sq. deg with accurate photometric redshifts, down to $R < 23$ mag (AB). We reconstructed the density contrast maps for the whole galaxy sample of the HS 47.5-22 ROSAT field in narrow slices for full range of redshifts. We select groups and clusters of galaxies with adaptive kernel based on density peaks which are larger than two times the mean density. The reconstructed overdensity field of galaxies consists of cluster-like structures outlining void-like regions for full redshift range $0 \leq z \leq 0.8$. We detect known galaxy clusters in this field with software specially developed for this project. This gives us a possibility to study how star formation properties and galaxy morphology depend on the environments of the galaxies in this field.

Key words: methods – data analysis – galaxies – clusters

1. Introduction

Galaxy evolution and physical properties must be in strong correlation with their environment. There are a several dependencies of galaxy physical properties and the environment. The dependence "morphology - density of the environment" was discovered by Oemler (1974) and Dressler (1980). These authors stated that the early type galaxies are more often located in overdensity areas in the center of groups and clusters, and that the late type galaxies are preferentially found in the periphery of groups and clusters. More recent studies based on 2dFGRS (Two-degree-Field Galaxy Redshift Survey, Madgwick et al., 2003) and SDSS (Sloan Digital Sky Survey, Guo et al., 2013, 2014) have found that this correlation is maintained for the entire range of local densities up to the field galaxies.

For nearby galaxies the dependencies of H_α equivalent width, 4000 \AA break (or the ratio between the average flux density in $\text{ergs s}^{-1} \text{cm}^{-2} \text{Hz}^{-1}$ between 4050 and 4250 \AA and that between 3750 and 3950 \AA Bruzual, 1983) and colors on the environment were found on scales of the order of 1 Mpc h^{-1} (Kauffmann et al., 2004). In the recent article of Cucciati et al. (2010) it was shown that more massive galaxies were formed in the most dense areas earlier than galaxies

with a smaller mass and the evolution of less massive galaxies occurs under the influence of complex physical processes determined by their environment.

Galaxies located in areas of high density of groups and clusters of galaxies are formed and evolve differently than galaxies in the low density voids. One of the main methods for determination of galaxies belonging to a large-scale structure, in the optical and infrared ranges, is density contrast maps based on filtering algorithms (Lopes et al., 2004; Koester et al., 2007).

In this paper we describe the survey observations and the data reduction in Section 2. We review filtering algorithm with adaptive kernel, basic statistics and overdensity field reconstruction in Section 3. We discuss our results and make conclusion in Section 4. Throughout this paper, we assume a flat cosmology described with $\Omega_m = 0.3$, $\Omega_\Lambda = 0.7$ and $H_0 = 70 \text{ km s}^{-1}$.

2. Observations

We observed the HS47.5-22 ROSAT field (Fig. 1) defined by the medium deep ROSAT survey with center coordinates $09^h50^m00^s + 47^d35^m00^s$ (Molthagen et al., 1997). The survey consists of 48 overlapping ROSAT pointings which were added to produce a final catalog containing 574 X-ray sources with broad band (0.1 – 2.4 keV) count rates between $\sim 3 \times 10^{-3} \text{ cts s}^{-1}$ and $\sim 0.2 \text{ cts s}^{-1}$, in a field of view of $\sim 2.3 \text{ sq. deg.}$ Molthagen et al. (1997) used an X-ray error circle of $2\sigma + 10 \text{ arcsec}$ in radius, with the positioning error box σ for ROSAT objects taken from ROSAT observations.

Observations of the field HS47.5-22 were carried out with 1-m Schmidt Telescope of the Byurakan Observatory (Armenia) during several sets in February, March, April, and November of 2017, and in February and November of 2018. Telescope field of view with $4k \times 4k$ CCD was $58 \times 58 \text{ arcmin}$, scale $0.868 \text{ arcsec pixel}^{-1}$. To get data for near all pointings of HS47.5-22 ROSAT field we observed four positions with 10 arcmin overlaps. From these observations we created the mosaic with total area of 2.386 sq. degree (Dodonov et al., 2017).

Each position was observed in four broad band filters (u , g , r and i *SDSS*) and in 16 medium band ($FWHM = 250 \text{ \AA}$, with FWHM defined as full width at half maximum) filters with homogeneous covering optical spectral range from 4000 \AA till 8000 \AA (see Tab. 1 and Fig. 2). In each filter we obtained from 12 to 25 individual images with 5-6 arcmin shifts between each one. Total exposure times in filters were varied from 60 min to 120 min depending from the spectral sensitivity of the CCD. Long term objects variability was controlled by the observations in $r - SDSS$ filter in each set of observations.

Photometry of the objects obtained using SExtractor (Bertin & Arnouts, 1996) in dual image mode. Base image were created from the sum of deep ($\sim 25^m$) images obtained in g , r and i filters. Before the photometry all images were convolved to common seeing quality and transformed to common coordi-

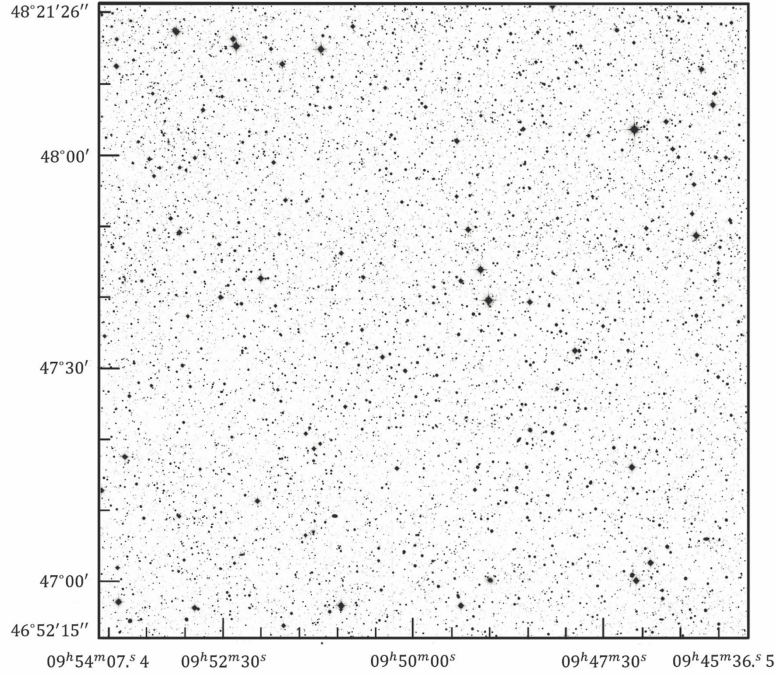


Figure 1. The composite optical image in g, r and i filters of the HS47.5-22 field is about 2.39 sq. degree with center coordinates $09^h50^m00^s + 47^d35^m00^s$. The 574 X-ray sources up to level $3.5 \cdot 10^{-14} \text{ erg cm}^{-2} \text{ s}^{-1}$ were detected by the ROSAT X-ray satellite (Molthagen et al., 1997).

nates system. We got photometry in $1.45 \times FWHM$ apertures and corrected received fluxes for light loss using light curve obtained from bright stars, and using MAG_AUTO SExtractor photometry we receive Kron-like fluxes for all objects in the field. Photometric calibration was developed using spectral and photometrical data from SDSS survey for the objects detected in the field. By using field objects as a standard stars within each exposure, we were independent from photometrical conditions for imaging.

Galaxies sample is extracted from the full catalog of objects (near 100000 objects) using following criteria:

- Objects brighter then $R_{AB} = 23$ mag (AB magnitude in R filter)
- Extended index < 0.8 (Bertin & Arnouts, 1996) for the objects with $R_{AB} < 21$ mag, extended index < 0.9 for the objects with $21 \text{ mag} < R_{AB} < 22$ mag and extended index < 0.96 for the objects with $R_{AB} < 23$ mag
- Index of contamination ≤ 2 (Bertin & Arnouts, 1996)

Table 1. 1m Schmidt Telescope Filter set. Effective Wavelength, $FWHM$, Limiting Magnitude measured at F/2.

Filter	$\lambda_{\text{cen}}, \text{\AA}$	$FWHM(\text{\AA})$	$m_{\text{lim}, 5\sigma}$
u_SDSS	3578	338	24.23
g_SDSS	4797	860	25.22
r_SDSS	6227	770	24.97
i_SDSS	7624	857	24.15
MB_400	3978	250	24.37
MB_425	4246	250	24.31
MB_450	4492	250	24.20
MB_475	4745	250	24.31
MB_500	4978	250	24.30
MB_525	5234	250	24.37
MB_550	5496	250	23.86
MB_575	5746	250	24.29
MB_600	5959	250	23.89
MB_625	6234	250	23.51
MB_650	6499	250	23.41
MB_675	6745	250	23.78
MB_700	7002	250	23.47
MB_725	7253	250	23.20
MB_750	7519	250	23.07
MB_775	7758	250	22.97

The sample of objects which follow the first two criteria includes 40194 objects and after applying the third one - we have 32637 objects with clean photometry. Due to the contamination we lose 8.12 % of the objects.

We check sample completeness using comparison of galaxies number-counts in g , r and i *SDSS* filters from our sample with already published data in Fig. 3. The galaxies sample completeness up to $R_{AB} = 23$ mag with no color selection effects in all optical range.

Photometric measurements from 17 filters ($u - SDSS$ plus 16 medium band filters) provide low resolution spectra Fig. 4 for each object which are analyzed by a statistical technique for classification and redshift estimation based on spectral template matching. We used for these galaxies spectra templates library from Dodonov & Chilingarian (2008), and a set of programs ZEBRA (Zurich's Extragalactic Bayesian Redshift Analyzer, Feldmann et al., 2006).

The obtained redshift accuracy $\sigma_z < 0.01$ and the fraction of catastrophic outliers is $(\Delta z / (1 + z) > 5 \cdot \sigma_z) \sim 4.0\%$ (in Fig. 5). Accuracy σ_z changes from 0.01 in magnitude range $r - SDSS = 16$ mag – 21 mag till 0.03 in magnitude range $r - SDSS = 21$ mag – 23 mag.

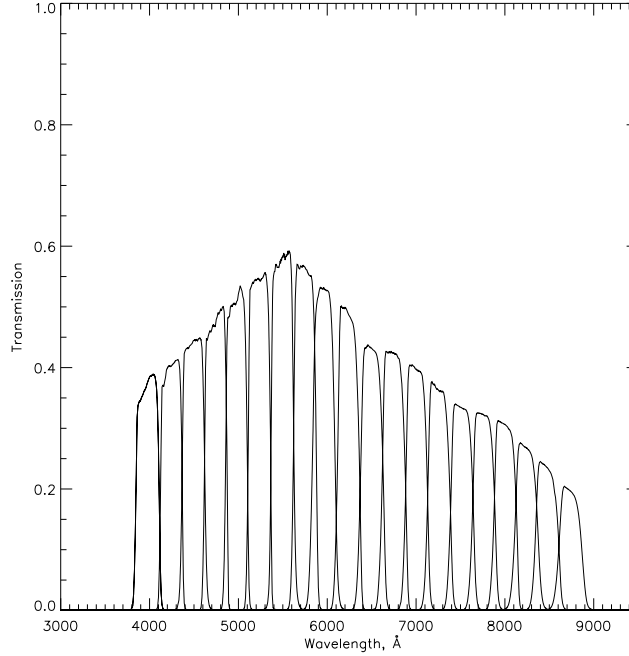


Figure 2. 1m Schmidt Telescope Filter set. Filter transmission measured at F/2. CCD spectral response included.

3. Data analysis

3.1. Filtering algorithm with adaptive kernel

In this work we use the algorithm with adaptive kernel to reconstruct the density contrast field. In this method we calculate the density value in the vicinity of each galaxy:

$$\delta_i = \frac{s}{\frac{4}{3}\pi R^3},$$

where R is three dimensional distance from the galaxy to its N -th nearest neighbor and s is number of nearest neighbor galaxy. Next we divide the light cone into thin redshift slices with $\Delta z = 0.056 \cdot (1+z)$ and 25% overlap from each side of slice. The width of slices is based on $1\sigma = 0.028$ photometric redshift error for all type galaxies. For each slice the mean density is estimated as

$$\bar{\delta} = \frac{1}{n} \sum_{i=1}^n \delta_i,$$

where n is the total number of galaxies in the each slice.

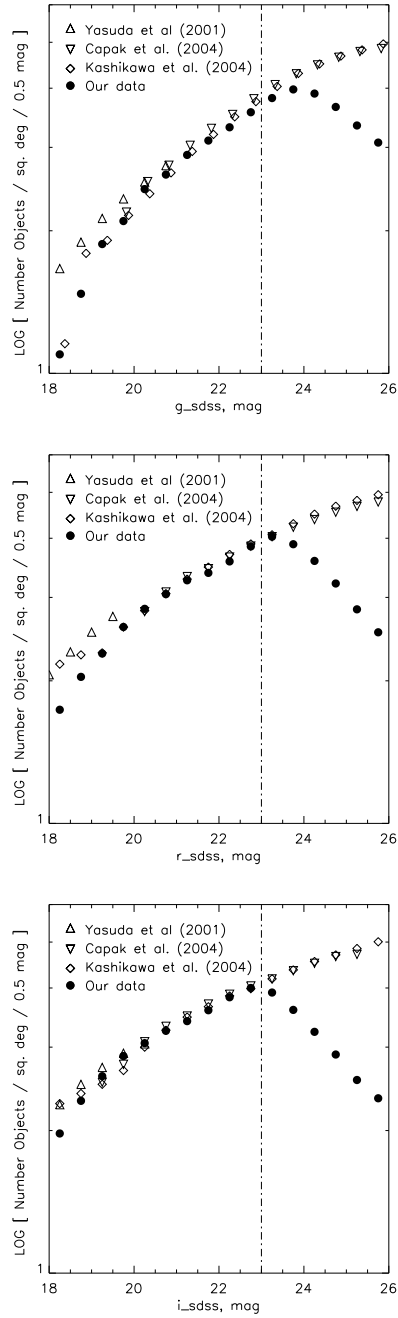


Figure 3. Galaxy sample completeness in g , r and i SDSS filters.

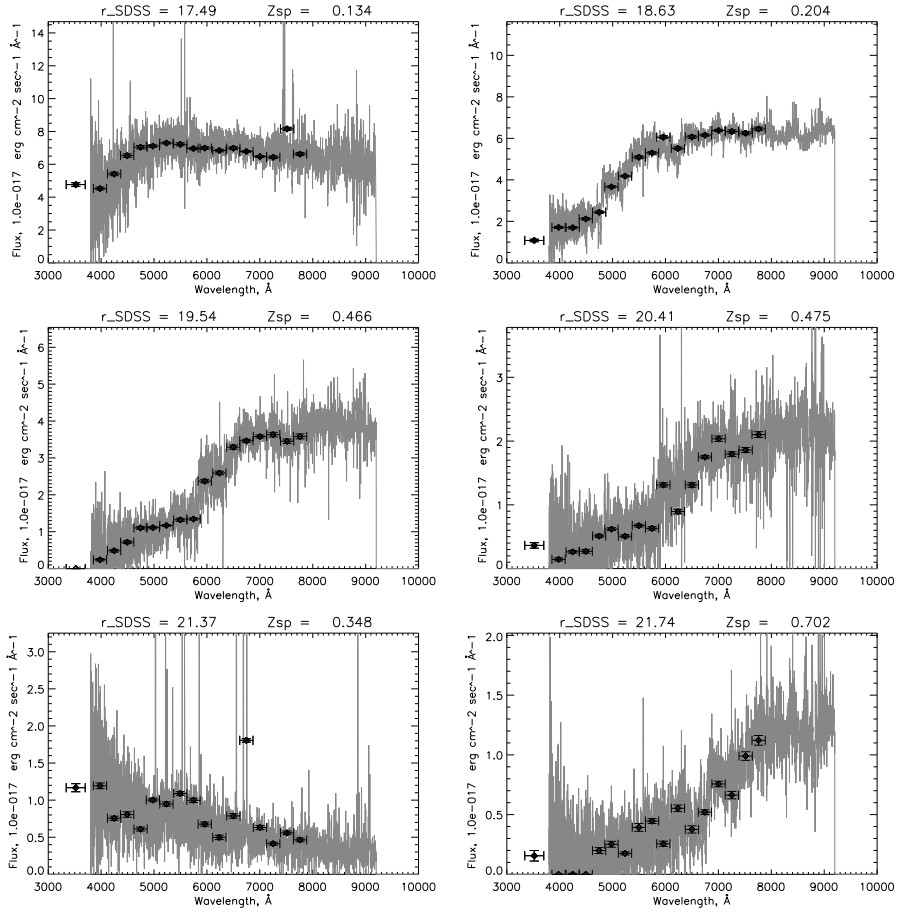


Figure 4. Comparison of the Spectral Energy Distribution (SED) obtained from the photometric data with 1-meter Schmidt telescope (points with bars) with the SDSS spectra (solid gray line). Points in the SED are scaled to 3 arcsec to match the SDSS fiber diameter. Horizontal bars corresponds to filter width and vertical bars to 1σ flux error.

The density contrast σ_i for each galaxy position is calculated as

$$\sigma_i + 1 = \frac{(\delta_i - \bar{\delta})}{\bar{\delta}} + 1.$$

The candidate to clusters and group of galaxies are detected as density peaks which are larger than two times the average density and the candidate to voids

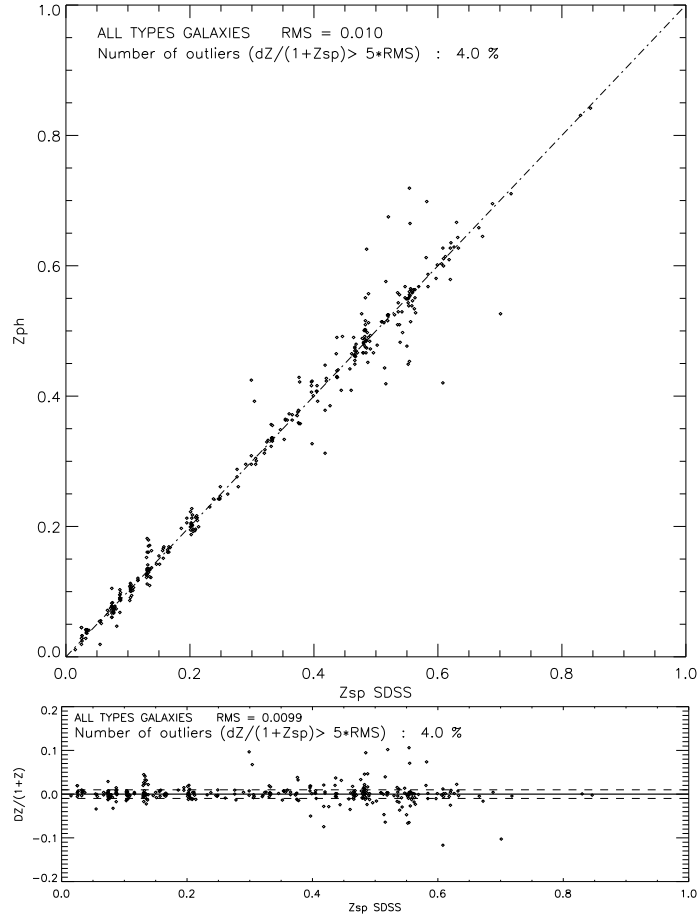


Figure 5. Comparison between photometric redshifts z_{ph} obtained with ZEBRA in Maximum Likelihood mode with SDSS spectroscopic redshifts z_{sp} along with error distribution $\Delta z/(1+z)$ for all galaxies with known spectroscopic redshifts

are detected as density cavity smaller than ten times the average density in each redshift slice.

3.2. Basic statistics

For testing filtering algorithm with adaptive kernel we use galaxy mock-catalog MICECAT v2 (Carretero et al., 2017). It is a fake or simulated galaxy catalogue which resembles a genuine galaxy redshift survey catalogue, but is built from a cosmological simulation. Mock catalog is useful for cluster-determination

algorithms because it has information about dark halo id. Thus we can estimate statistical parameters of detecting clusters sample over mock sample. Obviously, it is impossible to obtain a perfect match between structures of the model catalog and the recovered groups and clusters. Moreover completeness and purity of reconstructed structures tend to be mutually exclusive. In the process of determining the elements of a large-scale structure, it is possible to obtain the following cases: over-merging (several real groups combined to one reconstructed group), fragmentation (one real group divided to a several reconstructed groups), spurious group (reconstructed group with no one real group matching), undetected group (real group is missing in reconstructed catalog).

Basic statistic term are: I) the completeness, which is a measure of the fraction of real groups with N or more members that are successfully recovered in the reconstructed group catalogue, II) the purity, which is a measure of the fraction of reconstructed groups with N or more members that belong to real groups, III) "galaxy success rate" which is the fraction of galaxies belonging to real groups of special richness that have ended up in any reconstructed group, and IV) "interloper fraction" is the fraction of galaxies belonging to reconstructed groups of special richness which are field galaxies (Knobel et al. (2009), see also Grokhovskaya & Dodonov (2019)).

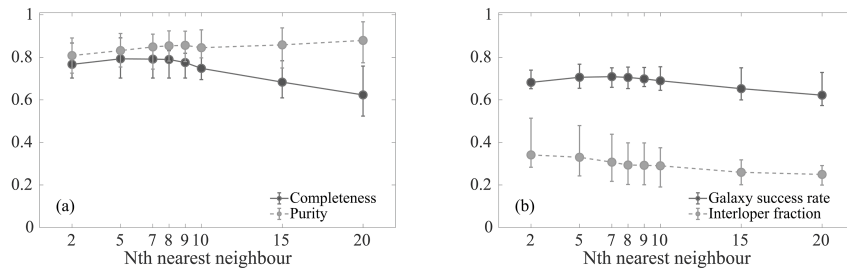


Figure 6. Basic static parameters of the sample of groups, clusters and galaxies obtained by filtering algorithm with adaptive kernel. On the left the figures show completeness (solid line) and purity (dashed line) of the sample, on the right - the percentage of successful detection of galaxies from clusters of the model catalog (solid line) and the percentage of galaxies defined automatically as galaxies of clusters, but being field galaxies in the model catalog (dotted line). The bars correspond to the standard deviation for 10 samples of galaxies of the MICE simulation.

We use 10 mock samples with the same physical properties like observation data (2 sq. degree field, $z \leq 0.8$ and $R_{AB} \leq 23$ mag) for estimation of all basic statistical parameters for detected clusters by filtering algorithm with adaptive kernel (Fig. 6). For this method we can variate size of aperture as number of nearest neighbor for calculation and compare statistics for choosing best size

of aperture. The 8 nearest neighbours is optimal variant of completeness and purity.

3.3. The HS47.5-22 overdensity field

We reconstructed 3D overdensity maps for observational data of the HS 47.5-22 field. We obtained a broad range of reliably reconstructed local overdensities of the sample of galaxies by using filtering algorithm with variable aperture. The size of aperture was defined by the distance to the 8th nearest neighbour from basic statistics. Based on the tests on the mock catalogue, 8 is the optimal number of neighbours which can be used to reliably reconstruct density at all redshifts. An increase in the size of the adaptive aperture (e.g. 10, 15 or 20) leads to a smoothing of the peaks on the contrast maps of the density of galaxies and the underdetermination of large-scale structures. Decrease in the size of the adaptive aperture (e.g. 2, 5 or 7) leads to decrease of the purity of the reconstructed cluster sample.

Figure 7 shows isosurfaces for a density contrast which are larger than two times the average density (grey surfaces) and clusters with spectral redshifts from WHL (by the name of the authors of the catalog Wen, Han and Liu) catalog (black triangles) which was completed by Wen & Han (2015) from spectroscopic and photometric data of the SDSS.

4. Conclusion

We used observational data from 1-m Schmidt Telescope of the Byurakan Observatory (Armenia) to reconstruct the overdensity maps in the HS47.5-22 ROSAT field. We explored the photometric properties of the sample of 36447 galaxies in the field and obtained spectral types and photometric redshifts for all objects. An accuracy of redshift allows one to determine whether a galaxy belongs to a cluster or group.

We applied the filtering algorithm with adaptive aperture for the reconstruction. This algorithm have been tested on the MICECAT v2 mock catalog. We estimated basic statistical parameters (completeness, purity, galaxy success rate and interloper fraction) for reconstructed clusters from mock catalog. Evaluation of the main statistical parameters allowed us to choose the optimal aperture size for further work with observational data.

We obtain a broad band of large scale structures up to $z = 0.8$ for observational data. Also we found the most part of clusters from the WHL cluster catalog with spectroscopic redshift in our field.

Obtained results allow us to begin a study of the connection between star formation rate in galaxies and their position in the large scale distribution.

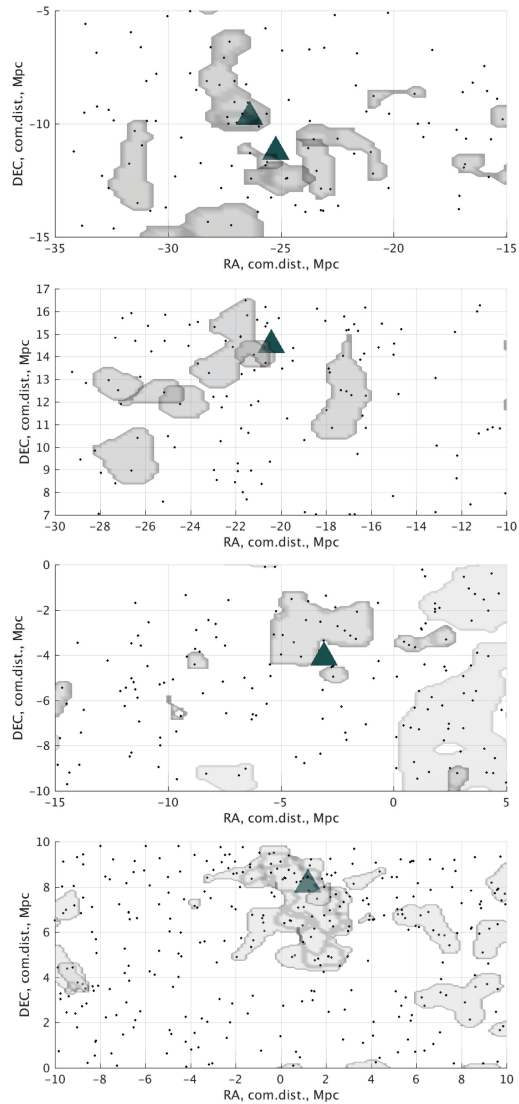


Figure 7. Overdensity maps (grey surfaces are isosurfaces with a density contrast two times above the mean density mean density) of narrow slices HS 47.5-22 field with WHL clusters (black triangles, from top to bottom): 1. WHL J094645.7 + 471107 and WHL J094637.9 + 471440 2. WHL J094657.3 + 481526 3. WHL J094913.0 + 472248 4. WHL J095027.9 + 481435. Axis are shown in comoving distance (x-axis is distance from the survey centre in right ascension, y-axis is distance from the survey centre in declination).

Acknowledgements. This work has made use of CosmoHub. CosmoHub has been developed by the Port d'Informacio Cientifica (PIC), maintained through a collaboration of the Institut de Fisica d'Altes Energies (IFAE) and the Centro de Investigaciones Energeticas, Medioambientales y Tecnologicas (CIEMAT), and was partially funded by the "Plan Estatal de Investigacion Cientifica y Tecnica y de Innovacion" program of the Spanish government.

The methodological part of the work was supported by the Russian Science Foundation under grant no. 17-12-01335 (observation, development of methods for processing and calibrating data).

The data analysis and the study of the large-scale structure were performed as part of the government contract of the SAO RAS approved by the Ministry of Science and Higher Education of the Russian Federation.

References

- Bertin, E. & Arnouts, S., SExtractor: Software for source extraction. 1996, *Astronomy and Astrophysics Supplement*, **117**, 393, DOI: 10.1051/aas:1996164
- Bruzual, A., G., Spectral evolution of galaxies. I. Early-type systems. 1983, *Astrophysical Journal*, **273**, 105, DOI: 10.1086/161352
- Carretero, J. et al., CosmoHub and SciPIC: Massive cosmological data analysis, distribution and generation using a Big Data platform. 2017, *PoS, EPS-HEP2017*, 488, DOI: 10.22323/1.314.0488
- Cucciati, O., Iovino, A., Kovac, K., et al., The zCOSMOS 10k-sample: the role of galaxy stellar mass in the colour-density relation up to $z \sim 1$. 2010, *Astronomy and Astrophysics*, **524**, 18, DOI: 10.1051/0004-6361/200912585
- Dodonov, S. N. & Chilingarian, I. V., Library of reference spectral energy distributions for galaxies for the classification and determination of photometric redshifts of objects. 2008, *Astrophysical Bulletin*, **63**, 1, DOI: 10.1007/s11755-008-1001-y
- Dodonov, S. N., Kotov, S. S., Movsesyan, T. A., & Gevorkyan, M., One-meter Schmidt telescope of the Byurakan Astrophysical Observatory: New capabilities. 2017, *Astrophysical Bulletin*, **72**, 473, DOI: 10.1134/S1990341317040113
- Dressler, A., Galaxy morphology in rich clusters - Implications for the formation and evolution of galaxies. 1980, *The Astrophysical Journal*, **236**, 351, DOI: 10.1086/157753
- Feldmann, R., Carollo, C. M., Porciani, C., et al., The Zurich Extragalactic Bayesian Redshift Analyzer and its first application: COSMOS. 2006, *Monthly Notices of the Royal Astronomical Society*, **372**, 565, DOI: 10.1111/j.1365-2966.2006.10930.x
- Grokhovskaya, A. A. & Dodonov, S. N. 2019, in prep.
- Guo, H., Zehavi, I., Zheng, Z., et al., The Clustering of Galaxies in the SDSS-III Baryon Oscillation Spectroscopic Survey: Luminosity and Color Dependence and Redshift Evolution. 2013, *The Astrophysical Journal*, **767**, 1, DOI: 10.1088/0004-637X/767/2/122
- Guo, H., Zheng, Z., Zehavi, I., et al., The clustering of galaxies in the SDSS-III Baryon Oscillation Spectroscopic Survey: modelling of the luminosity and colour depen-

- dence in the Data Release 10. 2014, *Mon. Not. R. Astron. Soc.*, **441**, 2398, DOI: 10.1093/mnras/stu763
- Kauffmann, G., White, S. D. M., Heckman, T. M., et al., The environmental dependence of the relations between stellar mass, structure, star formation and nuclear activity in galaxies. 2004, *Mon. Not. R. Astron. Soc.*, **353**, 713, DOI: 10.1111/j.1365-2966.2004.08117.x
- Knobel, C., Lilly, S. J., Iovino, A., et al., An Optical Group Catalog to $z = 1$ from the zCOSMOS 10 k Sample. 2009, *The Astrophysical Journal*, **697**, 1842, DOI: 10.1088/0004-637X/697/2/1842
- Koester, B. P., McKay, T. A., Annis, J., et al., MaxBCG: A Red-Sequence Galaxy Cluster Finder. 2007, *The Astrophysical Journal*, **660**, 221, DOI: 10.1086/512092
- Lopes, P. A. A., de Carvalho, R. R., Gal, R. R., et al., The Northern Sky Optical Cluster Survey. IV. An Intermediate-Redshift Galaxy Cluster Catalog and the Comparison of Two Detection Algorithms. 2004, *The Astrophysical Journal*, **128**, 1017, DOI: 10.1086/423038
- Madgwick, D. S. and Hawkins, E., Lahav, O., Maddox, S., et al., The 2dF Galaxy Redshift Survey: galaxy clustering per spectral type. 2003, *Mon. Not. R. Astron. Soc.*, **344**, 847, DOI: 10.1046/j.1365-8711.2003.06861.x
- Molthagen, K., Wendker, H. J., & Briel, U. G., Multiwavelength observations of the field HS 47.5/22 in Ursa Major. I. The X-ray catalogue of a medium deep ROSAT survey. 1997, *Astronomy & Astrophysics Supplement series*, **126**, 509, DOI: 10.1051/aas:1997391
- Oemler, A. 1974, The systematic properties of clusters of galaxies, PhD dissertation, California Institute of Technology
- Wen, Z. L. & Han, J. L., Calibration of the Optical Mass Proxy for Clusters of Galaxies and an Update of the WHL12 Cluster Catalog. 2015, *The Astrophysical Journal*, **807**, 11pp, DOI: 10.1088/0004-637X/807/2/178

Line shapes in narrow-line Seyfert 1 galaxies: a tracer of physical properties?

M. Berton^{1,2}, I. Björklund³, A. Lähteenmäki^{2,3}, E. Congiu⁴,
E. Järvelä^{5,2}, G. Terreran⁶ and G. La Mura⁷

¹ *Finnish Centre for Astronomy with ESO (FINCA), University of Turku, Quantum, Vesilinnantie 5, FI-20014, University of Turku, Finland, (E-mail: marco.berton@utu.fi)*

² *Aalto University Metsähovi Radio Observatory, Metsähovintie 114, FI-02540 Kylmälä, Finland*

³ *Aalto University Department of Electronics and Nanoengineering, P.O. Box 15500, FI-00076, Aalto, Finland*

⁴ *Las Campanas Observatory - Carnegie Institution of Washington, Colina El Pino Casilla 601, La Serena, Chile*

⁵ *Department of Physics, University of California, Santa Barbara, CA 93106-9530, USA*

⁶ *Center for Interdisciplinary Exploration and Research in Astrophysics CIERA, Department of Physics and Astronomy, Northwestern University, Evanston, IL 60208, USA*

⁷ *Laboratory of Instrumentation and Experimental Particle Physics, Av. Prof. Gama Pinto, 2 - 1649-003 Lisboa, Portugal*

Received: July 31, 2019; Accepted: September 26, 2019

Abstract. Line profiles can provide fundamental information on the physics of active galactic nuclei (AGN). In the case of narrow-line Seyfert 1 galaxies (NLS1s) this is of particular importance since past studies revealed how their permitted line profiles are well reproduced by a Lorentzian function instead of a Gaussian. This has been explained with different properties of the broad-line region (BLR), which may present a more pronounced turbulent motions in NLS1s with respect to other AGN. We investigated the line profiles in a recent large NLS1 sample classified using SDSS, and we divided the sources into two subsamples according to their line shapes, Gaussian or Lorentzian. The line profiles clearly separate all the properties of NLS1s. Black hole mass, Eddington ratio, [O III], and Fe II strength are all very different in the Lorentzian and Gaussian samples. We interpret this in terms of evolution within the class of NLS1s. The Lorentzian sources may be the youngest objects, while Gaussian profiles may be typically associated to more evolved objects. Further detailed spectroscopic studies are needed to fully confirm our hypothesis.

Key words: Galaxies: active – quasars: emission lines – Line: profiles – Galaxies: evolution

1. Introduction

Among active galactic nuclei (AGN), narrow-line Seyfert 1 galaxies (NLS1s) are often considered as “rebels”, which hardly fit into the unified models (Antonucci, 1993; Urry & Padovani, 1995). Recognized as a separate class more than 30 years ago (Osterbrock & Pogge, 1985), by definition they are those AGN in which the full width at half maximum (FWHM) of $H\beta$ is lower than 2000 km s^{-1} and the flux ratio $[O \text{ III}]\lambda 5007/H\beta < 3$ (Osterbrock & Pogge, 1985). An additional criterion for NLS1s is the presence of strong Fe II multiplets (Goodrich, 1989), although their presence is not always required, and the origin of the iron abundance and its physics are still not clear (Marziani et al., 2018b, Bon et al., 2019, submitted). Their steep X-ray spectral indexes (Boller et al., 1992) and the presence of relativistic jets in these AGN (Abdo et al., 2009a,b; Berton, 2018) further complicate the NLS1 picture.

Some of these characteristics can be explained, from a physical point of view, by the presence of a relatively low-mass black hole (10^6 - $10^8 M_{\odot}$, see Peterson, 2011) which is accreting close to or above the Eddington limit (Boroson & Green, 1992; Boller et al., 1996; Sulentic et al., 2000; Marziani et al., 2001; Zhou et al., 2006; Cracco et al., 2016; Rakshit et al., 2017; Chen et al., 2018). Due to this, NLS1s are located at the extreme end of the so-called eigenvector 1 (EV1), and constitute a class of extreme accretors (Sulentic & Marziani, 2015; Śniegowska et al., 2018; Marziani et al., 2018b), a property which would allow a more physically accurate definition than the classic FWHM-based criterion (Marziani et al., 2018a).

An explanation which accounts for the low black hole mass, the high accretion rate, and several other NLS1 properties, is that these AGN are younger with respect to classical broad-line Seyfert 1 (BLS1s, e.g., see Mathur, 2000; Berton et al., 2016a, 2017; Järvelä et al., 2017)¹. In this phase, these AGN are growing fast to eventually turn into fully-developed BLS1s. Although this point is still debated (e.g., see D’Ammando et al., 2018; Sbarrato et al., 2018), much evidence has been accumulated in support of the evolutionary hypothesis (for full reviews on their multiwavelength properties, see Komossa, 2008; Gallo, 2018; Komossa, 2018; Lister, 2018).

Interestingly enough, a property which seems to differ in NLS1s and BLS1s is the profile of their permitted lines, particularly that of $H\beta$. While most type 1 AGN typically have a Gaussian line profile, in NLS1s the profile is instead well reproduced by a Lorentzian function (Moran et al., 1996; Véron-Cetty et al., 2001; Sulentic et al., 2002; Cracco et al., 2016). This is particularly true when only the broad component of $H\beta$ is considered. Most broad-line profiles indeed can be well fitted by a broad component, either Gaussian or Lorentzian, and a weaker narrow Gaussian component.

¹Unless otherwise specified, in the following we will use the term BLS1s referring to both non-jetted sources, like classical Seyfert 1, and jetted sources with broad permitted lines such as high-excitation radio galaxies and flat-spectrum radio quasars.

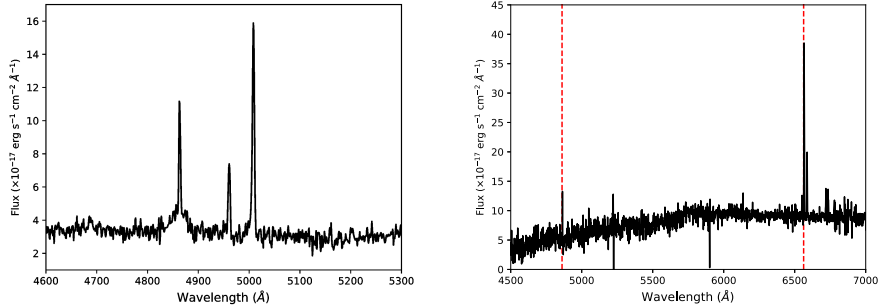


Figure 1. Two examples of spurious sources present in R17. **Left panel:** the spectrum of SDSS J143900.17+431440.9 (spec-6061-56076-0704). The three lines are, from left to right, H β , [O III] λ 4959, [O III] λ 5007. Although classified as an NLS1, this object is an intermediate type AGN, as shown by the presence of two well-separated kinematic components in the H β profile. **Right panel:** the spectrum of SDSS J155806.47+523748.2 (spec-0618-52049-0008), which can be classified as a LINER. The NLS1 classification was likely due to a wrong redshift reported in SDSS ($z = 0.401$ in SDSS, while the correct value is 0.069). The lines marked with the vertical red dashed lines are H β and H α , which were used to measure the correct redshift value.

However, it is known that a small fraction of NLS1s have Gaussian line profiles. Whether the different line profile is connected to different physical properties is still unclear. To answer this question, we decided to study the new large sample of NLS1s selected from the Sloan Digital Sky Survey (SDSS) by Rakshit et al. (2017, hereafter R17). In this proceeding we will carry out a simple statistical analysis of the line profiles, connect them with the other observed properties of NLS1s, and provide a physical interpretation for these results based on the evolutionary hypothesis. In Sect. 2 we present the sample selection, in Sect. 3 we discuss the impact of redshift on our sample, in Sect. 4 we present our results, in Sect. 5 we discuss them, and in Sect. 6 we provide a brief summary of this work. In the following, we adopt the standard Λ CDM cosmology, with $H = 70 \text{ km s}^{-1} \text{ Mpc}^{-1}$, $\Omega_m = 0.3$, $\Omega_\Lambda = 0.7$ (Komatsu et al., 2011).

2. Sample selection

As mentioned above, we used the sample of 11101 NLS1s selected by R17. They selected the sample starting from the SDSS DR12, using the standard classification criteria of $\text{FWHM}(\text{H}\beta)$ and $[\text{O III}]/\text{H}\beta$ flux ratio. The redshift limit of R17 is $z < 0.8$. Among the sources they selected, we considered only those whose signal-to-noise ratio (SNR) in the $\lambda 5100\text{\AA}$ continuum is higher than 5, finding

7070 sources. The SNR criterion decreases the chances of finding sources where an appropriate spectral analysis cannot be performed. As shown by Sulentic & Marziani (2015), spectral measurement can often be unreliable in noisy spectra. Indeed, in R17 some spurious non-NLS1 sources are definitely present, in particular intermediate type AGN, which R17 did not consider but meet both the FWHM and [O III]/H β criteria of NLS1s. Examples of an intermediate Seyfert and of a wrong identification are shown in Fig. 1.

On the remaining 7070 sources, we performed an extremely simple test. The profile of permitted lines in type 1 AGN typically shows two kinematic components, physically corresponding to the broad-line region (BLR) and the narrow-line region (NLR). However, in the NLS1 population the H β line usually has an extremely weak narrow component (see Fig. 3 by Sulentic et al., 2002). The line profile, after redshift correction and continuum subtraction, can indeed be fitted with a single function to reproduce the BLR emission. Therefore, we fitted each line profile with a Lorentzian and Gaussian profiles and used the reduced chi-squared χ^2_ν test to select the best fit. We included only sources which are well-reproduced with either of these simple models to our final sample.

By means of visual inspection of the spectra and of all the results of the fitting procedure, we decided to apply the following selection criteria also on the χ^2_ν . We excluded all those sources for which the $\chi^2_\nu \leq 0.5$ and $\chi^2_\nu \geq 5$, because in most cases their spectra were either noisy or misclassified as shown in Fig. 1. The lower limit in χ^2_ν was introduced to avoid overfitting. When $3.5 < \chi^2_\nu < 5$, we accepted only sources with SNR > 20. Only in high SNR objects, in fact, such high χ^2_ν still indicates a good representation of the H β profile. Between $2.5 < \chi^2_\nu < 3.5$, we also imposed the criterion SNR > 15, while if $2 < \chi^2_\nu < 2.5$ we imposed SNR > 10. All remaining sources with $0.5 < \chi^2_\nu < 2$ were included in the samples. To decide whether a source is to be included in the Lorentzian (L) or the Gaussian (G) subsample, we considered the minimum distance from a $\chi^2_\nu = 1$. These selection criteria inevitably miss some NLS1s. However, our aim is not to obtain complete subsamples, but to include a statistically significant number of sources both in G and L sample, and selecting at the same time only genuine NLS1s. Using this technique, we found 3933 NLS1s whose line profile can be reproduced with a single component, either Gaussian or Lorentzian. In particular, 2894 of them exhibit a Lorentzian profile (L sources), while the remaining 1039 sources are better reproduced with a single Gaussian profile (G sources).

We recognize the simplicity of this model. Firstly, we did not correct for the Galactic absorption, because on the very short wavelength interval we are considering (4000-5500 Å) it is basically a constant and it can be neglected. We also did not subtract the host galaxy contribution and the Fe II multiplets. However, our procedure selects those sources where a single component is a good representation of the H β line. This means that if the host galaxy contribution and the Fe II pseudo-continuum cause a significant deviation from an extremely simple line profile, the source was rejected and not included in the sample because of our selection criteria. In conclusion, this technique automatically selects sources

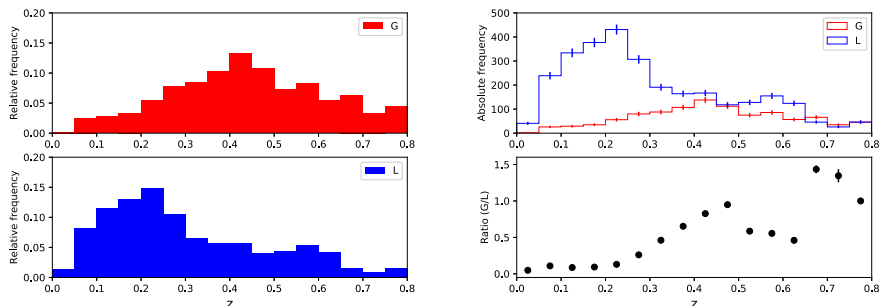


Figure 2. Redshift distributions of the two samples. The red color represents sources with a Gaussian profile, while the blue color indicates Lorentzian profiles. In the left figure we show the normalized distribution of sources per redshift bin. Hereafter each redshift bin has a width of 0.05. In the right figure, the top panel shows the total number of sources per redshift bin, while the bottom panel shows the ratio between the number of G and L sources as a function of redshift.

in which Fe II and host galaxy do not significantly contribute to the $H\beta$ profile. A more detailed analysis of the other line profiles, including an accurate subtraction of host galaxy and Fe II components, will be published in an upcoming paper (Berton et al., in prep.).

These factors not accounted for the line fitting would have a much stronger influence in measurements of the physical quantities. However, all the properties we are using are extracted from the R17 catalog, in which the Galactic absorption, the host galaxy, and the Fe II contribution have been taken into account. For each source, we used the measurements of redshift, $R4570^2$, black hole mass, Eddington ratio, and $[O\ III]\lambda 5007$ luminosity. For each property we carried out a Kolmogorov-Smirnov (K-S) test to compare the distributions of Lorentzian and Gaussian sources. In this case, the null hypothesis is that the two distributions of sources originate from the same population of objects. The p-values of each test are shown in the last column of Table 1. When the distributions are not normal but log-normal like, we also tested the differences between their tails by applying the Anderson-Darling (A-D) test (Hou et al., 2009; Berton et al., 2016b). The null hypothesis, again, is that the two distributions originate from the same population. In both cases we rejected the null hypothesis only at a 99% confidence level, thus when the p-value is lower than 0.01.

² $R4570$ is defined as the flux ratio between the Fe II multiplets and the $H\beta$ line.

3. Redshift distributions

The first result is that the redshift distribution of G and L sources are very different (p-value 1×10^{-97}). The normalized frequencies of the distributions are shown in the left panel of Fig. 2, while in the right panel we show the total number of L and G sources per redshift bin, and the ratio between G and L sources. The error associated to each bin assumes a Poisson distribution, so it is the square root of the number of sources in each bin. The ratio remains roughly constant up to $z = 0.25$, with approximately $\sim 10\%$ of G sources and 90% of L sources. This result is comparable to the results by Cracco et al. (2016), who found that up to $z = 0.35$ the fraction of L sources is 96% . The small difference between these result can be accounted to different selection criteria. Cracco et al. (2016), in fact, selected only sources with very high SNR, and this could introduce a small bias toward luminous objects.

Above $z = 0.25$, the number of Gaussian sources tends to increase rapidly, while the number of L objects decreases. Above $z = 0.5$ there are more sources in the G sample than in the L sample. This result could be attributed to a selection effect. When the redshift increases, the SNR tends to decrease, so the wings typical of Lorentzian profiles tend to disappear in the continuum noise. Therefore, without prominent wings a Lorentzian profile can be easily modeled with a Gaussian. We tried to test the effect of redshift on line profiles by comparing it with the SNR ratio. In fact, a selection effect should be present if SNR systematically decreases with redshift.

Indeed, we found that SNR has a non-negligible dependence on the redshift, with a Pearson correlation coefficient of -0.54 (p-value ~ 0), and a Spearman rank of -0.58 (p-value ~ 0). Therefore, redshift may play a role, even if it may not be the only factor causing a the difference between Lorentzian and Gaussian sources. In fact, we note that Gaussian sources are found also when the SNR is high. Therefore, the difference between these two samples does not seem to be solely due to a selection effect. However, to make our results more robust we decided to test the distributions of physical properties of G and L sources not only on the entire sample, but also at $z < 0.25$, where the ratio between L and G sources is roughly constant and redshift effects are very likely negligible.

4. Physical properties of the sources

As mentioned above, the physical quantities we extracted from R17 are black hole mass, Eddington ratio, relative Fe II strength (R4570), monochromatic continuum luminosity at 5100 \AA , and [O III] integrated luminosity. Their mean and median values, and the standard deviation of each sample are shown in Table 1. The distributions of each physical property for both samples are shown in Figs. 3, 4, 5, 6, and 7. All left panels refer only to sources with $z < 0.25$, while the right panel shows the entire sample up to $z = 0.8$.

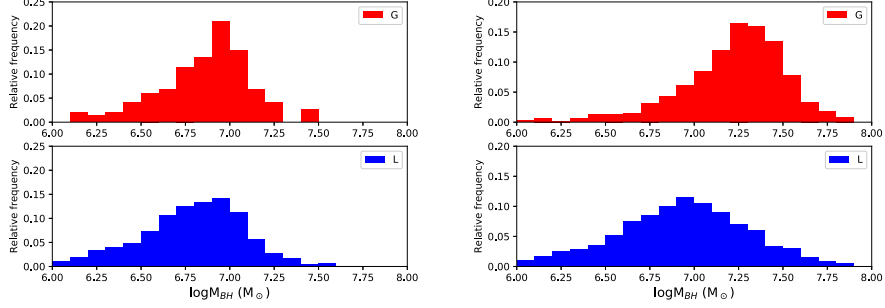


Figure 3. Distribution of black hole masses of the two samples. **Left panel:** distribution of sources up to the redshift limit $z=0.25$; **right panel:** distributions of the whole samples, with redshift limit $z=0.8$. Colors as in Fig. 2.

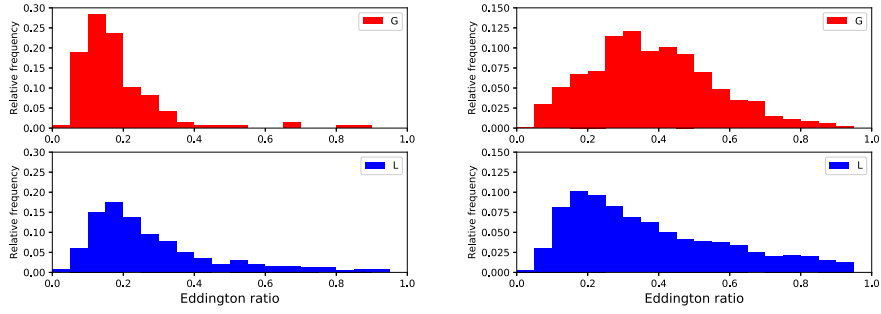


Figure 4. Distribution of Eddington ratio of the two samples. Colors as in Fig. 2 and panels as in Fig. 3.

The black hole mass in R17 was estimated under the assumption of virialized gas, with:

$$M_{BH} = f \frac{v^2 R_{BLR}}{G}. \quad (1)$$

The FWHM($H\beta$) broad component was used as a proxy for the rotational velocity of the gas surrounding the black hole. They assumed that the broad component can be always represented with a Lorentzian function. Therefore, they decomposed the $H\beta$ profile using a Lorentzian to represent the broad component, and a Gaussian to represent the narrow component. The BLR radius was calculated from the $\lambda 5100 \text{ \AA}$ continuum luminosity with the relation by Bentz et al. (2013). The factor f , which is dependent on the BLR geometry, was fixed to $3/4$ assuming a spherical distribution of clouds. The use of FWHM in black

Table 1. Statistical properties of the samples. Columns: (1) measured property (black hole mass in M_{\odot} , Eddington ratio and R4570 adimensional, logarithm of the monochromatic continuum luminosity (λL_{λ}) at 5100 Å in erg s^{-1} , and logarithm of the [O III] luminosity in erg s^{-1}); (2) mean in the Gaussian sample; (3) median in the Gaussian sample; (4) standard deviation in the Gaussian sample; (5) mean in the Lorentzian sample; (6) median in the Lorentzian sample; (7) standard deviation in the Lorentzian sample; (8) K-S test p-value.

Property	Mean	Median	σ	Mean	Median	σ	p-value
$z < 0.8$	G			L			
$\log M_{BH}$	7.21	7.26	0.32	6.90	6.93	0.41	1×10^{-111}
Edd ratio	0.43	0.38	0.41	0.60	0.38	0.75	4×10^{-21}
R4570	0.62	0.59	0.37	0.67	0.62	0.40	2×10^{-3}
$\log \lambda L_{\text{cont}}$	43.92	44.0	0.48	43.66	43.66	0.53	1×10^{-49}
$\log L_{[\text{OIII}]}$	41.54	41.55	0.47	41.35	41.34	0.52	5×10^{-22}
$z < 0.25$	G			L			
$\log M_{BH}$	6.82	6.90	0.32	6.75	6.80	0.35	5×10^{-3}
Edd ratio	0.19	0.16	0.13	0.35	0.24	0.36	3×10^{-14}
R4570	0.60	0.60	0.42	0.63	0.56	0.40	2×10^{-1}
$\log \lambda L_{\text{cont}}$	43.18	43.20	0.43	43.33	43.34	0.42	5×10^{-4}
$\log L_{[\text{OIII}]}$	42.11	42.11	0.42	41.84	41.88	0.70	2×10^{-11}

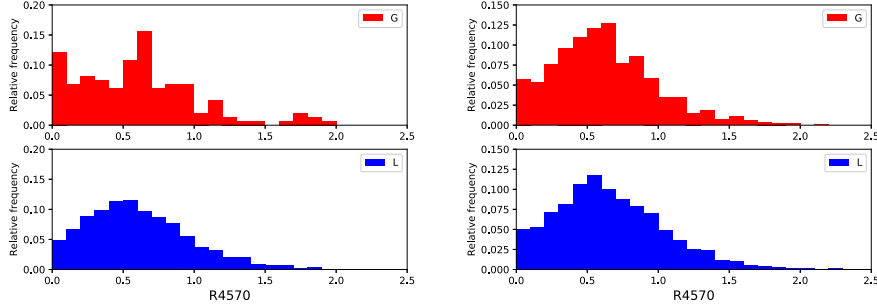


Figure 5. Distribution of R4570 of the two samples. Colors as in Fig. 2 and panels as in Fig. 3.

hole mass calculation is not ideal, since it has been shown that the second-order moment of the line is a better proxy for the velocity and less dependent on BLR geometry (Peterson, 2011; Foschini et al., 2015; Berton et al., 2015; Peterson & Dalla Bontà, 2018). However, since our aim is to compare the two distributions and not to obtain precise mass values, the use of FWHM is acceptable. The K-S

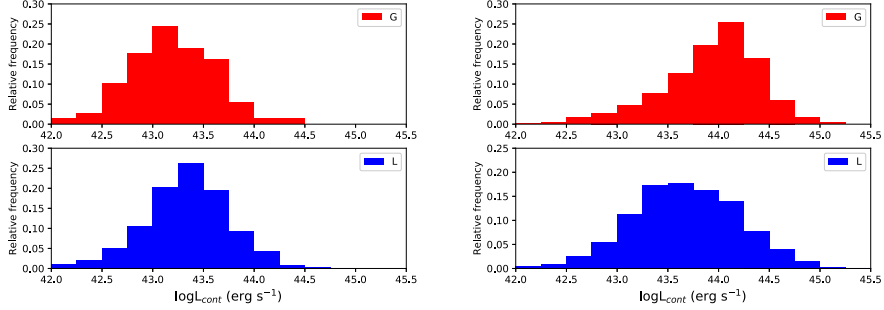


Figure 6. Distribution of the monochromatic continuum luminosity at 5100 Å of the two samples. Colors as in Fig. 2 and panels as in Fig. 3.

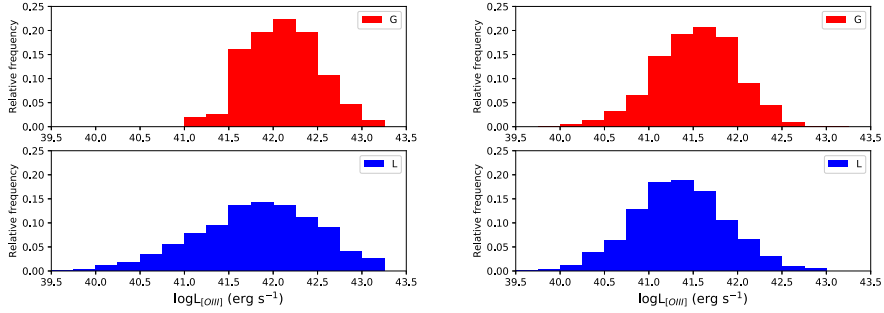


Figure 7. Distribution of [O III] luminosity of the two samples. Colors as in Fig. 2 and panels as in Fig. 3.

test rejects the null hypothesis at high confidence level both at low redshift and in the whole sample. The difference however is relatively small up to $z=0.25$, while it is remarkably large when the whole sample is considered. In both cases, mean and median mass are lower among L sources, but the mass of G sources at high redshift is significantly larger than those at low z .

The Eddington ratio was calculated, following R17, as the ratio between the bolometric luminosity and the Eddington luminosity. For the bolometric luminosity they assumed it to be nine times the monochromatic luminosity at $\lambda 5100$ Å. The Eddington luminosity was calculated as $L_{Edd} = 1.3 \times 10^{38} M_{BH}/M_{\odot}$, where M_{BH} is the black hole mass. The distributions are rather different, but at $z < 0.25$ this difference seems to be more significant. Given the shape of the distributions, seen in Fig. 4, we also carried out the A-D test to understand whether the tails of the two distributions are also statistically different. The

test confirms the difference both at low redshift and for the whole sample, rejecting the null hypothesis at a 99% confidence level. Indeed, it seems that the Eddington ratio is higher in L sources, and this is particularly evident at low redshift. At high redshift, the median values of the two samples are the same. However, there is a much larger number of high Eddington objects in the L sample than in the G sample, and this is in agreement with the larger mean value for this parameter in L sources, and with the result of the A-D test.

The Fe II multiplets flux was measured by R17 using the template provided by Kovačević et al. (2010), and later divided by the $H\beta$ flux to obtain the R4570 parameter. The two distributions are not statistically different below $z=0.25$. This result is confirmed both by the K-S test and by the A-D test. Both, in fact, do not reject the null hypothesis. When instead the whole samples are compared, the null hypothesis is rejected by both tests at 99% confidence level, suggesting that R4570 is in fact different between G and L sources. In particular, it seems that R4570 is slightly larger in L sources than in G sources.

The monochromatic luminosity of the continuum at 5100 Å was measured directly on the spectrum. The K-S test allows us to reject the null hypothesis in both redshift intervals. However, the behavior radically changes with the redshift. While up to $z=0.25$ on average L sources are brighter than G sources, when high- z objects are considered the result is the opposite, with G sources becoming brighter.

Finally, the [O III] flux was measured by fitting the $\lambda\lambda 4959, 5007$ lines with two Gaussians each, one to represent the core component, and the second to reproduce the wing (e.g., see Sulentic et al., 2000; Marziani et al., 2003; Komossa et al., 2008). Both in the low redshift domain and in the whole sample, the K-S test allows us to reject the null hypothesis, suggesting that the two sample do not originate from the same population of sources. The [O III] luminosity is indeed larger in G sources than in L sources. The difference becomes more evident when sources at high redshift are included. This result is particularly interesting in the light of the behavior found in the continuum luminosity, where the ionizing photons originate. While at high- z an increase in continuum luminosity corresponds to an increased [O III] luminosity, as expected, at low- z this does not happen, suggesting that another factor contributes to the larger [O III] luminosity observed in G sources (see next Section).

5. Discussion

As shown in Sect. 4, basically all physical properties of Gaussian and Lorentzian NLS1s are different. In the following we will discuss them one by one, and in the end provide a speculative picture regarding the evolution of these objects.

First of all, out of 3933 sources, approximately 2894 ($\sim 74\%$) can be better reproduced by a Lorentzian profile, while the remaining $\sim 26\%$ have a Gaussian line profile. The fraction of G sources is larger than what found by other studies.

For example, Cracco et al. (2016) found 96% of the profiles to be Lorentzian. However, as discussed above, we found that the redshift distribution of Gaussian profiles is concentrated at higher redshifts than Lorentzian, therefore a selection effect may be present. Indeed, when the sample is limited to $z=0.25$, the percentage of L sources is $\sim 90\%$, rather close to what was found in other works.

The different line profiles can be interpreted in terms of BLR geometry. As shown by Gaskell (2009), the BLR geometry in AGN seems to have a bird's nest appearance with velocity components

$$v_{keplerian} > v_{turbulent} \gtrsim v_{inflow} . \quad (2)$$

The presence of Keplerian motion was remarkably showed with VLTI observations of 3C 273 (Gravity Collaboration et al., 2018), and several authors (e.g., Kollatschny & Zetzl, 2011; Goad et al., 2012; Kollatschny & Zetzl, 2013a) claimed that the Gaussian profile originates when the BLR motion is dominated by a Keplerian rotation. However, in NLS1s the relation may be different, with

$$v_{keplerian} \sim v_{turbulent} , \quad (3)$$

while nothing can be said (yet) about the inflow velocity. Lorentzian profiles seem in fact to be associated with microturbulence (Goad et al., 2012), possibly pointing out that this kind of motion is significantly stronger in NLS1s. Such turbulent motion is likely associated with the vertical structure of the BLR, since it is due to random motion of the clouds above and below the equatorial plane (Kollatschny & Zetzl, 2013b). Indeed, a prominent fountain-like vertical structure has been also observed in AGN with Lorentzian line profiles of the Mg II line (Popović et al., 2019). All of this may indicate that the BLR geometry in NLS1s is less flattened than in other AGN, in agreement with the independence of line width from AGN inclination (Vietri et al., 2018).

5.1. Black hole mass

Black hole mass has always been the most discussed property of NLS1s, in particular after the discovery of γ -ray emission from those with a beamed relativistic jet (Abdo et al., 2009a,b). The presence of relativistic jets in these low-mass AGN was indeed a shocking discovery, since it contradicted the well-established paradigm according to which only high mass black holes are able to launch a relativistic jet (Laor, 2000). Some authors, indeed, tried to reconcile NLS1s, and extreme accretors in general, with the paradigm (Decarli et al., 2008; Chiaberge & Marconi, 2011). However, reverberation mapping (Peterson & Dalla Bontà, 2018) confirmed that NLS1s are characterized by a black hole with a mass lower than $10^8 M_{\odot}$. Furthermore, the low jet power observed in jetted NLS1s is likely associated with their low black hole mass (Foschini, 2014; Foschini et al., 2015). Jet power, indeed, scales non-linearly with black hole mass (Heinz & Sunyaev, 2003). For the same reason, the radio luminosity of beamed jetted NLS1s (Foschini, 2017) is lower with respect to other blazars, suggesting that they may

be the low-luminosity tail of the blazar population (Berton et al., 2016a). Last but not least the fact that, unlike other AGN, NLS1s are typically hosted in disk galaxies (both non-jetted and jetted, see Crenshaw et al., 2003; Deo et al., 2006; Orban de Xivry et al., 2011; Mathur et al., 2012; Kotilainen et al., 2016; Olguín-Iglesias et al., 2017; Järvelä et al., 2018; Berton et al., 2019), suggests that their black hole mass is lower than that of BLS1s, since the black hole mass tends to scale with the host galaxy morphology (Kormendy & Ho, 2013).

Our findings indicate that black hole masses change within the NLS1 population. The L and G distributions, both at low redshift and among the whole sample, are different from each other. This difference seems to be more prominent at large z . A selection effect could be present since the most luminous sources, seen at larger distances, may have a larger black hole mass and, as mentioned above, they preferentially belong to G sample. However, the presence of this difference at low z seems to indicate that it is not entirely a selection effect. Furthermore, this result is somewhat expected. The black hole mass is linearly dependent on the FWHM of $H\beta$ and a Lorentzian profile, for simple geometrical reasons, has a lower FWHM than a Gaussian profile with the same flux. If the $H\beta$ flux does not change, therefore, the derived black hole mass will be lower in Lorentzian sources (which in turn gives a higher Eddington ratio, a feature we also observe).

We must stress that such different behavior is not a bias: the line profile reflects a difference in the physical properties of the sources, therefore the different black hole mass distribution is a real effect. Furthermore, the black hole mass calculation we adopted in this work is the same for both line profiles. As mentioned above, the black hole mass we used are the same estimated by R17. In addition to a Gaussian to represent the narrow component, they decomposed the $H\beta$ profile fitting the broad component with either a Lorentzian or two Gaussians, according to the χ^2 statistics, when both $H\alpha$ and $H\beta$ were present in the spectrum (low z). They used instead a Lorentzian profile when only $H\beta$ is present in the spectrum. Assuming that the narrow component is the same in both cases, a Lorentzian broad component would yield to a lower FWHM with respect to a Gaussian broad component, thus slightly underestimating the black hole mass in the Gaussian sample. As a result, the intrinsic separation between the mass distributions of L and G sources should be even larger, and this would be evident particularly for high- z sources.

5.2. Eddington ratio, continuum and [O III] luminosity

It is widely known that NLS1s are extreme accretors, typically showing a rather high Eddington ratio (Boroson & Green, 1992; Marziani et al., 2018b, 2019). This phenomenon is believed to be the driver of the EV1 properties of AGN, and it actually accounts for many attributes of NLS1s. Strong disk winds are often observed in these sources (e.g., Jin et al., 2017a,b; Gallo et al., 2019), and the high Eddington ratio could also be responsible for the bulk outflowing

motion often observed in their NLR (Zamanov et al., 2002; Marziani et al., 2003; Komossa et al., 2008).

In our samples, we found that Lorentzian sources have a systematically different Eddington ratio, usually higher with respect to Gaussian sources. The mean and median values of Eddington ratio of the whole sample are higher than the mean and median of low redshift objects. Since black hole masses tend also to be larger when the entire sample is considered, this indicates that the bolometric luminosity of sources at high redshift is larger. This is expected, since low-luminosity sources at high z are simply not visible. Therefore, the effect of redshift is very prominent on the results we obtained for the whole sample.

What we observe in the redshift-limited sample is way more interesting. The difference between the two distribution is very large, and significantly larger than the difference observed between the two black hole mass distributions. This indicates that the bolometric luminosity of G sources and L sources are also different at low z , as shown by the different distributions of continuum luminosity³. In particular, it seems that at low redshift L sources are brighter than G sources. Indeed, as found from the continuum luminosity, in our low- z sample the median value of bolometric luminosity of G sources is 1.4×10^{44} erg s⁻¹, while in L sources the median is 2.0×10^{44} erg s⁻¹. Even if the difference is not so pronounced, this is an interesting result since it is in contradiction with what we observe in the [O III] luminosity. The G sources, indeed, are brighter than L sources (1.3×10^{42} erg s⁻¹ for G sources and 6.9×10^{41} erg s⁻¹ for L sources), but the brighter continuum in L sources should indeed produce brighter high ionization lines, such as [O III], within the same class of objects. The difference in [O III] distribution also rules out the possibility that the difference between L and G sources is inclination. Since [O III] luminosity is an isotropic property, if L and G sources were seen at different angles their [O III] luminosities should be the same.

5.3. Iron and R4570

The origin of iron in NLS1s is still unclear. However, it is well known that iron originates in supernova explosions, particularly from Ia and core-collapse supernovae (Ib, Ic, II). Authors already suggested that the origin of metals in AGN can be connected with starburst events (Heller & Shlosman, 1994; Collin & Zahn, 1999). NLS1s, in particular, are well known to be objects with an enhanced star formation rate with respect to BLS1s (Sani et al., 2010; Caccianiga et al., 2015). A high star formation rate can naturally lead to the explosion of several core-collapse supernovae in addition to Ia SNe, thus increasing the metallicity of these AGN (Chen et al., 2009; Million et al., 2011). When galaxy-galaxy interaction is ongoing, as observed in the hosts of several jetted NLS1s (Antón et al., 2008; D’Ammando et al., 2018; Järvelä et al., 2018; Berton et al., 2019),

³We remind that the bolometric luminosity was estimated by multiplying the monochromatic luminosity times a constant value.

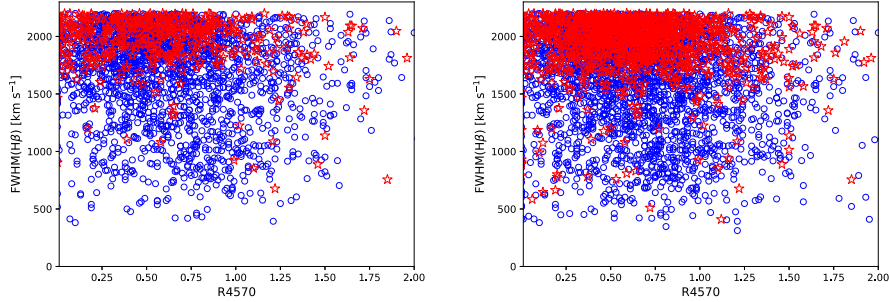


Figure 8. Position of our sources on the EV1 plane. The x-axis is the R4570, the y-axis is the FWHM($H\beta$). Colors as in Fig. 2 and panels as in Fig. 3.

star formation events and supernovae explosions may be even more common. For example, in the case of IRAS 20181-2244, the star formation rate was estimated from the near infrared to be close to $300 M_{\odot} \text{ yr}^{-1}$ (Caccianiga et al., 2015), and its host galaxy is clearly undergoing a major merging event (Berton et al., 2019). These events may trigger a large number of core-collapse supernovae explosions in a rather short timescale. Additionally, given the typical velocity of supernovae ejecta (5000 km s^{-1}), the products of the explosion can cross a Milky Way-sized galaxy in a few 10^6 years, a timescale possibly shorter than a typical NLS1 activity event (10^8 years, Komossa, 2018). If the star formation is circumnuclear, as pointed out by Sani et al. (2010), the timescale to feed iron and other metals into the nuclear region is even shorter.

The distributions of R4570 are statistically different when the whole sample is considered, but at low z the R4570 seems identical in L and G sources. It is worth noting that R4570 does not depend only on Fe II strength, but also on the $H\beta$ flux. Therefore, a lower R4570 does not necessarily reflect on the Fe II flux directly (Cracco et al., 2016). In the case of our low- z sample, in analogy with what happens for [O III], the $H\beta$ luminosity is higher in the G sample than in the L sample (median logarithmic values 42.45 vs 42.18 for G and L, respectively). If the R4570 in L and G sources is approximately the same, this result implies that the Fe II strength is higher in G sources. The same result is found when using the whole samples. In this case the ratio R4570 is generally lower in G sources. As before, $H\beta$ is instead significantly brighter in G sources, therefore the Fe II strength is even higher when high- z sources are included in the sample.

5.4. A complete picture? EV1 and intraclass evolution

To have a better understanding of the previous results, we plotted our sources on the EV1 plane. Although in general the y-axis of EV1 is the FWHM of H β broad component, in our case the H β line is well represented by a single component, therefore we used the total FWHM of the line. What is shown in Fig. 8 is extremely interesting. While L sources are basically spread on the whole diagram, the bulk of G sources is located close to the FWHM threshold of NLS1s, and on the left part of the diagram. This is the region where the vertical branch of the EV1 begins. This may suggest that G sources act like a “bridge”, connecting Lorentzian sources of the so-called population A (FWHM < 4000 km s⁻¹, Sulentic et al., 2000) with the mostly Gaussian sources that belong to population B (FWHM > 4000 km s⁻¹).

As already mentioned, many authors suggested that the driver of EV1 is the Eddington ratio (Boroson & Green, 1992). This idea is consistent with what we see in our plot, since G sources are located on the upper part of the diagram, where the Eddington ratio is supposed to decrease. However, some authors suggested that the EV1 represents the equivalent of a main sequence for quasars (Sulentic & Marziani, 2015), and that the position of the sources on this sequence may be connected to their age (Fraix-Burnet et al., 2017a,b). Indeed, the black hole mass could be used as a sort of an “arrow of time”. Since black hole mass can only grow, young sources must have lower masses than old sources. On the EV1, this would mean that population A sources are the progenitors of population B objects, with NLS1s being the youngest of all. Furthermore, given the different distributions of G and L sources on the EV1, and the fact that population B sources are largely dominated by Gaussian line profiles, we hypothesize that intraclass evolution could occur within the NLS1 population, and that L sources are the progenitors of G sources. It is already well known, in fact, that there is no sharp transition between NLS1s and BLS1s, but their properties form a continuous distribution (e.g., Cracco et al., 2016). It is therefore natural to expect the existence of an intermediate class of sources, which constitutes a link between the youngest NLS1s and their older evolved counterparts.

This evolutionary scenario could account for our previous results. The black hole mass increases going from L to G sources, in agreement with what mentioned before. If L sources are recently switched-on AGN, it is possible that they are surrounded by a dense environment consisting of gas clouds, dust, and stars. In these initial phases the accreting material is more abundant, which could account for the higher Eddington ratio. When the activity goes on for a long time, the Eddington ratio slightly decreases, while the AGN approaches the BLS1 phase and moves on the EV1 toward population B. We highlight that this model does not require a continuous single accretion episode. Separate activity episodes, possibly due to disk instabilities (Czerny et al., 2009), do not affect this hypothesis. The [O III] luminosity could be due to a change in the BLR geometry, reflected by the different line profiles. As mentioned above, L sources

may have a non-negligible vertical structure, which could increase the covering factor for the NLR. The ionizing continuum produced by the accretion disk that could reach the NLR may be absorbed by a more spherical BLR, accounting for weaker high ionization lines. With time, disk winds and radiation pressure may blow away the turbulent clouds, leaving a BLR dominated by Keplerian motion, and decreasing the covering factor for the NLR.

Finally, Fe II strength may also be included into this scenario, if we assume that the Fe II abundance is connected to the star formation rate. AGN activity is known to heat the gas and suppress star formation (Morganti, 2017). Therefore, supernova events may be less common in sources where the AGN activity has been ongoing for a long time. However, if NLS1s evolve from Lorentzian objects to Gaussian objects, we should observe an increasing amount of iron with increasing age. All the iron atoms, indeed, are formed during the early phase of the AGN life, and this behavior is essentially what we observe among our samples.

An interesting example that may fit into our picture is that of Mrk 783. This NLS1 was not included in our study, since its $H\beta$ profile cannot be reproduced by a single component (Berton et al., 2015; Congiu et al., 2017a,b). However, when the narrow component is subtracted, its line profile can be classified as Gaussian. In radio this NLS1 shows a prominent diffuse radio emission on kpc-scale, which can be interpreted in terms of relativistic jet precession or even as a relic emission. Therefore, despite being an NLS1, it is unlikely to be a very young source since, unlike most jetted NLS1s (Berton et al., 2018), it already had the time to develop a prominent diffuse emission. Its other properties are reminiscent of those of Gaussian sources. The black hole mass is in the higher end of NLS1s distribution ($4.3 \times 10^7 M_{\odot}$, Berton et al., 2015), its Eddington ratio is quite low (0.11, Berton et al., 2015), and its [O III] line is quite strong with respect to $H\beta$ ($R_{5007} \sim 2.9$). Only the iron is slightly different from the typical properties of the Gaussian sample, since the iron is basically not present with the only exception of a few high ionization lines (Congiu et al., in prep.). However, Mrk 783, in conclusion, could be a good example for this scenario, since its properties seem to fit this evolutionary picture.

6. Summary

In this work we analyzed the physical properties of two subsamples of NLS1 galaxies extracted from the SDSS. We divided them into Lorentzian and Gaussian sources according to the profile that better represents their $H\beta$ line. We later introduced a redshift limit at $z=0.25$ in the sample, in order to study both low-redshift objects and the sample as a whole. Our main result is that most of their physical properties seem to differ. From Lorentzian to Gaussian sources the black hole mass tends to increase, the Eddington ratio decreases, the Fe II strength decreases, and the [O III] luminosity increases.

We try to fit these differences into the context of the quasar main sequence and the EV1, suggesting that Lorentzian sources are the progenitors of Gaussian sources. This groundbreaking scenario seems to account for most of the observed results. In particular, the increased black hole mass may be used as an arrow of time which is representative of AGN evolution. If this hypothesis is correct, AGN may be born as NLS1s with Lorentzian line profiles, later evolve to NLS1s with a Gaussian profile, and eventually move in the EV1 region where population B sources are.

This model is still rather speculative, and needs further confirmation. A more careful analysis of the line profiles on large samples of NLS1s is needed in order to better separate Gaussian and Lorentzian sources. Furthermore, this study should be extended to the entire population A of the EV1, to see if this trend can be confirmed, and eventually to all type 1 AGN. An upcoming paper will be dedicated to the careful analysis of NLS1 spectra, and will provide a more complete view on this important issue.

Acknowledgements. MB would like to warmly thank the organizers of the 12th Serbian Conference on Spectral Line Shapes in Astrophysics for the interesting and fruitful meeting. The authors are grateful to P. Marziani, W. Kollatschny, E. Bon, S. Ciroi, and L. Foschini for helpful suggestions and discussions. This research has made use of the NASA/IPAC Extragalactic Database (NED) which is operated by the Jet Propulsion Laboratory, California Institute of Technology, under contract with the National Aeronautics and Space Administration. Funding for the Sloan Digital Sky Survey has been provided by the Alfred P. Sloan Foundation, and the U.S. Department of Energy Office of Science. The SDSS web site is <http://www.sdss.org>. SDSS-III is managed by the Astrophysical Research Consortium for the Participating Institutions of the SDSS-III Collaboration including the University of Arizona, the Brazilian Participation Group, Brookhaven National Laboratory, Carnegie Mellon University, University of Florida, the French Participation Group, the German Participation Group, Harvard University, the Instituto de Astrofísica de Canarias, the Michigan State/Notre Dame/JINA Participation Group, Johns Hopkins University, Lawrence Berkeley National Laboratory, Max Planck Institute for Astrophysics, Max Planck Institute for Extraterrestrial Physics, New Mexico State University, University of Portsmouth, Princeton University, the Spanish Participation Group, University of Tokyo, University of Utah, Vanderbilt University, University of Virginia, University of Washington, and Yale University.

References

- Abdo, A. A., Ackermann, M., Ajello, M., et al., Fermi/Large Area Telescope Discovery of Gamma-Ray Emission from a Relativistic Jet in the Narrow-Line Quasar PMN J0948+0022. 2009a, *Astrophys. J.*, **699**, 976, DOI: 10.1088/0004-637X/699/2/976
- Abdo, A. A., Ackermann, M., Ajello, M., et al., Radio-Loud Narrow-Line Seyfert 1 as a New Class of Gamma-Ray Active Galactic Nuclei. 2009b, *Astrophys. J., Lett.*, **707**, L142, DOI: 10.1088/0004-637X/707/2/L142

- Antón, S., Browne, I. W. A., & Marchã, M. J., The colour of the narrow line Sy1-blazar 0324+3410. 2008, *Astron. Astrophys.*, **490**, 583, DOI: 10.1051/0004-6361:20078926
- Antonucci, R., Unified models for active galactic nuclei and quasars. 1993, *ARA&A*, **31**, 473, DOI: 10.1146/annurev.aa.31.090193.002353
- Bentz, M. C., Denney, K. D., Grier, C. J., et al., The Low-luminosity End of the Radius-Luminosity Relationship for Active Galactic Nuclei. 2013, *Astrophys. J.*, **767**, 149, DOI: 10.1088/0004-637X/767/2/149
- Berton, M., An updated view on the parent population of γ -ray emitting narrow-line Seyfert 1 galaxies. 2018, in *Proceedings of Science, vol. Revisiting narrow-line Seyfert 1 galaxies and their place in the Universe. 9-13 April 2018*, 26
- Berton, M., Caccianiga, A., Foschini, L., et al., Compact steep-spectrum sources as the parent population of flat-spectrum radio-loud narrow-line Seyfert 1 galaxies. 2016a, *Astron. Astrophys.*, **591**, A98, DOI: 10.1051/0004-6361/201628171
- Berton, M., Congiu, E., Ciroi, S., et al., The Interacting Late-type Host Galaxy of the Radio-loud Narrow-line Seyfert 1 IRAS 20181-2244. 2019, *Astron. J.*, **157**, 48, DOI: 10.3847/1538-3881/aaf5ca
- Berton, M., Congiu, E., Järvelä, E., et al., Radio-emitting narrow-line Seyfert 1 galaxies in the JVLA perspective. 2018, *Astron. Astrophys.*, **614**, A87, DOI: 10.1051/0004-6361/201832612
- Berton, M., Foschini, L., Caccianiga, A., et al., An orientation-based unification of young jetted active galactic nuclei: the case of 3C 286. 2017, *Frontiers in Astronomy and Space Sciences*, **4**, 8, DOI: 10.3389/fspas.2017.00008
- Berton, M., Foschini, L., Ciroi, S., et al., [O III] line properties in two samples of radio-emitting narrow-line Seyfert 1 galaxies. 2016b, *Astron. Astrophys.*, **591**, A88, DOI: 10.1051/0004-6361/201527056
- Berton, M., Foschini, L., Ciroi, S., et al., Parent population of flat-spectrum radio-loud narrow-Line Seyfert 1 galaxies. 2015, *Astron. Astrophys.*, **578**, A28
- Boller, T., Brandt, W. N., & Fink, H., Soft X-ray properties of narrow-line Seyfert 1 galaxies. 1996, *Astron. Astrophys.*, **305**, 53
- Boller, T., Meurs, E. J. A., Brinkmann, W., et al., ROSAT All Sky Survey observations of IRAS galaxies. 1992, *Astron. Astrophys.*, **261**, 57
- Boroson, T. A. & Green, R. F., The emission-line properties of low-redshift quasi-stellar objects. 1992, *Astrophys. J., Suppl.*, **80**, 109, DOI: 10.1086/191661
- Caccianiga, A., Antón, S., Ballo, L., et al., WISE colours and star formation in the host galaxies of radio-loud narrow-line Seyfert 1. 2015, *Mon. Not. R. Astron. Soc.*, **451**, 1795, DOI: 10.1093/mnras/stv939
- Chen, S., Berton, M., La Mura, G., et al., Probing narrow-line Seyfert 1 galaxies in the southern hemisphere. 2018, *Astron. Astrophys.*, **615**, A167, DOI: 10.1051/0004-6361/201832678
- Chen, Y.-M., Wang, J.-M., Yan, C.-S., Hu, C., & Zhang, S., The Starburst-Active Galactic Nucleus Connection: The Role of Young Stellar Populations in Fueling Su-

- permassive Black Holes. 2009, *Astrophys. J., Lett.*, **695**, L130, DOI: 10.1088/0004-637X/695/2/L130
- Chiaberge, M. & Marconi, A., On the origin of radio loudness in active galactic nuclei and its relationship with the properties of the central supermassive black hole. 2011, *Mon. Not. R. Astron. Soc.*, **416**, 917, DOI: 10.1111/j.1365-2966.2011.19079.x
- Collin, S. & Zahn, J.-P., Star Formation in Accretion Disks Around Massive Black Holes and Pregalactic Enrichment. 1999, *Astrophys. Space Sci.*, **265**, 501, DOI: 10.1023/A:1002191506811
- Congiu, E., Berton, M., Giroletti, M., et al., Kiloparsec-scale emission in the narrow-line Seyfert 1 galaxy Mrk 783. 2017a, *Astron. Astrophys.*, **603**, A32, DOI: 10.1051/0004-6361/201730616
- Congiu, E., Contini, M., Ciroi, S., et al., Extended Narrow-Line Region in Seyfert Galaxies. 2017b, *Frontiers in Astronomy and Space Sciences*, **4**, 27, DOI: 10.3389/fspas.2017.00027
- Cracco, V., Ciroi, S., Berton, M., et al., A spectroscopic analysis of a sample of narrow-line Seyfert 1 galaxies selected from the Sloan Digital Sky Survey. 2016, *Mon. Not. R. Astron. Soc.*, **462**, 1256, DOI: 10.1093/mnras/stw1689
- Crenshaw, D. M., Kraemer, S. B., & Gabel, J. R., The Host Galaxies of Narrow-Line Seyfert 1 Galaxies: Evidence for Bar-Driven Fueling. 2003, *Astron. J.*, **126**, 1690, DOI: 10.1086/377625
- Czerny, B., Siemiginowska, A., Janiuk, A., Nikiel-Wroczyński, B., & Stawarz, L., Accretion Disk Model of Short-Timescale Intermittent Activity in Young Radio Sources. 2009, *Astrophys. J.*, **698**, 840, DOI: 10.1088/0004-637X/698/1/840
- D'Ammando, F., Acosta-Pulido, J. A., Capetti, A., et al., The host galaxy of the γ -ray-emitting narrow-line Seyfert 1 galaxy PKS 1502+036. 2018, *Mon. Not. R. Astron. Soc.*, **478**, L66, DOI: 10.1093/mnrasl/sly072
- Decarli, R., Dotti, M., Fontana, M., & Haardt, F., Are the black hole masses in narrow-line Seyfert 1 galaxies actually small? 2008, *Mon. Not. R. Astron. Soc.*, **386**, L15, DOI: 10.1111/j.1745-3933.2008.00451.x
- Deo, R. P., Crenshaw, D. M., & Kraemer, S. B., The Host Galaxies of Narrow-Line Seyfert 1 Galaxies: Nuclear Dust Morphology and Starburst Rings. 2006, *Astron. J.*, **132**, 321, DOI: 10.1086/504894
- Foschini, L., The Unification of Relativistic Jets. 2014, *International Journal of Modern Physics Conference Series*, **28**, 1460188, DOI: 10.1142/S2010194514601884
- Foschini, L., What we talk about when we talk about blazars? 2017, *Frontiers in Astronomy and Space Sciences*, **4**, 6, DOI: 10.3389/fspas.2017.00006
- Foschini, L., Berton, M., Caccianiga, A., et al., Properties of flat-spectrum radio-loud narrow-line Seyfert 1 galaxies. 2015, *Astron. Astrophys.*, **575**, A13, DOI: 10.1051/0004-6361/201424972
- Fraix-Burnet, D., D'Onofrio, M., & Marziani, P., Phylogenetic Analyses of Quasars and Galaxies. 2017a, *Frontiers in Astronomy and Space Sciences*, **4**, 20, DOI: 10.3389/fspas.2017.00020

- Fraix-Burnet, D., Marziani, P., D’Onofrio, M., & Dultzin, D., The phylogeny of quasars and the ontogeny of their central black holes. 2017b, *Frontiers in Astronomy and Space Sciences*, **4**, 1, DOI: 10.3389/fspas.2017.00001
- Gallo, L., X-ray perspective of Narrow-line Seyfert 1 galaxies. 2018, in *Proceedings of Science, vol. Revisiting narrow-line Seyfert 1 galaxies and their place in the Universe*, 34
- Gallo, L. C., Gonzalez, A. G., Waddell, S. G. H., et al., Evidence for an emerging disc wind and collimated outflow during an X-ray flare in the narrow-line Seyfert 1 galaxy Mrk 335. 2019, *Mon. Not. R. Astron. Soc.*, **484**, 4287, DOI: 10.1093/mnras/stz274
- Gaskell, C. M., What broad emission lines tell us about how active galactic nuclei work. 2009, *NewAR*, **53**, 140, DOI: 10.1016/j.newar.2009.09.006
- Goad, M. R., Korista, K. T., & Ruff, A. J., The broad emission-line region: the confluence of the outer accretion disc with the inner edge of the dusty torus. 2012, *Mon. Not. R. Astron. Soc.*, **426**, 3086, DOI: 10.1111/j.1365-2966.2012.21808.x
- Goodrich, R. W., Spectropolarimetry of ‘narrow-line’ Seyfert 1 galaxies. 1989, *Astrophys. J.*, **342**, 224, DOI: 10.1086/167586
- Gravity Collaboration, Sturm, E., Dexter, J., et al., Spatially resolved rotation of the broad-line region of a quasar at sub-parsec scale. 2018, *Nature*, **563**, 657, DOI: 10.1038/s41586-018-0731-9
- Heinz, S. & Sunyaev, R. A., The non-linear dependence of flux on black hole mass and accretion rate in core-dominated jets. 2003, *Mon. Not. R. Astron. Soc.*, **343**, L59, DOI: 10.1046/j.1365-8711.2003.06918.x
- Heller, C. H. & Shlosman, I., Fueling nuclear activity in disk galaxies: Starbursts and monsters. 1994, *Astrophys. J.*, **424**, 84, DOI: 10.1086/173874
- Hou, A., Parker, L. C., Harris, W. E., & Wilman, D. J., Statistical Tools for Classifying Galaxy Group Dynamics. 2009, *Astrophys. J.*, **702**, 1199, DOI: 10.1088/0004-637X/702/2/1199
- Järvelä, E., Lähteenmäki, A., & Berton, M., Near-infrared morphologies of the host galaxies of narrow-line Seyfert 1 galaxies. 2018, *Astron. Astrophys.*, **619**, A69, DOI: 10.1051/0004-6361/201832876
- Järvelä, E., Lähteenmäki, A., Lietzen, H., et al., Large-scale environments of narrow-line Seyfert 1 galaxies. 2017, *Astron. Astrophys.*, **606**, A9, DOI: 10.1051/0004-6361/201731318
- Jin, C., Done, C., & Ward, M., Super-Eddington QSO RX J0439.6-5311 - I. Origin of the soft X-ray excess and structure of the inner accretion flow. 2017a, *Mon. Not. R. Astron. Soc.*, **468**, 3663, DOI: 10.1093/mnras/stx718
- Jin, C., Done, C., Ward, M., & Gardner, E., Super-Eddington QSO RX J0439.6-5311 - II. Multiwavelength constraints on the global structure of the accretion flow. 2017b, *Mon. Not. R. Astron. Soc.*, **471**, 706, DOI: 10.1093/mnras/stx1634
- Kollatschny, W. & Zetzl, M., Broad-line active galactic nuclei rotate faster than narrow-line ones. 2011, *Nature*, **470**, 366, DOI: 10.1038/nature09761

- Kollatschny, W. & Zetzl, M., The shape of broad-line profiles in active galactic nuclei. 2013a, *Astron. Astrophys.*, **549**, A100, DOI: 10.1051/0004-6361/201219411
- Kollatschny, W. & Zetzl, M., Vertical broad-line region structure in nearby active galactic nuclei. 2013b, *Astron. Astrophys.*, **558**, A26, DOI: 10.1051/0004-6361/201321685
- Komatsu, E., Smith, K. M., Dunkley, J., et al., Seven-year Wilkinson Microwave Anisotropy Probe (WMAP) Observations: Cosmological Interpretation. 2011, *Astrophys. J., Suppl.*, **192**, 18, DOI: 10.1088/0067-0049/192/2/18
- Komossa, S., Narrow-line Seyfert 1 Galaxies. 2008, in Revista Mexicana de Astronomia y Astrofisica Conference Series, Vol. **32**, *Revista Mexicana de Astronomia y Astrofisica Conference Series*, 86–92
- Komossa, S., Multi-wavelength properties of radio-loud Narrow-line Seyfert 1 galaxies. 2018, in *Proceedings of Science, vol. Revisiting narrow-line Seyfert 1 galaxies and their place in the Universe*, 15
- Komossa, S., Xu, D., Zhou, H., Storchi-Bergmann, T., & Binette, L., On the Nature of Seyfert Galaxies with High [O III] λ 5007 Blueshifts. 2008, *Astrophys. J.*, **680**, 926, DOI: 10.1086/587932
- Kormendy, J. & Ho, L. C., Coevolution (Or Not) of Supermassive Black Holes and Host Galaxies. 2013, *Ann. Rev. Astron. Astrophys.*, **51**, 511, DOI: 10.1146/annurev-astro-082708-101811
- Kotilainen, J. K., León-Tavares, J., Olgún-Iglesias, A., et al., Discovery of a Pseudobulge Galaxy Launching Powerful Relativistic Jets. 2016, *Astrophys. J.*, **832**, 157, DOI: 10.3847/0004-637X/832/2/157
- Kovačević, J., Popović, L. Č., & Dimitrijević, M. S., Analysis of Optical Fe II Emission in a Sample of Active Galactic Nucleus Spectra. 2010, *Astrophys. J., Suppl.*, **189**, 15, DOI: 10.1088/0067-0049/189/1/15
- Laor, A., On Black Hole Masses and Radio Loudness in Active Galactic Nuclei. 2000, *Astrophys. J., Lett.*, **543**, L111, DOI: 10.1086/317280
- Lister, M., Radio Properties of Narrow-Line Seyfert 1 Galaxies. 2018, in *Revisiting narrow-line Seyfert 1 galaxies and their place in the Universe. 9-13 April 2018. Padova Botanical Garden*, 22
- Marziani, P., Bon, E., Bon, N., et al., Quasars: From the Physics of Line Formation to Cosmology. 2019, *Atoms*, **7**, 18, DOI: 10.3390/atoms7010018
- Marziani, P., del Olmo, A., D’Onofrio, M., et al., Narrow-line Seyfert 1s: what is wrong in a name? 2018a, in *Proceedings of Science, vol. Revisiting narrow-line Seyfert 1 galaxies and their place in the Universe*, 2
- Marziani, P., Dultzin, D., Sulentic, J. W., et al., A main sequence for quasars. 2018b, *Frontiers in Astronomy and Space Sciences*, **5**, 6, DOI: 10.3389/fspas.2018.00006
- Marziani, P., Sulentic, J. W., Zwitter, T., Dultzin-Hacyan, D., & Calvani, M., Searching for the Physical Drivers of the Eigenvector 1 Correlation Space. 2001, *Astrophys. J.*, **558**, 553, DOI: 10.1086/322286

- Marziani, P., Zamanov, R. K., Sulentic, J. W., & Calvani, M., Searching for the physical drivers of eigenvector 1: influence of black hole mass and Eddington ratio. 2003, *Mon. Not. R. Astron. Soc.*, **345**, 1133, DOI: 10.1046/j.1365-2966.2003.07033.x
- Mathur, S., Narrow-line Seyfert 1 galaxies and the evolution of galaxies and active galaxies. 2000, *Mon. Not. R. Astron. Soc.*, **314**, L17, DOI: 10.1046/j.1365-8711.2000.03530.x
- Mathur, S., Fields, D., Peterson, B. M., & Grupe, D., Supermassive Black Holes, Pseudobulges, and the Narrow-line Seyfert 1 Galaxies. 2012, *Astrophys. J.*, **754**, 146, DOI: 10.1088/0004-637X/754/2/146
- Million, E. T., Werner, N., Simionescu, A., & Allen, S. W., Core-collapse supernova enrichment in the core of the Virgo cluster. 2011, *Mon. Not. R. Astron. Soc.*, **418**, 2744, DOI: 10.1111/j.1365-2966.2011.19664.x
- Moran, E. C., Halpern, J. P., & Helfand, D. J., Classification of IRAS-selected X-Ray Galaxies in the ROSAT All-Sky Survey. 1996, *Astrophys. J., Suppl.*, **106**, 341, DOI: 10.1086/192341
- Morganti, R., The many routes to AGN feedback. 2017, *Frontiers in Astronomy and Space Sciences*, **4**, 42, DOI: 10.3389/fspas.2017.00042
- Olguín-Iglesias, A., Kotilainen, J. K., León Tavares, J., Chavushyan, V., & Añorve, C., Evidence of bar-driven secular evolution in the gamma-ray narrow-line Seyfert 1 galaxy FBQS J164442.5+261913. 2017, *Mon. Not. R. Astron. Soc.*, **467**, 3712, DOI: 10.1093/mnras/stx022
- Orban de Xivry, G., Davies, R., Schartmann, M., et al., The role of secular evolution in the black hole growth of narrow-line Seyfert 1 galaxies. 2011, *Mon. Not. R. Astron. Soc.*, **417**, 2721, DOI: 10.1111/j.1365-2966.2011.19439.x
- Osterbrock, D. E. & Pogge, R. W., The spectra of narrow-line Seyfert 1 galaxies. 1985, *Astrophys. J.*, **297**, 166, DOI: 10.1086/163513
- Peterson, B. & Dalla Bontà, E., Reverberation Mapping and Implications for Narrow-Line Seyfert 1 Galaxies. 2018, in *Proceedings of Science, vol. Revisiting narrow-line Seyfert 1 galaxies and their place in the Universe*, 8
- Peterson, B. M., Masses of Black Holes in Active Galactic Nuclei: Implications for Narrow-Line Seyfert 1 Galaxies. 2011, in *Narrow-Line Seyfert 1 Galaxies and their Place in the Universe*, 32
- Popović, L. Č., Kovačević-Dojčinović, J., & Marčeta-Mandić, S., The structure of the Mg II broad line emitting region in Type 1 AGNs. 2019, *Mon. Not. R. Astron. Soc.*, **484**, 3180, DOI: 10.1093/mnras/stz157
- Rakshit, S., Stalin, C. S., Chand, H., & Zhang, X.-G., A Catalog of Narrow Line Seyfert 1 Galaxies from the Sloan Digital Sky Survey Data Release 12. 2017, *Astrophys. J., Suppl.*, **229**, 39, DOI: 10.3847/1538-4365/aa6971
- Sani, E., Lutz, D., Risaliti, G., et al., Enhanced star formation in narrow-line Seyfert 1 active galactic nuclei revealed by Spitzer. 2010, *Mon. Not. R. Astron. Soc.*, **403**, 1246, DOI: 10.1111/j.1365-2966.2009.16217.x

- Sbarrato, T., Dotti, M., Ghirlanda, G., & Tavecchio, F., Study of the orientation of narrow-line Seyfert I. 2018, *Astron. Astrophys.*, **616**, A43, DOI: 10.1051/0004-6361/201732451
- Śniegowska, M., Czerny, B., You, B., et al., Properties of active galaxies at the extreme of Eigenvector 1. 2018, *Astron. Astrophys.*, **613**, A38, DOI: 10.1051/0004-6361/201730433
- Sulentic, J. & Marziani, P., Quasars in the 4D Eigenvector 1 Context: a stroll down memory lane. 2015, *Frontiers in Astronomy and Space Sciences*, **2**, 6, DOI: 10.3389/fspas.2015.00006
- Sulentic, J. W., Marziani, P., Zamanov, R., et al., Average Quasar Spectra in the Context of Eigenvector 1. 2002, *Astrophys. J., Lett.*, **566**, L71, DOI: 10.1086/339594
- Sulentic, J. W., Zwitter, T., Marziani, P., & Dultzin-Hacyan, D., Eigenvector 1: An Optimal Correlation Space for Active Galactic Nuclei. 2000, *Astrophys. J., Lett.*, **536**, L5, DOI: 10.1086/312717
- Urry, C. M. & Padovani, P., Unified Schemes for Radio-Loud Active Galactic Nuclei. 1995, *Publ. Astron. Soc. Pac.*, **107**, 803, DOI: 10.1086/133630
- Véron-Cetty, M.-P., Véron, P., & Gonçalves, A. C., A spectrophotometric atlas of Narrow-Line Seyfert 1 galaxies. 2001, *Astron. Astrophys.*, **372**, 730, DOI: 10.1051/0004-6361:20010489
- Vietri, A., Berton, M., Ciroi, S., et al., The link between X-ray complexity and optical lines in NLS1s. 2018, in *Proceedings of Science, vol. Revisiting narrow-line Seyfert 1 galaxies and their place in the Universe*, 47
- Zamanov, R., Marziani, P., Sulentic, J. W., et al., Kinematic Linkage between the Broad- and Narrow-Line-emitting Gas in Active Galactic Nuclei. 2002, *Astrophys. J., Lett.*, **576**, L9, DOI: 10.1086/342783
- Zhou, H., Wang, T., Yuan, W., et al., A Comprehensive Study of 2000 Narrow Line Seyfert 1 Galaxies from the Sloan Digital Sky Survey. I. The Sample. 2006, *Astrophys. J., Suppl.*, **166**, 128, DOI: 10.1086/504869

Main trends of the quasar main sequence - effect of viewing angle

S. Panda^{1,2}, P. Marziani³ and B. Czerny¹

¹ *Center for Theoretical Physics, Polish Academy of Sciences Al. Lotników 32/46, Warsaw, Poland, (E-mail: panda@cft.edu.pl)*

² *Nicolaus Copernicus Astronomical Center, Polish Academy of Sciences ul. Bartycka 00-716, Warsaw, Poland*

³ *INAF-Astronomical Observatory of Padova, Vicolo dell'Osservatorio 5, 35122 Padova PD, Italy*

Received: July 18, 2019; Accepted: October 3, 2019

Abstract. We address the effect of viewing angle of the accretion disk plane and the geometry of the broad line region (BLR) with the goal of interpreting the distribution of quasars along the main sequence (MS). We utilize photoionization code CLOUDY to model the BLR FeII emission, incorporating the grossly underestimated role of the form factor (f). We recover the dependence of the strength of the FeII emission in the optical (R_{FeII}) on $L_{\text{bol}}/L_{\text{Edd}}$ ratio and related observational trends - as a function of the spectral energy distribution (SED) shape, cloud density, composition and intra-cloud dynamics, assumed following prior observational constraints. With this approach, we are now able to explain the diversity of quasars and the change of the quasar properties along the Main Sequence (MS). Our approach also explains the rarity of the highest FeII emitters known as the extreme xA sources and can be used as a predictive tool in future reverberation mapping studies of Type-1 AGNs. This approach further justifies the use of quasars as ‘cosmological probes’.

Key words: Physical data and processes – Accretion, accretion disks – Line: formation – Radiative transfer – Turbulence – Galaxies: active – quasars: emission lines

1. Introduction

From a theoretical scenario, a quasar spectrum can be modelled using 4 basic ingredients: (a) black hole mass; (b) mass accretion rate; (c) viewing angle; and (d) black hole spin (see Campitiello et al. (2018) for a recent review). Boroson & Green (1992) incorporated the principal component analysis (PCA) to study the systematic trends between the numerous observed parameters of quasars. A long-standing issue in quasar astronomy has been the connection between observational and physical parameters (D’Onofrio et al., 2012). The eigenvector 1 of the original PCA paved way for the quasar main sequence picture as we know it today (Sulentic et al., 2000; Shen & Ho, 2014). The main sequence (MS) connects the velocity profile of ‘broad’ H β with the strength of the FeII emission

(R_{FeII}), i.e., the intensity of the FeII blend within 4434-4684 Å normalized with the ‘broad’ H β intensity.

FeII is a complex ion that comprises of numerous multiplets and transitions. These transitions are produced via a number of line excitation processes (e.g. photoionisation, continuum fluorescence, collisional excitation, self-fluorescence within FeII fluorescent excitation by Ly α and Ly β lines). The local physical conditions shape the spectrum and to make a deduction of these physical conditions, e.g., density, temperature, and iron abundance of the emitting regions, we require a complete simulation incorporating the various physical mechanisms that affect the FeII spectrum (Verner et al., 1999). In the new version of CLOUDY (Ferland et al., 2013, 2017), the FeII emission is modelled with 371 levels up to 11.6 eV, including 68,535 transitions based on the FeII model of Verner et al. (1999), which is a big improvement from the previous versions. The number of transitions is so large that the blended lines of FeII take the form of a pseudo-continuum, in which only few features can be unambiguously resolved. The modelled FeII pseudo-continuum shows quite good agreement with many observational FeII templates in the optical (Boroson & Green 1992; Véron-Cetty & Véron 2003; Kovačević et al. 2010).

In our previous works (Panda et al., 2017, 2018, 2019a) we were successful in modelling almost the entire MS diagram constructed for over 20,000 SDSS quasars. In the past studies, we had incorporated only two of the aforementioned physical parameters of the super massive black hole i.e., black hole mass and accretion rate. The modelling was affected also by the cloud density, metallicity and microturbulence.

In Panda et al. (2019b), we have shown that taking into account the viewing angle along with systematic trends in $L_{\text{bol}}/L_{\text{Edd}}$, local cloud density, cloud chemical composition and the shape of the ionizing continua which are known from prior observations, we can (a) explain the quasar main sequence starting from the low- R_{FeII} high FWHM sources (Population B, FWHM H β > 4000 km s $^{-1}$) to the high- R_{FeII} low FWHM sources (Population A, FWHM H β \leq 4000 km s $^{-1}$); and (b) explain why the highly accreting sources are also high-FeII emitters. These sources are of special importance in view of their potential use as Eddington standard candles i.e., sources for which the $L_{\text{bol}}/L_{\text{Edd}}$ and not the luminosity can be assumed to scatter around a well-defined value (Wang et al., 2013; Marziani & Sulentic, 2014).

In the current work, we present the model which incorporates the viewing angle effects in a much more careful way. Instead of discreet values of the density and metallicity, fixed for each AGN spectral type along the main sequence, we now allow for a range of densities and metallicities in each bin. We also analyze the effect of the SED, microturbulence and the black hole mass. The method allows to obtain more generic constraints for a viewing angle for each spectral type class. However, the method is now much more computational time consuming so at present we show the full results only for one representative spectral bin A1. In Section 2, we describe the derivation of the form factor and

how it is incorporated in our modelling. In Section 3, we describe the outcomes from these photoionisation simulations performed with *CLOUDY* in terms of (a) viewing angle, (b) shape of the SEDs, (c) micro-turbulence, and (d) increasing black hole mass. We show the relevance of this model to be used as a predictive tool to estimate the BLR sizes. In Section 4, we summarize the results and provide a road-map for the future work.

2. Method and Analysis

We perform the theoretical modelling of the quasar properties assuming, as in Panda et al. (2017, 2018), that the central black hole is surrounded by an accretion disk which provides the optical/UV continuum, and a hot corona, which is the source of the X-ray radiation. This continuum illuminates the BLR clouds located at a distance given by the BLR size. Photoionization modeling allow us to calculate BLR line intensities, and the BLR radius is reflected in the kinematic line width under the assumption of the Keplerian motion.

However, there are several new elements in the current study. First, we now allow for the dependence of the AGN appearance on the viewing angle, instead of using universal (average) viewing angle for all objects as in Panda et al. (2018, 2019a). Second, we approximate the trends noticed before between the model parameters and the source location in the $R_{\text{FeII}} - \text{FWHM}(\text{H}\beta)$ plane, and we model separately the spectral bins of the quasar MS plane assuming the representative values appropriate for each bin. Below we describe step by step our new approach to quasar MS modelling.

2.1. Effect of viewing angle on the main sequence

The virial relation is used to estimate the inner radius (r_{BLR}) of the broad, ionized cloud (Woltjer, 1959):

$$r_{BLR} \propto \frac{GM_{BH}}{\sigma_{line}^2} \quad (1)$$

where, G is the Gravitational constant, M_{BH} is the mass of the black hole, and, σ_{line}^2 is the square of the velocity dispersion of the emission line that is considered. This velocity dispersion can be replaced with the line's full-width at half maximum (FWHM) which is the radial velocity projection of the the "true" Keplerian velocity (v_k). Replacing the proportionality sign with a constant, we can write

$$r_{BLR} = \left(\frac{1}{f}\right) \frac{GM_{BH}}{FWHM^2} \quad (2)$$

The line FWHM can be expressed as:

$$FWHM^2 = 4(v_{iso}^2 + v_K^2 \sin^2 \theta) \quad (3)$$

where v_{iso} is the isotropic velocity component and θ is the viewing angle (Collin et al., 2006). The viewing angle is defined as the angle between the axis perpendicular to the disc and the line of sight to the observer. The full range of the viewing angles considered for the modelling is 0-60 degrees. This range is chosen to select only those sources that are un-obscured in accordance with unification schemes (Antonucci (1993); Urry & Padovani (1995), see Padovani et al. (2017) for a recent review). The FWHM is related to the v_k by

$$v_k^2 = f FWHM^2 \quad (4)$$

This proportionality constant has been a factor of debate (see Yu et al. 2019 for a recent review and references therein). Known as form factor (or structure factor or virial factor), f depends on the structure, kinematics, and inclination of the BLR (Collin et al., 2006). Combining Equations 3 and 4, we get

$$f = \frac{1}{4} \left[\frac{1}{\kappa^2 + \sin^2 \theta} \right] \quad (5)$$

where, κ is the ratio between v_{iso} and v_K , which decides how isotropic the gas distribution is around the central potential. If the value is close to zero, it represents a flat disk with thickness almost zero. On the other hand, if the value of κ is close to unity, it represents an almost spherical distribution of the gas.

2.2. Photoionisation modelling of the main sequence

We use the latest version of the publicly available photoionisation code *CLOUDY* (Ferland et al., 2017) to solve the radiative transfer under local thermodynamic equilibrium (LTE), satisfying ionization balance under a plane-parallel approximation. We assume a single cloud model where the density (n_{H}) of the ionized gas cloud is varied from 10^9 cm^{-3} to 10^{13} cm^{-3} with a step-size of 0.25 (in log-scale). We utilize the *GASS10* model (Grevesse et al., 2010) to recover the solar-like abundances and vary the metallicity within the gas cloud, going from a sub-solar type ($0.1 Z_{\odot}$) to super-solar ($100 Z_{\odot}$) with a step-size of 0.25 (in log-scale). The size of the BLR is estimated from the virial relation, assuming a black hole mass, a distribution in the viewing angle [0-90 degrees] and FWHM as described in Section 3.2. The total luminosity of the ionizing continuum is derived assuming a value of the $L_{\text{bol}}/L_{\text{Edd}}$ and the respective value for the black hole mass. We utilize different SEDs to highlight the differences in the shape of the ionizing continuum that is found to be relevant for the recovered values of the intensities of the line emissions (see Panda et al. (2019b) for more details).

3. Results and Discussions

3.1. Interpretation of the quasar main sequence

As an initial test, we assume a fixed black hole mass ($M_{\text{BH}} = 10^8 M_{\odot}$). Two Populations are identified in Figure 1 – the quasar main sequence diagram: Pop-

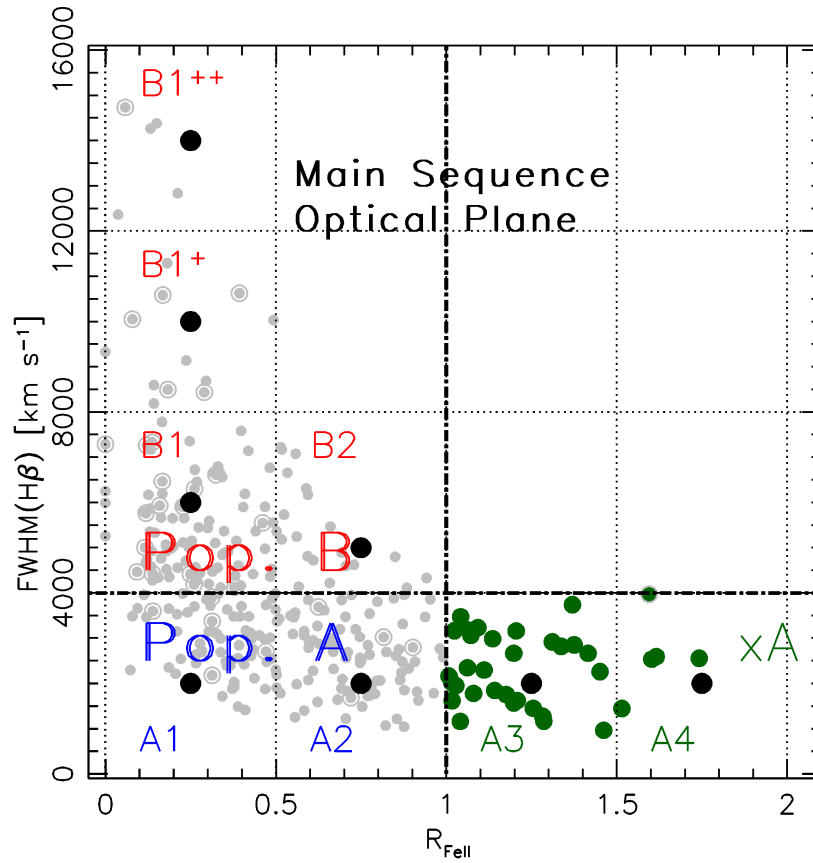


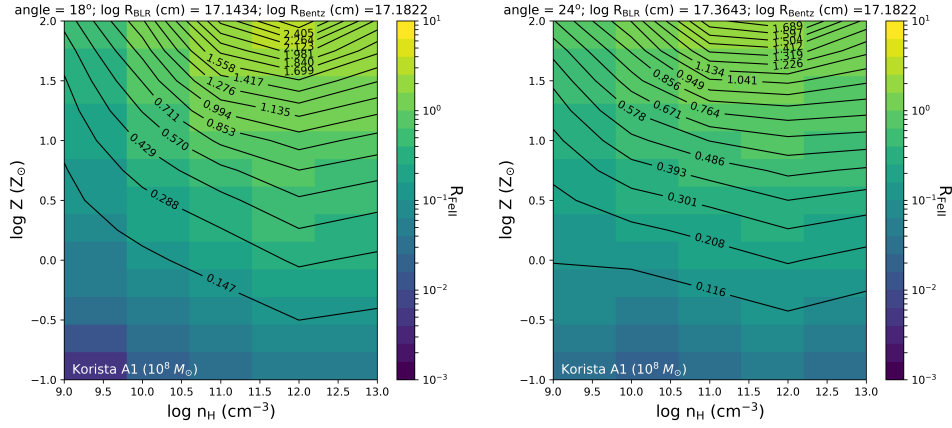
Figure 1. The diagram shows the optical plane of the Eigenvector 1 MS, $\text{FWHM}(\text{H}\beta)$ vs. R_{FeII} . Circled symbols identify radio-loud sources. The thick horizontal dot-dashed line separates populations A and B. The plane has been further subdivided in spectral bins as defined by Sulentic et al. (2002). The vertical dot-dashed line marks the limit for extreme Population A (xA) sources with $R_{\text{FeII}} \gtrsim 1$, whose data-points are in dark-green colors. The large black dots mark the average values in each spectral type which are incorporated in the modelling. The diagram is adapted from Fig. 2 of Marziani et al. (2018).

ulation A with $\text{FWHM H}\beta \leq 4000 \text{ km s}^{-1}$, and Population B of sources with $\text{H}\beta$ broader than 4000 km s^{-1} (for a rational justification about the distinction between the two populations and a description of the main systematic differences, see Marziani et al. 2018, 2019b). We consider the mean FWHM values in each spectral type depicted in Figure 1 to see the effect of changing the FWHM across the main sequence plane i.e., going from the lowest FWHM to the extreme Population B sources that have the highest values of $\text{FWHM} \gtrsim 10000 \text{ km/s}$. Hence, as a first test, we take the mean values in each spectral bin. For the Population A spectral types, we use $\text{FWHM} = 2000 \text{ km s}^{-1}$; for Population B spectral type B1, $\text{FWHM} = 6000 \text{ km s}^{-1}$ and for B1+ $\text{FWHM} = 10000 \text{ km s}^{-1}$. We also investigate the B2 spectral type and use $\text{FWHM} = 5000 \text{ km s}^{-1}$ in this case. This is justified as the source count in this spectral bin (B2) is quite low ($\sim 3\%$) and spans out the lower triangular region. The rationale to separate two quasars populations stems from the spectral differences recognizable by eye: Pop. A sources usually show low [OIII] emission, the strongest FeII emission; Pop. B sources give the impression of a much higher degree of ionization, with weak FeII, prominent [OIII] and CIV λ 1549 emission. By considering trends in metallicity, density, and Eddington ratio derived from earlier work, we were able to account for the R_{FeII} values (even for the highest ones!) in the spectral bins of the MS, and gain constraint on the viewing angle assuming an appropriate value of the BLR radius. These results are presented and discussed in Panda et al. (2019b). For the purpose of this paper, we will only concentrate on a representative case i.e., spectral type A1.

3.2. Constraints on the viewing angle

The use of angle-dependent form factor (see Eq. 2 and 5) is a crucial extension of the quasar MS modelling done by Panda et al. (2017, 2018, 2019a). Viewing angle directly affects the line width, and the object luminosity, and indirectly the estimated distance to the BLR and the location of an object on the quasar MS diagram. Inverting this dependence, we can obtain interesting constraints on the viewing angle of a source if its the location on the quasar MS diagram and the BLR size are known.

In Figure 2, we show two consecutive snapshots from one of the simulation results ($\theta = 18^\circ$ and $\theta = 24^\circ$). The plots show the distribution of R_{FeII} as a function of gas density (n_{H}) and cloud composition (in terms of the metallicity, Z). The colorbar represents the values of R_{FeII} which are also reported in the form of overlaid contours of the 2D distribution of Z and n_{H} as a function of R_{FeII} . The case shown is for a black hole mass, $M_{\text{BH}} = 10^8 M_{\odot}$ and for a bolometric luminosity, $L_{\text{bol}} = 0.2L_{\text{Edd}}$. To obtain the monochromatic luminosity at 5100\AA , we utilize the mass and the Eddington ratio and compute the bolometric luminosity. Using the normalization coefficient as a function of mass and accretion rate, we estimate the monochromatic luminosity at 5100\AA (see Equation 5 in Panda et al. (2018) for details).



and consider the full parameter range with respect to density, metallicity and Eddington ratio.

From Figure 1, we can obtain the range of the R_{FeII} for the spectral type A1 – [0,0.5]. Taking this upper limit and comparing it with the panels in Figure 2, we see that contrary to our previous assumption – the local cloud density is an almost constant entity within each spectral type, the density actually shows a broad distribution. In the considered grid on local densities i.e., from 10^9 cm^{-3} to 10^{13} cm^{-3} , the corresponding value of the R_{FeII} ([0,0.5]) can be recovered. But we find that there exists a coupling between density and metallicity that was not studied in the previous works, that is, relatively higher densities require slightly super-solar metallicities ($\sim 3\text{-}5Z_{\odot}$), while for the lower density cases the metallicity can be as high as $\sim 100Z_{\odot}$. This suggests that the BLR cloud can indeed exist at densities higher than those predicted from radiation-pressure confinement estimates, i.e. $\sim 10^{11} \text{ cm}^{-3}$ (Baskin et al., 2014). With an increase in the viewing angle under the same parameterization, we see that there is a requirement of higher metallicities, especially for the higher densities ($> 10^{10} \text{ cm}^{-3}$) which goes up by a factor ~ 2 .

We have made an extensive set of simulations with a broad range of parameters and we will discuss this in detail in a forthcoming paper (Panda et al. in prep).

3.3. Comparison of the spectral energy distributions

Motivated by the fact that there is a broad distribution of quasars in the main sequence and that no singular ionizing continuum shape can effectively explain all the quasars, we have used 4 different spectral energy distributions that are appropriate for explaining the sources based on their spectral types. In Panda et al. (2019b), each spectral type in the MS diagram, namely in Population A (A1, A2, A3, A4 and A1*) and in Population B (B1, B1+ and B2) is modelled with a specific SED shape. In this paper, our approach is different and we incorporate the four SEDs for spectral type A1 to understand the effect of the shape of the ionizing continuum which affects the recovery of the R_{FeII} . These SEDs are adopted from Mathews & Ferland (1987), Korista et al. (1997), Laor et al. (1997) and Marziani & Sulentic (2014). Figure 1 in Panda et al. (2019b) shows the differences in these SED shapes, especially in the 1 - 25 Rydberg energy range which corresponds to the the optical-UV bump feature in a characteristic quasar SED i.e. the Big Blue Bump (Czerny & Elvis, 1987; Richards et al., 2006).

Figure 3 compares the effect on R_{FeII} due to the four different SEDs used in the modelling. It shows four 2D shaded contour plots which map the R_{FeII} values as a function of cloud density and metallicity for a black hole mass $10^8 M_{\odot}$. The colorbar depicts the values of R_{FeII} . This is shown for a representative case at a viewing angle (18 degrees) that corresponds to a radius of the BLR which is in close agreement to the radius estimation from the standard $r_{\text{BLR}}\text{-}L_{5100}$

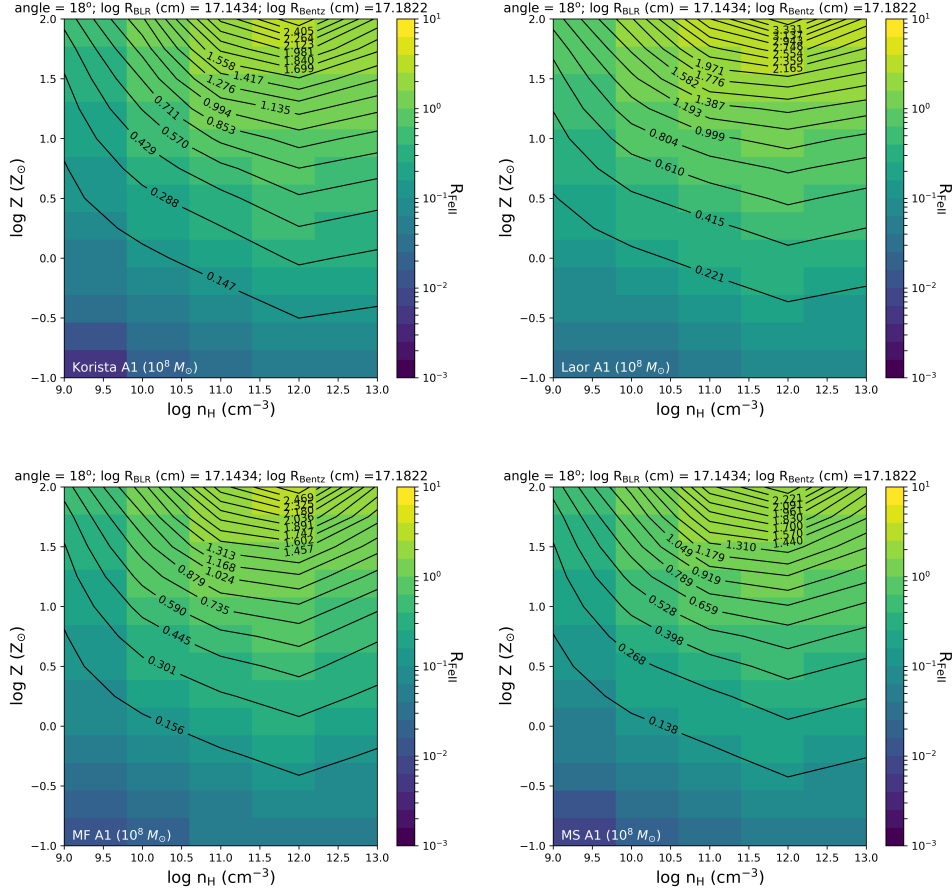


Figure 3. Comparison between the four SEDs (Korista et al., 1997; Laor et al., 1997; Mathews & Ferland, 1987; Marziani & Sulentic, 2014) used in the modelling. The figure shows four 2D density plots which map the distribution of the cloud density as a function of the metallicity for a black hole mass $10^8 M_\odot$. The colorbar depicts the value of R_{FeII} . This is shown for a representative case (spectral type A1 with $\text{FWHM} = 2000 \text{ km s}^{-1}$) at a viewing angle (here 18 degrees) that corresponds to a inner radius of the BLR which is close agreement to the radius estimation from the standard $r_{\text{BLR}}-L_{5100}$ relation (Bentz et al., 2013). The bolometric luminosity is assumed at $0.2L_{\text{Edd}}$.

relation (Bentz et al., 2013). The bolometric luminosity is assumed $0.2L_{\text{Edd}}$. The effect of the SEDs we have considered is modest over the full density-metallicity parameter plane. For example, for $n_{\text{H}} = 10.6$, and $\log Z \approx 0.7 [Z_\odot]$,

R_{FeII} ranges between 0.4 and 0.6. The largest achievable R_{FeII} values are also similar, in the range 2.2 – 2.5.

3.4. Effect of microturbulence

The effect of micro-turbulence to model the MS has been shown to be of importance (Panda et al., 2018, 2019a), where the optical plane of quasars is indeed positively affected by inclusion of modest values of micro-turbulence². In Figure 4, we show the 2D shaded contour plots for 4 different values of microturbulence values, starting from zero turbulent velocity up to 100 km s⁻¹. We recover the trends that were first estimated in Panda et al. (2018) where we found that the maximum R_{FeII} is recovered for the case with a modest value of microturbulence (10–20 km s⁻¹). Increasing the microturbulence any higher than these values suppressed the FeII emission and thereby resulting in a decrease in the R_{FeII} . It was also found that for $v_{\text{turb}} = 100$ km s⁻¹, the R_{FeII} reverts to the values that were obtained for the case with zero microturbulence.

The effect of the inclusion of microturbulence can be especially important for retrieving the R_{FeII} values that correspond to the high accretors - the xA quasars. Also, we have found that there is an intrinsic coupling between the metallicity and microturbulence. In Panda et al. (2019b), we have also shown that for theoretical templates that are generated using CLOUDY for the FeII pseudo-continuum, there is quite good agreement with the overall line profiles of FeII when compared with templates derived from observation (we have currently tested with two sources: an A1 spectral type – Mrk 335, and a A3 spectral type – I Zw 1). To retrieve the closest agreement to the spectral line profiles and the corresponding R_{FeII} between the observed and theoretical FeII templates³, there is a requirement to combine a realistic value of metallicity confirmed from the observations with a certain value of microturbulence. The value of microturbulence varies from case to case and we infer that it is linked with the spectral types. In Panda et al. (in prep.), we will also test the effect of conjugating the increase in mass of the black hole on the MS and the effect that the microturbulence has on it.

3.5. Effect of increasing M_{BH}

Another interesting inference that was drawn from the analyses in Panda et al. (2019b) was that the higher FWHM sources ($\gtrsim 6000$ km s⁻¹) couldn't be explained assuming a fixed mass of $10^8 M_{\odot}$. The issue becomes relevant for spectral type B1⁺ and above. These sources are with the broadest line profiles and this can be accounted for with increase in the viewing angle although with

²there is a $\sim 50\%$ increase in the R_{FeII} when the turbulent velocity is increased to 10–20 km s⁻¹.

³for the comparison between the templates, we have applied a Gaussian broadening of ~ 800 km s⁻¹.

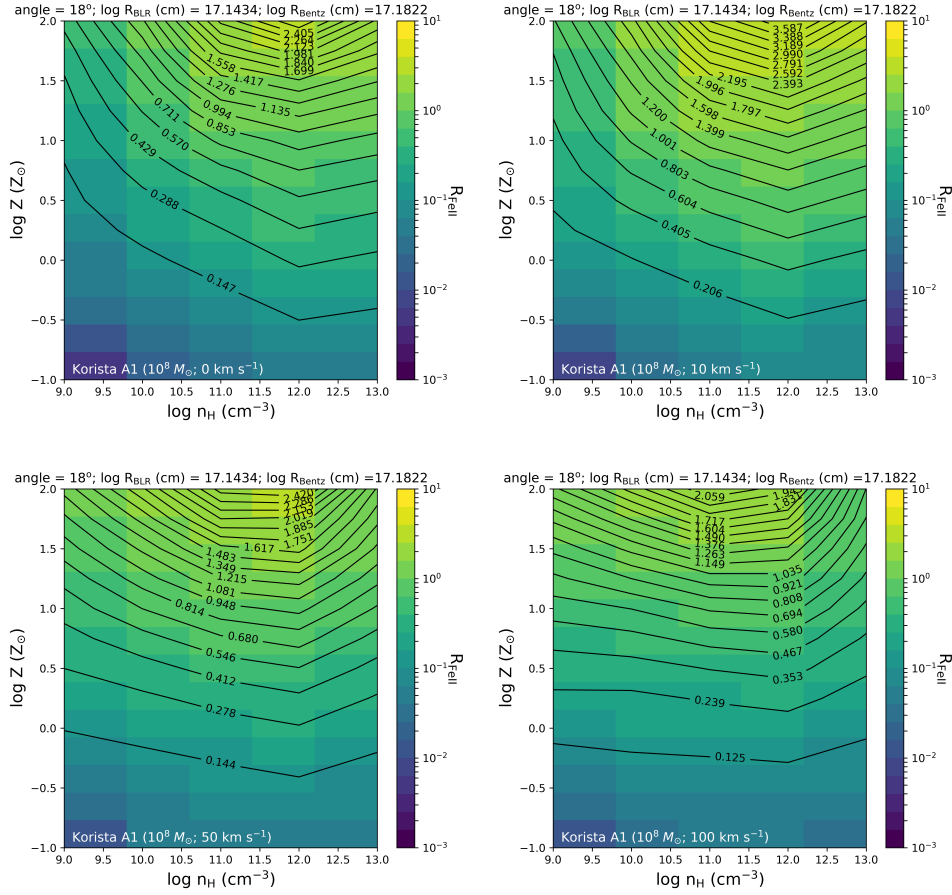
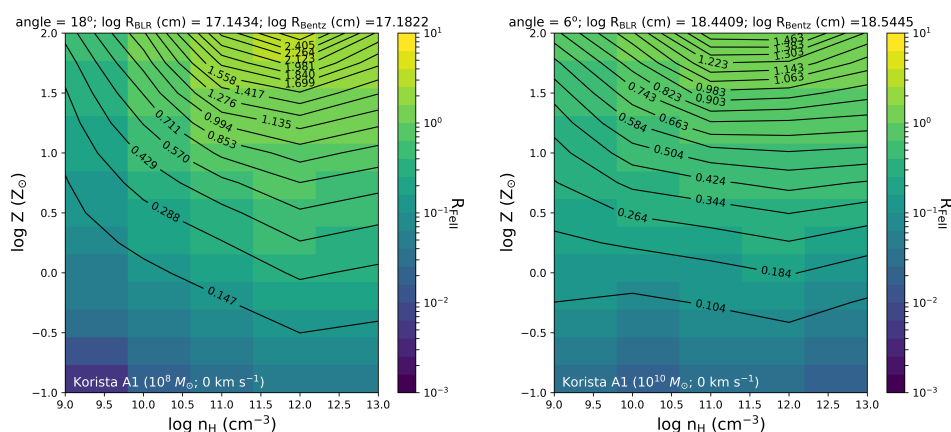


Figure 4. Effect of microturbulence – The figure shows four 2D density plots (for 4 different values of microturbulence: 0, 10, 50 and 100 km s^{-1}) which map the distribution of the cloud density as a function of the metallicity for a black hole mass $10^8 M_\odot$. The colorbar depicts the value of R_{FeII} . This is shown for a representative case (spectral type A1 with $\text{FWHM} = 2000 \text{ km s}^{-1}$) at a viewing angle (here 18 degrees) that corresponds to a inner radius of the BLR which is close agreement to the radius estimation from the standard $r_{\text{BLR}}-L_{5100}$ relation (Bentz et al., 2013). The bolometric luminosity is assumed at $0.2L_{\text{Edd}}$ and a representative SED from Korista et al. (1997) is used.

implausibly large values, $\gtrsim 60$ degrees. Such large θ values are problematic because the MS is made of the Type-1 sources i.e., sources that offer an unimpeded view of their central core. There is another way high FWHM values can be accounted for – a higher mass of the black hole. We have tested this possibility by considering a case with $M_{BH} = 10^{10} M_{\odot}$ alongside the original case with $M_{BH} = 10^8 M_{\odot}$, and comparing the R_{FeII} distribution as a function of the viewing angle and correspondingly the radius of the BLR in the vertical bins (see Figure 4 in Panda et al. 2019b). We find that increasing the M_{BH} to such masses (consistent for quasars in evolved systems) increases the net FeII emission, and yields viewing angles within the acceptable range for un-obscured sources.

In Figure 5, we show an example of how an increase in the black hole mass (going from $10^8 M_{\odot}$ to $10^{10} M_{\odot}$) affects the parameter space. For this exemplary case, we have assumed a $FWHM=2000 \text{ km s}^{-1}$ and Eddington ratio, $L_{bol}/L_{Edd} = 0.2$. Yet, this simple test already reveals quite interesting preliminary conclusions. First, due to this increase in the black hole mass, we obtain a much larger r_{BLR} from the standard Bentz et al. (2013) relation. To be consistent with our



approach, we find the solution for the r_{BLR} from the virial relation that is closest to the $r_{\text{BLR}}-L_{5100}$ relation, and retrieve back the corresponding value for the viewing angle. We see that the viewing angles in the case of higher black hole mass (here, $10^{10} M_{\odot}$) are relatively smaller. From the point of view of the recovered R_{FeII} values, there is a $\sim 30\text{-}40\%$ drop, when we go from $10^8 M_{\odot}$ to $10^{10} M_{\odot}$. But, these results are driven by our assumption of fixed FWHM value and the Eddington ratio. In principle, we need an extensive study of the evolution of the parameter space as a function of increasing FWHM and Eddington ratio. This will be reported in Panda et al. (in prep.).

Similar to the interpretation in Section 3.2 and Figure 2, we find that with an increase in the black hole mass under the same parameterization, we see that there is a requirement of higher metallicities for the higher densities ($> 10^{9.75} \text{ cm}^{-3}$) which goes up by a factor ~ 2 . But, in the lower density regime ($< 10^{9.75} \text{ cm}^{-3}$), the metallicities required to recover the optimal R_{FeII} are lower by factor ~ 2.5 when going from $10^8 M_{\odot}$ to $10^{10} M_{\odot}$.

4. Conclusions and the Future: a predictive tool to estimate BLR size?

We addressed the effect of viewing angle in the accretion disk plane and the geometry of the BLR in the context of the distribution of quasars in the plane FWHM $\text{H}\beta - R_{\text{FeII}}$. Treating the viewing angle along with a broad range of physically motivated parameters that affect FeII emission in Type-1 AGNs i.e., Eddington ratio, local cloud density, metallicity, microturbulence and the shape of the ionizing SED, we have covered the full extent of the quasar main sequence. The values of these physical parameters were known from prior studies.

In this paper, we summarily described the following results:

1. We are now able to constrain the viewing angle for each spectral type corresponding to these sources.
2. We have incorporated four different SEDs to justify the differences in the ionizing continua observed for a broad distribution of quasars.
3. The inclusion of the turbulent velocity inside the cloud (microturbulence) recovers the trends that were obtained in Panda et al. (2018): the maximum FeII emission and the maximum R_{FeII} values correspond to the case with modest values of microturbulence ($10\text{-}20 \text{ km s}^{-1}$).
4. We briefly described the effect of increasing black hole mass to explain the sources with high FWHM.

In Panda et al. (2019b) and in this paper, we have explored the possibility of constraining the viewing angle for the broad distribution of quasars. Our model can also explain the physical parameters responsible for high accretors which

turn out to be predominantly strong FeII emitters (the xA sources in Fig. 1). With this model, we can test for reliability by comparing the results with real sources⁴. The results we have shown here are a ‘snapshot’ and more detailed analysis will be shown in a forthcoming work (Panda et al. in prep.).

The parameter R_{FeII} which can be estimated from a single epoch spectrum for a given source and the metallicity from the line diagnostics from emission lines mostly in the UV (Hamann et al., 2002; Marziani et al., 2019a). These data make it possible to extend our analysis. Values of R_{FeII} and metallicity can be projected in the parameter space maps (see Figure 2) to ultimately recover the virial radius of the broad-line region. Although this possibility needs robust testing, it might be applicable as a predictor for future reverberation mapping studies. The prediction would be specially valuable for high accretors that show high $R_{\text{FeII}} (\gtrsim 1)$ shorter time delays with respect to the ones derived from the scaling law of Bentz et al. (2013). By the same token, we may become able to constrain the $r_{\text{BLR}}-L_{5100}$ relation that has been shown to offer prospects of application for cosmology by building the Hubble diagram for quasars (Risaliti & Lusso, 2015; Martínez-Aldama et al., 2019).

Acknowledgements. The project was partially supported by the Polish Funding Agency National Science Centre, project 2017/26/A/ST9/00756 (MAESTRO 9) and MNiSW grant DIR/WK/2018/12. PM acknowledges the Programa de Estancias de Investigación (PREI) No. DGAP/DFA/2192/2018 of UNAM, and funding from the INAF PRIN-SKA 2017 program 1.05.01.88.04. SP and PM would like to acknowledge the organizers of “Breaking the limits 2018: Super-Eddington accretion onto compact objects” where this project was first realized. SP would like to acknowledge Mary Loli Martínez Aldama, Deepika Bollimpalli and Abbas Askar for fruitful discussions that helped in the realization of the project. We thank the anonymous referee for useful comments that helped to improve the content of the paper.

References

- Antonucci, R., Unified models for active galactic nuclei and quasars. 1993, *ARA&A*, **31**, 473, DOI: 10.1146/annurev.aa.31.090193.002353
- Baskin, A., Laor, A., & Stern, J., Radiation pressure confinement - II. Application to the broad-line region in active galactic nuclei. 2014, *MNRAS*, **438**, 604, DOI: 10.1093/mnras/stt2230
- Bentz, M. C., Denney, K. D., Grier, C. J., et al., The Low-luminosity End of the Radius-Luminosity Relationship for Active Galactic Nuclei. 2013, *ApJ*, **767**, 149, DOI: 10.1088/0004-637X/767/2/149
- Boroson, T. A. & Green, R. F., The emission-line properties of low-redshift quasi-stellar objects. 1992, *ApJS*, **80**, 109, DOI: 10.1086/191661

⁴We checked this for two sources – for Mrk 335: 0-10 km s⁻¹ ; I Zw 1: 40-50 km s⁻¹ with super-solar metallicities 1-2.5 Z_⊙ and 4.8-5.4 Z_⊙, respectively (see Panda et al. 2019b)

- Campitiello, S., Ghisellini, G., Sbarato, T., & Calderone, G., How to constrain mass and spin of supermassive black holes through their disk emission. 2018, *A&A*, **612**, A59, DOI: 10.1051/0004-6361/201731897
- Collin, S., Kawaguchi, T., Peterson, B. M., & Vestergaard, M., Systematic effects in measurement of black hole masses by emission-line reverberation of active galactic nuclei: Eddington ratio and inclination. 2006, *A&A*, **456**, 75, DOI: 10.1051/0004-6361:20064878
- Czerny, B. & Elvis, M., Constraints on quasar accretion disks from the optical/ultraviolet/soft X-ray big bump. 1987, *ApJ*, **321**, 305, DOI: 10.1086/165630
- D'Onofrio, M., Marziani, P., & Sulentic, J. W. 2012, *Fifty Years of Quasars* (Springer, <https://doi.org/10.1007/978-3-642-27564-7>)
- Ferland, G. J., Chatzikos, M., Guzmán, F., et al., The 2017 Release Cloudy. 2017, *RMxAA*, **53**, 385
- Ferland, G. J., Porter, R. L., van Hoof, P. A. M., et al., The 2013 Release of Cloudy. 2013, *RMxAA*, **49**, 137
- Grevesse, N., Asplund, M., Sauval, A. J., & Scott, P., The chemical composition of the Sun. 2010, *Astrophys. Space Sci.*, **328**, 179, DOI: 10.1007/s10509-010-0288-z
- Hamann, F., Korista, K. T., Ferland, G. J., Warner, C., & Baldwin, J., Metallicities and Abundance Ratios from Quasar Broad Emission Lines. 2002, *ApJ*, **564**, 592, DOI: 10.1086/324289
- Korista, K., Baldwin, J., Ferland, G., & Verner, D., An Atlas of Computed Equivalent Widths of Quasar Broad Emission Lines. 1997, *ApJS*, **108**, 401, DOI: 10.1086/312966
- Kovačević, J., Popović, L. Č., & Dimitrijević, M. S., Analysis of Optical Fe II Emission in a Sample of Active Galactic Nucleus Spectra. 2010, *ApJS*, **189**, 15, DOI: 10.1088/0067-0049/189/1/15
- Laor, A., Fiore, F., Elvis, M., Wilkes, B. J., & McDowell, J. C., The Soft X-Ray Properties of a Complete Sample of Optically Selected Quasars. II. Final Results. 1997, *ApJ*, **477**, 93, DOI: 10.1086/303696
- Martínez-Aldama, M., Czerny, B., Panda, S., et al., Can reverberation-measured quasars be used for cosmology? 2019, *Accepted for publication in ApJ*, arXiv:1903.09687
- Marziani, P., Bon, E., Bon, N., et al., Quasars: From the Physics of Line Formation to Cosmology. 2019a, *Atoms*, **7**, 18, DOI: 10.3390/atoms7010018
- Marziani, P., del Olmo, A., Martínez-Carballo, M. A., et al., Black hole mass estimates in quasars. A comparative analysis of high- and low-ionization lines. 2019b, *A&A*, **627**, A88, DOI: 10.1051/0004-6361/201935265
- Marziani, P., Dultzin, D., Sulentic, J. W., et al., A main sequence for quasars. 2018, *FrASS*, **5**, 6, DOI: 10.3389/fspas.2018.00006
- Marziani, P. & Sulentic, J. W., Highly accreting quasars: sample definition and possible cosmological implications. 2014, *MNRAS*, **442**, 1211, DOI: 10.1093/mnras/stu951

- Mathews, W. G. & Ferland, G. J., What Heats the Hot Phase in Active Nuclei? 1987, *ApJ*, **323**, 456, DOI: 10.1086/165843
- Padovani, P., Alexander, D. M., Assef, R. J., et al., Active galactic nuclei: what's in a name? 2017, *A&Ar*, **25**, 2, DOI: 10.1007/s00159-017-0102-9
- Panda, S., Czerny, B., Adhikari, T. P., et al., Modeling of the Quasar Main Sequence in the Optical Plane. 2018, *ApJ*, **866**, 115, DOI: 10.3847/1538-4357/aae209
- Panda, S., Czerny, B., Done, C., & Kubota, A., CLOUDY View of the Warm Corona. 2019a, *ApJ*, **875**, 133, DOI: 10.3847/1538-4357/ab11cb
- Panda, S., Czerny, B., & Wildy, C., The physical driver of the optical Eigenvector 1 in Quasar Main Sequence. 2017, *FrASS*, **4**, 33, DOI: 10.3389/fspas.2017.00033
- Panda, S., Marziani, P., & Czerny, B., The Quasar Main Sequence explained by the combination of Eddington ratio, metallicity and orientation. 2019b, *Accepted for publication in ApJ*, arXiv:1905.01729
- Richards, G. T., Lacy, M., Storrie-Lombardi, L. J., et al., Spectral Energy Distributions and Multiwavelength Selection of Type 1 Quasars. 2006, *ApJS*, **166**, 470, DOI: 10.1086/506525
- Risaliti, G. & Lusso, E., A Hubble Diagram for Quasars. 2015, *ApJ*, **815**, 33, DOI: 10.1088/0004-637X/815/1/33
- Shen, Y. & Ho, L. C., The diversity of quasars unified by accretion and orientation. 2014, *Nature*, **513**, 210, DOI: 10.1038/nature13712
- Sulentic, J. W., Marziani, P., & Dultzin-Hacyan, D., Phenomenology of Broad Emission Lines in Active Galactic Nuclei. 2000, *ARA&A*, **38**, 521, DOI: 10.1146/annurev.astro.38.1.521
- Sulentic, J. W., Marziani, P., Zamanov, R., et al., Average Quasar Spectra in the Context of Eigenvector 1. 2002, *ApJL*, **566**, L71, DOI: 10.1086/339594
- Urry, C. M. & Padovani, P., Unified Schemes for Radio-Loud Active Galactic Nuclei. 1995, *PASP*, **107**, 803, DOI: 10.1086/133630
- Verner, E. M., Verner, D. A., Korista, K. T., et al., Numerical Simulations of Fe II Emission Spectra. 1999, *ApJS*, **120**, 101, DOI: 10.1086/313171
- Véron-Cetty, M. P. & Véron, P., A catalogue of quasars and active nuclei: 11th edition. 2003, *A&A*, **412**, 399, DOI: 10.1051/0004-6361:20034225
- Wang, J.-M., Du, P., Valls-Gabaud, D., Hu, C., & Netzer, H., Super-Eddington Accreting Massive Black Holes as Long-Lived Cosmological Standards. 2013, *PRL*, **110**, 081301, DOI: 10.1103/PhysRevLett.110.081301
- Woltjer, L., Emission Nuclei in Galaxies. 1959, *Astrophys. J.*, **130**, 38, DOI: 10.1086/146694
- Yu, L.-M., Bian, W.-H., Wang, C., Zhao, B.-X., & Ge, X., Calibration of the virial factor f in supermassive black hole masses of reverberation-mapped AGNs. 2019, *MNRAS*, DOI: 10.1093/mnras/stz1766

Extended ionized-gas structures in Seyfert 2 galaxy Mrk 78

D.V. Kozlova^{1,2}, A.V. Moiseev² and A.A. Smirnova²

¹ *Laboratory of Astrochemistry and Extraterrestrial Physics, Ural Federal University, 620002, Russia*

² *Special Astrophysical Observatory of the Russian Academy of Sciences, 369167, Russia*

Received: July 31, 2019; Accepted: October 24, 2019

Abstract. The search and study of extended emission-line regions (EELRs) related to AGN in early-type galaxies is interesting to probe the history of nuclear ionization activity and also to understand the process of external gas accretion. In this work, we present observations of the EELR in Mrk 78 obtained at the 6-m Russian telescope using the long-slit and 3D spectroscopy methods. We show that ionized-gas clouds at 12-16 kpc projected distances from the nucleus are ionized by the AGN radiation. Also we have checked if the galaxy appearing in the optical images in the immediate neighbourhood of Mrk 78 near the external clouds is a dwarf companion or a part of a tidal structure. However, the spectrum of this galaxy, SDSS J074240.37+651021.4, obtained at the 6-m telescope corresponds to a distant background galaxy with $z = 0.38$.

Key words: galaxies: individual: Mrk 78 – galaxies: active – galaxies: Seyfert – galaxies: interactions – galaxies: ISM

1. Introduction

According to the unified model of active galactic nuclei (AGN), the radiation of the central accretion engine comes out in broad axisymmetrical cones collimated by the circumnuclear obscuring torus. The impact of AGN ionizing radiation together with radio jet mechanical energy on the surrounding interstellar medium appears in the shape of ionizing cones from hundreds pc to a few kpc in typical size. In some fraction of Seyfert galaxies, extended emission-line regions (EELRs) are also detected at radial distances of tens of kpc. EELRs can be used to measure the AGN energetic output at both time and spatial scales and also to study the gas distribution in the galactic environment. Indeed, a significant fraction of EELR traces the off-plane gas related with tidal debris (Keel et al., 2012) or even the gas in a companion galaxy (Keel et al., 2019). One of the intriguing cases is the well-known AGN Mrk 6: deep imaging and spectroscopic observations revealed an extended system of gaseous filaments up to 40 kpc from the nucleus accreted by the Seyfert galaxy (Smirnova et al., 2018). Therefore,

the detailed study of EELRs is topical even around well-studied nearby active galaxies.

The Seyfert 2 galaxy Mrk 78 is a good illustration of the picture described above. The spectrophotometric properties of the inner ($r < 4 - 5''$, or 3–4 kpc) elongated emission-line structure studied with HST (Whittle & Wilson, 2004; Kewley et al., 2006) can be explained in terms of jet-cloud interaction together with the mass outflow and a cone of UV-radiation emerging from the Seyfert nucleus (Fischer et al., 2011, see the corresponding HST image in Fig. 1). Ground-based narrow-band images obtained by De Robertis (1987) and Pedlar et al. (1989) also revealed a weak extended ionized gas emission outside the central region with an extensive asymmetric structure at $r > 15''$ in the south-west. The presence of the gas emitting in [O III] in the western direction up to 12–14'' was confirmed in spectroscopic observations by Unger et al. (1987). Also, Afanasiev & Silchenko (1991) detected the [O III] line emission even at $r = 18 - 20''$. Pedlar et al. (1989) have shown that the weak narrow-line region extending out to 10 kpc to the west is consistent with AGN ionizing cones, however, the actual ionization state of the most distant part of the EELR is still unknown. Mrk 78 was included in the sample of the confirmed EELR selected from the Galaxy Zoo survey, but the follow-up spectra were obtained along $PA = 90^\circ$ (Keel et al., 2012), therefore, the properties of the southwestern external emission knots were not measured.

In this paper, we analysed the large-scale ionized gas distribution and spectral properties of the most distant parts of the EELR in Mrk 78 derived from new long-slit and 3D spectroscopic observations at the 6-m telescope of Special Astrophysical Observatory of Russian Academy of Sciences (SAO RAS). The gas and stellar kinematics will be considered in the forthcoming paper. In the present paper, we assumed a distance to the galaxy of 165 Mpc with a corresponding scale of 0.80 kpc/'' (according to NED¹).

2. Observations and data reduction

Observations were carried out at the prime focus of the 6-m SAO RAS telescope with the multi-mode focal reducers: SCORPIO (Afanasiev & Moiseev, 2005) and SCORPIO-2 (Afanasiev & Moiseev, 2011). We used the 3D spectroscopy with the Fabry-Perot interferometer (FPI), long-slit spectroscopy, and direct-image modes. Also, we used the data obtained with the integral-field Multi-Pupil Field Spectrograph (Afanasiev et al., 2001). The log of observations and parameters of the used instruments are listed in the Table 1.

SCORPIO and SCORPIO-2 both have the 6:1 fields of view with the 0.36-arcsec pixel size. The slit has the 6:1 length and the 1'' width. The scanning FPI mapped the spectral region around the redshifted [O III] λ 4959 emission line. We made the binning of these data to reach a higher signal-to-noise ratio

¹<http://ned.ipac.caltech.edu/>

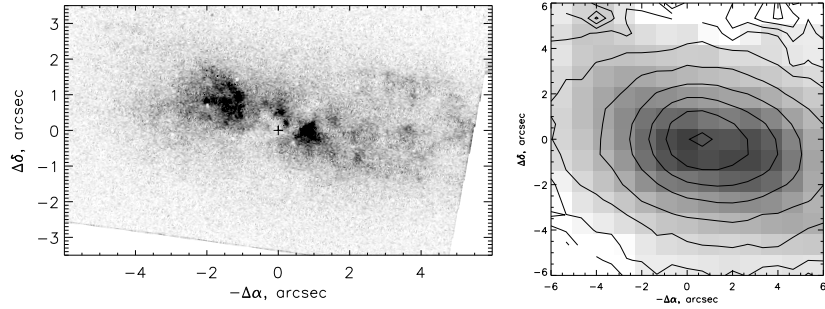


Figure 1. Left: the HST/FOC image with the F520M filter showing the [O III] emission (see Fischer et al., 2011). Right: the MPFS image in the [O III] λ 5007 line with the superimposed continuum isophotes.

Table 1. Log of observations at the SAO RAS telescope

Date	Instrument/mode	Exp. time, s	Sp. range	FWHM	Seeing
14/15 Mar 2007	SCORPIO/FPI	32×250	[O III] λ 4959	1.2 Å	1".2
22/23 Oct 2008	SCORPIO/DI	5×120	R _C -filter		1".2
03/04 Feb 2008	MPFS	6 × 1200	3650–5900 Å	5 Å	1".3
03/04 Feb 2008	MPFS	6 × 1200	4300–7380 Å	5 Å	1".3
12/13 Feb 2019	SCORPIO-2/LS	3x900	3650–8530 Å	7 Å	2".7

in the resulting data cube with $0.7''/\text{px}$. The MPFS data cube had the 16×16 arcsec² field-of-view centered on the nucleus with the $1''/\text{spaxel}$ spatial scale and covered a wide spectral range.

Calibration of the SCORPIO-2 and MPFS spectra into the absolute energy flux units was carried out using spectrophotometric standard stars observed in the same night as Mrk 78. The data reduction was performed in a standard way (see Smirnova et al., 2018, for references on the software and algorithms).

Fig. 2 shows the maps derived from the Voigt fitting of the [O III] spectra in the FPI data cube: the monochromatic image, the velocity field, and the velocity dispersion map free from instrumental effects. The emission-line fluxes in the MPFS and long-slit data were derived from the single-component Gaussian fitting. The map of the [O III] emission in the circumnuclear region according to the MPFS data is shown in Fig. 1. For the internal region, where well-known multi-component lines were observed (see Afanasiev & Silchenko, 1991, and references therein), only a brighter peak was fitted in the MPFS and FPI data.

3. External gas clouds

The ionization state of the EELR inside the galaxy disc ($r < 10 - 15''$) was analysed in the papers cited above in Sec. 1. However, the FPI map also revealed separate ionized gas clouds (labeled as C1 and C2 in Fig. 2) at a distance of $\sim 15-20''$ ($\sim 12-16$ kpc) southwest of the galaxy. The line-of-sight velocity field shows that the cloud velocities lie in the range of the gas disc ($10900-11500$ km s $^{-1}$). Whereas the velocities of C1 and C2 exceed by $50-200$ km s $^{-1}$ the nearest S-W side of the galactic disc. This indicates that both clouds are moving in the Mrk 78 gravitational potential, but rotate out of the galaxy plane on retrograde orbits possibly.

To determine the C1 and C2 ionization state, the SCORPIO-2 long-slit spectra were obtained along PA=127°. The slit position has been selected according to the centers of both clouds and a neighbouring galaxy with an unknown spectroscopic redshift (see Sec. 4).

To determine the ionization mechanism of the gas in C1 and C2, the emission-line ratio diagnostic diagrams (BPT-diagrams after Baldwin et al., 1981) were used with the branches from Kewley et al. (2006) to separate different mechanisms of gas excitation: the HII-regions and AGN (Seyfert or LINER). These diagrams involve the following line flux ratios independent from the interstellar extinction: [N II] $\lambda 6583/H\alpha$, [O III] $\lambda 5007/H\beta$, and [S II] $\lambda 6717 + 6731/H\alpha$.

The integrated spectrum of the C1+C2 clouds is shown in Fig. 3, the BPT diagrams are presented in Fig. 4. We designated the EELR ionization mechanism according to the long-slit spectroscopy. To compare their ionization state to that of the circumnuclear region, the MPFS intergal-field spectroscopic data were used. It is clearly seen that the C1 and C2 ionization state is the same as that in the internal part of the EELR: the Seyfert-type AGN radiation predominates. This result is in agreement with the diagrams based on the long-slit spectroscopy along the major galactic axis (PA=90°) presented in Keel et al. (2012).

Fischer et al. (2011) estimated the parameters of the ionized cones according to the HST data for the inner ($r < 4''$) brightest part of the emission-line structure. We overlaid the western side of this bicone (having an opening angle of $\sim 75^\circ$) on the FPI dispersion map (Fig. 2): C1 and C2 both fall into the projected cone borders. Therefore, the ionization state of the distant gas in the EELR is consistent with the model based on the analysis of the circumnuclear gas kinematics and ionization state. The ionized-gas velocity dispersion in C1 and C2 ($40 < \sigma < 100$ km s $^{-1}$, see Fig. 2) is similar to the gas in the outer part of the galaxy disc and significantly smaller than that observed in the inner region, where jet-cloud interaction takes place. It means that the external part of the EELR is dynamically cold, i.e., the AGN ionized off-plane gas clouds are related with the external accretion or tidal structures, but are not the result of the AGN outflow. The similar picture is observed in most EELRs in Seyfert galaxies (see Keel et al., 2015, and references therein).

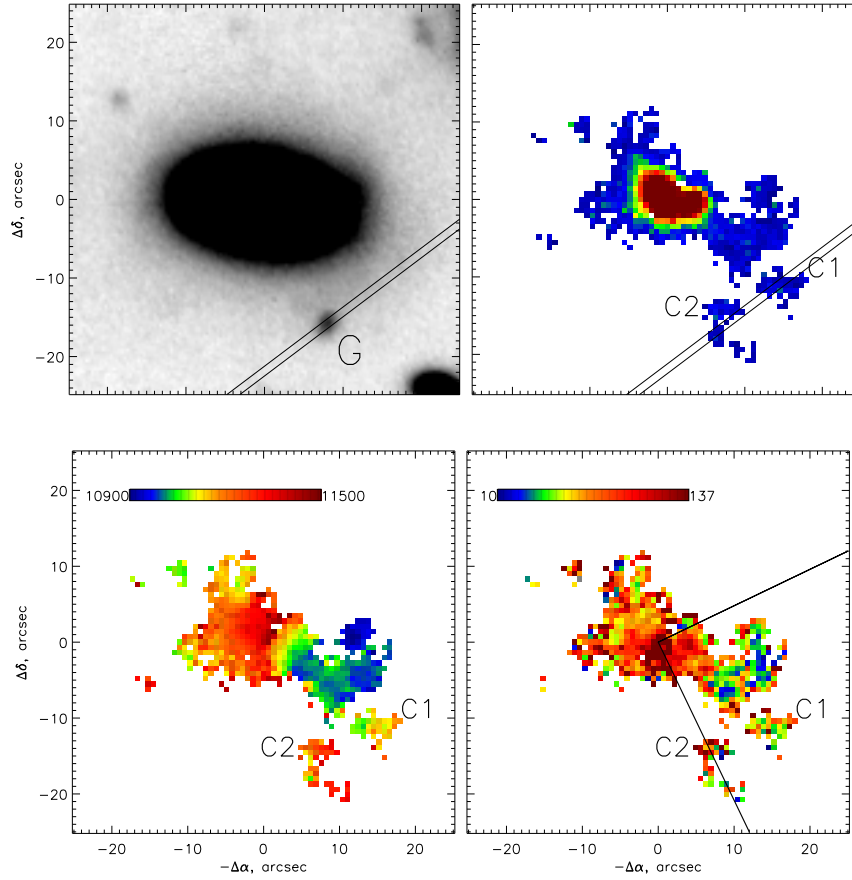


Figure 2. Mrk 78 observations. Top left: the SCORPIO R -band image with the long-slit position, the candidate companion galaxy is marked as ‘G’. Top right: the map of the $[\text{O III}]\lambda 4959$ emission derived from the FPI data. Bottom: the line-of-sight velocity field in the $[\text{O III}]$ emission line (left) and the velocity dispersion map with the marked ionization cone position (right). The colour bars are in the km s^{-1} , the external gaseous clouds are marked as ‘C1’ and ‘C2’.

4. Possible dwarf companion

Assumptions that Mrk 78 is a post-merging system were considered in a number of papers since the eighties of the last century. Morphological peculiarities on different spatial scales were considered as the galaxy interaction imprints: the nuclear dust lane (Whittle & Wilson, 2004), the disturbed external isophotes in the S-W part of the galactic disc (De Robertis, 1987; Pedlar et al., 1989; Keel

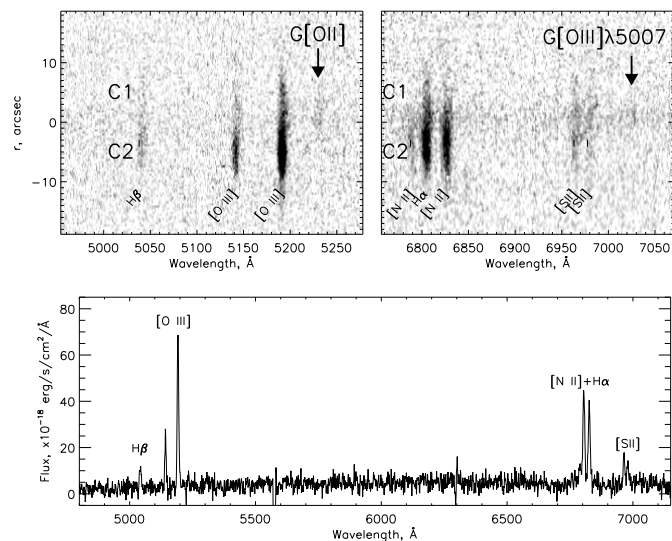


Figure 3. Top: identification of the emission lines in the ionized-gas clouds (C1 and C2) and the nearby galaxy long-slit spectra. Bottom: the integrated spectrum of both clouds.

et al., 2015), the asymmetric distribution of the external [O III] emission (Unger et al., 1987; Afanasiev & Silchenko, 1991).

De Robertis (1987) suggested that the disturbed external isophotes are caused by passing through a companion galaxy and the emission of this region due to the companion galaxy nucleus, but the forthcoming HST data disproved this idea (Fischer et al., 2011).

The SDSS DR15 and SCORPIO *R*-band images reveal the galaxy SDSS J074240.37+651021.4 with an unknown redshift in the nearest neighbourhood of the C1 and C2 clouds at a distance of $\sim 18''$ from the Mrk 78 nucleus (marked as ‘G’ in Fig. 2). We have checked the possibility that this galaxy is a dwarf companion of Mrk 78 or a remnant of a tidal structure. The obtained long-slit spectra (see the slit position in Fig. 2, PA=127°) show the continuum of ‘G’ with weak emission lines ($\lambda=5230 \text{ \AA}$ and $\lambda=7016 \text{ \AA}$) marked with arrows in Fig. 3. We interpreted them as [O II] $\lambda 3727$ and [O III] $\lambda 5007$ at the redshift $z = 0.382$. In this case, the H β should be blended with [S II] $\lambda 6731$ in the C1 and C2 clouds. This spectroscopic redshift is comparable to the photometric SDSS DR15 (Aguado et al., 2019) redshift: $z = 0.367 \pm 0.130$. Therefore, it is a distant background galaxy.

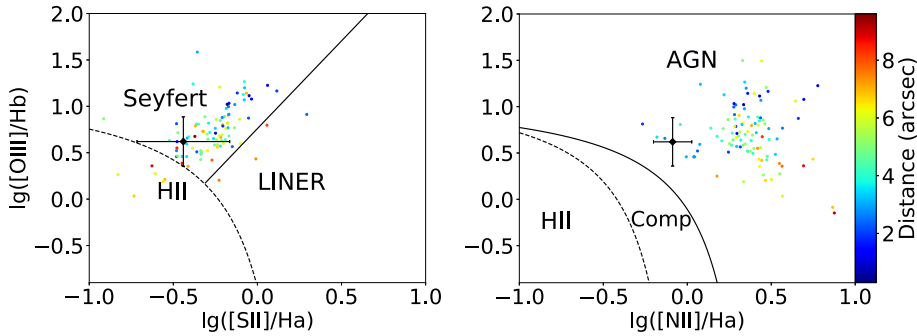


Figure 4. BPT diagrams. The separate lines are taken from Kewley et al. (2006). The circles denote the MPFS data for the circumnuclear region, the colour bar shows the projected distance of pixels on the MPFS maps from the nucleus. The diamond shows the line ratio of C1+C2 derived from the long-slit spectrum.

5. Summary

The 6-m telescope observations reveal a pair of ionized-gas clouds southwest from the stellar disc of Mrk 78 at 12–16 kpc projected distance from the AGN located beyond the galactic disc plane. The BPT diagrams have demonstrated that the AGN radiation makes the main contribution to the ionization state of these clouds. Moreover, the location of both clouds together with other external [O III]-emitting structures in the west side of the Mrk 78 disc is in a good agreement with the ionization cone borders proposed by Fischer et al. (2011) according only to the circumnuclear region structure and kinematics.

The AGN outflow as a source of the described ionized-gas clouds is the contrary to the dynamically cold gas in this part of the EELR. The most possible scenario is an external accretion, a minor merging, or a tidal interaction with the companion. The galaxy SDSS J074240.37+651021.4 at a projected distance of $\sim 18''$ from the Mrk 78 nucleus in the southwest direction was considered a candidate. However, the long-slit spectroscopy data gave a redshift of 0.382; it is a distant background galaxy. Thereby, the origin of the gas in the outer part of the Mrk 78 EELRs is still unclear.

Acknowledgements. This study was supported by the Russian Science Foundation, project no. 17-12-01335 ‘Ionized gas in galaxy discs and beyond the optical radius’ and based on the observations conducted with the 6-m telescope of the Special Astrophysical Observatory of the Russian Academy of Sciences carried out with the financial support of the Ministry of Science and Higher Education of the Russian Federation. Authors are grateful to Victor Afanasiev for his interest to this work. This research has made use of the NASA/IPAC Extragalactic Database (NED), which is operated by the Jet Propulsion Laboratory, California Institute of Technology, under contract with the National Aeronautics and Space Administration.

References

- Afanasiev, V. L., Dodonov, S. N., & Moiseev, A. V., Kinematics of Circumnuclear Regions of Galaxies: 2D Spectroscopy on SAO RAS 6m Telescope. 2001, in *Stellar Dynamics: from Classic to Modern*, ed. L. P. Ossipkov & I. I. Nikiforov, 103
- Afanasiev, V. L. & Moiseev, A. V., The SCORPIO universal focal reducer of the 6-m telescope. 2005, *Astronomy Letters*, **31**, 194, DOI: 10.1134/1.1883351
- Afanasiev, V. L. & Moiseev, A. V., Scorpio on the 6 m Telescope: Current State and Perspectives for Spectroscopy of Galactic and Extragalactic Objects. 2011, *Baltic Astronomy*, **20**, 363, DOI: 10.1515/astro-2017-0305
- Afanasiev, V. L. & Silchenko, O. K., Gas Kinematics in the Central Regions of Seyfert Galaxies - Part Six - MARKARIAN:34 MARKARIAN:78 and MARKARIAN:270. 1991, *Astrofizicheskie Issledovaniia Izvestiya Spetsial'noj Astrofizicheskoy Observatorii*, **33**, 144
- Aguado, D. S., Ahumada, R., Almeida, A., & Anderson, S. F., The Fifteenth Data Release of the Sloan Digital Sky Surveys: First Release of MaNGA-derived Quantities, Data Visualization Tools, and Stellar Library. 2019, *Astrophys. J., Suppl.*, **240**, 23, DOI: 10.3847/1538-4365/aaf651
- Baldwin, J. A., Phillips, M. M., & Terlevich, R., Classification parameters for the emission-line spectra of extragalactic objects. 1981, *Publ. Astron. Soc. Pac.*, **93**, 5, DOI: 10.1086/130766
- De Robertis, M. M., Spectroscopy and Imaging of Markarian 78 and I ZW 92. 1987, *Astrophys. J.*, **316**, 597, DOI: 10.1086/165228
- Fischer, T. C., Crenshaw, D. M., Kraemer, S. B., et al., Hubble Space Telescope Observations of the Double-peaked Emission Lines in the Seyfert Galaxy Markarian 78: Mass Outflows from a Single Active Galactic Nucleus. 2011, *ApJ*, **727**, 71, DOI: 10.1088/0004-637X/727/2/71
- Keel, W. C., Bennert, V. N., Pancoast, A., et al., AGN photoionization of gas in companion galaxies as a probe of AGN radiation in time and direction. 2019, *Mon. Not. R. Astron. Soc.*, **483**, 4847, DOI: 10.1093/mnras/sty3332
- Keel, W. C., Chojnowski, S. D., Bennert, V. N., et al., The Galaxy Zoo survey for giant AGN-ionized clouds: past and present black hole accretion events. 2012, *Mon. Not. R. Astron. Soc.*, **420**, 878, DOI: 10.1111/j.1365-2966.2011.20101.x
- Keel, W. C., Maksym, W. P., Bennert, V. N., et al., HST Imaging of Fading AGN Candidates. I. Host-galaxy Properties and Origin of the Extended Gas. 2015, *AJ*, **149**, 155, DOI: 10.1088/0004-6256/149/5/155
- Kewley, L. J., Groves, B., Kauffmann, G., & Heckman, T., The host galaxies and classification of active galactic nuclei. 2006, *MNRAS*, **372**, 961, DOI: 10.1111/j.1365-2966.2006.10859.x
- Pedlar, A., Meaburn, J., Axon, D. J., et al., Collimated radio and optical emission associated with the Seyfert galaxy Markarian 78. 1989, *Mon. Not. R. Astron. Soc.*, **238**, 863, DOI: 10.1093/mnras/238.3.863

- Smirnova, A. A., Moiseev, A. V., & Dodonov, S. N., A close look at the well-known Seyfert galaxy: extended emission filaments in Mrk 6. 2018, *Mon. Not. R. Astron. Soc.*, **481**, 4542, DOI: 10.1093/mnras/sty2569
- Unger, S. W., Pedlar, A., Axon, D. J., et al., The extended narrow-line region in radio Seyferts : evidence for a collimated nuclear UV field ? 1987, *Mon. Not. R. Astron. Soc.*, **228**, 671, DOI: 10.1093/mnras/228.3.671
- Whittle, M. & Wilson, A. S., Jet-Gas Interactions in Markarian 78. I. Morphology and Kinematics. 2004, *AJ*, **127**, 606, DOI: 10.1086/380940

Spectral changes and BLR kinematics of eruptive changing-look AGN

M. W. Ochmann¹, W. Kollatschny¹ and M. Zetzl¹

*Institut für Astrophysik, Universität Göttingen, Friedrich-Hund-Platz 1, 37077
Göttingen, Germany, (E-mail: mochmann@astro.physik.uni-goettingen.de)*

Received: August 15, 2019; Accepted: October 4, 2019

Abstract. We present results of recent optical spectroscopic variability campaigns for HE 1136-2304 and NGC 1566 which exhibited X-ray outbursts in July 2014 and June 2018, respectively. We show that the broad line region (BLR) structure in the changing-look AGN HE 1136-2304 is similar to that of non-changing-look AGN and that the BLR kinematics is dominated by Keplerian accretion disk (AD) rotation. Furthermore, we present an optical spectrum of NGC 1566 taken only a few weeks after its X-ray outburst, clearly showing drastic spectral changes.

Key words: active galactic nuclei – changing-look – broad line region – accretion disk – spectroscopy – HE 1136-2304 – NGC 1566

1. Introduction – The changing-look phenomenon

Active galactic nuclei (AGN) are known to exhibit variability in several frequency regimes. However, despite the mostly stochastic variations in the flux of AGN, their spectral type generally does not change. This is not true for optical changing-look (CL) AGN which exhibit significant spectral changes leading to a change of the source’s classification (e.g. from Sy-2 to Sy-1 or vice versa). Interestingly, these changes may happen on time scales of weeks to months and are often accompanied by outbursts in several frequency regimes. Up to now a few dozen examples of CL AGN have been found. Very early observations of this phenomenon include – amongst others – NGC 351 (Collin-Souffrin et al., 1973), NGC 4151 (Penston & Perez, 1984) and Fairall 9 (Kollatschny & Fricke, 1985). However, despite increasing interest in this topic, the cause for the changing-look phenomenon is still unknown. Possible explanations include accretion disk instabilities, tidal disruption events and a change of obscuration. Therefore, line profile studies of these eruptive spectral changes offer unique insight into AGN variability and allow – in combination with spectroscopic reverberation mapping – to determine the BLR structure and kinematics.

2. The changing-look AGN HE 1136-2304

HE 1136-2304 ($\alpha_{2000} = 11\text{h } 38\text{m } 51.1\text{s}$, $\delta = -23^\circ 21' 36''$) was detected as a variable X-ray source in 2014 (Parker et al., 2016). In comparison to the ROSAT survey in 1990, its $0.2 - 2\text{ keV}$ flux increased by a factor of ~ 30 . An optical spectroscopic follow-up observation revealed significant spectral changes, changing the classification of the galaxy. HE 1136-2304 is therefore classified as a changing-look AGN.

2.1. Observations and Data Reduction

The optical spectrum directly following the X-ray outburst was taken with the 10 m Southern African Large Telescope (SALT) (Parker et al., 2016) on July 7, 2014. To further investigate the variability behaviour of HE 1136-2304 we started a spectroscopic campaign with SALT on December 25, 2014, lasting until July 13, 2015. The mean cadence was ~ 9 days between February and July 2015. We reduced the spectra according to the standard procedure (bias and dark subtraction, flat-fielding, cosmic ray correction, illumination correction, wavelength calibration, night sky subtraction, and flux calibration). The resulting reduced spectra cover a spectral range of $4240 \text{ \AA} - 7040 \text{ \AA}$ in the rest frame. As the flux of

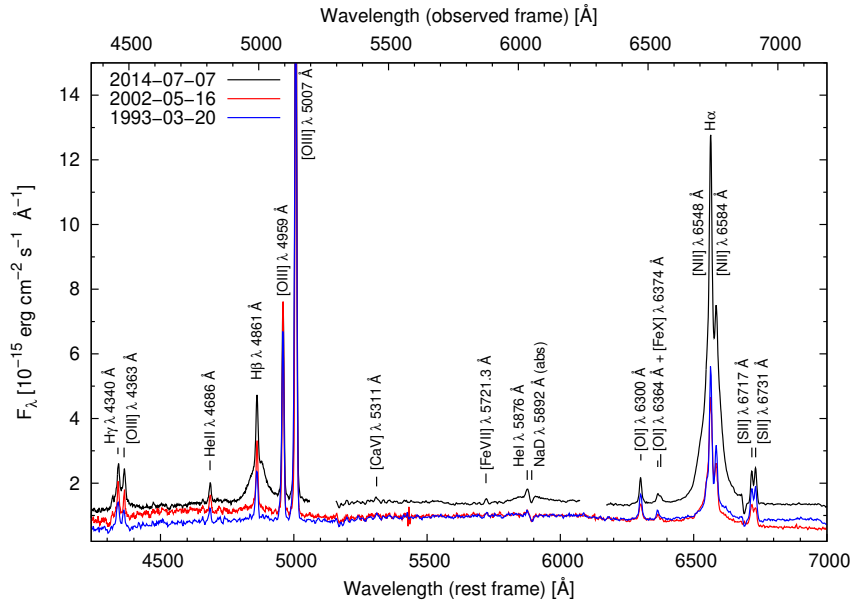


Figure 1. Optical spectra of HE 1136-2304 taken in 1993 (Hamburg/ESO), 2002 (6dF), and 2014. All spectra were calibrated to the absolute [OIII] $\lambda 5007$ flux from 1993-03-20.

the narrow emission line [OIII] $\lambda 5007$ is treated to be constant on time scales of several years, the reduced spectra were calibrated to the absolute [OIII] $\lambda 5007$ flux given in Reimers et al. (1996). For further details on the instrumental setup and the data reduction we refer to Kollatschny et al. (2018).

2.2. Results

We show a comparison of optical spectra taken in 1993 (Hamburg/ESO survey; Reimers et al. (1996)), 2002 (6dF) and 2014 (Parker et al., 2016) in Fig. 1. In contrast to the spectra from 1993 and 2002, the post-outburst spectrum from 2014 especially shows strong and very broad H α and H β lines with line widths of several thousand km s^{-1} (FWHM). While HE 1136-2304's spectral classification corresponded to a Seyfert 1.9 type in 1993 and 2002, respectively, it changed its classification to a Seyfert 1.5 type after the X-ray outburst in 2014 (Zetzl et al., 2018).

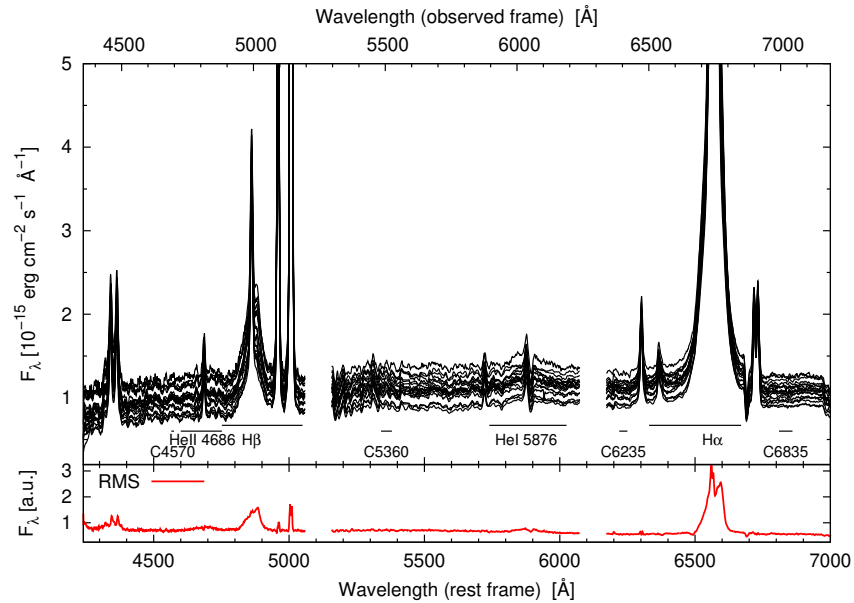


Figure 2. Finally reduced and intercalibrated optical spectra of the variability campaign of HE 1136-2304 with spectral ranges for light curve extraction (top). RMS spectrum of the variability campaign (bottom).

The finally reduced and calibrated spectra taken during our variability campaign and the resulting residual mean square (RMS) spectrum are shown in Fig. 2. Evidently, the spectrum of HE 1136-2304 exhibits clear variations of its continuum level. Furthermore, the RMS spectrum clearly shows variations not

Table 1. Cross-correlation time lags with respect to the 4570 Å continuum, FWHM (RMS), and line dispersion σ (RMS) of the Balmer and Helium lines.

Line	τ (days)	FWHM (RMS) (km s ⁻¹)	σ (RMS) (km s ⁻¹)
H α	15.0 ^{+4.2} _{-3.8}	2668±150	1816±150
H β	7.5 ^{+4.6} _{-5.7}	3791±150	1767±150
He I λ 5876	7.3 ^{+2.8} _{-4.4}	4131±400	2098±400
He II λ 4686	3.0 ^{+5.3} _{-3.7}	5328±500	2962±500

only in the broad Balmer lines but also – albeit lower – in the very broad higher ionization lines He I λ 5876 and He II λ 4686 (Kollatschny et al., 2018)¹. In order to determine the time-lag between continuum and broad emission line variations – a method known as reverberation mapping – we extracted continuum and emission line light curves from all of the spectra. The corresponding spectral ranges for extraction are also shown in Fig. 2. To determine the integrated emission line flux, pseudo-continua to the left and right of each emission line were used to subtract the underlying continuum.

We present the resulting light curves of the continuum flux at 4570 Å and 5360 Å, respectively, and the integrated fluxes of H α , H β , He I λ 5876 and He II λ 4686 in Fig. 3. According to the notion of reverberation mapping, the emission line flux in the broad line region responds with a delay to the ionizing continuum considering that the continuum emission is generated close to the black hole. Hence, time delay measurements between the emission line and continuum light curves allow to determine the mean distance between the central ionizing source and the broad emission line region. Please note that the optical continuum can merely function as a surrogate for the ionizing X-ray and UV emission as it lags behind the X-ray and UV light curves (e.g. Zetzl et al., 2018). This additional delay has to be taken into account when evaluating the kinematics of the system (e.g. calculating the mass of the SMBH).

The time-lags between the continua and emission lines were determined by correlating the continuum and emission line light curves. We used the interpolation cross-correlation function method (ICCF) developed by Gaskell & Peterson (1987) and implemented in our own ICCF code (Dietrich & Kollatschny, 1995). The time-lags were calculated using the centroids τ_{cent} of the ICCFs above 80% of the maximum correlation coefficient value r_{max} . The resulting time-delays with respect to the continuum at 4570 Å are given in Tab. 1. The errors were

¹Please note the variations in the [OIII] lines are entirely due to minor line profile variations during the campaign. The absolute [OIII] λ 5007 flux is constant.

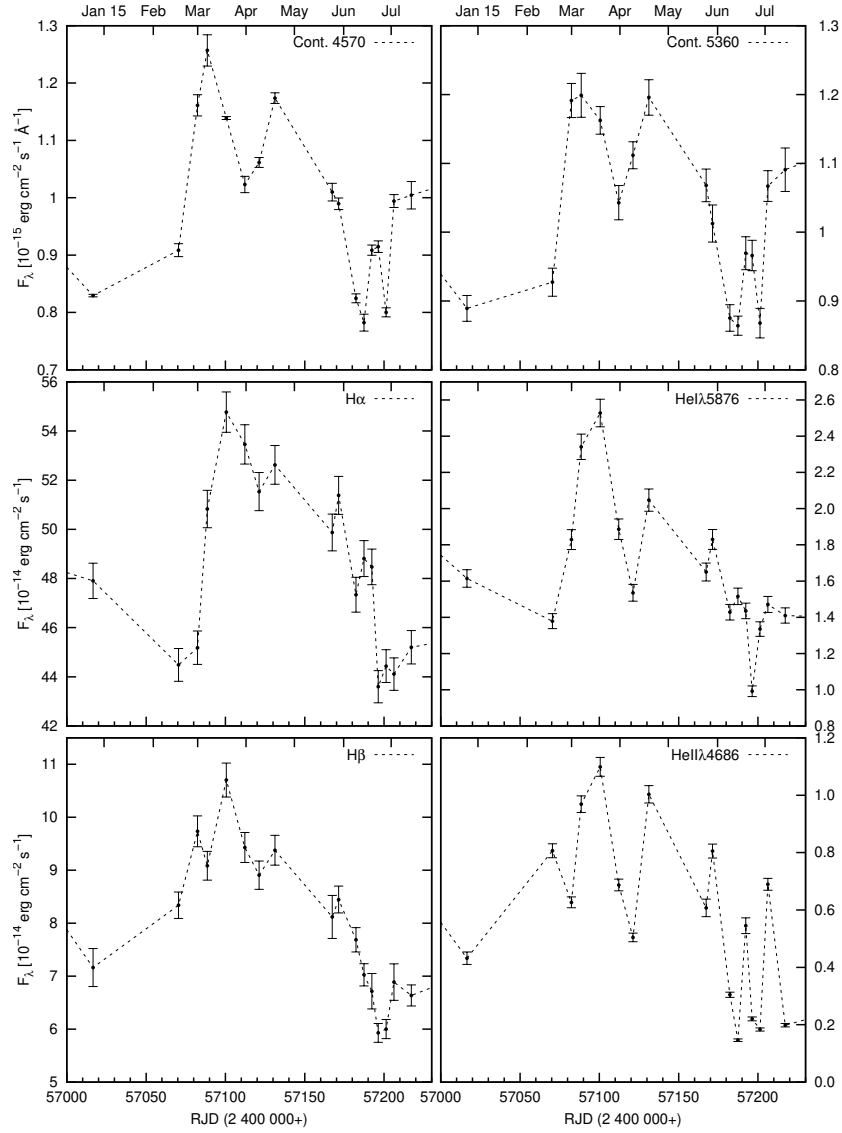


Figure 3. Light curves of the continua 4570 Å and 5380 Å as well as of the emission lines H α , H β , HeI λ 5876 and HeII λ 4686 for the campaign between December 25, 2014 and July 13, 2015.

estimated applying the flux redistribution/random subset selection (FR/RSS) method described in Peterson et al. (1998).

The results indicate an ionization stratification of the BLR, i.e. the averaged $H\alpha$ line originates the furthest away ($15.0^{+4.2}_{-3.8}$ d), the averaged $H\beta$ line originates at approximately half of this distance ($7.5^{+4.6}_{-5.7}$ d) while the Helium I and II line – with higher ionization energy – originate closer inwards ($7.3^{+2.8}_{-4.4}$ d and $3.0^{+5.3}_{-3.7}$ d, respectively). In order to determine the vertical BLR structure we parametrized the line profiles by the ratio of their full-width at half maximum (FWHM) to their line dispersion σ_{line} . In this model the rotational line broadening of intrinsic Lorentzian profiles manifests as the FWHM while the intrinsic Lorentzian profiles are due to turbulent motions of the BLR gas (Kollatschny & Zetzl, 2011, 2013a,b,c). To calculate the FWHM/ σ ratios we measured the FWHM and line dispersion σ in the RMS profile for each line. The values are presented in Tab. 1. The model calculations allow to determine the height of the line-emitting gas above the midplane for each line individually. The resulting cross-section of the BLR structure is shown in Fig. 4. The black dot denotes the supermassive black hole (SMBH) at the center of the AGN.

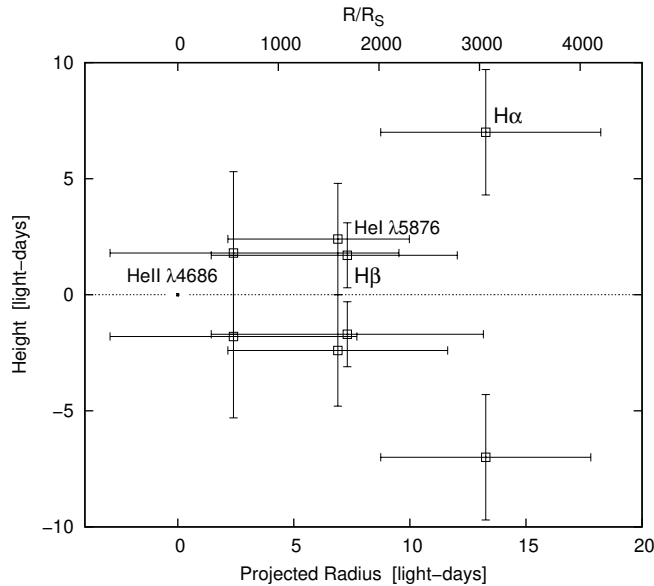


Figure 4. Cross-section of the line-averaged BLR structure in HE 1136-2304. The dot denotes the SMBH. The radius is given in both light-days and Schwarzschild radii of the SMBH in HE 1136-2304.

So far, we only analysed the line-averaged structure of the BLR. However, since the broadening of the lines is due to rotation, different parts of the line profile correspond to different rotational velocities and therefore distances. Particularly, we expect the outer line wings to originate closer to the SMBH than

the line center. To investigate the profile variations in more detail we calculated the lags of individual line segments. We sliced the velocity profiles of the emission lines into segments with a width of $v = 400 \text{ km s}^{-1}$ and extracted the light curve for each individual segment. We then correlated these light curves with the 4570 \AA light curve (Kollatschny et al., 2018). The result is a 2D velocity delay map showing the time delay for each velocity line profile segment. The 2D velocity maps of $\text{H}\alpha$ and $\text{H}\beta$ are shown in Figs. 5 and 6. The line centers show delays of $10 - 30 \text{ d}$ whereas the line wings exhibit a faster response of $0 - 10 \text{ d}$.

3. NGC 1566 – a periodic changing-look AGN?

NGC 1566 is a near ($z = 0.005$) face-on Seyfert galaxy which is known to have shown recurrent significant flux changes in several frequency bands. The outbursts have been accompanied by spectral changes, i.e. NGC 1566 changed from a nearly Sy-2 type classification in its low state to a nearly Sy-1 type classification after the outbursts (Parker et al. (2019) and references therein). In addition, the long-term light curves point towards a periodicity of the eruptive flux changes. A possible mechanism explaining the periodic outbursts was recently presented by Śniegowska & Czerny (2019).

3.1. Observations and Results

We took an optical spectrum of NGC 1566 with SALT shortly after an X-ray outburst was detected in 2018 (Parker et al., 2019). This spectrum is shown in Fig. 7 together with an archival spectrum we took with the same instrument in 2012. The outburst spectrum shows a strong increase in continuum flux, especially towards the UV. Several lines now show strong broad components which have not been present when NGC 1566 was in its low state in 2012.

4. Summary

For the changing-look AGN HE 1136-2304, we were able to show an ionization stratification of the BLR similar to that of other AGN (e.g. Kollatschny et al., 2014). Furthermore, the vertical BRL structure is consistent with the bowl-shaped geometry proposed by Goad et al. (2012), e.g. tested by Ramolla et al. (2018) for 3C 120. The 2D velocity maps of the Balmer line profiles reveal a faster response of the line wings ($0 - 10 \text{ d}$) in comparison to a slower response of the line centers ($10 - 30 \text{ d}$). A similar behaviour is observed in the $\text{He I } \lambda 5876$ and $\text{He II } \lambda 4686$ line (Kollatschny et al., 2018). The resulting kinematics is consistent with thin Keplerian disk BLR models (Horne et al., 2004). Overall, the BLR structure and kinematics of HE 1136-2304 is similar to that of non-changing-look AGN.

For the changing-look AGN NGC 1566, our optical outburst spectrum from 2018 reveals drastic spectral changes in comparison to the low state spectrum

from 2012. A thorough analysis of the outburst spectrum together with an archival spectroscopic campaign is in progress.

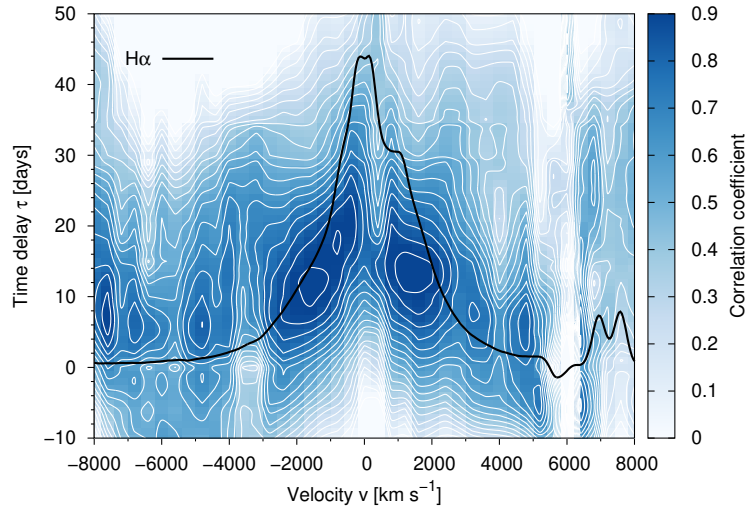


Figure 5. 2D velocity delay map of the H α profile in HE 1136-2304 showing the correlation coefficient as a function of velocity and time delay (blue scale). The campaign-averaged line profile without narrow component is plotted in black.

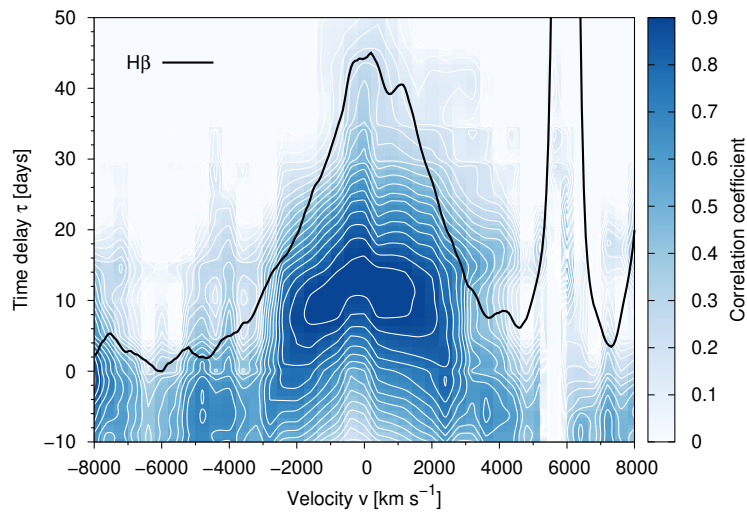


Figure 6. 2D velocity delay map of the H β profile in HE 1136-2304 showing the correlation coefficient as a function of velocity and time delay (blue scale). The campaign-averaged line profile without narrow component is plotted in black.

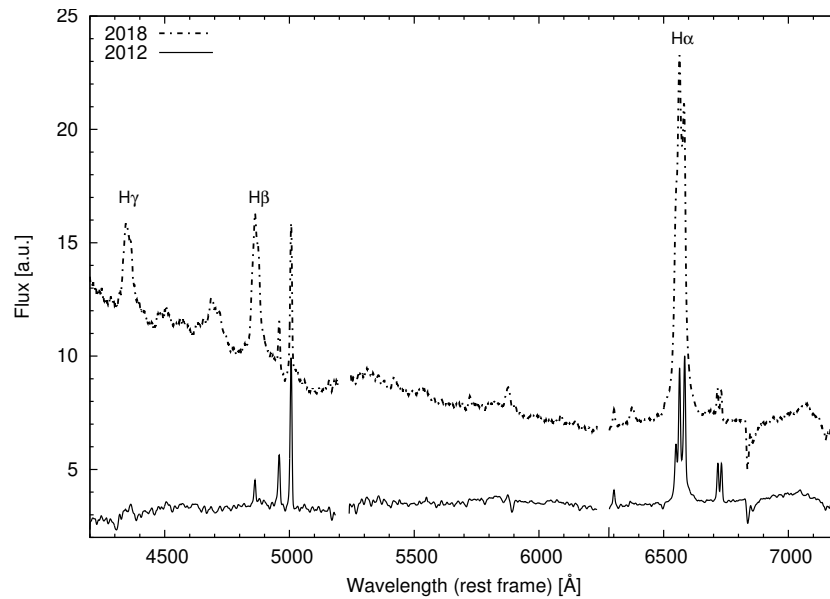


Figure 7. Optical calibrated spectra of NGC 1566 in its low state (2012) and in its high state after the outburst (2018). Both spectra were taken with SALT and reduced the same way as the spectra of HE 1136-2304.

Acknowledgements. This work has been supported by the DFG grant Ko 857/33-1.

References

- Collin-Souffrin, S., Alloin, D., & Andrillat, Y., A discussion of the new variations observed in the nucleus of the Seyfert galaxy NGC 3516. 1973, *Astron. Astrophys.*, **22**, 343
- Dietrich, M. & Kollatschny, W., Optical and ultraviolet emission-line variability of NGC 5548. The coordinated UV and optical monitoring campaign of 1989. 1995, *Astron. Astrophys.*, **303**, 405
- Gaskell, C. M. & Peterson, B. M., The accuracy of cross-correlation estimates of quasar emission-line region sizes. 1987, *Astrophys. J., Suppl.*, **65**, 1
- Goad, M. R., Korista, K. T., & Ruff, A. J., The broad emission-line region: the confluence of the outer accretion disc with the inner edge of the dusty torus. 2012, *Mon. Not. R. Astron. Soc.*, **426**, 3086
- Horne, K., Peterson, B. M., Collier, S. J., & Netzer, H., Observational Requirements for High-Fidelity Reverberation Mapping. 2004, *Publ. Astron. Soc. Pac.*, **116**, 465

- Kollatschny, W. & Fricke, K. J., The fading of the Seyfert galaxy F-9. 1985, *Astron. Astrophys.*, **146**, L11
- Kollatschny, W., Ochmann, M. W., Zetzl, M., et al., Broad-line region structure and line profile variations in the changing look AGN HE 1136-2304. 2018, *Astron. Astrophys.*, **619**, A168
- Kollatschny, W., Ulbrich, K., Zetzl, M., Kaspi, S., & Haas, M., Broad-line region structure and kinematics in the radio galaxy 3C 120. 2014, *Astron. Astrophys.*, **566**, A106
- Kollatschny, W. & Zetzl, M., Broad-line active galactic nuclei rotate faster than narrow-line ones. 2011, *Nature*, **470**, 366
- Kollatschny, W. & Zetzl, M., Accretion disk wind as explanation for the broad-line region structure in NGC 5548. 2013a, *Astron. Astrophys.*, **551**, L6
- Kollatschny, W. & Zetzl, M., The shape of broad-line profiles in active galactic nuclei. 2013b, *Astron. Astrophys.*, **549**, A100
- Kollatschny, W. & Zetzl, M., Vertical broad-line region structure in nearby active galactic nuclei. 2013c, *Astron. Astrophys.*, **558**, A26
- Parker, M. L., Komossa, S., Kollatschny, W., et al., The detection and X-ray view of the changing look AGN HE 1136-2304. 2016, *Mon. Not. R. Astron. Soc.*, **461**, 1927
- Parker, M. L., Schartel, N., Grupe, D., et al., X-ray spectra reveal the reawakening of the repeat changing-look AGN NGC 1566. 2019, *Mon. Not. R. Astron. Soc.*, **483**, L88
- Penston, M. V. & Perez, E., An evolutionary link between Seyfert I and II galaxies? 1984, *Mon. Not. R. Astron. Soc.*, **211**, 33P
- Peterson, B. M., Wanders, I., Bertram, R., et al., Optical Continuum and Emission-Line Variability of Seyfert 1 Galaxies. 1998, *Astrophys. J.*, **501**, 82
- Ramolla, M., Haas, M., Westhues, C., et al., Simultaneous H α and dust reverberation mapping of 3C 120: Testing the bowl-shaped torus geometry. 2018, *Astron. Astrophys.*, **620**, A137
- Reimers, D., Koehler, T., & Wisotzki, L., The Hamburg/ESO survey for bright QSOs. II. Follow-up spectroscopy of 160 quasars and Seyferts. 1996, *Astron. Astrophys. Suppl.*, **115**, 235
- Śniegowska, M. & Czerny, B., Mechanism of the Changing Look phenomenon in Active Galactic Nuclei. 2019, *arXiv*, **1904.06767**
- Zetzl, M., Kollatschny, W., Ochmann, M. W., et al., Long-term optical, UV, and X-ray continuum variations in the changing-look AGN HE 1136-2304. 2018, *Astron. Astrophys.*, **618**, A83

Medium-band photometric reverberation mapping of AGNs at $0.1 < z < 0.8$

Techniques and sample

E. Malygin¹, R. Uklein², E. Shablovinskaya², A. Grokhovskaya² and
A. Perepelitsyn²

¹ *Kazan Federal University, Kazan, Russia, (E-mail: playground@mail.ru)*

² *Special Astrophysical Observatory RAS, Nizhny Arkhyz, Russia, (E-mail: uklein.r@gmail.com)*

Received: July 31, 2019; Accepted: November 5, 2019

Abstract. The most popular method of the broad-line region size estimation in active galactic nuclei (AGN) is the reverberation mapping based on measuring the time delay between the continuum flux and the flux in the emission lines. In our work, we apply the method of photometric reverberation mapping in mid-band filters, adapted for observations on the 1-m Zeiss-1000 telescope of Special Astrophysical Observatory of Russian Academy of Sciences, for the study of AGN with broad lines in the range of redshifts $0.1 < z < 0.8$. This paper provides a sample of 8 objects, describes the technique of observations and data processing for 2 studied objects to demonstrate the stability of the used method.

Key words: galaxies: active – techniques: photometric

1. Introduction

Active galactic nuclei (AGN) are bright compact areas, emitting up to 90% of the energy of the entire galaxy. Because of the small size of the central object and the high gas velocity, it is now assumed that the supermassive black hole (SMBH) is present in the center of the galactic nucleus, and the enormous luminosity is provided by the processes of the matter accretion into the SMBH. The observed energy distribution, as well as the AGN spectrum, indicates that the nucleus is a multicomponent system, which observational properties depend on the orientation relative to the observer. This is known as the Unified model (Antonucci, 1993; Urry & Padovani, 1995), which is illustrated in Fig. 1. According to this model, the SMBH is surrounded by a hot disk of accreting matter (~ 0.001 pc from the central source), which hard radiation excites the gas in the broad-line region (BLR) at scales of 0.01-0.1 pc and is re-emitted in emission lines broadened due to the high gas velocity (up to 10^4 km/s).

The reverberation mapping method (RM, Blandford & McKee, 1982) consists of measuring the time lag τ between the continuum radiation of the ac-

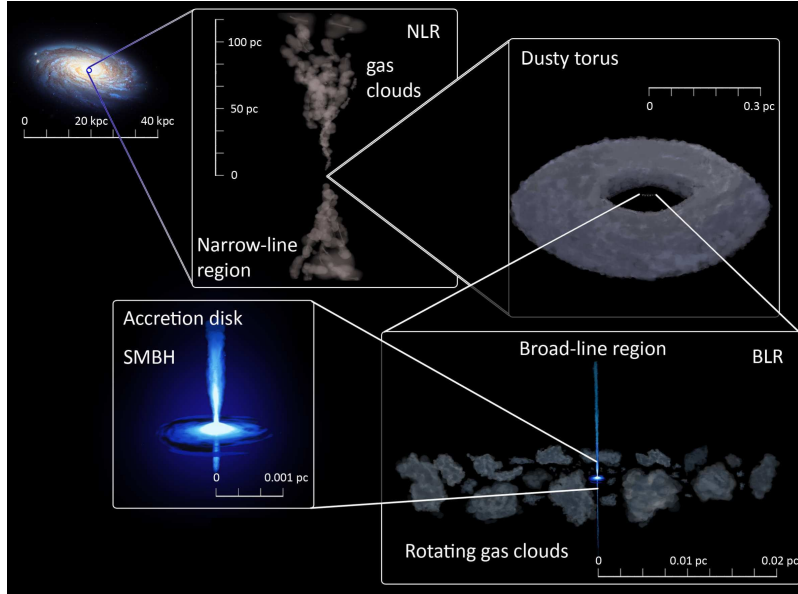


Figure 1. The illustration of modern conceptions of AGN structure.

cretion disk and the radiation in the emission lines produced in the BLR in AGN. The BLR size is assumed to be $R_{\text{BLR}} \equiv c\tau$, where c is the speed of light (Peterson, 1993). Then, the R_{BLR} can be determined by measuring the time lag τ between the continuum and line light curves. According to the virial ratio the SMBH mass is related to the BLR size $c\tau$ and the gas velocity in the BLR v_{line} as:

$$M_{\text{SMBH}} = f c \tau v_{\text{line}}^2 G^{-1},$$

where G is the gravitational constant and f is a dimensionless factor of the order of one depending on the BLR structure and kinematics and the inclination of the system relative to the observer. Thus, measuring the time delays provides one with the SMBH mass estimation. Yet, the RM method requires the accumulation of a long series of observational data that makes harder its wide application. That is the reason why presently this method was applied only for approximately 100 nearest quasars (e.g. Shapovalova et al., 2009; Bentz & Katz, 2015; Du et al., 2016; Jiang et al., 2016; Pozo Nuñez et al., 2017; Ilić et al., 2017).

However, to trace the evolution of the SMBH masses the extension of the AGN sample with known sizes R_{BLR} to more distant redshifts is needed. For AGN the linear relation between the BLR size and AGN luminosity was found: $R_{\text{BLR}} \propto L^\alpha$, where L could be measured in different spectral bands such as

5100Å (Kaspi et al., 2005; Bentz et al., 2009b) or definite emission lines (e.g. MgII in Czerny et al., 2019, and references therein).

Our investigation is dedicated to complement the existing relation of $R_{\text{BLR}}(L)$ by new measurements of $R_{\text{BLR}} = c\tau$ for the distant AGNs up to $z \sim 0.8$ using a sample of objects that have not been studied in other reverberation campaigns. Besides, we adopt the photometric RM method (Haas et al., 2011) to mid-band observation with the 1-meter class telescope.

The paper is formed as following. In Sec. 2 the sample and the methods of observations and data reduction are given. Sec. 3 contains the first results of the applied observational technique with the description of the local standards and the preliminary light curves. The conclusions and main ideas are shortly given in Sec. 4.

2. Observations

2.1. Sample

Our sample consists of 8 AGNs with broad lines (equivalent width $W_\lambda > 200\text{\AA}$) in the range the redshifts $0.1 < z < 0.8$ with the brightness limited to $m < 20$ mag. The sample includes only near-polar objects ($\text{Dec} > 68^\circ$), thus we were able to observe them throughout the whole year. The final sample is shown in Table 1.

(#)	Name (1)	RA Dec (2)	Mag (3)	z (4)	τ (5)	Filters (6)
1	2MASX J08535955+7700543	08 ^h 53 ^m 59 ^s .4 +77°00'55''	17.0	0.106	27	SED725 SED700
2	VII Zw 244	08 ^h 44 ^m 45 ^s .3 +76°53'09''	15.7	0.131	34	SED550 SED525
3	SDSS J093702.85+682408.3	09 ^h 37 ^m 02 ^s .9 +68°24'08''	18.0	0.294	47	SED625 SED600
4	SDSS J094053.77+681550.3	09 ^h 40 ^m 53 ^s .8 +68°15'50''	19.4	0.371	59	SED900 SED875
5	SDSS J100057.50+684231.0	10 ^h 00 ^m 57 ^s .5 +68°42'31''	19.0	0.499	80	SED725 SED700
6	2MASS J01373678+8524106	01 ^h 37 ^m 36 ^s .7 +85°24'11''	16.6	0.499	79	SED725 SED700
7	SDSS J095814.46+684704.8	09 ^h 58 ^m 14 ^s .4 +68°47'05''	19.7	0.662	92	SED800 SED775
8	GALEX 2486024515200490156	10 ^h 01 ^m 51 ^s .6 +69°35'27''	19.6	0.847	124	SED900 SED875

Table 1. Observed sample of AGN: (#) identification number in the sample; (1) galaxy name; (2) coordinates for the J2000 epoch; (3) magnitude in V band; (4) redshift z ; (5) roughly estimated time delay τ in days from the continuum or emission line luminosity (see text for details); (6) filters used to measure line and continuum fluxes.

Each object is observed in two filters selected so that they cover the broad emission line $H_{\beta(\alpha)}$ and the near-by continuum, which was used to subtract the contribution of the variable continuum from the emission line. The experiment uses medium-band interference filters¹ with the spectral energy distribution (SED) of a 250Å bandwidth, covering the 5000–9000Å range with 250Å-step. The selection of filters with their bandwidth overplotted on the spectra of the studied objects is illustrated in Fig. 2. The spectra are taken from Abolfathi et al. (2018), Boroson & Green (1992), and Wei et al. (1999).

From the known radius-luminosity relation $R_{\text{BLR}} - L$ for the H_{β} line the expected time delays τ were calculated for the sample (see Table 1, column 5) in the following way. For the objects with redshifts up to 0.5 - objects #1,3-5 - the flux F_{λ} at 5100Å was integrated in the range 4400–5850Å in the rest frame from the spectra obtained from the literature; the flux F_{λ} was divided by the window-width in order to get the monochromatic luminosity. The 4400–5850Å range contains some strong emission lines as variable H_{β} and approximately constant O[III] but as the integrated band is wide we assume that the lines contribution is not crucial especially for rough estimation of the time delays. To convert the flux to the luminosity L_{λ} at 5100 Å it was multiplied with $4\pi D^2$, where D is the AGN luminosity distance calculated using the cosmological parameters $\Omega_0 = 0.3036$ and $H_0 = 68.14$ km/s/Mpc. Note here that the contribution of the host galaxy was not considered. Then we applied the relation $R_{\text{BLR}} - L_{\lambda}(5100)$:

$$\lg(R_{\text{BLR}}) = -21.3_{-2.8}^{+2.9} + 0.519_{-0.066}^{+0.063} \lg(\lambda L_{\lambda}),$$

where $L_{\lambda} = L_{\lambda}(5100)$ is a luminosity at 5100Å, and R_{BLR} is the BLR size in the H_{β} line (Bentz et al., 2009a).

In the case of $z > 0.5$, as well as for the object #2, which spectral data used by us in calculations are available only in a small wavelength range (4075–5883Å), the $L_{\lambda}(5100)$ range goes beyond the available optical spectra. In this regard, for objects #2,6-8 we used the relation with the line $L_{\lambda}(H_{\beta})$ from Greene et al. (2010):

$$\lg(R_{10}) = 0.85 \pm 0.05 + (0.53 \pm 0.04) \lg[L_{43}(H_{\beta})],$$

where $R_{10} = R_{\text{BLR}}/10$ lt days is the size of the BLR region, normalized to 10 lt days, $L_{43}(H_{\beta}) = L_{\lambda}(H_{\beta})/10^{43}$ erg/s is the luminosity in the H_{β} line, normalized to 10^{43} erg/s. In Table 1 the rough estimate of the expected time delays τ are given with an accuracy of 10%.

2.2. Observational technique and reduction

Since February 2018, observations of the AGN sample have been carried out monthly on gray and bright nights at 1-m Zeiss-1000 telescope of the Spe-

¹Edmund Optics, <https://www.edmundoptics.com>.

For the main parameters of middle-band SED filters see: https://www.sao.ru/hq/lsvfo/devices/scorpio-2/filters_eng.html.

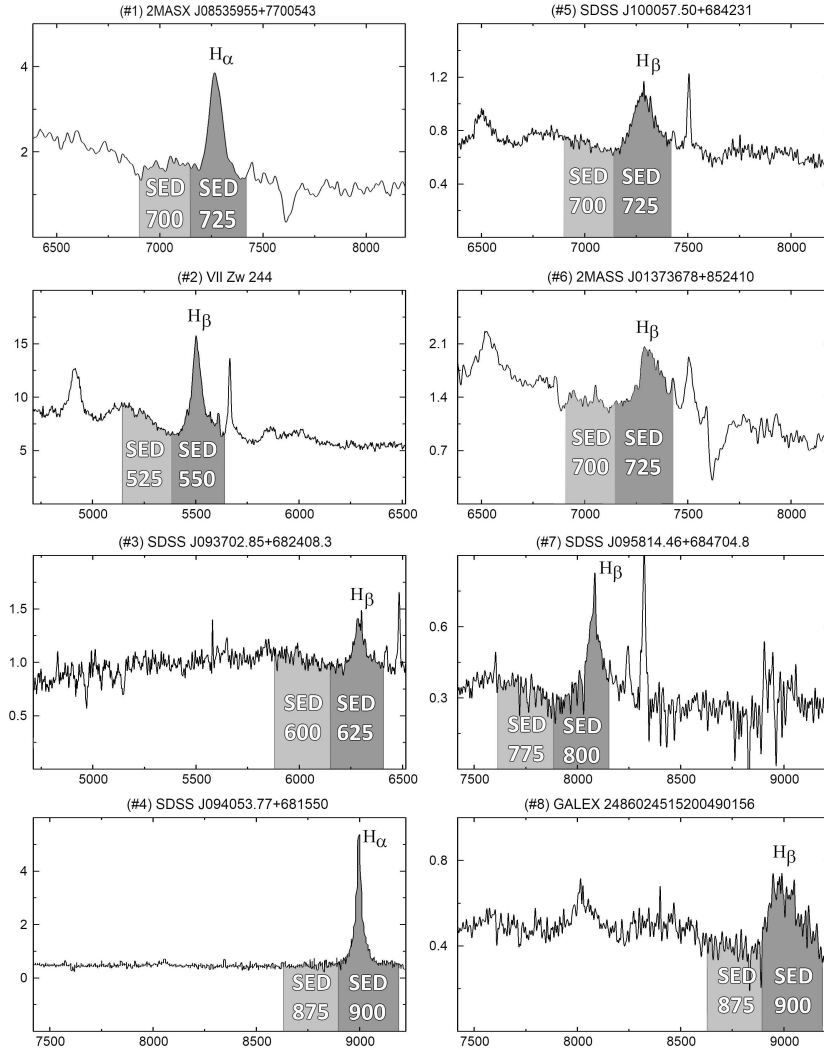


Figure 2. SED filters bands overlapped on the spectra of the studied AGN. Flux F_{λ} in units of 10^{-16} erg/cm²/s/Å depending on the wavelength in Å given in the observer rest frame. The spectra of #1 and #6 are obtained from Wei et al. (1999), #2 is from Boroson & Green (1992) and the others are from Abolfathi et al. (2018).

cial Astrophysical Observatory of Russian Academy of Sciences (SAO RAS) using MaNGaL (MApper of Narrow GALaxy Lines, Perepelitsyn et al., 2018) and MMPP (Multi-Mode Photometer-Polarimeter) devices in photometric mode with 10 medium-band interference SED filters. The size of the field of view (FoV) was 8.7×8.7 for MaNGaL and 7.2×7.2 for MMPP. Up to now, around 15 epochs were acquired on average for majority of the objects in the sample.

Three different detectors were used during the observations: Andor CCD iKon-M 934 (1024×1024 px), Andor Neo sCMOS (2560×2160 px) and Raptor Photonics Eagle V CCD (2048×2048 px). The quantum efficiency of these receivers in the needed bands is shown in Table 2. Water cooling was used for all three cases to minimize noise.

Detector	5500Å	6000Å	7000Å	8000Å	9000Å
Andor iKon-M 934	95%	96%	91%	77%	47%
Andor Neo sCMOS	54%	56%	49%	31%	14%
Raptor Eagle V CCD	92%	95%	89%	75%	50%

Table 2. Quantum efficiency of detectors in the studied photometric bands.

Observations of the sample were alternated with observations of spectrophotometric standard stars provided by Oke (1990). The standards were observed almost simultaneously with the object field in the same filter to minimize the variations of atmospheric transmission; moreover, even observing the standards at the close zenith distance we tried to obtain the extinction coefficient every night and take it into account. Such strategy was used to create a list of comparison stars with known AB-magnitudes in the FoV of the sample.

During each observational night, we received calibration images (flat frames at the twilight sky for each filter, bias/dark) to correct data for additive and multiplicative errors. For each object the series of images (3 and more) were taken, the exposure times depend on the object brightness, weather conditions and are ranged from 2 to 10 minutes. For correct statistics each frame is processed independently, and statistical evaluation is made by averaging the random value by robust methods giving its unbiased estimate. In this case, the photometric errors are the rms of the robust distribution.

The method of aperture photometry was used to determine the absolute flux of the objects in instrumental units. Therefore, to correctly estimate the sky background, the traces of cosmic rays which were close to the object were removed from images.

For better photometric accuracy needed for the variability studies of AGN, the AB fluxes were first calculated using the spectrophotometric standards, and further step was to re-calibrate them with the differential photometry using the local standards from the object image FoV.

3. Results

3.1. Local standards

The main methodological result obtained during the first year of observations is the definition of local standards in the field of each sample objects. In Fig. 3 we show the field of the object #1 (2MASX J08535955+7700543) obtained in the SED725 filter and object #2 (VII Zw 244) obtained in the SED550 filter by Raptor Eagle V CCD (MMPP) with marked local standards. Within the stable photometric nights, we bind the field with known spectrophotometric standards. To examine the variability of the stars in the fields, the obtained fluxes were normalized to the most frequently observed and the most stable star flux. Thus, the resulting fluxes of stars do not depend on weather conditions on the selected night. Fig. 4 presents the normalized light curves of local standards in objects #1 and #2 fields in AB-magnitudes. In Fig. 4 the regions corresponding to the 3σ confidence area are also shown. For differential photometry, the stars with the smallest scatter were chosen. It is also seen that the average error of the absolute binding was of the order of 0.03 mag.

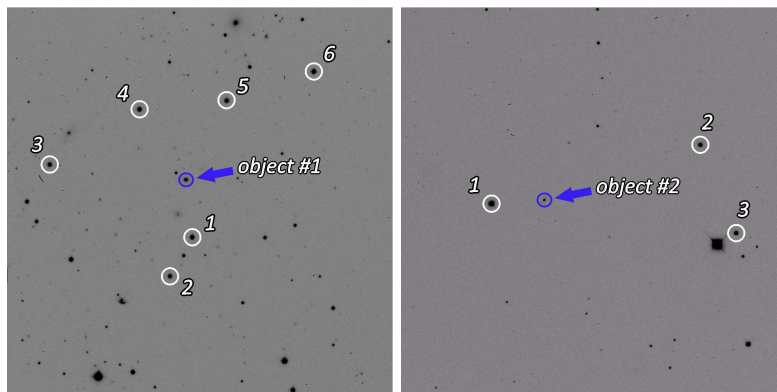


Figure 3. Direct images of AGNs: the object #1 obtained in the SED725 filter with 6 local standards candidates marked (*left*) and object #2 obtained in the SED550 filter by CCD Eagle V [MMPP] with 3 local standards candidates marked (*right*).

Once local standards have been defined, the flux of the object is measured relatively to them, minimizing errors introduced by variations in the atmosphere.

3.2. First light of light curves

The fluxes of the studied AGN were carried out relatively to the most stable reference stars — local standards. The light curves in the continuum and the

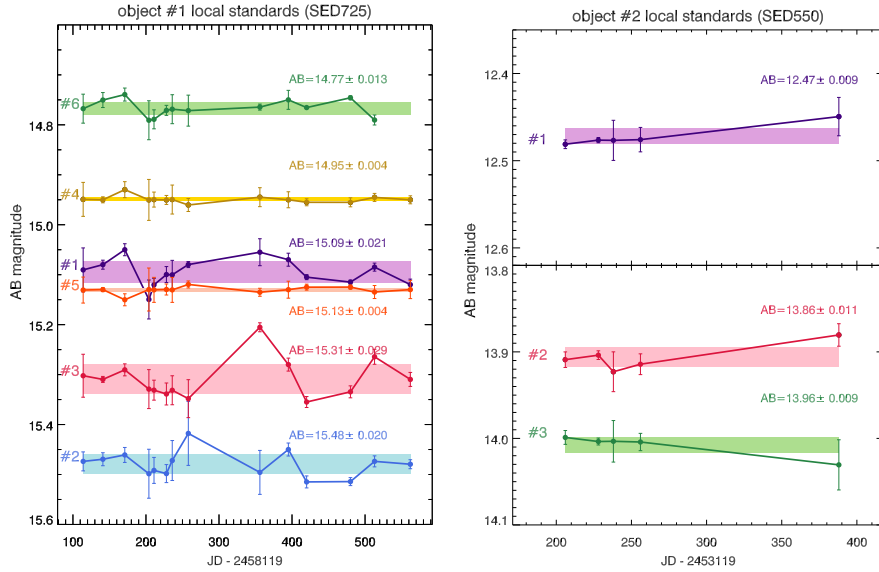


Figure 4. The light curves of the local standards candidates: 6 stars for object #1 in SED725 (*left*) and 3 stars for object #2 in SED550 filter (*right*).

line for one of the most intensively observed AGN, object #1 are presented in Fig. 5, left. Also, in Fig. 5, right, the same light curves for object #2 are shown.

To investigate the time lag between the light curves we have used the **JAVELIN** code (Zu et al., 2016; Mudd et al., 2018). The first step is to build a continuum model to determine the dumped random walk (DRW) parameters of the continuum light curve. As a result, the posterior distribution of the two DRW parameters (amplitude and timescale) of the continuum variability is calculated by **JAVELIN** using Markov chain Monte Carlo (MCMC). The second step is to interpolate the continuum light curve based on the posteriors derived on the first step, and then to shift, smooth, and scale each continuum light curve to compare with the observed line light curve. Finally, it derives the posterior distribution of the time lag and other parameters.

Fig. 6 shows the posterior distribution of **JAVELIN** time delays for objects #1 and #2. This is a distribution of the number of hits N during the MCMC sampling, which sum across all bins gives the sample size. We used at least 10,000 samples. Solid red line marks position of the local peak median, whereas dashed blue line marks expected lag from calibration relations (Table 1, column 5). Our preliminary lags are $44.9^{+13.8}_{-12.7}$ and $30.9^{+15.1}_{-12.2}$ days for objects #1 and #2 respectively. Low and high estimates of the lags correspond to the highest posterior density interval calculated by **JAVELIN**.

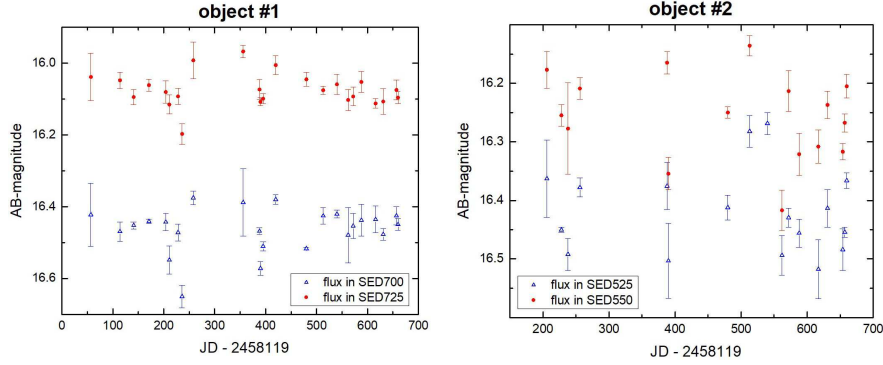


Figure 5. The light curves of object #1 (*left*) and object #2 (*right*) in the line (circles) and near-by continuum (triangles). The Julian dates starts on January 1, 2018.

3.2.1. JAVELIN analysis for object #1

The JAVELIN method involves sampling using the DRW, which ultimately gives us slightly different results from one chain to another. In general, the overall picture for the data set can be traced, however, we can choose the clearest histograms for analysis.

In case of the object #1, we see a stable result for 24 epochs (Fig. 6, left panel):

1. the most powerful peak with a median value of ~ 45 days is near the expected time delay from the calibrations;
2. the second and the less significant peak appears with a median value of ~ 125 days.

The expected value from the calibration relation for the object #1 is ~ 27 days, and we confidently take the position of a powerful peak $\tau_1 = 44.9^{+13.8}_{-12.7}$ days as a preliminary result.

Clearly, with an increase in the number of epochs, we can reveal a narrowing of the main peak, thereby reducing the error in estimating the time delay value.

3.2.2. JAVELIN analysis for object #2

For the object #2, the number of epochs is only 17, and we see a less clear picture (Fig. 6, right panel). For the range of time delays from 0 to 150 days sampling results are divided into two main solutions with a comparable level of significance:

- peak at ~ 30 days, which is quite close to the value expected from the calibrations;

– wider peak with a median value of ~ 90 days.

Despite the fact that we see two comparable peaks, we prefer the first peak, which is closer to the expected value ~ 34 days from calibrations. An additional argument is that with an increase in the number of epochs we trace the growth of the first peak and hope to see this trend after additional observations. So, for the object #2 we take $\tau = 30.9^{+15.1}_{-12.2}$ days as a rough preliminary result. The peaks are wide and still indistinguishable, so more data are needed for a more clear histogram.

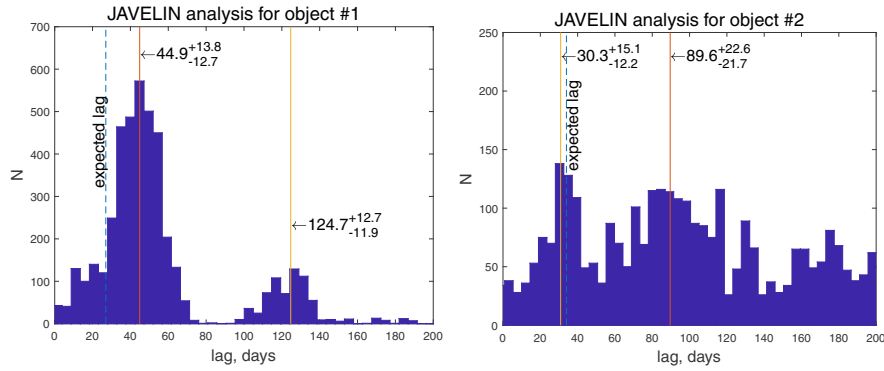


Figure 6. The time lag posterior distributions using JAVELIN code for the object #1 (*left*) and objects #2 (*right*). Solid red lines indicate significant peaks and their values, and the expected values from calibrations are indicated by dashed blue lines.

3.2.3. General comments

We should not exclude the possibility of mismatch between the roughly expected time delays and the obtained peaks in the histogram, since the observed luminosity of AGN is variable. That is, the fainter the state of the nucleus we observe, the smaller BLR size estimate is. Moreover, the spectral data for objects #1 and #2 were obtained more than 20 years ago, so the new spectral observation should be done. Also, certainly, the effect of sparse and poor sampling and low number of epochs influence the analysis of light curves. Obviously, we would increase the number of epochs and to clarify our results further we would also compare different cross-correlation methods.

4. Conclusions

In this paper we present the first results of the photometric reverberation mapping project started in 2018 on the 1-m telescope of SAO RAS. The ongoing

project is focused on the regular observations of the sample of 8 broad line AGNs, and here the technique of observation and data reduction is shown and the preliminary results demonstrating the method stability. Within this work, the following was obtained.

1. The observations by the photometric reverberation mapping method are adapted for telescopes of 1-meter class and are independent of the device used.

2. For each of the studied AGN in the range of redshifts $0.1 < z < 0.8$, a list of local standards was determined, which allows further use of the differential photometry method. The photometric accuracy is on average 0.03 mag, which is an order of magnitude greater than the expected amplitude of the AGN variability.

3. The use of the JAVELIN analysis revealed time delays $\tau_1 = 44.9^{+13.8}_{-12.7}$ and $\tau_2 = 30.9^{+15.1}_{-12.2}$ days for objects #1 and #2, respectively.

It is clear that the first obtained results are in agreement, within the error-bars, with our predictions based on the empirical radius-luminosity relations. However, the data should be processed more carefully and other cross-correlation methods should be applied to reveal whether the calculated time delays are correct. Also, it is particularly important to clean the series from the additional harmonics. Presently, for the majority of the objects the sampling of the observations and the number of epochs is still not sufficient for the reliable analysis, and this is probably the reason why the cross-correlation peaks are so wide. We continue with the observations and in the next stage of the project we are going to obtain and analyze more data, and compare different cross-correlation methods.

Acknowledgements. The work is executed at support of RFBR grant 18-32-00826. The authors thank V. L. Afanasiev for useful discussions and comments. Observations on the telescopes of SAO RAS are carried out with the support of the Ministry of science of the Russian Federation.

References

- Abolfathi, B., Aguado, D. S., Aguilar, G., Allende Prieto, C., & Almeida, A., The Fourteenth Data Release of the Sloan Digital Sky Survey: First Spectroscopic Data from the Extended Baryon Oscillation Spectroscopic Survey and from the Second Phase of the Apache Point Observatory Galactic Evolution Experiment. 2018, *Astrophys. J., Suppl.*, **235**, 42, DOI: 10.3847/1538-4365/aa9e8a
- Antonucci, R., Unified models for active galactic nuclei and quasars. 1993, *Ann. Rev. Astron. Astrophys.*, **31**, 473, DOI: 10.1146/annurev.aa.31.090193.002353
- Bentz, M. C. & Katz, S., The AGN Black Hole Mass Database. 2015, *Publ. Astron. Soc. Pac.*, **127**, 67, DOI: 10.1086/679601
- Bentz, M. C., Peterson, B. M., Netzer, H., Pogge, R. W., & Vestergaard, M., The Radius-Luminosity Relationship for Active Galactic Nuclei: The Effect of Host-Galaxy Starlight on Luminosity Measurements. II. The Full Sample of

- Reverberation-Mapped AGNs. 2009a, *Astrophys. J.*, **697**, 160, DOI: 10.1088/0004-637X/697/1/160
- Bentz, M. C., Walsh, J. L., Barth, A. J., et al., The Lick AGN Monitoring Project: Broad-line Region Radii and Black Hole Masses from Reverberation Mapping of H β . 2009b, *Astrophys. J.*, **705**, 199, DOI: 10.1088/0004-637X/705/1/199
- Blandford, R. D. & McKee, C. F., Reverberation mapping of the emission line regions of Seyfert galaxies and quasars. 1982, *Astrophys. J.*, **255**, 419, DOI: 10.1086/159843
- Boroson, T. A. & Green, R. F., The Emission-Line Properties of Low-Redshift Quasistellar Objects. 1992, *Astrophys. J., Suppl.*, **80**, 109, DOI: 10.1086/191661
- Czerny, B., Olejak, A., Ralowski, M., et al., Time delay measurement of Mg II line in CTS C30.10 with SALT. 2019, *arXiv e-prints*, arXiv:1901.09757
- Du, P., Lu, K.-X., Zhang, Z.-X., et al., Supermassive Black Holes with High Accretion Rates in Active Galactic Nuclei. V. A New Size-Luminosity Scaling Relation for the Broad-line Region. 2016, *Astrophys. J.*, **825**, 126, DOI: 10.3847/0004-637X/825/2/126
- Greene, J. E., Hood, C. E., Barth, A. J., et al., The Lick AGN Monitoring Project: Alternate Routes to a Broad-line Region Radius. 2010, *Astrophys. J.*, **723**, 409, DOI: 10.1088/0004-637X/723/1/409
- Haas, M., Chini, R., Ramolla, M., et al., Photometric AGN reverberation mapping - an efficient tool for BLR sizes, black hole masses, and host-subtracted AGN luminosities. 2011, *Astron. Astrophys.*, **535**, A73, DOI: 10.1051/0004-6361/201117325
- Ilić, D., Shapovalova, A. I., Popović, L. Č., et al., Long-term monitoring of the broad-line region properties in a selected sample of AGN. 2017, *Frontiers in Astronomy and Space Sciences*, **4**, 12, DOI: 10.3389/fspas.2017.00012
- Jiang, L., Shen, Y., McGreer, I. D., et al., Reverberation Mapping with Intermediate-band Photometry: Detection of Broad-line H α Time Lags for Quasars at $0.2 < z < 0.4$. 2016, *Astrophys. J.*, **818**, 137, DOI: 10.3847/0004-637X/818/2/137
- Kaspi, S., Maoz, D., Netzer, H., et al., The Relationship between Luminosity and Broad-Line Region Size in Active Galactic Nuclei. 2005, *Astrophys. J.*, **629**, 61, DOI: 10.1086/431275
- Mudd, D., Martini, P., Zu, Y., et al., Quasar Accretion Disk Sizes from Continuum Reverberation Mapping from the Dark Energy Survey. 2018, *Astrophys. J.*, **862**, 123, DOI: 10.3847/1538-4357/aac9bb
- Oke, J. B., Faint spectrophotometric standard stars. 1990, *Astron. J.*, **99**, 1621, DOI: 10.1086/115444
- Perepelitsyn, A. E., Moiseev, A. V., & Oparin, D. V., The focal reducer MaNGaL with tunable interference filter for small and medium-size telescopes (in Russian). in , *Proceedings of the VII Pulkovo astronomical conference for young astronomers (Pulkovo, St. Petersburg, 28–31 may 2018)*, Vol. **226**, Main Astronomical Observatory of RAS, 65–70
- Peterson, B. M., Reverberation Mapping of Active Galactic Nuclei. 1993, *Publ. Astron. Soc. Pac.*, **105**, 247, DOI: 10.1086/133140

- Pozo Nuñez, F., Chelouche, D., Kaspi, S., & Niv, S., Automatized Photometric Monitoring of Active Galactic Nuclei with the 46cm Telescope of the Wise Observatory. 2017, *Publ. Astron. Soc. Pac.*, **129**, 094101, DOI: 10.1088/1538-3873/aa7a55
- Shapovalova, A. I., Popović, L. Č., Bochkarev, N. G., et al., Long-term variability of the Broad Emission Line profiles in AGN. 2009, *New Astronomy Reviews*,, **53**, 191, DOI: 10.1016/j.newar.2009.08.004
- Urry, C. M. & Padovani, P., Unified Schemes for Radio-Loud Active Galactic Nuclei. 1995, *Publ. Astron. Soc. Pac.*, **107**, 803, DOI: 10.1086/133630
- Wei, J. Y., Xu, D. W., Dong, X. Y., & Hu, J. Y., An AGN sample with high X-ray-to-optical flux ratio from RASS. I. The optical identification. 1999, *Astron. Astrophys., Suppl.*, **139**, 575, DOI: 10.1051/aas:1999514
- Zu, Y., Kochanek, C. S., Kozłowski, S., & Peterson, B. M., Application of Stochastic Modeling to Analysis of Photometric Reverberation Mapping Data. 2016, *Astrophys. J.*, **819**, 122, DOI: 10.3847/0004-637X/819/2/122

Intraday variability of the polarization vector in AGN S5 0716+714

E. Shablovinskaya and V. Afanasiev

*Special Astrophysical Observatory of the Russian Academy of Science, Nizhnii
Arkhyz, 369167, Russia, (E-mail: e.shablie@yandex.com, vafan@sao.ru)*

Received: July 28, 2019; Accepted: September 28, 2019

Abstract. The bright radio source S5 0716+714, which is usually classified as a BL Lac object, is one of the most intensively studied blazar. S5 0716+714 demonstrates extremely peculiar properties, such as the shortest time-scale of optical and polarimetric variations observed in blazars. In the given talk, we present the results of a 8-h polarimetric monitoring of S5 0716+714 with a ~ 70 -sec resolution carried out using the 6-m telescope BTA of the SAO RAS. The observation data analysis reveals the variability both in total and polarized light on the 1.5-hour timescales that specifies the size of the unresolved emitting region. The numerical model of polarization in jet with helical structure of magnetic field is suggested, and fitting the model reveals a magnetic field precession with a period of about 15 days.

Key words: BL Lacertae objects: individual: S5 0716+714 – polarization – galaxies: jets – galaxies: distances and redshifts

1. Introduction

BL Lac type objects or blazars¹ are a special type of active galactic nucleus (AGN) with the jet directed almost toward the observer. Because of such orientation, the synchrotron (non-thermal) component formed in the jet makes a very large contribution in the blazar optical radiation, and short-term brightness and polarization variations are observed (the polarization degree in flashes is up 40% and higher, see e.g. polarization light curve of PKS 1510-089 in the paper by Marscher et al. (2010)).

S5 0716+714 is considered to be a typical BL Lac object. It shows flat power-law spectrum ($\alpha \geq -0.5$, $S_\nu \propto \nu_\alpha$ in the radio band), as well as intraday variability in all spectral ranges: from 8-12 hours in radio band (6 cm, Gorshkov et al., 2011; Gorshkov et al., 2011) to 2.2-3.2 min flares in X-rays (Pryal et al., 2015). The observed polarization is also variable as within the night (e.g. Impey et al., 2000; Amirkhanyan, 2006), and on the scale of tens of days (e.g. Larionov et al., 2013). However, the increase in the polarization is not correlated with optical flashes.

¹Though the terms "BL Lacs" and "blazars" are not equal to each other, within this paper we would assume it interchangeably.

It is assumed the plasma motion in a relativistic jet is responsible for the observed object variability. In this regard, this work is devoted to the detection of the polarization vector motion associated with the plasma, as well as the construction of a model of polarization changes within the night.

2. S5 0716+714 - what are you?

The biggest question related to object S5 0716+714 is the redshift estimation. The lines weakness and their small equivalent width in the blazar spectra are normal since the contribution of the non-thermal jet component is too large. However, in the case of S5 0716+714, no details up to 0.3% are detected in the spectrum that is also mentioned in the work by Nilsson et al. (2008).

In February the spectroscopic observations of S5 0716+714 were carried out at the BTA telescope using the SCORPIO-2 device (Afanasiev et al., 2017) while the object was in an almost record low activity state, when its luminosity was about 14.8 mag in R band². Three 600 sec exposure spectra were obtained with a VPHG940@600 grating. The slit was oriented so that the spectrum of the neighbouring star was observed simultaneously with the object. In Fig. 1 the object and the star spectra are presented in the range 3700-8200Å in residual intensities. As it can be seen from the figure, in the spectrum of S5 0716+714 there is no detail, despite low activity state, except noted atmospheric lines common to the object and the stars.

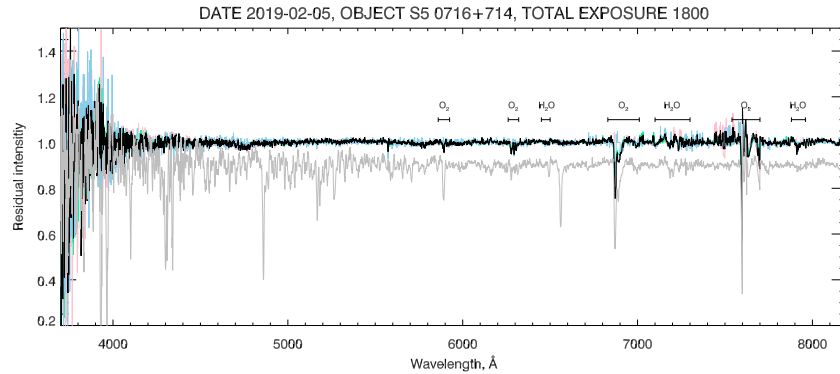


Figure 1. The spectrum of S5 0716+714 in residual intensities obtained while the object was in inactive state: the average S5 0716+714 spectrum is plotted in black and the comparison star is in gray. The telluric O₂ and H₂O lines are marked.

²According to the monitoring provided by Saint Petersburg State University observatory <http://vo.astro.spbu.ru/en/program>.

Also, the spectrum obtained at the BTA with the SCORPIO device in 2010 is shown (Fig. 2, upper panel). The object was in a brighter state (~ 13 mag in the R band), but its lines are still not visible. The spectrum contains interstellar molecular bands (DIBs) and H&K CaII lines (Fig. 2, bottom panel). The H&K CaII equivalent width is $W_\lambda = 185 \pm 6$ mÅ, and according to the calibration (Beers et al., 1990) is insufficient for an extragalactic object and corresponds to a distance less than 1 kpc.

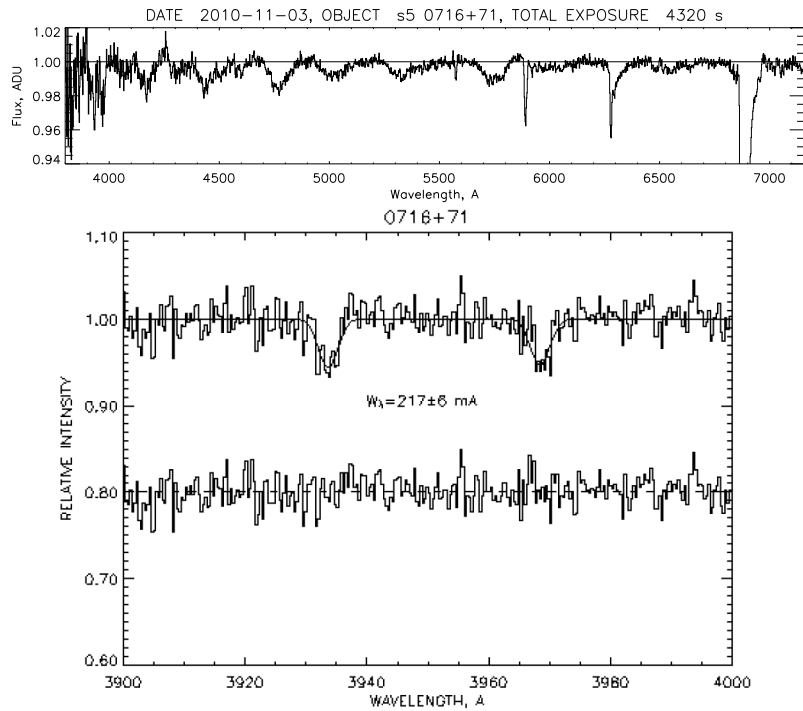


Figure 2. *Upper panel:* the spectrum of S5 0716+714 in residual intensities with DIBs. *Bottom panel:* equivalent width of Galactic H&K CaII in S5 0716+714 spectrum.

Other indirect methods were also used to find the S5 0716+714 redshift. The first try was described in the paper (Stickel et al., 1993). Two weak galaxies (at distances of $27''$ and $55''$ from the source - 0.11 Mpc and 0.23 Mpc for $z \sim 0.3$, respectively) with redshifts of ~ 0.26 were found and it was concluded the source z is close to this value. However, the assumption about the galaxy cluster is not confirmed by X-ray data (see e.g. X-ray galaxy cluster surveys by Romer et al. (2000); Burenin et al. (2007)). Attempts were also made to detect the host galaxy. In the works (Nilsson et al., 2008; Stadnik & Romani, 2014) the PSF fitting was used giving an inconsistent result: $z \sim 0.3$ and 0.127 respectively.

It is important to note that in the BL Lac type objects survey made by *HST* (Urry et al., 2000) no evidence of the host galaxy was detected in S5 0716+714 despite the inactive state (14.18 mag in R), and a restriction on the redshift $z > 0.5$ was given.

Another specific feature of the S5 0716+714 object is its brightness. Based on the *HST* survey, the maximum brightness difference between the core and the host is 4 mag on average for the blazar sample. Yet for S5 0716+714 it is up 7 mag. The reason for such a tremendous brightness remains unclear.

The above-mentioned features of the object doubt on its extragalactic nature. The observed synchrotron radiation is typical for all accreting systems both active nuclei and compact galactic systems, for example, low-mass X-ray binaries. In fact, when the system is oriented so that the relativistic jet points toward the observer and such details are absent as any marks of the surroundings or spectral features it is hard or even impossible to unambiguously answer the question about its type. This fact makes us free to raise an issue if S5 0716+714 is an extragalactic object or it is just a system with a jet in the Galaxy, and we are looking for a critical test.

Within the frames of this work, we will consider the object S5 0716+714 belongs to the BL Lac type, although the conclusions we give about the jet radiation can be applied to sources of a different nature.

3. Polarimetric observations

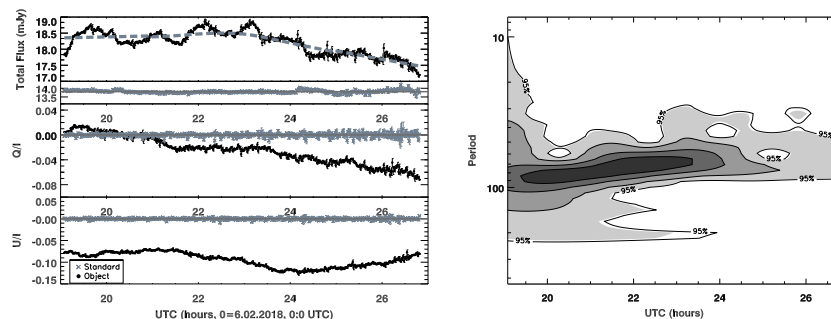


Figure 3. *Left:* the variations of the total flux and the Stokes parameters Q and U during the night. The observations started at 19:08 on 2018 February 2 (UTC). *Right:* The magnitude of the wavelet transform for the total flux.

In February 2018, we conducted 8-hour polarimetric monitoring of the S5 0716+714 object with a 1-minute temporal resolution at the BTA telescope with the SCORPIO-2 device. There are two important methodic features:

- (i) the observations of the object and the comparison star at a distance of $\sim 1'$ occur simultaneously. Since the star is photometrically constant and has zero polarization (Amirkhanyan, 2006), it is possible to minimize the transmission variations and the atmospheric depolarization;
- (ii) the double Wollaston prism (Geyer et al., 1996; Oliva, 1997) was used as a polarization analyzer to measure both linear polarization parameters – the Stokes parameters Q and U – simultaneously.

The obtained accuracy was about 0.005 mag for photometry and 0.1% for polarimetry.

As a result, an 8-hour data series was obtained (Fig. 3, left), where significant changes in both flux and polarization are observed. To study the total flux variability the long-period trend was approximated by the robust smoothing 2-degree polynomial function³ and subtracted. The wavelet analysis (Grossmann & Morlet, 1984) provided a period of 77 ± 10 min of rapid variations (Fig. 3, right).

To study the variability of the Q and U parameters, they were plotted on the QU -plane (Fig. 4). During the night the polarization vector changed its direction several times about every 1.5-3 hours, and the changes are perpendicular to the jet direction. Therefore, "loops" and "arcs" are observed on the QU -plane. Moreover, the period of the polarization vector direction and the total flux changes are similar. Indeed, if we assume that the observed motion of the polarization vector is caused by the plasma motion in the jet, then the polarization vector rotation will be due to the plasma changing direction and, consequently, a change in the Doppler amplification of its brightness for the observer.

4. Data comparison and model

Similar results were found for S5 0716+714 in earlier papers. Thus, the discovery that the polarization of an object changes on the QU -plane not stochastically but along the definite trajectories was made in the work by Impey et al. (2000). However, the time sets duration was not enough to investigate the way the polarization vector change.

Furthermore, in the case of the object BL Lacertae (ancestor of the class blazars), a similar picture was found. We have examined polarimetric data, obtained in the paper by Covino et al. (2015) as the angle and degree of polarization separately, on the QU -plane, where we also obtained the rotation of the polarization vector on the scales of several hours. Besides, for BL Lac, such a conclusion was made earlier in the almost forgotten work Moore et al. (1982): BL Lac showed the rotation of the polarization vector on the scales of hours in more than 7-day monitoring.

³The function was close to 6-degree polynomial one.

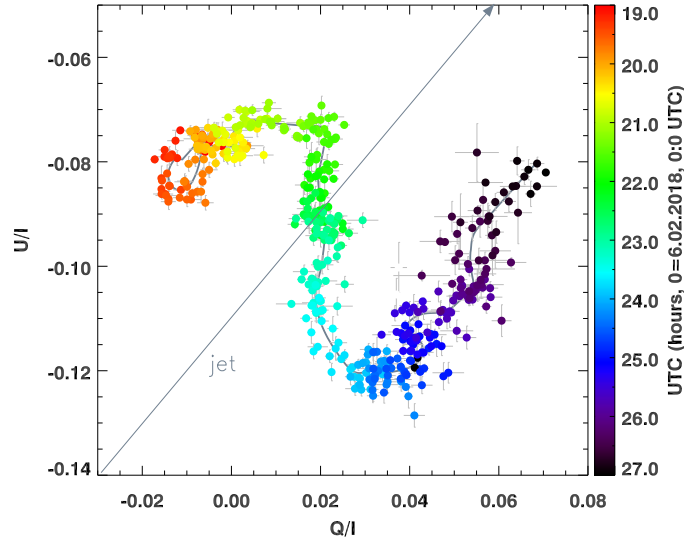


Figure 4. The variations of the normalized Stokes parameters Q and U during the night on the QU -diagram.

Also, the rotation of the polarization vector along the arcs was found in the radio band in observations of blazar CTA 102 (Li et al., 2018). It was assumed there that the plasma in the jet should rotate along helical trajectories. On the other hand, according to the commonly used model (Marscher et al., 2008), it is known that the optical synchrotron radiation in the AGN jet is formed at a distance of $\sim 10^{-3}$ pc from the central source, where the magnetic field has a helical structure.

Based on these principles, we constructed a geometric model of polarization change in the jet helical magnetic field (in more details - Shablovinskaya & Afanasiev, 2019). However, the numerical model of polarization change showed that it is impossible to describe the observed motion of the polarization vector by a stable configuration of the field. An important feature of our model was the field precession as an additional kinematic component. Then the rotation of the polarization vector on the QU -plane observed during the 8-hour monitoring is described by the motion of the plasma in a helical magnetic field precessing with a period of ~ 15 days. Moreover, the linear size of the region where the optical polarization is formed is associated with the time of its variability, that is, they are about 1.5 lt hours or 10 a.u. Comparison of the model with observational data is shown in Fig. 5, where 3σ confidence area of the smoothed polarization vector rotation is plotted light grey. The model fits the data good except the

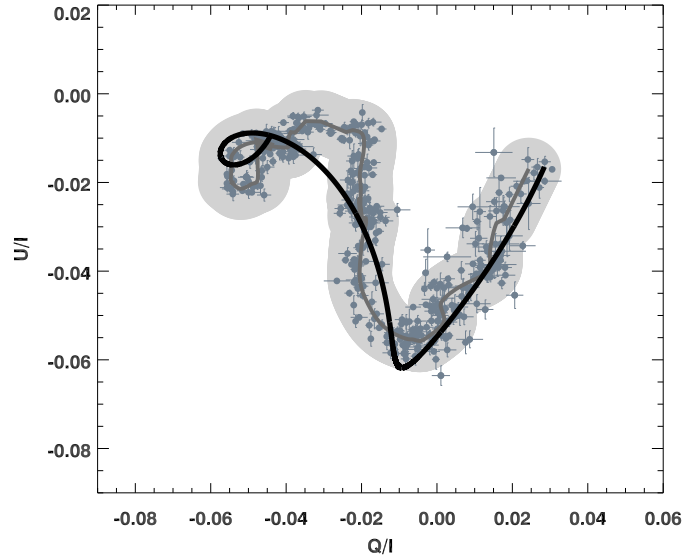


Figure 5. The model of linear polarization in the QU -plane in the case of jet precession. The observational data are plotted with grey dots with error bars. The 3σ confidence area is coloured light grey.

region between 21 and 22 hours. We attribute this divergence to the physical processes (radiation transfer and etc.) that we have not considered as our model describes the geometry of the plasma motion, and this neglect does not affect our quantitative results.

5. Conclusions

During the polarimetric monitoring of the S5 0716+714 object we obtained the following results.

- (i) We found the variability of the total ($\Delta=0.04$ mag) and polarized ($\Delta=7\%$) fluxes on a time-scale ~ 1.5 hours.
- (ii) We discovered the specific pattern of the polarization vector on the QU -plane – arches and loops.
- (iii) The estimation of the linear size of the field identifying with the emitting region $1.5 \cdot 10^{-5}$ pc, or 10 a.u. at $\sim 10^{-3}$ pc from the central BH.
- (iv) The polarization vector rotations mark the magnetic field precessing with the 15 days period.
- (v) The similar pattern was found in other papers and also for BL Lac.

Acknowledgements. We sincerely thank V. R. Amirkhanyan for valuable discussions and useful remarks. The results of observations were obtained with the 6-m BTA telescope of the Special Astrophysical Observatory Academy of Sciences, operating with financial support from the Ministry of Education and Science of Russian Federation.

References

- Afanasiev, V. L., Amirkhanyan, V. R., Moiseev, A. V., Uklein, R. I., & Perepelitsyn, A. E., SCORPIO-2 guiding and calibration system in the prime focus of the 6-m telescope. 2017, *Astrophysical Bulletin*, **72**, 458, DOI: 10.1134/S1990341317040095
- Amirkhanyan, V. R., BV RI observations of the radio source S5 0716+71. 2006, *Astronomy Reports*, **50**, 273, DOI: 10.1134/S1063772906040020
- Beers, T. C., Preston, G. W., Shectman, S. A., & Kage, J. A., Estimation of Stellar Metal Abundance. I. Calibration of the CA II K Index. 1990, *Astron. J.*, **100**, 849, DOI: 10.1086/115568
- Burenin, R. A., Vikhlinin, A., Hornstrup, A., et al., The 400 Square Degree ROSAT PSPC Galaxy Cluster Survey: Catalog and Statistical Calibration. 2007, *Astrophys. J., Suppl.*, **172**, 561, DOI: 10.1086/519457
- Covino, S., Baglio, M. C., Foschini, L., et al., Short timescale photometric and polarimetric behavior of two BL Lacertae type objects. 2015, *Astron. Astrophys.*, **578**, A68, DOI: 10.1051/0004-6361/201525674
- Geyer, E. H., Jockers, K., Kiselev, N. N., & Chernova, G. P., A novel quadruple beam imaging polarimeter and its application to Comet Tanaka-Machholz 1992 X. 1996, *Astrophys. Space Sci.*, **239**, 259, DOI: 10.1007/BF00645780
- Gorshkov, A. G., Ipatov, A. V., Konnikova, V. K., et al., Rapid variability of the radio flux density of the blazar J0721+7120 (S5 0716+714) in 2010. 2011, *Astronomy Reports*, **55**, 1096, DOI: 10.1134/S1063772911120043
- Gorshkov, A. G., Ipatov, A. V., Konnikova, V. K., et al., Variability of the radio flux density of the Blazar S5 0716+714 on time scales less than a month. 2011, *Astronomy Reports*, **55**, 97, DOI: 10.1134/S106377291102003X
- Grossmann, A. & Morlet, J., Decomposition of Hardy Functions into Square Integrable Wavelets of Constant Shape. 1984, *SIAM Journal on Mathematical Analysis*, **15**, 723, DOI: 10.1137/0515056
- Impey, C. D., Bychkov, V., Tapia, S., Gnedin, Y., & Pustilnik, S., Rapid Polarization Variability in the BL Lacertae Object S5 0716+714. 2000, *Astron. J.*, **119**, 1542, DOI: 10.1086/301286
- Larionov, V. M., Jorstad, S. G., Marscher, A. P., et al., The Outburst of the Blazar S5 0716+71 in 2011 October: Shock in a Helical Jet. 2013, *Astrophys. J.*, **768**, 40, DOI: 10.1088/0004-637X/768/1/40
- Li, X., Mohan, P., An, T., et al., Imaging and Variability Studies of CTA 102 during the 2016 January γ -ray Flare. 2018, *Astrophys. J.*, **854**, 17, DOI: 10.3847/1538-4357/aaa5ac

- Marscher, A. P., Jorstad, S. G., D’Arcangelo, F. D., et al., The inner jet of an active galactic nucleus as revealed by a radio-to- γ -ray outburst. 2008, *Nature*, **452**, 966, DOI: 10.1038/nature06895
- Marscher, A. P., Jorstad, S. G., Larionov, V. M., et al., Probing the Inner Jet of the Quasar PKS 1510-089 with Multi-Waveband Monitoring During Strong Gamma-Ray Activity. 2010, *Astrophys. J., Lett.*, **710**, L126, DOI: 10.1088/2041-8205/710/2/L126
- Moore, R. L., Angel, J. R. P., Duerr, R., et al., The noise of BL Lacertae. 1982, *Astrophys. J.*, **260**, 415, DOI: 10.1086/160266
- Nilsson, K., Pursimo, T., Sillanpää, A., Takalo, L. O., & Lindfors, E., Detection of the host galaxy of S5 0716+714. 2008, *Astron. Astrophys.*, **487**, L29, DOI: 10.1051/0004-6361:200810310
- Oliva, E., Wedged double Wollaston, a device for single shot polarimetric measurements. 1997, *Astron. Astrophys., Suppl.*, **123**, 589, DOI: 10.1051/aas:1997175
- Pryal, M., Falcone, A., & Stroh, M., A Search for Fast X-Ray Variability from Active Galactic Nuclei Using Swift. 2015, *Astrophys. J.*, **802**, 33, DOI: 10.1088/0004-637X/802/1/33
- Romer, A. K., Nichol, R. C., Holden, B. P., et al., The Bright SHARC Survey: The Cluster Catalog. 2000, *Astrophys. J., Suppl.*, **126**, 209, DOI: 10.1086/313302
- Shablovinskaya, E. S. & Afanasiev, V. L., The intraday variations of the polarization vector direction in radio source S5 0716+714. 2019, *Mon. Not. R. Astron. Soc.*, **482**, 4322, DOI: 10.1093/mnras/sty2943
- Stadnik, M. & Romani, R. W., Imaging Redshift Estimates for Fermi BL Lac Objects. 2014, *Astrophys. J.*, **784**, 151, DOI: 10.1088/0004-637X/784/2/151
- Stickel, M., Fried, J. W., & Kuehr, H., The complete sample of 1 Jy BL Lac objects. II. Observational data. 1993, *Astron. Astrophys., Suppl.*, **98**, 393
- Urry, C. M., Scarpa, R., O’Dowd, M., et al., The Hubble Space Telescope Survey of BL Lacertae Objects. II. Host Galaxies. 2000, *Astrophys. J.*, **532**, 816, DOI: 10.1086/308616

Narrow lines correlations in an SDSS sample of type 1 quasars

I. Jankov¹ and D. Ilić²

¹ *Department of Physics, Faculty of Sciences, University of Novi Sad,
Trg Dositeja Obradovica 3, 21000 Novi Sad, Serbia
(E-mail: isidora.jankov@gmail.com)*

² *Department of Astronomy, Faculty of Mathematics, University of Belgrade,
Studentski trg 16, 11000 Belgrade, Serbia (E-mail: dilic@matf.bg.ac.rs)*

Received: August 12, 2019; Accepted: September 2, 2019

Abstract. Investigation of quasar emission line properties and relationships between spectral parameters is important for understanding the physical mechanisms that originate inside different regions of the active galactic nuclei. In this paper, we investigate the optical spectral parameters of type 1 quasars taken from the Sloan Digital Sky Survey Data Release 7 Quasar Catalog (Shen et al., 2011). Spectral parameters, such as equivalent widths and full widths at half maximum of both narrow and broad lines are taken into account. We perform the analysis of correlation matrix and principal component analysis of our sample. We obtain that the narrow line Baldwin effect is significant enough and deserves further investigation. We provide the correlation coefficients and slope values for Baldwin effect in several narrow lines.

Key words: galaxies: active–multivariate analysis: principal component analysis

1. Introduction

Active galactic nuclei (AGN) or quasars are extremely bright objects with rapidly accreting supermassive black hole at their center. They exhibit a wide range of spectral characteristics, which can give us valuable information about the physical conditions in these extreme environments. Large surveys of quasars showed that there are some correlations between their spectral parameters. Most notable correlations are anti-correlation between [O III] and optical Fe II line strength, as well as the anti-correlation between full width at half maximum (FWHM) of broad H β line and ratio of optical Fe II line and broad H β line equivalent widths ($R_{\text{Fe II}}$). These correlations were investigated using principal component analysis (PCA) and represented in the parameter space known as Eigenvector 1 (see e.g. Sulentic et al., 2000b). In addition to the Eigenvector 1 correlations, the strength of some spectral lines appears to decrease with luminosity of the underlying continuum. This trend was first detected in C IV line and is known as the Baldwin effect (Baldwin, 1977).

There is distinction between the Baldwin effect for narrow and broad emission lines because these lines are associated with different regions of AGN with different geometrical and dynamical properties. In case of broad emission lines, it has been studied in great detail (see e.g. Dietrich et al., 2002; Shields, 2007; Bian et al., 2012), but its physical origin is still a matter of debate (see e.g. Rakić et al., 2017). One possible explanation for Baldwin effect that is associated with broad emission lines, is that the continuum shape is luminosity-dependent, in a way that more luminous objects have softer UV/X-ray spectra and this results in reduced ionization and photoelectric heating in the broad line region (BLR) gas (e.g. Boroson & Green, 1992; Korista et al., 1998). The narrow line Baldwin effect is still not entirely understood (Shields, 2007), and has been studied by several authors in the past. For example, Kovačević et al. (2010) did a careful spectral measurement of a sample of ~ 300 AGN and noticed a strong anti-correlation between the narrow $H\beta$ and [O III] lines with continuum luminosity, with the correlation coefficients of -0.36 and -0.43, respectively. The explanation of the effect could be due to different scale of narrow line region (NLR) compared to the BLR, or due to the extinction of the continuum luminosity by dust located between the BLR and NLR (e.g. Heard & Gaskell, 2016), or due to some other factors that also need to be taken into account (for more details see Boroson & Green, 1992; McIntosh et al., 1999; Croom et al., 2002; Dietrich et al., 2002; Netzer et al., 2004, 2006; Zhang et al., 2013; Shields, 2007).

The Sloan Digital Sky Survey (SDSS) quasars were previously investigated for the Baldwin effect in narrow lines by Zhang et al. (2013), who studied a large sample of broad-line (i.e. type 1), radio-quiet AGN taken from SDSS Data Release 4. They found that narrow lines show a similar Baldwin effect with slope value of approximately -0.2, which could be explained with the combination of continuum variation and a lognormal distribution of the luminosity. In addition they show that there is no evidence for a relationship between Baldwin effect slope and ionization potential of the narrow lines (Zhang et al., 2013). However, in their analysis they did not consider the host galaxy starlight contamination, which overestimates continuum luminosity, especially for low luminosity quasars (e.g. Bentz et al., 2006; Shen et al., 2011), which is resulting in steeper Baldwin effect slope.

In this paper, we report the results of our analysis based on the correlation matrices and PCA on a sample of type 1 quasars taken from the SDSS Data Release 7 (SDSS DR7) quasar catalog (Shen et al., 2011), with a special focus on the narrow line Baldwin effect, which was not investigated before in case of this catalog.

2. Data Reduction and Analysis

We use the measured spectral line properties of the SDSS quasars from Shen et al. (2011) catalog, and we select our sample putting the following constraints:

the signal to noise ratio $S/N > 10$ and redshift $z < 0.39$. The higher S/N ratio was set in order to have more precisely measured quantities (Shen et al., 2011) and redshift was limited so both $H\alpha$ and $H\beta$ spectral ranges are covered. This has resulted with a sample of 2,224 type 1 quasars. All objects in the sample have the following spectral parameters measured: the FWHM of broad $H\alpha$ and $H\beta$ lines; equivalent widths (EW) of narrow $H\alpha$, $H\beta$, $[O\ III] \lambda 5007 \text{ \AA}$, $[S\ II] \lambda\lambda 6718, 6732 \text{ \AA}$ and $[N\ II] \lambda 6585 \text{ \AA}$ lines; continuum luminosity at 5100 \AA (L_{5100}), R_{FeII} and luminosity ratio of $[O\ III]$ and narrow $H\beta$ line. We emphasize that the final number of objects is obtained so that there are no null values for all spectral parameters.

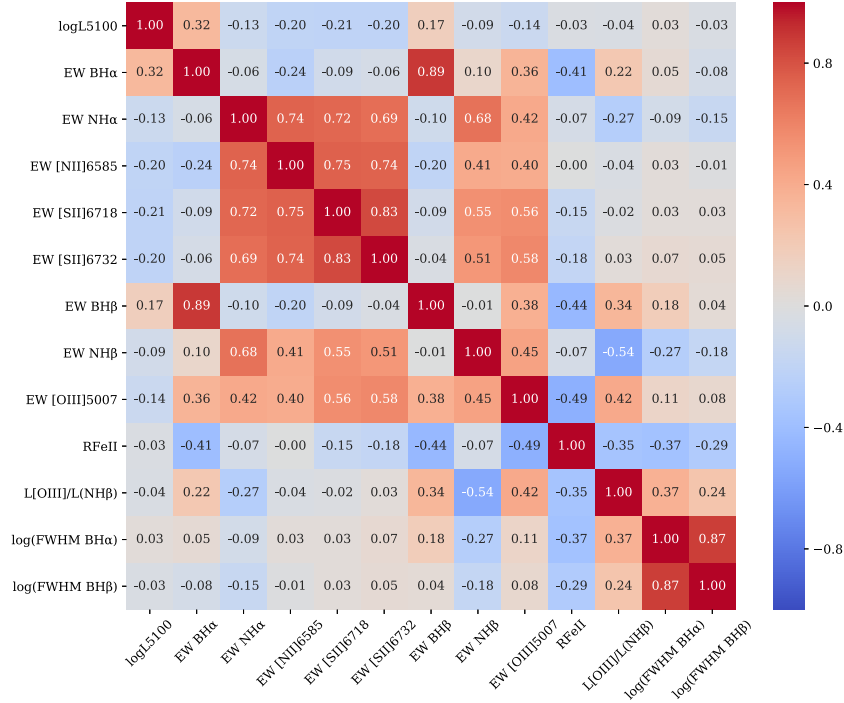


Figure 1. Correlation matrix of the entire sample. The color bar on the right represents the color associated with a correlation coefficient value. Red is associated with correlations and blue is associated with anti-correlations. The numbers represent Spearman correlation coefficients.

To analyze the correlations between quasar optical spectral parameters, we constructed a correlation matrix of our sample using Spearman correlation co-

efficients. The correlation matrix served as a useful tool for the selection of parameters later for PCA, but also for the analysis of correlation coefficients separately from the PCA results.

PCA is sometimes considered to be an unsupervised machine learning algorithm, because it can be used on unlabeled datasets, i.e. it can be applied even if we don't have a target variable that we want to predict (for more details on PCA see e.g. Boroson & Green, 1992; Francis & Wills, 1999; Grupe, 2004). In this work, the PCA was applied using the scikit-learn Python library where dimensionality reduction is conducted using Singular Value Decomposition of the data to project it to a lower dimensional space. In this way, only a few components are needed to completely describe total variance in our dataset and each component is representation of the dominant trends in the data.

To calculate the Baldwin effect slope, we performed linear regression for each narrow emission line in our sample. For further analysis of the Baldwin effect, the continuum luminosity was divided onto 9 bins of length 0.2 dex, starting from $\log L_{5100} = 43.75$ and ending with $\log L_{5100} = 45.55$. The last bin was excluded from the analysis because it contained only one object and it was not representative enough to be taken into account. Finally, to test the effect of the starlight contamination on the Baldwin effect, we corrected the continuum luminosity using the empirical fitting formula of the average host contamination given in Shen et al. (2011), see their Eq. 1, and obtained the pure continuum luminosity of the quasar. The luminosity at 5100 Å has been corrected up to $\log L_{5100} < 45.053$, since above this value no correction is needed.

3. Results and Discussion

Fig. 1 gives the correlation matrix of all spectral parameters in our sample of type 1 quasars. The most evident result is the presence of correlations between parameters which populate Eigenvector 1 (E1) parameter space, which was well established and investigated previously (for a review see Sulentic et al., 2000a): the anti-correlations between the [O III] equivalent width and the Fe II strength R_{FeII} ($r = -0.49$), and the FWHM of broad H β line and R_{FeII} ($r = -0.29$). The strongest correlations are found between the equivalent widths of broad H α and H β lines ($r = 0.89$) as well as between their narrow components ($r = 0.68$), which is an expected result.

However, the matrix clearly reveals the apparent anti-correlation between continuum luminosity at 5100 Å and equivalent widths of several narrow lines, which include: [O III] $\lambda 5007$ Å, [N II] $\lambda 6585$ Å, [S II] $\lambda\lambda 6718, 6732$ Å, narrow H α and narrow H β . This anti-correlation represents the Baldwin effect for narrow lines in AGN. While Baldwin effect for broad lines in AGN is well established, narrow line Baldwin effect is still under investigation and it may result from different physical mechanisms.

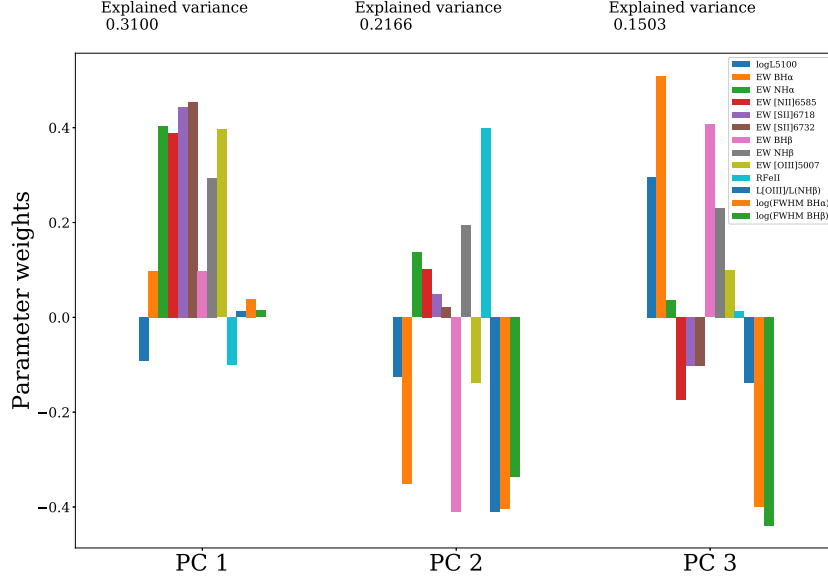


Figure 2. Results of the PCA, applied on the whole sample of 2,224 quasars, presented with bar charts. The three most significant principal components (eigenvectors) are labeled on the horizontal axis and on the vertical axis they are described in terms of the parameter weights. Each principal component is a linear combination of our 13 parameters, where the weights represent the components of the eigenvector. Note here that if the weight of at least two parameters is of the same sign, they are correlated and if the weights are of the opposite sign, they are anti-correlated. The parameters with the largest absolute value of the weights show the largest correlations/anti-correlations. The extent to which each component is describing the data sample is presented with the fraction of the total variance in the data sample and this number is indicated on top of each components bar chart. The width of the bars is arbitrary and serves only to illustrate the results.

The results of the PCA, which are presented in Fig. 2, are also indicating the presence of these anti-correlations. Furthermore, PCA suggests that this is the dominant trend in our data sample because the relationship between continuum luminosity and narrow line equivalent widths is represented with the first principal component (PC 1). PC 1 explains 31% of the variance in our data sample. The second principal component (PC 2) is dominated by the anti-correlation between R_{FeII} and FWHM of broad H β (Sulentic et al., 2000b) and anti-correlation between R_{FeII} and [O III] λ 5007 (discovered by Boroson & Green, 1992). One

Table 1. (β) - the log EW - log L_{5100} slope; (r) - correlation coefficient; (P_0) - p-value of the null hypothesis; (χ_{ion}) - line ionization energy in eV; (n_c) - logarithm of the line critical density in cm^{-3} .

Emission line	β	r	P_0	χ_{ion}	$\log n_c$
[O III] λ 5007	-0.20 \pm 0.03	-0.14	1.06E-10	35.11	5.80
[N II] λ 6585	-0.42 \pm 0.04	-0.20	7.28E-22	14.50	4.82
[S II] λ 6718	-0.38 \pm 0.03	-0.21	9.06E-24	10.36	2.30
[S II] λ 6732	-0.38 \pm 0.03	-0.20	2.48E-22	10.36	2.30
Narrow H α	-0.26 \pm 0.04	-0.13	1.32E-09	13.60	infinity
Narrow H β	-0.15 \pm 0.04	-0.09	1.94E-05	13.60	infinity

other correlation that is very prominent on PC2 is the correlation between the ratio of [O III] and H β luminosity $L([\text{O III}])/L(\text{H}\beta)$ and FWHM of broad H α which was recently discussed by Baron & Ménard (2019).

The summary of correlation coefficients with p-values of the null hypothesis for all narrow lines, along with the values of slopes obtained from linear regression is given in Table 1. These values are also presented on Fig. 3. Table 1 also lists the ionization energy and critical density in case of forbidden lines. The strongest Baldwin effect appears to be associated with [N II] and [S II] lines, however the p-values suggests that these anti-correlations are significant in all narrow lines. The Baldwin effect of the H α and H β lines shows the lowest correlation with the smallest significance.

We find that the slope for [O III] and H α are in agreement with the findings of Zhang et al. (2013), however, for [N II] and [S II] lines the slope is much steeper ($\beta = -0.41$ and $\beta = -0.38$, respectively) than previously reported by Zhang et al. (2013), who received the value of $\beta = -0.10$ and $\beta = -0.20$. This could be the result of the selection effect, since our sample contains low-redshift objects, and both radio loud and radio quiet objects.

In order to quickly test if the Baldwin effect slope for narrow lines depends on the ionization potential or critical density of the lines, which was noticed to be relevant in case of the broad line Baldwin effect (e.g., Espey & Andreadis, 1999; Dietrich et al., 2002), we plotted those dependencies in Fig. 4, and compared our results with the data obtained from previous studies of narrow line Baldwin effect (Zhang et al., 2013; Keremedjiev et al., 2009; Dietrich et al., 2002). The p-values of the null hypothesis of correlations in question indicate that there is no significant correlation between Baldwin effect slopes and ionization potential ($P_0 = 0.87$), and no correlation between Baldwin effect slopes and line critical densities ($P_0 = 0.17$) for narrow lines. This is in agreement with findings of Zhang et al. (2013).

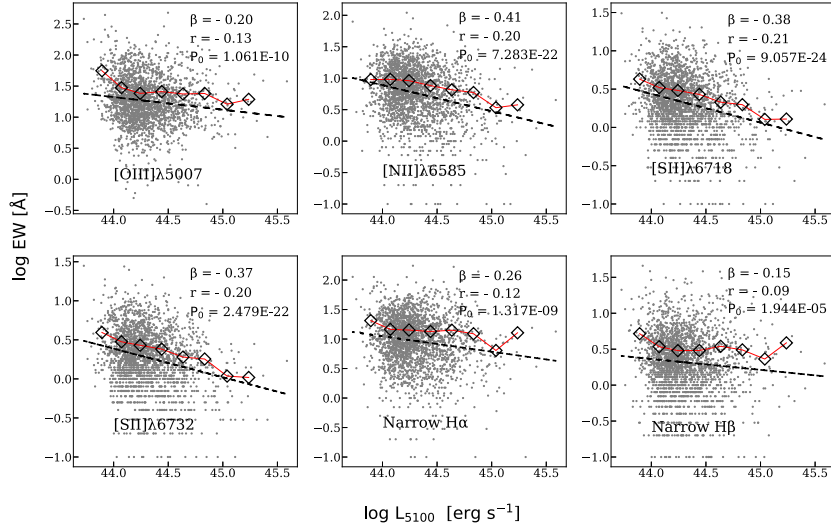


Figure 3. The Baldwin effect ($\log L_{5100} - \log EW$) in case of six narrow lines for all data in our sample (gray dots). Slopes (β) are obtained from linear regression (black dashed line) applied on the whole sample. Diamond markers (connected with red full line) represent points that resulted from continuum luminosity binning. The correlation coefficient (r) and the p-value of the null hypothesis (P_0) is also given on each plot.

Furthermore, we selected from our sample a sub-sample of 405 radio-loud quasars based on detection by the FIRST survey (both lobe- and core-dominated objects are included), and a sub-sample of 1,694 radio-quiet quasars, for which the FIRST survey reported no radio emission. Preliminary results of this analysis indicate that narrow line Baldwin effect slopes are steeper for radio-loud than for radio-quiet quasars. In the case of radio-loud quasars [O III] λ 5007 line has a slope (β) of -0.36, correlation coefficient (r) is -0.24 and p-value of the null hypothesis (P_0) is 7.48E-07. On the other hand, in the case of radio-quiet quasars the same line has $\beta = -0.20$, $r = -0.14$ and $P_0 = 2.06E-08$. For the [N II] λ 6583 line the results also differ substantially, such that we have for radio-loud sample $\beta = -0.56$, $r = -0.35$ and $P_0 = 4.85E-13$ and for radio-quiet $\beta = -0.41$, $r = -0.19$ and $P_0 = 3.02E-15$. The difference that appears in these two sub-samples may originate from the fact that in radio-loud quasars the narrow line emission may be enhanced by the jet-ISM interaction (Labiano, 2008) and also the continuum emission can be enhanced as the result of relativistic beaming. Further investigations are needed to confirm if this is the case.

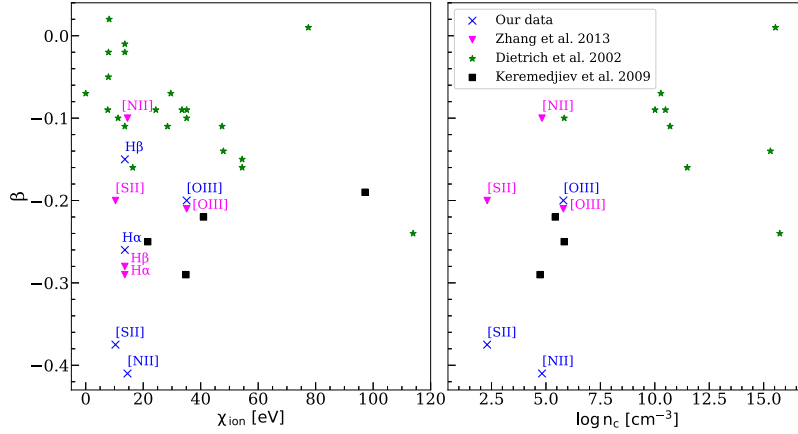


Figure 4. Dependence of Baldwin effect slope on ionization potential (χ_{ion}) and critical density (n_c) of lines in question. The blue crosses represent our data and data from Zhang et al. (2013); Dietrich et al. (2002); Keremedjiev et al. (2009) is represented with pink triangles, green stars and black squares, respectively.

Finally, we tested how would starlight contamination of the continuum luminosity affect the Baldwin effect in narrow lines. Using the continuum luminosity corrected for the host contribution, we still detect the Baldwin effect in all considered narrow lines, but with consistently smaller slope. The slope of the [O III] $\lambda 5007$ is decreased from -0.20 to -0.16 , for [N II] $\lambda 6585$ to -0.32 , for [S II] $\lambda 6718$ and [S II] $\lambda 6732$ to -0.29 , for $H\alpha$ to -0.20 , and for $H\beta$ to -0.12 . The correlation coefficients remain the same.

4. Conclusions

In this paper, we reported the results of the analysis performed on the sample of 2,224 low-redshift ($z < 0.39$) quasars from SDSS quasar catalog by Shen et al. (2011), for which we constructed the correlation matrix and applied the PCA on their optical spectral parameters. From our results, we came to the following conclusions: (i) we confirmed the Eigenvector 1 parameter space correlations for our data sample; ii) the Baldwin effect is present in all studied narrow lines, but with different slopes; iii) the slopes and correlation coefficients indicate that the Baldwin effect is the strongest for [N II] $\lambda 6585$ and [S II] $\lambda\lambda 6718, 6732$ lines, whereas in the case of the $H\alpha$ and $H\beta$ lines it shows the lowest correlation with the smallest significance; iv) ionization energies needed to create the ions and critical densities of the narrow lines have no correlation with Baldwin effect slopes for narrow lines; and v) the host galaxy contamination of the contin-

uum luminosity is steepening the Baldwin effect, but even with the corrected luminosity, the Baldwin effect remains in all narrow lines. Future investigation should be done to test if the continuum variation could be an explanation of the Baldwin effect as suggested by Zhang et al. (2013).

Acknowledgements. This work is supported by the project (176001) Astrophysical Spectroscopy of Extragalactic Objects of the Ministry of Education, Science and Technological Development of the Republic of Serbia.

References

- Baldwin, J. A., Luminosity Indicators in the Spectra of Quasi-Stellar Objects. 1977, *Astrophys. J.*, **214**, 679, DOI: 10.1086/155294
- Baron, D. & Ménard, B., Black hole mass estimation for active galactic nuclei from a new angle. 2019, *Mon. Not. R. Astron. Soc.*, **487**, 3404, DOI: 10.1093/mnras/stz1546
- Bentz, M. C., Peterson, B. M., Pogge, R. W., Vestergaard, M., & Onken, C. A., The Radius-Luminosity Relationship for Active Galactic Nuclei: The Effect of Host-Galaxy Starlight on Luminosity Measurements. 2006, *Astrophys. J.*, **644**, 133, DOI: 10.1086/503537
- Bian, W.-H., Fang, L.-L., Huang, K.-L., & Wang, J.-M., The C IV Baldwin effect in quasi-stellar objects from Seventh Data Release of the Sloan Digital Sky Survey. 2012, *Mon. Not. R. Astron. Soc.*, **427**, 2881, DOI: 10.1111/j.1365-2966.2012.22123.x
- Boroson, T. A. & Green, R. F., The Emission-Line Properties of Low-Redshift Quasi-stellar Objects. 1992, *Astrophys. J., Suppl.*, **80**, 109, DOI: 10.1086/191661
- Croom, S. M., Rhook, K., Corbett, E. A., et al., The correlation of line strength with luminosity and redshift from composite quasi-stellar object spectra. 2002, *Mon. Not. R. Astron. Soc.*, **337**, 275, DOI: 10.1046/j.1365-8711.2002.05910.x
- Dietrich, M., Hamann, F., Shields, J. C., et al., Continuum and Emission-Line Strength Relations for a Large Active Galactic Nuclei Sample. 2002, *Astrophys. J.*, **581**, 912, DOI: 10.1086/344410
- Espey, B. & Andreadis, S., Observational Evidence for an Ionization-Dependent Baldwin Effect. 1999, in *Astronomical Society of the Pacific Conference Series*, Vol. **162**, *Quasars and Cosmology*, ed. G. Ferland & J. Baldwin, 351
- Francis, P. J. & Wills, B. J., Introduction to Principal Components Analysis. 1999, in *Astronomical Society of the Pacific Conference Series*, Vol. **162**, *Quasars and Cosmology*, ed. G. Ferland & J. Baldwin, 363
- Grupe, D., A Complete Sample of Soft X-Ray-selected AGNs. II. Statistical Analysis. 2004, *Astron. J.*, **127**, 1799, DOI: 10.1086/382516
- Heard, C. Z. P. & Gaskell, C. M., The location of the dust causing internal reddening of active galactic nuclei. 2016, *Mon. Not. R. Astron. Soc.*, **461**, 4227, DOI: 10.1093/mnras/stw1616

- Keremedjiev, M., Hao, L., & Charmandaris, V., The Mid-Infrared Narrow-Line Baldwin Effect Revealed by Spitzer. 2009, *Astrophys. J.*, **690**, 1105, DOI: 10.1088/0004-637X/690/2/1105
- Korista, K., Baldwin, J., & Ferland, G., Quasars as Cosmological Probes: The Ionizing Continuum, Gas Metallicity, and the W_λ -L Relation. 1998, *Astrophys. J.*, **507**, 24, DOI: 10.1086/306321
- Kovačević, J., Popović, L. Č., & Dimitrijević, M. S., Analysis of Optical Fe II Emission in a Sample of Active Galactic Nucleus Spectra. 2010, *Astrophys. J., Suppl.*, **189**, 15, DOI: 10.1088/0067-0049/189/1/15
- Labiano, A., Tracing jet-ISM interaction in young AGN: correlations between [O III] λ 5007 Å and 5-GHz emission. 2008, *Astron. Astrophys.*, **488**, L59, DOI: 10.1051/0004-6361:200810399
- McIntosh, D. H., Rieke, M. J., Rix, H. W., Foltz, C. B., & Weymann, R. J., A Statistical Study of Rest-Frame Optical Emission Properties in Luminous Quasars at $2.0 < z < 2.5$. 1999, *Astrophys. J.*, **514**, 40, DOI: 10.1086/306936
- Netzer, H., Mainieri, V., Rosati, P., & Trakhtenbrot, B., The correlation of narrow line emission and X-ray luminosity in active galactic nuclei. 2006, *Astron. Astrophys.*, **453**, 525, DOI: 10.1051/0004-6361:20054203
- Netzer, H., Shemmer, O., Maiolino, R., et al., Near-Infrared Spectroscopy of High-Redshift Active Galactic Nuclei. II. Disappearing Narrow-Line Regions and the Role of Accretion. 2004, *Astrophys. J.*, **614**, 558, DOI: 10.1086/423608
- Rakić, N., La Mura, G., Ilić, D., et al., The intrinsic Baldwin effect in broad Balmer lines of six long-term monitored AGNs. 2017, *Astron. Astrophys.*, **603**, A49, DOI: 10.1051/0004-6361/201630085
- Shen, Y., Richards, G. T., Strauss, M. A., et al., A Catalog of Quasar Properties from Sloan Digital Sky Survey Data Release 7. 2011, *Astrophys. J., Suppl.*, **194**, 45, DOI: 10.1088/0067-0049/194/2/45
- Shields, J. C., Emission-Line versus Continuum Correlations in Active Galactic Nuclei. 2007, in *Astronomical Society of the Pacific Conference Series*, Vol. **373**, *The Central Engine of Active Galactic Nuclei*, ed. L. C. Ho & J. W. Wang, 355
- Sulentic, J. W., Marziani, P., & Dultzin-Hacyan, D., Phenomenology of Broad Emission Lines in Active Galactic Nuclei. 2000a, *Ann. Rev. Astron. Astrophys.*, **38**, 521, DOI: 10.1146/annurev.astro.38.1.521
- Sulentic, J. W., Zwitter, T., Marziani, P., & Dultzin-Hacyan, D., Eigenvector 1: An Optimal Correlation Space for Active Galactic Nuclei. 2000b, *Astrophys. J., Lett.*, **536**, L5, DOI: 10.1086/312717
- Zhang, K., Wang, T.-G., Gaskell, C. M., & Dong, X.-B., The Baldwin Effect in the Narrow Emission Lines of Active Galactic Nuclei. 2013, *Astrophys. J.*, **762**, 51, DOI: 10.1088/0004-637X/762/1/51

Preliminary Spectral Analysis of the NLS1 Galaxy WPVS48

M.A. Probst and W. Kollatschny

*Institut für Astrophysik, Göttingen University
Friedrich-Hund-Platz 1
37073 Göttingen
Germany*

Received: August 15, 2019; Accepted: October 3, 2019

Abstract. A spectroscopic campaign was carried out on the Narrow Line Seyfert 1 (NLS1) Galaxy WPVS 48 (2MASX J09594263-3112581) at the Southern African Large Telescope (SALT) from December 2013 to June 2014. The final objective is to perform reverberation mapping on the acquired light curves in order to calculate the Black Hole (BH) mass and to characterise the Broad Line Region (BLR) of the galaxy. To date, the spectra of one third of the observations are reduced and intercalibrated. Therefore, we will provide spectra displaying the spectral variability of WPVS 48 and preliminary light curves of the continuum at $\lambda 5100 \text{ \AA}$ as well as the emission lines $H\alpha$, $H\beta$ and $HeII \lambda 4686$.

Key words: galaxies: active – galaxies: NLS1 – galaxies: nuclei – galaxies: individual: WPVS 48

1. Introduction

Among Active Galactic Nuclei (AGN), the subclass of NLS1 galaxies is identified by the widths of their optical Balmer lines ($\text{FWHM} \leq 2000 \text{ km s}^{-1}$) as well as a relatively weak $[\text{OIII}]\lambda 5007$ emission in comparison to $H\beta$ (Osterbrock & Pogge, 1985). Little is known about whether the variability pattern of NLS1 differs from those of Broad Line Seyfert 1 Galaxies (BLS1). The method of reverberation mapping, which is used to study the internal structure of AGN as well as their BH mass, is very time consuming and was therefore applied to less than a handful of NLS1s (Pozo Nuñez et al., 2014; Pei et al., 2014; Huang et al., 2019, e.g.). We will use light curves comprising of data obtained in various nights over the course of several months in order to calculate the mass of the BH and to study the BLR structure.

WPVS 48 is a NLS1 galaxy at the distance of 161 Mpc with a redshift of $z = 0.0377$ (Véron-Cetty & Véron, 2010). Its host is a spiral galaxy and has a luminous nucleus ($V = 14.78$), as it was shown by Winkler (1997). Photometric reverberation mapping on WPVS 48 was realised by Pozo Nuñez et al. (2014) using data in the B, R, J and K bands. The retrieved light curves from all these

bands display high variability and the found sharp dust echo argues for a face-on torus. In the subsequent discussion, Pozo Nuñez et al. (2014) proposed two scenarios:

1. A flattened inner region of the torus coming close to the accretion disk in the equatorial plane.
2. The torus being geometrically and optically thick and only the facing rim being visible to the observer.

For our investigation, spectroscopic SALT data is used. In our analysis we consider the continuum at $\lambda 5100 \text{ \AA}$ and the emission lines $H\alpha$, $H\beta$ and $HeII \lambda 4686$. The analysis of the spectrum will be extended in the near future.

2. Observations and Data Reduction

We obtained 27 spectra with the SALT 10 m telescope over the time period from December 1, 2013 to June 29, 2014. The Robert Stobie Spectrograph with a PG0900 grating was used at all nights of observation. The observations are taken at the same airmass as a result of the construction of the telescope. The slit width was fixed to 2 arcsecs.

The optical spectra were taken in the wavelength regime from 4350 to 7375 \AA , this corresponds to the wavelengths of 4200 to 7100 \AA in the rest frame. Spectra taken at SALT are divided into 3 segments. Hence, two gaps are seen, the first being between 5363 and 5415 \AA (5162 and 5226 \AA in rest frame) and the second one between 6408 and 6454 \AA (6172 and 6227 \AA in rest frame).

Flat field, arc images (xenon and argon lamps) and spectra of standard stars were taken for the reduction and calibration process. The spectra were reduced in a homogeneous way (bias subtraction, cosmic ray correction, flat-field correction, 2D-wavelength calibration, night-sky subtraction and flux calibration) using IRAF reduction packages according to (Kollatschny et al., 2018). No further denoising was performed.

To date, the spectra of 9 out of 27 nights of observation were reduced, covering the time period from December 1, 2013 to February 7, 2014. LTT 4364 was used as the standard star for the flux calibration. Following data reduction and flux calibration, the spectra were intercalibrated according to the fluxes of the narrow [OIII] and [SII] lines, as these are considered to remain constant over timescales of years. Constant, narrow lines should vanish in the rms spectrum, when the spectra are intercalibrated. This was tested including further narrow [OI] and [NII] lines.

3. Results

We present three reduced and intercalibrated spectra of WPVS 48 in Fig. 1. The spectra were obtained on December 13, 2013, December 26, 2013 and February

7, 2014. These spectra show variability in both continuum and line fluxes. All wavelengths are given in the rest frame.

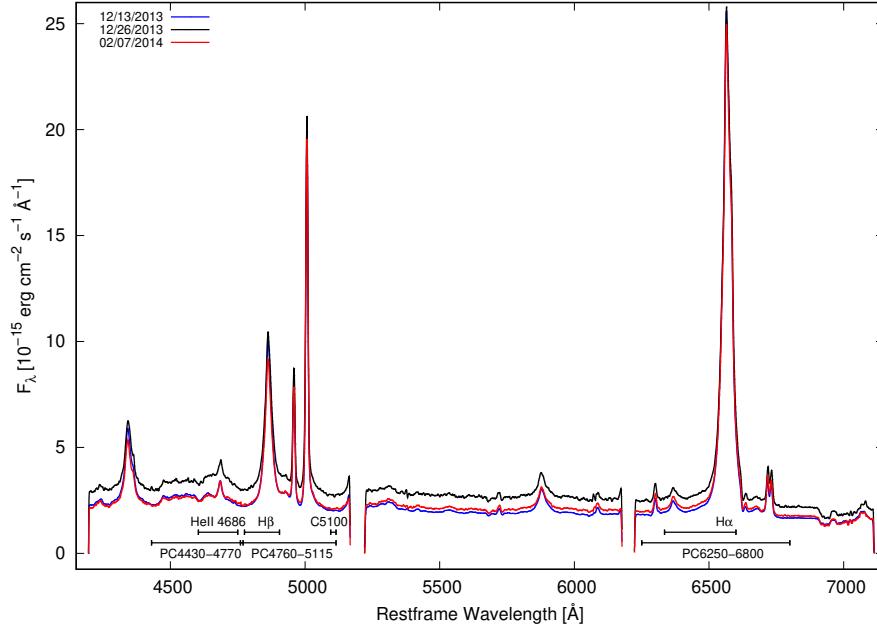


Figure 1. Optical spectra of WPVS 48 taken with the SALT telescope for our variability campaign on December 13, 2013, December 26, 2013 and February 7, 2014.

The mean flux density of the continuum is usually measured at the wavelength of 5100 \AA , as this wavelength regime is free of strong emission and absorption lines. Furthermore, three sections of the spectra were chosen to create pseudo-continua for each spectrum. These sections encompass the wavelengths between 6250 \AA and 6800 \AA , 4760 \AA and 5115 \AA as well as 4430 \AA and 4770 \AA respectively for H α , H β and HeII λ 4686. These pseudo-continua are also displayed in Fig. 1.

We integrated the flux densities of the two Balmer lines H α and H β as well as the helium line HeII λ 4686. The integration limits are given in Tab. 1 and included into Fig. 1. Before integration, the pseudo-continua were subtracted from the corresponding spectrum. The resulting, preliminary light curves are presented in Fig. 2. The preliminary light curves cover the period from December 1, 2013 till February 7, 2014. In this time, the variability in the emission lines are measured to be 19% for H α , 17% for H β and 66% for HeII λ 4686. For the continuum at λ 5100, we found a variability of 31%. For comparison, Pozo Nuñez

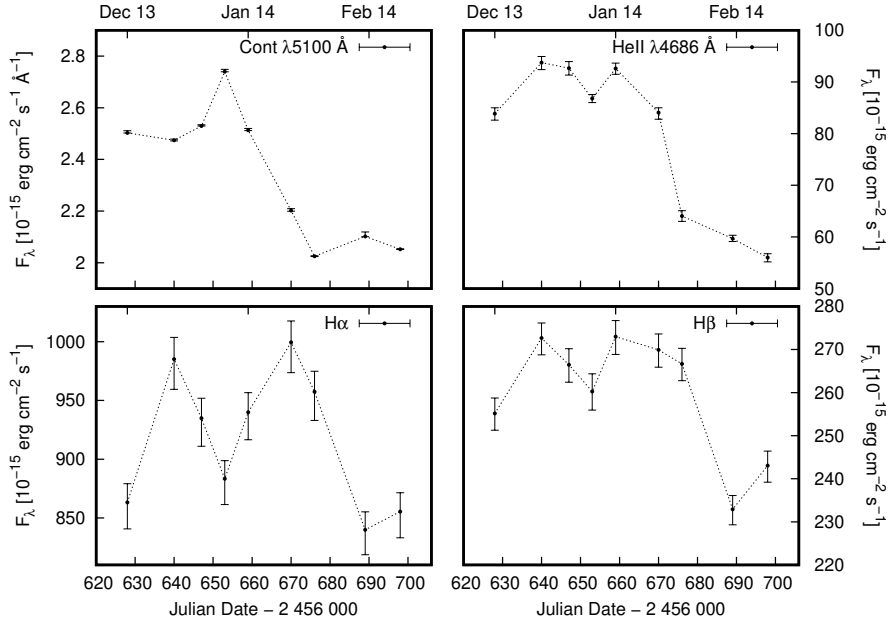


Figure 2. Preliminary light curves of the continuum flux density at 5100 Å (in units of $10^{-15} \text{ erg cm}^{-1} \text{ \AA}^{-1}$) as well as integrated line fluxes of H α , H β and HeI $\lambda 5876$ (in units of $10^{-15} \text{ erg cm}^{-1}$) for our variability campaign between December 2013 and February 2014.

Table 1. Rest frame continuum boundaries and integration limits.

Cont./Line (1)	Wavelength range (2)	Pseudo-continuum (3)
Cont. 5100	5095 Å - 5115 Å	
H α	6335 Å - 6600 Å	6250 Å - 6800 Å
H β	4775 Å - 4905 Å	4760 Å - 5115 Å
HeII $\lambda 4686$	4604 Å - 4750 Å	4430 Å - 4770 Å

et al. (2014) found a variability of roughly 13% in both the B and R band, which encompass the H β and H α line, respectively.

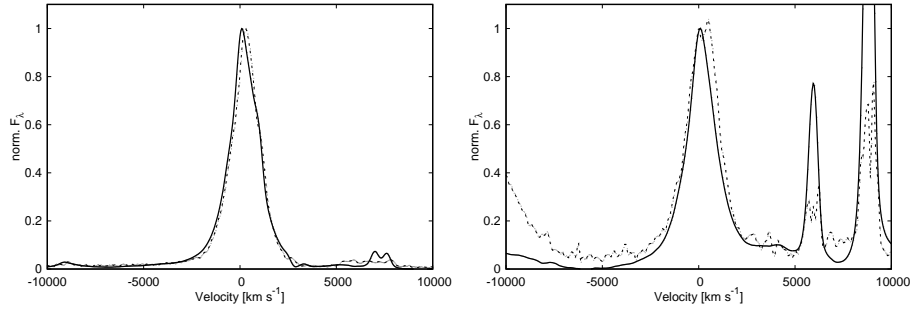


Figure 3. Normalised mean (solid) and rms (dashed) line profile of H α (a) and H β (b) in velocity space.

The mean line profiles of H α and H β in the velocity space are presented in Fig 3. Both the mean and rms profiles are determined in reference to the available data of the 9 nights of observation and after the pseudo-continua were subtracted. The mean profiles show both narrow and broad components. The FWHM was calculated for both lines based on the rms spectrum. As a result, we obtained $1890 \pm 60 \text{ km s}^{-1}$ for H β and $1660 \pm 50 \text{ km s}^{-1}$ for H α .

4. Summary and Outlook

The spectra and light curves reveal flux variations of WPVS 48 in the continuum as well as in Balmer and He emission lines. The number of reduced nights is yet not sufficient to perform a robust cross correlation and hence, neither the mass of the BH nor any details about the BLR are presented. Agreeing with the results of Pozo Nuñez et al. (2014), we observed high variability in the emission lines. We also confirm that the FWHM of H β corresponds to a galaxy of type NLS1.

Acknowledgements. This work has been supported by DFG grant Ko 857/33-1. We also want to thank Martin W. Ochmann for his helpful advice.

References

- Huang, Y.-K., Hu, C., Zhao, Y.-L., et al., Reverberation Mapping of the Narrow-line Seyfert 1 Galaxy I Zwicky 1: Black Hole Mass. 2019, *Astron. J.*, **876**, 14
- Kollatschny, W., Ochmann, M., Zetzl, M., et al., Broad-line region structure and line profile variations in the changing look AGN HE 1136-2304. 2018, *Astron. Astrophys.*, **619**, A168
- Osterbrock, D. & Pogge, R., The Spectra of Narrow-Line Seyfert 1 Galaxies. 1985, *Astrophys. J.*, **297**, 166

- Pei, L., Barth, A. J., Aldering, G. S., et al., Reverberation Mapping of The Keplerfield AGN KA1858+4850. 2014, *Astron. J.*, **795**, 15
- Pozo Nuñez, F., Haas, M., Chini, R., et al., Dust reverberation-mapping of the Seyfert 1 galaxy WPVS48. 2014, *Astron. Astrophys.*, **561**, L8
- Véron-Cetty, M.-P. & Véron, P., A catalogue of quasars and active nuclei: 13th edition. 2010, *Astron. Astrophys.*, **518**, A10
- Winkler, H., The extinction, flux distribution and luminosity of Seyfert 1 nuclei derived from $UBV(RI)_C$ aperture photometry. 1997, *Mon. Not. R. Astron. Soc.*, **292**, 273

PRÁCE ASTRONOMICKÉHO OBSERVATÓRIA
NA SKALNATOM PLESE
L, číslo 1

Zostavovatelia:	Dr. Dragana Ilić Dr. Anđelka Kovačević Dr. Luka Č. Popović Dr. Evgeny Stambulchik
Výkonný redaktor:	RNDr. Richard Komžík, CSc.
Vedecký redaktor:	RNDr. Augustín Skopal, DrSc.
Vydal:	Astronomický ústav SAV, Tatranská Lomnica
IČO vydavateľa:	00 166 529
Periodicita:	3-krát ročne
ISSN (on-line verzia):	1336-0337
CODEN:	CAOPF8
Rok vydania:	2020
Počet strán:	366

Contributions of the Astronomical Observatory Skalnaté Pleso are processed using
L^AT_EX 2_ε CAOSP DocumentClass file 3.07 ver. 2019.